



Deciphering the aging dynamics using microfluidics and deep-learning

Théo Aspert

► To cite this version:

Théo Aspert. Deciphering the aging dynamics using microfluidics and deep-learning. Human health and pathology. Université de Strasbourg, 2021. English. NNT : 2021STRAJ078 . tel-03967029

HAL Id: tel-03967029

<https://theses.hal.science/tel-03967029>

Submitted on 1 Feb 2023

HAL is a multi-disciplinary open access archive for the deposit and dissemination of scientific research documents, whether they are published or not. The documents may come from teaching and research institutions in France or abroad, or from public or private research centers.

L'archive ouverte pluridisciplinaire **HAL**, est destinée au dépôt et à la diffusion de documents scientifiques de niveau recherche, publiés ou non, émanant des établissements d'enseignement et de recherche français ou étrangers, des laboratoires publics ou privés.

ÉCOLE DOCTORALE DES SCIENCES DE LA VIE ET DE LA SANTÉ



CNRS UMR 7104 – Inserm U 964

Thèse présentée par Théo ASPERT

Soutenue le 17 décembre 2021

Pour obtenir le grade de : **Docteur de l'université de Strasbourg**

Discipline/ Spécialité : **Sciences de la vie/ Biophysique**

**Deciphering the aging dynamics using
microfluidics and deep-learning**

Dr. Gilles CHARVIN

Université de Strasbourg – CNRS - INSERM

DIRECTEUR DE THESE

Pr. Liesbeth VEENHOFF

European Research Institute for the Biology of Ageing

RAPPORTRICE EXTERNE

Dr. Damien COUDREUSE

IGDR - CNRS

RAPPORTEUR EXTERNE

Pr. Michael RYCKELYNCK

Université de Strasbourg - IBMC

EXAMINATEUR INTERNE

To life
&
A mon père

Remerciements

First of all, I would like to thank the jury members, Liesbeth Veenhoff, Damien Coudreuse, Mickael Ryckelynck and Sahand Rahi for accepting to evaluate my work, and especially to Liesbeth and Damien for reviewing the manuscript.

Aussi et bien sûr, j'aimerais remercier Gilles Charvin pour m'avoir accueilli dans son labo. Presque 5 ans et un terrain de jeu quasiment illimité : microscopes, microfluidique et gadgets à volonté, le rêve ! C'était aussi un plaisir de plonger dans le monde du deep-learning, de développer et d'interagir ensemble quotidiennement. On a pas mal fait chauffer les serveurs de Teams et RocketChat !

Merci aussi au reste de l'équipe, Audrey, Sandrine et Sophie pour la bonne humeur, les chit-chats et l'interaction scientifique.

Merci à l'équipe Mendoza pour les discussions scientifiques, et notamment à Mercè : it was « *super cool* » to crush yeast cells with you late in the lab!

Merci à Erwan, Didier et Serge pour leur aide technique en microscopie et en mécanique.

Merci aux voisins d'en face et squatteurs de machine à café : Hélène, Sara et Elena, et le voisin plus éloigné, Simon.

Basile, sans toi cette thèse aurait eu une saveur bien différente, alors merci pour les interactions et collaborations scientifiques et humaines. *"Je sais que je suis venu officiellement pour tenter de retirer l'épée, mais j'ai trouvé ici quelque chose de beaucoup plus précieux, j'ai trouvé la sérénité affective."* ;)

And thanks to you for reading this thesis and taking an interest in my work! I hope you're not here only for the acknowledgement page :)

Table of content

PREAMBLE	1
CHAPTER I: DECIPHERING THE AGING DYNAMICS AT THE SINGLE-CELL LEVEL	2
INTRODUCTION I: THE BIOLOGY OF AGING AND THE SPECIFIC CASE OF <i>SACCHAROMYCES CEREVISIAE</i>	2
1. GENERAL AGING CONCEPTS	2
1.1. Definition of aging	4
1.2. Evolutionary theories of aging	7
1.3. Molecular models of aging	10
1.4. Universality of aging.....	15
1.5. Laboratory models	16
2. AGING IN BUDDING YEAST: DIFFERENT MODELS	25
INTRODUCTION II: METHODS TO STUDY REPLICATIVE AGING IN YEAST	62
1. MICRODISSECTION.....	62
2. POPULATIONAL ENRICHMENT OF OLD CELLS	64
2.1. Density gradient and Elutriation	64
2.2. Mother Enrichment Program.....	65
2.3. Cell wall labeling	66
2.4. Conclusions on traditional assays	67
3. CAPTURING SINGLE-CELL DYNAMICS.....	68
SUMMARY OF THE INTRODUCTION AND OBJECTIVES.....	82
4. OBJECTIVES.....	88
RESULTS.....	89
5. RESULTS I: SETTING UP A PLATFORM FOR AUTOMATED AND HIGH-THROUGHPUT TRACKING OF REPLICATIVE LIFESPAN	89
1.1. Introduction.....	89
1.2. Results	89
1.3. Perspectives	128
6. RESULTS II: MEASURING THE PROBABILITY OF ERC EXCISION WITH AGE.....	130
1.1. Introduction.....	130
1.2. Results	130
1.3. Perspectives	136

GENERAL DISCUSSION.....	140
1. The ERCs pathway of aging: A countdown to death started by a stochastic trigger.....	141
2. Relevance of the ERC/rDNA pathway in other organisms.....	145
3. Other pathways of aging.....	145
4. A general framework to classify hallmarks of aging into pathways	147
5. Observing the daughters to understand aging factors	150
REFERENCES CHAPTER I	153
CHAPTER 2: MONITORING SINGLE-CELL DYNAMICS OF ENTRY INTO QUIESCENCE DURING AN UNPERTURBED LIFE-CYCLE	181
INTRODUCTION	181
1. GENERAL CONCEPTS OF QUIESCENCE	181
2. THE MOLECULAR PATHWAYS OF ENTRY INTO QUIESCENCE.....	181
3. STRUCTURAL REARRANGEMENTS IN QUIESCENCE	182
3.1. Cytoskeleton	183
3.2. Mitochondrial network and respiration.....	184
3.3. Proteasome	184
3.4. Phase transition of the cytoplasm	184
4. QUIESCENCE AND LIFE-CYCLE OF BUDDING YEAST	186
4.1. The life-cycle of budding yeast.....	186
4.2. Quiescence: one unique cellular state?	186
4.3. Assessing quiescence.....	188
SUMMARY AND MOTIVATIONS.....	189
RESULTS.....	190
DISCUSSION	215
REFERENCES CHAPTER II	217
APPENDIXES.....	221
APPENDIX 1: MICROFLUIDIC ENRICHMENT OF OLD CELLS AND SORTING ACCORDING TO THEIR SENESCENT STATE	221
APPENDIX 2: VERSATILE HEATING SYSTEM FOR LONG-TERM MICROFLUIDIC CULTURE.....	227
APPENDIX 3: (COLLABORATION) SPECIALIZATION OF CHROMATIN-BOUND NUCLEAR PORE COMPLEXES PROMOTES YEAST AGING	230
APPENDIX 4: DISTINCT MECHANISMS UNDERLIE H₂O₂ SENSING IN C. ELEGANS HEAD AND TAIL	257

APPENDIX 5: (COLLABORATION) SELF-LEARNING MICROFLUIDIC PLATFORM FOR SINGLE-CELL IMAGING AND CLASSIFICATION IN FLOW	302
PUBLICATIONS (AS OF DECEMBER 2021)	324
RESUME LONG	325
CHAPITRE 1: DECHIFFRER LES DYNAMIQUES DU VIEILLISSEMENT A L'AIDE DE LA MICROFLUIDIQUE ET DE L'APPRENTISSAGE PROFOND.....	325
Introduction générale	325
Partie méthodologique	325
Partie biologique.....	327
CHAPITRE 2 : SUIVI DE LA DYNAMIQUE DE L'ENTREE EN QUIESCENCE A L'ECHELLE DE LA CELLULE UNIQUE	329
Introduction.....	329
Résultats	329
ABSTRACT	331
RESUME COURT	331

Abbreviations

ANN: Artificial Neural Network

ARS: Autonomously Replicative Sequence

DNA: Deoxyribonucleic acid

DSB: Double Strand Break

E. coli: *Escherichia coli*

ERC: Extrachromosomal rDNA Circle

GFP: Green Fluorescent Protein

ISC: Iron-Sulfur Cluster

LSTM: Long Short Term Memory network

NPC: Nuclear Pore Complex

PDMS: Polydimethylsiloxane

R- cells: Cells unable to respire, as opposed to R+ cells.

rDNA: ribosomal Deoxyribonucleic Acid

RLS: Replicative Lifespan

RNN: Recurrent Neural Network

ROS: Reactive oxygen species

rRNA: ribosomal Ribonucleic Acid

S. cerevisiae: *Saccharomyces cerevisiae*

S. pombe: *Schizosaccharomyces pombe*

SEP: Senescence Entry Point

TOR: Target Of Rapamycin

USCR: Unequal Sister Chromatid Recombination

WT: Wild type

Preamble

If I had two words to summarize my thesis, I would use *single-cell* and *homeostasis*.

During the 4 years of my Ph.D., I focused on understanding how cells maintain and lose their homeostasis, mainly in two different contexts: replicative aging and quiescence. Since these phenomena are highly heterogeneous in a population and very dynamic at the cellular level, longitudinal single-cell approaches are required to accurately capture them. For that, I developed and used several tools based on microfluidics, timelapse microscopy and image analysis. Thus, this Ph.D. thesis has a strong methodological content but also aims at addressing biological questions.

This manuscript is split into two independent chapters. Chapter I is relative to replicative aging and is the core of the thesis. Chapter II is a side-project about quiescence, which has been done in close collaboration with Basile Jacquelin, another Ph.D. student from the lab.

The appendix part contains a preliminary side-project, the development of a small tool and three published collaborations.

Chapter I: Deciphering the aging dynamics at the single-cell level

A substantial part of my thesis consisted in developing methodological tools to address questions relative to aging. Hence, I decided to introduce the biology and the methodology in two different introductions, I and II.

Then come a short summary of the two introductions and the enunciation of the objectives of this part of the Ph.D.

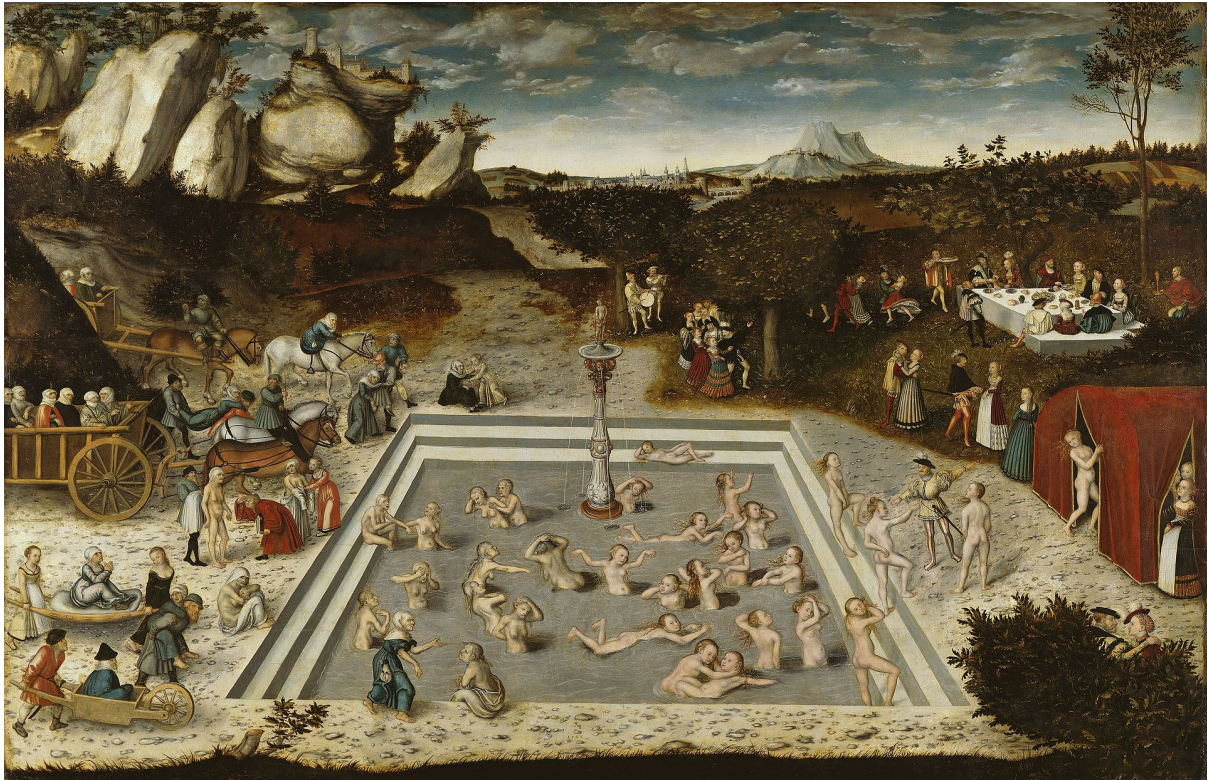
The Results section is also split into two parts relative to the methodology and to the biological question, with their own Perspectives paragraphs.

The chapter ends with a General discussion of the project on its globality.

Introduction I: The biology of aging and the specific case of *Saccharomyces cerevisiae*

1. General aging concepts

Aging is one of the most familiar biological concepts, and anyone can observe its effects on older individuals and on themselves. At first sight, we could analogize it as the wearing of a machine due to its daily use. Nevertheless, understanding which gears are failing is challenging due to the complexity of the living machines. Indeed, most of the biological processes affect or are affected by aging. Consequently, a plethora of studies has been describing potential cellular or molecular causes over the years, which Medvedev tried to rationalize in the late 20th century [1]. Even though modern approaches and technologies now allow a more systematic and comprehensive analysis of this phenomenon, it remains a complex and poorly understood phenomenon.



The Fountain of Youth, 1546 by Lucas Cranach.

Beyond the fundamental scientific question, aging is also an increasingly important concern for public health and demographic reasons. Indeed, it is the main risk (cancer, cardiovascular diseases, age-related diseases like Alzheimer or Parkinson, etc) and hazard (COVID19 [2], etc) factor of many diseases, in addition to be the main driver of a general state of frailty. This is problematic knowing that the population's average age keeps increasing every year (Figure 2), especially in wealthy countries. At the individual level, aging has been a major source of apprehension for at least 2500 years, with Herodotus reporting the existence of a mythological fountain of youth. Hence, understanding the origins and the molecular processes involved in this phenomenon is as interesting as it is important.

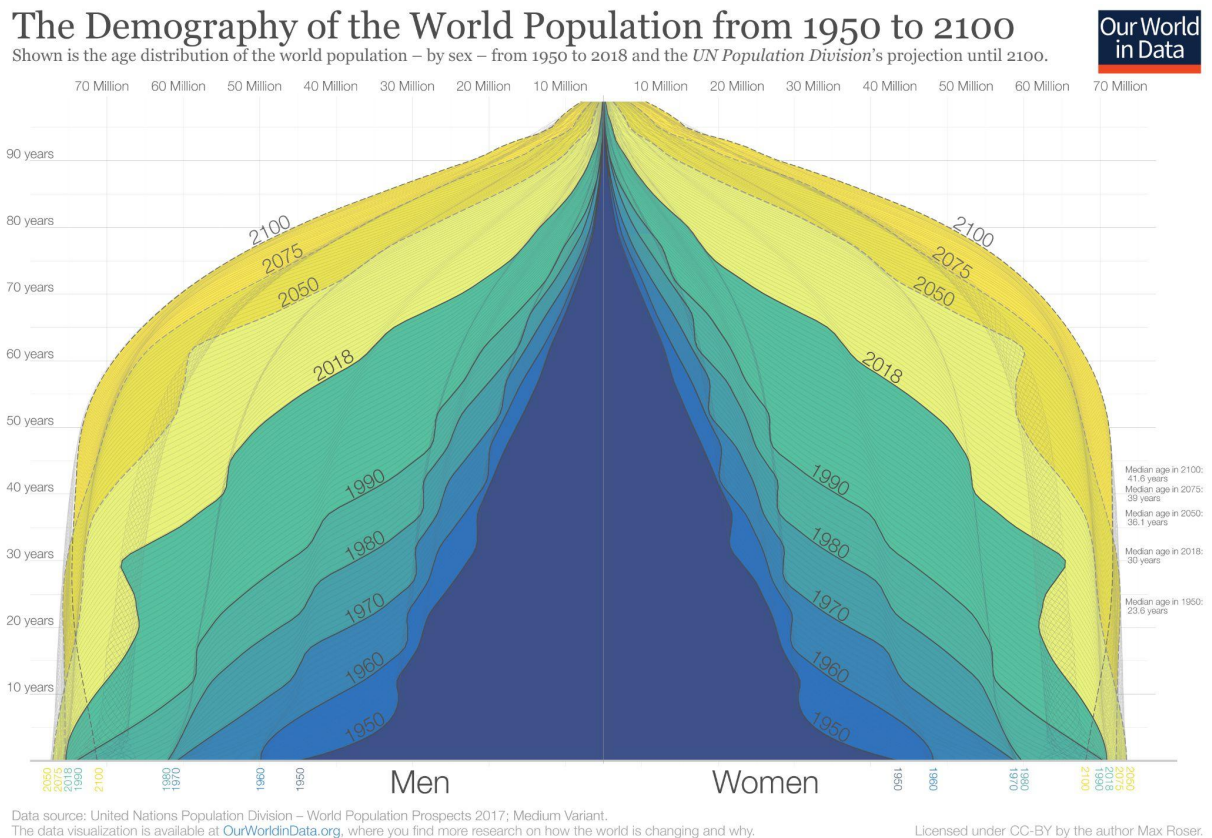


Figure 2: The demography of the world population from 1950 (blue shade) to 2100 (dark yellow shade) (From [3])

In this introduction, we will first describe the concept of aging, the different theories proposed so far and the classical models to study it. Then, a specific focus will be made on the unicellular *Saccharomyces cerevisiae* and the various suggested aging pathways.

1.1. Definition of aging

Aging can be defined as “a persistent decline in the age-specific fitness components of an organism due to internal physiological deterioration” [4] or by an increase in the mortality rate with age. It is possible to measure parts of the biological decline with specific readouts, such as the world record, for human aging (Figure 3). However, such a definition of aging makes a generalization across species difficult and requires different assays for each model organism.

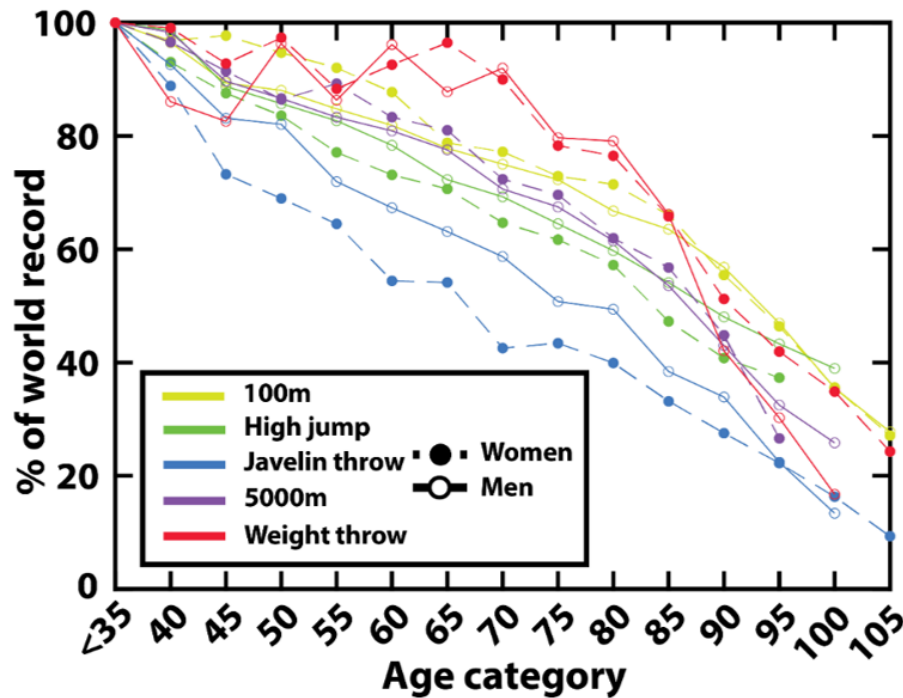


Figure 3: World records of different athletic sports from different age categories, normalized to the world record in the <35 years old category. (Data from [5])

The increase of the mortality rate, which is in fact a consequence of the first definition, is a more general readout and can easily be derived from the survival curve of a population. Indeed, be n the number of individuals still alive at time t from a given population of N individuals at $t = 0$. The survival rate at a given time is $s(t) = \frac{n(t)}{N(t)}$ and the hazard rate (or mortality) is $h(t) = -\frac{s'(t)}{s(t)}$, with s' the derivative of s relative to t (Figure 4).

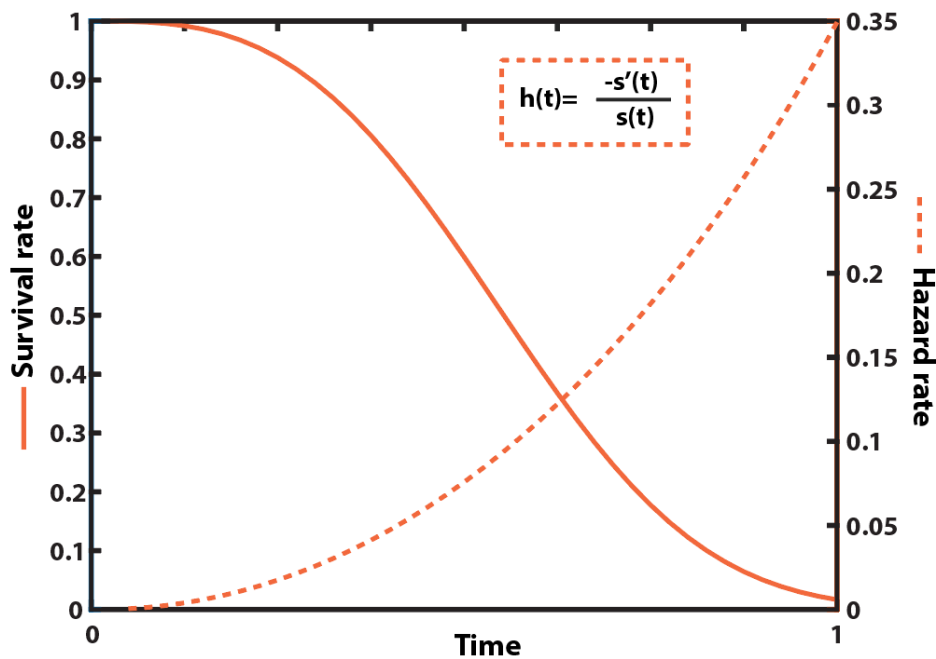


Figure 4: Theoretical survival and hazard rate

Gompertz law

Taking this definition, we also observe that aging in humans exists and that the hazard rate increases exponentially with age (Figure 5) after the infantile period has passed.

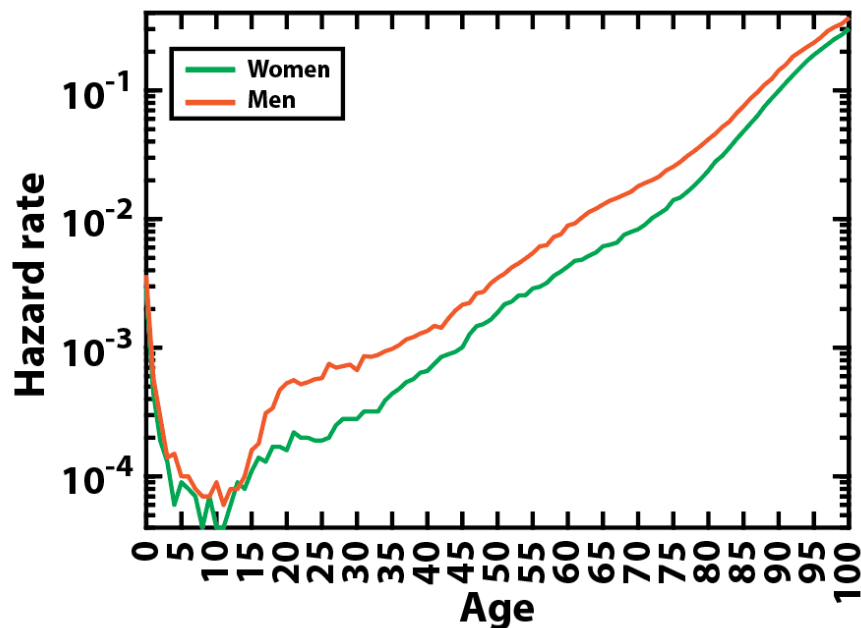


Figure 5: Hazard rate in the French population in 2019 (Data from INSEE).

Benjamin Gompertz first described this in 1825 [6], where he showed that the mortality $h(t)$ was equal to $\alpha * \exp(\beta * t)$, with α being the basal death rate and β describing how fast the rate of dying increases with age.

This law also describes the mortality of many mammals such as mice, rats, horses [7], but also of worms [8], fruit flies [9] or budding yeast [10], and many other animals [11]. Later on, William Makeham proposed a refinement of this law by adding a constant term to the hazard rate $h(t) = \alpha * \exp(\beta * t) + \lambda$ to take into account age-independent death (λ is also called extrinsic mortality). However, this term is often negligible under a protected environment such as modern society or lab conditions.

Therefore, following a population can help us understand if individuals from a species are submitted to aging or not. However, it does not indicate which mechanisms are at stake nor how aging has arisen in the living.

1.2. Evolutionary theories of aging

Other approaches have emerged to try to understand aging, including evolutive theories. Georges Williams expressed in 1957 that "It is indeed remarkable that after a seemingly miraculous feat of morphogenesis, a complex metazoan should be unable to perform the much simpler task of merely maintaining what is already formed." [12]

Thus, despite its apparent drawbacks regarding Darwinian fitness, evolution has selected (or at least not discarded) aging, and a few theories have emerged to explain this selection.

1.2.1. Programmed aging

The first essay trying to explain the evolutionary origin of aging arose in the late 19th century from August Weismann with his theory of programmed aging "*When one or more individuals have provided a sufficient number of successors they, as consumers of nourishment to a constantly increasing degree, are an injury to those successors [...] natural selection, therefore, will weed them out.*" [13].

In other words, aging would be a mechanism to remove older, less fertile and less fit individuals from the species to benefit the younger and healthier ones. Some kind of programmed aging indeed exists in very specific contexts. For example, telomere shortening in an *in vitro* culture of mammalian somatic cells leads to the death of cells after a given number of divisions [14-16] (discussed later).

Nonetheless, the programmed aging theory lacks generality and was criticized for its many flaws. For example, the base of this reasoning is circular since aging is supposed to clear worn-out individuals, but is also causing this deterioration. Besides, if it is programmed, a set of genes controlling it must have evolved specifically for this function. Hence, it should be possible to stop aging by modifying these genes. However, despite having identified hundreds of longevity genes in different organisms, such as in *C. elegans* [17, 18], no combination of mutations has been able to stop it. If aging is programmed, then evolution has made this program very robust.

1.2.2. The selection shadow & the theory of mutation accumulation

Another evolutionary approach is based on the idea that natural selection declines progressively past a given age and that aging has arisen from the negligence of evolution. Indeed, different essays from the first part of the 20th century [19,20] used this idea to explain the high prevalence of the allele causing Huntington disease, which expresses after the age of 30, at which most individuals would have died pre-modern societies. Building on that,

Peter Medawar proposed in 1952 a more general model on how aging could have evolved in the wild.

It is based on the idea that most animals in the wild will die shortly after reaching sexual maturity and that deleterious phenotypes that are expressed later in life would not be affected by selection (in other words, be in the shadow of selection) (Figure 6).

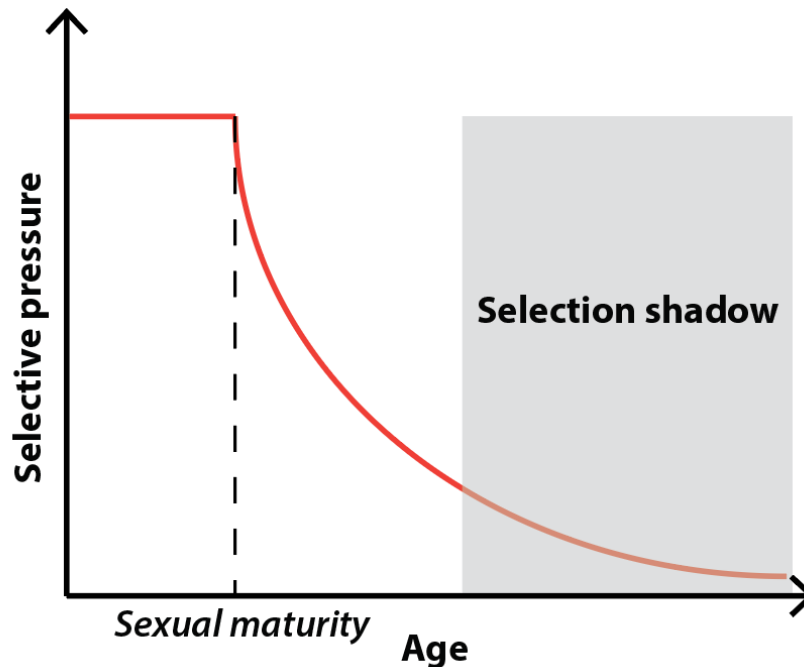


Figure 6: The Selection shadow concept

Hence, mutations that affect early life will be highly subjected to selection because reproduction has not occurred yet. In contrast, mutations expressed later could be passed to the offspring before they show any fitness problem.

Thus, species would accumulate mutations with late-acting deleterious effects in their genome, and this would cause aging. This theory is called the mutation accumulation theory and was later mathematically formalized by Hamilton [21].

This theory - though giving an attractive framework to consider gene actions in aging - raised several critics. Indeed, increasing evidence shows that aging is more common in the wild than previously expected [22,23] and influences the life tables of species [23-25]. Moreover, in social animals, knowledge transfer and material help such as parental care from the elders to the younger generation brings a fitness advantage [26]. For example, there is an increasing body of evidence that grandmothering in humans increases fitness by reducing mother hazards and child survival, which could explain why menopause (a consequence of aging) has been selected in humans [27-31].

Furthermore, this theory was also criticized because aging would still have a selective cost over individuals who do not age, even if it expresses late. Hence, it would ultimately be affected by natural selection [12].

Together, these critics suggest that aging is seen by natural selection. Then, why has it been selected?

1.2.3. Antagonistic pleiotropy

A refinement of the mutation accumulation theory was proposed by George Williams a few years later [12].

It states that if a gene has *pleiotropic* and *antagonistic* effects - one beneficial early in life (when selective pressure is high and survival and reproduction must be maximized), and one detrimental at a later age (such as the accumulation of damages) - then this gene will be selected and enriched in the population.

While direct evidence of the existence of such genes remains thin [32], they still exist. For example, in *C. elegans* and *S. cerevisiae*, competitive assays between long-lived mutants and wildtype (WT) showed that the mutant disappeared in a handful of generations due to an almost undetectable reduction in fertility [33,34,35].

Antagonistic pleiotropy can also mean an increase in fitness in varying environments. For example, *C. elegans* have shown that some long-lived mutants show no competitive disadvantage under normal conditions. Yet, the WT outcompetes the mutants once exposed to different feeding regimes (variation between starvation and feeding) [36].

Recently, more examples of antagonistic pleiotropy have been found and are discussed in [37,38].

A corollary of this theory is that since there is a trade-off between early reproduction and late fitness effects, genotypes with high reproductive capacity should be shorter-lived than those with lower fecundity and vice-versa [39]. This has been partly verified in field studies and in lab experiments, where a change in extrinsic mortality (thus, lower selective pressure at an early age) induces a change in aging [23,40,41]. On the contrary, selection experiments for long-lived individuals led to reduced fertility in *Drosophila* [42-45]. An extreme example of the trade-off between longevity and reproduction is the case of *Somniosus microcephalus* (Greenland shark) which can live more than 400 years but is thought to reach maturity at about 150 years old [46].

1.2.4. The disposable soma theory

As an extension of these ideas, Kirkwood proposed in 1977 the *disposable soma* theory [47], which predicts that each species must maintain a given ratio between reproduction and maintenance of the existing structure. Indeed, organisms have limited resources (especially energy) and must allocate them between these two biological outputs in order to maximize their Darwinian fitness. Consequently, somatic cells would accumulate damages while germline cells are protected and immortal.

In line with that, some embryonic stem cells in murine models have a lower mutation frequency than somatic cells and a stronger oxidative stress detoxification system [48,49]. Similarly to the previous theory (and supported by the same set of evidence), it suggests that extrinsic mortality also drives this trade-off between maintenance and reproduction, with harsh survival conditions favoring rapid growth and sexual maturity over longevity [50].

Thus, aging would be an accumulation of damages due to the imbalance between soma maintenance and germline generation (see next paragraph)

A corollary of this theory is that aging must have appeared in the tree of life simultaneously as the distinction between the soma and the germline, *i.e.*, alongside asymmetric division.

Indeed, if symmetrically dividing organisms were deteriorating over successive divisions, it would lead to the extinction of the whole lineage. This implies that symmetrically dividing organisms must keep a constant level of damage and allocate as much energy to division as they do to maintenance [51,52]. This idea is supported by data on symmetrically and asymmetrically dividing unicellulars (see p.22).

1.3. Molecular models of aging

Although these theories on the emergence of aging give a conceptual frame, they are not directly informative on which molecular players are at stake in this phenomenon.

The idea arising in the later theories is that damages and errors would accumulate with age in somatic cells, thus leading to the deterioration of tissues, as first suggested in 1963 by Leslie Orgel [53]. From then, many different types of damage accumulation have been described (Figure 7), such as (non-exhaustively) free radicals [54, 55], protein aggregates [56], telomeres shortening [15,16], mutations [57,58], DNA damages [59-61] and epigenetics alterations [62-65].

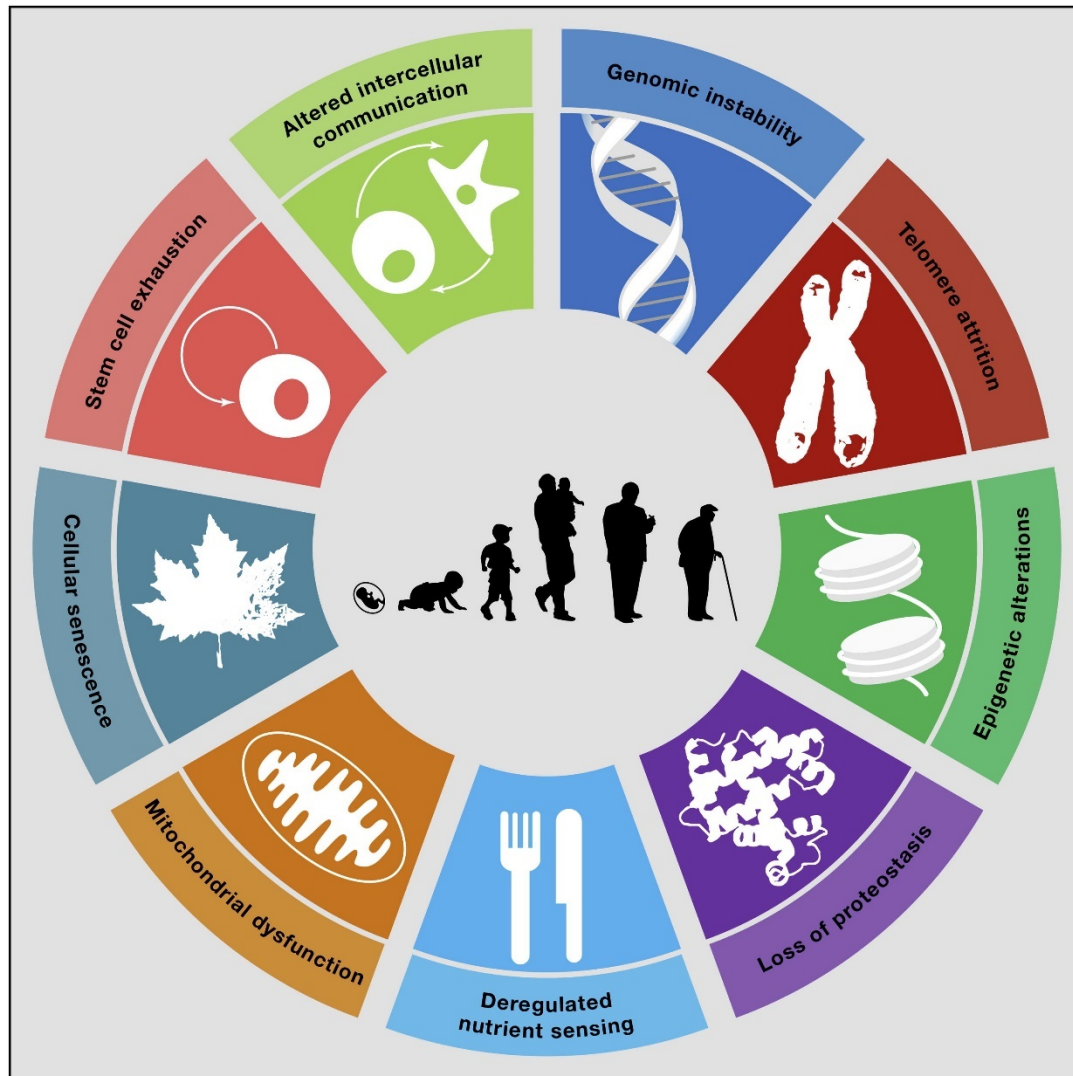


Figure 7: The hallmarks of aging, from [99].

In the following paragraphs, we will briefly review the main molecular theories of aging.

1.3.1. Free radicals

The free radicals theory of aging was proposed in 1956 and stood as one of the first models to explain how organisms lose fitness with time [54,55,66]. It states that cells accumulate free radicals (i.e., a molecule with a single unpaired electron from its outer shell) with time. These highly reactive species would damage the DNA and other molecules of the cell. It was later established that mitochondria produce Reactive Oxygen Species (ROS), which are free radicals, giving more substrate to this theory [66].

In line with that, ROS and other oxidative species levels increase during aging, even in mammals [67]. Besides, deleting the superoxide dismutase (an enzyme implied in oxidative stress detoxification) in yeast decreases the replicative [68,69] and chronological lifespan [70,71]. In *C. elegans*, increasing the level of superoxide dismutase has been reported to

extend lifespan [72]. However, reducing its level can also lead to increased longevity [73]. In *Drosophila melanogaster*, studies also reached opposing results regarding oxidative stress and longevity [74,75]. In ants, overexpression of the dismutase is not needed to reach extreme longevity in queens [76]. In mice, mutants lacking the superoxide dismutase have a decreased lifespan [77], but its overexpression does not lead to increased longevity [78].

Besides, reactive oxygen species also serve in signaling, and their average level might have evolved to ensure the proper functioning of the cell [79]. Moreover, hormetic effects exist regarding oxidative stress or antioxidants. Indeed, mild exposure to H₂O₂ could have beneficial effects on longevity, potentially by overexpressing the detoxification machinery [80]. In contrast, excessive antioxidant supplementation can have negative consequences such as higher risks of cancers and increased mortality in humans [81-83]. The pleiotropic effect of oxidative stress in the cell and the way cells maintain their oxidative homeostasis might explain the discrepancy between the studies.

Overall, the free radical theory is one of the oldest molecular theories of aging and is still seriously considered and debated.

1.3.2. The somatic mutations theory of aging

Another early model proposes that the accumulation of mutations in somatic cells drives aging [57,58]. This is supported by evidence that the genome is constantly exposed to harmful reagents such as oxidative stress (see previous section), UVs and replication problems [84], which can create DNA damages (for example, single- or double-strand breaks). Endogenous DNA damages are widespread in cells since they occur tens of thousands of times per cell and per day in mammal cells (reviewed here [85]), which can lead to a mutation if not correctly repaired. In multicellular organisms, it can lead to the generation of a tumor or the altered function of the cell. In line with that, somatic mutations accumulate during aging in model organisms and humans [86].

Nevertheless, specific mutant mice defective in a protein for DNA mismatch repair have about a 100-fold elevated mutation frequency (and cancer) in all tissues, yet do not appear to age more rapidly [87]. Similarly, it has been recently reported in yeast and humans that mutation accumulation is not linked with aging [88,89]. Therefore, the somatic mutation theory of aging is strongly contested nowadays ¹.

¹ Update 04/2022: This theory has received new support with a study showing a scaling of somatic mutation rates with lifespan across different species: Cagan, A., Baez-Ortega, A., Brzozowska, N. *et al.* Somatic mutation rates scale with lifespan across mammals. *Nature* **604**, 517–524 (2022). <https://doi.org/10.1038/s41586-022-04618-z>

1.3.3. DNA damage and epigenetic alteration

Contrariwise, the DNA damage theory of aging has received substantial support since it was first expressed in 1967 [61]. If they can create mutations in dividing cells, these damages can not be repaired and lead to the mistranscription of the affected genes in post-mitotic (or slowly dividing) cells. The accumulation of such abnormalities is considered a driver of aging. Experimental evidence indeed found increased levels of DNA damage in old cells and identified oxidative stress as a substantial cause [59,90-92]. In agreement with that, a very recent comparative study on 102 species of rockfishes, whose lifespan ranges from 11 to more than 200 years, identified the DNA repair pathways as a trait of longevity [93].

Interestingly, this model bridges with a more recent one, which states that the accumulation of epigenetic alterations drives aging. Indeed, the repair of DNA damages often leaves epigenetic marks such as DNA methylation or chromatin reorganization. These marks are enriched during aging, notably in mammal tissues [62-65,94-96]. Moreover, the DNA methylation state of human blood cells was shown to have predictive value on later-life mortality [97,98], which led to the famous term “epigenetic clock” of aging. Whether this clock plays a role in aging or is just indicative of the epigenomic state of the cell is not clear. Yet, preventing some of these epigenetic remodeling increases lifespan in yeast, flies, worms, and even mammals, according to a recent study [96,99-102].

Overall, the DNA damage theory of aging is still receiving attention from the aging community. Its link with the epigenetic alteration is not fully understood, and DNA methylation and chromatin reorganization can likely occur in a DNA damage-independent manner. This last theory is still young and emerging, and further study will tell us how much this hallmark of aging [103] is a cause of it.

1.3.4. Telomere attrition

Telomere shortening is also an early theory of aging with the observation that somatic cells cultured *in vitro* experience an irreversible cell-cycle (termed *senescence*) after a given number of divisions, linked to telomere shortening in [14,15]. Yet, only a little evidence supports that it could cause aging in organisms. Indeed, normal somatic cells in tissue do not divide enough times for that [104,105], and telomere shortening could only be a mechanism of tumor prevention [106]. Besides, even though other studies report a global telomere shortening in old tissues [103] and an increased lifespan in mice with longer telomeres [107], it is still debated as to whether telomeres attrition is causal of aging [108,109].

1.3.5. Decline in protein homeostasis

Since proteins are the basis of most cellular functions and their synthesis costs many resources (energy and amino acids), tight control of their content and quality is necessary. Thus, protein homeostasis is regulated by several processes such as protein production and degradation, folding, and autophagy. In humans, proteostasis can change with age [110], and age-related disorders such as Huntington, Parkinson or Alzheimer's disease are caused by a loss of protein homeostasis [111]. Besides, increasing chaperone protein levels increase longevity in flies and worms [112- 115], and so does autophagy in mice [116].

1.3.6. Decline of repair functions

In addition to the previously suggested damages, repair and maintenance machinery such as the proteasome [117], chaperons [118], autophagy [119], and DNA damage repair [120] have also been reported to decline with age, amplifying the accumulation of damages. This is in line with the disposable soma theory (see p.10), in which aging arises from a rupture of homeostasis between repair and damages [50].

A link exists between the cellular, tissue, and organismal level. Indeed, senescent cells are enriched in old tissues of many organisms, including mice, apes [121], and humans [106,122]. Besides, these cells often trigger inflammation and senescence, in part due to their secretory functions (secretion of Senescence Associated Secretory Phenotype, SASP [123]). Hence, senolytics recently received much attention for their ability to kill senescence cells specifically. However, it is still not clear if these cells are a simple byproduct or a cause of aging. Consequently, if senescence at the single-cell level causes aging at the organismal level is still debated [124].

1.3.7. The network theory of aging

Yet, none of these processes can explain aging on their own. More generally, many hallmarks of aging have been identified [103,125], but no theory has emerged to link all the potential players and distinguish drivers from byproducts of aging.

Besides and as described all along this section, processes in one organism may not be at stake in another one. If a general theory of aging exists, it needs to be validated across many organisms.

Therefore, new concepts are emerging to try studying aging as a complex system with different interacting processes that have different dynamics instead of separate causes. This approach aims to link the many existing theories by considering the interactions and synergies between the molecular players implied in aging and across biological sub-systems (molecules, metabolic pathways, organelles, cells, tissue, and organism) [126]. It can be termed the *network theory of aging* [127,128], or with a more recent terminology, the *system biology of aging* [129,130], and is discussed in the General discussion.

1.4. Universality of aging

Interestingly, aging is not universal across the tree of life. Many species have reported to not age at all (*i.e.*, to have a constant probability of dying, see p.4), and this phenomenon is termed *negligible senescence* [132].

Examples are the hydra (probability close to zero, *i.e.*, quasi-immortal [131], the red abalone, the collared flycatcher, or the great rhododendron (Figure 8). Other organisms experience *negative senescence* - namely a decrease in mortality with age - such as the desert tortoise or the white mangrove [11,133]. More recently, the famous *Heterocephalus glaber* (naked mole rat) has been reported as the first mammal not experiencing aging [134].

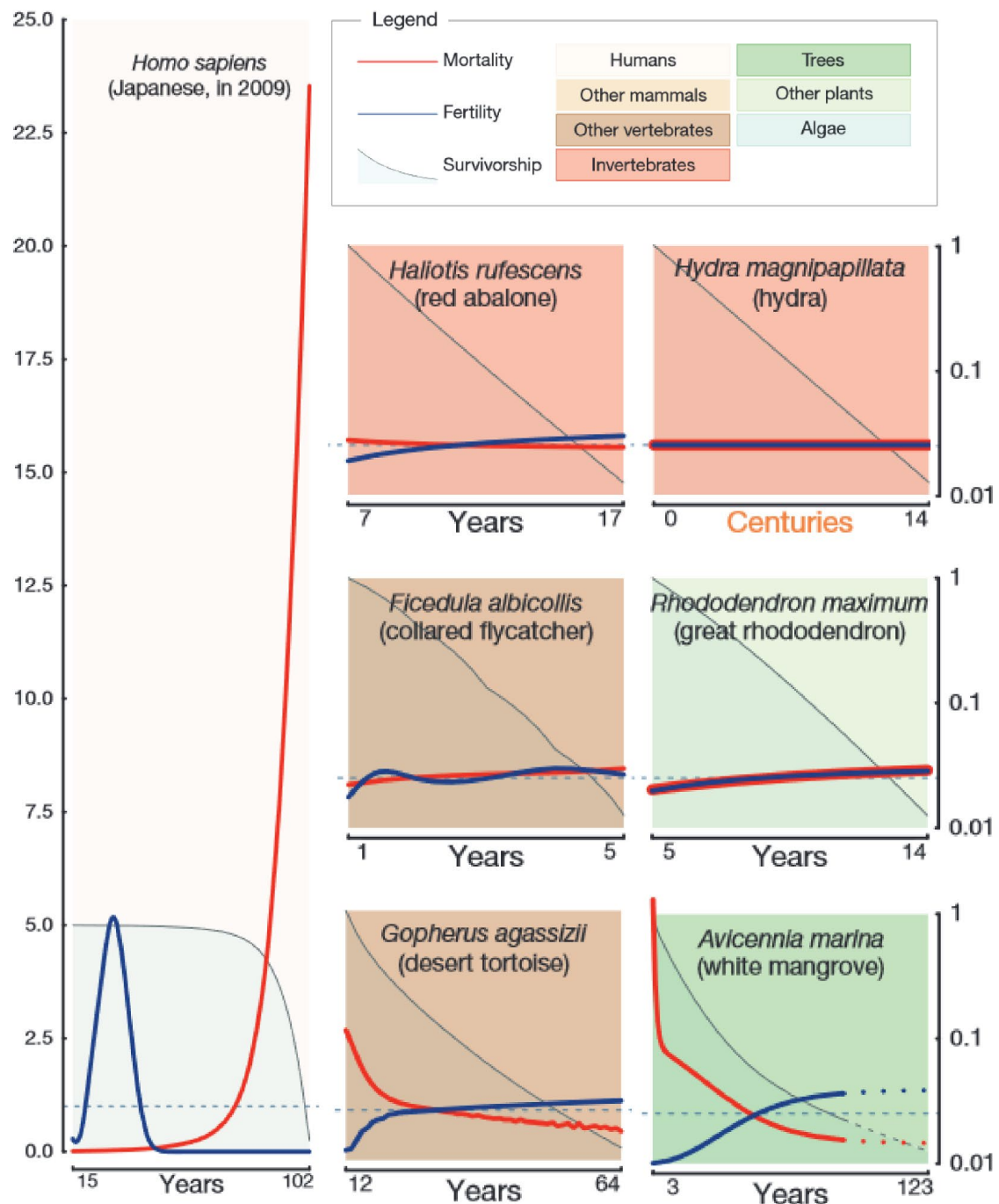


Figure 8: Mortality, fertility, and survivorship across several species. From [11]

Studying these models, especially in light of already known theories, can help us understand the different evolutionary and molecular aspects of aging.

1.5. Laboratory models

As previewed in the previous sections, aging can be studied at the cellular or organismal level. Besides, genes do not solely influence it since homogenic individuals can have different

lifespans. Thus, monitoring aging in laboratory conditions by varying the genetic background or the environment is a powerful approach.

1.5.1. Clonal aging

A simple way of studying aging is by observing cultures of dividing mammal cells *in vitro*. As discussed earlier (p.13), somatic cells can do only a limited number of divisions before entering senescence, and telomere shortening is mainly responsible for this arrest. In fact, since telomeres size is equal in cells dividing symmetrically and shortens at each division in somatic cells (lacking the telomerase enzyme), the whole culture stops dividing after about 60 divisions [14-16,106]. This phenomenon is termed clonal senescence (Figure 9) and is convenient to study since the whole process takes about ten days instead of years for mammal organisms.

Clonal senescence

Mammalian somatic cells

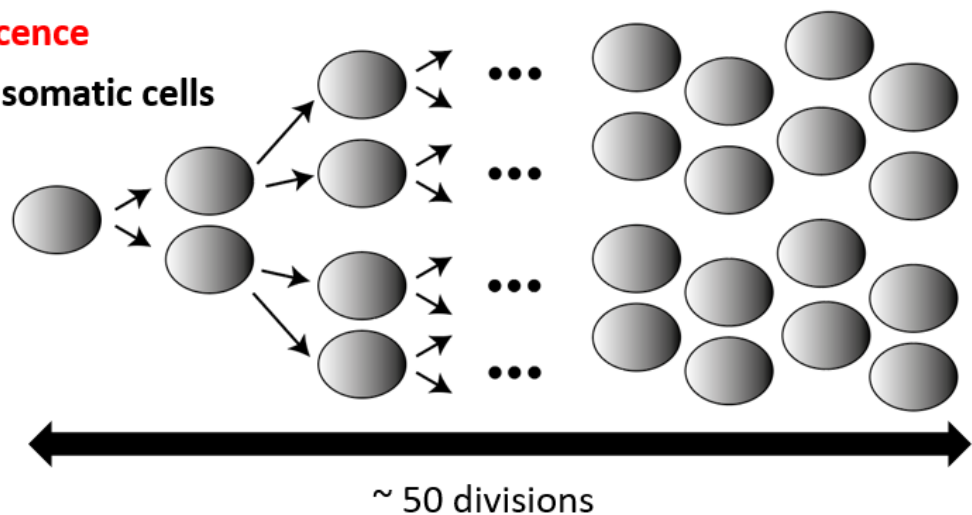


Figure 9: Schematics describing clonal senescence. A culture of cells originating from the same telomerase deficient cell will senesce after a given number of divisions.

Nevertheless, although it is interesting to study senescence and its involvement in development and tumor suppression, the relevance of such a model to study aging at the organismal scale is debated.

1.5.2. Organoids

An intermediate model has been emerging for the past few years, in which cells are cultured to grow in an organized 3D microenvironment to mimic micro organs [135]. These *organoids* are particularly interesting for morphogenesis and developmental research. They also happen to be useful for aging research since they age at the scale of a few months while having a tissue structure, therefore conserving the cell-cell interactions. Besides, they can be used with various cell types, especially derived from humans [136,137].

1.5.3. Model organisms

As stated before, it is essential to consider aging by integrating all the scales on which it has an influence.

Therefore, several model organisms have been extensively studied in the past decades.

For example, the fly *Drosophila melanogaster*, which has a lifespan of about 50 days under normal conditions, is a common model to study aging, and several mutants of longevity have been described [74,138-143]

Another valuable and popular model organism to explore the genetic influence of aging is the worm *C. elegans*, which lives about ten days and allows facile genetic screens thanks to the famous interfering RNA [144] tool. Again, many pathways affecting its longevity have been identified [17,18,145,146].

Concerning mammal models, the most used models are the mice *Mus musculus* [147] and the rat *Rattus norvegicus* because they offer an interesting trade-off between easiness of manipulation, aging kinetics, and similarities with humans (similar organs and diseases).

Aging can also be investigated using unicellulars such as budding yeast (*Saccharomyces cerevisiae*), which ages in a few days and is a historical model for this purpose [148,149]. This model organism will be thoroughly developed in the following sections.

Interestingly, in all of these organisms, blocking the main metabolic pathways (TOR, Sch9, PKA, and IGF) results in increased longevity [150]

Besides genetic manipulations, environmental modifications can also affect aging, with caloric restriction (CR) being the most widely used and documented. Indeed, it was found to positively impact longevity on most of the tested organisms. Already 90 years ago in the rat [151,152], and then in mice [153-155], worms [156], flies [9], budding yeast [157,158], fission yeast [159], and many other model organisms. In monkeys, it delays the onset of age-associated disease and increases lifespan (though it was debated during a few years, it now seems consensual) [160-162].

However, the range of effects of CR is still debated, and some could be due to the overfeeding of control groups or other analysis biases [163,164,331]. Furthermore, it is

unclear which CR regimes induce an effect (constant and low level of nutrients, or alternate periods of fasting) [155-165].

Caloric restriction is known to repress the growth metabolic pathways presented above. However, as these pathways impact most other biological processes, it is complex to understand, and the exact molecular mechanisms at stake remain unknown or controversial [166].

Nevertheless, working on different organisms and trying to identify the common pathways is interesting. In this sense, it has been shown quantitatively that the genetic components of lifespan are quite conserved across eukaryote species [167].

Thus, since unicellulars share many longevity pathways with other *taxa*, that they are simultaneously a cell and an organism, that they age very fast and are very convenient to manipulate, they seem to be of particular interest for aging studies.

1.5.4. Unicellulars

Like in complex organisms, it is possible to measure aging in unicellulars, either by looking at their mortality rate with time or by measuring the decline of their physiological functions, such as the cell-cycle slowdown or growth rate. Interestingly, the division pattern varies among the classical unicellular models with the bacteria *E. coli* and the yeast *S. pombe* dividing symmetrically, while *S. cerevisiae* divides in an asymmetric manner.

1.5.4.1. *Bacteria*

E. coli is a small (2µm long, 0.25-1µm diameter, Figure 10) rod-shaped bacterium that divides very quickly (~20min) under favorable conditions, giving two daughter cells.

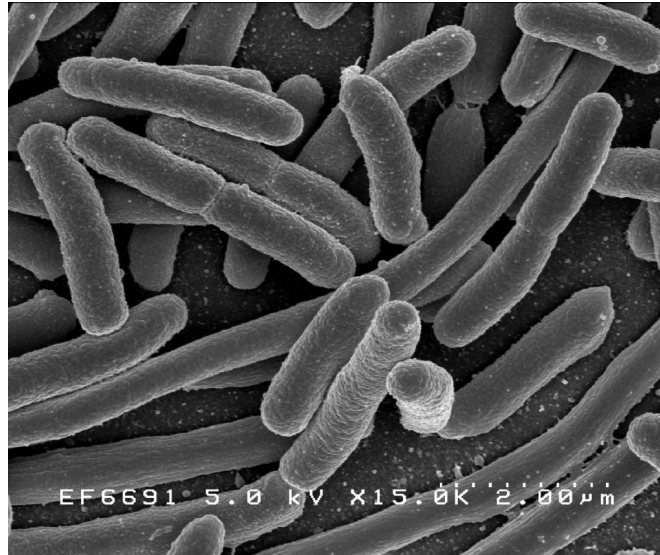


Figure 10: Electron microscopy image of *E. coli* cells. (Image from Rocky Mountain Laboratories, NIAID, NIH)

Historically, *E. coli* and other symmetrically dividing organisms were thought to not age for reasons explicated before (see p.10). In reality, the *E. coli* division is not exactly symmetrical because after forming a septum and the septation, one daughter receives an old pole while the other gets a new one (Figure 11).

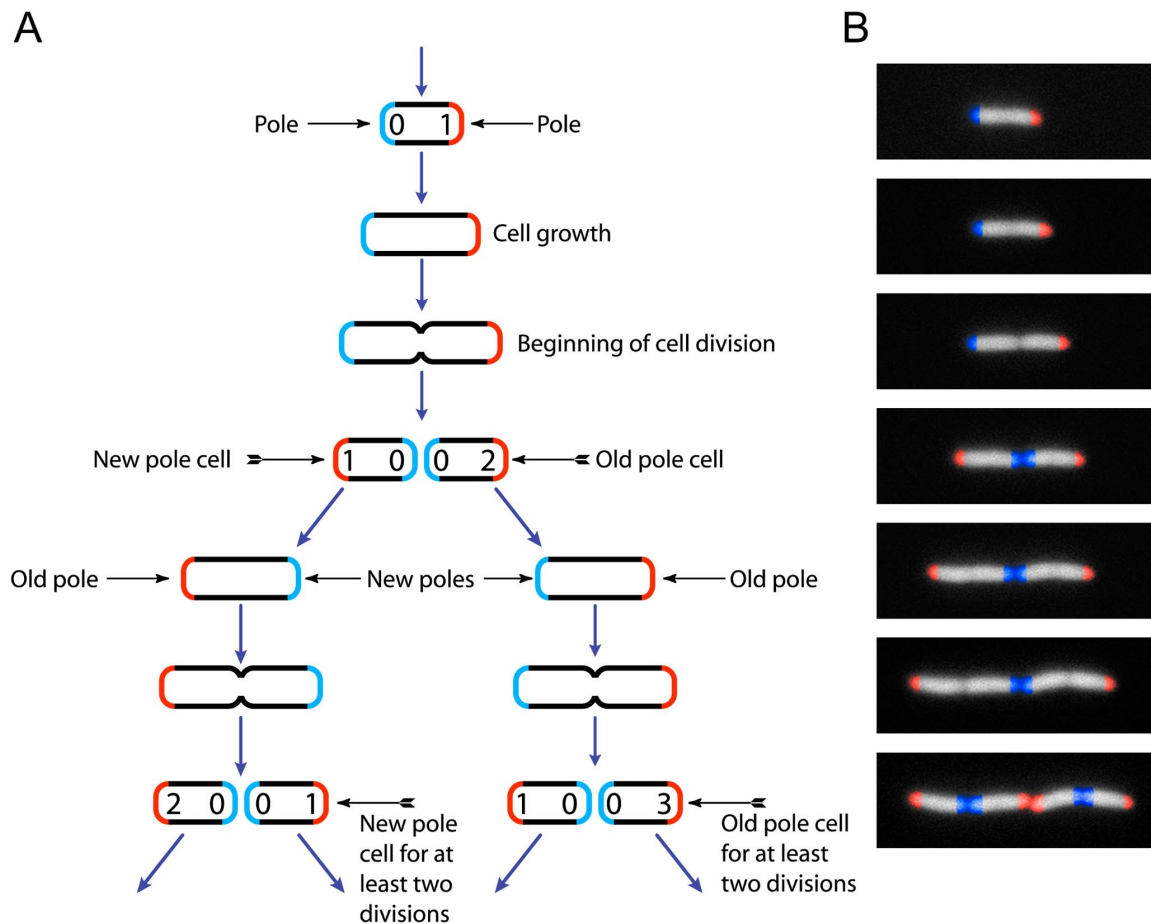


Figure 11: Division pattern of *E. coli*. (From [164]). (A): Schematics of the old and new pole distribution among the progeny. The numbers indicate the replicative age of the pole. The blue overlay: new poles, red overlay: old pole.; (B): Images of an *E. coli* dividing with the same color code as (A).

The first piece of work studying aging in *E. coli*, by following the first nine divisions of single-cells, concluded that the “old pole cell” was experiencing a decrease in division time after a few divisions [168] while new pole cells were gaining fitness during this interval.

However, a more recent study using microfluidics (discussed later, p.68) was able to track old pole cells for more than 100 divisions and showed that the division time of old and new pole cells was indeed evolving but reaching an equilibrium state - later identified as a stable attractor [169] - after a few divisions [170]. Besides, old pole cells were found to keep a constant growth rate throughout their lifespan after the first ten divisions (Figure 12).

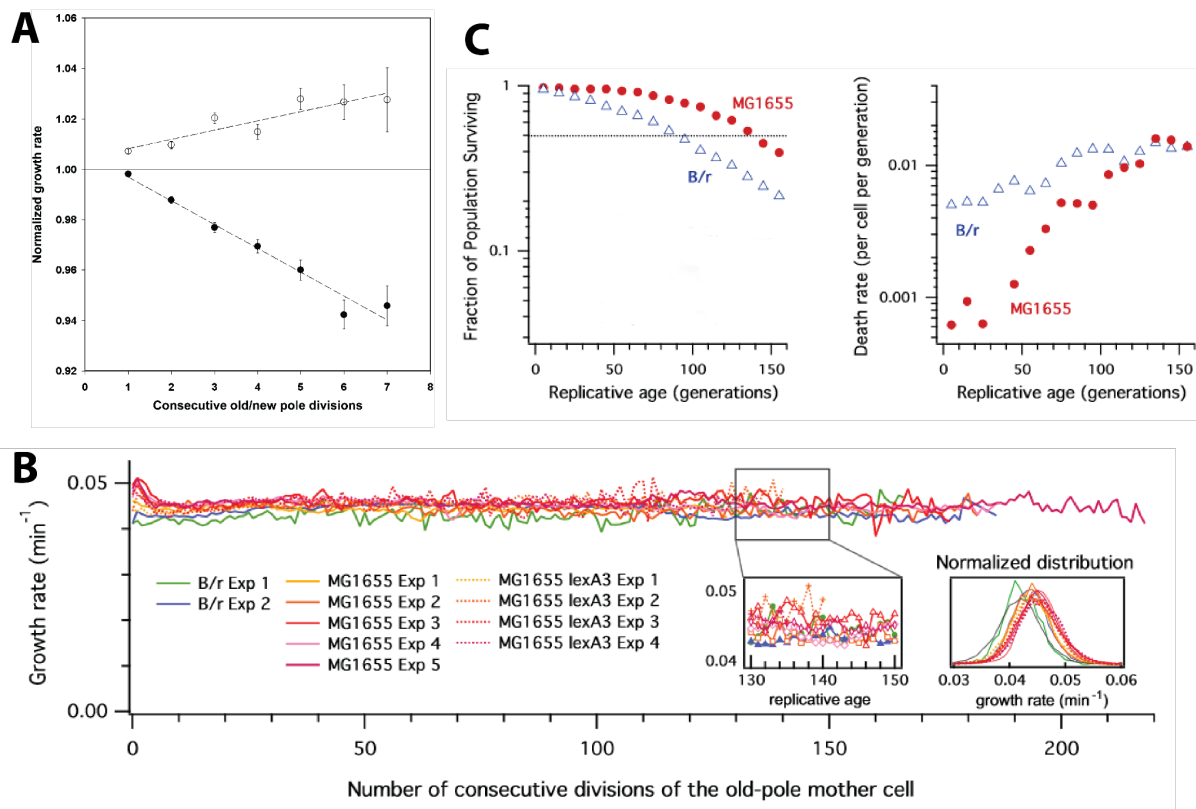


Figure 12: (A): Normalized growth rate of new (top) and old (bottom) pole cells during the eight first divisions (From [166]). ; (B): Growth rate of the old pole cell across different strains and replicates plotted versus replicative age of the old pole cell. (C): Survival rate (left) and death rate (right) of the old pole cells from the MG1655 and B/r strains.

Importantly, this study has also shown that the mortality of the old pole increases throughout the divisions.

Two interesting ideas emerge from this set of studies. Firstly, an increase in mortality can occur without a detectable decrease in fitness (such as growth rate). Secondly, aging can exist even in the case of seemingly symmetrical division.

How to explain this aging molecularly? First, the cell wall of the old pole is not renewed and is unable to avoid deterioration [17-173]. Moreover, protein aggregates have also been

proposed to segregate asymmetrically between the old and the new pole [174,175]. Even though more asymmetrically segregated factors could be involved and no causal link has been identified, this could explain the old pole lineage is aging.

1.5.4.2. *Schizosaccharomyces pombe*

Schizosaccharomyces pombe, a rod-shaped yeast historically used to study cell-cycle and cell size control [176]–[182], divides in a similar fashion to *E. coli*, with each division giving rise to two daughter cells, “an old pole cell” and “a new pole cell” (Figure 13). Thus, if this unicellular eukaryote displays any sort of aging or not is of major interest.

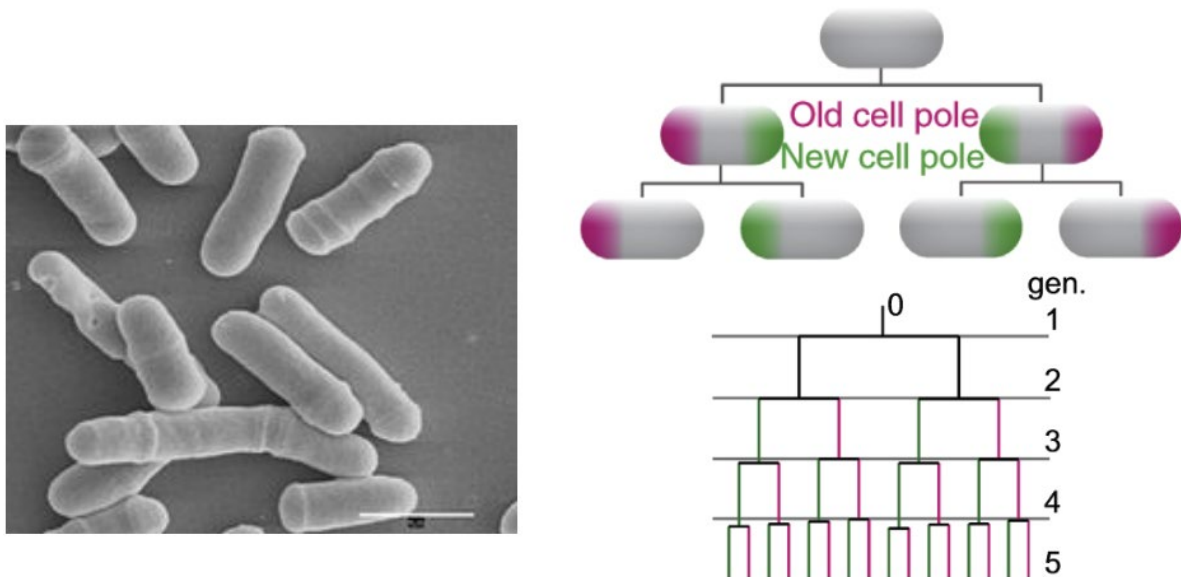


Figure 13: (Left): Electron microscopy image of *S. pombe* cells (scalebar: 10µm) from [179]; (Right): Division pattern of *S. pombe* cells and the repartition of the old (purple) and new (green) poles along with the divisions (from [180])

By following the old pole cell using microdissection techniques, it was first reported that the old pole was aging [185]. In contradiction, recent studies have shown that it was not the case [159,184,186]. Neither division time nor the death rate increases in the old pole lineage, and cells die without any aging-associated changes. One way to explain the difference with *E. coli* is that *S. pombe* is growing polarly, with newly synthesized cell wall materials being exclusively incorporated at the ends of the cells [187-189]. Instead, the new pole inherits a more significant proportion of old lateral cell walls and a birth scar [179,190]. Hence, the new pole lineage may experience aging, but no current method allows the tracking of the new pole for an extended number of divisions.

On top of that, the spindle pole body (SPB) and protein aggregates are also segregated asymmetrically and randomly [191] (or partly randomly in the case of aggregates). Indeed,

one cell inherits a new SPB or a protein aggregate while the other is born with the old SPB or no protein aggregate. However, none of these factors have been clearly shown to affect mortality or the division frequency.

So far, the distinction of lineages was based on the new versus old pole, new versus old SPB, or presence of a protein aggregate versus free of protein aggregate at birth, and no aging effect has been detected based on these markers. However, it is possible that a factor, transmitted asymmetrically and randomly, would cause aging in the lineage of the cells inheriting this factor, but that no one could not follow this lineage. Another option is that the generation of damages per division is slower than the division itself. Consequently, symmetrical damage segregation would lead to a constant average amount of damage in each cell, close to zero.

Again, new methods and further studies would be required to tackle these questions.

1.5.4.3. Asymmetrically dividing cells

In other unicellular organisms, the division's output is two different entities - at least morphologically - making it easier to isolate a given lineage and measure its aging.

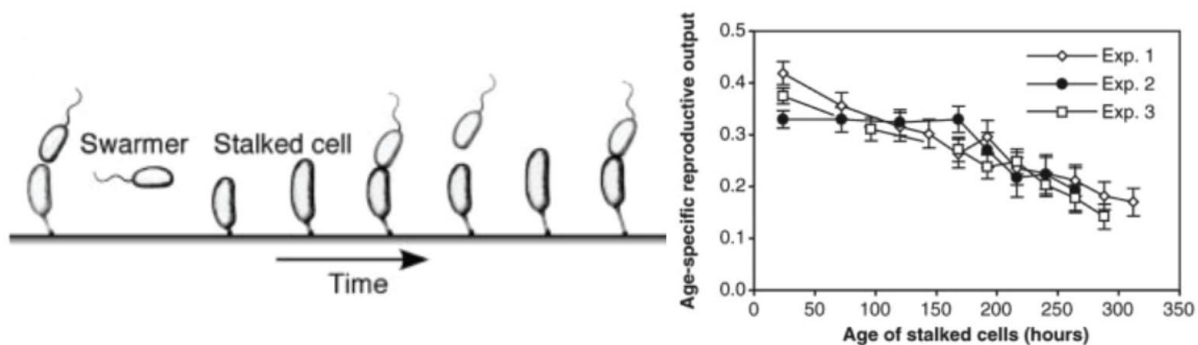


Figure 14: (Left): Schematics of the division of *Caulobacter crescentus*. (Right): Average division rate of single stalked cells versus replicative age. (From [192])

For example, in the bacterium *Caulobacter crescentus*, only the "stalked cells" attach to a surface. It then divides and gives rise to a "swarmer" cell that freely swims until it finds a substrate to attach to and differentiates into a stalked cell (Figure 14). In this context, it has been established that the division frequency of a given stalked cell was decreasing with time, whereas its progeny recovered a normal reproductive output [192]. Interestingly, young cells born from old stalked cells had the same division time as young cells from the beginning of the experiment, indicating a rejuvenation of the progeny of stalked cells.

Similarly, in the budding yeast *Saccharomyces cerevisiae* (Figure 15), the result of the successive divisions is a mother lineage and a daughter lineage, which are distinguishable by

several properties such as the morphology or protein expressed. After the division completion, the daughter will grow and become a mother itself. From that, it was found that mother cells can only undergo a finite number of divisions before dying, while the progeny is rejuvenated (described in detail in the next section).

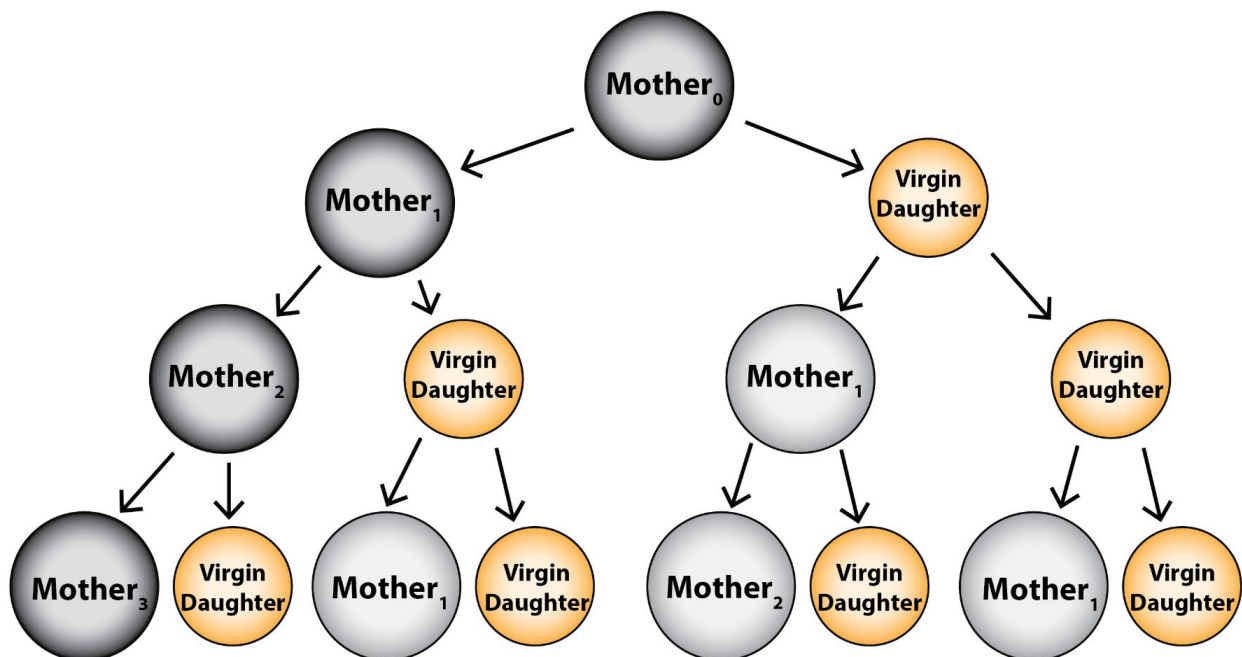
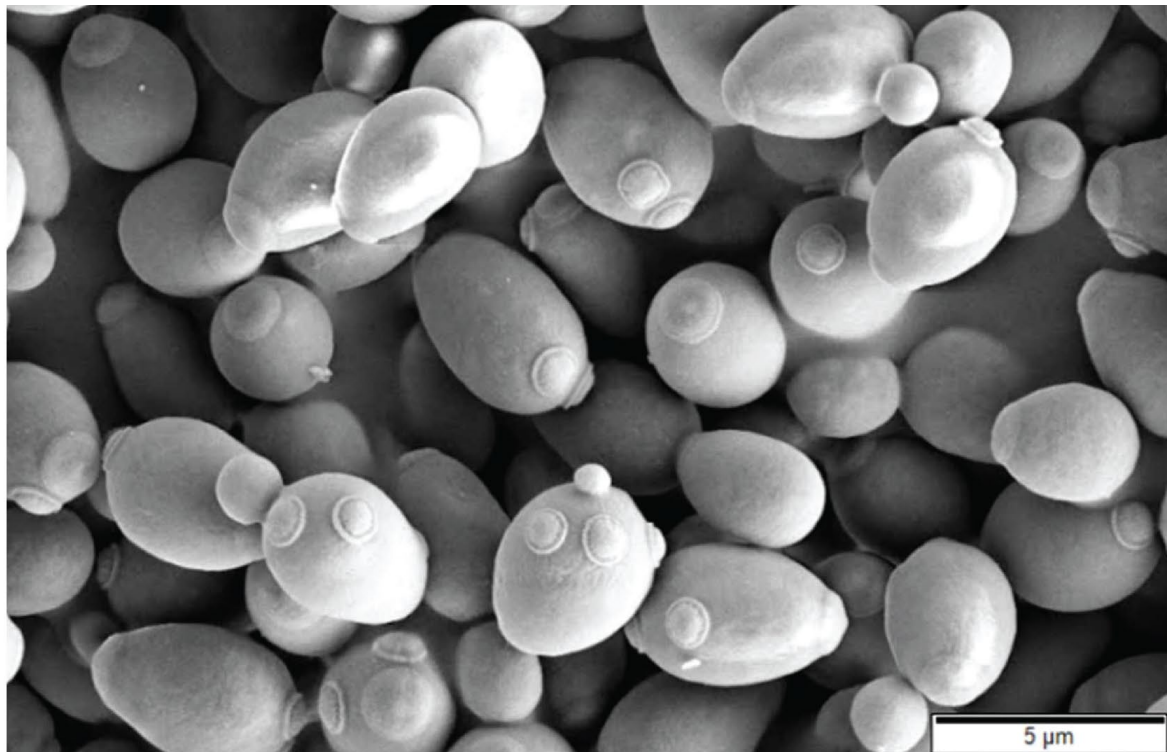


Figure 15: (Top): Electron microscopy image of *S. cerevisiae* cells (from [188]).; (Bottom): Phylogeny of an original mother cell (dark grey). The indices represent the replicative age.

This model is particularly interesting to study aging for several reasons. Firstly, it perfectly illustrates the disposable soma theory, where the mother cell (*i.e.*, the disposable soma) produces healthy daughter cells at the expense of accumulating damage. Indeed, it is thought that mother cells accumulate damages that are not passed to the daughters (see next section), which is another strategy (compared to *S. pombe*, for example) to ensure that the offspring survives and reproduces to maintain the lineage. Besides, it can also be a model for stem cell replicative aging, where the mother lineage mimics the differentiating lineage while the daughter lineage represents the stem cell lineage [194,195].

Secondly, though the relevance of this model to study human aging is debatable [196,197], many molecular pathways and hallmarks of aging remain conserved with higher eukaryotes [198]. Moreover, it is very convenient to manipulate thanks to its unicellularity, to the fact that the mother lineage is easily isolable from the daughter lineage, and to its short lifespan when replicating (a few tens of hours). In addition, even though there is increased ease to generate mutants in other model organisms thanks to CRISPR-Cas9 and other new genetic technologies, budding yeast remains one of the easiest for mutant and genetic variety generations. Indeed, it is compatible with many genome editing techniques (classical and new), can adopt sexual reproduction, and offers exhaustive mutant collections (deletion and GFP [199]). Furthermore, the species *S. cerevisiae* contains more than 1000 natural isolates [200], so studying the similarities and the differences regarding aging across the isolates can be helpful to understand the genetic drivers of longevity evolution [201-204].

For these reasons, our lab uses this model organism to study aging, and the following sections of this manuscript will focus on it by calling it “yeast” for simplicity.

2. Aging in budding yeast: different models

One strength of yeast when studying aging is the multiplicity of approaches. For example, one can focus on the time a yeast cell survives in a non-dividing state, which mimicks post-mitotic cells' aging in higher organisms such as neurons [71]. Technically, this chronological lifespan is assayed by measuring the viability of a culture of cells left in the stationary phase at given timepoints (typically, by replating cells on rich media and counting the number of colonies forming). From that, several longevity mutants were reported, such as mutants of the SCH9 and TORC1 pathway (metabolic pathways controlling growth which are strongly conserved across organisms, see p.44). Nevertheless, the parallel with post-mitotic cells is

debatable because post-mitotic cells are metabolically very active while yeast in the stationary phase are dormant cells [205].

The second widely used model is to observe mother cells dividing from birth to death, and in particular, to count how many daughters are generated before death (termed Replicative lifespan, **RLS**). This replicative aging approach will be the focus of the rest of this chapter.

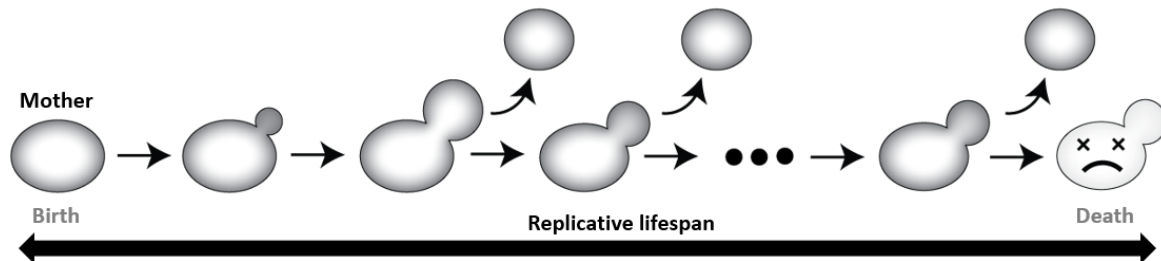


Figure 16: Schematics of the replicative lifespan of an *S. cerevisiae* cell

Finally, it is also possible to mimic clonal aging (which happens in telomerase deficient mammal cells, (see p.13 for detailed definition). In fact, in certain mutant strains, the culture fails to propagate indefinitely, which is the case for telomerase deficient cells in mammals) [206-208].

2.1. The dogma of replicative aging

Concerning replicative aging, it has been known for 60 years that yeast mother cells can undergo a finite number of divisions before dying [148].

The replicative survival curve of yeast mother cells is sigmoidal (or Gompertzian or a Weibull distribution), not only in lab strains, both haploid and diploid, but also in natural isolates [209,210]. This demonstrates that aging occurs in budding yeast (see p.4 for aging definitions).

Besides, yeast shows a decline in physiological functions with age (described later), which also conforms to the definition of aging.

Then, the central hypothesis to explain replicative aging is that a toxic factor would accumulate in mother cells, leading to their death [211].

Interestingly, daughter cells recover a full replicative lifespan, which is called rejuvenation. This is not true for daughters from very old mothers, but in this case the progeny of the daughter eventually recover its full replicative potential [212].

From that, we can define the dogma of the replicative aging paradigm as [213] (Figure 17): Aging occurs in the mother lineage due to aging factors that 1. Accumulate in the mother, 2. Are not transmitted to the daughter and 3. Are toxic for the cell, directly or indirectly, and modulating the level of the factor should impact lifespan.

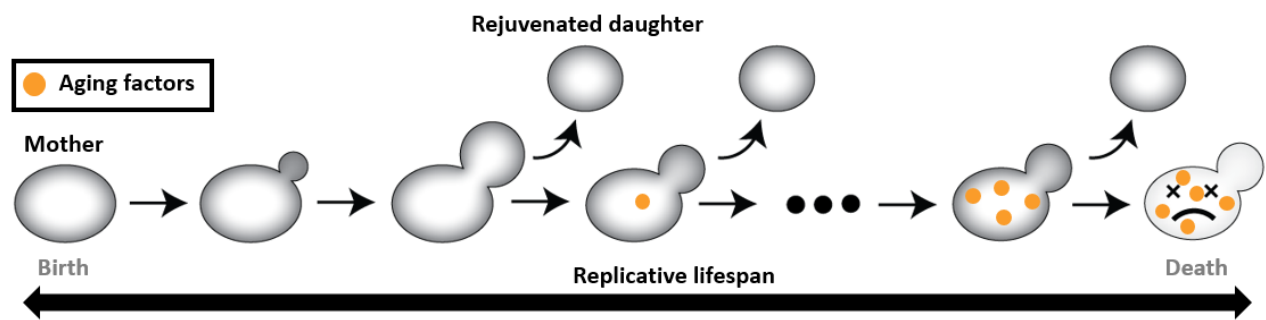


Figure 17: Schematics of the replicative aging dogma

This field of research focuses on identifying aging factors, determining how they are toxic, and by what mechanisms they asymmetrically segregate.

Hence and similarly to general theories of aging (see p.10), many different hallmarks of aging and candidate aging factors have been proposed [194,198,214-216](Figure 18). In the following sections of this introduction, we will review a few of these aging phenotypes, starting with changes at the whole-cell level, before describing changes at the organellar and molecular level, and finishing with a focus on a particular aging factor.

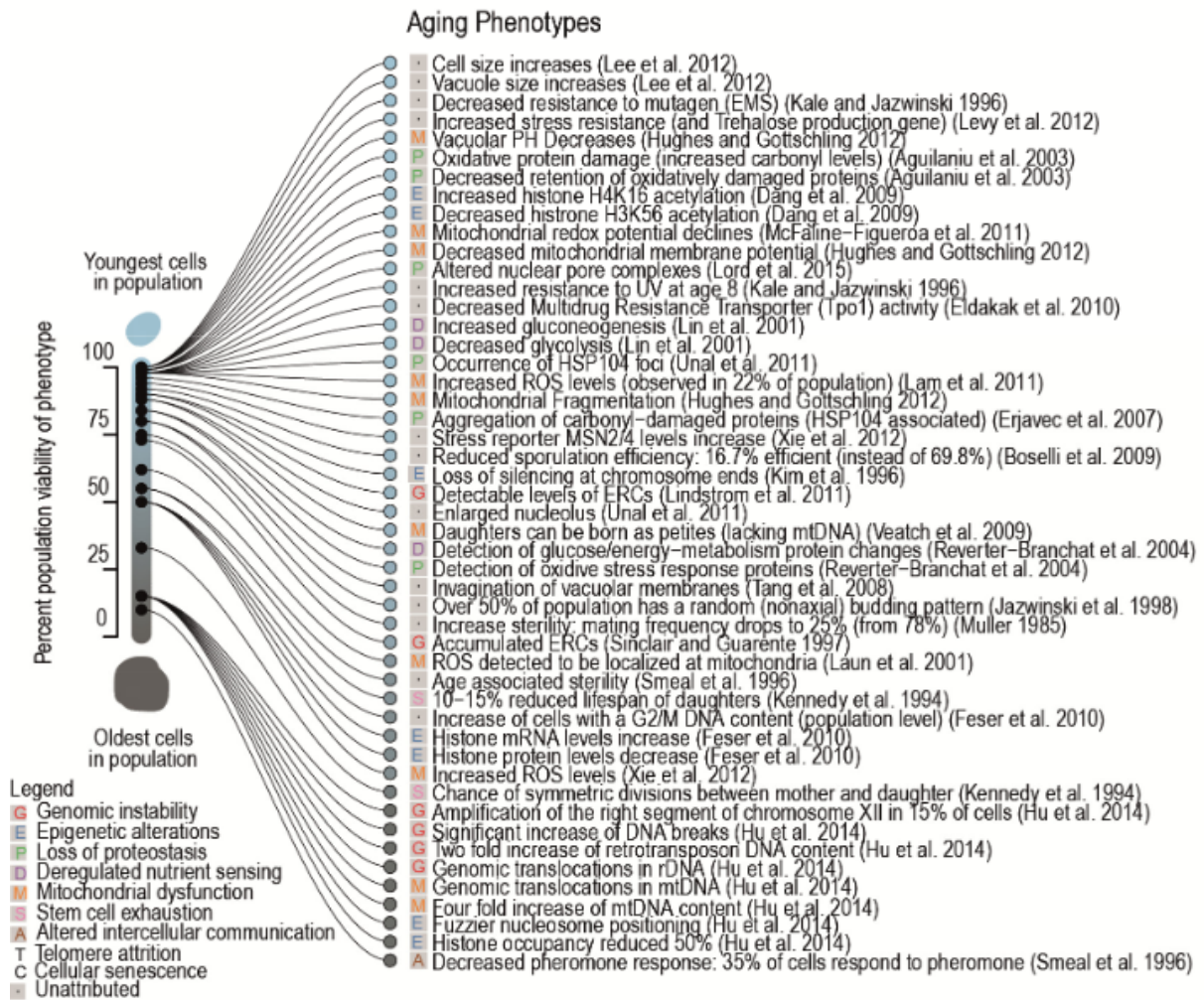


Figure 18: List of replicative aging phenotypes in yeast, sorted by category and by the approximate percentage of viability at which age-related phenotype occurs in the population (Figure from [198])

2.2. Bud scars and budding pattern

After each cytokinesis, a chitin ring remains in the cell wall of the mother, at the place of the former bud neck. These “bud scars” can be revealed by simple staining and counted to determine the replicative age of a cell [217] (Figure 19). They accumulate in the mother cell and are not passed to the daughters (daughters only inherit a *birth scar*) [149,218]. Hence, they have been proposed as aging factors by early studies [148,219] as a source of decreased metabolic exchange with the external media and obstruction for new bud necks.

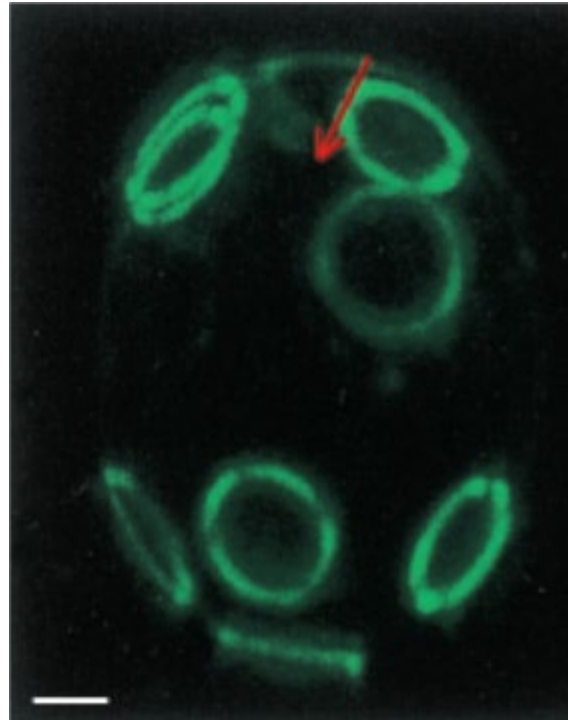


Figure 19: Bud scars of a mother cell, stained with a FITC-labelled wheat-germ agglutinin. Scale bar: 1.25 μ m (From [217], ignore the red arrow))

However, the toxicity of these scars has never been established. Furthermore, it is now known that the ratio between the scars surface and the total surface decreases with age, and artificial increase of cell volume fails to increase replicative lifespan [212].

Another hallmark of aging relative to budding is the budding pattern of cells. Indeed, its polarity is normally tightly controlled for the cell to bud in the same direction, but often becomes random with age [220]. Similarly, the morphology of the bud changes during aging, with buds becoming more elongated or more round [221-223]. Yet, these phenotypes are more likely to be a pure byproduct of aging instead of a cause.

2.3. Hypertrophy and crowding

Another striking morphological feature of yeast aging is the increase in cell size throughout lifespan, as reported by many studies [221,224-226]. In particular, quantitative measurements show a doubling in average size between birth and death (in apparent surface, not volume) [221,226]. Enlargement is mainly due to the cell constantly producing matter directed to the bud during all the cycle phases, except in G1 (absence of bud) when only the mother grows. Therefore, it is possible to modulate cell size by using mutants of the G1 or by arresting cells in G1 for a certain time.

Remarkably, the cell size of the daughter cell lineage is quickly reset, even from big mothers. Thus, the increase in cell size would be an aging factor if it is toxic. The first study to test this hypothesis used a pheromone to block cells in G1 for a certain time before releasing them and measure their RLS [212]. However, no effect on the lifespan was detected on arrested cells compared to unarrested cells. From then, other studies using artificial volume increase proposed that, on the contrary, the increase of cell size is a driver of replicative aging and named this model the *hypertrophy theory of aging* [227-229]. In line with that, a correlation exists between size and lifespan in some mutants affecting the size [225,230].

Moreover, the replicative lifespan negatively correlates with the size at birth [225,231] among isogenic strains, although this result is debated [234]. The ideas that emerge from this model is that there is a critical size upon which the cell cannot maintain its homeostasis and that what determines longevity is the size at birth and the growth per generation (in other words, how fast the cell will reach this threshold size, Figure 20) [230,232].

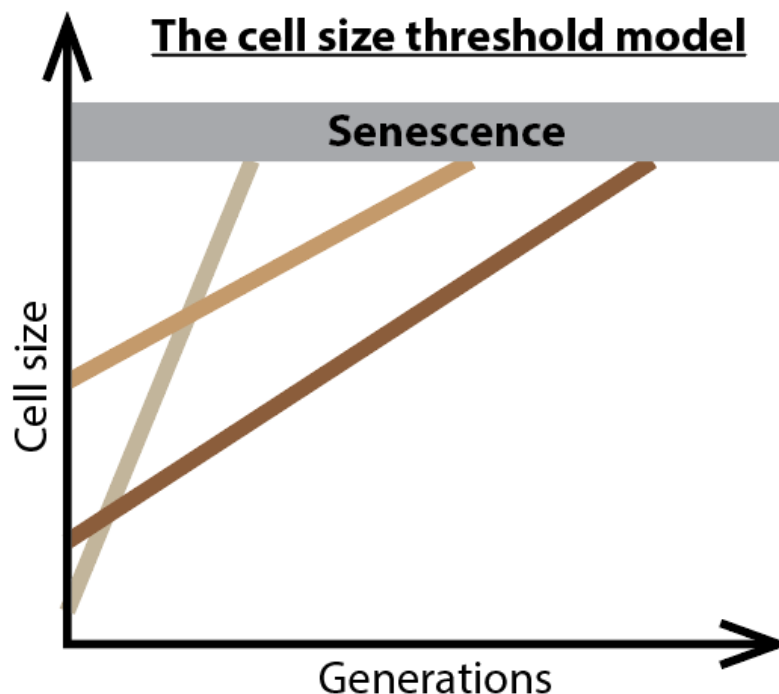


Figure 20: Schematics of the size threshold model of aging. Cells (3 brown lines) are born at different sizes (among an isogenic population or across mutants) and grow at different rates. What determines lifespan in this model is the time to reach a threshold size.

On the other hand, other studies show that mother cells die at a wide range of sizes [221,233,234] and that the size at birth does not correlate with lifespan [234,235], contradicting the threshold volume theory. Furthermore, long-lived mutants are not particularly mutants of size [236,237]. Besides, if cells growing faster and with a high metabolic activity have a reduced lifespan (and vice-versa) [234,235] does not necessarily

mean that this effect on lifespan is due to hypertrophy. Indeed, it could be that these accumulate more damages per generation.

Beyond these discrepancies, the major weakness of this theory is that it is mostly correlative and lacks mechanistic insights. Only recently, a study found that the loss of scaling between the protein & RNA biosynthesis and the volume was due to a limitation in the transcriptional and translational machinery [229]. This reduction could be due to the activation of a general stress response, leading to the dilution of the cytosol and the impairment of several processes like cell-cycle progression. However, the G1 arrests performed in this study led to cell volumes way beyond what is usually reached during normal aging (by a factor 2), which questions the physiological relevance of such strong perturbations. Moreover, another study tracking cells throughout their lifespan in physiological conditions found that the cytosolic macromolecular crowding was only slightly reduced - if not unchanged - during aging (although a correlation exists between change in crowding and lifespan) [238].

Apart from the cytoplasm, most organelles also become larger with age, such as the vacuole (see p.38) and the nucleus (see p.45). Insightful studies comparing cellular structures at the Correlative Light and Electron Microscopy between young and old cells [238] showed that the distance between organelles (also called organellar crowding) was strongly reduced during aging.

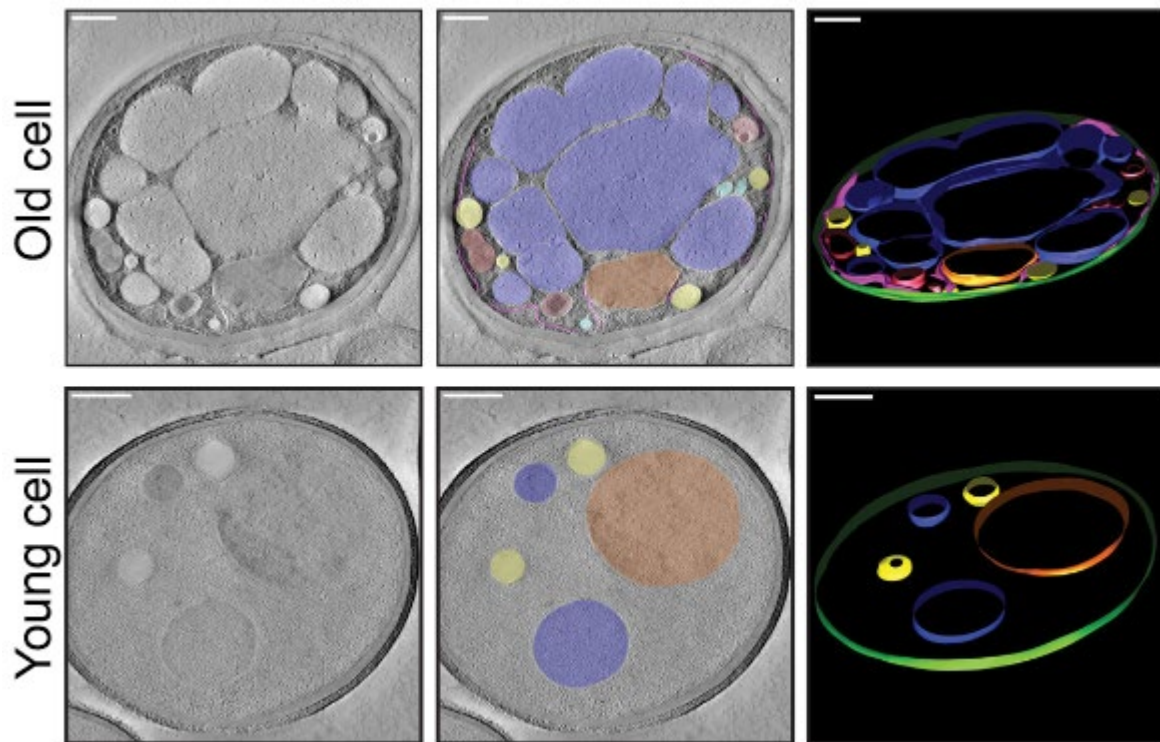


Figure 21: Single slices of tomograms without (left panel) and with an overlay to emphasize organelles (middle panel). 3D isosurface rendering (right panel) of tomograms of young or old cells. Nuclei (orange), vacuoles (blue), lipid droplets (yellow), mitochondria (red), ER (magenta), and plasma membrane (green). Scale bars: 500 nm. (Figure from [238])

This could affect cytoskeletal dynamics or the movement of structures above a specific size (for instance, ribosomes or lipid droplets), their interaction with organelles or the cell membrane. Besides, the increased surface area of organelles could lead to more interaction with their immediate environment (adsorption or molecule exchanges), hence disrupting their homeostasis.

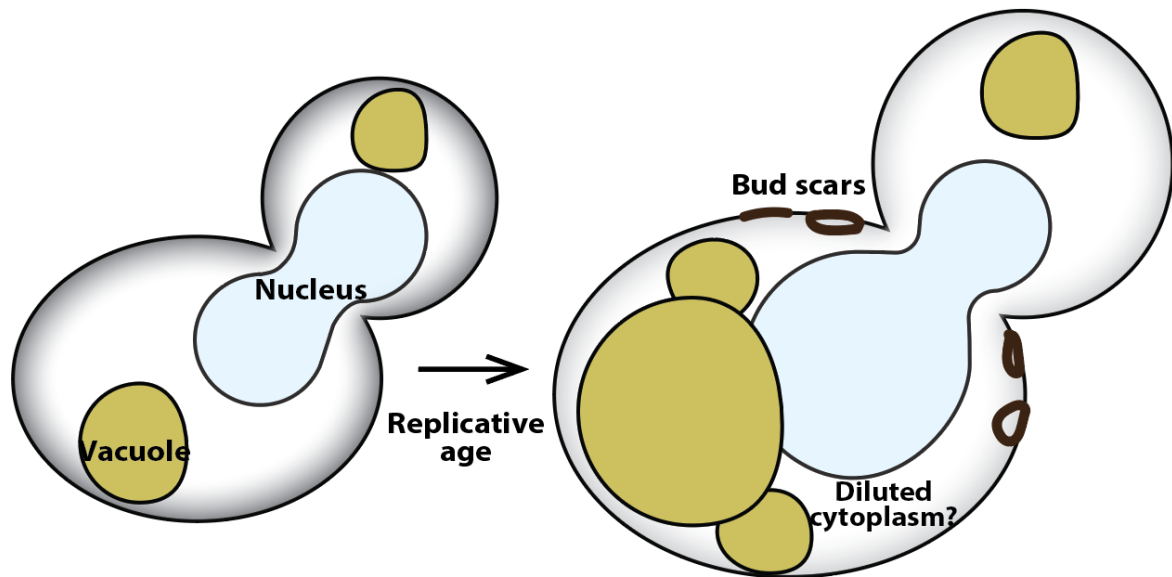


Figure 22: Schematics of the evolution of the physical state of the cell with replicative age. Young cells (left) represent the normal state, while old cells (right) have bud scars, larger cytoplasm and organelles.

Altogether, the fact that cell size increases during aging and resets in daughter cells is consensual (Figure 22). Yet, it is still not clear and openly debated whether the hypertrophy of the cell and its organelles is a cause, a consequence, or just an unrelated effect of aging [230,232,233,239]. However, since cell size affects many processes such as nutrient sensing and transcription regulation [240,241] - two processes known to be involved in aging (discussed in later sections) - the hypertrophy theory of aging should not be ignored. Of note, the control of cell and organelles size during aging has recently seemed to regain interest, not only in yeast but also in mammal cells [229,242-244,244b].

2.4. Division time

Early studies already noticed an increasing division time at late ages [211], later validated by timelapse microscopy [221,245,246] (Figure 23).

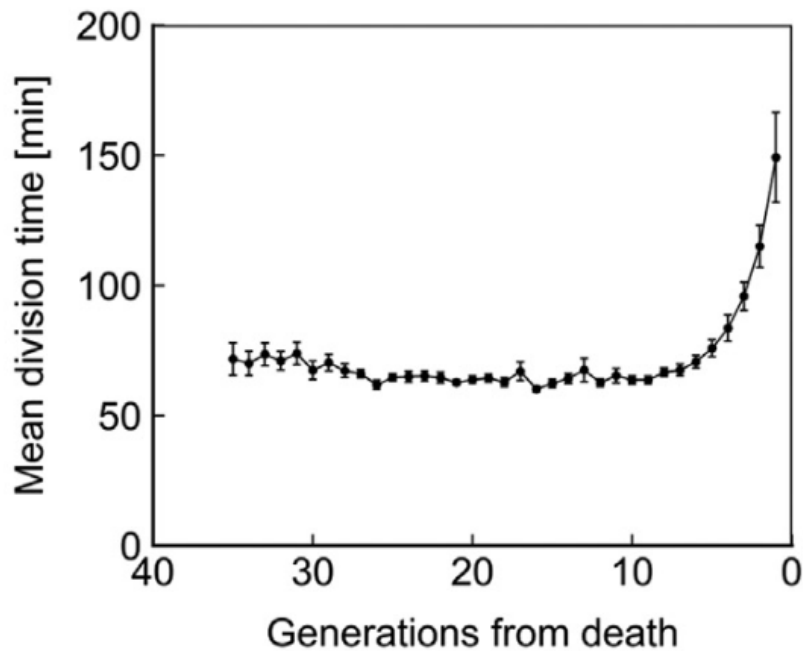


Figure 23: Averaged division time of 50 cells with age, aligned from their death (From [247])

Remarkably, daughters recover a normal division time at birth, unless they are born from an old mother, and in this case, it takes a few divisions of the cell to be back to normal [211]. This suggests that some aging factors affect the division time of the cell and all the cell cycle stages seem affected [248]. For example, the G1/S transition is delayed, which is thought to be caused by an inefficient induction of the G1/S transition gene cluster [248]. In particular, the induction of *CLN1* and *CLN2* (G1 cyclins in budding yeast) becomes less efficient as the cell approaches death. Similarly, the S-phase cyclin *CLB5* is induced less efficiently in old cells. Such defects could be due to accumulation and longer residency in the nucleus of *Whi5* (a *Cln2* and G1/S transition repressor) of old mothers. However, more insights are needed to understand the causes of this cell-cycle lengthening properly.

Nevertheless, instead of antagonizing lifespan, longer cell cycles could occur to let the aged cells repair accumulating DNA damage [249]. On the other hand, old cells spend more time in G1, making them grow larger (if their growth rate is not decreased) and could drive the hypertrophy described earlier.

Overall, the cell cycle becomes longer with age and resets in daughter cells. Yet, the mechanisms underlying this phenotype are not really identified, nor is it clear as to whether it participates in the worsening of the cell fitness or if it is a compensatory mechanism.

2.5. Response to environmental changes and sterility

Another well-observed general phenotype of old cells is their difficulty in responding to environmental stimuli. For example, they become less responsive to sexual pheromones, which leads to sexual sterility [250-252]. Similarly, the ability of diploid cells to form spores strongly decreases with age [253].

Overall, the loss of homeostasis of the general processes described in these paragraphs seems to be the consequences of aging rather than causes (though they could worsen the cell's fitness). Therefore, we must describe which organellar and molecular processes fail to better understand the bigger picture of the aging decay.

2.6. DNA damage, mutations, aneuploidy, and loss of heterozygosity

An increase in DNA damages is a conserved hallmark of aging across the tree of life, as seen in the introduction. In yeast, RAD52 foci and other DNA damage markers are more frequent in old cells [248]. Besides, old cells have decreased capacities in repairing single and double-strand breaks (DSB) [254].

In diploid cells, DNA damages, and in particular DSB, can lead to the loss of heterozygosity (LOH) from a gene, and it was shown that the rate of LOH increases with age [255-257].

Similarly, missegregation of chromosomes, aneuploidy, and multinucleated cells [226,248], [258], most likely due to spindle pole body problems (such as multiple SPB per cell) are also more frequent with age [226,248,258].

Of note, telomere attrition, which is also a genomic problem discussed as a potential cause of aging in mammals, is not happening in normal yeasts [259], although telomeres stability has been implicated in yeast aging [260,261].

Nevertheless, it is widely accepted that DNA mutations are not a cause of aging in yeast but rather a late consequence since these defects are inheritable and that daughters cells are rejuvenated (except from very old mothers). Besides, the accumulation of DNA mutations does not correlate with age in yeast [88]. Therefore, the genome most likely remains intact until extreme late ages.

Overall, although DNA damage could be a source of aging, DNA mutations, aneuploidy, and LOH cannot be considered as such since they are propagated to the progeny.

2.7. Mitochondria

Mitochondria have been a major center of attention for aging, not only in yeast [262-264] but also in mammals [265-269]. These complex organelles play a significant role in the homeostasis of the cell since they control many metabolic pathways, in addition to producing Reactive Oxygen Species (see p.41).

Of note, mitochondria have their own DNA, and some cells lose it (often called *ρ0*, or *petite* cells in yeast) [262]. Interestingly, the fraction of petite cells is highly variable (up to a factor of 100) from one strain to the other [257-270], and many lab strains suffer from a high percentage of this defect².

Nevertheless, cells are still viable without mtDNA since respiration is not essential for survival, and the cell can still divide if it can fermentate sugars. However, in this case, the whole lineage is affected [246,262,272,273]; that is, all the daughters also become petite.

As a consequence, the loss of mtDNA does not fit the definition of aging factor. Besides, it has been shown that the probability of this event was not affected by age and was rather purely stochastic [246].

Beyond the petiteness, it seems that mitochondria can be damaged and oxidized during aging but be retained in the mother [274]. Active mechanisms that rely on an actin retrograde transports [275,276] and other molecular complexes [277] are involved in the retention, but how the defective mitochondria are filtered from the healthy one is still unclear. A differential movement speed between oxidized and healthy mitochondria during the actin-mediated transport could explain the filtering [276].

Nonetheless, knowing this risk of transmissible loss of mtDNA, studying mitochondria and aging in yeast can lead to inexact or biased conclusions because of the difficulty to differentiate between transmissible loss of mtDNA and asymmetrical mitochondrial damages. For example, it has been proposed that mitochondria's potential decreases with the cell's age and that the mitochondrial network goes from a tubular to a fragmented morphology to end forming aggregates until their death [264] (Figure 24).

² This questions the relevance of studying natural phenomena in domesticated yeast strains. Indeed, lab strains have evolved towards a more efficient fermentation over a less efficient respiration and stress tolerance [271], and have a different lifespans compared to natural isolates [10].

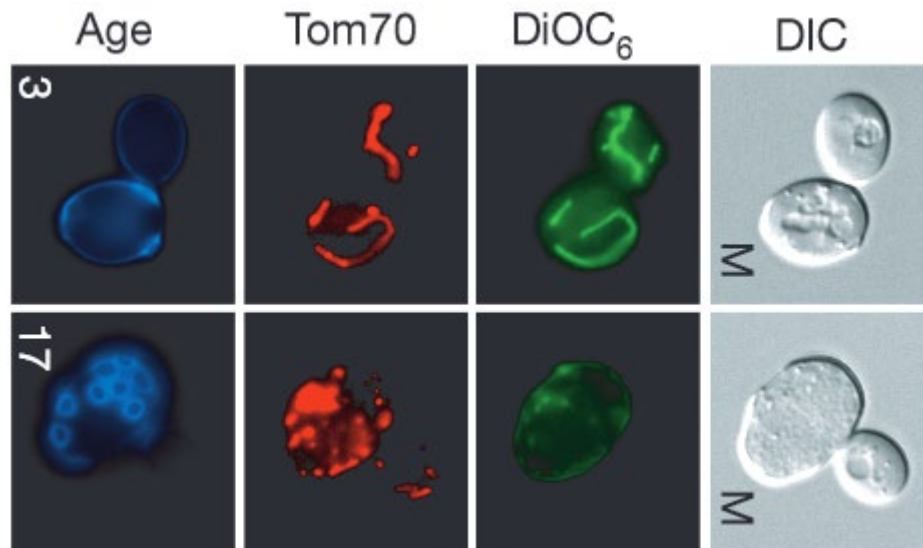


Figure 24: Bud scars (blue), mitochondrial network (red), mitochondrial potential (green), and DIC images of a young (top) and old (bottom) cell. (From [264])

Although mitochondrial fragmentation occurs during respiration [278] and that cells are suspected of going from a fermentative to a respiratory metabolism during aging [279], mitochondrial aggregation can be a sign of petiteness [278]. Thus, this famous study perhaps just describes petiteness (age-independent and transmissible defect) and not mitochondrial aging.

With this being clarified, it is still relevant to understand how mitochondria homeostasis declines with age. Many studies have pointed out the role of iron homeostasis in this phenomenon. Indeed, iron is crucial for the mitochondrial respiratory machinery, and defects in the iron-sulfur (Fe-S) cluster (a form of iron in the cell) pathways have been described as causal for petiteness and mitochondrial decline during aging. In line with that, reinforcing these pathways with mutants leads to increased longevity [262,274,280,281]. Similarly, heme metabolism has been described as a critical factor of mitochondrial decay and aging, with its increase leading to higher RLS [282,283].

How defective mitochondria are toxic to the cell remains unclear since these organelles are central to many metabolic pathways of the cell. The most proposed mechanism is that damaged mitochondria could contribute to the loss of the redox homeostasis by producing more ROS [284,285], which in turn could damage proteins, DNA and lead to genomic instabilities (see p.41). Besides, since the Fe-S clusters are often co-factors of DNA repair enzymes, declining mitochondria could drive genomic instabilities [255].

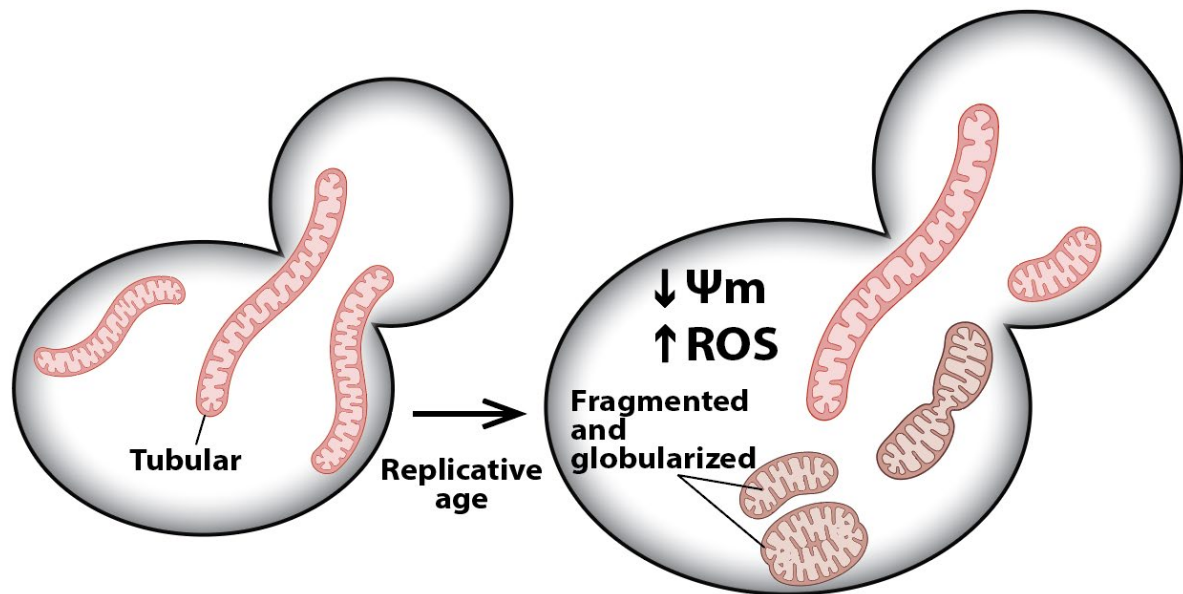


Figure 25: Schematics of the evolution of the mitochondrial state of the cell with replicative age. Young cells (left) represent the normal state with functional tubular mitochondria, while old cells (right) have fragmented and globularized mitochondria with a reduced potential.

Altogether, mitochondria decline with age and are partly causal for aging Figure 25, but it is difficult to distinguish this age-related decline from the accidental loss of mtDNA present in the laboratory strains. Furthermore, the precise mechanisms of rejuvenation and toxicity remain unclear.

Interestingly, mitochondrial functions have been extensively linked to the homeostasis of another cell organelle: the vacuole [264,280,281,286,287].

2.8. Vacuole, cytosolic pH, and mitochondria homeostasis

The vacuole in fungal is an acidic organelle that possesses degradative and storage capacities, in addition to its role in pH- and ion-homeostasis [288,289]. In this sense, it has many similarities with the vacuole in plants or with the lysosome in mammal cells. In the context of aging, this organelle enlarges as the cell ages [221,238,290]. It has been proposed that the morphology of the vacuole has an impact on the replicative lifespan since mutants deleted for vacuolar fusion proteins produce fragmented vacuoles and have a decreased lifespan [290,291], while overexpressing these proteins lead to an increased lifespan. However, this result should be taken with caution since these proteins also affect sterol and ergosterol biosynthesis and could thus influence longevity through other pathways.

Apart from their morphology, the pH of the vacuole has also been described as involved in aging [264,280]. Indeed, acidity in the vacuole is high in young cells and starts dropping very early, whereas daughter cells recover an acidic vacuole. The vacuolar pH is mainly controlled by the V-ATPase, a proton pump encoded in part by VMA1. Overexpression of Vma1 delays the pH drop in the vacuole of old mothers and increases lifespan, placing vacuolar alkalinization as an aging factor.

Interestingly, it turns out that the pH increase in the vacuole is responsible for the mitochondrial declines described in the previous section. Indeed, changing the acidity of the vacuole also alters its ability to store (through proton-dependent amino-acid transporters) essential or toxic amino acids for the mitochondria [264,281].

These results seem to indicate that vacuolar homeostasis, and in particular vacuolar pH, can impact other organelles' homeostasis. However, why this pH fluctuates with aging is still not consensual. It has been proposed that the cell's cytosolic pH increases with age due to an enrichment of Pma1 (an efflux pump of protons) at the membrane of old cells and that daughter cells recover a normal Pma1 concentration and a normal pH. Therefore, the lack of protons in the cytoplasm would, in turn, lead to a loss of acidification of the vacuole since less protons can be pumped into it.

However, this study was, in reality, measuring the cortical pH of the cell and not the cytosolic pH. Indeed, more recent studies tracking cells throughout their lifespan described contrarily that the cytoplasmic pH of cells was dropping with age (from 7.1 to 6.7) as well as the isoelectric point of the proteome [238,292]. They also propose that the alkalinization of the vacuole [293] could be due to a loss of functional V-ATPases, as suggested by a large-scale study on protein stoichiometry [294].

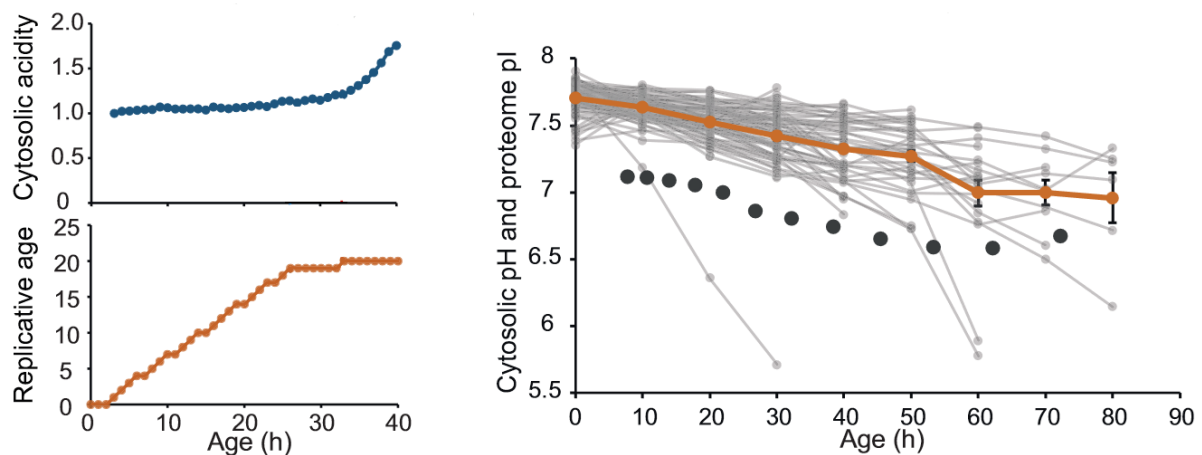


Figure 26: (Left)/ Trace of a single cell's cytosolic acidity and replicative age along time. (Right)/ Cytosolic acidity (single traces in grey, mean, and SEM in orange & black) and estimated proteome pI (black dots) along time.

Further suggesting that vacuolar and cytosolic pH are linked and influence lifespan, a recent report shows that overexpressing VPH2 (a protein required for assembly of V-ATPases) is delaying the cytosolic pH drop during aging, as well as increasing lifespan [292]. Hence, it could be that the loss of vacuolar homeostasis drives the drop in cytosolic pH, and not the contrary.

If vacuolar pH seems to influence lifespan, it is ambiguous for cytosolic pH. Indeed, the drop in cytosolic pH is a late event in life and is not predictive of longevity [238,295]. It could be the direct effect of a metabolic slowdown and lower energy availability occurring in late ages [226,295] since the major proton pumps work with ATP. In line with that, starvation or lower energy states of the cell can cause acidification of the cytoplasm [295-297].

On the other hand, the identity of the cytosol and vacuole are converging during aging, both in size and in pH, which could participate in the multiple problems enunciated previously, such as the proper compartmentalization of amino acids and damaged proteins.

Furthermore, any change of intracellular pH (in any direction) could profoundly impact cell physiology. Indeed, pH influences proton gradient and proton-dependent transports (see previous paragraphs) but also redox potential, enzyme activity, protein folding and solubility, phase separation [296], and many other general processes [298].

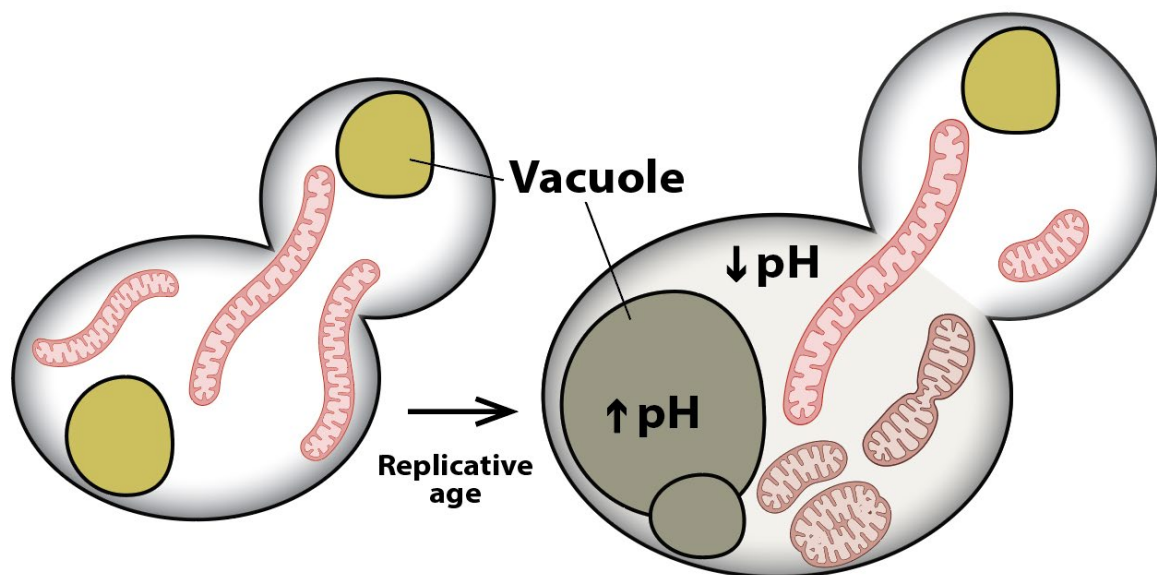


Figure 27: Schematics of the evolution of the vacuolar, mitochondrial, and acidity state of the cell with replicative age. Young cells (left) represent the normal state with small vacuoles and functional tubular mitochondria, while old cells (right) have larger and less acidic vacuoles, which lead to fragmented and globularized mitochondria.

Overall, intracellular pH modification is a consensual hallmark of aging and is reset in daughter cells. Vacuolar alkalization seems to be an aging factor since correcting it

leads to an increased lifespan, but it is less clear if cytosolic pH is a cause or a consequence of aging (Figure 27).

2.9. Reactive Oxygen Species

As discussed earlier (p.11), the link between Reactive Oxygen Species (ROS) and aging has been extensively debated since 1956 [54] in many different organisms, and the conclusions are not consensual.

In yeast, it has been shown that old cells have increased ROS levels [245,285,299]. Moreover, mitochondria from old mothers have a lower redox potential and produce more ROS compared to their daughters [275]

However, some reports show that cells with increased ROS live longer under particular conditions [300] or that the redox state of the cell does not correlate with its lifespan [295]. Besides, mild exposure to oxidative stress is shown to have a hormetic effect by increasing the lifespan [80,301]. **Therefore, ROS could have a hormetic role and whether or not their natural accumulation is causal or consequential of aging, and protective or toxic, is not clear** [302,303]³.

2.10. Carbonylated proteins and protein aggregates

Since ROS levels are high in old cells, one could wonder how this could affect proteostasis. Indeed, upon oxidation, proteins can be cleaved or carbonylated [304] (among other modifications), especially by ROS during aging [305].

Carbonylated proteins and other denatured proteins tend to form aggregates. They are known to interact with chaperon proteins (such as Hsp104 [306]) in charge of the disassembly of these aggregates. Interestingly, carbonylated proteins and Hsp104 foci are found in aging cells [307-312].

These proteins segregate asymmetrically in the mothers, and different models have come up to explain this asymmetry. For example, it has been proposed that this asymmetry is dependent on the actin cytoskeleton and the polarisome, where protein aggregates would be retrogradely transported from the bud to the mother [308,311,313,314]. On the other hand, the geometry of the cell division (growth directed to the bud and low diffusivity between the mother and the bud) and the slow and random movement of these aggregates could explain by themselves the lower amount of aggregates in the bud [310,315].

³ I know, it starts to be repetitive

Besides, it has been shown that Hsp104 is required for asymmetric segregation and that mutants lacking this gene are short-lived. Therefore, it is still unclear if Hsp104 aggregates (and other protein aggregates) act as an aging factor or if they are protective for the cell by sequestering otherwise toxic content [195,316].

Very recently, P-bodies (protein aggregates formed by RNA-binding proteins), known to form under stress or low pH, have been found enriched during aging. Interestingly, their quantity correlates with the remaining lifespan, and cells that leak P-bodies to their bud tend to live longer [292].

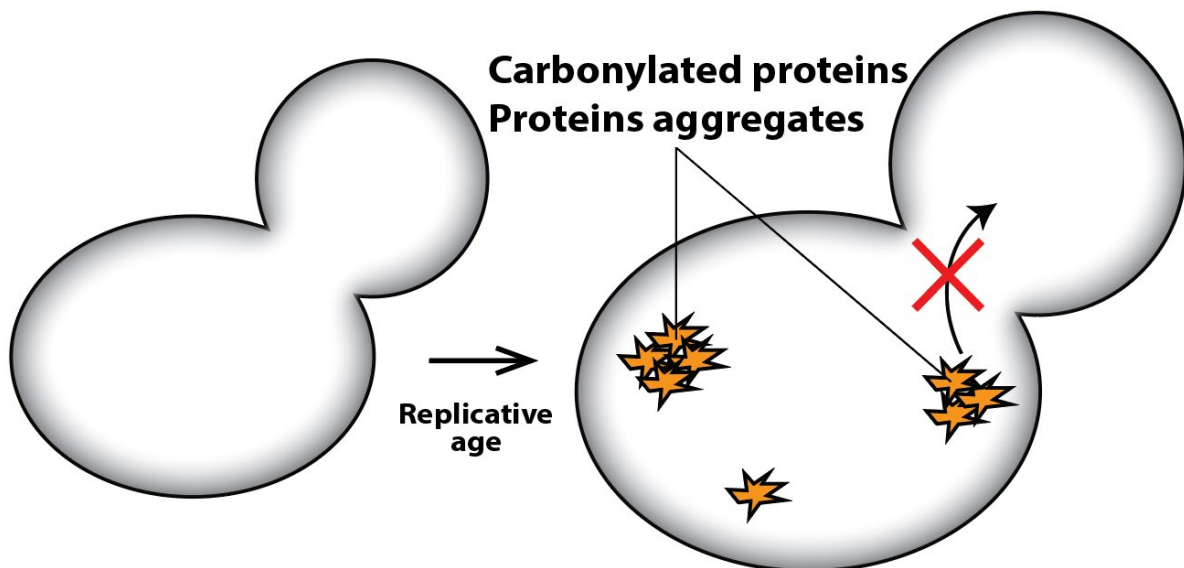


Figure 28: Schematics of the evolution of the presence of protein aggregates with age. Young cells (left) are devoid of these aggregates, while old cells (right) have enriched levels of them, which are not passed to the progeny.

Overall, protein aggregates accumulate in old cells and are not passed to the daughter (Figure 28). However, if these aggregates are toxic or if they participate in the maintenance of cell homeostasis is not consensual.

2.11. Proteostasis and protein stoichiometry

As seen previously (p.14), protein homeostasis is implied in the aging of complex eukaryotes. In yeast, it is mediated by chaperones (as discussed in the previous paragraph) but also by proteasomal activity and autophagy.

A comprehensive study that performed proteome- and transcriptome-wide analysis of aging mother cells [294] showed that the stoichiometry of protein complexes is affected during aging.

Though the cause of this mismatch is not fully explained, the accumulation of P-bodies during aging (detailed in the previous section) - sequestering certain mRNA away from the translation machinery - could play a role in this loss of stoichiometry.

Moreover, old cells also show a decoupling between protein and transcript levels for biogenesis machinery genes such as translation regulation, ribosomes, and tRNA synthesis genes [294].

Interestingly, mutants with increased proteasomal activity have one of the longest RLS described in the literature so far [236,317], much clearer than mutants with improved chaperon activity. This result is to be nuanced since they are also thought to have fewer rDNA instabilities and less ERCs (another aging factor, discussed later) [318] and could therefore act on two different causes of aging simultaneously. However, increasing the proteasomal activity could solve the loss of stoichiometry and the imbalance between proteins and transcript, which would explain the longevity of such mutants.

Similarly, deletion of ribosomal proteins, translation initiation factors, or caloric restriction, all affect protein translation and lead to robust lifespan extension [167,236,319]. Interestingly, pre-ribosome contents have also been noted as upregulated during aging in different studies [226] but do not show loss of stoichiometry, suggesting that they are still functional and active.

Altogether, loss of proteostasis and excessive translation are a strong hallmark of aging - though all the underlying mechanisms are not yet defined.

2.12. Epigenetic alterations

In yeast, epigenetic control of DNA expression is solely mediated by the chromatin state, which is mainly controlled by histone content and acetylation since there is no known DNA methylation pattern in this organism [320] (as opposed to drosophila or mammals).

During aging, acetylation of H4 at lysine 16 (H4K16) increases, notably at the rDNA and subtelomeric regions, and deacetylation of H3K56 decreases [321]. Of note, the H4K16 acetylation state is mediated by the sirtuin Sir2, an NAD⁺-dependent histone deacetylase, which levels decrease during aging [321]. In line with that, deletion or overexpression of Sir2 greatly reduces or increases lifespan (respectively), though this effect is also due to modified recombinations in the rDNA (discussed later) [99,322]. Similarly, specific deletion in the chromatin-modifying SAGA complex greatly enhances longevity [323].

Additionally, histone levels are also reported as going down during aging, which could be partly due to increased DNA damages in old cells (see p.35) since it can trigger histone degradation [99,258]. This phenotype does not seem to be a pure byproduct of aging but to be part of its cause, since increasing histone transcription, translation, or blocking histone degradation, increases lifespan [99,258] while decreasing the amount of histone negatively affects lifespan [324].

However, these results are not consensual since several studies report an increase of histones H2B levels with aging [226]. In addition, partial deletion of histones H3 and H4 (hence, theoretical decrease in histone content) promotes longevity, though this has been attributed to hormetic activation of the chromatin architecture defect response [325].

Moreover, not only are the histone state and content thought to be modified during aging, but also the nucleosomes, which show a decreased abundance in the chromatin as well as increasing mispositioning [326]. Yet, whether this is an aging factor is contested because deletion of ISW2, a chromatin remodeling enzyme, decreases nucleosome levels and increases lifespan [327].

Contrariwise, a recent study using ATAC-seq assays showed that the nucleosome occupancy was globally unchanged with age [318] and that the previous measurements were most probably biased by the dead cells from the population (since dead cells lose their nucleosomes).

Despite these discrepancies, pervasive transcription of non-coding RNA [318,328-330] and general transcriptional induction of all genes [326] seems to happen during aging.

Altogether, epigenetic alterations and loss of silencing appear to be a hallmark of aging, even though the causality of these phenotypes relative to aging is debated.

2.13. Nutrient sensing and metabolism

Nutrient sensing and metabolic pathways are the most conserved players in aging (see p.18). In yeast, aging is accompanied by a change in carbon metabolism, with cells decreasing glycolysis while increasing gluconeogenesis, energy storage, and respiration [279,303,331]. The fact that cells grow larger with age leads to a decrease in surface-to-volume ratio, and it has been proposed that fluxes with the environment - such as nutrient uptake - could be reduced and trigger starvation cues [279,332,333]. This is supported by proteomic analyses in which proteins of the starvation response are enriched in old cells [294]. Besides, the

growth rate of cells decreases in late ages [226], which could be a consequence of nutrient availability.

However, and as for many aging phenotypes, if this is a cause of aging or just a consequence remains unclear.

Besides, it seems that the nutrient-sensing pathways such as TOR are somewhat hyperactivated during aging. In line with that, deletion of TOR1 or SCH9 (a protein kinase downstream of TOR1) increases lifespan [150], as well as caloric restriction [157,231,334] or caloric restriction mimetics in strains deleted for a glucose transporter [334]. Of note, a meta-analysis argues that caloric restriction does not elicit such a robust effect on lifespan in yeast and that the previous positive results were due to analysis biases [335].

To explain their lifespan extension properties (if they exist), it is proposed that since these pathways control ribosome biogenesis and protein translation, their deregulation could be linked with the loss of protein stoichiometry and proteostasis described in the previous section. Moreover, they regulate histone remodeling [325,327] as well as the rDNA stability [336], which has been extensively pointed as involved in yeast aging (discussed p.48).

Altogether, nutrient sensing and metabolism seem to be central in the modulation of aging and are deregulated during this process. Yet, their strong pleiotropy makes it difficult to conclude about their effect on specific pathways.

2.14. Nucleus and nuclear pores

The karyoplasmic ratio (also called nuclear-cytoplasmic ratio, abbreviated N/C ratio here) is the quotient of the nucleus volume divided by the total volume of the cell. This value is very tightly regulated under normal conditions and conserved in many contexts, not only in budding yeast but also in *S. pombe*, mammal cells, and *Xenopus* [337-340]. Its homeostasis is thought to play a role in the global homeostasis of the cell since it dictates, and is dictated by, the flux of matters between the two major compartments of the cell [339,340].

Despite this tight regulation, the size of the nucleus increases with age, and at a faster rate than the cytoplasm [226]. This increase of the N/C ratio is accompanied by an increase of nuclear content, ranging from histones to fluorescent proteins with a simple Nuclear Localization Signal (NLS) [226,341]. Of note, a known regulator of the N/C ratio is the transport of matter in and out of the nucleus (called nucleocytoplasmic transport)[339,340], which mainly goes through the Nuclear Pore Complexes (NPCs)(Figure 29).

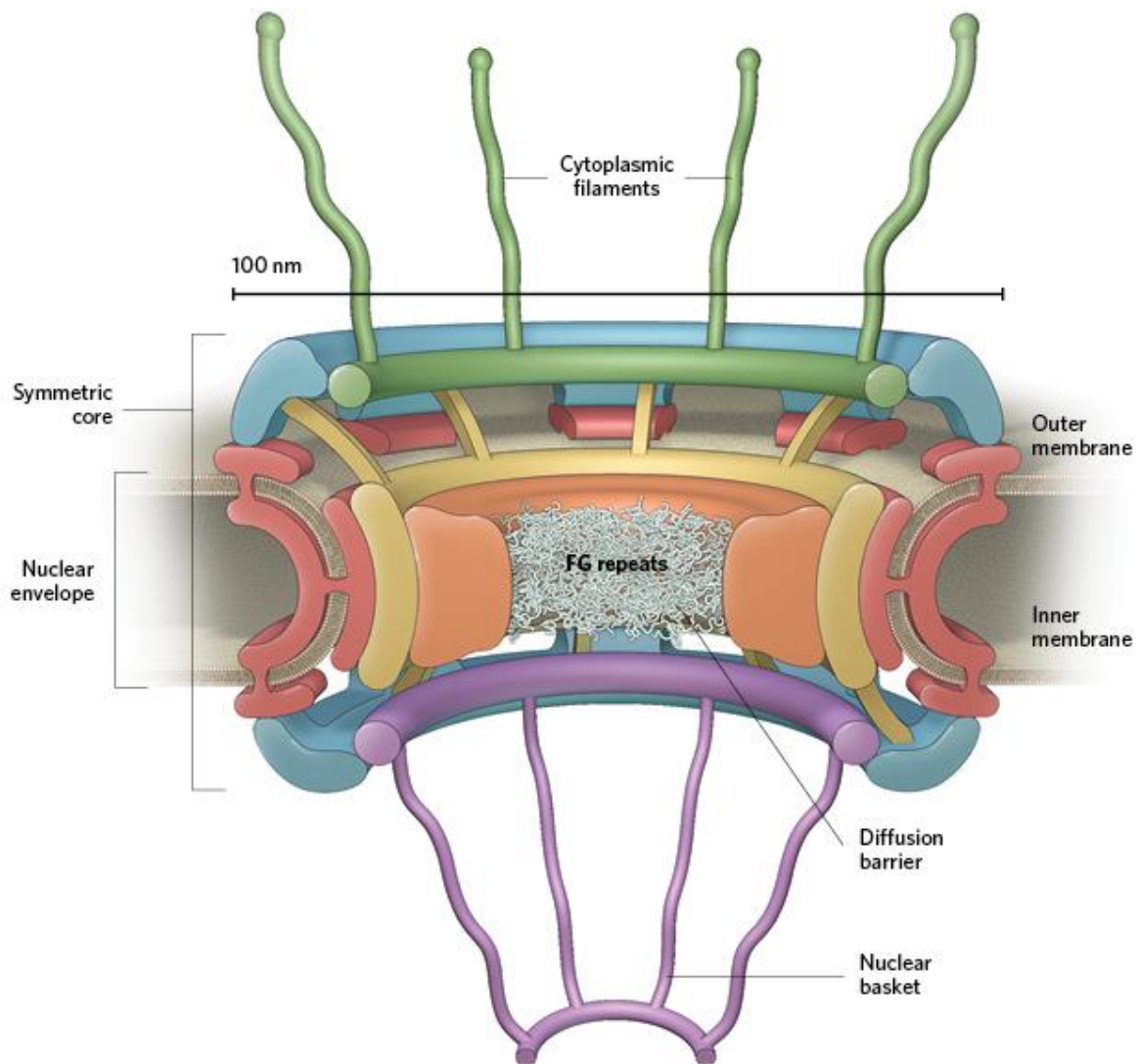


Figure 29: Schematics of one nuclear pore complex (Figure from [342])

The NPC is one of the largest complexes in yeast in terms of protein numbers and size [343] and has several crucial functions required for cell homeostasis. It is primarily known for allowing exchanges of proteins and RNA between the cytosol and the nucleoplasm, and this exchange is mediated by karyopherins (importins and exportins). However, NPCs also have gene regulation functions with their ability to interact with chromatin and therefore promote efficient transcription [344] by bringing the transcriptional, splicing, and nuclear export machinery into close functional context [345,346]. Similarly, NPCs, and in particular their nuclear basket, can filter pre-mRNA from mature mRNA and therefore play a role in splicing quality control [347].

Along the same line, they also seem to be involved in DNA repair (including rDNA) [348-351], and more generally, they can exert spatial control on DNA by tethering it to the nuclear membrane.

In yeast, a growing body of evidence suggests that NPCs also play a role in cell identity between the daughter and the mother. In fact, they get specifically deacetylated in daughter cells which then impact other cellular processes such as the cell cycle [352,353]. Moreover, studies suggest that old or damaged pores are kept in the mother [194,354,355], further contributing to the segregation of biological material between mother and daughter and to the asymmetry in general.

In the aging context, it has been established that the NPC homeostasis was destabilized, not only in yeast but also in other cell types (mitotic and non-mitotic) [341,356-358]. For example, the NPCs stoichiometry is one of the most affected complex during yeast replicative aging [294]. This could partly be explained by the fact that some components of the pores, such as the core scaffold, are very long-lived, while others (such as FG-Nups) have a high turnover [359]. Consequently, a change in protein homeostasis would differentially affect these different components.

Moreover, NPC assembly, quality control, and maintenance machinery are also decreasing during aging [341], which leads to more pores being misassembled and not cleared from the nuclear envelope of old mothers, thus accumulating. Indeed, signals of NPC assembly problems are detected in old cells three times more frequently than in young cells. In addition, it seems that old misassembled pores are covered by the nuclear envelope (NE), leading to local herniation of the NE [341].

Notably, a decrease in several nucleoporins (components of the NPCs) was correlated with a shorter lifespan, while deletion of some other nucleoporins led to increased longevity [341,360,361]. Furthermore, affecting specific nucleoporins can, in turn, have beneficial effects by tuning down other pathways implied in aging, such as translation [360,361].

If NPCs lose their integrity during aging and if this loss is toxic to the cell, how to explain the daughter cell rejuvenation? Several studies show that NPCs from the mother are not passed to the daughter because of a diffusion barrier present during mitosis at the nuclear membrane (discussed p.45) [354-356]. Hence, old and damaged pores can be retained in the mother, and daughter cells are born with new functional pores.

Then, how are the NPCs damaged during aging? It has been proposed that some nucleoporins are carbonylated during aging (due to a high level of ROS, for example) [362], but recent studies and modeling suggest that it might not be the case for several nucleoporins [341,363].

This destabilization could then come from the binding to the pores of rDNA circles (discussed later), which lead to the loss of the nuclear basket from the NPC [358]. In line with that, proteomics on old cells found that several proteins from the nuclear basket were missing (though, not precisely the same) [341,357]

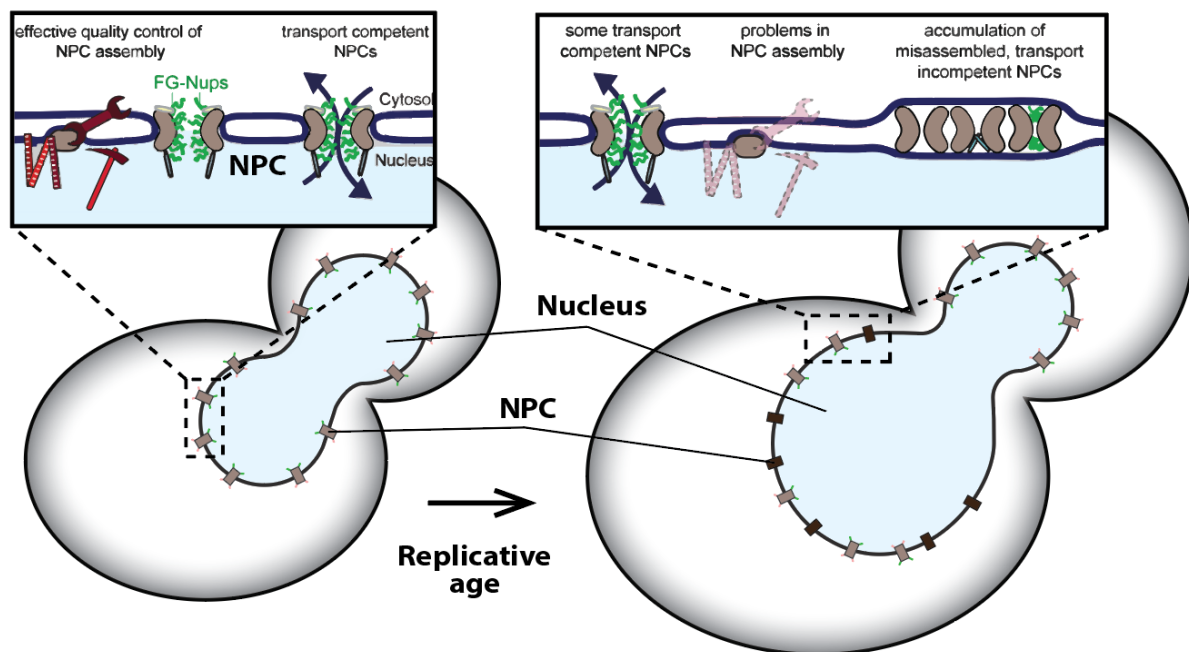


Figure 30: Schematics of the evolution of the nuclear state of cells with replicative age. Young cells (left) represent the normal state with a normal N/C ratio, functional pores, and active NPC assembly and quality control machinery. Old cells (right) have a larger nucleus with defective or remodeled pores (adapted from [238])

Altogether, NPC remodeling and destabilization can be considered as an aging factor (Figure 30). They are increasingly present in old cells but not in daughters, and alteration of the NPCs' stoichiometry can positively affect the lifespan. Besides, this loss of NPC integrity could explain the increased N/C ratio and compartmentalization in the nucleus.

2.15. Nucleolus and rDNA

Another source of deregulation in the nucleus could arise from the nucleolus. This crescent-shaped sub-compartment of the nucleus contains the ribosomal DNA (rDNA) and is the place of rRNA transcription, processing, and parts of the ribosomal assembly [364,365] (Figure 31).

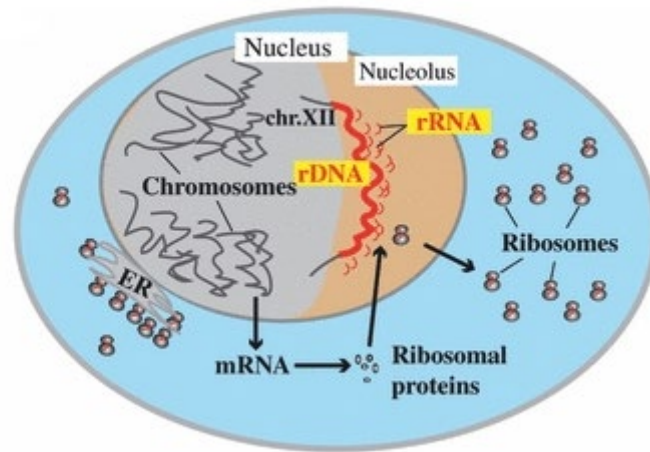


Figure 31: Schematics of the nucleolus place and role in the cell. This crescent shape subcompartment (brown) of the nucleus (grey) contains the rDNA (thick red line). rRNA (small red lines) are also transcribed in the nucleolus. Besides, the mRNA of ribosomal proteins is exported to the cytoplasm to be translated. Then, the ribosomal proteins are imported to the nucleolus to form mature ribosomes. Then, ribosomes are exported to the cytoplasm to translate various proteins, mostly at the endoplasmic reticulum (ER)(From [366])

In the context of aging, it is found to increase in size, to become fragmented, and the transcriptional activity happening there is also strongly upregulated [226,258,367,368]. Moreover, more DNA recombinations happen at this particular locus, which is thought to be causal for aging (see following paragraphs).

This makes it not only a hallmark of aging but also a significant center of aging deregulation since it is where the ribosomes biogenesis starts, and that ribosomes are highly implied in aging (see p.44).

Interestingly, this hallmark is conserved across many organisms and predictive of longevity [367,369,370].

For these reasons and because we will partly focus on the rDNA in the results part, a particular elaboration will be made in the next section.

2.15.1. The architecture of the rDNA locus

In most eukaryotes, the rDNA locus is composed of long tandem repeats [371,372]. In yeast, it is made of 100-200 repeats [373] of size 9.1kb and located on chromosome XII. The number of repeats is not fixed and can vary between mutants, strains, and culture conditions [374]. Importantly, each repeat comprises a 35S and a 5S gene coding for the precursors of the ribosome subunits. The RNA Polymerase I transcribes the 35S (abbreviated Pol I here) to form different rRNA precursors after processing, while the 5S is transcribed by Pol III.

The metabolic cost of rRNA and ribosomes synthesis is immense since 60% of all the ribonucleotides are consumed by Pol I for the sole transcription of the 35S, and 50% of the total activity of Pol II is dedicated to ribosomal proteins. [375,376]. Hence, the transcription of a single rDNA gene is not sufficient to allow fast cellular growth, which explains why the rDNA locus is composed of several dozens of repeats [377]. Interestingly, the number of rDNA repeats can rapidly adapt by recombinations (in a matter of tens of generations at the population level [240]), depending on the environment [378] (which can be considered as an evolutive adaptation). Besides, the repeats are transcriptionally controlled, with approximately half of them being transcribed by Pol I at a given time and the other half being silenced by chromatin organization [377,379-381]. Altogether, this shows that the rDNA locus is very adaptable at the timescale of the cell division but also in the longer term to ensure tight regulation of the rRNA levels and fit cellular demands. This also means that the ribosome biogenesis (and in particular, rRNA transcription), is very dependent on the nutrient availability in the cell [336,382-384]. For example, the TORC1 complex (whose repression increases lifespan, see p.44) controls many steps of the ribosome biogenesis and, in particular, the Pol I transcription of the 35S [385,386] and the Pol III transcription of the 5S [387].

These particular properties are in part conferred by sequences present on two intergenic spacers (IGS1 and IGS2) that lie in between the 35S and the 5S (Figure 32).

For example, in the IGS1, the bidirectional promoter known as E-pro, transcribed by Pol II and silenced by Sir2 (Sir2 is a histone deacetylase, see p.43), is thought to regulate rDNA recombination by modulating the cohesion of sister chromatids [329,330] (discussed in the next section). Each repeat also has an origin of replication (or Autonomously Replication Sequence, ARS) for efficient replication of the whole rDNA locus. In the IGS2, a Replication Fork Barrier (RFB) sequence, active when Fob1 binds to it [388-390], prevents collisions between the transcription and the replication machinery.

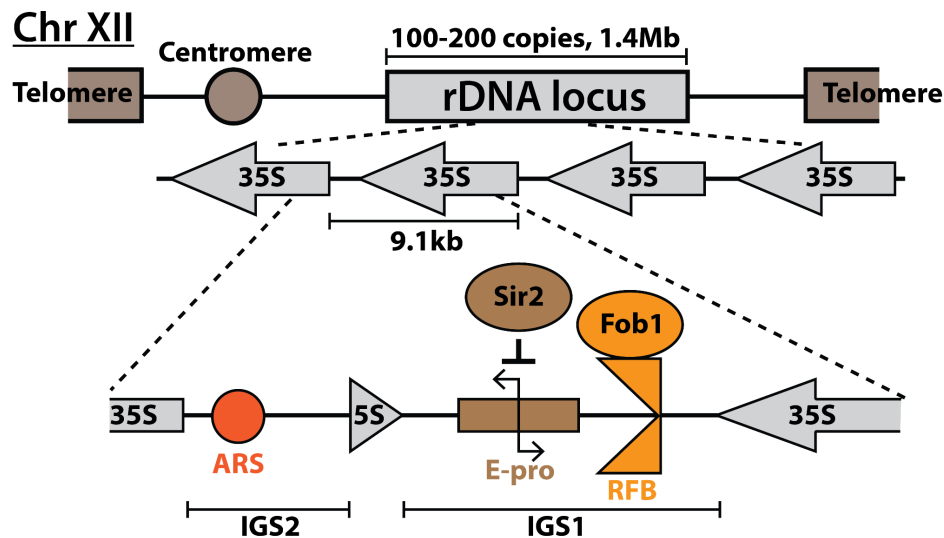


Figure 32: Schematics of the architecture of the rDNA locus

2.15.2. rDNA silencing

An important regulatory part of the rDNA passes through the Pol II transcription of the IGS1 and IGS2. Initially, these spacers were called NST1 and NTS2 (for Non Transcribed Spacer). However, it is now known that they are naturally transcribed by Pol II, producing non-coding RNA (ncRNA) [391-394], and in particular from the E-pro promoter. IGS1 and IGS2 are mainly silenced by Sir2 [389,395] via its histone deacetylase function, and of note, **Sir2 does not directly regulate Pol1 transcription or silencing** [396,397]. Interestingly and non-intuitively, the rDNA silencing of Pol II requires Pol I transcription [394,398,399], though only a part of the mechanism is understood ([400] for more details).

As to Pol I transcription, the repeats are transcriptionally controlled, with approximately half of them being transcribed by Pol I at a given time and the other half being silenced by chromatin organization [377,379-381] (as enunciated previously). Adding more repeats does not modify the number of active genes (*i.e.*, not silenced), and modifying the number of active genes does not modify the number of genes being transcribed. Altogether, this suggests that rRNA synthesis is controlled by the chromatin state of the repeats and by the initiation of Pol I onto them [381].

Nevertheless, what controls these two processes remains partially unknown. Relative to the chromatin state, its control is very complex and will not be detailed here. Briefly, several complexes are known to affect the acetylation, methylation, or ubiquitination of different histones at the 35S, such as Nop1 or Torc1 [401-403].

Concerning the activation of Pol I, several proteins such as Rrn3 and Net1 are known to promote its transcription of the 35S gene [404-407].

However, more research needs to be done to unveil the exact molecular mechanisms of these regulations and understand how the cell decides to transcribe some repeats and silence others.

Altogether, the transcription and silencing of the rDNA repeats are tightly controlled, not only in its coding sequences but also in the intergenic one. Interestingly, a link exists between the transcription of the repeats and their ability to change their number.

2.15.3. rDNA plasticity

The rDNA is the most unstable region of the genome because of its highly repetitive nature, its high recombination rate, and because it is heavily and constantly transcribed (except in anaphase) [374,408]. This high recombination rate gives the ability to the rDNA array to modify its number of copies to fit the cell needs (in a matter of hundreds of divisions) but can be detrimental and toxic in specific contexts, such as replicative aging.

The recombination mechanisms are well described. Indeed, recombination occurs after a DSB, most of them (but not all [409]) being caused by a stalling of the replication fork at the RFB formed by Fob1 [388-390,410] (Figure 33, top).

The repair can be done (mainly) in three ways: equal sister chromatid recombination, unequal sister chromatid recombination (USCR), and intrachromosomal homologous recombination. The first one uses the copy at the same location on the sister chromatid, and in this case, the repair does not change the number of copies (Figure 33, left). In the case of USCR, the broken end invades into a misaligned sequence on the sister chromatid, and the repair results in amplification or deletion of rDNA copies [411,412] (Figure 33, middle). This is the primary way the rDNA array changes its copy number [372,373,408]. **Similarly, the broken strand can recombine with itself at another repeat (Figure 33, right), which will lead to the formation of an rDNA circle, also called Extrachromosomal rDNA Circle (ERC).**

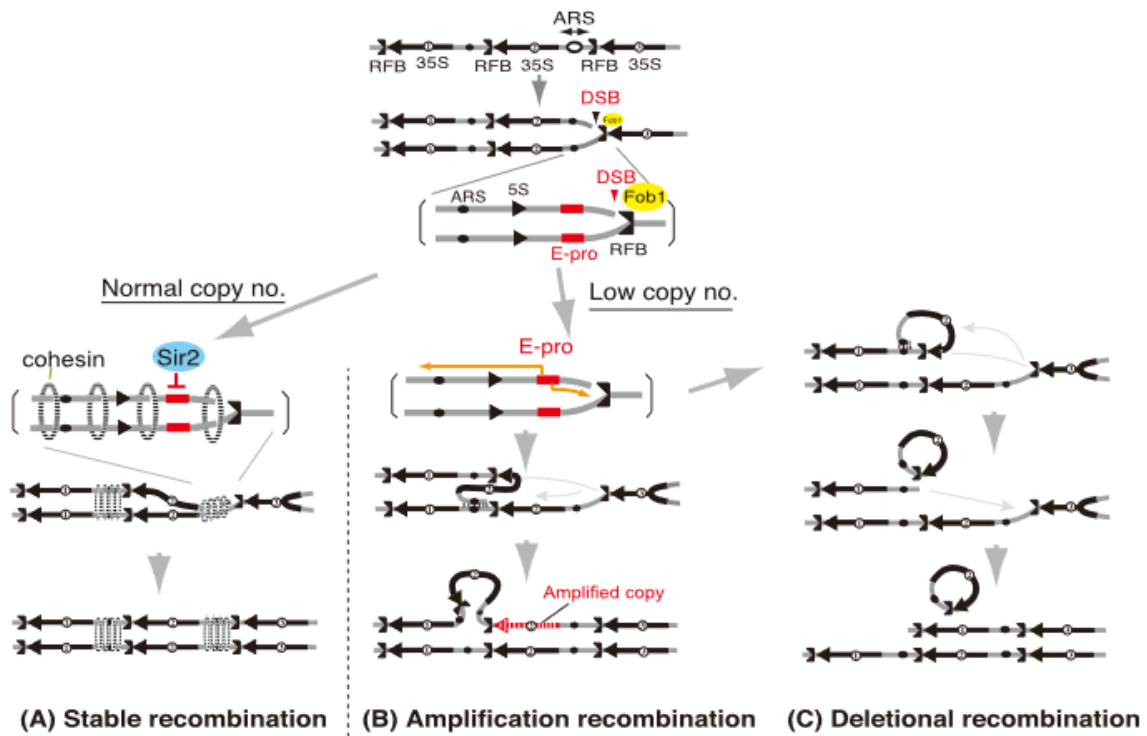


Figure 33: Schematics of the different scenarios after a DSB in the rDNA, mostly occurring at the RFB (top). (From [374])

Interestingly, the cell is able to sense its number of copies and control it since halving the copy number in a strain results in a gradual expansion of the array to get back to equilibrium in a Fob1 dependent manner [410]. Of note, more recent reports show that ERCs can reintegrate into the genome to help modulate the rDNA copy number as well [378,413]. How the cells “count” their number of copies and active copies is a fascinating question that is still not fully answered [414,415].

If these recombination mechanisms confer expansion and contraction properties to the rDNA array, it can also create instabilities in certain contexts. The rDNA instability refers to the heterogeneity of the rDNA array size among a population that can be measured by the sharpness of the band of a gel generated by pulsed-field electrophoresis (Figure 34). Screening the deletion mutant database using this technique reveals that 10% of the genome impacts rDNA stability [374,416].

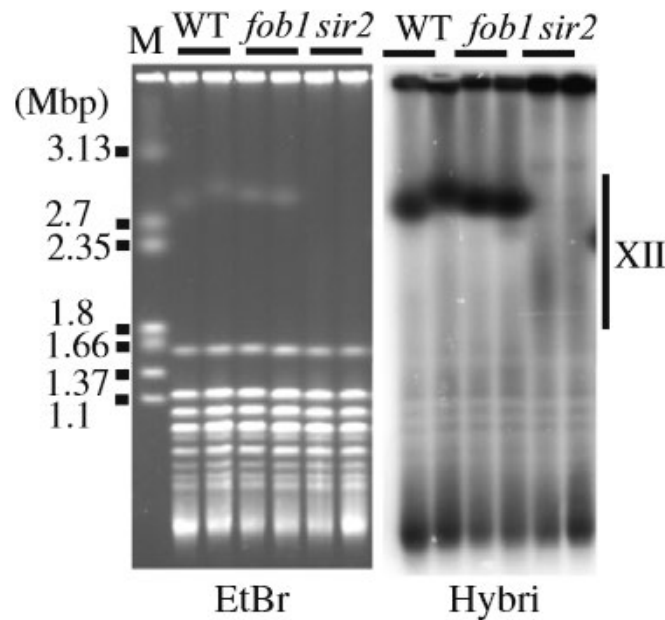


Figure 34: Total DNA gel revealed by EtBr (left) and rDNA revealed by a specific hybridization probe (right). WT and fob1 conditions have sharp bands, while the sir2 bands are smeared and undetectable due to the size variation among cells (From [417])

2.15.4. The link between rDNA transcription, silencing, and recombination

A close link exists between Pol I & Pol II transcription and rDNA recombinations.

First, the silencing activity of Sir2 at the ncRNA is necessary to repress the expansion of the array [372,415]. The main explanation is that transcription at the E-pro - which is repressed by Sir2 - stimulates USCR and intra-chromosomal recombinations by removing cohesin from the DSB [330,418-420](see Figure 33). Additionally, Pol I transcription on the repeat seems necessary for the RFB to be in place and the DSB to appear [409].

To summarize the main points of this section, rDNA recombinations are a way for the cells to control their rDNA copy number. Transcription of the E-pro promoter, normally silenced by Sir2, is linked with modifications of the rDNA size and ERC excision after a DSB that mainly depends on Fob1 association with the RFB.

2.15.5. rDNA instability during aging

Back to aging, the rDNA silencing of Pol II targets and Pol II transcription impacts lifespan, with increasing H4K16 acetylation or decreasing Sir2 levels negatively impacting longevity and vice-versa [321]. This is thought to be mediated by unwanted variation in the rDNA array size (called rDNA instability) as well as the production of ERCs.

The rDNA instability theory of aging [417,421,422] suggests that the rDNA copy numbers variates during aging, which would, in turn, alter the expression of important genes (typically,

ribosomal genes). In addition, rDNA instability would trigger global genomic instabilities and increase replication stress, leading to senescence [330,421,422]. If this theory is seducing because a correlation between the rDNA stability and certain longevity mutants exists, it lacks an important criterion. According to the definition of an aging factor, if rDNA instability causes aging, it should be present in the mother but not in the daughter. However, the same DNA (and in particular, rDNA) segregates to both cells, and even if putative mechanisms have been proposed to solve this contradiction [366,421], further experiments will be required to back this model.

Apart from variabilities in the rDNA size, several other rDNA-related phenotypes are observed during aging. For example, old cells show more Pol I transcription, suggesting a global loss of silencing of Pol I transcription and an increase of its activation [226]. Pol II silencing also decreases at the rDNA locus, with an accumulation of ncRNA transcripts from the two IGS being detected [328,330,423] as well as an increase in H3K16 acetylation [321]. Besides, cohesin is lost during aging, which could participate in the increase of USCR observed during aging [330].

Finally, ERCs are also enriched in old mother cells [226,424].

How these nucleolus and rDNA deregulations - namely a larger and fragmented nucleolus, greater variation in the rDNA array size, a higher number of ERCs, a higher Pol I transcription, and a higher Pol II transcription of IGS1/2 - are linked during aging remains unclear and debated (Figure 35). Nevertheless, it seems that the rDNA regulation is a core feature of the process of replicative aging, which is confirmed by Quantitative Trait Locus analyses across very different budding yeast strains [202,210].

From that, another model of aging implies the rDNA has received extensive backing, namely: the ERC theory of aging.

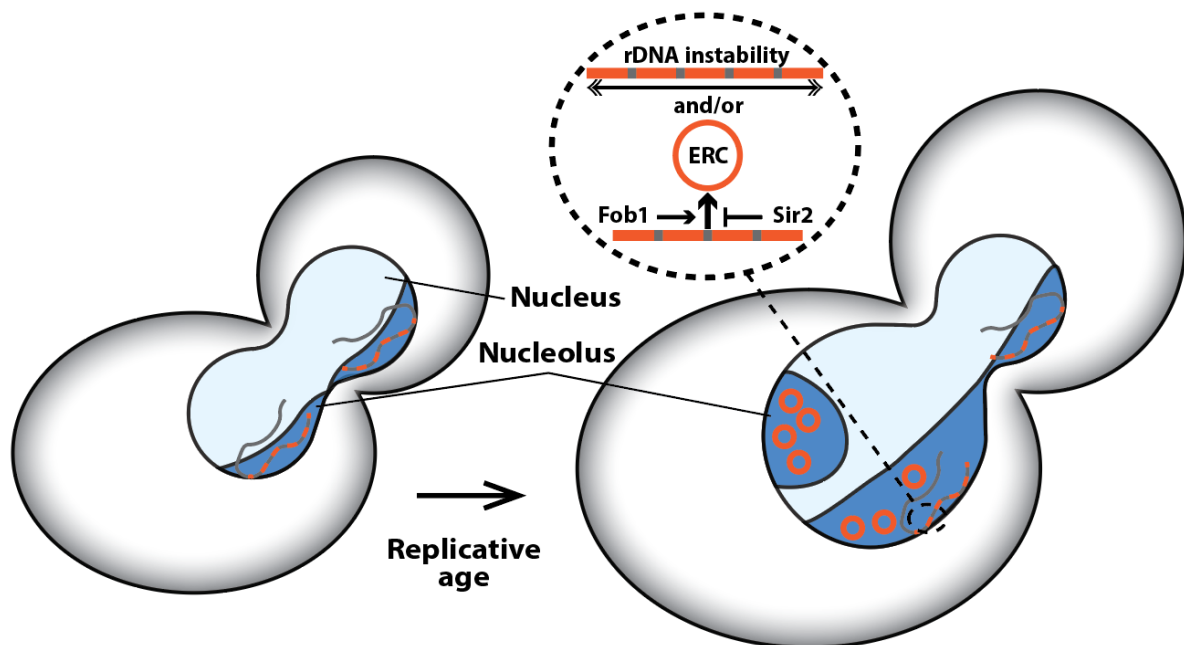


Figure 35: Schematics of the evolution of the nucleolus and rDNA state with replicative age. Young cells (left) represent the normal state, while old cells have a bigger nucleolus, rDNA instabilities, and ERCs (right).

2.16. Extrachromosomal rDNA Circles

As briefly enunciated in the previous section, ERCs are created after a DSB repair caused by a stalling of the DNA polymerase at Fob1 if the recombination occurs when the sister chromatids are not held together by cohesin (which is mediated by Sir2 silencing). Interestingly, ERCs can be observed using gel electrophoresis and have been shown to accumulate in old mothers and be an aging factor [424]. Indeed, the *fob1Δ* mutant as well as mutants overexpressing Sir2, accumulate less ERCs during aging and are long-lived [322,425]. On the contrary, the *sir2Δ* mutant accumulates many ERCs and is short-lived. More recently, ERCs accumulation has been monitored at the single-cell level and their level correlates with the RLS [226]. Importantly, their level is reset to zero in daughter cells [226]. **Overall, ERCs accumulate in old cells, are not transmitted to the daughter, and are toxic for the cell.**

In the following sections, we will see how ERCs accumulate in old cells and the putative mechanisms behind their toxicity.

2.16.1. Accumulation of ERCs

So far, we have described how ERCs are excised from the genome but not how they accumulate in the mother cell. In fact, since each rDNA repeat (and therefore, each ERC) contains an origin of replication (ARS, see p.49), each ERCs can replicate at each division.

Recently, a study tagging each ERC with a LacO LacI-GFP system and tracking them throughout aging showed that the doubling time of the ERC pool takes 1.5 divisions, suggesting that two-thirds of the ERCs are replicated at each division [226].

Besides, since the daughter cells are born free of ERCs (except daughters of very old mothers) [226], it means that the ERCs are highly retained in the mother and thus, that their number increases exponentially.

Therefore, how to explain this highly asymmetric segregation? Previous mathematical modeling predicted that a retention of 0.99 was needed to recapitulate experimental survival curves [426]. Later on, a diffusion model suggested that freely diffusing plasmids are not likely to go through the bud neck since it is a small area only opened during the short window of anaphase and that plasmids are not highly diffusive. Nevertheless, such a model can only account for a retention frequency of 0.75-0.90 [427].

This suggests that another mechanism of segregation is at play. Indeed, yeast has a closed mitosis during which a septin-dependent lateral diffusion barrier is formed around the outer nuclear membrane. This barrier strongly impairs the diffusion of proteins embedded in the outer nuclear membrane [428], such as NPCs (Figure 36). Indeed, using Fluorescence Loss in Photobleaching (FLIP) on tagged nucleoporins showed that the pores from the mother are not passed to the daughter, thanks to a septin-dependent diffusion barrier [354]. Similar results were obtained by tagging an artificial plasmid, suggesting that ERCs could bind to the NPCs. In line with that, weakening the barrier with mutants such as *bud6Δ* increases the leaking of old NPCs and of tagged plasmids to the daughter. Moreover, this mutant displays increased longevity that does not depend on Fob1, still experience excisions but accumulate less ERC, suggesting that the ERCs are leaked to the bud. Altogether, the retention of the nuclear pores of the mother cell could be the way cells retain ERCs in the mother (Figure 36).

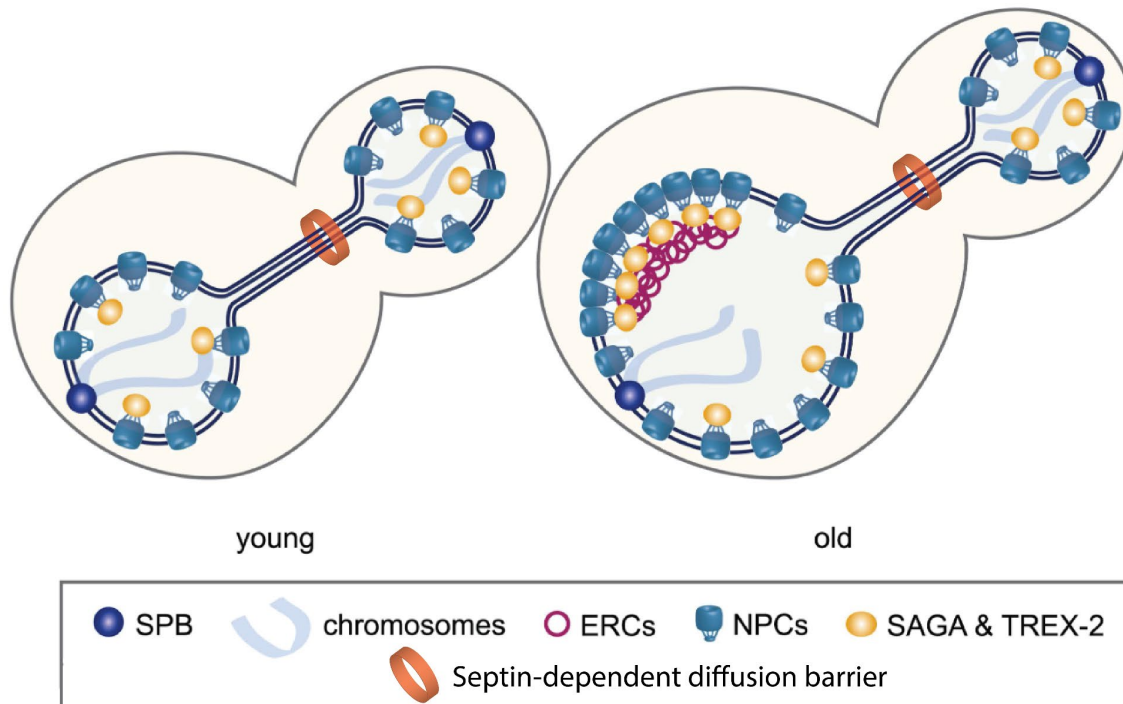


Figure 36: Schematics of a model of ERC retention in the mother. ERCs attach to the NPC with the SAGA & TREX2 complexes, and NPCs cannot pass the septin-dependent diffusion barrier. Hence, ERCs stay in the mother (adapted from [194]).

Further refinement of this model [354,356] showed that the circles need to be bound to stable parts of the NPCs in order to be able to not diffuse to the bud. Indeed, anchoring the circles to the nuclear basket (Mlp1 or Nup2, for example) leads to their free diffusion in the bud [429], whereas tethering to more stable parts ensures proper retention in the mother [356]. What mediates this anchoring is also partially known and involves the SAGA and TREX-2 (which associates with the NPCs) complexes. Indeed, deleting specific proteins from SAGA leads to the leaking of circles to the bud, while artificial tethering to the pores bypasses the need for these proteins for proper retention.

From then, how are these circles recognized by the cell compared to other transmitted plasmids? Beyond the fact that the presence of a centromere sequence leads to equal segregation, a long-standing observation is that plasmids with an ARS are highly retained in the mother cell (only 1 out of 10 leaks to the bud) [430] and that the stronger the ARS, the higher the retention [431]. In line with that, previous ChIP data indicate that ARS are targets of SAGA and that SAGA targets preferentially non-centromeric circles [356,432]. Thus, SAGA has a high affinity with non-centromeric and autonomously replicating plasmids.

Beyond the context of aging and ERCs, this could be a general mechanism for yeast to prevent the spread of extrachromosomal DNA (foreign or endogenous) in the population by retaining replicating circles in the mother.

Altogether, this suggests that asymmetric segregation of ERCs could be partially mediated by anchoring non-centromeric circles to the NPCs of the mother, which are not passed to the daughter. Yet, this model relies on experiments with artificial model plasmids and has never been assessed with ERCs directly.

2.16.2. Toxicity of ERCs

In addition to the fact that *fob1Δ*, *sir2Δ* and other mutants affecting the number of ERCs have a corresponding lifespan, the most substantial evidence of the toxicity of ERCs comes from the original study [368]. There, the authors used an ectopic plasmid containing an rDNA repeat as well as an excisable centromere (using a *LoxP* and *Cre*-recombinase system). When the plasmid has the CEN, it segregates symmetrically between the mother and the daughter, and the cells have a normal RLS. Excising the CEN leads to the accumulation of the plasmid in the mother and to a reduction of lifespan, hence proving the toxicity of having many ERC. However, some discrepancy remains since modifying the ARS of the rDNA, which influences ERC accumulation, does not always correlate with RLS [417]. Indeed, cells engineered with a weaker ARS are short-lived, even though cells with a stronger ARS are also short-lived, more than cells with the weaker ARS. Therefore, having a weaker ARS or an ARS that is not adapted to the rest of the array could induce detrimental effects, independently of ERC accumulation. Conversely, another study showed that exchanging ARS between different strains leads to a change in lifespan, with having a stronger ARS decreasing RLS and vice-versa [202], and mutants decreasing the ARS efficiency are also long-lived [424].

If the ERC accumulation is widely admitted as to be toxic for the cells, the reason behind this toxicity remains unclear.

Simple experiments with an empty plasmid containing an ARS show that these circles of DNA are sufficient to induce a reduction in lifespan, which is rescued by adding a CEN to the plasmid [424,433]. Hence, it is possible that accumulating plasmids causes aging, independently of if they contain rDNA sequence or not. To explain that, it has been proposed that ERCs could titrate important factors away from their usual action sites, thus disrupting the cell homeostasis. For example, ERCs could bind with histones, chromatin modifiers, and other parts of the silencing machinery, thus leading to the observed global derepression of expression. They could also induce longer DNA replication, as suggested by the fact that yeast mutant over-amplifying 2 μ DNA circles possess a longer S-phase [434].

If the sequence plays a role in the toxicity (though the few available data argue it is not the case), ERCs could also titrate important transcription factors for cell cycle and growth. In fact, the DNA sequence of these circles contains binding sites for the Swi4/Swi6 (SBF) and the Mbp1/Swi6 (MBF) transcription factors, on which depend the transcription of genes from the G1/S regulon (Wittenberg and Reed 2005). In line with that, it has been shown that reducing the number of ERCs in the mother during its lifespan makes it recover a normal Cln2 level activator of S phase). However, this result is weak since the authors used a nucleolar marker as a marker for ERCs, and did not check if the reduction of nucleolar size (interpreted as ERCs number) was linked to a reduction in cell-cycle duration [248].

Besides, since deletion of SBF and MBF lead to hypertrophy (in part due to a longer G1 phase) [338,435], titration of SBF and MBF by ERC could explain the cell-cycle slowdown observed in old cells, as well as their hypertrophy.

Another model proposes that the tethering of ERC to NPCs leads to their remodeling. Indeed, a recent study shows that plasmids-bound NPCs lose their nuclear basket due to the SAGA complex acetylating parts of its nucleoporins [358] (Figure 37). In line with that, blocking this acetylation results in a longer lifespan (even though the increase is very mild).

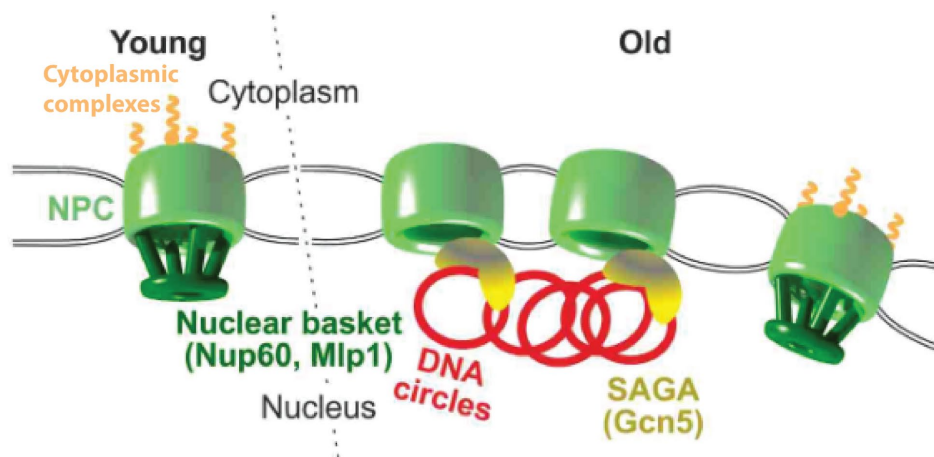


Figure 37: Schematics of young VS old pores. Pores from young cells are intact while certain pores in old cells tether ERCs, which leads to the loss of their nuclear basket (adapted from [358]).

Basket-less NPCs are known to be present under physiological conditions and have specific functions. Recent studies even suggest that basket-less pores are the default assembly state [436]. However, having more ERCs could disrupt the equilibrium between pores with and

without baskets, which could in turn disrupt the nuclear homeostasis (theory further discussed in the general discussion).

ERCs are a credible aging factor since they accumulate with age, are segregated asymmetrically, and are toxic for the cells. Yet, many questions remain unanswered: how the ERCs are toxic is still putative and if ERC excision is the result of the loss of regulation from other processes (such as rDNA stability) [257], or if they are also the cause of these losses, is still not clear.

Introduction II: Methods to study replicative aging in yeast

Studying replicative aging in budding yeast is a challenging task. Indeed, since the daughter cells are rejuvenated and that the daughter lineage grows exponentially, the fraction of cells of age N is equal to $\frac{1}{2^N}$. Therefore, separating the mother cells from their progeny is necessary to avoid such dilution (Figure 38).

This introduction will review the different strategies to tackle this challenge that exist since the birth of the field in the 1950s.

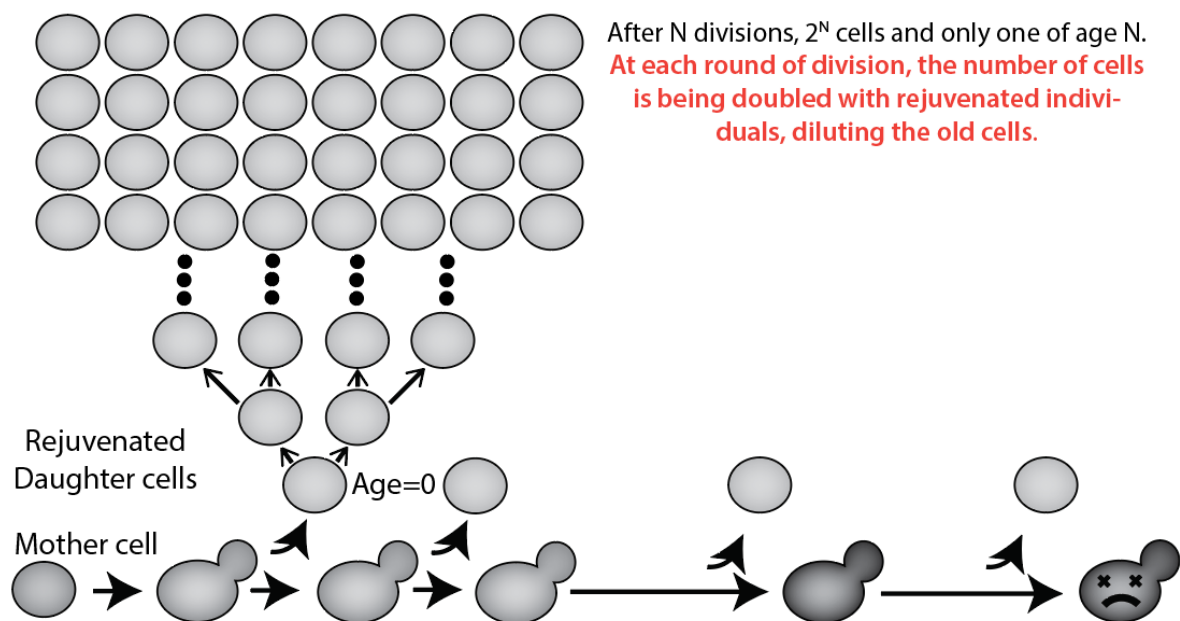


Figure 38: Schematics describing the exponential growth of a yeast population and the exponential dilution of cells of old cells.

1. Microdissection

The historical method consists in manually removing the daughter cells from a mother placed on a culture pad using a microneedle under a microscope after each division (Figure 39) [148,149].

Conventional dissection

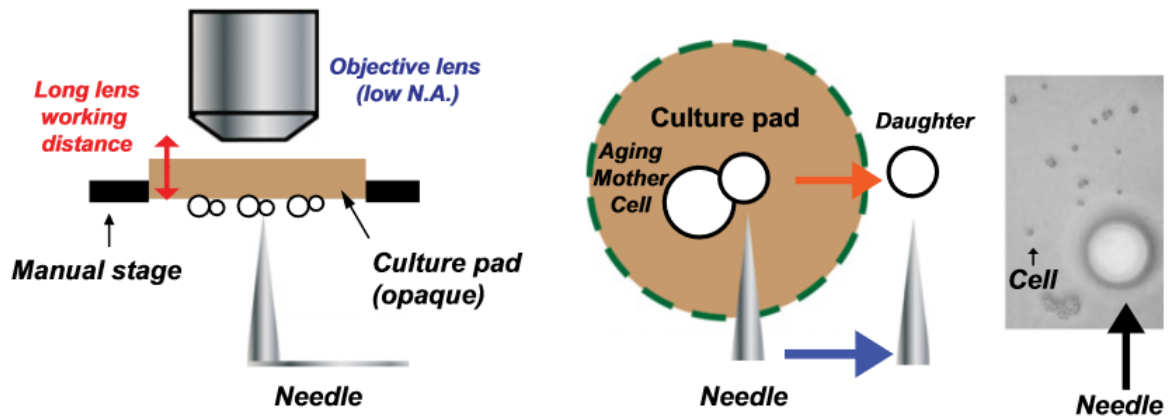


Figure 39: Principle of the microdissection manipulation. A microneedle under a microscope (left) can remove the successive daughter cells from the mother (middle). The diameter of the needle is ten times bigger than the cell (right). (From [221])

With that, one can assess the replicative lifespan of cells by counting how many divisions are performed before dying and plot the survival curves of populations (Figure 40). In this sense, it has been very instructive to identify longevity genes thanks to deletion mutants and to find molecular processes involved in aging [236].

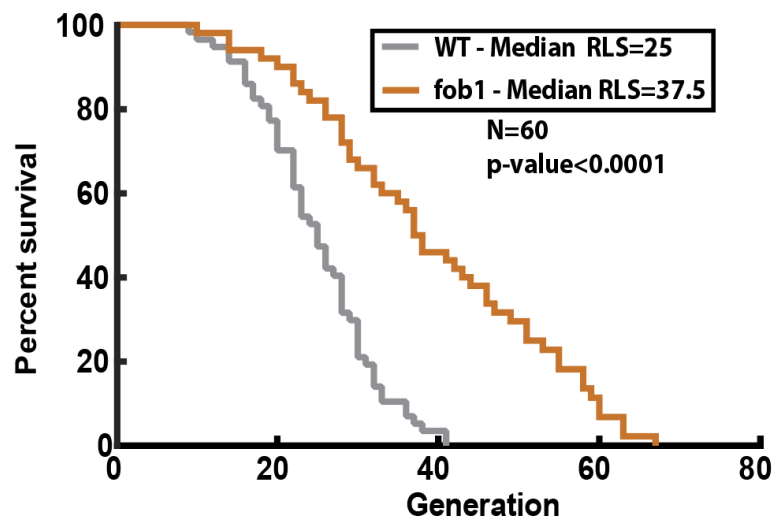


Figure 40: Replicative survival of a wild-type population VS a *fob1Δ* population. Each time a cell dies, the percentage of cells alive is decreased. (Data from a personal experiment)

However, the replicative lifespan of the cell is the only information that can be extracted from such assays, and understanding aging requires more physiological and dynamic metrics. Moreover, it has a very low throughput and is tedious (measuring the RLS of 60-100 cells takes between one and four weeks for an experimented manipulator). Indeed, the needle used to remove cells is more than ten times larger in diameter than the cells themselves, and cells need to be put at 4°C when no experimenter is available to remove the progeny.

2. Populational enrichment of old cells

To complement this method and do populational assays (for instance, biochemical or omics), other approaches have been developed in order to enrich a population with old mothers.

2.1. Density gradient and Elutriation

The historical enrichment method takes advantage of the size difference between young and old cells. Practically, it consists in making a population of cells migrate through a sucrose gradient during centrifugation, which leads to different bands (just like a DNA-gel during electrophoresis) of cells of the same size. By selecting the bands and repeating this migration process, one can separate millions of cells (up to 10^8 cells) of the same age (± 2 generations) with an accuracy of 90% [224]. Yet, this method is quite labor-intensive since it requires several rounds of purification for several days, is vulnerable to contaminations, and requires keeping the cells at 4°C overnight.

A similar technique using the morphological differences between daughters and old mothers, called elutriation, has been developed and improved several times to enrich a population with old mothers [285,437,438]. It involves applying a certain centrifugal force to the cells while exposing them to a flow in the opposite direction. Consequently, the trade-off of forces will have the small cells being removed by the flow, while the bigger ones will remain in the chamber (Figure 41). This method is less labor-intensive than sucrose migrations since cells can be grown and separated in the elutriation chamber in a continuous manner. Nevertheless, inspection and adjustment of the flux is still needed, in addition to vulnerability to contaminations

Elutriation

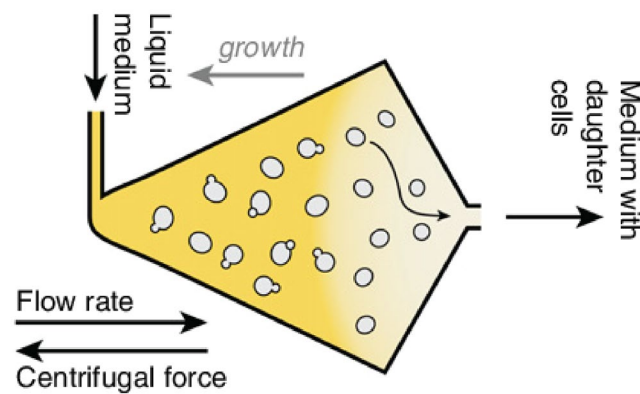


Figure 41: Principle of the elutriation enrichment of old cells. A trade-off from two forces, centrifugal and hydrodynamic, can separate cells according to their size. (From [194])

Interestingly, these methods allow the harvesting of daughter cells from a population of mothers of a given age to perform subsequent analysis, such as size and replicative lifespan measurement, or question the presence of a given potential aging factor.

2.2. Mother Enrichment Program

Another way of overcoming the exponential dilution of original mother cells is to utilize the fundamental asymmetry of budding yeast. Indeed, some genes are specifically expressed in virgin daughter cells just after their birth. By hacking this system, it is then possible to differentially express proteins in the daughter compared to the mother, which can be used to kill the daughter. With this idea, the Gottschling lab has developed a strain that expresses a Cre recombinase fused to an Estradiol Binding Domain (EBD) under a daughter-specific promoter. In the absence of estradiol, the protein is cytoplasmic in the daughter and does not exist in the mother. However, when in contact with estradiol, the protein translocates to the nucleus and is able to cut essential genes flanked by artificially engineered LoxP sites [439](Figure 42).

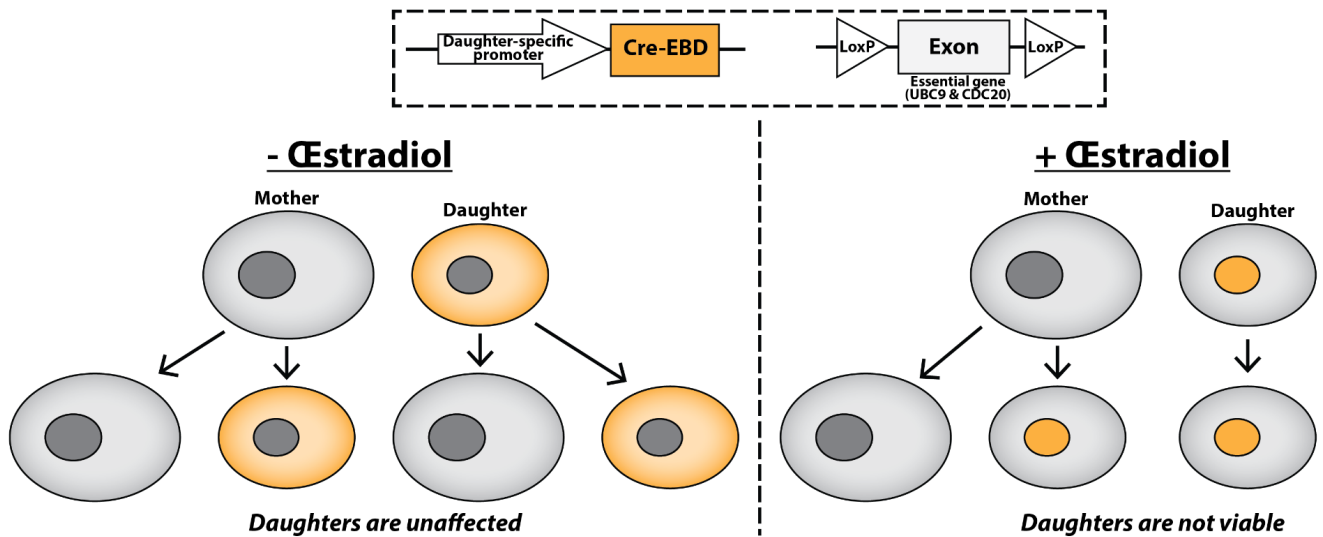


Figure 42: Principle of the Mother Enrichment Program. Upon addition of estradiol, a Cre recombinase, only expressed in daughter cells, enters the nucleus to excise essential genes, which prevents the cell from dividing.

Therefore, it is possible to render newborn cells unviable without affecting mother cells, transforming an ordinarily exponential growth into a linear growth, hence limiting the dilution of the mothers by their progeny.

Nevertheless, this *Mother Enrichment Program* (MEP) comprises certain caveats. First, it requires genetic manipulations of the strains of interest. Furthermore, it was found that some daughters do not undergo senescence immediately, especially if arrested during M-phase, and continue producing a few daughter cells before division arrest. Similarly, cells escape the selection by getting mutations in the Cre or EBD sequence at a rate ρ of 1.4×10^{-6} per division [439], which further limits the yield. Consequently, this genetic trick is often combined with other selection methods to allow efficient enrichment.

2.3. Cell wall labeling

Another method to enrich mother cells from a culture is to label them with iron beads using a biotin-streptavidin system. Since the cell wall of new daughter cells is newly synthesized [440] and thus, unlabeled, passing cells through magnetic columns [251] or directly culturing them on magnets [294,318] allows automatic separation between the original tagged cells (mothers) and their daughters (Figure 43).

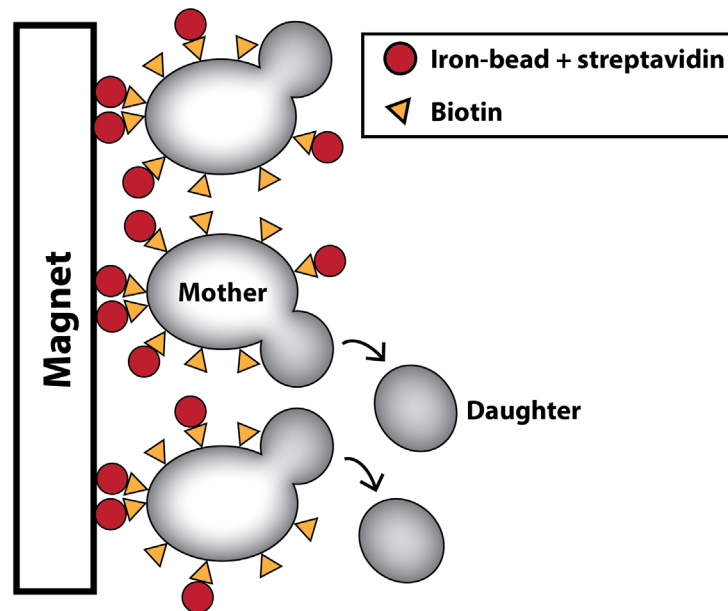


Figure 43: Principle of the magnetic enrichment of mother cells. The cell wall of mothers is decorated with iron beads which allow them to attach to a magnet, while daughter cells are born with a new cell wall and do not attach to the magnet.

Similarly, using the principle that daughter cell does not inherit cell wall from the mother, it is possible to select old mother cells by labeling the cell wall of progenitor cells with a fluorescent tag instead of iron beads, to stain their budscar at the end of the experiment, and to sort the population at the FACS using the two fluorescent channels [441].

These methods, often combined with the Mother Enrichment Program, are the state-of-the-art method to produce a population of old cells before conducting further assays on it.

2.4. Conclusions on traditional assays

Populational assays and genetic screens using microdissections have been extremely informative and influential in describing which biomolecular processes are changed during aging. However, these approaches fail to capture the proper dynamics of the processes and can only tell if they are affected - on average in the population and in time - or not.

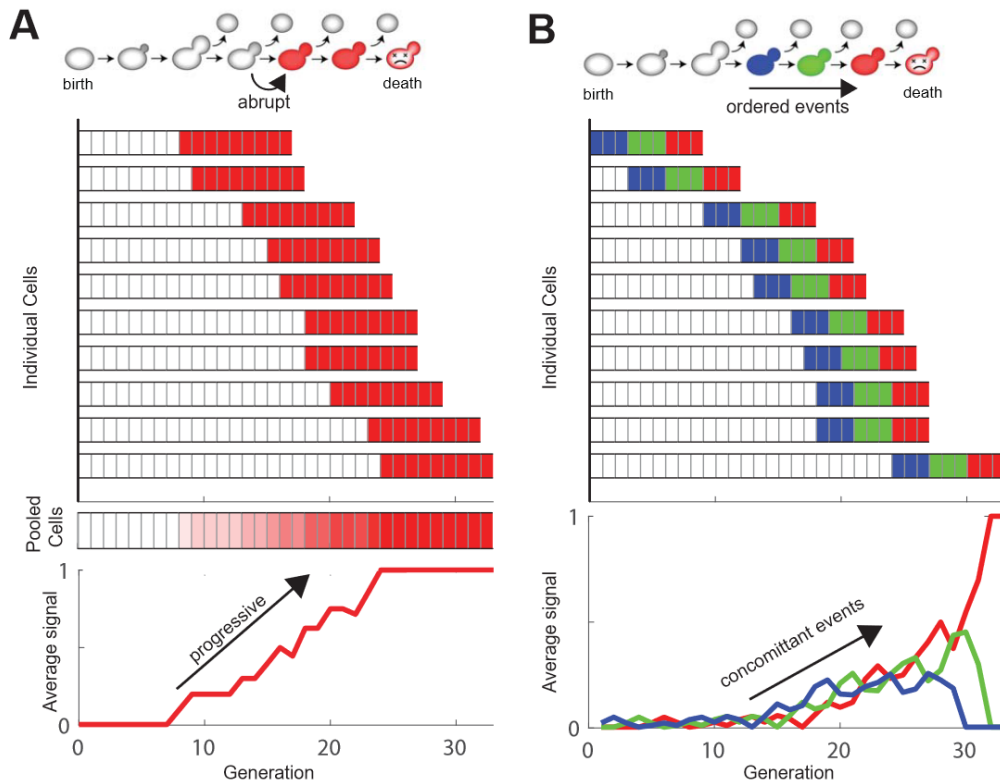


Figure 44: Schematics describing averaging biases. (A): The heterogeneous occurrence of an abrupt event (represented in red) at the single-cell level will give a progressive signal at the population level. (B): Similarly, an ordered series of events (represented by the colors) will look like a progressive and parallel accumulation of events (From [226])

Indeed, due to the cell-cell heterogeneity of most phenotypes during aging (at least in time), averaging biases can lead to misinterpreting an abruptly occurring phenomenon into a progressive or a series of ordered events into concomitant parallel processes (Figure 44).

Therefore, another way of studying replicative aging - while avoiding population biases - is to extract temporal signals directly from single cells.

3. Capturing single-cell dynamics

For a decade, the development of new technologies such as microfluidics has allowed the isolation of cells of interest as well as precise control of their environment, not only in budding yeast (described above) but in bacteria [170,174], fission yeast [159,186,442], *C. elegans* [443], or mammal cells [444,445]. When coupled with timelapse microscopy, this approach allows tracking cellular responses to various environments at the single-cell level, using direct light and epifluorescence with mutant strains harboring proteins with fluorescent tags. In the context of replicative aging, they permit the isolation of mother cells of interest in order to follow them throughout their lifespan. The next paragraph will briefly describe how these

microfluidic devices are fabricated, which designs are used for replicative aging, how to track aging cells, and how to analyze their images.

3.1. Microfabrication and soft-lithography

Many different techniques exist in order to create microfluidic devices. The most common one is called soft-lithography [446] and consists of pouring a polymer on a mold that will, after chemical treatment (such as the addition of a cross-linking reagent), take the negative shape of the mold (Figure 45, third column). Therefore, the mold has to contain structures of interest.

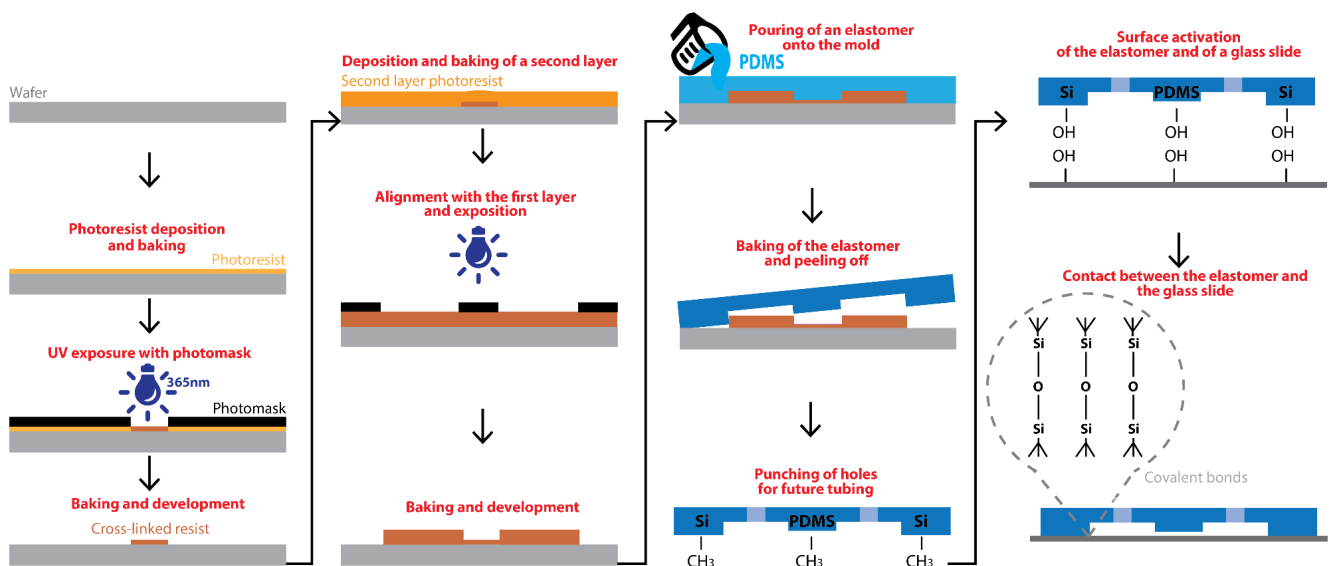


Figure 45: Schematics representing the main steps of the photolithography (two first columns) and of the softlithography and plasma activation (two last columns) for the preparation of microfluidic devices.

To create these structures, again, several approaches are possible depending on the resolution and size requirement. If 3D printing and micro-milling can reach a resolution of 50 μm in specific contexts, going lower often requires lithography techniques. Direct photolithography involves depositing a photosensitive resist on a substrate before exposing it to a given wavelength through a mask containing transparent and opaque parts. Exposed resist will release cross-linking agent, become solid and adhere to the substrate after heating, while unexposed resist can be removed using a solvent (Figure 45, first column). In theory, the resolution of such a technique is then only limited by the diffraction of light. In practice, one can achieve microstructures with a 1 μm resolution if the thickness of the resist does not exceed 10 μm .

Once the mold is done and the chip cast, baked, and peeled off, one can pierce holes for the future tubing and seal the device to a substrate such as a glass slide, using (for example) plasma activation to create covalent bonds between the polymer and the glass (Figure 45, last column).

3.2. Microfluidic designs for replicative aging

Using this approach, several microfluidic devices have been developed to study replicative aging.

Similar to enrichment techniques, their objective is to isolate mother cells from their exponentially growing progeny, but this time to observe them throughout their lifespan.

To do that, the first devices “glued” the cells to a coverslip using a biotin-streptavidin system before applying a gentle flow of media to remove the successive daughters [222]. This pioneering system is however relatively inefficient to retain cells over an extended period of time and can be toxic to them.

Therefore, it has quickly been replaced by mechanical trapping, for example by trapping the cells under pads (see “Micropads” in Figure 46) of polydimethylsiloxane (PDMS). In fact, if the ceiling has the proper height, the newborn daughters can be removed by the flow since they are smaller than the trapped mother [221,245]. These devices, which are still used nowadays by a few labs [248], also suffer from low retention of the mothers with age, are hardly adaptable to different cell sizes, and have low throughput.

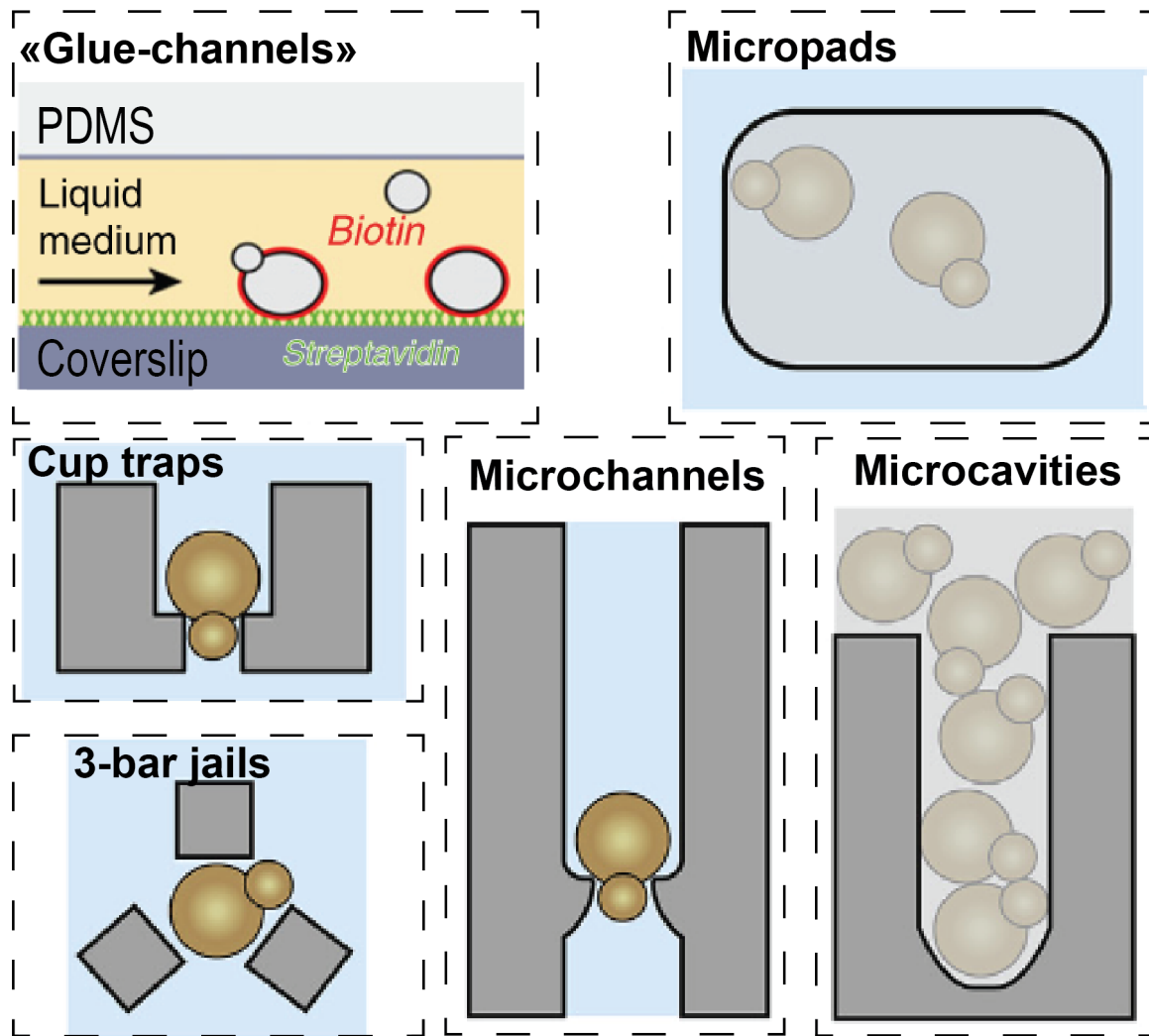


Figure 46: Schematics from the different microfluidic devices used to perform replicative lifespan assays in yeast (Adapted from [194], [447])

Inspired by the mother machine (introduced p.19), devices with cavities have been developed to work with budding yeast [246](see “Microcavities” in Figure 46). In this device, mother cells are trapped at the tip of the cavity and the successive daughters are pushed out of the cavity and removed by a lateral flow. It comes with a few caveats such as the requirement to use strains that always bud in the same direction. Moreover, the budding pattern sometimes becomes erratic during aging, leading to the loss of the mother cell, replaced by a daughter. Taking that point into account, microcavities with a hole have been developed [328], with the drawback that the number of traps is reduced in such devices (100 traps/device)(see “Microchannels” in Figure 46).

Alternatively, devices with an array of inflow traps are also used [231,247,448,449] in which the mother cell is blocked in-between pillars of different shapes. Trapping mother cells in between cup-shaped structures (see “Cup trap” in Figure 46) or chevrons is straightforward, efficient, and easy, but the retention is not perfect since big cells tend to leave the trap or be

replaced by their daughter. Using three pillars (see “3-bar jail” in Figure 46) solves this problem but is much more challenging to trap the original mothers since a cell has to come outside the jail and bud inside to inoculate it [449,450]. With inflow traps, the progeny is automatically dissected by the constant flow of media.

Depending on the strategy, the trapped cell will be guaranteed virgin [246,449] or might have any age. However, since the age distribution of an exponentially growing population is composed of 50% of virgin cells, 25% of cells with an age of one division, and 12.5% of cells with two divisions, most of the cells are virgin or very young when trapped at the beginning of the experiment (Verified experimentally: [231]).

Overall, microfluidic devices can isolate mother cells throughout their lifespan and avoid an exponential dilution by their progeny. Interestingly, the culture media is tightly controlled and can be changed in a matter of seconds to submit cells to stress, drugs, or to change their carbon or nitrogen source.

From that, they can be used to enrich a population with old cells before harvest (like enrichments methods presented in the previous section) (see Appendix 1), or Appendix 1: Microfluidic enrichment of old cells and sorting according to their senescent state to track them longitudinally during the aging process.

3.3. Longitudinal tracking: Image acquisition and processing

Most of the microfluidic devices are made of PDMS or other polymers transparent to visible light. Therefore, they are compatible with epifluorescence microscopy and can be imaged in week-long experiments with a constant frame interval using a camera (Figure 47). *Timelapses* of individual mother cells offer much information compared to microdissection since it is possible to measure the size of the cell, its morphology, its division duration, and many fluorescent reporters. However, this quantity of information, if analyzed manually, makes the whole pipeline low-throughput and comparable to microdissection in terms of tediousness. In other words, microfluidics has displaced the throughput bottleneck from isolating the cells to analyzing the data.

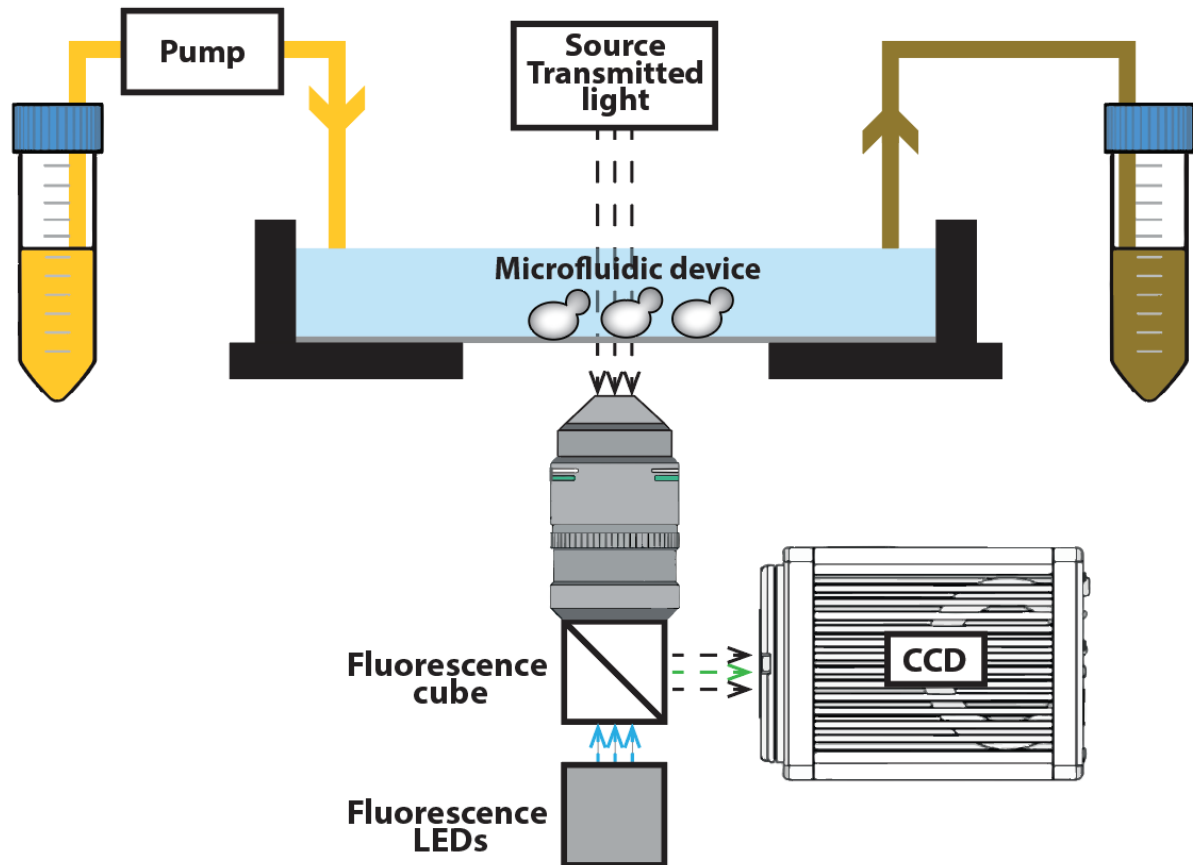


Figure 47: Schematic representation of a typical timelapse microscopy setup with a microfluidic device

It is possible to automate part of the analysis by using classical image processing algorithms. For example, it is very simple to segment (*i.e.*, create a mask of pixels corresponding to the object of interest) an object from an image of a fluorescent reporter (provided the signal-noise ratio is sufficient), using a threshold value on the signal. Similarly, cells can be segmented using watershed from phase-contrast images or using other similar sets of transformations and cost-algorithms from brightfield images [246,451-453,453b]

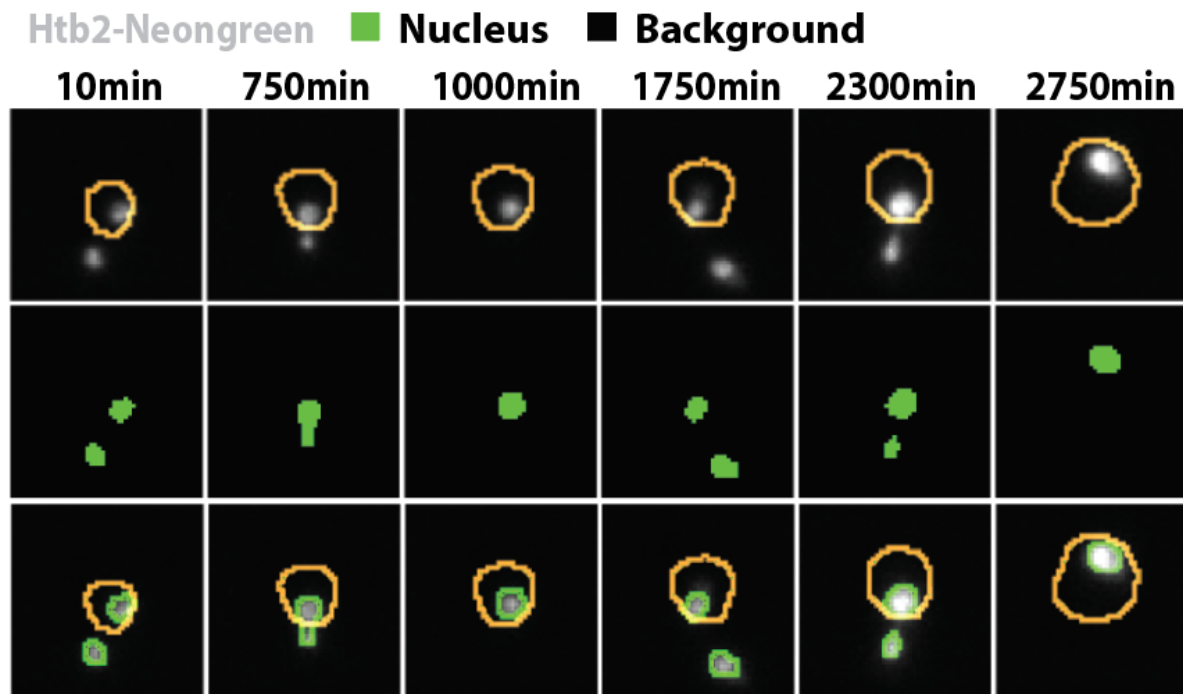


Figure 48: Timeseries of images from one cell. (Top): Gray level of the signal from a Htb2-Neongreen nuclear reporter. The orange contour represents the mother cell. (Middle): Pixel mask obtained by thresholding. Each pixel from the input image above a certain value is assigned to a green pixel on the mask. (Bottom): Mother cell contour (orange), mask contour (green) overlaid on the input fluorescence image.

Nevertheless, such algorithms require fine-tuning to analyze the specific set of images and could fail with a slightly different set. In particular, in the context of aging, cells and their vacuole become bigger, and their aspect can change, especially when the cell is close to death. These changes often trick algorithms tuned with young cells, and manual correction is necessary, which impairs the throughput.

Besides, other complex features can just not be automatically extracted and analyzed using classical approaches, such as detecting when a cell divides. **In other words, classical approaches are ad hoc rigid methods with a narrow range of applications and struggle to extract complex signals from an image.**

For a few years, machine learning (ML) is emerging as a state-of-the-art solution to fit complex models in biology ([454] and see Figure 49). It is used not only for automation of image analysis (*i.e.*, increase the throughput compared to manual work) but also for extracting information from data too complex for a human (for example, denoising with spatial or temporal interpolation [455,456] or detecting organelles from brightfield images).

It is also widely used in omics studies and structural biology with the recent development of AlphaFold to predict protein structures [457].

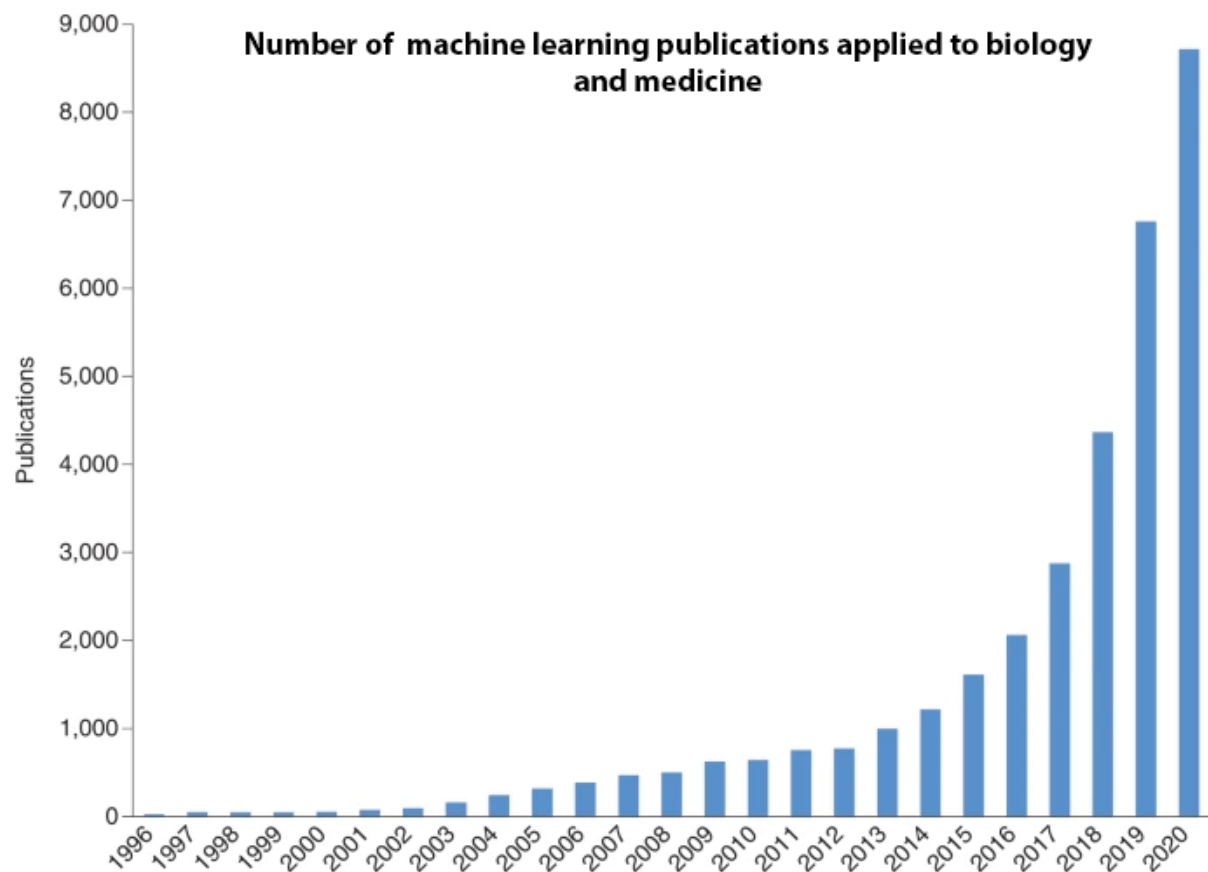


Figure 49: Number of publications in the "machine learning" category in combination with a topic category related to biology or medicine term (From [454]).

The general principle of machine-learning is similar to a fitting process. Indeed, the goal is to create a mathematical model from sample data (called "training data") during a training phase in which the algorithm will tune the parameters of the model to minimize the error (in other words, the algorithm will learn).

Then, the model can output a predicted value from input data (Figure 50).

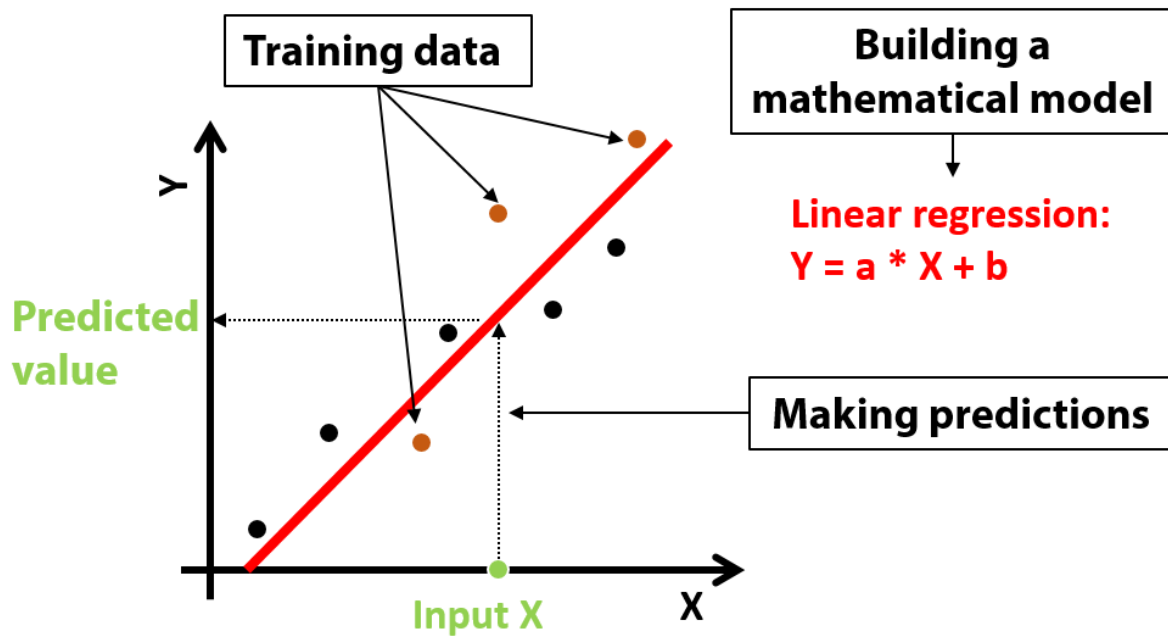


Figure 50: Principle of the creation of a model from a machine learning algorithm

If the model presented in Figure 50 is a simple linear regression that could be obtained with a simple classical algorithm, machine-learning can also fit highly non-linear models and is necessary when the relationship between the data is complex.

It can be used to classify an object between different classes (classification) or return an exact value from a continuum of possibilities (regression). For example, a machine-learning model could try to predict if a patient has a heart disease (classification between "Yes" or "No") based on its weight, age, if it is smoking and if it is exercising (these input data are called *descriptors*). Back to image processing, a ML model could tell if a pixel from an image belongs to a cell or to the background, based on its intensity, neighbors, and value after different image transforms. In this sense, Ilastik has been pioneering the ML approach in bioimage analysis by providing a software to segment cells and biological objects from raw images, based on a given list of descriptors [458].

However, the ability to extract complex relationships from data comes at a price. In fact, the main caveat of ML is that the model can memorize much information from the training data. Therefore, there is a risk of overfitting if the training set is not large enough to extract the general rules from the data. In other words, the algorithm can "learn-by-heart" the data and will have limited predictive power on new data (Figure 51).

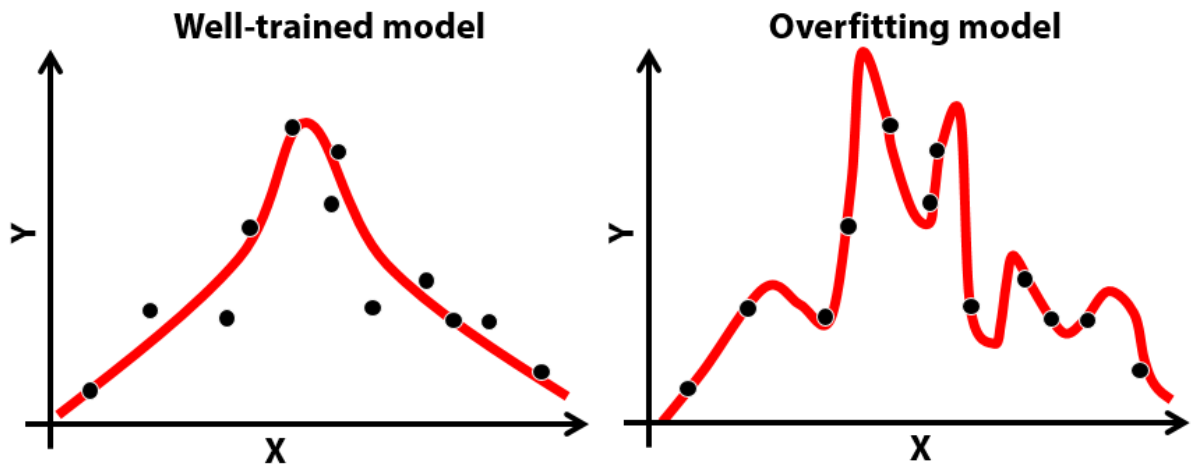


Figure 51: Schematics of the fit (red line) of real data (black dots) from a well-trained model (left) compared to an overfitting model (right).

Moreover, ML computational time can be longer than classical algorithms (depending on the complexity of both), and must therefore be used only when standard approaches fail or are slower.

From then, different learning algorithms exist such as decision trees and random forests, bayesian networks, and artificial neural networks (ANN). For the rest of this section, we will focus on ANN.

ANN are inspired by the biology of neurons, in which the cell body receives signals from the dendrites and, transduce (or not) the signal to the axon. Artificial neurons perform simple mathematical operations (weighted sum) based on inputs and transduce it into an output (after activation, see function $f()$ on Figure 52)). ANN are often organized in layers of neurons, and the weights of the different layers are tunable parameters that allow learning the complex relationships between the input and the output. An ANN can have a large number of hidden layers and is then considered as a deep learning (DL) network.

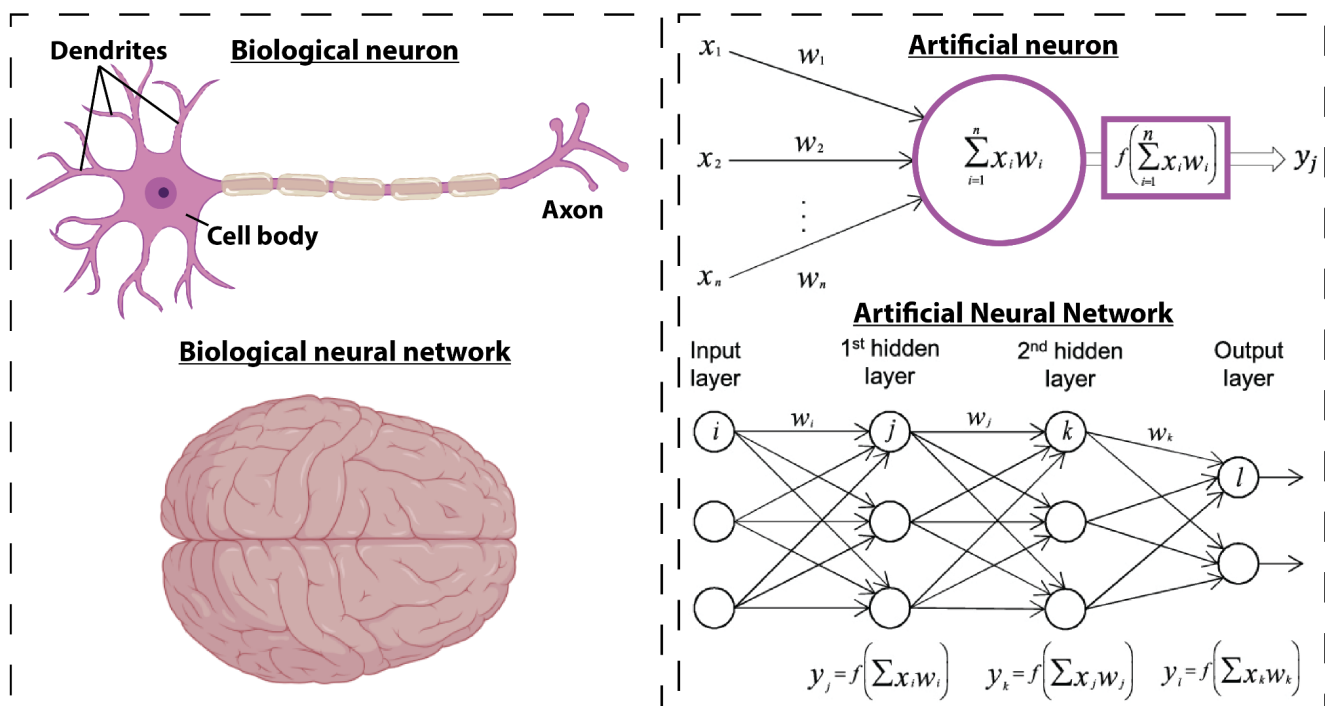


Figure 52: (Left) Simplistic representation of a biological neuron and neural network (brain). The neuron receives information from other neurons through its dendrites and potentialize a response towards its axon accordingly. Putting neurons together can transform complex inputs into complex output (behavior, movements,...). (Right) Representation of an artificial neuron and of a ANN. An artificial neuron receives weighted inputs $x \cdot w$ (data or other neurons' output). An activation function transforms the sum of these weighted inputs into an output value y (connecting to other neurons or to the output layer). The training consists solely in adjusting the different weights w of the network.

The advantage of ANN (and in particular of DL) compared to other ML approaches is that it does not require the user to select descriptors to make a prediction. Indeed, the nature of the network (*i.e.*, the kind of operations each neuron does and how the neurons are organized) alone is able to extract relevant features from input data. This is very convenient since defining accurate descriptors is difficult. On the other hand, it often requires more training data. Besides, the user does not know which particular feature of the data matters to create the model, which is why DL models are often described as “black boxes”.

Many different types of DL networks exist (with new types emerging every year). For example, Convolutional Neural Networks (CNN) are remarkably efficient with images since they perform convolutions on groups of pixels from the input image. Hence, they can extract the information stored in the value of the pixels themselves, but also of their neighborhood (Figure 53) [459].

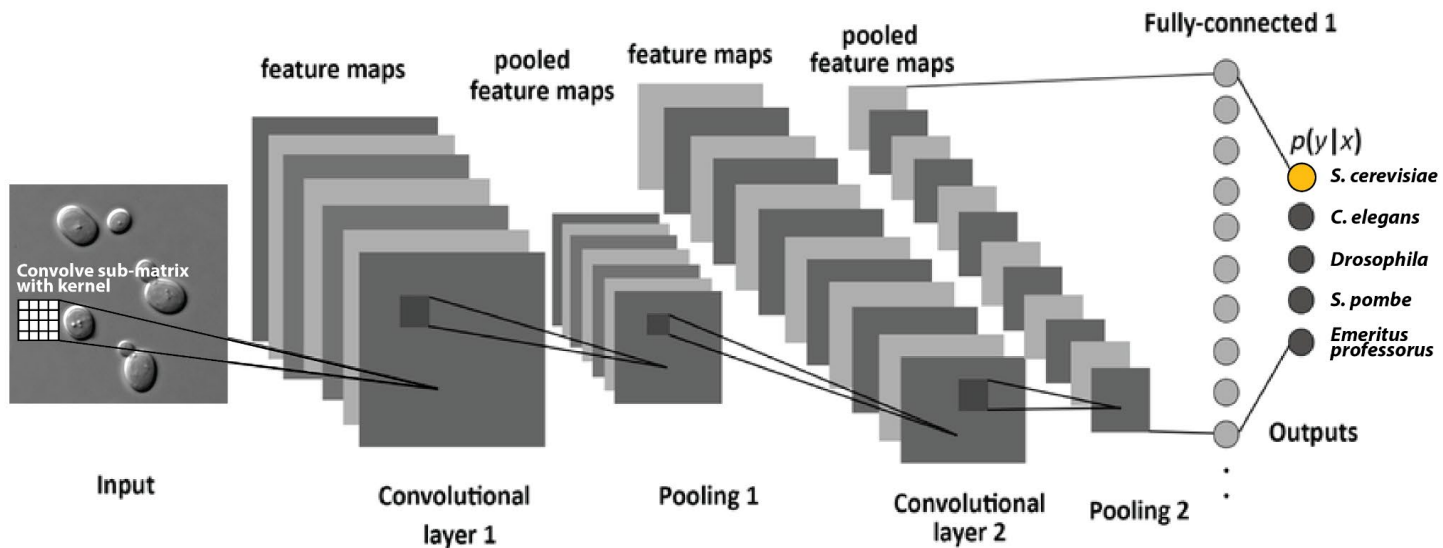


Figure 53: Representation of the architecture of a CNN. At each layer, the input and output are an image (except the last layers), and the operations are convolution with a mask (instead of simple weighted sums). Here, the CNN is used to classify an image into predefined classes. The output of the convolutional layers is connected to a classification layer that transforms images into an array of probabilities. During the training, the weights of the convolution masks and of the classification layer are tuned

Specific variants of CNN are adapted explicitly for semantic segmentation, such as U-net networks [460], and are so efficient that they are now state-of-the-art for such tasks.

These kinds of networks have been adapted to segmentations of broadscale bioimages [461], [462], but are also being developed to specifically segment yeast cells [463-468] (Figure 54).

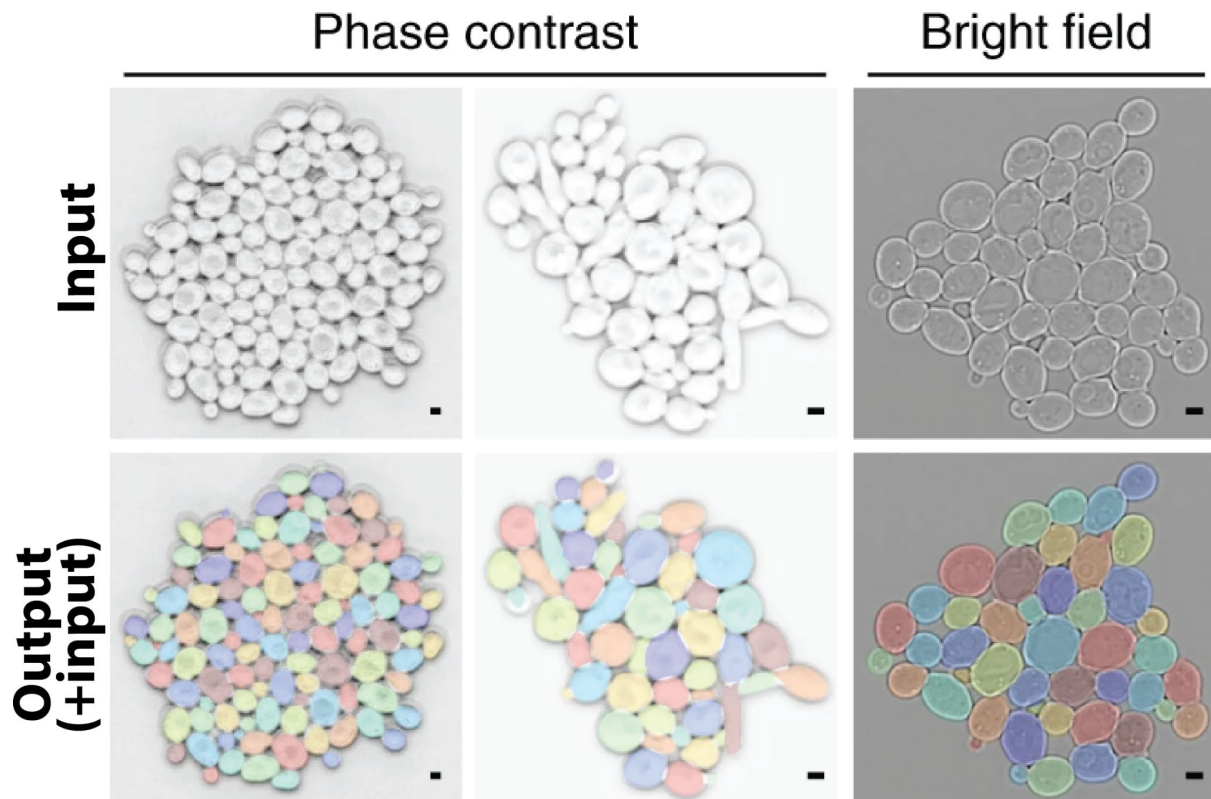


Figure 54: Examples of single-cell yeast segmentation from raw images. (Top): Raw phase contrast or brightfield images. (Bottom): Overlay of the segmentation with the raw image using a U-net. The different colors represent the predicted pixels of a cell. Scalebar: $2\mu\text{m}$ (From [463])

Deep-learning can also be used to track particle movements (like cells) [469] or detect divisions in very stereotyped organisms such as *E. coli* [470].

Another type of network is specifically efficient in analyzing temporal and repetitive signals. Indeed, Recurrent Neural Networks (RNN) can take into account the time dependencies between the timepoints by including the output of nodes in their input, therefore creating some kind of memory of the previous timepoints (Figure 55).

In particular, Long Short Term Memory (LSTM) networks are particularly suited for analyzing temporal data such as speech [471].

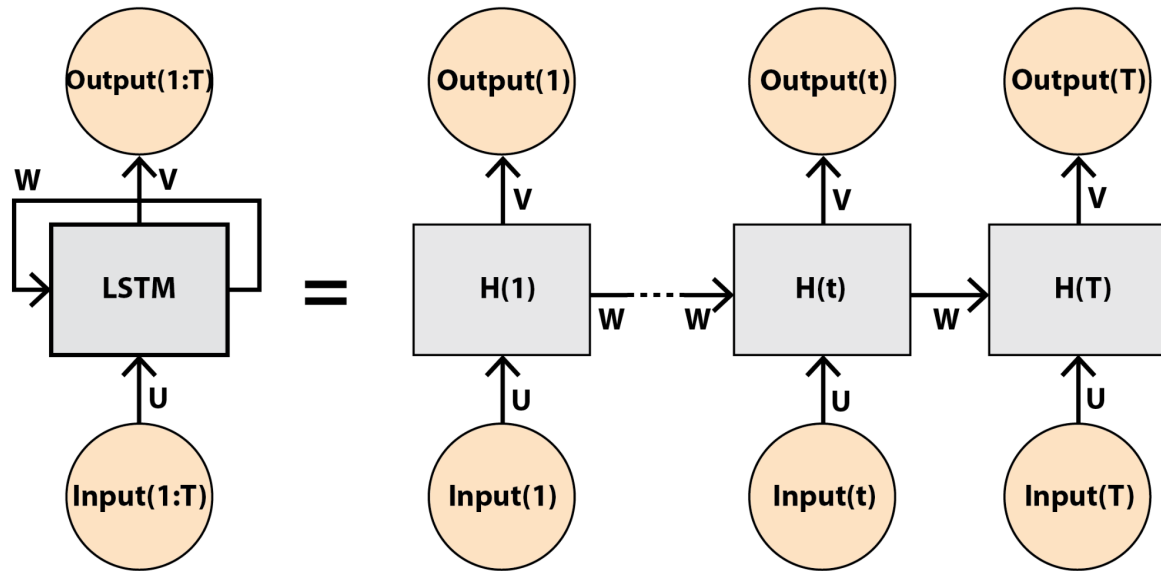


Figure 55: Representation of the architecture of a unidirectional RNN. Such networks take timeseries as an input, and the output from the function H of each timepoint is fed to the node treating the next timepoint. U , V , and W are the weights of the nodes.

However, even though deep-learning models provide unprecedented capabilities to extract meaningful information from images or temporal signals, its potential to exploit the time-dependencies in temporal sequences of images has been almost completely overlooked. Yet, the analysis of complex temporal behaviors of biological systems - a primary focus in cellular biology - may largely fail when using pipelines that do not exploit the underlying temporal correlations between images in time-lapse datasets. For example, no algorithm is capable of detecting yeast cell divisions efficiently.

Summary of the introduction and Objectives

As seen all along [Introduction I](#), a large number of biological processes are affected during aging. Yeast is a powerful model to study this phenomenon, and systematic studies, as well as more focused analyses, have identified many hallmarks of aging and genes of longevity.

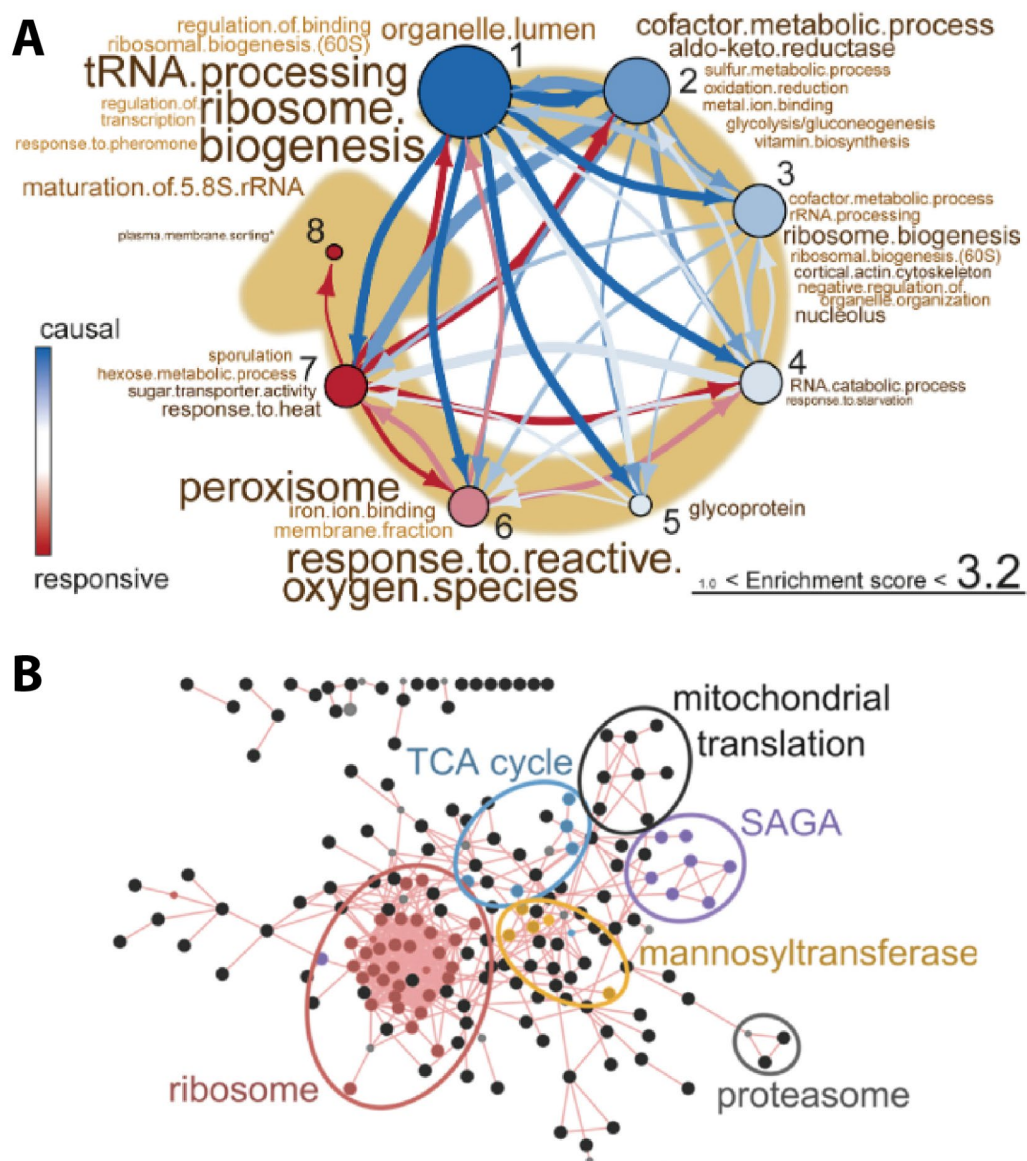


Figure 56: The output of two large-scale screening studies. (A): Functional clustering from proteome- and transcriptome-wide data from old cells. A specific data processing was used to infer the degree of causality of each cluster. Arrow thickness, colors, and direction represent the strength and causality of the connections between two nodes. In this model, the protein biogenesis-related genes are the primary causal force during aging (From [294]). (B): Functional clustering of long-lived deletions. The overrepresented categories are colored and circled [236])

However, understanding how these different hallmarks are linked between one another is necessary for the field to grasp this complex phenomenon. More precisely, it is important to try drawing aging pathways and define which processes are causal for the loss of fitness and

which are consequential among these pathways. This task is made difficult by the fact that certain alterations are mechanisms to keep the global homeostasis while others participate in its loss. Several comprehensive studies have tried to link different ontologies (Figure 56) and to bridge several hallmarks of aging.

For example, the loss of protein stoichiometry affects vacuolar proton-pumps, affecting the vacuole's pH in turn. Alkalinization of the vacuole in turn was linked with mitochondrial decline, which in turn promotes protein oxidation and genomic instabilities (see p.38).

Besides, some proteins or metabolic pathways seem to be at the core of aging. For example, Tor1 controls many processes described earlier, at many different levels (not only ribosome biogenesis and cell growth, but also rDNA stability in a Sir2-dependent and -independent manner [386], autophagy, proteostasis [472-475], and even cytosolic and vacuolar pH [476]) Similarly, Sir2 seems to be involved in most of the processes described in Introduction I. It controls ERC levels, rDNA stability, and silencing and is required to filter oxidized mitochondria from the daughter by acting on the polarisome and the retrograde actin transport [276]. Besides, having defective mitochondria elevates Sir2 levels [477]. Sir2 is also necessary for the asymmetric segregation of protein aggregates in a similar manner to oxidized mitochondria [308,309,478-480]. Sir2 also interacts with the SAGA complex, known for regulating the tethering of ERCs to the pores [323].

Therefore, while these hub proteins and pathways seem at the center of aging, studying them directly is challenging because of their strong pleiotropy [237,481].

On the other hand, other hallmarks are already known to happen very late in life, such as aneuploidy and DNA mutations. These phenotypes are not likely to be aging factors since they affect the whole progeny and are more likely proximal causes of death than primary causes of aging.

More generally, where all these hallmarks stand in the aging process, whether they form different parallel pathways or rather a network, is almost entirely undefined, and many contradicting studies exist on most of these hallmarks (see introduction). This is in part because traditional methods do not allow proper capture of the dynamics of the events (see p.67), which in turn participate in the idea that aging in yeast is a gradual decline of parallel functions (Figure 44, p.68), might it be true or not.

The relatively recent development of new technologies such as microfluidics and long-term timelapse microscopy enables longitudinal analyses of single-cells, thus circumventing the

population biases. Thanks to this approach, propositions of ordered series of events and pathways of aging are emerging.

Indeed, several longitudinal studies have noted that cells were dying with distinct terminal bud morphology, *i.e.*, with a spherical (or “rounded”) bud or ellipsoidal (or “elongated” bud. [221,223,245,283].

Similarly, our lab described that the progressive lengthening of the cell cycle, previously described at the population level (see p.33 Division time), was actually a very abrupt event when looking at the single-cell level [246], that was termed **Senescence Entry Point (SEP)**.

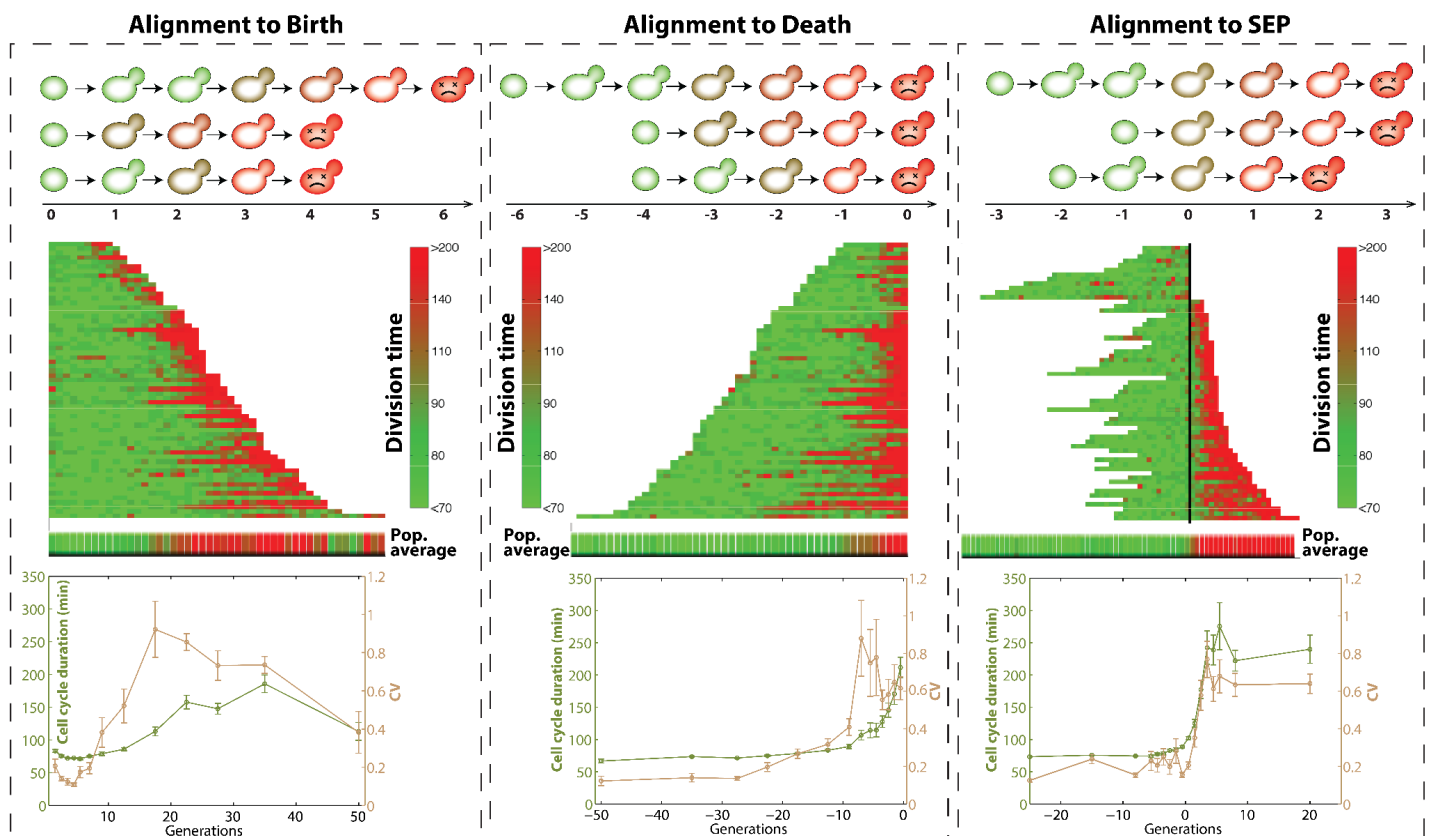


Figure 57: Different alignments (from birth, death, or the SEP) of single-cells division duration along lifespan. (Top): Schematics of the alignment method. (Middle) Each line represents a cell, and the colorcode represents the division duration. (Bottom): Mean division duration and coefficient of variation (CV). (Adapted from [246])

This is a striking illustration of how averaging a heterogeneous signal from a population can lead to misinterpretations if the single-cell trajectories are not correctly aligned. Hence, aligning cells relative to the occurrence of the phenotype of interest (here, the division slowdown) before averaging is necessary to reduce variability to its minimum (Figure 57, right). When this in-silico synchronization is not possible, aligning cells relative to their death is often better than aligning from birth (Figure 57, middle vs. left) since the onset of aging hallmarks is often closer to the death than to the birth of cells (as it is done with population assays).

Besides, the power of longitudinal tracking in this study showed that the loss of mitochondrial potential (*petiteness*) was a stochastic event, independent of age or of the SEP.

Building on that, further work tried to ordinate some of the known hallmarks of aging and proposed a choreography of events followed by most of the wild-type cells [226]. Indeed, nine cells out of ten (after removing *petite* cells from the analysis) are experiencing the same aging scenario (Figure 59), starting with **1/** the excision of an ERC. Then, **2/** this circle self-multiplies throughout the divisions until a threshold number of copies, at which the cell reaches the SEP.

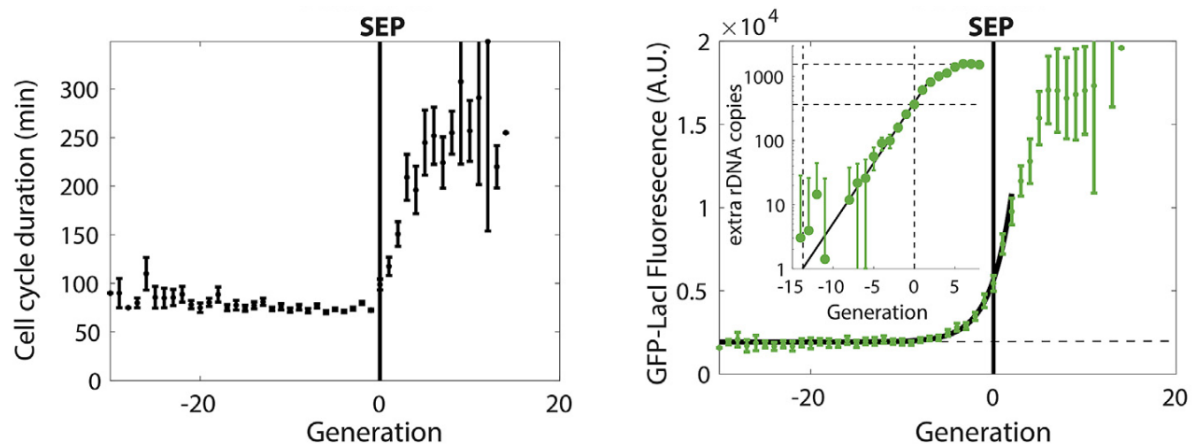


Figure 58: Average cell-cycle duration (left) and number of presumptive rDNA copies (including ERCs) (right), aligned to the SEP, as a function of age. $N=64$. Error bar represents the SEP. (From [226]).

Interestingly, the activity of the rDNA transcription machinery, as well as the pre-rRNA content, are upregulated before the SEP, following the ERCs accumulation dynamics. The fact that the ERC accumulation (followed using a LacO system inserted in each repeat of the rDNA) always precedes the SEP and that the SEP occurs at a threshold number of circles strongly suggests that ERCs are the cause (direct or indirect) of this cell-cycle slowdown (Figure 58). Moreover, that would explain why the SEP is so abrupt (happening in less than three divisions) since the ERC number goes from ~240 copies to ~550 copies around the SEP.

Then, from the SEP, **3/** the N/C ratio starts increasing, and the cells show accumulating defects such as nucleus fragmentation and aberrant nucleolus size, until death.

Supporting this model and the causality of ERCs, two-thirds of the cells lacking FOB1 (known to reduce the excision rate, see p.56) do not experience a SEP nor an ERC accumulation, and those who do have a SEP reach it later but also accumulate ERCs until the same threshold than WT cells.

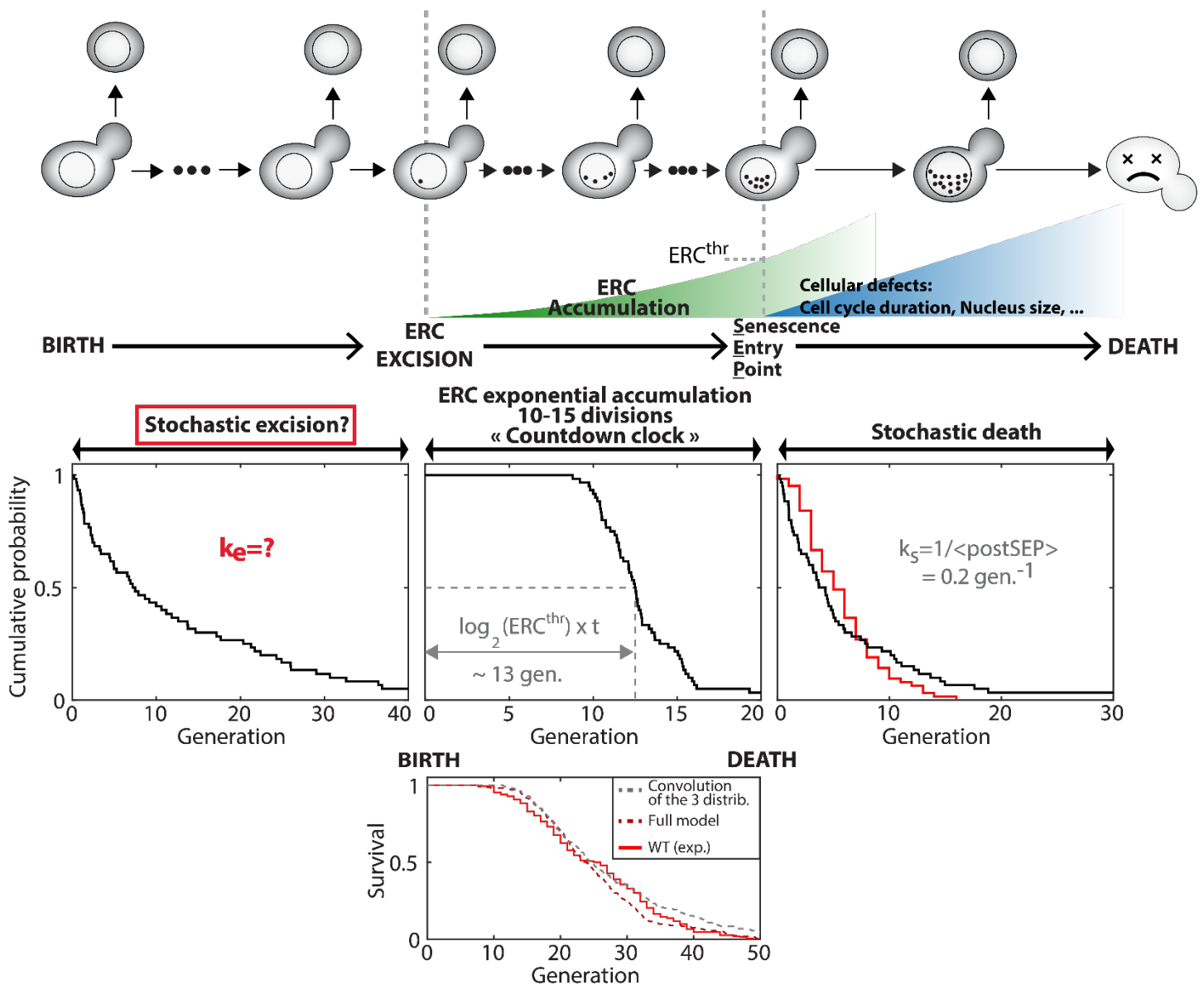


Figure 59: (Top): Schematic describing the three phases involved in the ERC-dependent senescence (ERC excision, self-multiplication, and post-SEP interval). (Middle): Cumulative probability associated with the three phases, numerically computed (black line) or from experimental data (red line). (Bottom): Survival curve obtained experimentally (solid line), by convoluting the three distributions from the middle lane (grey dashed lined), or by adding a mild ERC-independent cause of death to the convolution. (From [226])

This model raises several molecular questions raised by this model (discussed in the general discussion, p.141). Beyond that, we can note several points about the statistics of all the 3 phases:

Indeed, the period 2/ is quasi- deterministic (as modeled mathematically [226] and shown in Figure 59). This is explained by the well-controlled replication machinery which drives the accumulation until the threshold triggering the SEP.

Then, period 3/ between the SEP and death, is age-independent, with a constant 20% probability of dying at each division.

Therefore, none of these processes are age-dependent.

Thus, what are the statistics of the period 1/ from birth to excision?

Is 1/ an age-dependent or a stochastic distribution? In other words, is the probability of ERC excision influenced by other aging factors, or is it the first event of a pathway of aging?

Bulk assays report that Sir2 protein levels and silencing at the rDNA are decreased in replicatively old mothers while rDNA recombinations are increased [257,321], though unpublished data from our group suggest it is not the case. Similarly, a recent study suggests that the increase of cell size could decrease Sir2 levels (without direct evidence) [240].

Therefore, the few data available in the literature suggest that the probability of excision could increase with age.

On the other hand, numerical modeling shows that it is possible to recapitulate the survival curve of WT cells by convoluting an exponential decay (i.e., age-independent process, representing 1/ the excision phase), with a gaussian decay (pseudo-deterministic process, representing 2/ the accumulation phase) with another exponential decay (representing 3/ the post-SEP phase). In other words, ERC excision can be independent of age in this 3 phases model. This result differs from previous mathematical modeling in which a quadratic increase of the ERC excision probability with age is needed to recapitulate the experimental survival curve [426]. However, this model does not take into account the 3rd phase but only considers death at a threshold number of ERCs, which explains why it needs an age-dependent distribution for the first excision.

The hypothesis that the probability of ERC excision is independent of age raises a broader conceptual implication. In fact, this means that it is theoretically possible to reproduce a Gompertzian distribution (describing aging per definition) solely from age-independent processes. In other words, aging could arise from stochasticity.

To test this hypothesis experimentally but also to try rationalizing the different hallmarks of aging into pathways, a large number of cells must be analyzed in different mutants and conditions. Yet, despite recent progress in microfluidic-based approaches, replicative lifespan assays still suffer from throughput problems. Indeed, the low number of cells per experiment and the manual analysis of the timelapse data currently limit the potential for large-scale longevity screens.

4. Objectives

Consequently, my PhD thesis had two objectives:

1. Develop a platform to track and analyze cells throughout their replicative lifespan in a high-throughput manner.
2. Measure the excision rate of ERC during aging: Is it a stochastic or age-dependent process?

Results

This result section will be split into 2 parts:

Results I: Setting up a platform for automated and high-throughput tracking of replicative lifespan

Results II: Measuring the ERC excision probability with age

Each part has its own short introduction to remind the main challenges and its own discussion, and will be put into perspective in a later General discussion.

5. Results I: Setting up a platform for automated and high-throughput tracking of replicative lifespan

1.1. Introduction

The current microfluidic devices and imaging systems have a limited throughput due to the number of cells they can trap and image simultaneously. More importantly, replicative lifespan assays consist of counting divisions, and up to now, this task has to be performed by a human, which significantly impairs the analysis throughput.

Machine-learning could tackle this problem, but existing pipelines can only segment cells and never exploit the underlying temporal correlations between images in time-lapse datasets.

In order to increase the throughput power of replicative lifespan experiments, we created a platform to

1. Trap 32000 mother cells distributed in 16 different conditions
2. Track them using timelapse microscopy, and
3. Automatically detect when they divide, measure their size and fluorescence.

1.2. Results

(See attached paper along the next pages. Please check the latest version online, since modifications might be done after the publication of this thesis)

DetecDiv, a deep-learning platform for automated cell division tracking and replicative lifespan analysis

Théo Aspert^{1234*}, Didier Hentsch¹²³⁴ and Gilles Charvin^{1234*}

1) Department of Developmental Biology and Stem Cells, Institut de Génétique et de Biologie Moléculaire et Cellulaire, Illkirch, France

2) Centre National de la Recherche Scientifique, UMR7104, Illkirch, France

3) Institut National de la Santé et de la Recherche Médicale, U964, Illkirch, France

4) Université de Strasbourg, Illkirch, France

*: Corresponding authors: charvin@igbmc.fr, aspertt@igbmc.fr

Abstract

Automating the extraction of meaningful temporal information from sequences of microscopy images represents a major challenge to characterize dynamical biological processes. So far, strong limitations in the ability to quantitatively analyze single-cell trajectories have prevented large-scale investigations of the mechanisms that drive the entry into replicative senescence in yeast. Here, we have developed DetecDiv, a microfluidic-based image acquisition platform combined with deep learning-based software for high-throughput single-cell division tracking. We show that DetecDiv can reconstruct cellular replicative lifespans with outstanding accuracy. In addition, this methodology provides comprehensive temporal cellular metrics using time-series classification and image semantic segmentation. Hence, this methodology provides an all-in-one toolbox for quantitative division tracking assays that will pave the way for high-throughput phenotyping of single-cell dynamics and cellular aging studies.

Introduction

Yeast has a limited replicative lifespan (RLS, i.e., 20-30 divisions) before entering senescence and dying ¹. Over the last decades, this simple unicellular has become a reference model for understanding the fundamental mechanisms that control longevity ^{2,3}. Several independent mechanistic models have been proposed to explain entry into replicative senescence ⁴⁻⁶. In

this context, whether there are multiple parallel causes responsible for senescence remains highly debated ^{7,8}.

A crucial difficulty in solving this puzzle lies in the very labor-intensive nature of RLS assays ⁹ and the limited information derived from them regarding the dynamics of senescence entry. The initial development of microfluidic systems for RLS assays has partially alleviated this problem by allowing continuous observation of individual cell divisions and relevant fluorescent cellular markers under the microscope from birth to death ^{10–12}. Recent efforts further increased data acquisition throughput ^{13,14} and attempted to automate data analysis ^{15,16}. Yet, retrieving individual cellular lifespans from large sets of image sequences so far remained an insurmountable bottleneck to characterize senescence entry quantitatively or to screen large numbers of mutants and environmental conditions.

Here, we report the development of DetecDiv, an integrated platform that combines high-throughput observation of cell divisions using a microfluidic device, a simple benchtop image acquisition system, and a deep learning-based image processing software with several image classification frameworks. Using this methodology, one can accurately track cell division in an automated manner with outstanding accuracy. By combining this pipeline with additional deep learning models for time series classification and semantic segmentation, we provide a comprehensive toolset for an in-depth quantification of single-cell trajectories during entry into senescence.

Results

To overcome the current limitations inherent to replicative lifespan assays, we have developed an imaging platform that combines a custom benchtop microscope, a microfluidic device, and a set of deep learning-based image processing pipelines.

The microscope was built using a rigid frame with inverted epifluorescence optics, transmission (bright field) illumination, a camera, and a motorized stage (Fig. S1A and B). The motorized frame carries the microfluidic device to trap individual cells and follow their successive divisions from birth to death (Fig. 1A, S1C, and S1D). Even though its principle is similar to previously reported designs ^{13,14,17}, we have brought significant improvements to the trap geometry to increase cell retention, avoid replacement of a mother cell by its daughter, and prevent device clogging and any source of contamination (see Fig S1E-G and supplementary text for details). The device includes 16 independent chambers (with 2000

traps per chamber) to image different strains in parallel or to varying environmental conditions (Fig. 1A and 1B). Altogether, this system allows following the successive divisions and the entry into senescence of typically 30000 individual cells in parallel with a 5-min resolution (knowing that there are ~500 traps per field of view using a 20x objective), i.e., about 1 to 2 orders of magnitude above the previously described techniques ^{10,13}.

This image acquisition system generates a large amount of cell division data (on the Terabytes scale depending on the number of channels, frames, and fields of view), only a tiny part of which can be manually curated in a reasonable time. In particular, the determination of replicative lifespans requires counting successive cell divisions until death, hence, reviewing all images acquired for each cell in each field of view over time. In addition, automating the division counting process is complicated by the heterogeneity in cell fate (i.e. division times, cell shape), especially during the entry into senescence. To overcome this limitation, we have developed an image classification pipeline to count divisions and reconstruct the entire lifespan of individual cells dividing in the traps (Fig. 1C). For this, we have trained a GoogleNet convolutional neural network (CNN) ¹⁸ to determine the budding state of the trapped cells by assigning one of six possible classes (unbudded, small-budded, large-budded, dead, empty trap, clogged trap) to each frame, see Fig. S2 and S3A. In this framework, the alternation between the 'large budded' and the 'unbudded'/'small budded' states revealed the successive cell divisions, and the occurrence of the 'dead' class allowed us to reconstruct the cell's lifespan (Fig. 1C)

However, the assignment of the cellular state based on the CNN, which processes the images independently of one another, led to sporadic ambiguities and errors that compromise the identification of division events (Fig. 2A), hence the distribution of division times (Fig. 2B) and *a fortiori* of the lifespans (Fig. 2A and 2C). These problems could be partially alleviated by post-processing the predictions made by the CNN (see "CNN+PP" in Fig. 2A-C and supplementary text for details). Yet, to improve the robustness of the method, we have combined the CNN with a long short-term memory network (LSTM) ^{19,20}, to take into account the time-dependencies between images (Fig. 1C). Thus, by providing full image sequences rather than individual images, we obtained an outstanding accuracy and recall for both division quantification and lifespan reconstruction (Fig. 2B, 2C, S3D, S3E, and Movie M1). Comparing the predictions by the classifier to the manually annotated data ("ground truth") revealed a non-significant difference in the distributions and an excellent correlation ($R^2=0.99$ for both divisions and lifespans, Fig 2B and 2C). To estimate the robustness of the classification model which was only trained on images of WT cells, we measured the large-

scale RLS in classical longevity mutants. Remarkably, we recapitulated the increase (resp. decrease) in longevity observed in the *fab1Δ* (resp. *sir2Δ*) mutant ^{21,22} and we could compute the related death rate with a high-confidence interval using a large-scale dataset (Fig 2D) ²³. Importantly, only 200 manually annotated lifespans (i.e. used during the training procedure) were necessary to achieve robust RLS reconstruction. Thus, rapid user annotation of a small cohort of cells allows the model to be deployed on larger datasets in different genetic contexts and/or environments.

We then sought to apply other classification schemes of DetecDiv to further characterize the trajectories of the cells as they transition to senescence. First, we set up an LSTM sequence-to-sequence classifier to detect the onset of cell-cycle slowdown during entry into senescence (also referred to as the senescence entry point or SEP ¹²), see Fig. 3A and S4. We thus trained the classifier to assign a 'pre-SD' or 'post-SD' label (before and after the cell-cycle slowdown, respectively) to each frame, using the sequence of cellular state probabilities (i.e., the output of the CNN/LSTM image classifier described in Fig. 1C) as input. Using this method, we could successfully identify the transition to a slow division mode (Fig. 3B and 3C) and recapitulate the evolution of average division times after aligning individual trajectories from that transition (Fig. 3D).

Second, we used an encoder/decoder network based on a Resnet50 CNN ²⁴ and the DeepLab v3+ architecture ²⁵, see Fig. S5, to segment brightfield and fluorescence images of cells carrying a histone-Neongreen fusion (see Fig 4A, Movie M2 and supplementary text) ²⁵. After training the model on ~1500 manually segmented brightfield images using three output classes (i.e., 'background,' 'mother cell,' 'other cell'), we obtained accurate mother cells contours (Fig. 4A-C and S6). This allowed us to quantify the cellular volume increase (4C and 4D), as previously reported ²³. A similar training procedure with ~3000 fluorescence images yielded accurate nuclei contours (see Fig. 4E, 4F, and S7). It successfully recapitulated the sharp burst in histone fluorescence that follows cell-cycle slowdown (Fig. 4G, 4H) ²³, hence further validating our methodology for automated quantitative analyses of division tracking and replicative lifespan assays.

Discussion

In this study, we report the development of a microscopy pipeline to acquire and track cell division events with high throughput, hence unleashing the potential of microfluidic cell trapping devices to perform fully automated replicative lifespan analyses.

The imaging system was designed to perform heavy-duty image acquisition sequences (i.e, no filter wheel, fixed objective) to generate high-throughput microscopy datasets. The hardware could be easily assembled from simple optical components -for a price of about one-third that of a commercial automated microscope. By processing temporal sequences of images rather than individual ones, our software demonstrated an outstanding accuracy that matches human capabilities for image classification yet with much higher throughput.

The robustness of the imaging pipeline benefited from improvements made in the design of the microfluidic device (see supplementary text). Therefore, our framework now overcomes all intrinsic technical limitations of conventional RLS assays and provides an unprecedented potential to perform large screens for players and environmental perturbations that dynamically control replicative longevity.

More broadly, this work illustrates how temporal dependencies in image sequences can be exploited using a combined CNN and LSTM architecture to accurately reveal and quantify dynamic cellular processes. Despite large efforts to make deep-learning models available to the community of microscopists, very little work has attempted to fully exploit information encoded in image sequences. With its comprehensive set of generic classification schemes that can be fully user-parameterized, DetecDiv may be used well beyond the scope of the present study and applied to any biological context with complex temporal patterns (cellular differentiation, cell division, organelles dynamics, etc).

Methods

Strains

All strains used in this study are congenic to S288C (see Supplementary Table 1 for details). See supplementary methods for detailed protocols for cell culture.

Microfabrication and microfluidics

The designs were created on AutoCAD to produce chrome photomasks (jd-photodata, UK). The microfluidic master molds were then made by standard photolithography processes (see supplementary text for details).

The microfluidic device is composed of geometric microstructures that allow mother cells trapping and flushing of successive daughter cells (see Fig. S2 and supplementary text). The cell retention efficiency of the traps is 99% after the five first divisions. We designed a particle filter with a cutoff size of 5 μm to prevent dust particles or debris from clogging the chip. The microfluidic chips were fabricated with PDMS using standard methods (PDMS, Sylgard 184, Dow Chemical, USA, see supplementary text for detailed protocols). We connected the chip using PTFE tubing (1mm OD), and we used a peristaltic pump to ensure media replenishment (Ismatec, Switzerland). We used standard rich media supplemented with 2% dextrose (YPD). See supplementary methods for additional details.

Microscopy

The microscope was built from a modular microscope system with a motorized stage (ASI, USA, see the supplementary text for the detailed list of components), a 20x objective 0.45 (Nikon, Japan) lens, and an sCMOS camera (ORCA flash 4.0, Hamamatsu, Japan). A dual-band filter (#59022, Chroma Technology, Germany) coupled with a two-channel LED system (DC4104 and LED4D067, Thorlabs, USA). Sample temperature was maintained at 30°C thanks to a heating system based on an Indium Thin Oxide coated glass and an infrared sensor coupled to an Arduino-based regulatory loop. Micromanager v2.0²⁶ was used to drive all hardware, including the camera, the light sources, and the stage and objective motors. We developed a custom autofocus routine to minimize the autofocus time (https://github.com/TAspert/DetecDiv_Hardware). The interval between two frames for all the experiments was 5min. We could image approximately 80 fields of view (0.65mmx0.65mm) in brightfield and fluorescence (using a dual-band GFP-mCherry filter) with this interval.

Image processing

We developed Matlab software, DetecDiv, which provides different classification models: image classification, image sequence classification, time series classification, and pixel classification (semantic segmentation), see Fig. S9. DetecDiv was developed using Matlab, and additional toolboxes (TB), such as the Computer Vision TB, the Deep-learning TB, and the Image Processing TB. A graphical user interface was designed to facilitate the generation

of the training sets. The DetecDiv software is available for download on GitHub: <https://github.com/gcharvin/DetecDiv>

Image classification for division tracking and lifespan reconstruction

DetecDiv was used to classify images into six classes after supervised training using a GoogleNet¹⁸ network combined with an LSTM network²⁰. See supplementary text for details.

Image segmentation from brightfield and fluorescent images

DetecDiv was used to segment images using a pixel classification model called Deeplab v3+²⁵, after supervised training based on 1000-3000 manually annotated images. See supplementary text for details.

Cell-cycle slowdown detection

DetecDiv was used to detect cell-cycle slowdown from a temporal sequence of classes obtained using the division tracking network. The training was based on manual annotation of 200 lifespans. See supplementary text for details.

Statistics

All experiments have been replicated at least twice. Data are presented in Results and Figures as the mean \pm SEM (curves) or median. Group means were compared using the Two-sample t-test. A P value of < 0.05 was considered significant.

Computing

Image processing was performed on a computing server with 8 Intel Xeon E5-2620 processors and 8 co-processing GPU units (Nvidia Tesla K80), each of them with 12Go RAM. Under these conditions, the image classification of a single trap (roughly 60x60pixels) with 1000 frames took between 3 and 5s for the CNN/LSTM classifier. For image segmentation, it took about 30s to classify 1000 images.

Acknowledgments

We thank Audrey Matifas for constant technical support throughout this work, Sophie Quintin and Nacho Molina for carefully reading the manuscript. We are grateful to Olivier Tassy for their insightful discussions. We thank Denis Fumagalli at the IGBMC Mediaprep facility for media preparation. We are grateful to the IT service for efficient support and providing the computing resources. We thank the Charvin lab members, Bertrand Vernay, Jerome Mutterer,

Serge Taubert, and the IGBMC imaging facility for discussions and technical support. This work was supported by the Agence Nationale pour la Recherche (T.A. and G.C.), the grant ANR-10-LABX-0030-INRT, a French State fund managed by the Agence Nationale de la Recherche under the frame program Investissements d'Avenir ANR-10-IDEX-0002-02.

Data Availability

Annotated datasets and trained classifiers used in this study are available for download as indicated:

- Lifespan analyses:
 - Data: doi.org/10.5281/zenodo.5552642
 - Trained Network (CNN+LSTM): doi.org/10.5281/zenodo.5553862
- Brightfield image segmentation:
 - Data: doi.org/10.5281/zenodo.5553771
 - Trained Network (Encoder-Decoder Deeplabv3+): doi.org/10.5281/zenodo.5553851
- Cell-cycle slowdown detection:
 - Data: doi.org/10.5281/zenodo.5553796
 - Trained Network (LSTM): doi.org/10.5281/zenodo.5553829

Information regarding the microfluidic device, the custom imaging system are available on https://github.com/TAspert/DetecDiv_Data.

Code availability

The custom MATLAB software DetecDiv, used to analyze imaging data with deep-learning algorithms, is available on <https://github.com/gcharvin/DetecDiv>.

This software distribution features a tutorial on how to use the graphical user interface:

https://github.com/gcharvin/DetecDiv/blob/master/Tutorial/GUI_tutorial.md

It also provides the main commands to use the DetecDiv pipeline in custom user-defined scripts:

https://github.com/gcharvin/DetecDiv/blob/master/Tutorial/commandline_tutorial.md

A demo project that contains all the necessary files to learn how to use DetecDiv can be downloaded from zenodo :

<https://doi.org/10.5281/zenodo.5771536>

References

1. Mortimer, R. K. & Johnston, J. R. Life span of individual yeast cells. *Nature* 183, 1751–1752 (1959).
2. Denoth-Lippuner, A., Julou, T. & Barral, Y. Budding yeast as a model organism to study the effects of age. *FEMS Microbiol. Rev.* 38, 300–325 (2014).
3. Janssens, G. E. & Veenhoff, L. M. Evidence for the hallmarks of human aging in replicatively aging yeast. *Microb. Cell Fact.* 3, 263–274 (2016).
4. Hughes, A. L. & Gottschling, D. E. An early age increase in vacuolar pH limits mitochondrial function and lifespan in yeast. *Nature* 492, 261–265 (2012).
5. Sinclair, D. A. & Guarente, L. Extrachromosomal rDNA circles--a cause of aging in yeast. *Cell* 91, 1033–1042 (1997).
6. Aguilaniu, H., Gustafsson, L., Rigoulet, M. & Nyström, T. Asymmetric inheritance of oxidatively damaged proteins during cytokinesis. *Science* 299, 1751–1753 (2003).
7. Dillin, A., Gottschling, D. E. & Nyström, T. The good and the bad of being connected: the integrons of aging. *Curr. Opin. Cell Biol.* 26, 107–112 (2014).
8. He, C., Zhou, C. & Kennedy, B. K. The yeast replicative aging model. *Biochim. Biophys. Acta Mol. Basis Dis.* 1864, 2690–2696 (2018).
9. McCormick, M. A. et al. A Comprehensive Analysis of Replicative Lifespan in 4,698 Single-Gene Deletion Strains Uncovers Conserved Mechanisms of Aging. *Cell Metab.* 22, 895–906 (2015).
10. Lee, S. S., Vizcarra, I. A., Huberts, D. H. E. W., Lee, L. P. & Heinemann, M. Whole lifespan microscopic observation of budding yeast aging through a microfluidic dissection platform. *Proceedings of the National Academy of Sciences* 109, 4916–4920 (2012).
11. Xie, Z. et al. Molecular phenotyping of aging in single yeast cells using a novel microfluidic device. *Aging Cell* (2012).
12. Fehrmann, S. et al. Aging yeast cells undergo a sharp entry into senescence unrelated to the loss of mitochondrial membrane potential. *Cell Rep.* 5, 1589–1599 (2013).
13. Jo, M. C., Liu, W., Gu, L., Dang, W. & Qin, L. High-throughput analysis of yeast replicative aging using a microfluidic system. *Proc. Natl. Acad. Sci. U. S. A.* 112, 9364–9369 (2015).
14. Liu, P., Young, T. Z. & Acar, M. Yeast Replicator: A High-Throughput Multiplexed Microfluidics Platform for Automated Measurements of Single-Cell Aging. *Cell Rep.* 13, 634–644 (2015).

15. Ghafari, M. et al. Complementary performances of convolutional and capsule neural networks on classifying microfluidic images of dividing yeast cells. *PLoS One* 16, e0246988 (2021).
16. Ghafari, M., Mailman, D. & Qin, H. Application Note: μ Polar - An Interactive 2D Visualization Tool for Time-Series Microscopic Images. (2021) doi:10.2139/ssrn.3827406.
17. Crane, M. M., Clark, I. B. N., Bakker, E., Smith, S. & Swain, P. S. A Microfluidic System for Studying Ageing and Dynamic Single-Cell Responses in Budding Yeast. 9, e100042 (2014).
18. Szegedy, C. et al. Going deeper with convolutions. in 2015 IEEE Conference on Computer Vision and Pattern Recognition (CVPR) 1–9 (2015).
19. Venugopalan, S. et al. Sequence to sequence -- video to text. in 2015 IEEE International Conference on Computer Vision (ICCV) (IEEE, 2015). doi:10.1109/iccv.2015.515.
20. Hochreiter, S. & Schmidhuber, J. Long Short-Term Memory. *Neural Comput.* 9, 1735–1780 (1997).
21. Defossez, P. A. et al. Elimination of replication block protein Fob1 extends the life span of yeast mother cells. *Mol. Cell* 3, 447–455 (1999).
22. Lin, S. J., Defossez, P. A. & Guarente, L. Requirement of NAD and SIR2 for life-span extension by calorie restriction in *Saccharomyces cerevisiae*. *Science* 289, 2126–2128 (2000).
23. Morlot, S. et al. Excessive rDNA Transcription Drives the Disruption in Nuclear Homeostasis during Entry into Senescence in Budding Yeast. *Cell Rep.* 28, 408–422.e4 (2019).
24. He, K., Zhang, X., Ren, S. & Sun, J. Deep Residual Learning for Image Recognition. in 2016 IEEE Conference on Computer Vision and Pattern Recognition (CVPR) 770–778 (2016).
25. Chen, L.-C., Zhu, Y., Papandreou, G., Schroff, F. & Adam, H. Encoder-decoder with atrous separable convolution for semantic image segmentation. *arXiv [cs.CV]* (2018).
26. Edelstein, A. D. et al. Advanced methods of microscope control using μ Manager software. *J Biol Methods* 1, (2014).
27. Pokhrel, A., Dyba, T. & Hakulinen, T. A Greenwood formula for standard error of the age-standardised relative survival ratio. *Eur. J. Cancer* 44, 441–447 (2008).

Figure 1

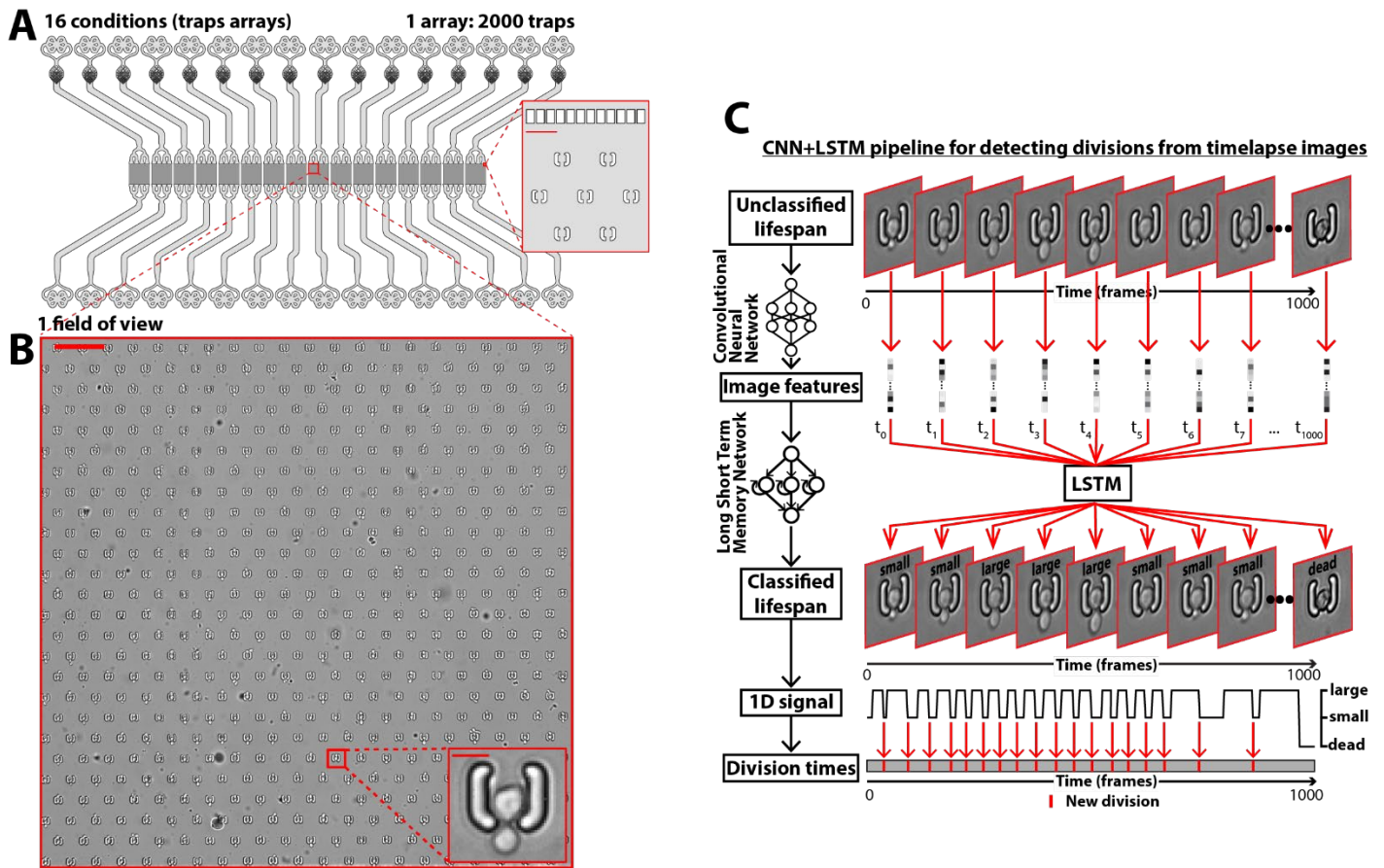


Figure 1 - DetectDiv division tracking and RLS reconstruction pipeline

A) Left: Sketch of the microfluidic device, featuring 16 independent channels with 2000 individual cell traps in each; Right: zoom on the cellular traps, scale bar: 20 μ m.

B) Brightfield image from a typical field of view obtained with the imaging setup, scale bar: 60 μ m; Inset: Zoom on one trap containing a budding yeast, scale bar: 5 μ m.

C) Principles of the DetectDiv division tracking and lifespan reconstruction pipeline; Brightfield images are processed by a convolutional neural network (CNN) to extract representative image features. The sequence of image features is then processed by a long short-term memory network (LSTM) that assigns one of the 6 predefined classes ('unbud', 'small', 'large', 'dead', 'clog', 'empty'), taking into account the time dependencies. Temporal oscillations between "large" and "small" or "large" and "unbudded" indicate the completion of the division cycle. The appearance of the "dead" class marks the end of the lifespan.

Figure 2

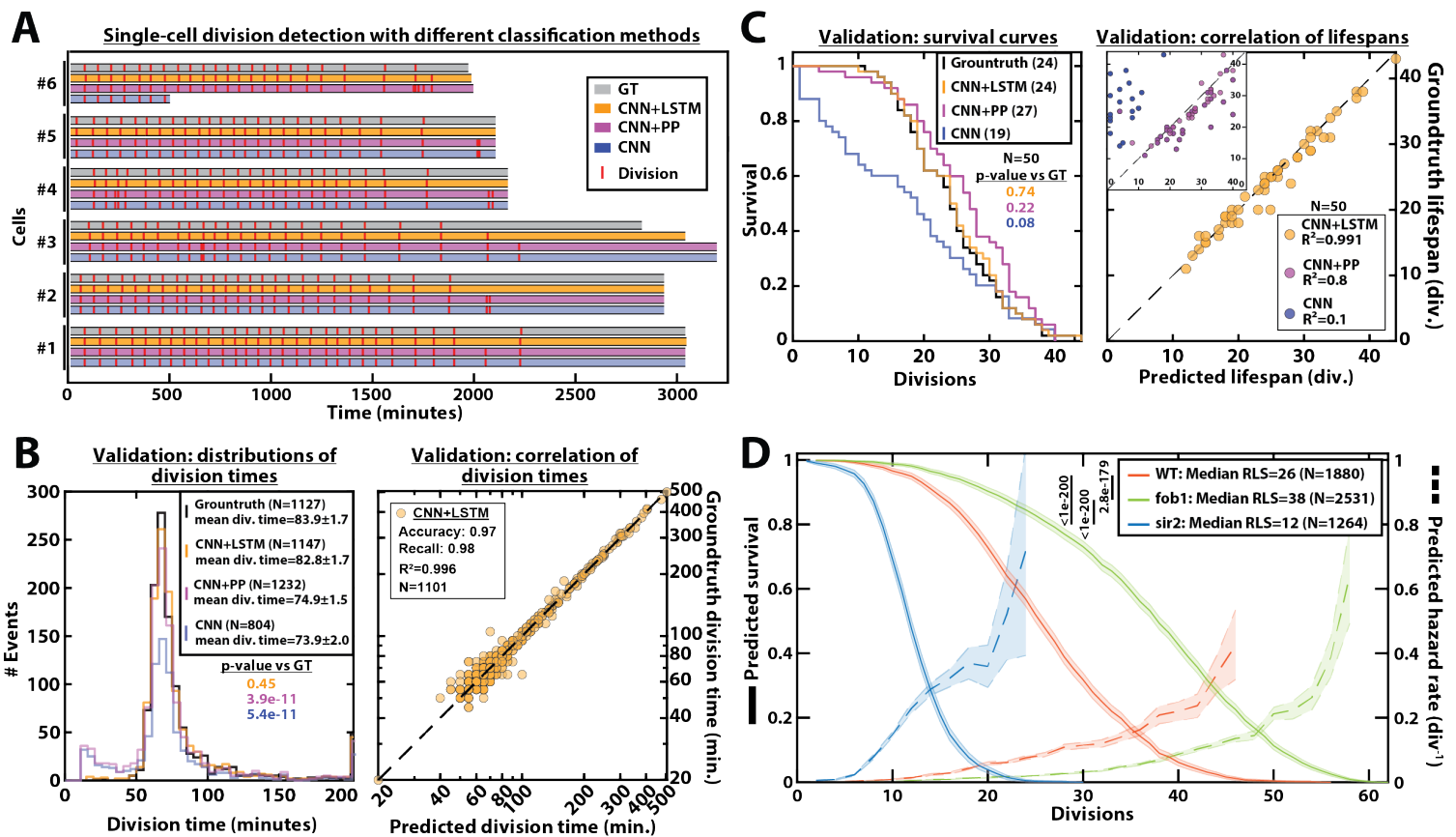


Figure 2 - Validations of the division tracking and RLS reconstruction

A) Comparison of the different methods used for 6 sample cells. The gray bars represent the ground truth data made from manually annotated image sequences. Colored lines indicate the corresponding predictions made by CNN/LSTM (orange), the CNN + post-processing (magenta), and the CNN (blue) networks (see Methods and supplementary text for details). The red segments indicate the position of division events.

B) Left: histogram of division times representing ground truth data and predictions using different processing pipelines). The p-value indicates the results of a rank-sum test comparing the predictions to the ground truth for the different pipeline variants. The total number of division events annotated in the ground truth or detected by the networks are indicated in the legend. Right: Scatter plot in log scale representing the correlation between ground-truth-calculated division times and those predicted by the CNN/LSTM network. R² represents the coefficient of correlation between the two datasets. Accuracy and recall are defined in the supplementary text.

C) Left: cumulative distribution showing the survival of cells as a function of the number of divisions (N=50 cells). The numbers in the legend indicate the median replicative lifespans. The p-value indicates the results from a statistical rank-sum test. Right: Scatter plot showing

the correlation of the replicative lifespans of individual cells obtained from the ground truth with that predicted by the CNN/LSTM architecture (N=50). Inset: same as the main plot, but for the CNN and CNN with post-processing pipelines. R^2 indicates the coefficient of correlation between the two datasets.

D) Replicative lifespans obtained using the CNN/LSTM network for longevity mutants (solid colored lines, genotype indicated). The shading represents the 95% confidence interval calculated using the Greenwood method ²⁷. The median RLS and the number of cells analyzed are indicated in the legend. The dashed lines with shading represent the hazard rate and its standard deviation estimated with a bootstrap test (N=100). Results from log-rank tests (comparing WT and mutant distributions) are indicated on the left of the legend.

Figure 3

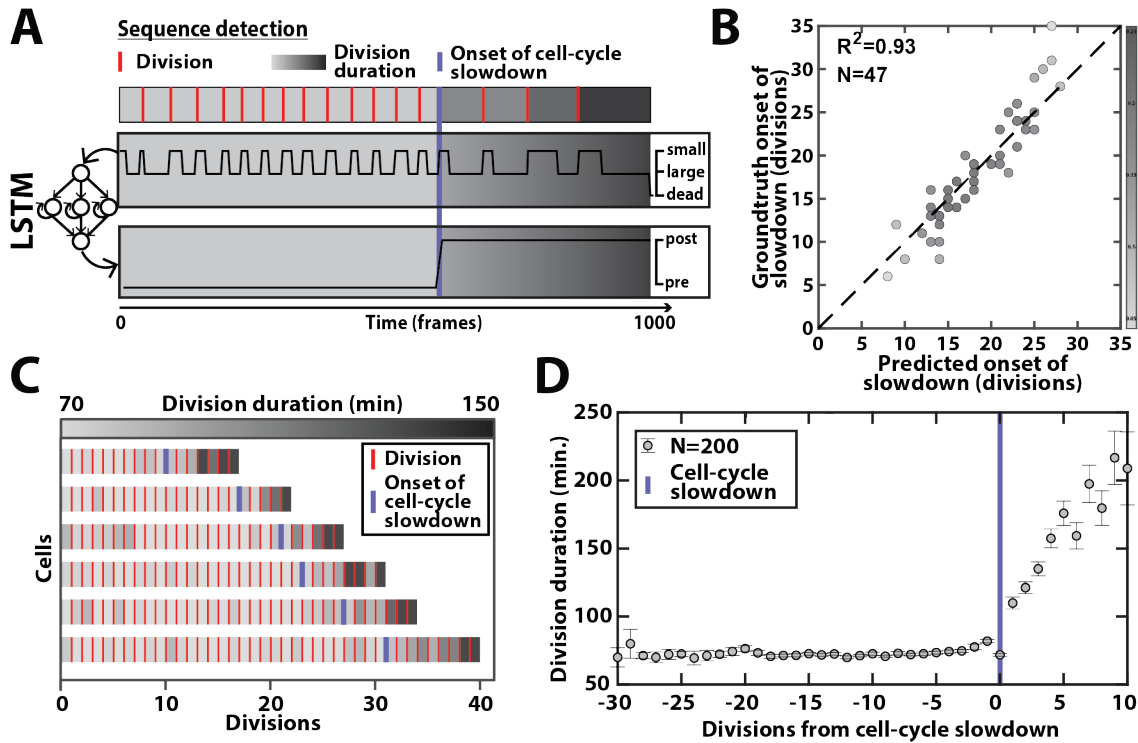


Figure 3 - Deep learning-based measurement of the dynamics of entry into senescence

A) Sketch depicting the detection of the time of slow division (SD) state. The temporal sequence of classes probabilities (ie, unbud, small, large, dead) is fed into an LSTM network that predicts the onset of cell-cycle slowdown by assigning one of the two predefined classes pre-SD or post-SD to each frame.

B) Correlogram showing the correlation between the onset of cell-cycle slowdown predicted by the LSTM network and the ground truth data, obtained as previously described ¹². The color code indicates the local density of the points using arbitrary units as indicated by the color bar.

C) Sample trajectories indicating the successive divisions of individual cells (red lines) along with the division times (color-coded as indicated).

D) Average division time versus division index after aligning all individual trajectories from the onset of cell-cycle slowdown ¹². Each point represents an average over up to 200 cell trajectories. The error bar represents the standard error-on-mean.

Figure 4

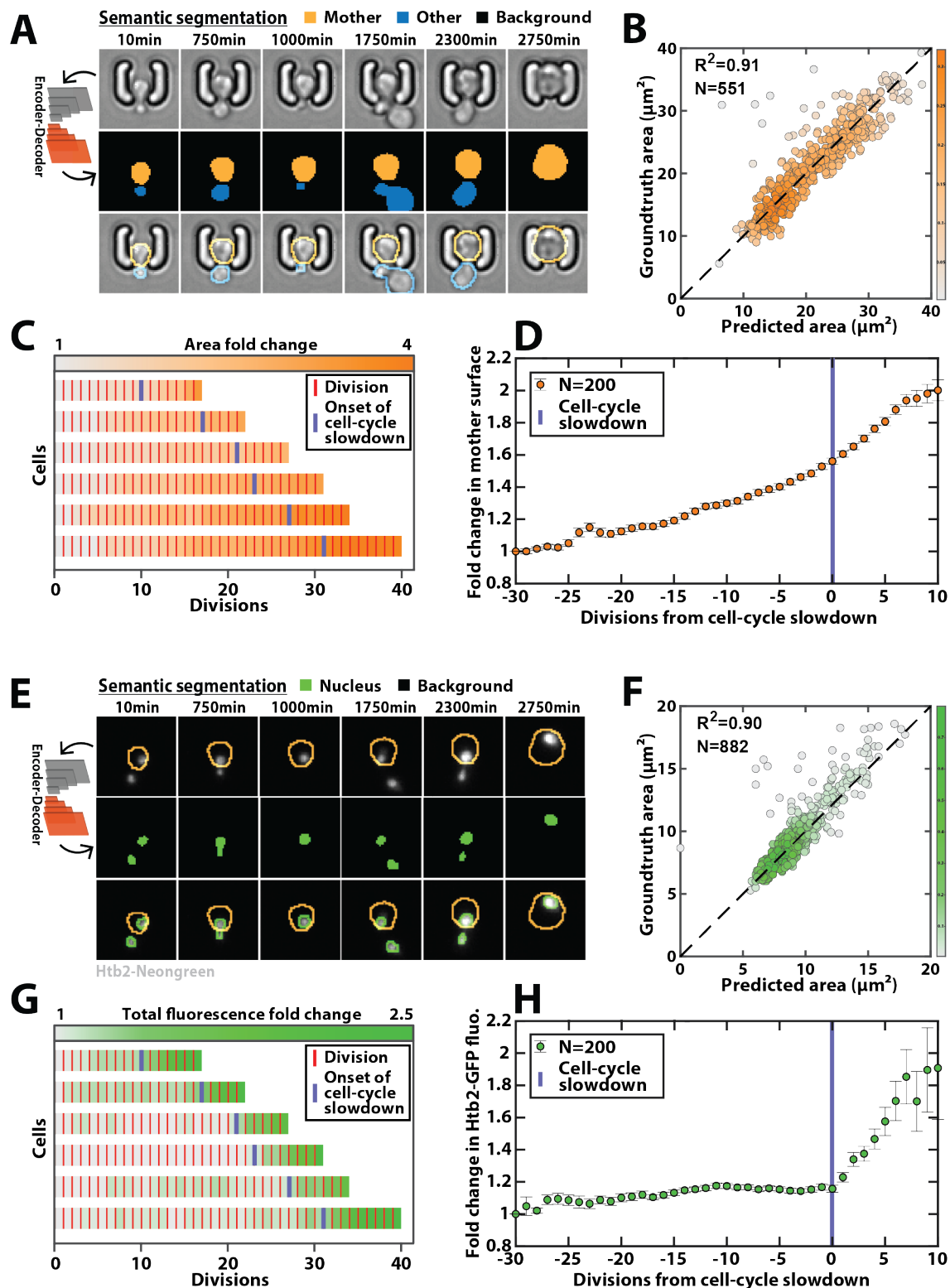


Figure 4- Deep learning-based semantic segmentation of cells and nuclei

A) Principles of semantic cell contours segmentation based on brightfield images ; Top and middle row) Individual brightfield images were processed by the DeeplabV3+ network that was trained to perform pixel classification using three predefined classes representing the

background (black), the mother cell of interest (orange), or any other cell in the image (blue).

B) Bottom row: overlay of brightfield images with segmented cellular contours .

C) Correlogram showing the correlation between individual cell area predicted by the segmentation pipeline and the ground truth data, obtained by manual annotation of the images. The color code indicates the local density of the points using arbitrary units.

Sample trajectories indicating the successive divisions of individual cells (red lines) along with the cell surface (color-coded as indicated).

D) Average mother cell surface versus division index after aligning all individual trajectories from the onset of cell-cycle slowdown¹². Each point represents an average over up to 200 cell trajectories. The error bar represents the standard error-on-mean.

E) Principles of semantic cell nuclei segmentation based on fluorescent images of cells expressing a histone-Neongreen fusion. The semantic segmentation network was trained to classify pixels between two predefined classes ('background' in black, 'nucleus' in green).

F) Same as B) but for nuclear surface.

G) Same as C) but for nuclear fluorescence.

H) Same as in D) but for nuclear fluorescence.

Supplementary text

Théo Aspert^{1234*}, Didier Hentsch¹²³⁴ and Gilles Charvin^{1234*}

1) Department of Developmental Biology and Stem Cells, Institut de Génétique et de Biologie Moléculaire et Cellulaire, Illkirch, France

2) Centre National de la Recherche Scientifique, UMR7104, Illkirch, France

3) Institut National de la Santé et de la Recherche Médicale, U964, Illkirch, France

4) Université de Strasbourg, Illkirch, France

*: Corresponding authors: charvin@igbmc.fr, aspertt@igbmc.fr

Supplementary Methods

Cell culture

For each experiment, freshly thawed cells were grown overnight, diluted in the morning, and allowed to perform several divisions (~5 hours at 30°C) before injection into the microfluidic device. Yeast extract Peptone Dextrose (YPD) medium was used throughout the experiments. We found that synthetic media (SCD) tend to form small crystals that escape the microfluidic filter and may be detrimental to long-term cell growth. However, this phenomenon was not observed with YPD media.

Microfluidic mold fabrication

The designs were created on AutoCAD (see https://github.com/TAspert/DetecDiv_Data to download the design) to produce chrome photomasks (jd-photodata, UK). Then, the microfluidic master molds were made using two rounds of classical photolithography steps. The array of 2000 traps was created from a 5.25µm deposit by spinning (WS650 spin coater, Laurell, France) 3mL of SU8-2005 negative photoresist at 2500rpm for 30sec on a 3" wafer (Neyco, FRANCE). Then, a soft bake of 3min at 95°C on heating plates (VWR) was performed, followed by exposure to 365nm UVs at 120 mJ/cm² with a mask aligner (UV-KUB3, Kloeé, FRANCE). Finally, a post-exposure bake identical to the soft bake was performed before development using SU-8 developer (Microchem, USA).

The second layer with channel motifs was made of a 30µm deposit of SU8-2025, by spinning it at 2500rpm for 30s. Subsequently, a soft bake of 3min at 65°C and 6min at 95°C was performed. The wafer was then aligned with the mask containing the motif of the second

layer before a 160mJ/cm² exposure. A post-exposure bake similar to the soft bake was then performed.

After each layer, we performed a hard bake at 150°C for 15min to anneal potential cracks and stabilize the photoresist. Finally, the master molds were treated with chlorotrimethylsilane to passivate the surface.

Microfluidics chip design, fabrication, and handling

The microfluidic device is composed of an array of 2050 microstructures able to trap a mother cell while removing successive daughter cells, as previously designed (Ryley and Pereira-Smith 2006; Zhang et al. 2012; Lee et al. 2012), (Crane et al. 2014; Jo et al. 2015; Liu, Young, and Acar 2015). The traps are composed of two symmetrical structures separated by 3μm (see Fig. 1 and S1C and S1D), in such a way that only one cell can be trapped and remain in between the structures. We have measured that 99% of the cells that underwent at least 5 divisions in the trap would stay inside until their death. Moreover, a particle filter with a cutoff size of 15μm is present before each array of traps, preventing dust particles or debris from clogging the chip (Fig. S1C).

The microfluidic devices were fabricated using soft-lithography by pouring polydimethylsiloxane (PDMS, Sylgard 184, Dow Chemical, USA) with its curing agent (10:1 mixing ratio) on the different molds. The chips were punched with a 1mm biopsy tool (KAI, Japan) and covalently bound to a 24 × 50 mm coverslip using plasma surface activation (Diener Zepto, Germany). The assembled chips were baked for 1 hour at 60°C to consolidate covalent bonds between glass and PDMS. The chip was then plugged using a 1mm Outer Diameter (O.D.) PTFE tubing (Adtech, UK) and the channels were primed using culture media for 5min. After that, cells were injected through the outlet using a 5mL syringe and a 26G needle for approximately 1 minute per channel by applying very gentle pressure. The cell filter placed upstream of the trapping area prevented the cells from entering the tubing connected to the inlet (see Figure S1E). Then, the inlet of each microfluidic channel was connected to a peristaltic pump (Ismatec, Switzerland) with a 5μL/min rate to ensure a constant replenishment of the media and dissection of the daughter cells (Fig. S1E). This procedure avoids potential contamination by cells forming colonies upstream of the trapping area, which would induce the clogging of the device after 1-2 days of experiment, therefore making long lasting experiments more robust.

Microscopy

Microscope

The microscope was built from a modular microscope system (RAMM, ASI, USA) with trans- (Oly-Trans-Illum, ASI, USA) and epi- (Mim-Excite-Cond20N-K, ASI, USA) illumination. This microscope frame provides a cost-effective solution to build a minimal microscopy apparatus to perform robust image acquisition over several days (Fig. S1B).

It is equipped with a motorized XY stage (S551-2201B, ASI, USA), a stage controller (MS200, ASI, USA), and a stepper motor to drive the 20x N.A. 0.45 Plan Fluor objective (Nikon, Japan) and an sCMOS camera (ORCA flash 4.0, Hamamatsu, Japan) with 2048 x 2048 pixels (i.e., 650 microns x 650 microns field of view at 20x magnification). We used a dual-band filter (#59022, Chroma Technology, Germany) coupled with two-channel LED illumination (DC4104 and LED4D067, Thorlabs, USA), which allows fast imaging of GFP and mCherry without any filter switching.

Sample holder and temperature control

We designed a custom 3D-printed sample holder (by extruding PLA material with a MK3S+ printer, Prusa Research, Czech republic) for the microfluidic device to ensure the mechanical stability of the microfluidic device.

In addition, we developed a custom temperature control system to maintain a constant temperature (30°C) and guarantee optimal cell growth throughout the experiment. Briefly, we used an Indium Tin Oxide (ITO) Coated glass, an electrically conductive and transparent material, in direct contact with the PDMS chip. Therefore, applying a voltage to the ITO glass allowed the Joule effect to heat the glass and the adjacent PDMS chip.

To achieve a temperature control loop, we used an infrared sensor attached to the objective and facing towards the bottom glass coverslip in contact with the cells. The sensor allowed in situ temperature measurement and was used in an Arduino-based PID control loop to regulate the heating power to maintain the setpoint temperature. About 1W was sufficient to maintain a 30°C temperature at room temperature. Notably, the temperature profile obtained with this method was homogenous and constant throughout the experiment. Furthermore, the glass is fully transparent to visible light. In addition, it does not interfere with fluorescent light when using an inverted microscope since it is located at the end of the optical path, after the sample.

Software and time-lapse acquisition parameters

Micromanager v2.0. was used to drive the camera, the light source, the XYZ controller, and the LED light source for fluorescence epi-illumination. We developed a specific program in order to drive the temperature controller from the Arduino (The source code is available on github: github.com/TAspert/ITO_heating_device).

Unless specified otherwise, the interval between two brightfield frames for all the experiments was 5minutes, and images recorded over 1000 frames (i.e, ~3 days). We used three z-stack for brightfield imaging (spaced by 1.35 microns) to ease the detection of small buds during the image classification process for cell state determination. Fluorescent images were acquired with a 10min interval using 470nm illumination for 50ms. Up to 80 fields of view were recorded over the 5-min interval.

Autofocusing

To keep a stable focus through the whole experiment, we developed a custom software-based autofocus routine that finds the sharpest image on the first field of view and then applies the focus correction to the rest of the positions. This method provides faster scanning of all fields of view in a reasonable time. Nevertheless, it is almost as efficient as performing autofocusing on each position since the primary source of defocusing in our setup is the thermal drift, which applies identically to all the positions.

Image processing

DetecDiv software

We designed custom software DetecDiv as a Matlab backend to provide an expandable interface to perform microscopy data processing, based on existing resources in Matlab's Deep Learning Toolbox and Computer Vision Toolbox. DetecDiv can be used with an arbitrarily large number of classes, image channels, types, and sizes (Figure S9). Therefore, its capabilities go far beyond the scope of this study.

First, DetectDiv offers graphical tools to identify regions of interest in image sequences. In addition, a cross-correlation function can be used to automatically detect similar regions in images, such as the traps in the microfluidic device.

Then, several classification models can be defined to process the images: 1) Image classification using a convolutional network (CNN, see Fig. S2); 2) a combined CNN/LSTM classifier as reported in fig. 1; 3) an LSTM network to perform sequence-to-sequence (as in Fig. 2A) or sequence-to-one classification; 4) An encoder/decoder classifier to perform pixel classification (semantic segmentation) based on the Deeplab v3+ architecture (Chen et al. 2018), see Fig 2A and 2B; 5) Similar routines as in 1-4, but for regression analyses (not used

in the present study). DetecDiv allow the user to choose among several CNNs -such as GoogleNet or Resnet50 for all image classifications/segmentations applications.

DetecDiv provides a graphical user interface to generate the groundtruth required for both training and testing the classifiers used in the image classification, pixel classification, and time-series classification pipelines. Furthermore, we paid attention to making this step as user-friendly as possible. For instance, we used keyboard shortcuts to assign labels to individual frames (it takes about 5-10 min to annotate 1000 frames in the case of cell state assignment). Similarly, direct "painting" of objects with a mouse or a graph pad can be used to label images before launching the training procedure for pixel classification.

DetecDiv training and validation procedures are run at the command line, which allows using remote computing resources, such as a CPU/GPU cluster. All the relevant training parameters can be easily defined by the user. We designed generic routines to benchmark the trained classifiers that allow an in-depth evaluation of the classifiers' performances(Laine et al. 2021). Trained classifiers can be exported to user-defined repositories and classified data can be further processed using custom Matlab scripts, and images sequences can be exported as .mat or .avi video files.

Last, DetecDiv provides additional post-processing routines to extract division and lifespan data for further analysis, as performed in the present study.

Convolutional Neural Networks (CNN) for image classification

We used an image classifier to assess the state of cells in the cell cycle (small, large-budded, etc.) using brightfield images of individual traps. For each frame, we combined the three z-stack images described above into a single RGB image, which was used as input for the classifier.

We defined six classes, four of which representing the state of the cell, i.e., unbudded ('unbud'), small-budded ('small'), large-budded ('large'), dead ('dead'), as shown on Fig. S3A. Two additional classes are related to the state of the trap: trap with no a cell ('empty') and clogged trap ('clog'). We trained a pre-trained GoogleNet convolutional neural network (Szegedy et al. 2015) to classify images according to these six classes using a training set of 200000 representative manually annotated brightfield images (i.e., 200 traps monitored during 1000 frames). The training of the classifier was achieved using Adaptive Moment estimation (Adam) optimizer (Kingma and Ba 2015). Specific parameters used can be found in the supplementary table T2.

After the training procedure, we tested the classifier using a dataset composed of 50 independent cell traps (i.e. 50000 images) that were manually annotated and used for benchmarking (Fig. S3).

Division time measurement and replicative lifespan (RLS) reconstruction

As the image classifier outputs a label for each frame corresponding to one of the 6 classes defined above, we used the sequence of labels to reveal the successive divisions of the cells: the oscillations between the “large” and “small” or “large” and “unbudded” classes captured the entry into a new cell cycle. The appearance of the “dead” class was used to assess the end of the replicative lifespan. This set of rules was used to compute the division times and the RLS of each individual cell when using either the CNN or the combined CNN/LSTM architecture (see below). However, in order to improve the accuracy of the method based only on the CNN, we implemented an additional “post-processing” step (referred to as PP in Figure 1), namely that two consecutive frames with a “dead” label are necessary to consider a cell as dead.

Image sequence classification using combined CNN and a long short-term memory network (LSTM)

Based on the rules defined above, and despite very good benchmarks obtained for image classification (See Figure S3B and S3C), the CNN-based classifier was unable to accurately capture the replicative lifespan in the test set (see Fig. 1E). Indeed, the sporadic appearance of the “dead” class led to an underestimate of the actual RLS, and the incorrect classification of some small-budded and large-budded cells provided some abnormally short estimates of cell cycle durations (see the first peak in the distribution on Figure 1D). Additional post-processing steps, as mentioned above, alleviated the problem of short lifespan estimates (see CNN + PP on Figure 1E).

To provide a more accurate classification of the image according to the cellular state, we added a bidirectional long short-term memory (LSTM) network with 150 hidden units to the CNN network (Hochreiter and Schmidhuber 1997). The LSTM network takes the whole sequence of images as input (instead of independent images in the case of the CNN), hence taking the time-dependencies between successive images into account for improved classification. Two hundred image sequences (each with 1000 frames) were used to train the LSTM network independently of the CNN network (see training parameters in Supplementary table T3 and benchmarks on Figure S3D and S3E). The CNN and the LSTM network were

then assembled as described in Figure 1B in order to output a sequence of labels for each series of images.

Annotated dataset is available at: doi.org/10.5281/zenodo.5552642

Trained network is available at: doi.org/10.5281/zenodo.5553862

Assessment of cell-cycle slowdown using a LSTM network

After classifying an image sequence to reconstruct the lifespans of the cells, we further analyzed the data to determine the onset of cell-cycle slowdown. Unlike our previously developed method based on chi-square minimization with a piecewise linear fit (Fehrmann et al. 2013), we designed a time series classification method to identify when the cell cycle starts to slow down. For this, we trained a bidirectional LSTM network with 150 hidden units to classify all the frames in each lifespan between two classes, i.e., 'pre-slowdown' and 'post-slowdown'. We used class probabilities from the previously described CNN/LSTM (unbudded, small, large, dead), as an input for the classifier (see Figure S4 for benchmarking results on a test set with 50 lifespans).

Annotated dataset is available at: doi.org/10.5281/zenodo.5553796

Trained network is available at: doi.org/10.5281/zenodo.5553829

Brightfield and fluorescence images semantic segmentation using DeepLab v3+

Cell and nuclei contours were determined based on brightfield and fluorescence images, respectively, using the deep learning-based semantic segmentation architecture DeepLab v3+ (Chen et al. 2018). DeepLab v3+ possesses an encoder/decoder architecture allowing to classify pixels according to a number of user-defined classes. Here, we used 3 classes (i.e., background, mother cell, other cells) for cell segmentation to distinguish between the mother cell and its surrounding buds or daughter cells, see Figure 2 and S6). For nuclei segmentation, only two classes were defined (i.e., background and nucleus, see Fig. 2 and S6). We used the Resnet50 CNN in the encoder part of the network because it provided better segmentation results than Googlenet. We trained the network using a manually curated training set of 1500 and 3000 images for brightfield and fluorescence images, respectively (see Figure S7 and S8 for benchmarking results). Specific parameters used can be found in the supplementary table T4 (cell segmentation) and T5 (nucleus segmentation).

Annotated dataset is available at: doi.org/10.5281/zenodo.5553771

Trained network is available at: doi.org/10.5281/zenodo.5553851

Classifier benchmarking

We used standard benchmarking to estimate the efficiency of image and pixel classifiers. For each classifier, we computed the confusion matrix obtained by comparing the “groundtruth” manually annotated images (or timeseries) to the predictions made by the classifier. We computed the accuracy, the recall, and F-score for each class, which balances accuracy and recall. In the specific case of pixel classification (semantic segmentation), we computed these benchmarks for different values of prediction thresholds used to assign the “mother” and “nucleus” classes, as reported in Figure S7 and S8. Then, we performed the segmentation of images using the threshold value that maximizes the F-score (0.9 and 0.35 for brightfield and fluorescence image classification, respectively).

To benchmark the detection of divisions, we used a custom pairing algorithm to detect false positive and false negative divisions. Using this, we could compute the accuracy and recall of the division detection procedure, and plot the correlation between paired divisions (Fig. 1D).

Statistics

All experiments have been replicated at least twice. Error bars represent the standard error-on-mean, unless specified otherwise. Results of specific statistical tests are indicated in the figure legends.

Supplementary movies legends

Supplementary movie 1: Comparison of groundtruth versus classifier predictions for the CNN/LSTM classification of the cellular state
(<https://www.biorxiv.org/content/10.1101/2021.10.05.463175v2.supplementary-material>)

The left column represents the class predictions made by the CNN/LSTM classifier, while the right column represents the groundtruth (determined by manual annotation). The two numbers represent the number of buds generated by the cells according to the classifier predictions and manual annotation, respectively.

Supplementary movie 2: Sample movies of individual cells following cellular state classification, cell and nuclear contour segmentation

(<https://www.biorxiv.org/content/10.1101/2021.10.05.463175v2.supplementary-material>)

The left column represents the cellular state according to the prediction made by the CNN/LSTM classifier. The middle column shows the brightfield image along with mother cell contours obtained by a semantic segmentation classifier. The right column displays the Htb2-NeonGreen fluorescence channel, along with cells contours and nuclear contours obtained by a semantic segmentation classifier.

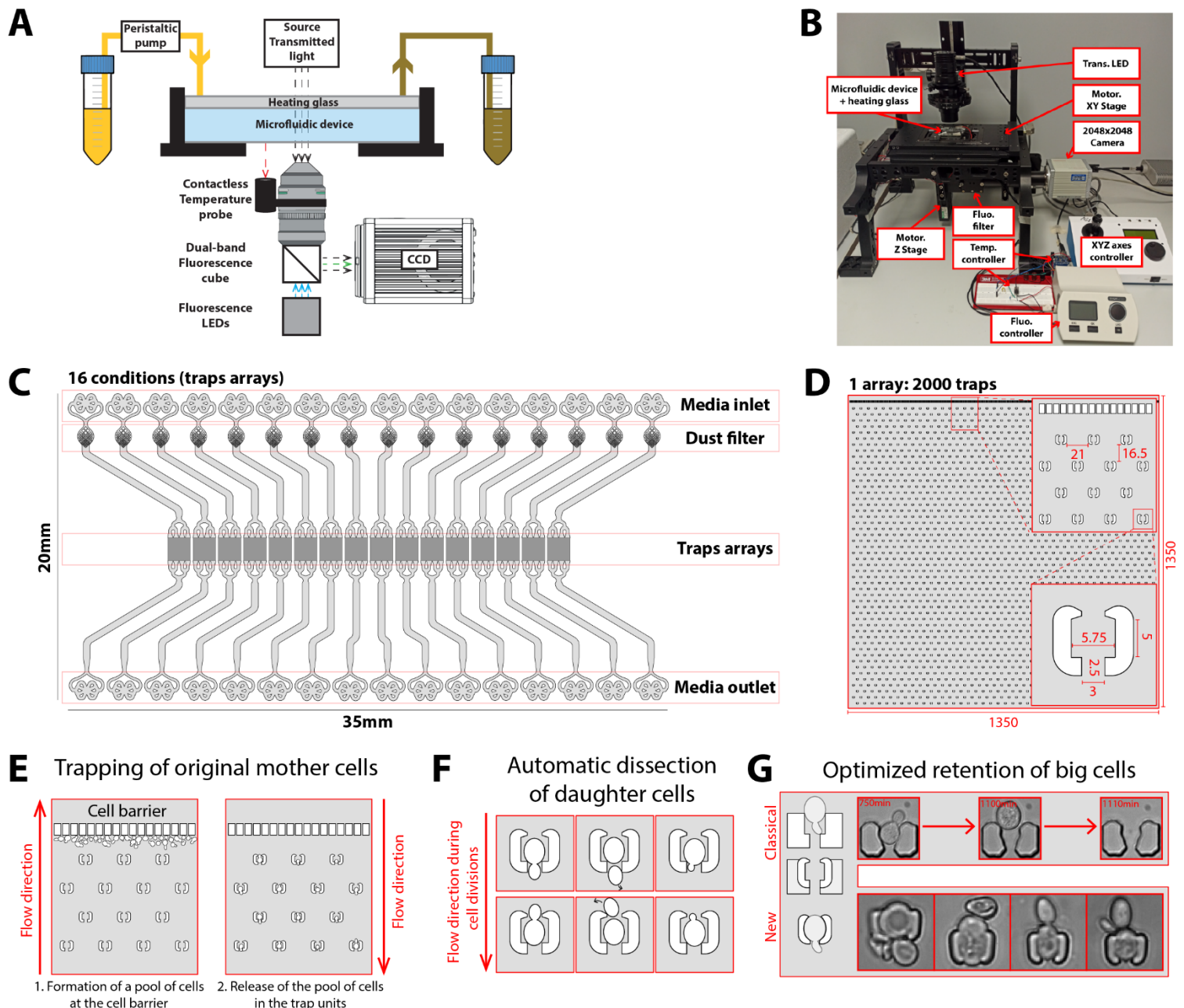
Additional references

- Chen, Liang-Chieh, Yukun Zhu, George Papandreou, Florian Schroff, and Hartwig Adam. 2018. "Encoder-Decoder with Atrous Separable Convolution for Semantic Image Segmentation." *arXiv [cs.CV]*. arXiv. https://openaccess.thecvf.com/content_ECCV_2018/papers/Liang-Chieh_Chen_Encoder-Decoder_with_Atrous_ECCV_2018_paper.pdf.
- Crane, Matthew M., Ivan B. N. Clark, Elco Bakker, Stewart Smith, and Peter S. Swain. 2014. "A Microfluidic System for Studying Ageing and Dynamic Single-Cell Responses in Budding Yeast" 9 (6): e100042.
- Fehrmann, Steffen, Camille Paoletti, Youlian Goulev, Andrei Ungureanu, Hugo Aguilaniu, and Gilles Charvin. 2013. "Aging Yeast Cells Undergo a Sharp Entry into Senescence Unrelated to the Loss of Mitochondrial Membrane Potential." *Cell Reports* 5 (6): 1589–99.
- Hochreiter, Sepp, and Jürgen Schmidhuber. 1997. "Long Short-Term Memory." *Neural Computation* 9 (8): 1735–80.
- Jo, Myeong Chan, Wei Liu, Liang Gu, Weiwei Dang, and Lidong Qin. 2015. "High-Throughput Analysis of Yeast Replicative Aging Using a Microfluidic System." *Proceedings of the National Academy of Sciences of the United States of America* 112 (30): 9364–69.
- Kingma, Diederik P., and Jimmy Ba. 2015. "Adam: A Method for Stochastic Optimization." <https://www.semanticscholar.org/paper/a6cb366736791bcccc5c8639de5a8f9636bf87e8>.
- Laine, Romain F., Ignacio Arganda-Carreras, Ricardo Henriques, and Guillaume Jacquemet. 2021. "Avoiding a Replication Crisis in Deep-Learning-Based Bioimage Analysis." *Nature Methods* 18 (10): 1136–44.
- Lee, Sung Sik, Ima Avalos Vizcarra, Daphne H. E. W. Huberts, Luke P. Lee, and Matthias Heinemann. 2012. "Whole Lifespan Microscopic Observation of Budding Yeast Aging through a Microfluidic Dissection Platform." *Proceedings of the National Academy of Sciences* 109 (13): 4916–20.
- Liu, Ping, Thomas Z. Young, and Murat Acar. 2015. "Yeast Replicator: A High-Throughput Multiplexed Microfluidics Platform for Automated Measurements of Single-Cell Aging." *Cell Reports* 13 (3): 634–44.
- Ryley, J., and O. M. Pereira-Smith. 2006. "Microfluidics Device for Single Cell Gene Expression Analysis in *Saccharomyces Cerevisiae*." *Yeast* 23 (14-15): 1065–73.
- Szegedy, Christian, Wei Liu, Yangqing Jia, Pierre Sermanet, Scott Reed, Dragomir Anguelov, Dumitru Erhan, Vincent Vanhoucke, and Andrew Rabinovich. 2015. "Going Deeper with Convolutions." In *2015 IEEE Conference on Computer Vision and Pattern Recognition*

(CVPR), 1–9.

Zhang, Yi, Chunxiong Luo, Ke Zou, Zhengwei Xie, Onn Brandman, Qi Ouyang, and Hao Li. 2012. "Single Cell Analysis of Yeast Replicative Aging Using a New Generation of Microfluidic Device" 7 (11): e48275.

Figure S1



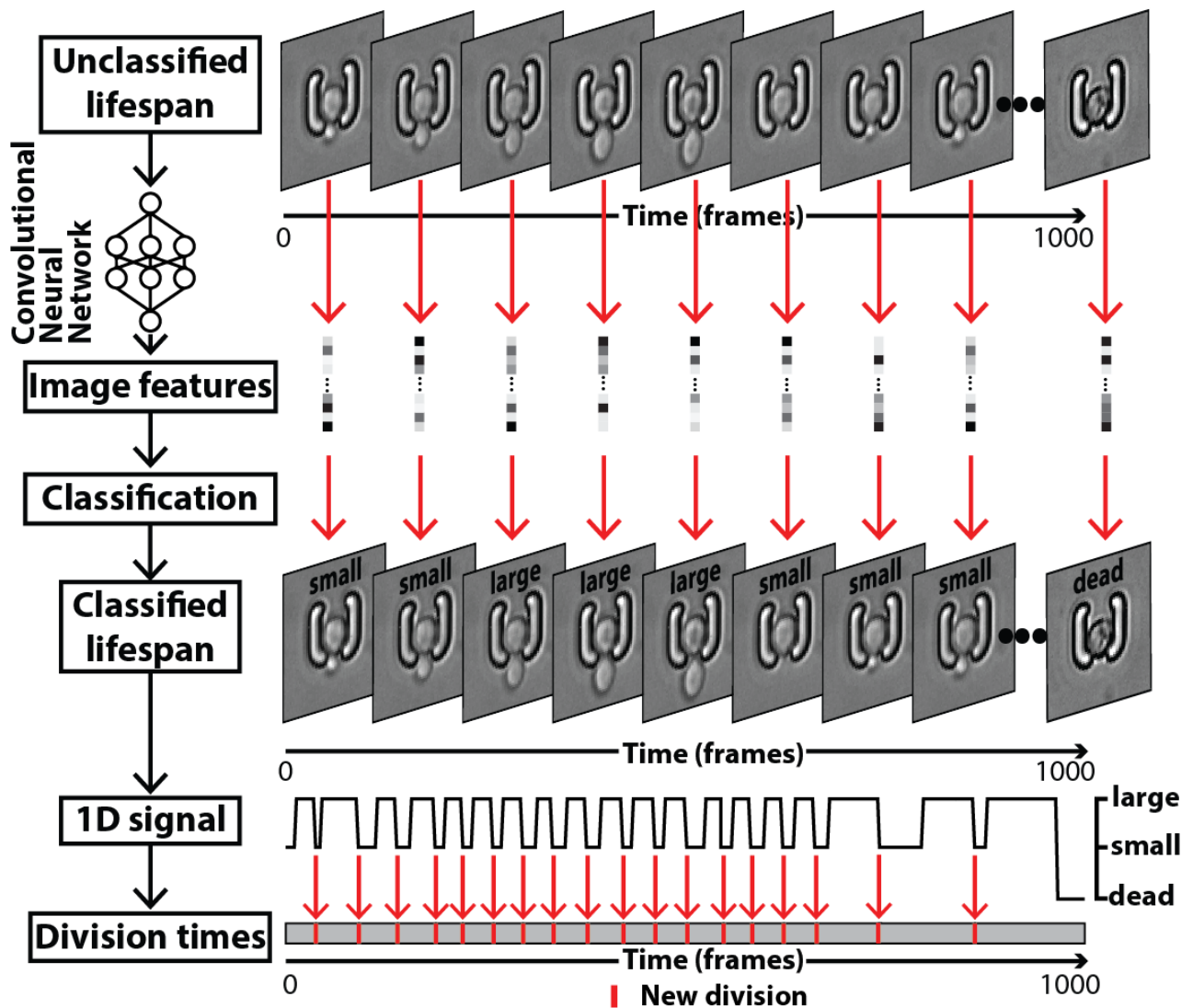
Supplementary figure 1: Experimental setup and microfluidic device

- A) Schematics of the custom imaging setup built for DetecDiv (see supplementary text for details).
- B) Picture of the imaging setup
- C) Schematics of the microfluidic device with 16 independent channels. Each channel has one inlet, a dust filter, and one outlet.

- D) Schematics of the array of cell traps. Dimensions are in microns. Inset represents close-ups on indicated areas.
- E) Principle of the cell barrier used to prevent the cells from moving towards the inlet when loading the cells from the outlet. Any cell upstream of the cell array may lead to the formation of colonies hence clog the device over time.
- F) Principle of the automated dissection of daughter cells: the mother is retained within the trap but their successive daughters are flushed away due to constant medium flow. Daughters may either exit the trap from the top or the bottom opening.
- G) Unlike previous cell trap geometries ("classical"), the current design ("new") features shallow PDMS walls that can be deformed by large cells, hence ensuring the long term retention of the cells. Two small claws on each side of the trap entrance further enhances retention.

Figure S2

Classification of images using the GoogleNet CNN (processing images separately)

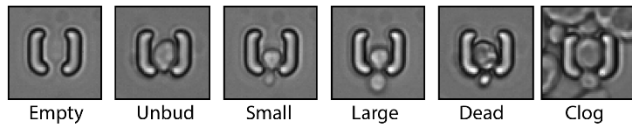


Supplementary figure 2: Principles of division tracking and lifespan reconstruction using a CNN-based image classification

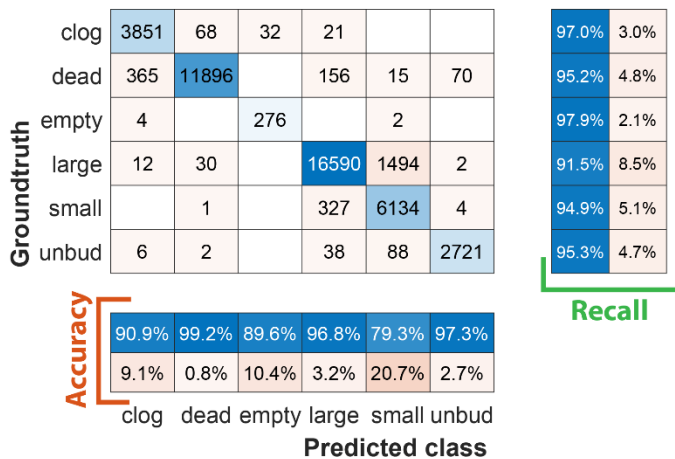
In this framework, the sequence of images is processed by a GoogleNet CNN that processes each image separately. The CNN extracts image features that are used to assign a label to each image among six possible classes (see supplementary methods for details). As with the CNN/LSTM architecture described in Figure 1, the sequence of labels is used to assign division events and the occurrence of cell death.

Figure S3

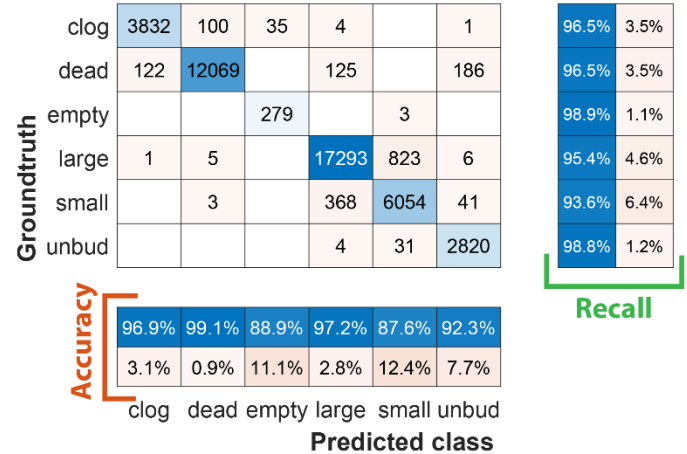
A Definition of classes



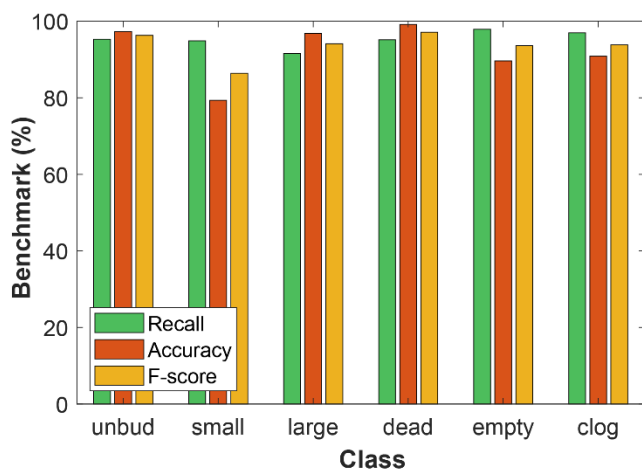
B GoogleNet (CNN) classification



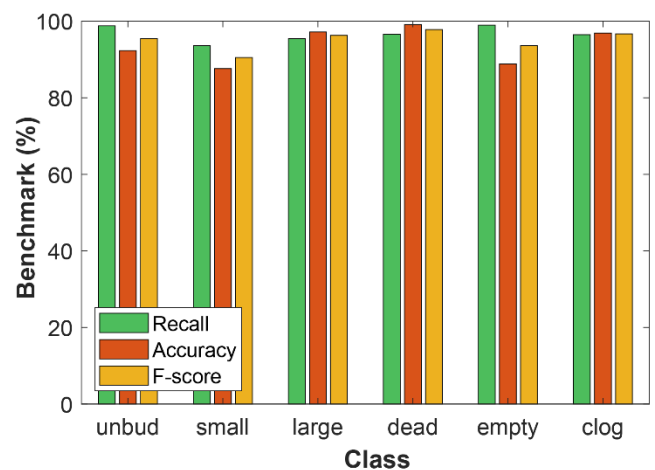
D GoogleNet (CNN) + LSTM classification



C



E

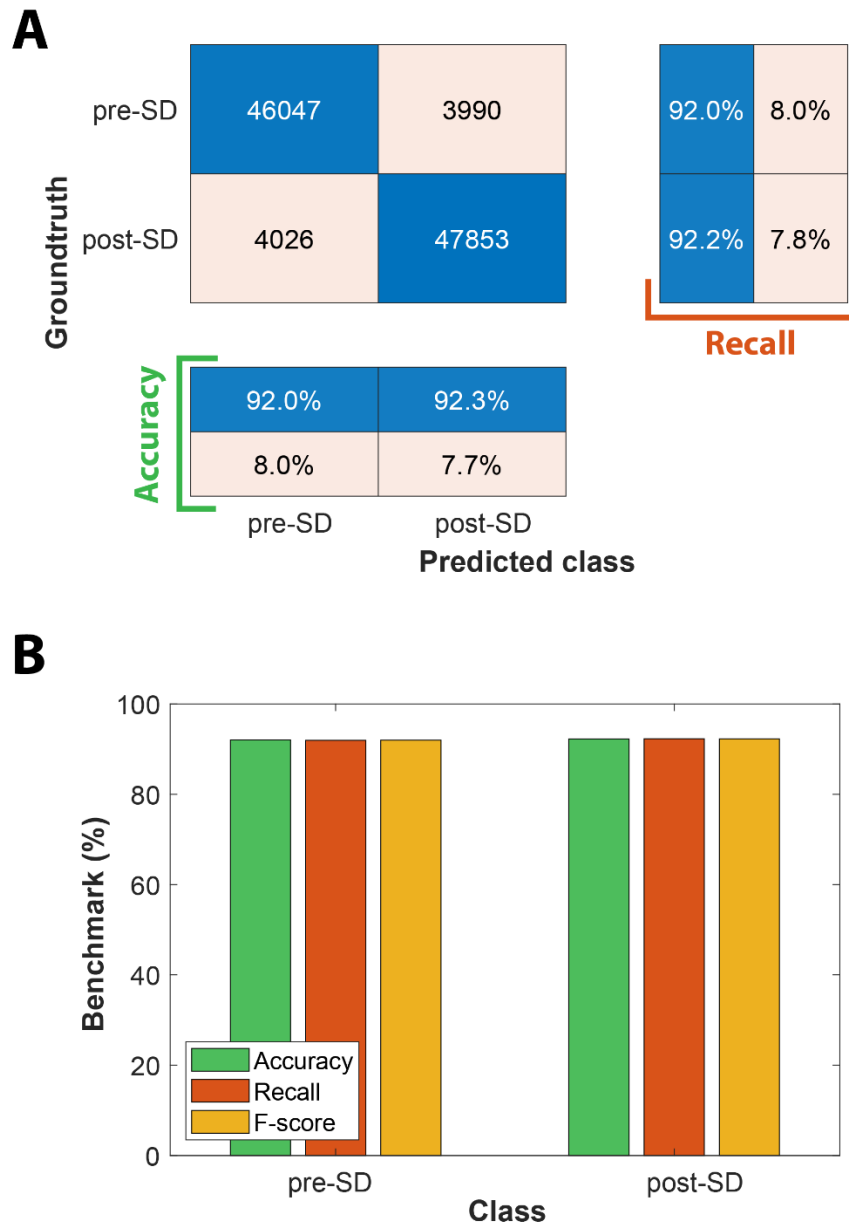


Supplementary figure 3: Class definition and image classification benchmarks

- A) Sample images indicating how each class was defined. "Empty": empty trap, i.e., no cell; "Unbud": unbudded cell; "Small": small-budded cell; "Large": large-budded cell; "Dead": dead cell; "Clogged": clogged trap.
- B) Confusion matrix obtained with a test dataset (50 trapped cells followed over 1000 frames) using the CNN image classifier. Each number in the matrix represents the number of detected events.

- C) Bar plot showing the recall, accuracy and F-score metrics obtained on each class for the CNN image classifier on the test dataset.
- D) Same as B), but for the combined CNN/LSTM architecture
- E) Same as C), but for the combined CNN/LSTM architecture

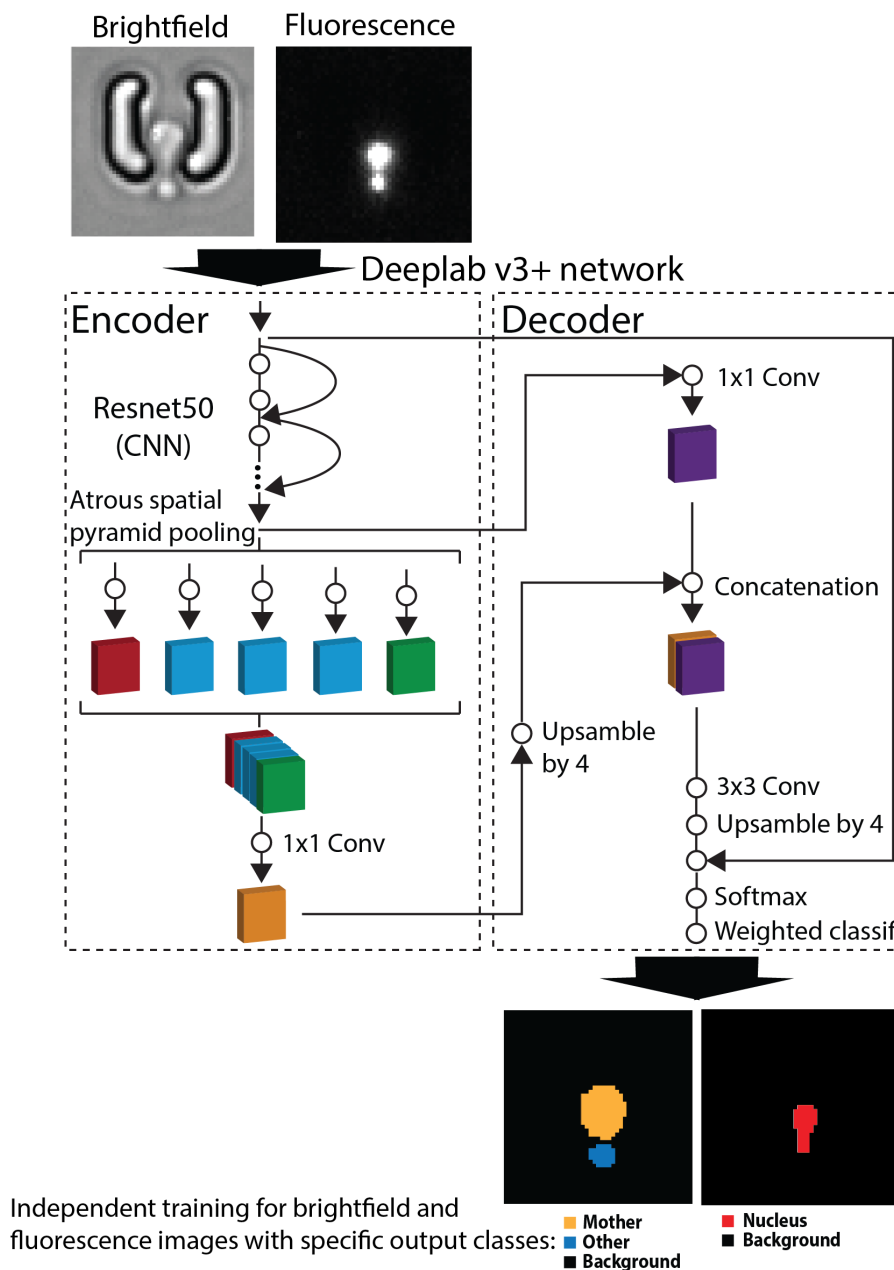
Figure S4



Supplementary figure 4: Classification benchmarks for the detection of the onset of slow division using an LSTM sequence-to-sequence classification

- A) Confusion matrix obtained with a test dataset (50 timeseries based on the cellular state probabilities output by the CNN/LSTM classifier) using a trained LSTM classifier. Each number in the matrix represents the number of detected events.
- B) Bar plot showing the recall, accuracy and F-score metrics obtained on each class for the LSTM classifier on the test dataset.

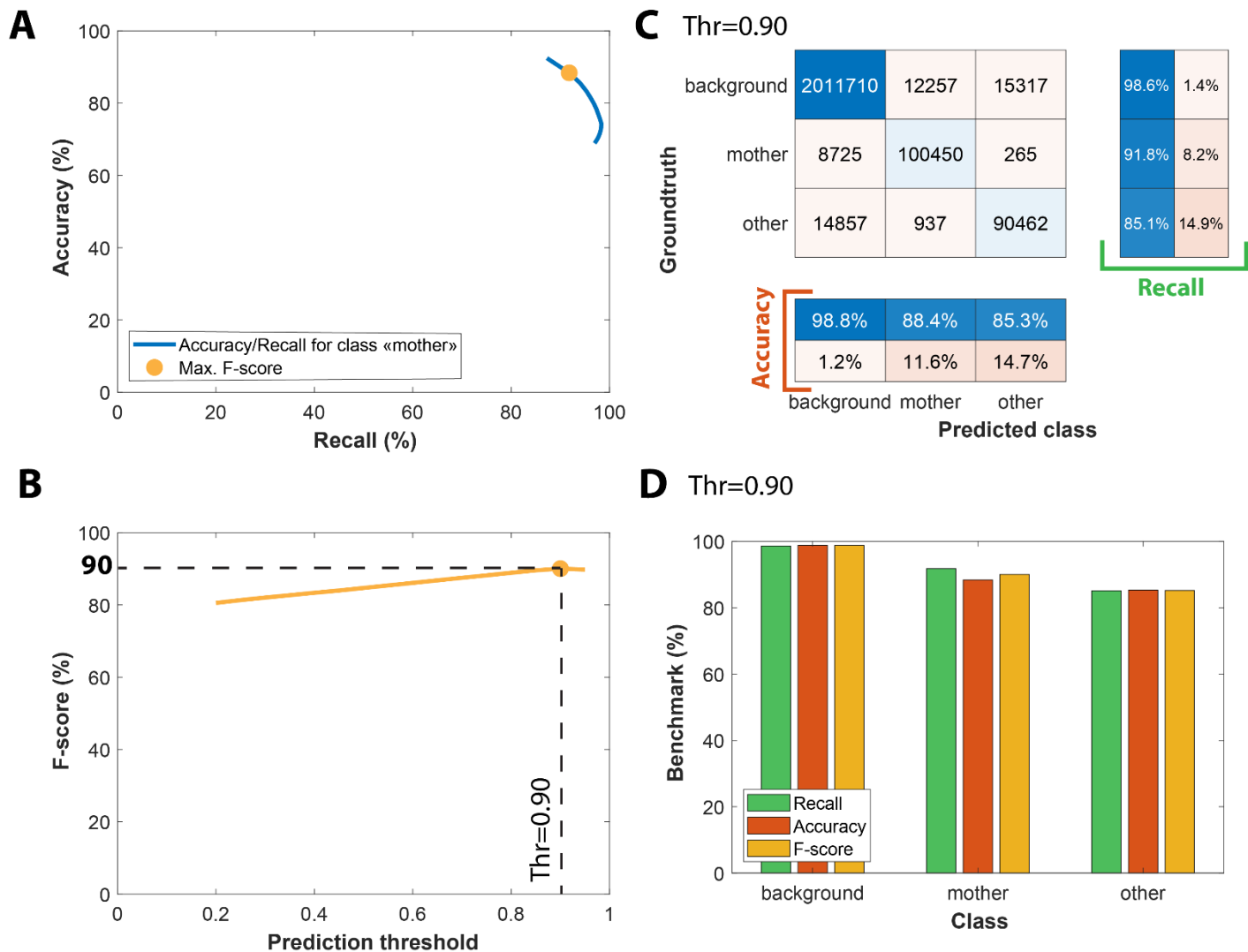
Figure S5



Supplementary figure 5: Principles of the pipeline used for semantic segmentation with DeepLab V3+

Brightfield or Fluorescence images are separately processed by the DeepLab V3+ encoder/decoder network (Chen et al. 2018) that has been modified to classify image pixels according to user-defined classes (mother /other /background & nucleus / background for brightfield and fluorescence images, respectively). A weighted classification layer is used to deal with class imbalance.

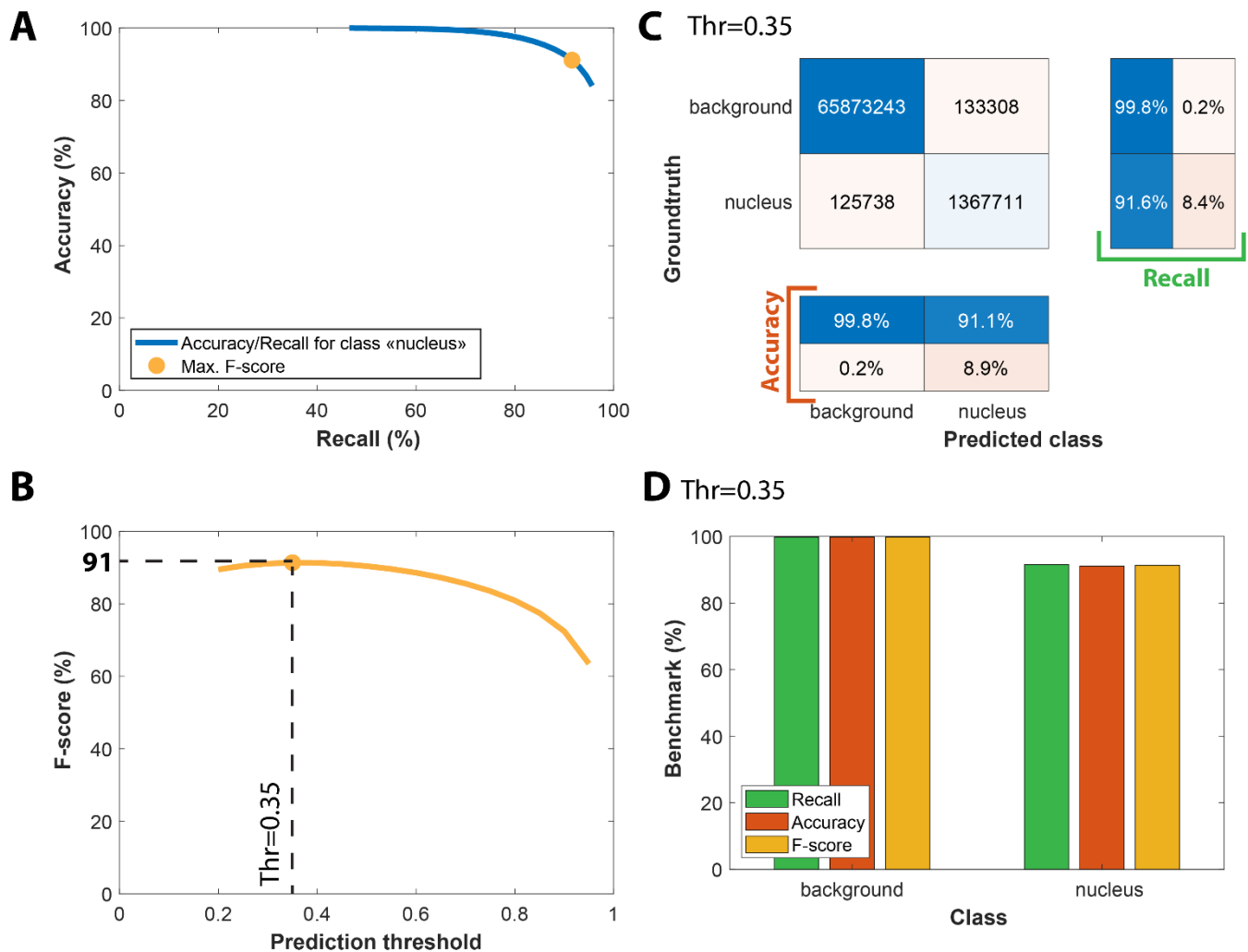
Figure S6



Supplementary figure 6: Benchmarks for the semantic segmentation of brightfield images

- A) Accuracy/Recall tradeoff plot obtained by varying the output prediction threshold for the class "mother" using a test dataset that contains 50 image sequences with 1000 frames. The orange dot indicates the point that maximizes the F-score.
- B) Evolution of F-score as a function of the output prediction threshold (computed on the [0.2 : 0.95] interval). A threshold value of 0.9 maximizes the F-score (90%).
- C) Confusion matrix obtained with the test dataset using a 0.9 prediction threshold.
- D) Bar plot showing the recall, accuracy and F-score metrics obtained on each class for the pixel classifier on the test dataset.

Figure S7



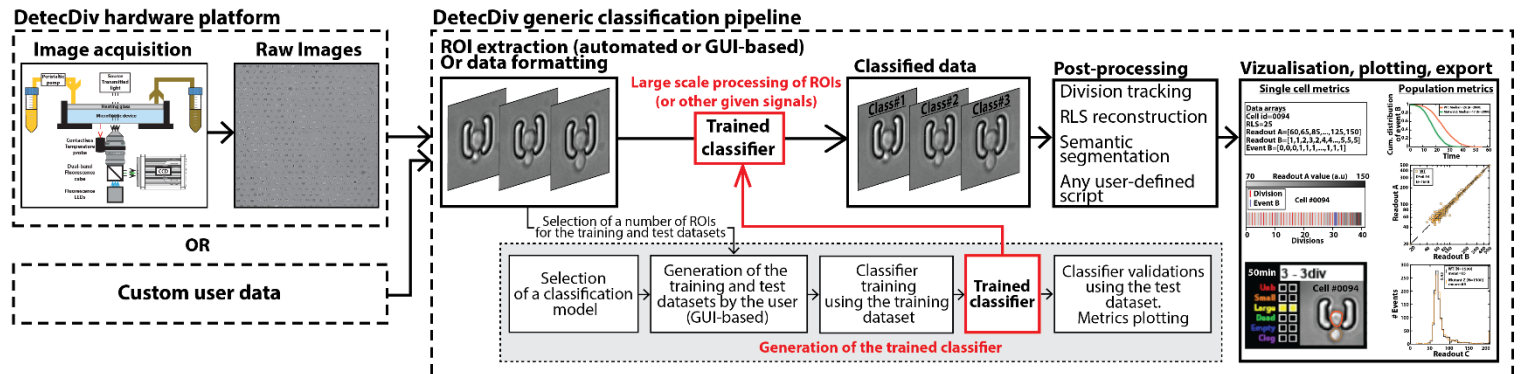
Supplementary figure 7: Benchmarks for the semantic segmentation of fluorescence images

- A) Accuracy/Recall tradeoff plot obtained by varying the output prediction threshold for the class "nucleus" using a test dataset that contains 25 image sequences with 1000 frames. The orange dot indicates the point that maximizes the F-score.
- B) Evolution of F-score as a function of the output prediction threshold (computed on the [0.2:0.95] interval). A threshold value of 0.35 maximizes the F-score (91%).
- C) Confusion matrix obtained with the test dataset using a 0.35 prediction threshold.
- D) Bar plot showing the recall, accuracy and F-score metrics obtained on each class for the pixel classifier on the test dataset.

Figure S8



DetecDiv workflow



Available classification models

Type	Description	Input	Output	Reference figures in article
Models used in the present article				
Image classification	CNN : GoogleNet, Resnet50, etc.	Individual images	M user-defined classes	Fig. 1 ("CNN"), S2 and S3. Table T2
Image sequence classification	Combined CNN/LSTM network for sequence-to-sequence classification	Sequence of N images	N (frames) x M (user-defined classes)	Fig. 1 ("CNN/LSTM"), S2 and S3. Table T2
Timeseries classification	LSTM network for sequence-to-sequence classification	N (frames) x L vector	N (frames) x M (user-defined classes)	Fig. 2A and S4. Table T3
Pixel classification (semantic segmentation)	Deeplab v3+ (with GoogleNet, Resnet50, etc. encoder)	Individual images	Labeled images (M user-defined classes)	Fig. 2B, 2C, S6-8. Table T4 and T5
Additional models available				
Image sequence classification	Combined CNN/LSTM network for sequence-to-one classification	Sequence of N images	M (user-defined classes)	N/A
Image regression	CNN : GoogleNet, Resnet50, etc.	Individual images	1 number	N/A
Image sequence regression	Combined CNN/LSTM network for sequence-to-sequence regression	Sequence of N images	N (frames) x 1 number	N/A
Timeseries classification	LSTM network for sequence-to-one classification	N (frames) x L vector	M (user-defined classes)	N/A
Timeseries regression	LSTM network for sequence-to-sequence regression	N (frames) x L vector	N (frames) x 1 number	N/A
Timeseries regression	LSTM network for sequence-to-one regression	N (frames) x L vector	1 number	N/A

Supplementary figure 8: DetecDiv software workflow

- Schematics showing the image processing steps performed for image classification with the DetecDiv software
- List of all available classification models available in DetecDiv.

Table 1

Strain Table				
Name	Mat	Background	Genotype	Origin
SF1.39	alpha	S288C	BY4742 his3delta1 leu2delta0 lys2delta0 TRP1 ura3delta0	Euroscarf
SF1.46	alpha	S288C	YDL042c::KanMX4 his3delta1 leu2delta0 lys2delta0 ura3delta0	Euroscarf
SF1.47	alpha	S288C	YDR110w::KanMX4 his3delta1 leu2delta0 lys2delta0 ura3delta0	Euroscarf
YAM4.38	alpha	S288C	HTB2-NeonGreen-CaURA his3-1 leu2-3 URA3 met15.0	Charvin lab

Table 2

CNN	Value			LSTM bidirectional	Value		
ROIs	200			ROIs	200		
Total images	200 000			Total data points	200 000		
classes	unbudded, small, large dead, empty, clogged			classes	unbudded, small, large dead, empty, clogged		
Network	Googlenet						
method	adam			method	adam		
split	0,7			split	0,7		
freeze	n			freeze	n		
ExecutionEnvironment	multi-gpu			ExecutionEnvironment	multi-gpu		
GradientDecayFactor	0.9			GradientDecayFactor	0.9		
SquaredGradientDecayFactor	0.999			SquaredGradientDecayFactor	0.999		
Epsilon	1,00E-08			Epsilon	1,00E-08		
InitialLearnRate	0.0003			InitialLearnRate	0.0003		
LearnRateScheduleSettings				LearnRateScheduleSettings			
	Method	piecewise			Method	piecewise	
	DropRateFactor	0.9			DropRateFactor	0.9	
	DropPeriod	10			DropPeriod	10	
L2Regularization	1,00E-05			L2Regularization	1,00E-05		
GradientThresholdMethod	l2norm			GradientThresholdMethod	l2norm		
MaxEpochs	6			MaxEpochs	50		
MiniBatchSize	128			MiniBatchSize	8		
ValidationPatience	Inf			ValidationPatience	Inf		
Shuffle	every-epoch			Shuffle	every-epoch		
TranslateAugmentation	-5 5						
RotateAugmentation	-30 30						

Table 3

LSTM	Value	
ROIs	200	
Total data points	90092	
classes	unbudded, small, large dead, empty, clogged	
method	adam	
split	0,7	
freeze	n	
ExecutionEnvironment	multi-gpu	
GradientDecayFactor	0.9	
SquaredGradientDecayFactor	0.999	
Epsilon	1,00E-08	
InitialLearnRate	0.0003	
LearnRateScheduleSettings		
	Method	piecewise
	DropRateFactor	0.9
	DropPeriod	10
L2Regularization	1,00E-05	
GradientThresholdMethod	l2norm	
MaxEpochs	50	
MiniBatchSize	8	
ValidationPatience	Inf	
Shuffle	every-epoch	

Table 4

CNN	Value	
Images	1404	
classes	Background, Mother, Other	
Network	resnet50	
method	adam	
split	0,9	
freeze	n	
ExecutionEnvironment	multi-gpu	
GradientDecayFactor	0.9	
SquaredGradientDecayFactor	0.999	
Epsilon	1,00E-08	
InitialLearnRate	0.00001	
LearnRateScheduleSettings		
	Method	piecewise
	DropRateFactor	0.7
	DropPeriod	2
L2Regularization	0,00E+00	
GradientThresholdMethod	l2norm	
MaxEpochs	10	
MiniBatchSize	8	
ValidationPatience	500	
Shuffle	every-epoch	
TranslateAugmentation	-7 7	
RotateAugmentation	-20 20	

Table 5

CNN	Value	
Images	3000	
classes	background, fluo	
Network	resnet50	
method	adam	
split	0,9	
freeze	n	
ExecutionEnvironment	multi-gpu	
GradientDecayFactor	0.9	
SquaredGradientDecayFactor	0.999	
Epsilon	1,00E-08	
InitialLearnRate	0.0003	
LearnRateScheduleSettings		
	Method	piecewise
	DropRateFactor	0.7
	DropPeriod	2
L2Regularization	1,00E-03	
GradientThresholdMethod	l2norm	
MaxEpochs	10	
MiniBatchSize	128	
ValidationPatience	20	
Shuffle	every-epoch	
TranslateAugmentation	-5 5	
RotateAugmentation	-20 20	

1.3. Perspectives

Though developed for general use (and not only replicative lifespan), this platform can accurately detect the division of cells and quantify many different readouts throughout their lifespan. The monitoring throughput is unprecedented, thanks to a new microfluidic device and a specific imaging system. Besides, analysis is no longer the throughput bottleneck since everything is automated using artificial intelligence with an error rate close to 1%, thanks to its architecture to exploit the time-dependencies in temporal sequences of images.

With that, 16x2000 cells can be screened and analyzed every 4 days, with only 6 hours of active human work. Therefore, this framework increases the screening throughput of 1 to 2 orders of magnitude, which opens new perspectives for understanding the system dynamics of aging.

As a perspective, it would be interesting to train a network to detect petite cells based on their morphology and division time (using mitochondrial markers to generate the groundtruth). Indeed, this artifact from the lab strains has been described as an aging path by many different studies [280,283], and it would be interesting to systematically separate these cells from the others. Similarly, we could classify the cells between the two morphologies often described during aging, “elongated bud” and “round bud” [223], to try to understand if they relate to different aging paths (which is probably also linked to mitochondria [283])

Another way of understanding aging, aging factors, and rejuvenation is to observe the progeny of old mothers. To study that, I have developed a microfluidic device that allows the tracking of a mother cell until a given timepoint before inverting the budding pattern and replacing the mother cell with its daughter.

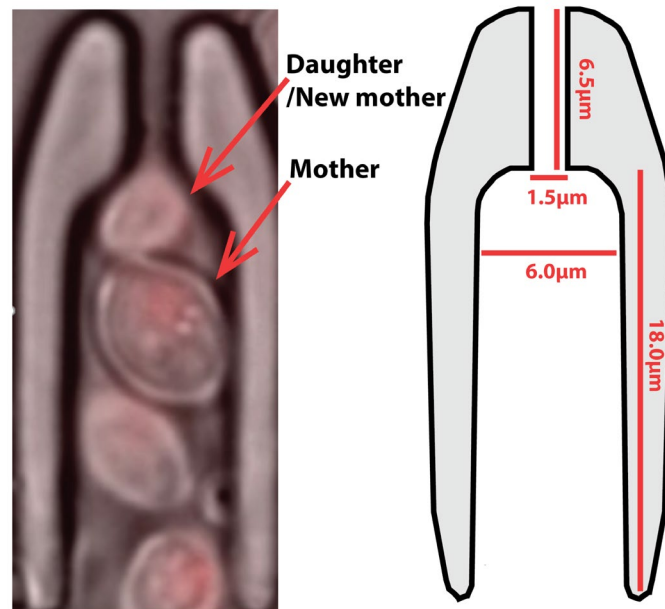


Figure 60: Image (left) and design (right) of a trap used to observe the RLS of a daughter after the replacement of its mother

Indeed, S288C cells have a unidirectional budding pattern and can therefore age in a unidirectional cavity. However, deleting the BUD4 or intermittently degrading Bud4 proteins with an Auxin Inducible Degron system during the experiment would cause a fraction of the mothers to be replaced by their daughter by budding against the tip of the trap instead of towards its exit. Consequently, we could track the partial lifespan of daughters born at different mother ages, in the same automated manner as with mother cells, using the system presented previously. It is indeed straightforward to detect such switch with image classification by using a class for the presence of a small bud at the tip of the cavity (Figure 60, left)

Beyond the replicative lifespan application, our software is designed to be used as a generic interface to set up custom classification pipelines to extract temporal features from any sequences of timelapse images, thanks to its architecture. It is proposed as a stand-alone software that includes all the steps to produce and use custom networks (pre-processing, classifier training and validation, raw data classification, post-processing, and data visualization).

6. Results II: Measuring the probability of ERC excision with age

1.1. Introduction

In order to determine if the excision of the first ERC - which is the starting point of a major cascade of events leading to death - is more probable in late ages than in early life or not, we need to capture excision events and link them with the replicative age of the cell.

One way of assaying the excision rate of a population is by inserting an ADE2 gene in one rDNA repeat in an *ade2Δ* strain. The absence of Ade2 promotes the accumulation of a red pigment due to a rupture in the adenine metabolic pathway [482]. Therefore, after the excision of the repeat containing the Ade2 gene in a cell, its progeny becomes red. Hence, it is possible to estimate the excision rate of a population by counting the ratio of red/white colonies [356,368]. However, this colony sectoring assay does not inform about the probability of excision with age at the single-cell level, but rather gives the average excision rate of the whole population in exponential phase.

Therefore, we thought to tag rDNA repeats with fluorescence. With this strategy, once an rDNA repeat is excised, it will be replicated at each division and retained in the mother, and the signal from the tag should increase exponentially.

A recent study from our group using a LacI-GFP expressing strain in which each of the ~150 rDNA repeats includes a LacO sequence showed that this exponential accumulation occurs. With that, they could measure the doubling time of the signal and determine that two-thirds of the circles are replicated at each division. However, since the basal fluorescence signal from this strain is 150 units, it is difficult to capture the exact excision time at which the signal goes from 150 to 151 units.

1.2. Results

To precisely capture the excision of a repeat with age at the single-cell level, I therefore used a strain on which only one repeat among the 150 has a GFP sequence under a TDH3 promoter, inserted in the intergenic region of the repeat (IGS1 or IGS2). This strain was used in a previous study [328] to study the loss of Pol II silencing at the rDNA with age. Indeed, as seen in the introduction (see p.49), the 35S and 5S genes are transcribed by Pol I and Pol III (respectively), and the IGS1/2 loci are transcribed by Pol II. Using this strain, they could observe an increase of fluorescence in the late ages (an increase of a factor ~4), which implies

that cells experience a sustained loss of silencing of the rDNA. They also validated that this loss of silencing depended on Sir2 (Sir2 is known to be the main silencer of the IGS1/2 [392]) since blocking Sir2 increased fluorescence. Interestingly, they reported that a tiny fraction of cells was displaying a massive increase of fluorescence (an increase of 2 to 3 orders of magnitude) and attributed that to ERC accumulation from the tagged repeat.

Therefore, this strain can act as a transcriptional reporter of the ERC accumulation, and the exponential dynamics of the signal can allow us to determine the time of excision, at which the exponential starts (Figure 61).

However, since the estimated average excision rate is about 10% per generation [226,356] the caveat of this approach is that only ~2% of the wildtype cells will excise the tagged repeat during their lifespan. Thus, having a high-throughput system is necessary in order to capture enough events.

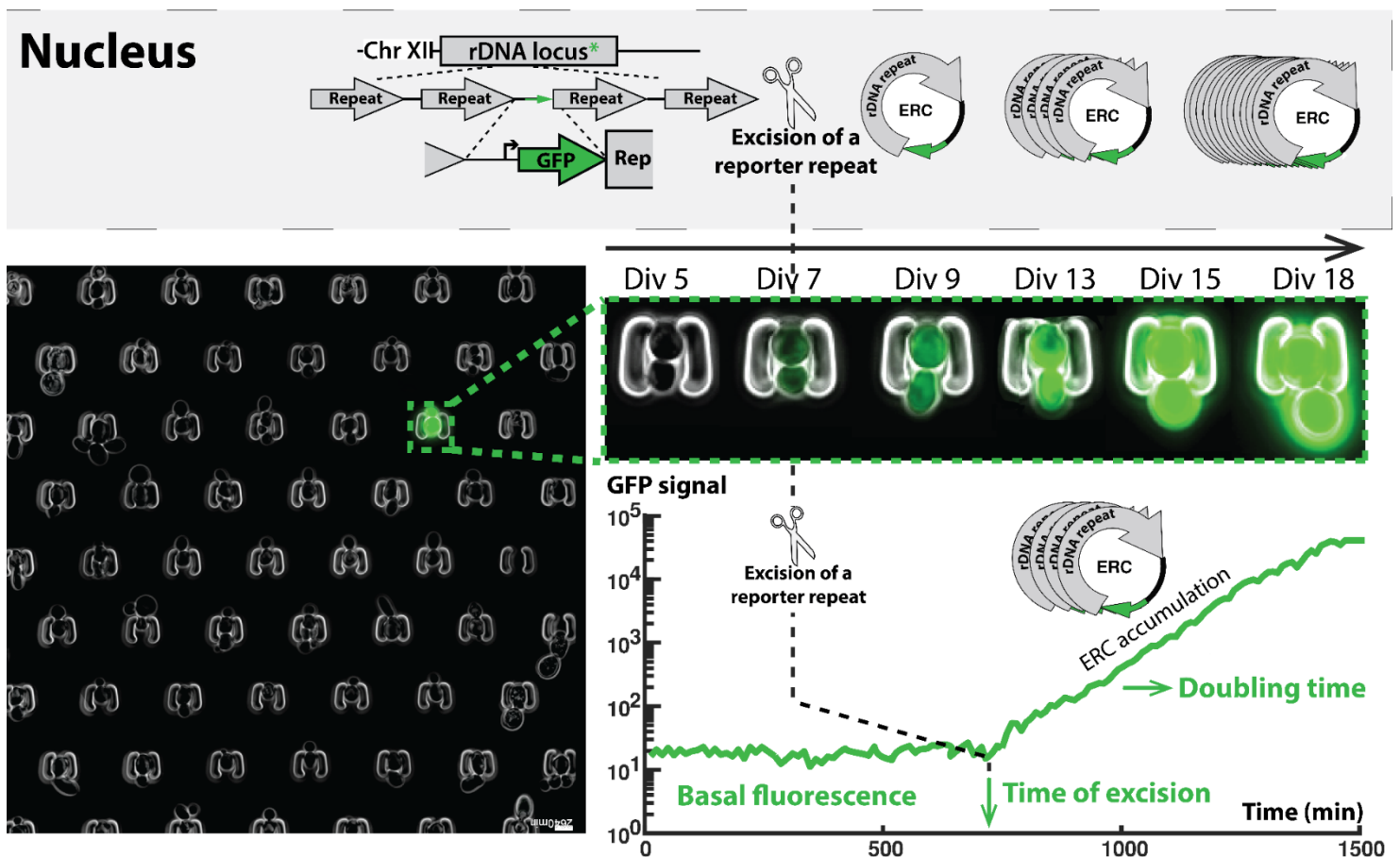


Figure 61: Experimental procedure to measure ERC excisions. An rDNA repeat is tagged with a transcriptional reporter of GFP in the IGS1 or 2 regions. When this repeat is excised, the number of DNA template of this gene increase and the cell emits a proportional amount of fluorescence. (Left): Phase contrast + GFP signal of a typical field of view after 10h showing the rarity of the event.

Using this strain with the previously described microfluidic chip, I was able to recapitulate the different signals observed in the original study, namely a loss of silencing (Figure 62, left), a recombination of the tagged repeat (leading to a doubling of the fluorescence, see Figure

33B, p.53 and Figure 62, middle), and the excision and accumulation of the tagged ERC (Figure 62, right).

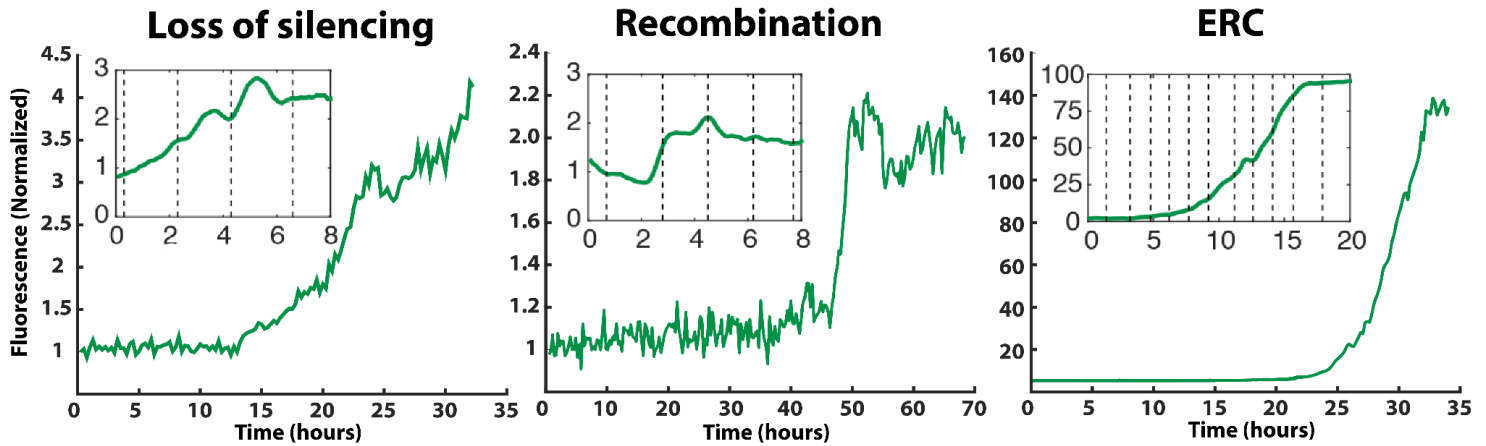


Figure 62: Different types of signals obtained with the transcriptional reporter of ERCs. The main graphs were obtained by us, while inset graphs represent what is reported in the original paper [328].

As expected, 2.4% of the cells (N=930) showed an exponential increase of the fluorescence over more than one order of magnitude (condition to consider the signal as the accumulation of a tagged repeat). Besides, these cells displayed the increase at very different moments, suggesting that the excision time was also very variable (Figure 63).

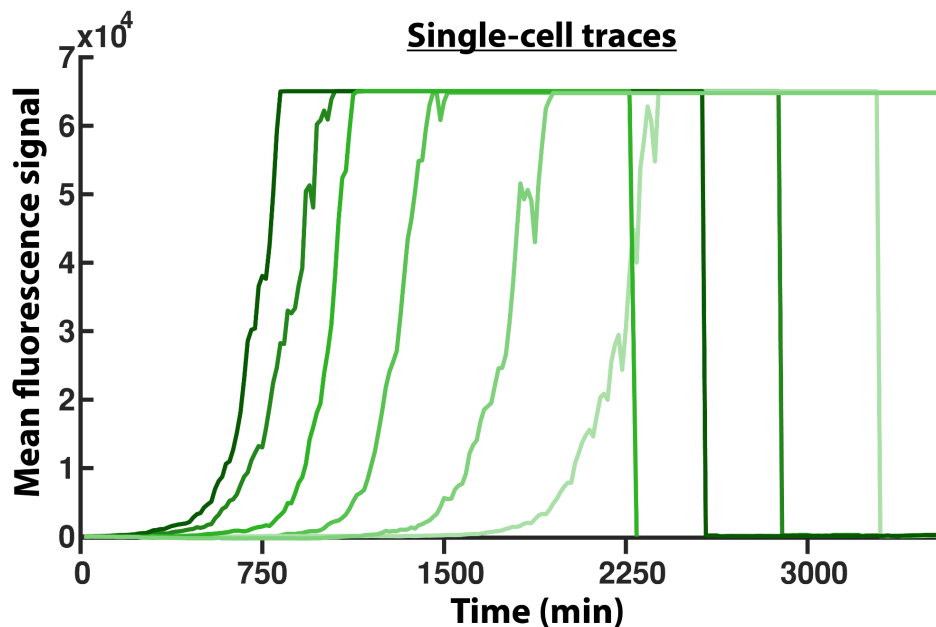


Figure 63: Mean GFP fluorescence of six different cells as a function of time

From such a signal, it is possible to extract many parameters, such as the time of excision or the doubling time, using a piecewise and an exponential fit, respectively (Figure 64).

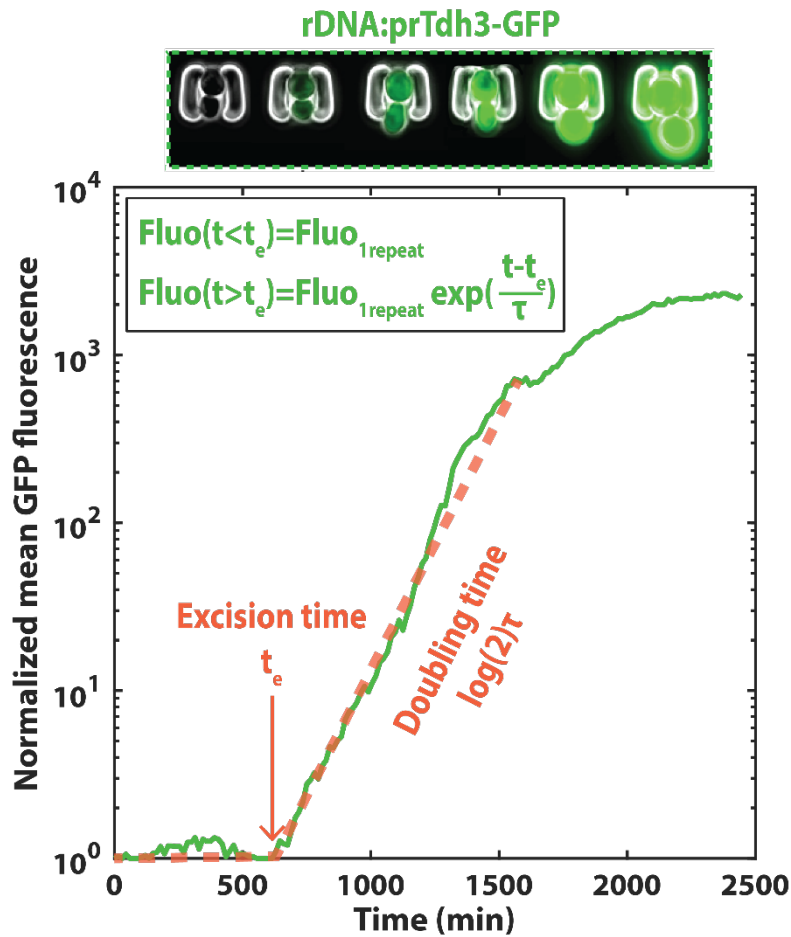


Figure 64: GFP fluorescence of one *rDNA::Tdh3pr-GFP* cell displaying a strong increase of fluorescence, as a function of time. The fitting of the data with a delayed exponential allows to decipher the time of excision and the doubling time of the fluorescence.

The doubling time of such a signal was found to be slightly higher than the division (1.36 divisions Figure 65), in agreement with the previous study [226], reinforcing the fact that this signal is linked to ERC accumulation and that not all ERCs are replicated at each division.

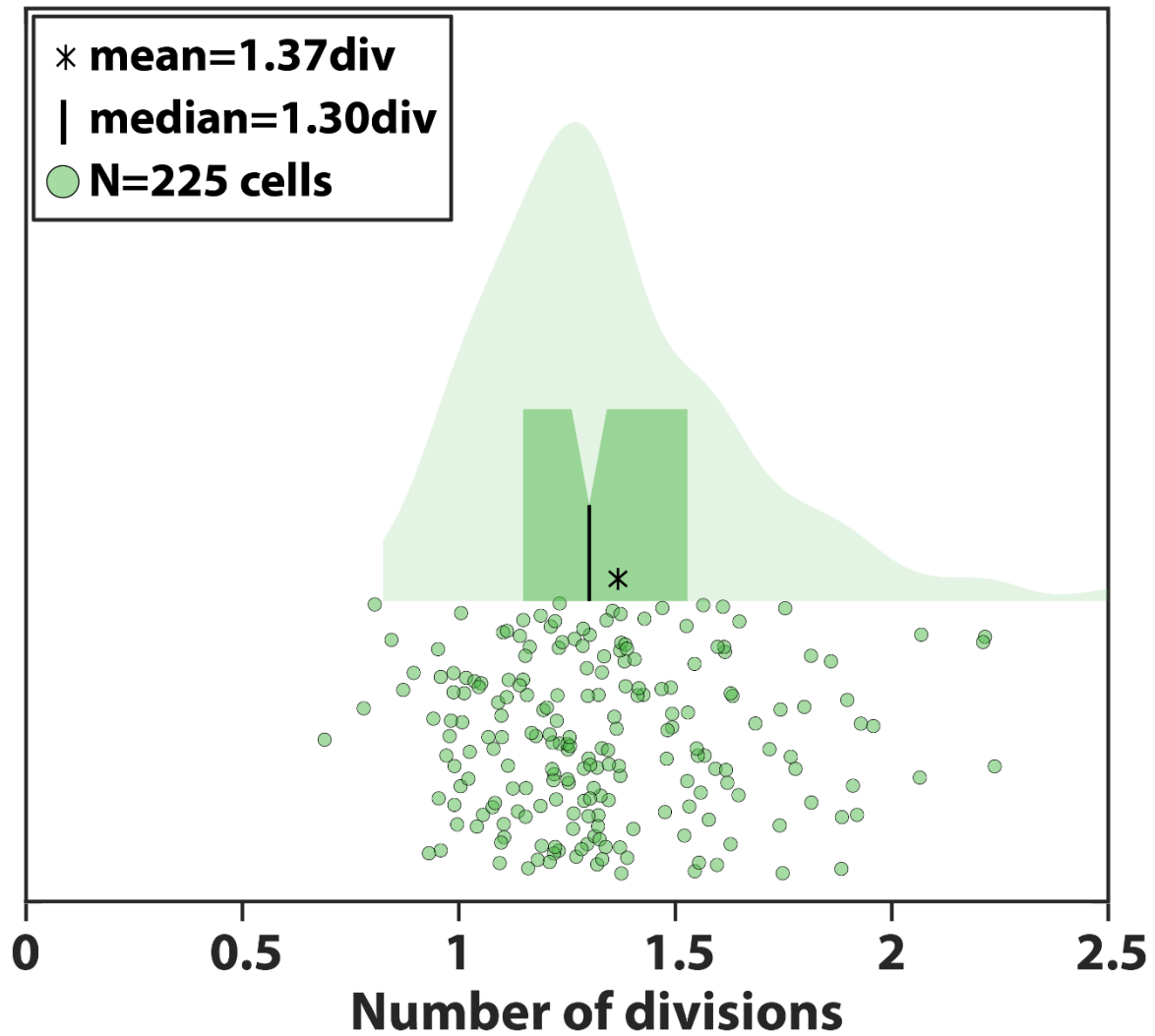


Figure 65: Distribution and boxplot of the fluorescence doubling time in *rDNA::Tdh3pr-GFP* cells displaying an exponential increase of fluorescence

To have access to the statistics of excision, one can plot the cumulative distribution of excision time (just like plotting a survival curve, see p.4). From that, the best fit is obtained with an exponential decay $F(t) = \exp\left(-\frac{t}{p_{\text{exc}}}\right)$, with p_{exc} a constant representing the probability of excision per unit of time (Figure 66). Therefore, the probability of excision is independent of age (from these preliminary results) and of about 10% per division, in agreement with previous numerical models [226].

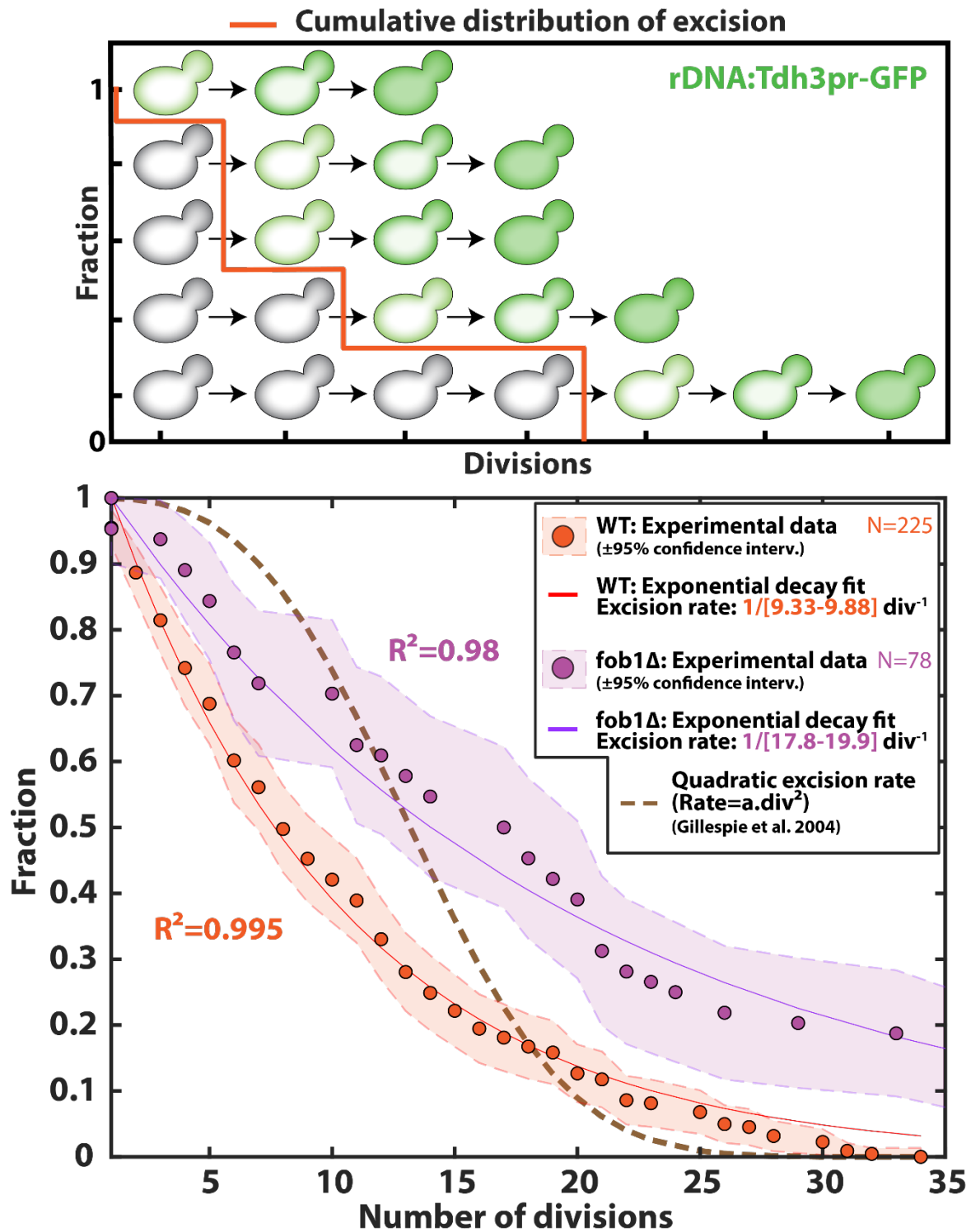


Figure 66: Cumulative fraction of cells in the birth to excision period, among all the cells that displayed an exponential fluorescence increase. Top: explanatory scheme of how the cumulative fraction is computed. Bottom: Data (dots) and fit (solid lines) (Wildtype in orange, *fob1Δ* in purple). The excision rate can be deciphered from the fit and is displayed in the inset with a 5% confidence interval.

Interestingly, the *fob1Δ* mutant (a mutant known to experience less ERC excision, see p.56) has a halved probability of excision per division compared to the WT, which is higher than what was predicted with a previous model [226].

1.3. Perspectives

Altogether, these preliminary results suggest that our marker can detect the excision of ERCs and measure the dynamics of their accumulation. In particular, it seems that **the probability of excision is constant with age and that cells can experience it even during their first S phase**. However, several controls must be done in order to validate the approach.

First, it is unclear in the literature whether ERCs are actively transcribed or not. On the one hand, non-coding RNA are enriched in old WT cells and not in *fob1Δ* cells [330]. Moreover, an exponential increase of Pol I, Pol I target transcripts are detected with the same dynamics as ERCs' during aging [226]. On the other hand, half of the rDNA is not transcribed, and adding more repeats to the rDNA array does not change the amount of Pol I transcription [381] (though Pol II transcription has not been looked at in these strains). Even though ERCs are probably not submitted to the same regulations as intrachromosomal repeats, whether or not they are transcribed and which polymerase transcribe them is not evident in literature. Nevertheless, our data provide direct evidence that ERCs are actively transcribed by Pol II, since the dynamics of the transcriptional reporter match with the increase of ERCs numbers [226].

To verify that, it would be interesting to isolate unmodified ERCs from old mothers [483] after enrichment and sorting (Appendix 2), and observe them with an electron microscope to see potential nascent transcription from Pol I [381], or perform ChIP targeting for Pol I.

Even if we could observe an exponential accumulation of fluorescence across several orders of magnitudes, it could be that the *bona fide* excision of the circle happens earlier than the increase of fluorescence. Indeed, it could be that part of the ERCs is silenced and that the observed increase occurs only later in life when the silencing is lost. This is not likely to be the case since we observe increases in fluorescence even after one division. Yet, we could verify that by several means. It is indeed possible to modulate rDNA silencing with drugs such as nicotinamide (an inhibitor of Sir2) or nicotinic acid (an activator of Sir2). Therefore, perfusing this drug in the media in the middle of the experiment and observing if cells with tagged ERCs dramatically change their fluorescence or not would indicate if ERCs are silenced.

To further verify this hypothesis and, more generally, assess if the transcriptional reporter faithfully reports the number of ERCs, we engineered a strain harboring a direct reporter of

ERC (LacO array in a strain expressing LacI-Neongreen) at the same locus as the transcriptional reporter (Figure 67).

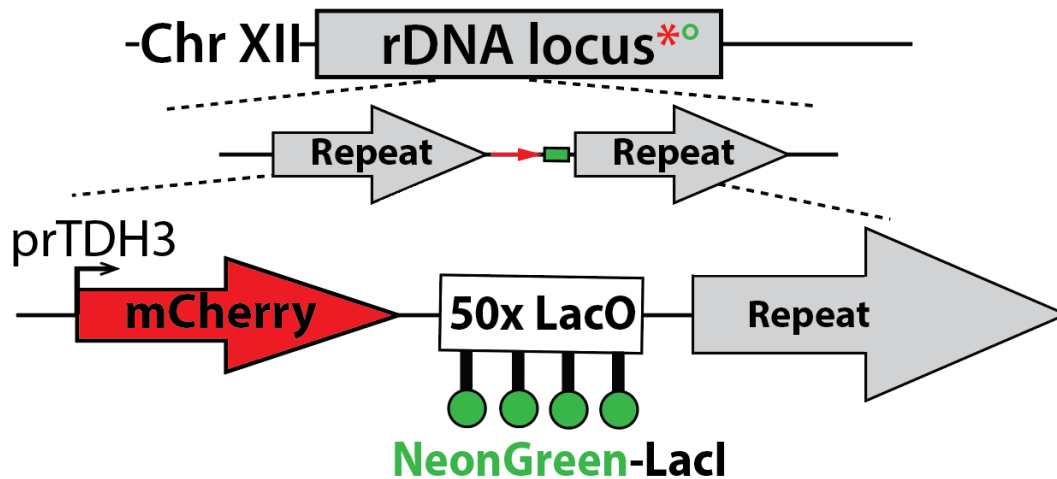


Figure 67: Genetical construction of a double ERC reporter strain. A transcriptional reporter (*prTDH3-mCherry*) is inserted in the *IGS1* and is followed by a *50xLacO* sequence. The cell is also expressing *NeonGreen-LacI* from another locus.

The LacO-LacI-Neongreen system is therefore a more direct reporter of ERCs but emits less fluorescent signal than the transcriptional reporter. Consequently, longer exposures are required to obtain a signal, which affects the temporal resolution (to avoid phototoxicity) and is the reason also why we opted for a transcriptional tag for routine experiments. However, for the control, comparing the dynamics of the two reporters (even at a low framerate) will show if there is a lag between the excision and the transcription of the reporter or not.

It is also possible that transcription of the GFP under the strong TDH3 promoter influences the probability of excision since it has been shown in different mutants that the number of ERC is linked with the number of ncRNA transcripts [423]. Nevertheless, in the light of our data and of recent studies [330], it is most likely that most of the increase of ncRNA transcripts numbers from population assays comes from ERCs. In other words, the accumulation of ERCs driving the accumulation of ncRNA is more probable than an upregulation of ncRNA transcription driving more ERC generations.

Besides, the RLS of our tagged strain and of the cells displaying the excision of a tagged repeat is identical to that of WT, suggesting that the excision rate is the same between the untagged WT and the tagged WT. However, though the measured excision rate fits with the mathematical model for the WT, that of *fob1Δ* is higher than that of the model. To understand if the transcriptional reporter affects excision rate, we engineered a strain with just a *50x LacO* inserted in one repeat (Figure 67 but without transcriptional reporter). Comparing the

excision rate in this strain with that of the transcriptional reporter strain will tell if adding a Pol II target in the intergenic spacer regions promotes excision or not.

Another caveat of having one repeat tagged among 150 untagged is that we cannot be sure that the observed excision is the first one in the life of the cell. If the excision of a repeat does not change the probability of further excisions, then the measured probability is valid. If the excision of a repeat impacts the probabilities of excising another repeat, we would expect even less late events, which would even less favor the age-dependent hypothesis. However, simulating the two hypotheses and generating the subsequent cumulative distribution of excision times needs to be done as an additional control.

This ERC marker would be interesting to be used in different context known to modify the excision rate (like I did with *fob1Δ*), or the accumulation rate (diffusion barrier mutants like *bud6Δ* [354] or perturbations [484], NPC tethering with *sgf73Δ* [356] or rDNA-ARS mutants [202,417]), to further validate the approach (Figure 68).

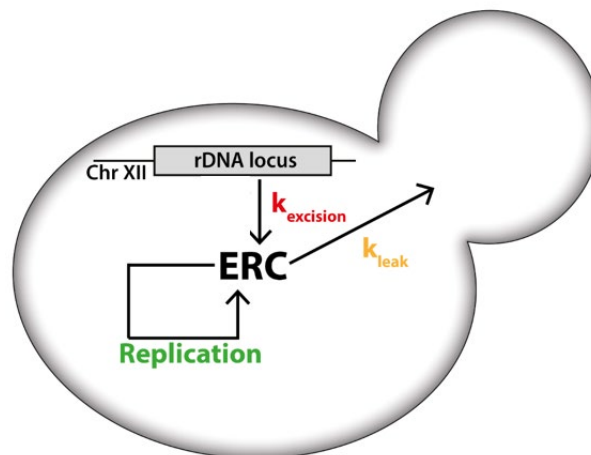


Figure 68: Framework of mutants and perturbations to further validate the ERC reporter. Acting on the excision rate, the replication, or the leaking should change the different dynamics of the signal.

Interestingly, the strain used for measuring ERC excision has another fluorescent reporter (promoter TDH3-mCherry) placed in another repeat [328]. The first advantage of that is that it doubles the probability of seeing an excision event.

In addition, it is possible to measure the loss of Pol II silencing in the rDNA relative to the excision and accumulation of ERCs (Figure 69). Is the loss of silencing causing ERC excision as suggested by the literature? Conversely, is the ERC accumulation causing the loss of silencing by titrating Sir2 proteins? Are these two events unlinked? A deeper analysis of the data will be required to conclude but would bring interesting data to the debate [240,257,321].

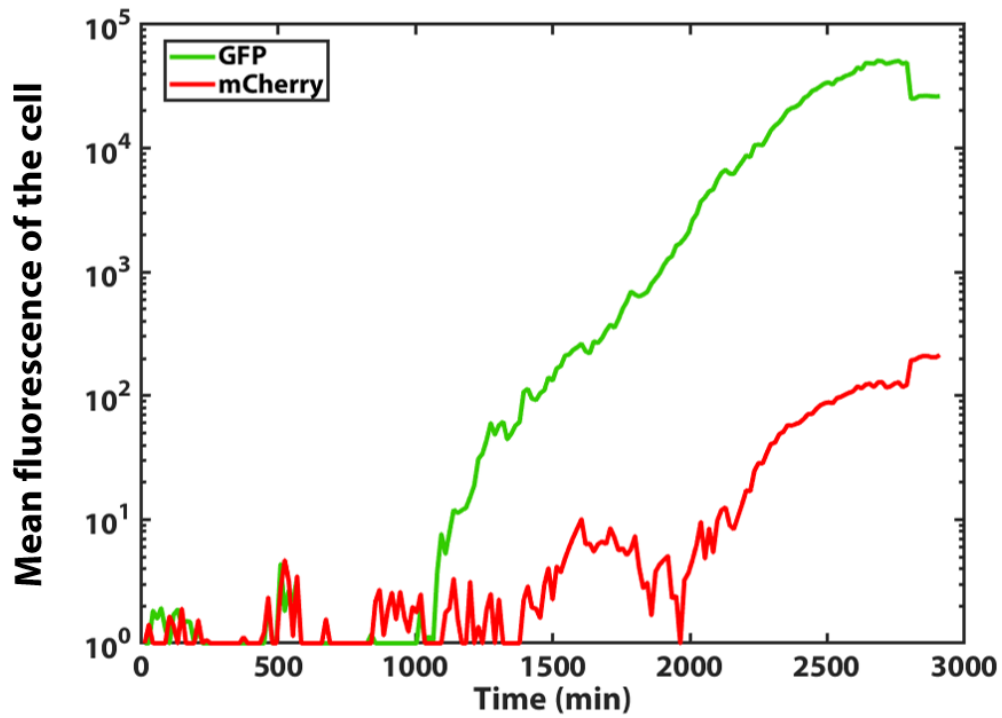


Figure 69: Mean fluorescence from a single cell with two rDNA transcriptional reporters. In this case, an exponential increase of the GFP (ERC accumulation) is followed by a mild increase of mCherry (loss of silencing of second ERC excision).

Moreover, these data were obtained before the development of the high-throughput methodology presented earlier, and more events and experimental replicates would be necessary to properly conclude about the time-dependency of the excision.

Finally, using this pipeline, it will also be interesting to verify that the period between the excision and the SEP is deterministic, as suggested by previous numerical modeling [226].

General discussion

Aging is a phenomenon affecting many different biophysical processes. In multicellular organisms such as humans, it is associated with an increased death rate and a progressive failure of the different organs due to the aging of the cells of their tissues. However, due to the different scales at play (organism - organs - tissue - cell - organelles - molecules) and the interplay between them, it is very complex to understand why organs fail, how these failures are linked together, or how the cells from these organs age. For this reason, unicellular eukaryotes can be relevant - to a certain extent - to study aging because they are both a cell and an organism while having no cell-cell interaction (in most contexts). In particular, *S. cerevisiae* is an attractive model because of its asymmetric division pattern and the rejuvenation of the progeny of a given cell.

Besides, it has exhaustive mutant collections (deletion and GFP [199]); it is easily manipulated thanks to the new microfluidic technologies and ages fast. Thus, it is possible to screen many different genes with immense statistical power and observe their effect and dynamics at the single-cell level throughout the lifespan. These are unique features of budding yeast and make it a still invaluable model in geroscience. It is true that the molecular mechanisms at play (such as the ERCs) might not all be entirely conserved in “higher” eukaryotes. Nevertheless, understanding how different processes are destabilized, driving to a general loss of homeostasis of the cell and leading to death, would **set a framework to address the system dynamics of aging in organisms in general.**

Indeed, among the many processes identified as losing their homeostasis during aging (see introduction), it is often difficult to separate the causes from the consequences and to differentiate what is a compensatory mechanism from what is a deleterious change [126]. This challenge is made even harder by the heterogeneity (in kinetics and in quality) between isogenic cells in an identical environment.

Double deletion mutants can help distinguish if two genes are from the same pathway or not, but this kind of epistasis analysis is often complex to interpret due to the pleiotropy of many genes.

Therefore, adopting a single-cell and longitudinal approach is almost necessary to tackle this question. For that, microfluidic coupled with timelapse is the state-of-the-art method and has allowed sorting certain known hallmarks of aging in ordered pathways.

1. The ERCs pathway of aging: A countdown to death started by a stochastic trigger

Doing that, our lab and others have identified a stereotyped pathway of aging, implying the rDNA followed by most of the wild-type cells. This pathway is triggered by the excision of an rDNA circle (ERC) that self-replicates exponentially throughout the divisions (almost $\frac{3}{4}$ of the ERCs being replicated at each division) in the mother cell, until a threshold number at which the cell enters a pathological state (Senescent Entry Point). This SEP is preceded by an increase of the rDNA transcription and is defined as a cell-cycle slowdown and an increase of the karyoplasmic ratio. Once passed the SEP, the cell dies with a constant probability at each division (see p.86).

Here, preliminary data suggest that the ERC excision is a stochastic (that is, age-independent) process. This indicates that **this event is most likely not caused by another age-dependent degradation and is instead an upstream event of the aging choreography.**

Interestingly, the cell-cell variability (due to the stochasticity of the process), the fact that ~13 divisions (amplifications of the circles) are needed before reaching the SEP, and the stochastic death once the SEP is reached, hide the fact that the aging curve is composed of age-independent processes (see p.86). In other words, **aging can arise from age-independent processes.**

Although, many questions about the links between the events of this pathway remain unanswered:

Why is the rDNA transcription increased around the SEP? Under normal conditions, the rate of rDNA transcription is buffered against variation in copy numbers [379,381,409]. Therefore, increasing the number of copies (like with ERCs) beyond basal numbers should not lead to an increased transcription (though this model has been recently debated [240,485]). If ERC accumulation is the cause of the whole nucleolus activity [226] is not sure, but the data presented previously using transcriptional reporters seems to prove that **ERCs are transcribed**, which was not directly established so far.

Why is the N/C ratio increasing at the SEP? Indeed and as discussed in the introduction (see p.45), the N/C ratio is very tightly regulated under normal conditions and conserved in many contexts, not only in budding yeast but also in *S. pombe*, mammal cells, and *Xenopus* [337-340]. The nucleocytoplasmic transport has been proposed as a regulator of the nucleus size

and modifying import and export rates, and in decreasing, mRNA export [339,340] is known to increase the N/C ratio.

In the context of aging, the NPC homeostasis is disrupted [341,356-358], and in particular old cells show an increased compartmentalization of proteins in the nucleus [226,341].

How to explain these changes? Since they happen every time at an approximate given number of ERCs, these DNA circles are a potential suspect. In line with that, ERCs are thought to attach to the NPC via the SAGA complex, leading to acetylation of several components of the NPCs, in particular, their nuclear basket (see Figure 37 p.60)[356-358]. Another possible explanation would be that the increase of nucleolus size (driven by ERCs) drives this massive specialization of the pores since NPCs adjacent to the nucleolus, even in young cells, are devoid of baskets [347,436,486,487].

Such remodeling of the NPCs could modify their nucleocytoplasmic transport. In fact, basketless NPCs tethered with plasmids have enriched importins (in particular Kap123 that mediates the nuclear import of ribosomal proteins and of histones), and depleted exportins (in particular exportins involved in mRNA export). Altogether, the increased N/C ratio could be explained by a disruption of the nucleocytoplasmic exchanges, in part altered by ERCs tethering to the NPCs.

Another possibility would be that the excess DNA from the ERC would signal to the nucleus. In fact, the quantity of ERC at the end of the lifespan is similar to the quantity of chromosomal DNA, and early studies proposed that the quantity of DNA controls the nuclear size (called the nucleoskeletal theory [488–490]. However, a more recent study established that it might not be the case [337], so this theory is less likely to explain the increase of nucleus size.

What is causing the SEP? Like the N/C ratio, the cell-cycle duration is tightly regulated under normal conditions, and homeostasis is lost at the SEP. Are ERCs directly causal for that? Is it simply because they increase the total amount of DNA in the cell, or because they are rDNA sequences? Is it linked to the massive upregulation of the rRNA transcription?

First, increased nucleus size and content could disrupt the homeostasis of cyclins, CDKs, and other proteins involved in cell-cycle duration. Indeed, some of these proteins are controlled in concentration [248,491], and the global increase of the concentration of nuclear proteins could affect this equilibrium. Hence, the SEP could be an indirect cause of ERCs, via nuclear deregulation.

On the other hand, the number of ERCs saturates in the post-SEP period, suggesting that the replication machinery is deregulated, potentially because too much DNA is to be replicated.

This is supported by the observation that yeast mutants over-amplifying a 2 μ DNA circle possess a relatively longer S-phase [434]. Moreover, and as enunciated in the introduction, the DNA sequence of these circles contains binding sites for the SBF and MBF transcription factors, which control the G1/S transition (Wittenberg and Reed 2005). Hence, the SEP could be directly caused by an accumulation of DNA titrating the replication machinery and transcription factors of the cell cycle.

If the massive upregulation of rRNA transcription is part of the SEP phenotype is currently assessed in our group. Unpublished data show that deleting *Rrn3* (an activator of Pol I) or degrading Pol I in the post-SEP phase do not prolong lifespan nor rescue the SEP phenotype. Therefore, the upregulation of the rRNA transcription is likely to be a simple byproduct of ERCs and not a cause of the SEP.

An interesting corollary of all these questions is that aging can also be used as a perturbation to study fundamental processes that are very well regulated under physiological conditions.

1.1. An integrative model of the ERC pathway of aging

One possible integrative model of the ERC pathway of aging starts with a stochastic excision of a circle that multiplies by self-replication with the cell divisions. These circles are tethered to the NPCs so they are not transmitted to the progeny, with the caveat that the affected NPCs get remodeled by losing their basket and disrupting their nucleoplasmic transport. In particular, they would import more matter (notably ribosomal proteins and histones) and export less (in particular, mRNA). Altogether, this overproduction of matter and modification of the import/export homeostasis would lead to an increase in nuclear size and content, which in addition to the DNA burden from these circles, would in turn affect the cell-cycle homeostasis. Then, many other processes, often described as hallmarks of aging, would appear (sharp loss of pH, loss of protein stoichiometry and ribosome biogenesis decline, multinucleation, genomic alterations, etc). Potentially, feedforward and feedback loops exist between these post-SEP processes (such as the loss of protein stoichiometry, affecting the NPC and the translation machinery [294,341], in turn worsening the loss of protein stoichiometry), and participate in the death of the cell.

Why has evolution selected ERCs? As seen in the introduction, the evolutionary theory of aging proposes that the toxicity of aging factors is the consequence of an antagonistic pleiotropy which gives a fitness advantage at early ages. In line with that, ERCs are a

byproduct of rDNA recombinations which is a rapid evolutive mechanism to modulate the size of the rDNA array. Besides, ERCs can reintegrate the rDNA locus and participate in replenishing the number of copies [378]. To validate this hypothesis, it would be interesting to perform competitive assays between WT and *fob1Δ* in different changing environments, and show that the WT outcompete the *fob1Δ* mutant that is unable to adapt its rDNA size.

Altogether, we provide a framework to explain one path of aging by separating three distinct phases: excision, replications, and post-SEP survival. This ordering seems crucial to understanding different mutants' role since the confusion between excision and accumulation is often made in the literature. For instance, a fairly recent study [202] used different rDNA-ARS (which impact the replication efficiency of ERC) and found that weaker ARS leads to increased lifespan. However, they found an additive effect with a SIR2 or a FOB1 deletion and thus concluded that modulating the ARS affects lifespan in an ERC-independent manner. In reality, Sir2 and Fob1 affect the excision rate, while the ARS affect the replication rate, which both affect the ERC quantity in a population.

More generally, to challenge this model, it would be necessary to screen known mutants of longevity and see if they are long-lived because of a decreased excision probability, a slower accumulation, if they trigger the SEP at a higher dose of ERCs, or if they survive better in the post-SEP period (Figure 70).

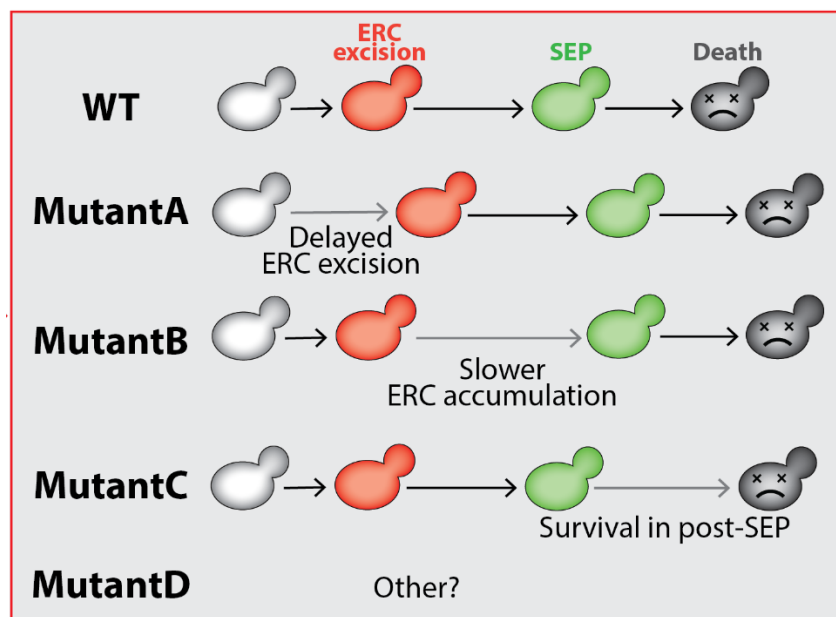


Figure 70: Scheme describing the potential effect of longevity mutants on the ERC-pathway of aging

2. Relevance of the ERC/rDNA pathway in other organisms

The molecular relevance of such a pathway in other organisms is debatable. Indeed, though ERCs exist in other organisms, they have not been found as enriched during aging. However, extrachromosomal circles (eccDNA) are a hallmark of cancer cells and have raised much attention in the past few years [492-495], thanks to the adaptive potential they can confer to a cell by increasing gene copy number [496,497]. Though in the case of cancer, eccDNA provides a fitness advantage, they have also been found implicated in the aging of the central nervous system and in neurodegeneration [498].

If ERCs are absent from aging tissues in mammals, the rDNA homeostasis is a recurrent hallmark of aging and cancer. Indeed, since all the cellular functions are dependent on the ribosome biogenesis across the living, the fact that the rDNA is organized in repetitive repeats is very conserved so that cells can crank out many ribosomes simultaneously. Consequently, rDNA sequences are also prone to genomic damage in these organisms and are strongly rearranged during aging and in cancer cells [499-501]. Besides, misregulated ribosome biogenesis and increased rRNA transcription is known to be linked with senescence in mouse and human fibroblasts [502,503]. Along the same line, small nucleoli and reduced ribosome biogenesis are also correlated with longevity in *C. elegans*, *Drosophila*, mice, and human muscle tissues [234,369,370,504]. In line with that, caloric restriction or TORC1 inhibition, two of the most conserved longevity interventions, decreases the nucleolus size [505]. Altogether, this points out that the nucleolus homeostasis and the rDNA pathway(s) of aging that we described have a crucial and conserved role in cancer and aging.

3. Other pathways of aging

At least one other pathway (or “mode”) of aging exists and has been described as mutually exclusive with an “rDNA mode” (loss of rDNA silencing, increase of nucleolus size [283]). This rDNA mode is most probably what we described as the ERC/rDNA pathway, while this second mode seems to implicate mitochondria homeostasis [283]. Recently, another independent but concomitant study also reported two divergent populations, this time regarding the vacuolar pH and the iron-sulfur cluster maintenance [280]. It would be interesting to see if these populations also represent the two modes, “rDNA” and “Mitochondria” (which is likely, knowing the link between mitochondria and vacuolar pH and ISC, see p. 38). Nonetheless, if this “mitochondrial pathway” is really aging or simply the age-independent and transmissible loss of mitochondrial potential that can occur in the life of

cells, as described previously [246], has not been carefully analyzed by the authors (though the phenotype seems to be inherited to the daughters, according to the raw data provided). In any way, the fact that two-thirds of the *fob1Δ* cells die without ERCs suggests that another path of aging exists. This idea is reinforced by the fact that mathematical modeling fails to perfectly recapitulate the aging curve by simply taking into account the ERC model, and a competing ERC-independent cause dictated by a Gompertzian law (age-dependent mortality, see introduction) needs to be added to the model to better fit the survival curve (Figure 59, p.86). Understanding what causes this age-dependent part, and how ERC-less cells die, is of particular interest.

In a more general manner, we could wonder where all the described hallmarks of aging from the introduction (and many more not presented here) stand on the aging picture.

Altogether, it is very likely that several pathways of aging with different kinetics compete together (potentially interconnected at some nodes), or alternatively, that one path is exclusive to the others [126,223,283,506,507] (Figure 71).

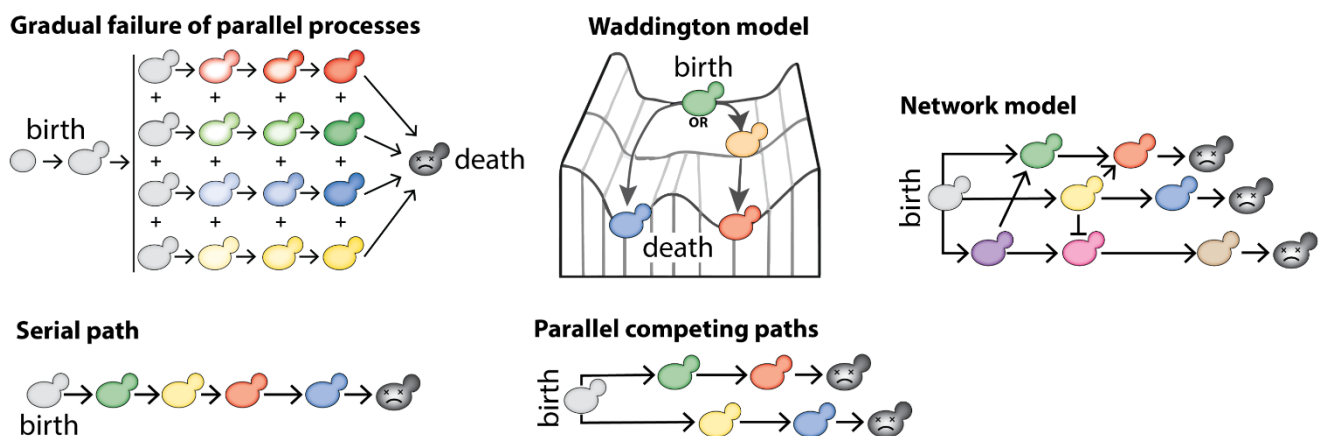


Figure 71: Different paradigms can model aging. Each color represents a biological process that is affected during aging.

Yet, the current tools have a limited power to test so many hypotheses. Even if microfluidics lifted a manipulation burden, the throughput and, in particular, the speed of analysis (mainly manual), remains an obstacle for systematic and comprehensive screens. For that, **we developed a high-throughput platform for automated and standardized aging assays, which will allow us to analyze all the known markers of aging at the single-cell level and classify them into aging pathways.**

4. A general framework to classify hallmarks of aging into pathways

4.1. Deciphering the choreography of aging

Indeed, since neither monitoring nor analysis represents a throughput problem (16x2000 cells can be screened and analyzed in 4 days) anymore, it is possible to screen 4 or 5 markers (division duration, growth, and 2-3 fluorescent tags) simultaneously in order to decipher their dynamics and where they stand one towards the others. With that, we will be able to temporally order the phenotypes to know if their occurrence is abrupt or progressive and classify them into one or another aging pathway (Figure 72).

Deciphering the choreography of aging

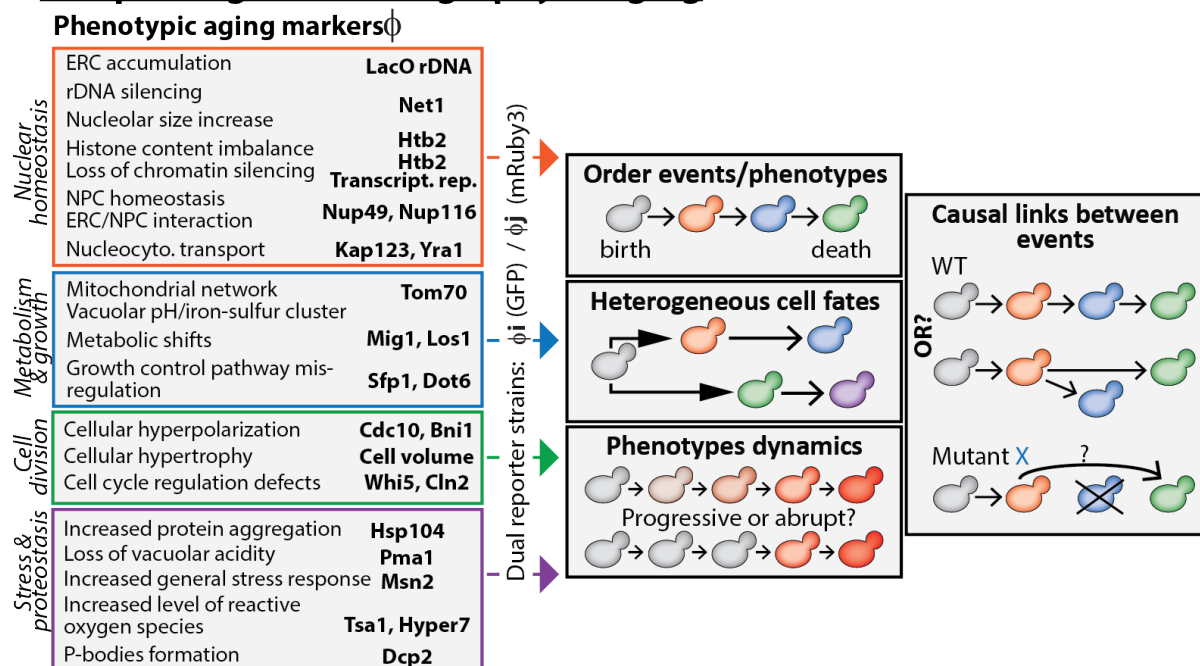


Figure 72: Experimental plan to decipher the choreography of aging. (Left): List of phenotypic aging markers, grouped in functional ontologies, that will be tagged fluorescently. (Right): Types of dynamics that can be assessed with these markers. The color of the cell represents a phenotype of aging, tagged using a fluorescent marker. It is possible to order them temporally (top left tile), to know if they are abrupt or progressive (bottom left tile), to know if they are independent of each other's (mid left tile), or to know if a marker is a link of a chain of causality or a pure byproduct (right tile)

For instance, we could systematically use a Net1-mRuby3 as a marker of the rDNA/ERC pathway (or simply look at the existence of a SEP, which always correlates with an ERC accumulation [226]), with another marker X. Does X belong to the ERC mode of aging? If so, does it occur before or after the nucleolar misregulation and the SEP? With this approach, we could, for example, assess if the NPC remodeling and the impairment of the nucleocytoplasmic exchange [341,358] are ERC-dependent or not (using tagged Nup116 and other nucleoporins from different parts of the NPCs, as well as karyopherins), and if yes, whether they occur progressively with the ERC accumulation, abruptly at the SEP, or only in late the post-SEP phase.

Another example application could be to determine if any of the described aging phenotypes (such as Whi5 accumulation [248] or proteostasis collapse [316]) *bona fide* paths of aging or only post-SEP and proximal causes of cell death.

Along the same line, a recent report described P-bodies formation in late ages and linked it to a change in cytoplasmic pH [292]. Could we show that the pH drop and the P-bodies formation are post-SEP events (as suggested in [238] for the pH)?

Beyond allowing the classification of hallmarks in aging pathways, looking at temporal sequences of events can be very informative on the causality. If event A systematically occurs before event B, then B is probably causally linked to A (directly or indirectly). However, this observation remains correlative, and deletion mutants are necessary to reinforce such conclusions and determine if an event is a cause or just a byproduct. Do we still have the rest of the chain of events when deleting a gene causing a marker? If so, then this marker is probably a byproduct of the pathway (Figure 72, top right).

Finally, without even looking at several markers at the same time, measuring the statistics of the occurrence of a given event can inform us about its causes. For example, if an event is not dependent on age or is observed at any age (like the loss of mitochondrial DNA [246] or the excision of an ERC, as presented in this dissertation), then it is not likely to be the result of a pathway of aging, but rather the genesis of a pathway (or a standalone event).

4.2. Classifying longevity genes

Similarly, screening the longevity mutants will also allow distinguishing the different paths of aging and the kinetics of each component of the paths.

For example, if two different paths of aging have different kinetics (Figure 73B “WT”), we could determine if longevity mutants are long-lived because they affect the kinetics of one path or the other (Figure 73B “Mutant1”), and which element of the path has its kinetics modified (Figure 73C, and example with the ERC pathway p.138). Along the same line, slowing down the kinetics of the fastest aging path should reveal the other (Figure 73B “Mutant2”).

For example, it could be that ERC accumulation (and all its downstream effects) is the first replicative limit encountered by the cell (Scenario “WT” in Figure 73B), but if the kinetics of this pathway is decreased (for example, in a *fob1Δ* mutant), then another competing pathway of aging becomes the new replicative limit, later than in the WT (scenario “Mutant 1” and “Mutant 2” on Figure 73B). In line with that, one-third of the *fob1Δ* cells die with a SEP and an ERC accumulation, but later than the WT cells (scenario “Mutant 1”), while two-thirds die without a SEP nor ERC accumulation (scenario “Mutant 2”).

Classifying known pro-longevity genes

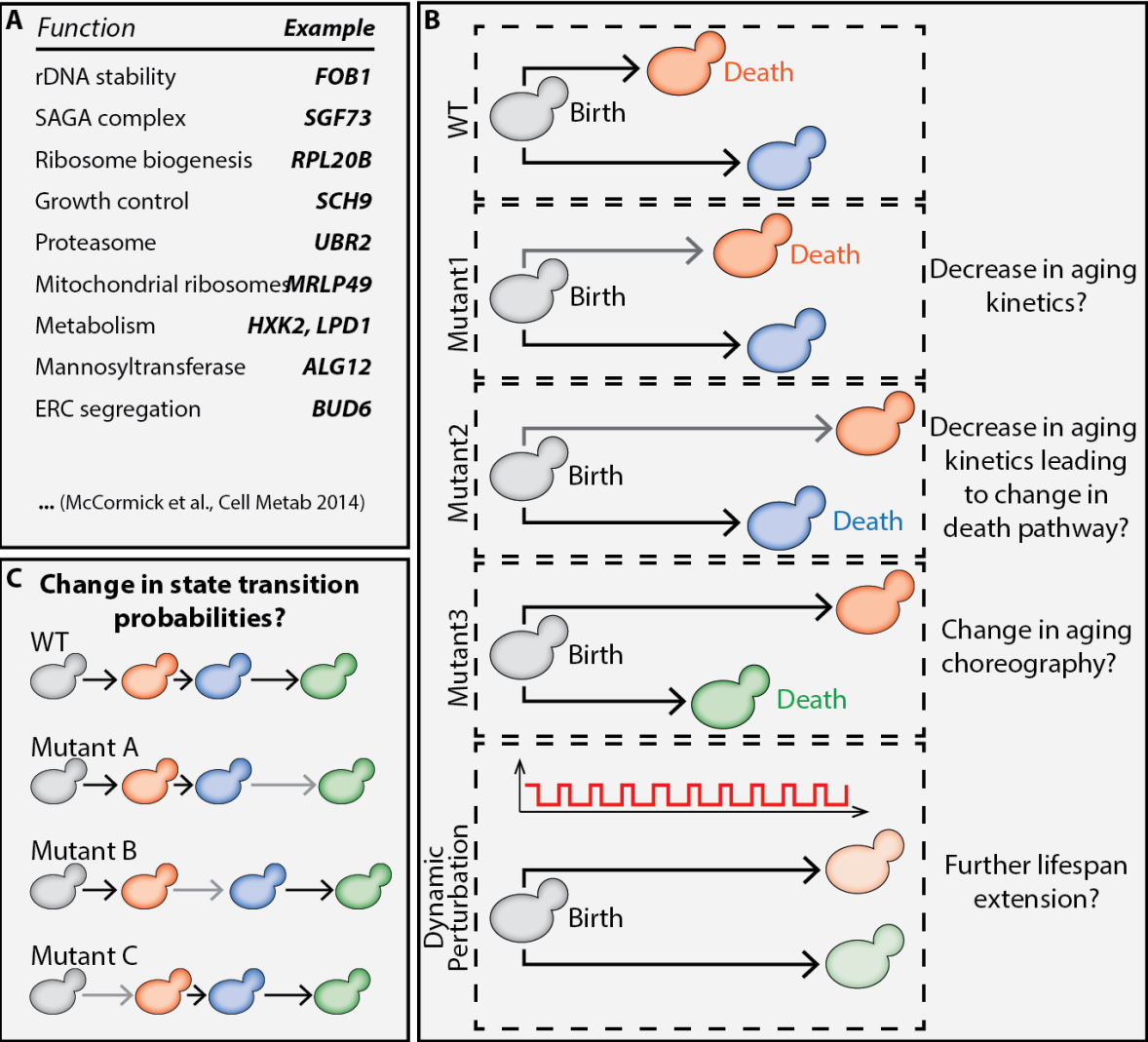


Figure 73: Experimental plan to classify longevity genes. (A): Non-exhaustive list of deletion mutant to screen using markers from Figure 72. (B): With the hypothesis of two concomitant aging pathways (WT scenario), we could observe mutants that are long-lived because they delay one path or the other, therefore changing the proportion of cells dying from one or the other and reveal new paths. (C): Among one pathway that is delayed, we could identify which transition between two nodes of the pathway is slowed down (grey arrow).

Instead of deletion mutants, dynamic genetic perturbations (with an AID- system, for instance [508]) are also a way to decipher the chains of causality. If a gene is thought to have an effect early in the chain of causality, then deleting it at later stages should not affect aging. For instance, deleting *FOB1* after the cells have excised an ERC should have no impact on the rest of the events, (namely the accumulation of ERC, the entry into senescence, and the post-SEP declines), nor on the RLS. Conversely, some deletions could have a deleterious effect early in life but be beneficial once advanced in the path of aging (such as a *GCN5* deletion, which is thought to have a higher excision probability, but a slower ERC accumulation [356]).

Similarly, definitive deletion can cause fitness defects, while an intermittent reduction of one protein quantity could increase lifespan. More generally, with such an approach, we could also test the antagonistic pleiotropy theory of aging by suppressing genes early or late in life and measuring the impacts on fitness (growth) and survival.

Along the same line, environmental perturbations such as caloric restriction, amino acid depletion, inhibition of TOR with rapamycin, or growth in respirative media are known to affect lifespan positively [157,158,295]. Understanding how these effects impact longevity is key to grasping aging because of their high degree of conservation and the fact that they act on different hallmarks of aging simultaneously. However, this pleiotropic nature makes the results difficult to interpret, but using our pipeline could help to determine precisely and systematically which aging markers are affected. Besides, no study exists about the lifespan of cells in fluctuating environments such as periodic pulses of caloric restrictions and if it could be possible to further extend the lifespan with such dynamic switches.

This ordering and classification of events in pathways and networks seem basic and obvious but are in reality rarely applied due to the cumbersome task of tracking cells manually throughout aging. We think that the new tool we developed will help realize such comprehensive and systematic analyses and that budding yeast remains the most suitable model for this approach.

5. Observing the daughters to understand aging factors

To better identify and understand the aging factors, one could also observe the progeny of old cells. So far, careful examination of daughters has been almost absent from the literature, except from early studies [211,212,224]. Nevertheless, this approach can be very informative about what drives aging in the mother, and help tell which hallmark is a *bona fide* aging factor (that is, not transmitted to the daughter).

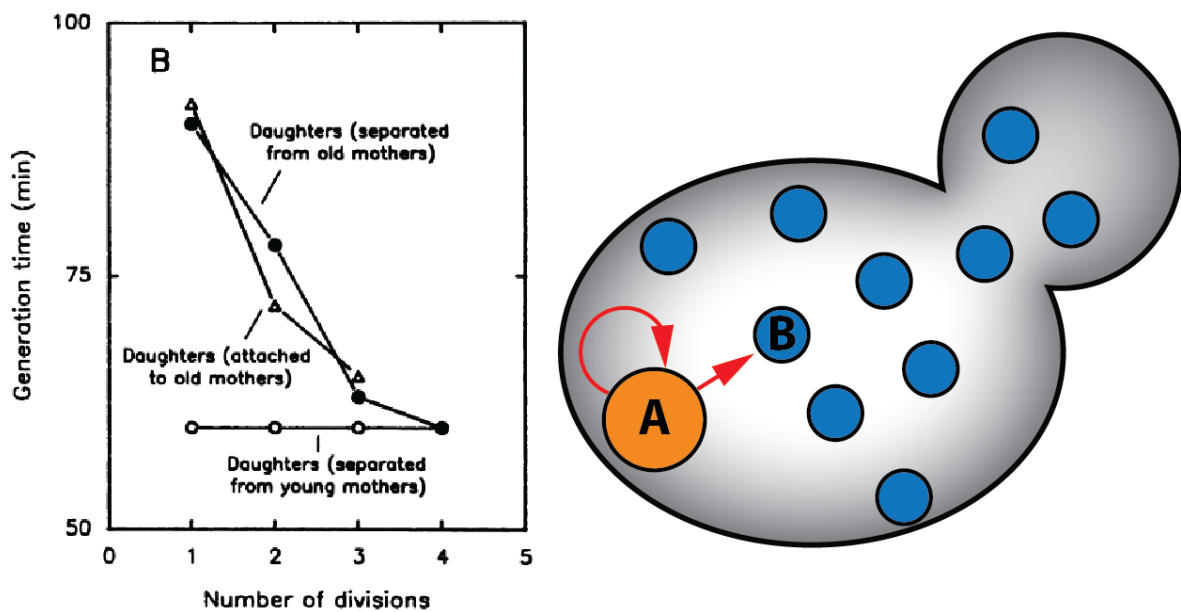


Figure 74: Examining the lifespan of daughters from old mothers can be informative. (Left) Division time as a function of the divisions, of daughters from old mothers (black circle and triangle) compared to daughters from young mothers (white circles) (From [211]). (Right): Hypothetic new model of aging factor. A factor A, non-necessarily toxic, asymmetrically segregated and accumulating in the mother, drives the accumulation of a factor B, toxic but not actively segregated and thus being diluted throughout the divisions in the daughter.

For example, daughters from old mothers divide slower than those from young mothers, but it is back to normal after a few divisions [211] and Figure 74). This suggests that these daughters inherit a factor that slows down the division time, which is not asymmetrically segregated and not self-amplifying (since it is diluted at each division).

In other words, it is possible that a toxic factor is evenly segregated to the daughter but does not accumulate there because its production relies on another factor retained in the mother (Figure 74). Such concepts question the validity of the aging factor definition and framework (accumulation in the mother, toxicity, and non-transmission to the daughter [213]).

Yet, these experiments are in practice difficult to realize with the current tools, since the only way to study daughters from old mothers so far is to use microdissection or to harvest them from enrichment methods. Either way, it is impossible to correlate the mother's lifespan with that of the daughters.

Using the device and experimental setup presented in the discussion of the first project (p.129), we could capture the entire lifespan of a daughter cell born at any mother age.

Beyond understanding aging factors, we could also determine which damages are irreversibly passed to the progeny, such as -among the obvious ones- loss of heterozygosity, nuclear

fragmentation, and loss of mtDNA. In this sense, we could adequately characterize mitochondrial damages that have often (and still recently) been described as aging factors, though they are inherited by the whole progeny in some cases [246,262,264].

However, though they cannot be described as an aging factor per se, traits that decrease the lifespan while being inherited (DNA mutations, nuclear fragmentation, loss of mtDNA, etc) contribute to aging and should not be ignored. Therefore, we could question the replicative aging model and consider the rejuvenation loss as a hallmark of aging, since genomic instabilities and some epigenetic alterations are part of human aging and are transmitted to the daughter cells as well.

Altogether, this suggests that studying how the daughters of old mothers age and rejuvenate has been overlooked so far but could become a powerful angle to tackle replicative aging thanks to newly available technologies.

References Chapter I

- [1] Z. A. Medvedev, "An attempt at a rational classification of theories of ageing," *Biol Rev*, vol. 65, no. 3, pp. 375–398, 1990, doi: 10.1111/j.1469-185x.1990.tb01428.x.
- [2] E. J. Williamson *et al.*, "Factors associated with COVID-19-related death using OpenSAFELY," *Nature*, vol. 584, no. 7821, pp. 430–436, 2020, doi: 10.1038/s41586-020-2521-4.
- [3] M. Roser, H. Ritchie, and E. Ortiz-Ospina, "World Population Growth," *Our World in Data*, 2013, [Online]. Available: <https://ourworldindata.org/world-population-growth>
- [4] M. R. Rose, *Evolutionary biology of aging*. 1991.
- [5] Wikipedia, "List of world records in masters athletics," n.d.
https://en.wikipedia.org/wiki/List_of_world_records_in_masters_athletics (accessed Nov. 14, 2021).
- [6] B. Gompertz, "On the nature of the function expressive of the law of human mortality, and on a new mode of determining the value of life contingencies. In a letter to Francis Baily, Esq. F. R. S. &c," *Philosophical Transactions Royal Soc Lond*, vol. 115, no. 115, pp. 513–583, 1825, doi: 10.1098/rstl.1825.0026.
- [7] C. E. Finch, M. C. Pike, and M. Witten, "Slow Mortality Rate Accelerations During Aging in Some Animals Approximate That of Humans," *Science*, vol. 249, no. 4971, pp. 902–905, 1990, doi: 10.1126/science.2392680.
- [8] J. W. Vaupel, T. E. Johnson, and G. J. Lithgow, "Rates of Mortality in Populations of *Caenorhabditis elegans*," *Science*, vol. 266, no. 5186, pp. 826–826, 1994, doi: 10.1126/science.7973641.
- [9] W. Mair, P. Goymer, S. D. Pletcher, and L. Partridge, "Demography of Dietary Restriction and Death in *Drosophila*," *Science*, vol. 301, no. 5640, pp. 1731–1733, 2003, doi: 10.1126/science.1086016.
- [10] H. Qin and M. Lu, "Natural variation in replicative and chronological life spans of *Saccharomyces cerevisiae*," *Exp Gerontol*, vol. 41, no. 4, pp. 448–456, 2006, doi: 10.1016/j.exger.2006.01.007.
- [11] O. R. Jones *et al.*, "Diversity of ageing across the tree of life," *Nature*, vol. 505, no. 7482, pp. 169–173, 2014, doi: 10.1038/nature12789.
- [12] G. C. Williams, "Pleiotropy, natural selection, and the evolution of senescence," *Evolution*, vol. 11, no. 4, pp. 398–411, 1957, doi: 10.1111/j.1558-5646.1957.tb02911.x.
- [13] A. Weismann, "Essays upon heredity and kindred biological problems," *Vol. 1. 2d ed. Oxford: Clarendon.*, 1891.
- [14] L. Hayflick and P. S. Moorhead, "The serial cultivation of human diploid cell strains," *Exp Cell Res*, vol. 25, no. 3, pp. 585–621, 1961, doi: 10.1016/0014-4827(61)90192-6.
- [15] A. M. Olovnikov, "A theory of marginotomy The incomplete copying of template margin in enzymic synthesis of polynucleotides and biological significance of the phenomenon," *J Theor Biol*, vol. 41, no. 1, pp. 181–190, 1973, doi: 10.1016/0022-5193(73)90198-7.
- [16] C. B. Harley, A. B. Futcher, and C. W. Greider, "Telomeres shorten during ageing of human fibroblasts," *Nature*, vol. 345, no. 6274, pp. 458–460, 1990, doi: 10.1038/345458a0.
- [17] B. Lakowski and S. Hekimi, "Determination of Life-Span in *Caenorhabditis elegans* by Four Clock Genes," *Science*, vol. 272, no. 5264, pp. 1010–1013, 1996, doi: 10.1126/science.272.5264.1010.
- [18] C. A. Wolkow, K. D. Kimura, M.-S. Lee, and G. Ruvkun, "Regulation of *C. elegans* Life-Span by Insulinlike Signaling in the Nervous System," *Science*, vol. 290, no. 5489, pp. 147–150, 2000, doi: 10.1126/science.290.5489.147.
- [19] R. A. Fisher, "Retrospect of the criticisms of the theory of natural selection," 1930.

- [20] J. B. S. Haldane, *New Paths in Genetics*. 1941.
- [21] W. D. Hamilton, "The moulding of senescence by natural selection," *J Theor Biol*, vol. 12, no. 1, pp. 12–45, 1966, doi: 10.1016/0022-5193(66)90184-6.
- [22] D. H. Nussey, H. Froy, J.-F. Lemaître, J.-M. Gaillard, and S. N. Austad, "Senescence in natural populations of animals: Widespread evidence and its implications for biogerontology," *Ageing Res Rev*, vol. 12, no. 1, pp. 214–225, 2013, doi: 10.1016/j.arr.2012.07.004.
- [23] R. E. Ricklefs, "Evolutionary Theories of Aging: Confirmation of a Fundamental Prediction, with Implications for the Genetic Basis and Evolution of Life Span," *Am Nat*, vol. 152, no. 1, pp. 24–44, 1998, doi: 10.1086/286147.
- [24] G. Libertini, "An adaptive theory of the increasing mortality with increasing chronological age in populations in the wild," *J Theor Biol*, vol. 132, no. 2, pp. 145–162, 1988, doi: 10.1016/s0022-5193(88)80153-x.
- [25] G. Libertini, "Evidence for aging theories from the study of a hunter—gatherer people (Ache of Paraguay)," *Biochem Mosc*, vol. 78, no. 9, pp. 1023–1032, 2013, doi: 10.1134/s0006297913090083.
- [26] R. D. Lee, "Rethinking the evolutionary theory of aging: Transfers, not births, shape senescence in social species," *Proc National Acad Sci*, vol. 100, no. 16, pp. 9637–9642, 2003, doi: 10.1073/pnas.1530303100.
- [27] T. Y. Pang, "On age-specific selection and extensive lifespan beyond menopause," *Roy Soc Open Sci*, vol. 7, no. 5, p. 191972, 2020, doi: 10.1098/rsos.191972.
- [28] S. N. Chapman, J. E. Pettay, V. Lummaa, and M. Lahdenperä, "Limits to Fitness Benefits of Prolonged Post-reproductive Lifespan in Women," *Curr Biol*, vol. 29, no. 4, pp. 645–650.e3, 2019, doi: 10.1016/j.cub.2018.12.052.
- [29] P. S. Kim, J. S. McQueen, and K. Hawkes, "Why does women's fertility end in mid-life? Grandmothering and age at last birth," *J Theor Biol*, vol. 461, pp. 84–91, 2019, doi: 10.1016/j.jtbi.2018.10.035.
- [30] K. Hawkes, J. F. O'Connell, and N. G. B. Jones, "Hadza Women's Time Allocation, Offspring Provisioning, and the Evolution of Long Postmenopausal Life Spans," *Curr Anthropol*, vol. 38, no. 4, pp. 551–577, 1997, doi: 10.1086/204646.
- [31] T. B. L. Kirkwood, "Evolution of ageing," *Mech Ageing Dev*, vol. 123, no. 7, pp. 737–745, 2002, doi: 10.1016/s0047-6374(01)00419-5.
- [32] A. M. Leroi et al., "What evidence is there for the existence of individual genes with antagonistic pleiotropic effects?," *Mech Ageing Dev*, vol. 126, no. 3, pp. 421–429, 2005, doi: 10.1016/j.mad.2004.07.012.
- [33] N. L. Jenkins, G. McColl, and G. J. Lithgow, "Fitness cost of extended lifespan in *Caenorhabditis elegans*," *Proc Royal Soc Lond Ser B Biological Sci*, vol. 271, no. 1556, pp. 2523–2526, 2004, doi: 10.1098/rspb.2004.2897.
- [34] J. R. Delaney, C. J. Murakami, B. Olsen, B. K. Kennedy, and M. Kaeberlein, "Quantitative evidence for early life fitness defects from 32 longevity-associated alleles in yeast," *Cell Cycle*, vol. 10, no. 1, pp. 156–165, 2011, doi: 10.4161/cc.10.1.14457.
- [35] D. M. Garcia et al., "A prion accelerates proliferation at the expense of lifespan," *Elife*, vol. 10, p. e60917, 2021, doi: 10.7554/elife.60917.
- [36] D. W. Walker, G. McColl, N. L. Jenkins, J. Harris, and G. J. Lithgow, "Evolution of lifespan in *C. elegans*," *Nature*, vol. 405, no. 6784, pp. 296–297, 2000, doi: 10.1038/35012693.
- [37] S. N. Austad and J. M. Hoffman, "Is Antagonistic Pleiotropy Ubiquitous in Aging Biology?," *Evol Medicine Public Heal*, vol. 2018, no. 1, pp. eoy033–, 2018, doi: 10.1093/emph/eoy033.
- [38] T. Flatt and D. E. L. Promislow, "Still Pondering an Age-Old Question," *Science*, vol. 318, no. 5854, pp. 1255–1256, 2007, doi: 10.1126/science.1147491.
- [39] B. Charlesworth, *Evolution in Age-structured Populations*. 1994.

- [40] S. N. Austad, "Retarded senescence in an insular population of Virginia opossums (*Didelphis virginiana*)," *J Zool*, vol. 229, no. 4, pp. 695–708, 1993, doi: 10.1111/j.1469-7998.1993.tb02665.x.
- [41] S. C. Stearns, M. Ackermann, M. Doebeli, and M. Kaiser, "Experimental evolution of aging, growth, and reproduction in fruitflies," *Proc National Acad Sci*, vol. 97, no. 7, pp. 3309–3313, 2000, doi: 10.1073/pnas.97.7.3309.
- [42] M. Rose and B. Charlesworth, "A test of evolutionary theories of senescence," *Nature*, vol. 287, no. 5778, pp. 141–142, 1980, doi: 10.1038/287141a0.
- [43] A. M. Leroi, A. K. Chippindale, and M. R. Rose, "Long-term laboratory evolution of a genetic life-history trade-off in *drosophila melanogaster*," *Evolution*, vol. 48, no. 4, pp. 1244–1257, 1994, doi: 10.1111/j.1558-5646.1994.tb05309.x.
- [44] M. R. Rose, "Laboratory Evolution of Postponed Senescence in *Drosophila melanogaster*," *Evolution*, vol. 38, no. 5, p. 1004, 1984, doi: 10.2307/2408434.
- [45] L. S. Luckinbill, R. Arking, M. J. Clare, W. C. Cirocco, and S. A. Buck, "Selection for delayed senescence in *drosophila melanogaster*," *Evolution*, vol. 38, no. 5, pp. 996–1003, 1984, doi: 10.1111/j.1558-5646.1984.tb00369.x.
- [46] J. Nielsen et al., "Eye lens radiocarbon reveals centuries of longevity in the Greenland shark (*Somniosus microcephalus*)," *Science*, vol. 353, no. 6300, pp. 702–704, 2016, doi: 10.1126/science.aaf1703.
- [47] T. B. L. Kirkwood, "Evolution of ageing," *Nature*, vol. 270, no. 5635, pp. 301–304, 1977, doi: 10.1038/270301a0.
- [48] R. B. Cervantes, J. R. Stringer, C. Shao, J. A. Tischfield, and P. J. Stambrook, "Embryonic stem cells and somatic cells differ in mutation frequency and type," *Proc National Acad Sci*, vol. 99, no. 6, pp. 3586–3590, 2002, doi: 10.1073/pnas.062527199.
- [49] G. Saretzki, L. Armstrong, A. Leake, M. Lako, and T. von Zglinicki, "Stress Defense in Murine Embryonic *Stem Cells* Is Superior to That of Various Differentiated Murine Cells," *Stem Cells*, vol. 22, no. 6, pp. 962–971, 2004, doi: 10.1634/stemcells.22-6-962.
- [50] T. B. L. Kirkwood and S. N. Austad, "Why do we age?," *Nature*, vol. 408, no. 6809, pp. 233–238, 2000, doi: 10.1038/35041682.
- [51] T. B. L. Kirkwood, "Asymmetry and the origins of ageing," *Mech Ageing Dev*, vol. 126, no. 5, pp. 533–534, 2005, doi: 10.1016/j.mad.2005.02.001.
- [52] M. Ackermann, L. Chao, C. T. Bergstrom, and M. Doebeli, "On the evolutionary origin of aging," *Aging Cell*, vol. 6, no. 2, pp. 235–244, 2007, doi: 10.1111/j.1474-9726.2007.00281.x.
- [53] L. E. Orgel, "The maintenance of the accuracy of protein synthesis and its relevance to ageing," *Proc National Acad Sci*, vol. 49, no. 4, pp. 517–521, 1963, doi: 10.1073/pnas.49.4.517.
- [54] D. Harman, "Aging: A Theory Based on Free Radical and Radiation Chemistry," *J Gerontology*, vol. 11, no. 3, pp. 298–300, 1956, doi: 10.1093/geronj/11.3.298.
- [55] D. Harman, "Free radical theory of aging," *Mutat Res Dnaging*, vol. 275, no. 3–6, pp. 257–266, 1992, doi: 10.1016/0921-8734(92)90030-s.
- [56] A. B. Lindner and A. Demarez, "Protein aggregation as a paradigm of aging," *Biochimica Et Biophysica Acta Bba - Gen Subj*, vol. 1790, no. 10, pp. 980–996, 2009, doi: 10.1016/j.bbagen.2009.06.005.
- [57] G. Failla, "The Aging Process And Cancerogenesis," *Ann Ny Acad Sci*, vol. 71, no. 6 Genetic Conce, pp. 1124–1140, 1958, doi: 10.1111/j.1749-6632.1958.tb46828.x.
- [58] L. Szilard, "On the Nature of the Aging Process," *Proc National Acad Sci*, vol. 45, no. 1, pp. 30–45, 1959, doi: 10.1073/pnas.45.1.30.
- [59] H. L. Gensler and H. Bernstein, "DNA Damage as the Primary Cause of Aging," *Q Rev Biology*, vol. 56, no. 3, pp. 279–303, 1981, doi: 10.1086/412317.
- [60] G. A. Garinis, G. T. J. van der Horst, J. Vijg, and J. H. J. Hoeijmakers, "DNA damage and ageing: new-age ideas for an age-old problem," *Nat Cell Biol*, vol. 10, no. 11, pp.

- 1241–1247, 2008, doi: 10.1038/ncb1108-1241.
- [61] P. Alexander, "The role of DNA lesions in the processes leading to aging in mice.," *Sym Soc Exp Biol*, vol. 21, pp. 29–50, 1967.
- [62] B. Sarg, E. Koutzamani, W. Helliger, I. Rundquist, and H. H. Lindner, "Postsynthetic Trimethylation of Histone H4 at Lysine 20 in Mammalian Tissues Is Associated with Aging*," *J Biol Chem*, vol. 277, no. 42, pp. 39195–39201, 2002, doi: 10.1074/jbc.m205166200.
- [63] M. F. Fraga and M. Esteller, "Epigenetics and aging: the targets and the marks," *Trends Genet*, vol. 23, no. 8, pp. 413–418, 2007, doi: 10.1016/j.tig.2007.05.008.
- [64] I. Cheung et al., "Developmental regulation and individual differences of neuronal H3K4me3 epigenomes in the prefrontal cortex," *Proc National Acad Sci*, vol. 107, no. 19, pp. 8824–8829, 2010, doi: 10.1073/pnas.1001702107.
- [65] S. Han and A. Brunet, "Histone methylation makes its mark on longevity," *Trends Cell Biol*, vol. 22, no. 1, pp. 42–49, 2012, doi: 10.1016/j.tcb.2011.11.001.
- [66] D. Harman, "The Biologic Clock: The Mitochondria?," *J Am Geriatr Soc*, vol. 20, no. 4, pp. 145–147, 1972, doi: 10.1111/j.1532-5415.1972.tb00787.x.
- [67] B. N. Ames, M. K. Shigenaga, and T. M. Hagen, "Oxidants, antioxidants, and the degenerative diseases of aging," *Proc National Acad Sci*, vol. 90, no. 17, pp. 7915–7922, 1993, doi: 10.1073/pnas.90.17.7915.
- [68] E. S. Unlun and A. Koc, "Effects of Deleting Mitochondrial Antioxidant Genes on Life Span," *Ann Ny Acad Sci*, vol. 1100, no. 1, pp. 505–509, 2007, doi: 10.1196/annals.1395.055.
- [69] J. Wawryn, A. Krzepiłko, A. Myszk, and T. Biliński, "Deficiency in superoxide dismutases shortens life span of yeast cells.," *Acta Biochim Pol*, vol. 46, no. 2, pp. 249–53, 1999.
- [70] V. D. Longo, L.-L. Liou, J. S. Valentine, and E. B. Gralla, "Mitochondrial Superoxide Decreases Yeast Survival in Stationary Phase," *Arch Biochem Biophys*, vol. 365, no. 1, pp. 131–142, 1999, doi: 10.1006/abbi.1999.1158.
- [71] V. D. Longo, G. S. Shadel, M. Kaeberlein, and B. Kennedy, "Replicative and Chronological Aging in *Saccharomyces cerevisiae*," *Cell Metab*, vol. 16, no. 1, pp. 18–31, 2012, doi: 10.1016/j.cmet.2012.06.002.
- [72] S. Melov et al., "Extension of Life-Span with Superoxide Dismutase/Catalase Mimetics," *Science*, vol. 289, no. 5484, pp. 1567–1569, 2000, doi: 10.1126/science.289.5484.1567.
- [73] J. M. V. Raamsdonk and S. Hekimi, "Deletion of the Mitochondrial Superoxide Dismutase *sod-2* Extends Lifespan in *Caenorhabditis elegans*," *Plos Genet*, vol. 5, no. 2, p. e1000361, 2009, doi: 10.1371/journal.pgen.1000361.
- [74] T. L. Parkes, A. J. Elia, D. Dickinson, A. J. Hilliker, J. P. Phillips, and G. L. Boulianne, "Extension of *Drosophila* lifespan by overexpression of human SOD1 in motoneurons," *Nat Genet*, vol. 19, no. 2, pp. 171–174, 1998, doi: 10.1038/534.
- [75] J. P. Phillips, S. D. Campbell, D. Michaud, M. Charbonneau, and A. J. Hilliker, "Null mutation of copper/zinc superoxide dismutase in *Drosophila* confers hypersensitivity to paraquat and reduced longevity," *Proc National Acad Sci*, vol. 86, no. 8, pp. 2761–2765, 1989, doi: 10.1073/pnas.86.8.2761.
- [76] J. D. Parker, K. M. Parker, B. H. Sohal, R. S. Sohal, and L. Keller, "Decreased expression of Cu–Zn superoxide dismutase 1 in ants with extreme lifespan," *P Natl Acad Sci Usa*, vol. 101, no. 10, pp. 3486–3489, 2004, doi: 10.1073/pnas.0400222101.
- [77] S. Elchuri et al., "CuZnSOD deficiency leads to persistent and widespread oxidative damage and hepatocarcinogenesis later in life," *Oncogene*, vol. 24, no. 3, pp. 367–380, 2005, doi: 10.1038/sj.onc.1208207.
- [78] V. I. Pérez, H. V. Remmen, A. Bokov, C. J. Epstein, J. Vijg, and A. Richardson, "The overexpression of major antioxidant enzymes does not extend the lifespan of mice," *Aging Cell*, vol. 8, no. 1, pp. 73–75, 2009, doi: 10.1111/j.1474-9726.2008.00449.x.
- [79] J. Viña, C. Borras, K. M. Abdelaziz, R. Garcia-Valles, and M. C. Gomez-Cabrera, "The

- Free Radical Theory of Aging Revisited: The Cell Signaling Disruption Theory of Aging," *Antioxid Redox Sign*, vol. 19, no. 8, pp. 779–787, 2013, doi: 10.1089/ars.2012.5111.
- [80] Y. Goulev et al., "Nonlinear feedback drives homeostatic plasticity in H₂O₂ stress response," *Elife*, vol. 6, p. e23971, 2017, doi: 10.7554/elife.23971.
- [81] E. R. Miller, R. Pastor-Barriuso, D. Dalal, R. A. Riemersma, L. J. Appel, and E. Guallar, "Meta-Analysis: High-Dosage Vitamin E Supplementation May Increase All-Cause Mortality," *Ann Intern Med*, vol. 142, no. 1, p. 37, 2005, doi: 10.7326/0003-4819-142-1-200501040-00110.
- [82] G. S. Omenn et al., "Effects of a Combination of Beta Carotene and Vitamin A on Lung Cancer and Cardiovascular Disease," *New Engl J Medicine*, vol. 334, no. 18, pp. 1150–1155, 1996, doi: 10.1056/nejm199605023341802.
- [83] T. A. Group, "The Effect of Vitamin E and Beta Carotene on the Incidence of Lung Cancer and Other Cancers in Male Smokers," *New Engl J Medicine*, vol. 330, no. 15, pp. 1029–1035, 1994, doi: 10.1056/nejm199404143301501.
- [84] J. H. J. Hoeijmakers, "DNA Damage, Aging, and Cancer," *New Engl J Medicine*, vol. 361, no. 15, pp. 1475–1485, 2009, doi: 10.1056/nejmra0804615.
- [85] Wikipedia, "DNA damage (naturally occurring)," DNA damage (naturally occurring), n.d.
[https://en.wikipedia.org/wiki/DNA_damage_\(naturally_occurring\)#A_major_problem_for_life](https://en.wikipedia.org/wiki/DNA_damage_(naturally_occurring)#A_major_problem_for_life) (accessed Nov. 14, 2021).
- [86] A. A. Moskalev et al., "The role of DNA damage and repair in aging through the prism of Koch-like criteria," *Ageing Res Rev*, vol. 12, no. 2, pp. 661–684, 2013, doi: 10.1016/j.arr.2012.02.001.
- [87] L. Narayanan, J. A. Fritzell, S. M. Baker, R. M. Liskay, and P. M. Glazer, "Elevated levels of mutation in multiple tissues of mice deficient in the DNA mismatch repair gene Pms2," *Proc National Acad Sci*, vol. 94, no. 7, pp. 3122–3127, 1997, doi: 10.1073/pnas.94.7.3122.
- [88] A. Kaya, A. V. Lobanov, and V. N. Gladyshev, "Evidence that mutation accumulation does not cause aging in *Saccharomyces cerevisiae*," *Aging Cell*, vol. 14, no. 3, pp. 366–371, 2015, doi: 10.1111/accel.12290.
- [89] P. S. Robinson et al., "Increased somatic mutation burdens in normal human cells due to defective DNA polymerases," *Nat Genet*, pp. 1–9, 2021, doi: 10.1038/s41588-021-00930-y.
- [90] B. N. Ames and L. S. Gold, "Endogenous mutagens and the causes of aging and cancer," *Mutat Res Fundam Mol Mech Mutagen*, vol. 250, no. 1–2, pp. 3–16, 1991, doi: 10.1016/0027-5107(91)90157-j.
- [91] G. E. Holmes, C. Bernstein, and H. Bernstein, "Oxidative and other DNA damages as the basis of aging: a review," *Mutat Res Dnaging*, vol. 275, no. 3–6, pp. 305–315, 1992, doi: 10.1016/0921-8734(92)90034-m.
- [92] K. S. Rao and L. A. Loeb, "DNA damage and repair in brain: relationship to aging," *Mutat Res Dnaging*, vol. 275, no. 3–6, pp. 317–329, 1992, doi: 10.1016/0921-8734(92)90035-n.
- [93] S. R. R. Kolora et al., "Origins and evolution of extreme life span in Pacific Ocean rockfishes," *Science*, vol. 374, no. 6569, pp. 842–847, 2021, doi: 10.1126/science.abg5332.
- [94] S. Pal and J. K. Tyler, "Epigenetics and aging," *Sci Adv*, vol. 2, no. 7, p. e1600584, 2016, doi: 10.1126/sciadv.1600584.
- [95] S. Horvath and K. Raj, "DNA methylation-based biomarkers and the epigenetic clock theory of ageing," *Nat Rev Genet*, vol. 19, no. 6, pp. 371–384, 2018, doi: 10.1038/s41576-018-0004-3.
- [96] J.-H. Yang et al., "Loss of Epigenetic Information as a Cause of Mammalian Aging," *Ssrn Electron J*, 2021, doi: 10.2139/ssrn.3951490.
- [97] M. J. Jones, S. J. Goodman, and M. S. Kobor, "DNA methylation and healthy human aging," *Aging Cell*, vol. 14, no. 6, pp. 924–932, 2015, doi: 10.1111/accel.12349.

- [98] R. E. Marioni et al., "DNA methylation age of blood predicts all-cause mortality in later life," *Genome Biol*, vol. 16, no. 1, p. 25, 2015, doi: 10.1186/s13059-015-0584-6.
- [99] J. Feser et al., "Elevated Histone Expression Promotes Life Span Extension," *Mol Cell*, vol. 39, no. 5, pp. 724–735, 2010, doi: 10.1016/j.molcel.2010.08.015.
- [100] E. L. Greer et al., "Members of the Histone H3 Lysine 4 Trimethylation Complex Regulate Lifespan in a Germline-dependent Manner in *C. elegans*," *Nature*, vol. 466, no. 7304, pp. 383–387, 2010, doi: 10.1038/nature09195.
- [101] A. P. Siebold, R. Banerjee, F. Tie, D. L. Kiss, J. Moskowitz, and P. J. Harte, "Polycomb Repressive Complex 2 and Trithorax modulate *Drosophila* longevity and stress resistance," *Proc National Acad Sci*, vol. 107, no. 1, pp. 169–174, 2010, doi: 10.1073/pnas.0907739107.
- [102] C. Jin et al., "Histone Demethylase UTX-1 Regulates *C. elegans* Life Span by Targeting the Insulin/IGF-1 Signaling Pathway," *Cell Metab*, vol. 14, no. 2, pp. 161–172, 2011, doi: 10.1016/j.cmet.2011.07.001.
- [103] C. López-Otín, M. A. Blasco, L. Partridge, M. Serrano, and G. Kroemer, "The Hallmarks of Aging," *Cell*, vol. 153, no. 6, pp. 1194–1217, 2013, doi: 10.1016/j.cell.2013.05.039.
- [104] H. Rubin, "The disparity between human cell senescence in vitro and lifelong replication in vivo," *Nat Biotechnol*, vol. 20, no. 7, pp. 675–681, 2002, doi: 10.1038/nbt0702-675.
- [105] M. H. Goyns and W. L. Lavery, "Telomerase and mammalian ageing: a critical appraisal," *Mech Ageing Dev*, vol. 114, no. 2, pp. 69–77, 2000, doi: 10.1016/s0047-6374(00)00095-6.
- [106] J. Campisi, "The biology of replicative senescence," *Eur J Cancer*, vol. 33, no. 5, pp. 703–709, 1997, doi: 10.1016/s0959-8049(96)00058-5.
- [107] M. A. Muñoz-Lorente, A. C. Cano-Martin, and M. A. Blasco, "Mice with hyper-long telomeres show less metabolic aging and longer lifespans," *Nat Commun*, vol. 10, no. 1, p. 4723, 2019, doi: 10.1038/s41467-019-12664-x.
- [108] K. L. Rudolph et al., "Longevity, Stress Response, and Cancer in Aging Telomerase-Deficient Mice," *Cell*, vol. 96, no. 5, pp. 701–712, 1999, doi: 10.1016/s0092-8674(00)80580-2.
- [109] P. J. Hornsby, "Telomerase and the aging process," *Exp Gerontol*, vol. 42, no. 7, pp. 575–581, 2007, doi: 10.1016/j.exger.2007.03.007.
- [110] H. Koga, S. Kaushik, and A. M. Cuervo, "Protein homeostasis and aging: The importance of exquisite quality control," *Ageing Res Rev*, vol. 10, no. 2, pp. 205–215, 2011, doi: 10.1016/j.arr.2010.02.001.
- [111] I. Saez and D. Vilchez, "The Mechanistic Links Between Proteasome Activity, Aging and Age-related Diseases," *Curr Genomics*, vol. 15, no. 1, pp. 38–51, 2014, doi: 10.2174/138920291501140306113344.
- [112] G. Morrow, M. Samson, S. Michaud, and R. M. Tanguay, "Overexpression of the small mitochondrial Hsp22 extends *Drosophila* life span and increases resistance to oxidative stress," *Faseb J*, vol. 18, no. 3, pp. 598–599, 2004, doi: 10.1096/fj.03-0860fje.
- [113] G. A. Walker and G. J. Lithgow, "Lifespan extension in *C. elegans* by a molecular chaperone dependent upon insulin-like signals," *Aging Cell*, vol. 2, no. 2, pp. 131–139, 2003, doi: 10.1046/j.1474-9728.2003.00045.x.
- [114] W.-C. Chiang, T.-T. Ching, H. C. Lee, C. Mousigian, and A.-L. Hsu, "HSF-1 Regulators DDL-1/2 Link Insulin-like Signaling to Heat-Shock Responses and Modulation of Longevity," *Cell*, vol. 148, no. 1–2, pp. 322–334, 2012, doi: 10.1016/j.cell.2011.12.019.
- [115] A.-L. Hsu, C. T. Murphy, and C. Kenyon, "Regulation of Aging and Age-Related Disease by DAF-16 and Heat-Shock Factor," *Science*, vol. 300, no. 5622, pp. 1142–1145, 2003, doi: 10.1126/science.1083701.
- [116] J.-O. Pyo et al., "Overexpression of Atg5 in mice activates autophagy and extends lifespan," *Nat Commun*, vol. 4, no. 1, p. 2300, 2013, doi: 10.1038/ncomms3300.

- [117] B. Friguet, A. BULTEAU, N. CHONDROGIANNI, M. CONCONI, and I. Petropoulos, "Protein Degradation by the Proteasome and Its Implications in Aging," *Ann Ny Acad Sci*, vol. 908, no. 1, pp. 143–154, 2000, doi: 10.1111/j.1749-6632.2000.tb06643.x.
- [118] A. J. L. Macario and E. C. de Macario, "Sick Chaperones, Cellular Stress, and Disease," *New Engl J Medicine*, vol. 353, no. 14, pp. 1489–1501, 2005, doi: 10.1056/nejmra050111.
- [119] D. C. Rubinsztein, G. Mariño, and G. Kroemer, "*Autophagy* and Aging," *Cell*, vol. 146, no. 5, pp. 682–695, 2011, doi: 10.1016/j.cell.2011.07.030.
- [120] V. Gorbunova, A. Seluanov, Z. Mao, and C. Hine, "Changes in DNA repair during aging," *Nucleic Acids Res*, vol. 35, no. 22, pp. 7466–7474, 2007, doi: 10.1093/nar/gkm756.
- [121] U. Herbig, M. Ferreira, L. Condel, D. Carey, and J. M. Sedivy, "Cellular Senescence in Aging Primates," *Science*, vol. 311, no. 5765, pp. 1257–1257, 2006, doi: 10.1126/science.1122446.
- [122] M. L. Idda et al., "Survey of senescent cell markers with age in human tissues," *Aging*, vol. 12, no. 5, pp. 4052–4066, 2020, doi: 10.18632/aging.102903.
- [123] J.-P. Coppé, P.-Y. Desprez, A. Krtolica, and J. Campisi, "The Senescence-Associated Secretory Phenotype: The Dark Side of Tumor Suppression," *Pathology Mech Dis*, vol. 5, no. 1, pp. 99–118, 2010, doi: 10.1146/annurev-pathol-121808-102144.
- [124] D. McHugh and J. Gil, "Senescence and aging: Causes, consequences, and therapeutic avenues," *J Cell Biol*, vol. 217, no. 1, pp. 65–77, 2018, doi: 10.1083/jcb.201708092.
- [125] M. Lemoine, "The Evolution of the Hallmarks of Aging," *Frontiers Genetics*, vol. 12, p. 693071, 2021, doi: 10.3389/fgene.2021.693071.
- [126] A. Dillin, D. E. Gottschling, and T. Nyström, "The good and the bad of being connected: the integrons of aging," *Curr Opin Cell Biol*, vol. 26, pp. 107–112, 2014, doi: 10.1016/j.ceb.2013.12.003.
- [127] A. Kowald and T. B. L. Kirkwood, "A network theory of ageing: the interactions of defective mitochondria, aberrant proteins, free radicals and scavengers in the ageing process," *Mutat Res Dnaging*, vol. 316, no. 5–6, pp. 209–236, 1996, doi: 10.1016/s0921-8734(96)90005-3.
- [128] T. B. L. Kirkwood and A. Kowald, "Network theory of aging," *Exp Gerontol*, vol. 32, no. 4–5, pp. 395–399, 1997, doi: 10.1016/s0531-5565(96)00171-4.
- [129] T. B. L. Kirkwood, "Systems biology of ageing and longevity," *Philosophical Transactions Royal Soc B Biological Sci*, vol. 366, no. 1561, pp. 64–70, 2011, doi: 10.1098/rstb.2010.0275.
- [130] R. Song, E. A. Sarnoski, and M. Acar, "The Systems Biology of Single-Cell Aging," *Iscience*, vol. 7, pp. 154–169, 2018, doi: 10.1016/j.isci.2018.08.023.
- [131] D. E. Martinez, "Mortality Patterns Suggest Lack of Senescence in Hydra," *Exp Gerontol*, vol. 33, no. 3, pp. 217–225, 1998, doi: 10.1016/s0531-5565(97)00113-7.
- [132] C. E. Finch, *Longevity, Senescence, and the Genome*. 1994.
- [133] J. W. Vaupel, A. Baudisch, M. Dölling, D. A. Roach, and J. Gampe, "The case for negative senescence," *Theor Popul Biol*, vol. 65, no. 4, pp. 339–351, 2004, doi: 10.1016/j.tpb.2003.12.003.
- [134] J. G. Ruby, M. Smith, and R. Buffenstein, "Naked Mole-Rat mortality rates defy gompertzian laws by not increasing with age," *Elife*, vol. 7, p. e31157, 2018, doi: 10.7554/elife.31157.
- [135] J. Kim, B.-K. Koo, and J. A. Knoblich, "Human organoids: model systems for human biology and medicine," *Nat Rev Mol Cell Bio*, vol. 21, no. 10, pp. 571–584, 2020, doi: 10.1038/s41580-020-0259-3.
- [136] L. Mesch et al., "Aged human iPSC-RPE organoid cultures display hallmarks of drusen formation," *bioRxiv*, 2021, doi: 10.1101/2021.10.12.463899.
- [137] J. L. Hu, M. E. Todhunter, M. A. LaBarge, and Z. J. Gartner, "Opportunities for

- organoids as new models of aging," *J Cell Biol*, vol. 217, no. 1, pp. 39–50, 2018, doi: 10.1083/jcb.201709054.
- [138] M. Tatar, A. Kopelman, D. Epstein, M.-P. Tu, C.-M. Yin, and R. S. Garofalo, "A Mutant *Drosophila* Insulin Receptor Homolog That Extends Life-Span and Impairs Neuroendocrine Function," *Science*, vol. 292, no. 5514, pp. 107–110, 2001, doi: 10.1126/science.1057987.
- [139] Y.-J. Lin, L. Seroude, and S. Benzer, "Extended Life-Span and Stress Resistance in the *Drosophila* Mutant *methuselah*," *Science*, vol. 282, no. 5390, pp. 943–946, 1998, doi: 10.1126/science.282.5390.943.
- [140] D. J. Clancy et al., "Extension of Life-Span by Loss of CHICO, a *Drosophila* Insulin Receptor Substrate Protein," *Science*, vol. 292, no. 5514, pp. 104–106, 2001, doi: 10.1126/science.1057991.
- [141] B. Rogina, S. L. Helfand, and S. Frankel, "Longevity Regulation by *Drosophila* Rpd3 Deacetylase and Caloric Restriction," *Science*, vol. 298, no. 5599, pp. 1745–1745, 2002, doi: 10.1126/science.1078986.
- [142] T. Maruzs, Z. Simon-Vecsei, V. Kiss, T. Csizmadia, and G. Juhász, "On the Fly: Recent Progress on Autophagy and Aging in *Drosophila*," *Frontiers Cell Dev Biology*, vol. 7, p. 140, 2019, doi: 10.3389/fcell.2019.00140.
- [143] M. D. W. Piper and L. Partridge, "*Drosophila* as a model for ageing," *Biochimica Et Biophysica Acta Bba - Mol Basis Dis*, vol. 1864, no. 9, pp. 2707–2717, 2018, doi: 10.1016/j.bbadis.2017.09.016.
- [144] A. Fire, S. Xu, M. K. Montgomery, S. A. Kostas, S. E. Driver, and C. C. Mello, "Potent and specific genetic interference by double-stranded RNA in *Caenorhabditis elegans*," *Nature*, vol. 391, no. 6669, pp. 806–811, 1998, doi: 10.1038/35888.
- [145] B. Hamilton et al., "A systematic RNAi screen for longevity genes in *C. elegans*," *Gene Dev*, vol. 19, no. 13, pp. 1544–1555, 2005, doi: 10.1101/gad.1308205.
- [146] L. R. Lapierre and M. Hansen, "Lessons from *C. elegans*: signaling pathways for longevity," *Trends Endocrinol Metabolism*, vol. 23, no. 12, pp. 637–644, 2012, doi: 10.1016/j.tem.2012.07.007.
- [147] K. Flurkey, J. Papaconstantinou, R. A. Miller, and D. E. Harrison, "Lifespan extension and delayed immune and collagen aging in mutant mice with defects in growth hormone production," *Proc National Acad Sci*, vol. 98, no. 12, pp. 6736–6741, 2001, doi: 10.1073/pnas.111158898.
- [148] R. K. Mortimer and J. R. Johnston, "Life Span of Individual Yeast Cells," *Nature*, vol. 183, no. 4677, pp. 1751–1752, 1959, doi: 10.1038/1831751a0.
- [149] A. A. Barton, "Some Aspects of Cell Division in *Saccharomyces cerevisiae*," *Microbiology+*, vol. 4, no. 1, pp. 84–86, 1950, doi: 10.1099/00221287-4-1-84.
- [150] S. C. Johnson, P. S. Rabinovitch, and M. Kaeberlein, "mTOR is a key modulator of ageing and age-related disease," *Nature*, vol. 493, no. 7432, pp. 338–345, 2013, doi: 10.1038/nature11861.
- [151] C. M. McCay, M. F. Crowell, and L. A. Maynard, "The Effect of Retarded Growth Upon the Length of Life Span and Upon the Ultimate Body Size," *J Nutrition*, vol. 10, no. 1, pp. 63–79, 1935, doi: 10.1093/jn/10.1.63.
- [152] M. J. P. Simons, W. Koch, and S. Verhulst, "Dietary restriction of rodents decreases aging rate without affecting initial mortality rate – a meta-analysis," *Aging Cell*, vol. 12, no. 3, pp. 410–414, 2013, doi: 10.1111/accel.12061.
- [153] F. Pifferi et al., "Caloric restriction increases lifespan but affects brain integrity in grey mouse lemur primates," *Commun Biology*, vol. 1, no. 1, p. 30, 2018, doi: 10.1038/s42003-018-0024-8.
- [154] R. Weindruch, R. L. Walford, S. Fligiel, and D. Guthrie, "The Retardation of Aging in Mice by Dietary Restriction: Longevity, Cancer, Immunity and Lifetime Energy Intake," *J Nutrition*, vol. 116, no. 4, pp. 641–654, 1986, doi: 10.1093/jn/116.4.641.
- [155] H. H. Pak et al., "Fasting drives the metabolic, molecular and geroprotective effects of

- a calorie-restricted diet in mice," *Nat Metabolism*, pp. 1–15, 2021, doi: 10.1038/s42255-021-00466-9.
- [156] E. L. Greer and A. Brunet, "Different dietary restriction regimens extend lifespan by both independent and overlapping genetic pathways in *C. elegans*," *Aging Cell*, vol. 8, no. 2, pp. 113–127, 2009, doi: 10.1111/j.1474-9726.2009.00459.x.
- [157] S.-J. Lin et al., "Calorie restriction extends *Saccharomyces cerevisiae* lifespan by increasing respiration," *Nature*, vol. 418, no. 6895, pp. 344–348, 2002, doi: 10.1038/nature00829.
- [158] J. C. Jiang, E. Jaruga, M. V. Repnevskaya, and S. M. Jazwinski, "An intervention resembling caloric restriction prolongs life span and retards aging in yeast," *Faseb J*, vol. 14, no. 14, pp. 2135–2137, 2000, doi: 10.1096/fj.00-0242fje.
- [159] E. C. Spivey, S. K. Jones, J. R. Rybarski, F. A. Saifuddin, and I. J. Finkelstein, "An aging-independent replicative lifespan in a symmetrically dividing eukaryote," *Elife*, vol. 6, p. e20340, 2017, doi: 10.7554/elife.20340.
- [160] J. A. Mattison et al., "Impact of caloric restriction on health and survival in rhesus monkeys from the NIA study," *Nature*, vol. 489, no. 7415, pp. 318–321, 2012, doi: 10.1038/nature11432.
- [161] R. J. Colman et al., "Caloric Restriction Delays Disease Onset and Mortality in Rhesus Monkeys," *Science*, vol. 325, no. 5937, pp. 201–204, 2009, doi: 10.1126/science.1173635.
- [162] J. A. Mattison et al., "Caloric restriction improves health and survival of rhesus monkeys," *Nat Commun*, vol. 8, no. 1, p. 14063, 2017, doi: 10.1038/ncomms14063.
- [163] R. S. Sohal and M. J. Forster, "Caloric restriction and the aging process: a critique," *Free Radical Bio Med*, vol. 73, pp. 366–382, 2014, doi: 10.1016/j.freeradbiomed.2014.05.015.
- [164] S. Caristia et al., "Is Caloric Restriction Associated with Better Healthy Aging Outcomes? A Systematic Review and Meta-Analysis of Randomized Controlled Trials," *Nutrients*, vol. 12, no. 8, p. 2290, 2020, doi: 10.3390/nu12082290.
- [165] M. Ulgherait et al., "Circadian autophagy drives iTRF-mediated longevity," *Nature*, vol. 598, no. 7880, pp. 353–358, 2021, doi: 10.1038/s41586-021-03934-0.
- [166] B. K. Kennedy, K. K. Steffen, and M. Kaeberlein, "Ruminations on dietary restriction and aging," *Cell Mol Life Sci*, vol. 64, no. 11, pp. 1323–1328, 2007, doi: 10.1007/s00018-007-6470-y.
- [167] E. D. Smith et al., "Quantitative evidence for conserved longevity pathways between divergent eukaryotic species," *Genome Res*, vol. 18, no. 4, pp. 564–570, 2008, doi: 10.1101/gr.074724.107.
- [168] E. J. Stewart, R. Madden, G. Paul, and F. Taddei, "Aging and Death in an Organism That Reproduces by Morphologically Symmetric Division," *Plos Biol*, vol. 3, no. 2, p. e45, 2005, doi: 10.1371/journal.pbio.0030045.
- [169] C. U. Rang, A. Y. Peng, and L. Chao, "Temporal Dynamics of Bacterial Aging and Rejuvenation," *Curr Biol*, vol. 21, no. 21, pp. 1813–1816, 2011, doi: 10.1016/j.cub.2011.09.018.
- [170] P. Wang et al., "Robust Growth of *Escherichia coli*," *Curr Biol*, vol. 20, no. 12, pp. 1099–1103, 2010, doi: 10.1016/j.cub.2010.04.045.
- [171] L. G. Burman, J. Raichler, and J. T. Park, "Evidence for diffuse growth of the cylindrical portion of the *Escherichia coli* murein sacculus," *J Bacteriol*, vol. 155, no. 3, pp. 983–988, 1983, doi: 10.1128/jb.155.3.983-988.1983.
- [172] M. A. de Pedro, J. C. Quintela, J. V. Høltje, and H. Schwarz, "Murein segregation in *Escherichia coli*," *J Bacteriol*, vol. 179, no. 9, pp. 2823–2834, 1997, doi: 10.1128/jb.179.9.2823-2834.1997.
- [173] D.-J. Scheffers and M. G. Pinho, "Bacterial Cell Wall Synthesis: New Insights from Localization Studies," *Microbiol Mol Biol R*, vol. 69, no. 4, pp. 585–607, 2005, doi: 10.1128/mmbr.69.4.585-607.2005.

- [174] A. B. Lindner, R. Madden, A. Demarez, E. J. Stewart, and F. Taddei, "Asymmetric segregation of protein aggregates is associated with cellular aging and rejuvenation," *Proc National Acad Sci*, vol. 105, no. 8, pp. 3076–3081, 2008, doi: 10.1073/pnas.0708931105.
- [175] J. Winkler et al., "Quantitative and spatio-temporal features of protein aggregation in *Escherichia coli* and consequences on protein quality control and cellular ageing," *Embo J*, vol. 29, no. 5, pp. 910–923, 2010, doi: 10.1038/emboj.2009.412.
- [176] M. G. Lee and P. Nurse, "Complementation used to clone a human homologue of the fission yeast cell cycle control gene *cdc2*," *Nature*, vol. 327, no. 6117, pp. 31–35, 1987, doi: 10.1038/327031a0.
- [177] P. Fantes and P. Nurse, "Control of cell size at division in fission yeast by a growth-modulated size control over nuclear division," *Exp Cell Res*, vol. 107, no. 2, pp. 377–386, 1977, doi: 10.1016/0014-4827(77)90359-7.
- [178] P. A. Fantes and P. Nurse, "Control of the timing of cell division in fission yeast Cell size mutants reveal a second control pathway," *Exp Cell Res*, vol. 115, no. 2, pp. 317–329, 1978, doi: 10.1016/0014-4827(78)90286-0.
- [179] J. M. Mitchison and P. Nurse, "Growth in cell length in the fission yeast *Schizosaccharomyces pombe*," *J Cell Sci*, vol. 75, pp. 357–76, 1985.
- [180] P. Nurse, P. Thuriaux, and K. Nasmyth, "Genetic control of the cell division cycle in the fission yeast *Schizosaccharomyces pombe*," *Mol Gen Genetics Mgg*, vol. 146, no. 2, pp. 167–178, 1976, doi: 10.1007/bf00268085.
- [181] D. Coudreuse and P. Nurse, "Driving the cell cycle with a minimal CDK control network," *Nature*, vol. 468, no. 7327, pp. 1074–1079, 2010, doi: 10.1038/nature09543.
- [182] D. García-Ruano et al., "Fluorescence exclusion: a rapid, accurate and powerful method for measuring yeast cell volume," *Biorxiv*, p. 2021.10.07.463508, 2021, doi: 10.1101/2021.10.07.463508.
- [183] D. O. Morgan, *The Cell Cycle: Principles of Control*. 2007.
- [184] M. Coelho et al., "Fission Yeast Does Not Age under Favorable Conditions, but Does So after Stress," *Curr Biol*, vol. 23, no. 19, pp. 1844–1852, 2013, doi: 10.1016/j.cub.2013.07.084.
- [185] M. G. Barker and R. M. Walmsley, "Replicative ageing in the fission yeast *Schizosaccharomyces pombe*," *Yeast*, vol. 15, no. 14, pp. 1511–1518, 1999, doi: 10.1002/(sici)1097-0061(199910)15:14<1511::aid-yea482>3.0.co;2-y.
- [186] H. Nakaoka and Y. Wakamoto, "Aging, mortality, and the fast growth trade-off of *Schizosaccharomyces pombe*," *Plos Biol*, vol. 15, no. 6, p. e2001109, 2017, doi: 10.1371/journal.pbio.2001109.
- [187] J. M. Mitchison, "The growth of single cells I. *Schizosaccharomyces pombe*," *Exp Cell Res*, vol. 13, no. 2, pp. 244–262, 1957, doi: 10.1016/0014-4827(57)90005-8.
- [188] B. F. Johnson, "Autoradiographic analysis of regional cell wall growth of yeasts *Schizosaccharomyces pombe*," *Exp Cell Res*, vol. 39, no. 2–3, pp. 613–624, 1965, doi: 10.1016/0014-4827(65)90064-9.
- [189] J. W. May, "Sites of cell-wall extension demonstrated by the use of fluorescent antibody," *Exp Cell Res*, vol. 27, no. 1, pp. 170–172, 1962, doi: 10.1016/0014-4827(62)90060-5.
- [190] S. Baumgärtner and I. M. Tolić-Nørrelykke, "Growth Pattern of Single Fission Yeast Cells Is Bilinear and Depends on Temperature and DNA Synthesis," *Biophys J*, vol. 96, no. 10, pp. 4336–4347, 2009, doi: 10.1016/j.bpj.2009.02.051.
- [191] M. Sohrmann, S. Schmidt, I. Hagan, and V. Simanis, "Asymmetric segregation on spindle poles of the *Schizosaccharomyces pombe* septum-inducing protein kinase Cdc7p," *Gene Dev*, vol. 12, no. 1, pp. 84–94, 1998, doi: 10.1101/gad.12.1.84.
- [192] M. Ackermann, S. C. Stearns, and U. Jenal, "Senescence in a Bacterium with Asymmetric Division," *Science*, vol. 300, no. 5627, pp. 1920–1920, 2003, doi: 10.1126/science.1083532.

- [193] M. D. Murtey and P. Ramasamy, "Modern Electron Microscopy in Physical and Life Sciences," 2016, doi: 10.5772/61720.
- [194] A. D. Lippuner, T. Julou, and Y. Barral, "Budding yeast as a model organism to study the effects of age," *Fems Microbiol Rev*, vol. 38, no. 2, pp. 300–325, 2014, doi: 10.1111/1574-6976.12060.
- [195] J. Saarikangas and Y. Barral, "Protein aggregates are associated with replicative aging without compromising protein quality control," *Elife*, vol. 4, p. e06197, 2015, doi: 10.7554/elife.06197.
- [196] H. Gershon and D. Gershon, "The budding yeast, *Saccharomyces cerevisiae*, as a model for aging research: a critical review," *Mech Ageing Dev*, vol. 120, no. 1–3, pp. 1–22, 2000, doi: 10.1016/s0047-6374(00)00182-2.
- [197] C. He, C. Zhou, and B. K. Kennedy, "The yeast replicative aging model," *Biochimica Et Biophysica Acta Bba - Mol Basis Dis*, vol. 1864, no. 9, pp. 2690–2696, 2018, doi: 10.1016/j.bbadis.2018.02.023.
- [198] G. E. Janssens and L. M. Veenhoff, "Evidence for the hallmarks of human aging in replicatively aging yeast," *Microb Cell*, vol. 3, no. 7, pp. 263–274, 2016, doi: 10.15698/mic2016.07.510.
- [199] W.-K. Huh et al., "Global analysis of protein localization in budding yeast," *Nature*, vol. 425, no. 6959, pp. 686–691, 2003, doi: 10.1038/nature02026.
- [200] J. Peter et al., "Genome evolution across 1,011 *Saccharomyces cerevisiae* isolates," *Nature*, vol. 556, no. 7701, pp. 339–344, 2018, doi: 10.1038/s41586-018-0030-5.
- [201] E. X. Kwan, E. Foss, L. Kruglyak, and A. Bedalov, "Natural Polymorphism in BUL2 Links Cellular Amino Acid Availability with Chronological Aging and Telomere Maintenance in Yeast," *Plos Genet*, vol. 7, no. 8, p. e1002250, 2011, doi: 10.1371/journal.pgen.1002250.
- [202] E. X. Kwan et al., "A Natural Polymorphism in rDNA Replication Origins Links Origin Activation with Calorie Restriction and Lifespan," *Plos Genet*, vol. 9, no. 3, p. e1003329, 2013, doi: 10.1371/journal.pgen.1003329.
- [203] A. Kaya, S. Ma, B. Wasko, M. Lee, M. Kaeberlein, and V. N. Gladyshev, "Defining molecular basis for longevity traits in natural yeast isolates," *Npj Aging Mech Dis*, vol. 1, no. 1, p. 15001, 2015, doi: 10.1038/npjamd.2015.1.
- [204] A. Kaya et al., "Evolution of natural lifespan variation and molecular strategies of extended lifespan," *Elife*, vol. 10, p. e64860, 2021, doi: 10.7554/elife.64860.
- [205] P. Laun, M. Rinnerthaler, E. Bogengruber, G. Heeren, and M. Breitenbach, "Yeast as a model for chronological and reproductive aging – A comparison," *Exp Gerontol*, vol. 41, no. 12, pp. 1208–1212, 2006, doi: 10.1016/j.exger.2006.11.001.
- [206] M. S. Singer and D. E. Gottschling, "TLC1: Template RNA Component of *Saccharomyces cerevisiae* Telomerase," *Science*, vol. 266, no. 5184, pp. 404–409, 1994, doi: 10.1126/science.7545955.
- [207] V. Lundblad and J. W. Szostak, "A mutant with a defect in telomere elongation leads to senescence in yeast," *Cell*, vol. 57, no. 4, pp. 633–643, 1989, doi: 10.1016/0092-8674(89)90132-3.
- [208] H. Martin, M. Doumic, M. T. Teixeira, and Z. Xu, "Telomere shortening causes distinct cell division regimes during replicative senescence in *Saccharomyces cerevisiae*," *Biorxiv*, p. 2021.06.16.448683, 2021, doi: 10.1101/2021.06.16.448683.
- [209] M. Kaeberlein and B. K. Kennedy, "Large-scale identification in yeast of conserved ageing genes," *Mech Ageing Dev*, vol. 126, no. 1, pp. 17–21, 2005, doi: 10.1016/j.mad.2004.09.013.
- [210] S. W. Stumpferl et al., "Natural genetic variation in yeast longevity," *Genome Res*, vol. 22, no. 10, pp. 1963–1973, 2012, doi: 10.1101/gr.136549.111.
- [211] N. K. Egilmez and S. M. Jazwinski, "Evidence for the involvement of a cytoplasmic factor in the aging of the yeast *Saccharomyces cerevisiae*," *J Bacteriol*, vol. 171, no. 1, pp. 37–42, 1989, doi: 10.1128/jb.171.1.37-42.1989.

- [212] B. K. Kennedy, N. R. Austriaco, and L. Guarente, "Daughter cells of *Saccharomyces cerevisiae* from old mothers display a reduced life span.," *J Cell Biology*, vol. 127, no. 6, pp. 1985–1993, 1994, doi: 10.1083/jcb.127.6.1985.
- [213] K. A. Henderson and D. E. Gottschling, "A mother's sacrifice: what is she keeping for herself?," *Curr Opin Cell Biol*, vol. 20, no. 6, pp. 723–728, 2008, doi: 10.1016/j.ceb.2008.09.004.
- [214] T. Nyström and B. Liu, "The mystery of aging and rejuvenation—a budding topic," *Curr Opin Microbiol*, vol. 18, pp. 61–67, 2014, doi: 10.1016/j.mib.2014.02.003.
- [215] D. Sinclair, K. Mills, and L. Guarente, "Aging in *Saccharomyces Cerevisiae*," *Annu Rev Microbiol*, vol. 52, no. 1, pp. 533–560, 1998, doi: 10.1146/annurev.micro.52.1.533.
- [216] B. M. Wasko and M. Kaeberlein, "Yeast replicative aging: a paradigm for defining conserved longevity interventions," *Fems Yeast Res*, vol. 14, no. 1, pp. 148–159, 2014, doi: 10.1111/1567-1364.12104.
- [217] C. D. Powell, D. E. Quain, and K. A. Smart, "Chitin scar breaks in aged *Saccharomyces cerevisiae*," *Microbiology+*, vol. 149, no. 11, pp. 3129–3137, 2003, doi: 10.1099/mic.0.25940-0.
- [218] J. W. Bartholomew and T. Mittwer, "Demonstration of yeast bud scars with the electron microscope.," *J Bacteriol*, vol. 65, no. 3, pp. 272–5, 1953.
- [219] J. R. Johnston, "Reproductive capacity and mode of death of yeast cells," *Antonie Van Leeuwenhoek*, vol. 32, no. 1, pp. 94–98, 1966, doi: 10.1007/bf02097448.
- [220] S. M. Jazwinski, S. Kim, C.-Y. Lai, and A. Benguria, "Epigenetic stratification: the role of individual change in the biological aging process," *Exp Gerontol*, vol. 33, no. 6, pp. 571–580, 1998, doi: 10.1016/s0531-5565(98)00029-1.
- [221] S. S. Lee, I. A. Vizcarra, D. H. E. W. Huberts, L. P. Lee, and M. Heinemann, "Whole lifespan microscopic observation of budding yeast aging through a microfluidic dissection platform," *Proc National Acad Sci*, vol. 109, no. 13, pp. 4916–4920, 2012, doi: 10.1073/pnas.1113505109.
- [222] Y. Zhang et al., "Single Cell Analysis of Yeast Replicative Aging Using a New Generation of Microfluidic Device," *Plos One*, vol. 7, no. 11, p. e48275, 2012, doi: 10.1371/journal.pone.0048275.
- [223] M. Jin et al., "Divergent Aging of Isogenic Yeast Cells Revealed through Single-Cell Phenotypic Dynamics," *Cell Syst*, vol. 8, no. 3, pp. 242–253.e3, 2019, doi: 10.1016/j.cels.2019.02.002.
- [224] N. K. Egilmez, J. B. Chen, and S. M. Jazwinski, "Preparation and Partial Characterization of Old Yeast Cells," *J Gerontology*, vol. 45, no. 1, pp. B9–B17, 1990, doi: 10.1093/geronj/45.1.b9.
- [225] J. Yang et al., "Cell size and growth rate are major determinants of replicative lifespan," *Cell Cycle*, vol. 10, no. 1, pp. 144–155, 2011, doi: 10.4161/cc.10.1.14455.
- [226] S. Morlot, J. Song, I. Léger-Silvestre, A. Matifas, O. Gadai, and G. Charvin, "Excessive rDNA Transcription Drives the Disruption in Nuclear Homeostasis during Entry into Senescence in Budding Yeast," *Cell Reports*, vol. 28, no. 2, pp. 408–422.e4, 2019, doi: 10.1016/j.celrep.2019.06.032.
- [227] R. Zdrag, G. Bartosz, and T. Bilinski, "Replicative aging of the yeast does not require DNA replication," *Biochem Bioph Res Co*, vol. 333, no. 1, pp. 138–141, 2005, doi: 10.1016/j.bbrc.2005.05.081.
- [228] R. Zdrag, M. Kwolek-Mirek, G. Bartosz, and T. Bilinski, "Relationship between the replicative age and cell volume in *Saccharomyces cerevisiae*," *Acta Biochim Pol*, vol. 53, no. 4, pp. 747–51, 2006.
- [229] G. E. Neurohr et al., "Excessive Cell Growth Causes Cytoplasm Dilution And Contributes to Senescence," *Cell*, vol. 176, no. 5, pp. 1083–1097.e18, 2019, doi: 10.1016/j.cell.2019.01.018.
- [230] J. Wright, H. Dungrawala, R. K. Bright, and B. L. Schneider, "A growing role for

- hypertrophy in senescence," *Fems Yeast Res*, vol. 13, no. 1, pp. 2–6, 2013, doi: 10.1111/1567-1364.12015.
- [231] M. C. Jo, W. Liu, L. Gu, W. Dang, and L. Qin, "High-throughput analysis of yeast replicative aging using a microfluidic system," *Proc National Acad Sci*, vol. 112, no. 30, pp. 9364–9369, 2015, doi: 10.1073/pnas.1510328112.
- [232] T. Biliński, R. Zdrażga-Tęcza, and G. Bartosz, "Hypertrophy hypothesis as an alternative explanation of the phenomenon of replicative aging of yeast," *Fems Yeast Res*, vol. 12, no. 1, pp. 97–101, 2012, doi: 10.1111/j.1567-1364.2011.00759.x.
- [233] A. R. D. Ganley, M. Breitenbach, B. K. Kennedy, and T. Kobayashi, "Yeast hypertrophy: cause or consequence of aging? Reply to Bilinski et al," *Fems Yeast Res*, vol. 12, no. 3, pp. 267–268, 2012, doi: 10.1111/j.1567-1364.2012.00796.x.
- [234] G. E. Janssens and L. M. Veenhoff, "The Natural Variation in Lifespans of Single Yeast Cells Is Related to Variation in Cell Size, Ribosomal Protein, and Division Time," *Plos One*, vol. 11, no. 12, p. e0167394, 2016, doi: 10.1371/journal.pone.0167394.
- [235] J. T. Smith, J. W. White, H. Dungrawala, H. Hua, and B. L. Schneider, "Yeast lifespan variation correlates with cell growth and SIR2 expression," *Plos One*, vol. 13, no. 7, p. e0200275, 2018, doi: 10.1371/journal.pone.0200275.
- [236] M. A. McCormick et al., "A Comprehensive Analysis of Replicative Lifespan in 4,698 Single-Gene Deletion Strains Uncovers Conserved Mechanisms of Aging," *Cell Metab*, vol. 22, no. 5, pp. 895–906, 2015, doi: 10.1016/j.cmet.2015.09.008.
- [237] J. R. Delaney et al., "Sir2 deletion prevents lifespan extension in 32 long-lived mutants," *Aging Cell*, vol. 10, no. 6, pp. 1089–1091, 2011, doi: 10.1111/j.1474-9726.2011.00742.x.
- [238] S. N. Mouton et al., "A physicochemical perspective of aging from single-cell analysis of pH, macromolecular and organellar crowding in yeast," *Elife*, vol. 9, p. e54707, 2020, doi: 10.7554/elife.54707.
- [239] M. Kaeberlein, "Hypertrophy and senescence factors in yeast aging. A reply to Bilinski et al," *Fems Yeast Res*, vol. 12, no. 3, pp. 269–270, 2012, doi: 10.1111/j.1567-1364.2012.00798.x.
- [240] J. E. Pérez-Ortín, A. Mena, M. Barba-Aliaga, A. Singh, S. Chávez, and J. García-Martínez, "Cell volume homeostatically controls the rDNA repeat copy number and rRNA synthesis rate in yeast," *Plos Genet*, vol. 17, no. 4, p. e1009520, 2021, doi: 10.1371/journal.pgen.1009520.
- [241] X.-M. Sun et al., "Size-Dependent Increase in RNA Polymerase II Initiation Rates Mediates Gene Expression Scaling with Cell Size," *Curr Biol*, vol. 30, no. 7, pp. 1217–1230.e7, 2020, doi: 10.1016/j.cub.2020.01.053.
- [242] M. C. Lanz et al., "Increasing cell size remodels the proteome and promotes senescence," *Biorxiv*, p. 2021.07.29.454227, 2021, doi: 10.1101/2021.07.29.454227.
- [243] S. Anzi et al., "Postnatal Exocrine Pancreas Growth by Cellular Hypertrophy Correlates with a Shorter Lifespan in Mammals," *Dev Cell*, vol. 45, no. 6, pp. 726–737.e3, 2018, doi: 10.1016/j.devcel.2018.05.024.
- [244] L. Cheng, J. Chen, Y. Kong, C. Tan, R. Kafri, and M. Björklund, "Size-scaling promotes senescence-like changes in proteome and organelle content," *Biorxiv*, p. 2021.08.05.455193, 2021, doi: 10.1101/2021.08.05.455193.
- [244b] J. Lengefeld et al., "Cell size is a determinant of stem cell potential during aging," *Sci Adv*, vol. 7, no. 46, p. eabk0271, 2021, doi: 10.1126/sciadv.abk0271.
- [245] Z. Xie et al., "Molecular phenotyping of aging in single yeast cells using a novel microfluidic device," *Aging Cell*, vol. 11, no. 4, pp. 599–606, 2012, doi: 10.1111/j.1474-9726.2012.00821.x.
- [246] S. Fehrmann, C. Paoletti, Y. Goulev, A. Ungureanu, H. Aguilaniu, and G. Charvin, "Aging Yeast Cells Undergo a Sharp Entry into Senescence Unrelated to the Loss of Mitochondrial Membrane Potential," *Cell Reports*, vol. 5, no. 6, pp. 1589–1599, 2013, doi:

- 10.1016/j.celrep.2013.11.013.
- [247] E. A. Sarnoski, R. Song, E. Ertekin, N. Koonce, and M. Acar, "Fundamental characteristics of single-cell aging in diploid yeast," *Iscience*, vol. 7, pp. 96–109, 2018, doi: 10.1016/j.isci.2018.08.011.
- [248] G. E. Neurohr, R. L. Terry, A. Sandikci, K. Zou, H. Li, and A. Amon, "Deregulation of the G1/S-phase transition is the proximal cause of mortality in old yeast mother cells," *Gene Dev*, vol. 32, no. 15–16, pp. 1075–1084, 2018, doi: 10.1101/gad.312140.118.
- [249] M. M. Crane et al., "Rb analog Whi5 regulates G1 to S transition and cell size but not replicative lifespan in budding yeast," *Transl Medicine Aging*, vol. 3, pp. 104–108, 2019, doi: 10.1016/j.tma.2019.10.002.
- [250] G. Schlissel, M. K. Krzyzanowski, F. Caudron, Y. Barral, and J. Rine, "Aggregation of the Whi3 protein, not loss of heterochromatin, causes sterility in old yeast cells," *Science*, vol. 355, no. 6330, pp. 1184–1187, 2017, doi: 10.1126/science.aaj2103.
- [251] T. Smeal, J. Claus, B. Kennedy, F. Cole, and L. Guarente, "Loss of Transcriptional Silencing Causes Sterility in Old Mother Cells of *S. cerevisiae*," *Cell*, vol. 84, no. 4, pp. 633–642, 1996, doi: 10.1016/s0092-8674(00)81038-7.
- [252] I. Müller, "Parental age and the life-span of zygotes of *Saccharomyces cerevisiae*," *Antonie Van Leeuwenhoek*, vol. 51, no. 1, pp. 1–10, 1985, doi: 10.1007/bf00444223.
- [253] M. Boselli, J. Rock, E. Ünal, S. S. Levine, and A. Amon, "Effects of Age on Meiosis in Budding Yeast," *Dev Cell*, vol. 16, no. 6, pp. 844–855, 2009, doi: 10.1016/j.devcel.2009.05.013.
- [254] T. Z. Young, P. Liu, G. Urbonaite, and M. Acar, "Quantitative Insights into Age-Associated DNA-Repair Inefficiency in Single Cells," *Cell Reports*, vol. 28, no. 8, pp. 2220–2230.e7, 2019, doi: 10.1016/j.celrep.2019.07.082.
- [255] M. A. McMurray and D. E. Gottschling, "An Age-Induced Switch to a Hyper-Recombinational State," *Science*, vol. 301, no. 5641, pp. 1908–1911, 2003, doi: 10.1126/science.1087706.
- [256] L. L. Carr and D. E. Gottschling, "Does age influence loss of heterozygosity?," *Exp Gerontol*, vol. 43, no. 3, pp. 123–129, 2008, doi: 10.1016/j.exger.2007.10.010.
- [257] D. L. Lindstrom, C. K. Leverich, K. A. Henderson, and D. E. Gottschling, "Replicative Age Induces Mitotic Recombination in the Ribosomal RNA Gene Cluster of *Saccharomyces cerevisiae*," *Plos Genet*, vol. 7, no. 3, p. e1002015, 2011, doi: 10.1371/journal.pgen.1002015.
- [258] M. M. Crane et al., "DNA damage checkpoint activation impairs chromatin homeostasis and promotes mitotic catastrophe during aging," *Elife*, vol. 8, p. e50778, 2019, doi: 10.7554/elife.50778.
- [259] N. P. D'Mello and S. M. Jazwinski, "Telomere length constancy during aging of *Saccharomyces cerevisiae*," *J Bacteriol*, vol. 173, no. 21, pp. 6709–6713, 1991, doi: 10.1128/jb.173.21.6709-6713.1991.
- [260] N. R. Austriaco and L. P. Guarente, "Changes of telomere length cause reciprocal changes in the lifespan of mother cells in *Saccharomyces cerevisiae*," *Proc National Acad Sci*, vol. 94, no. 18, pp. 9768–9772, 1997, doi: 10.1073/pnas.94.18.9768.
- [261] S. Kim, B. Villeponteau, and S. M. Jazwinski, "Effect of Replicative Age on Transcriptional Silencing Near Telomeres in *Saccharomyces cerevisiae*," *Biochem Bioph Res Co*, vol. 219, no. 2, pp. 370–376, 1996, doi: 10.1006/bbrc.1996.0240.
- [262] J. R. Veatch, M. A. McMurray, Z. W. Nelson, and D. E. Gottschling, "Mitochondrial Dysfunction Leads to Nuclear Genome Instability via an Iron-Sulfur Cluster Defect," *Cell*, vol. 137, no. 7, pp. 1247–1258, 2009, doi: 10.1016/j.cell.2009.04.014.
- [263] C. Q. Scheckhuber, N. Erjavec, A. Tinazli, A. Hamann, T. Nyström, and H. D. Osiewacz, "Reducing mitochondrial fission results in increased life span and fitness of two fungal ageing models," *Nat Cell Biol*, vol. 9, no. 1, pp. 99–105, 2007, doi: 10.1038/ncb1524.

- [264] A. L. Hughes and D. E. Gottschling, "An early age increase in vacuolar pH limits mitochondrial function and lifespan in yeast," *Nature*, vol. 492, no. 7428, pp. 261–265, 2012, doi: 10.1038/nature11654.
- [265] R. S. Balaban, S. Nemoto, and T. Finkel, "Mitochondria, Oxidants, and Aging," *Cell*, vol. 120, no. 4, pp. 483–495, 2005, doi: 10.1016/j.cell.2005.02.001.
- [266] A. Bratic and N.-G. Larsson, "The role of mitochondria in aging," *J Clin Invest*, vol. 123, no. 3, pp. 951–957, 2013, doi: 10.1172/jci64125.
- [267] N. Sun, R. J. Youle, and T. Finkel, "The Mitochondrial Basis of Aging," *Mol Cell*, vol. 61, no. 5, pp. 654–666, 2016, doi: 10.1016/j.molcel.2016.01.028.
- [268] J. Nunnari and A. Suomalainen, "Mitochondria: In Sickness and in Health," *Cell*, vol. 148, no. 6, pp. 1145–1159, 2012, doi: 10.1016/j.cell.2012.02.035.
- [269] D. C. Wallace, "A Mitochondrial Paradigm of Metabolic and Degenerative Diseases, Aging, and Cancer: a Dawn for Evolutionary Medicine," *Genetics*, vol. 39, no. 1, pp. 359–407, 2005, doi: 10.1146/annurev.genet.39.110304.095751.
- [270] L. N. Dimitrov, R. B. Brem, L. Kruglyak, and D. E. Gottschling, "Polymorphisms in Multiple Genes Contribute to the Spontaneous Mitochondrial Genome Instability of *Saccharomyces cerevisiae* S288C Strains," *Genetics*, vol. 183, no. 1, pp. 365–383, 2009, doi: 10.1534/genetics.109.104497.
- [271] M. D. Chiara et al., "Domestication reprogrammed the budding yeast life cycle," *Biorxiv*, p. 2020.02.08.939314, 2020, doi: 10.1101/2020.02.08.939314.
- [272] C.-Y. Lai, E. Jaruga, C. Borghouts, and S. M. Jazwinski, "A Mutation in the ATP2 Gene Abrogates the Age Asymmetry Between Mother and Daughter Cells of the Yeast *Saccharomyces cerevisiae*," *Genetics*, vol. 162, no. 1, pp. 73–87, 2002, doi: 10.1093/genetics/162.1.73.
- [273] S. M. Jazwinski, "Yeast replicative life span – the mitochondrial connection," *Fems Yeast Res*, vol. 5, no. 2, pp. 119–125, 2004, doi: 10.1016/j.femsyr.2004.04.005.
- [274] H. Klinger et al., "Quantitation of (a)symmetric inheritance of functional and of oxidatively damaged mitochondrial aconitase in the cell division of old yeast mother cells," *Exp Gerontol*, vol. 45, no. 7–8, pp. 533–542, 2010, doi: 10.1016/j.exger.2010.03.016.
- [275] J. R. McFaline-Figueroa et al., "Mitochondrial quality control during inheritance is associated with lifespan and mother–daughter age asymmetry in budding yeast," *Aging Cell*, vol. 10, no. 5, pp. 885–895, 2011, doi: 10.1111/j.1474-9726.2011.00731.x.
- [276] R. Higuchi et al., "Actin Dynamics Affect Mitochondrial Quality Control and Aging in Budding Yeast," *Curr Biol*, vol. 23, no. 23, pp. 2417–2422, 2013, doi: 10.1016/j.cub.2013.10.022.
- [277] P. W. Piper, G. W. Jones, D. Bringloe, N. Harris, M. MacLean, and M. Mollapour, "The shortened replicative life span of prohibitin mutants of yeast appears to be due to defective mitochondrial segregation in old mother cells," *Aging Cell*, vol. 1, no. 2, pp. 149–157, 2002, doi: 10.1046/j.1474-9728.2002.00018.x.
- [278] D. Laporte, L. Gouleme, L. Jimenez, I. Khemiri, and I. Sagot, "Mitochondria reorganization upon proliferation arrest predicts individual yeast cell fate," *Elife*, vol. 7, p. e35685, 2018, doi: 10.7554/elife.35685.
- [279] S. Leupold et al., "*Saccharomyces cerevisiae* goes through distinct metabolic phases during its replicative lifespan," *Elife*, vol. 8, p. e41046, 2019, doi: 10.7554/elife.41046.
- [280] K. L. Chen et al., "Loss of vacuolar acidity results in iron-sulfur cluster defects and divergent homeostatic responses during aging in *Saccharomyces cerevisiae*," *Geroscience*, vol. 42, no. 2, pp. 749–764, 2020, doi: 10.1007/s11357-020-00159-3.
- [281] C. E. Hughes, T. K. Coody, M.-Y. Jeong, J. A. Berg, D. R. Winge, and A. L. Hughes, "Cysteine Toxicity Drives Age-Related Mitochondrial Decline by Altering Iron Homeostasis," *Cell*, vol. 180, no. 2, pp. 296–310.e18, 2020, doi: 10.1016/j.cell.2019.12.035.
- [282] H. Atamna, D. W. Killilea, A. N. Killilea, and B. N. Ames, "Heme deficiency may be a factor in the mitochondrial and neuronal decay of aging," *Proc National Acad Sci*, vol. 99,

- no. 23, pp. 14807–14812, 2002, doi: 10.1073/pnas.192585799.
- [283] Y. Li et al., “A programmable fate decision landscape underlies single-cell aging in yeast,” *Sci New York N Y*, vol. 369, no. 6501, pp. 325–329, 2020, doi: 10.1126/science.aax9552.
- [284] A. Y. Seo, A.-M. Joseph, D. Dutta, J. C. Y. Hwang, J. P. Aris, and C. Leeuwenburgh, “New insights into the role of mitochondria in aging: mitochondrial dynamics and more,” *J Cell Sci*, vol. 123, no. 15, pp. 2533–2542, 2010, doi: 10.1242/jcs.070490.
- [285] P. Laun et al., “Aged mother cells of *Saccharomyces cerevisiae* show markers of oxidative stress and apoptosis,” *Mol Microbiol*, vol. 39, no. 5, pp. 1166–1173, 2001, doi: 10.1111/j.1365-2958.2001.02317.x.
- [286] Y. Ohya, N. Umemoto, I. Tanida, A. Ohta, H. Iida, and Y. Anraku, “Calcium-sensitive cts mutants of *Saccharomyces cerevisiae* showing a Pet- phenotype are ascribable to defects of vacuolar membrane H(+)-ATPase activity,” *J Biol Chem*, vol. 266, no. 21, pp. 13971–13977, 1991, doi: 10.1016/s0021-9258(18)92798-5.
- [287] A. L. Hughes, C. E. Hughes, K. A. Henderson, N. Yazvenko, and D. E. Gottschling, “Selective sorting and destruction of mitochondrial membrane proteins in aged yeast,” *Elife*, vol. 5, p. e13943, 2016, doi: 10.7554/elife.13943.
- [288] M. Thumm, “Structure and function of the yeast vacuole and its role in autophagy,” *Microsc Res Techniq*, vol. 51, no. 6, pp. 563–572, 2000, doi: 10.1002/1097-0029(20001215)51:6<563::aid-jemt6>3.0.co;2-8.
- [289] S. C. Li and P. M. Kane, “The yeast lysosome-like vacuole: Endpoint and crossroads,” *Biochimica Et Biophysica Acta Bba - Mol Cell Res*, vol. 1793, no. 4, pp. 650–663, 2009, doi: 10.1016/j.bbamcr.2008.08.003.
- [290] F. Tang et al., “A lifespan-extending form of autophagy employs the vacuole-vacuole fusion machinery,” *Autophagy*, vol. 4, no. 7, pp. 874–886, 2008, doi: 10.4161/auto.6556.
- [291] S. Gebre et al., “Osh6 overexpression extends the lifespan of yeast by increasing vacuole fusion,” *Cell Cycle*, vol. 11, no. 11, pp. 2176–2188, 2014, doi: 10.4161/cc.20691.
- [292] J. Choi, S. Wang, Y. Li, N. Hao, and B. M. Zid, “Age-induced P-bodies become detrimental and shorten the lifespan of yeast,” *bioRxiv*, 2021, doi: 10.1101/2021.11.05.467477.
- [293] K. A. Henderson, A. L. Hughes, and D. E. Gottschling, “Mother-daughter asymmetry of pH underlies aging and rejuvenation in yeast,” *Elife*, vol. 3, p. e03504, 2014, doi: 10.7554/elife.03504.
- [294] G. E. Janssens et al., “Protein biogenesis machinery is a driver of replicative aging in yeast,” *Elife*, vol. 4, p. e08527, 2015, doi: 10.7554/elife.08527.
- [295] R. A. Knieß and M. P. Mayer, “The oxidation state of the cytoplasmic glutathione redox system does not correlate with replicative lifespan in yeast,” *Npj Aging Mech Dis*, vol. 2, no. 1, p. 16028, 2016, doi: 10.1038/npjamd.2016.28.
- [296] M. C. Munder et al., “A pH-driven transition of the cytoplasm from a fluid- to a solid-like state promotes entry into dormancy,” *Elife*, vol. 5, p. e09347, 2016, doi: 10.7554/elife.09347.
- [297] B. Jacquél, T. Aspert, D. Laporte, I. Sagot, and G. Charvin, “Monitoring single-cell dynamics of entry into quiescence during an unperturbed lifecycle,” *Biorxiv*, p. 2020.11.25.395608, 2021, doi: 10.1101/2020.11.25.395608.
- [298] R. Orij, S. Brul, and G. J. Smits, “Intracellular pH is a tightly controlled signal in yeast,” *Biochimica Et Biophysica Acta Bba - Gen Subj*, vol. 1810, no. 10, pp. 933–944, 2011, doi: 10.1016/j.bbagen.2011.03.011.
- [299] M. H. Barros, B. Bandy, E. B. Tahara, and A. J. Kowaltowski, “Higher Respiratory Activity Decreases Mitochondrial Reactive Oxygen Release and Increases Life Span in *Saccharomyces cerevisiae* *,” *J Biol Chem*, vol. 279, no. 48, pp. 49883–49888, 2004, doi: 10.1074/jbc.m408918200.
- [300] P. K. Sharma, V. Agrawal, and N. Roy, “Mitochondria-mediated hormetic response in

- life span extension of calorie-restricted *Saccharomyces cerevisiae*," *Age*, vol. 33, no. 2, pp. 143–154, 2011, doi: 10.1007/s11357-010-9169-1.
- [301] M. Ristow and S. Schmeisser, "Extending life span by increasing oxidative stress," *Free Radical Bio Med*, vol. 51, no. 2, pp. 327–336, 2011, doi: 10.1016/j.freeradbiomed.2011.05.010.
- [302] A. J. Kowaltowski, N. C. de Souza-Pinto, R. F. Castilho, and A. E. Vercesi, "Mitochondria and reactive oxygen species," *Free Radical Bio Med*, vol. 47, no. 4, pp. 333–343, 2009, doi: 10.1016/j.freeradbiomed.2009.05.004.
- [303] A. Koc, A. P. Gasch, J. C. Rutherford, H.-Y. Kim, and V. N. Gladyshev, "Methionine sulfoxide reductase regulation of yeast lifespan reveals reactive oxygen species-dependent and -independent components of aging," *P Natl Acad Sci Usa*, vol. 101, no. 21, pp. 7999–8004, 2004, doi: 10.1073/pnas.0307929101.
- [304] Y. J. Suzuki, M. Carini, and D. A. Butterfield, "Protein Carbonylation," *Antioxid Redox Sign*, vol. 12, no. 3, pp. 323–325, 2010, doi: 10.1089/ars.2009.2887.
- [305] E. R. Stadtman, "Protein oxidation and aging," *Free Radical Res*, vol. 40, no. 12, pp. 1250–1258, 2009, doi: 10.1080/10715760600918142.
- [306] D. A. Parsell, A. S. Kowal, M. A. Singer, and S. Lindquist, "Protein disaggregation mediated by heat-shock protein Hsp104," *Nature*, vol. 372, no. 6505, pp. 475–478, 1994, doi: 10.1038/372475a0.
- [307] E. Ünal, B. Kinde, and A. Amon, "Gametogenesis Eliminates Age-Induced Cellular Damage and Resets Life Span in Yeast," *Science*, vol. 332, no. 6037, pp. 1554–1557, 2011, doi: 10.1126/science.1204349.
- [308] H. Aguilaniu, L. Gustafsson, M. Rigoulet, and T. Nyström, "Asymmetric Inheritance of Oxidatively Damaged Proteins During Cytokinesis," *Science*, vol. 299, no. 5613, pp. 1751–1753, 2003, doi: 10.1126/science.1080418.
- [309] N. Erjavec, L. Larsson, J. Grantham, and T. Nyström, "Accelerated aging and failure to segregate damaged proteins in Sir2 mutants can be suppressed by overproducing the protein aggregation-remodeling factor Hsp104p," *Gene Dev*, vol. 21, no. 19, pp. 2410–2421, 2007, doi: 10.1101/gad.439307.
- [310] C. Zhou, B. D. Slaughter, J. R. Unruh, A. Eldakak, B. Rubinstein, and R. Li, "Motility and Segregation of Hsp104-Associated Protein Aggregates in Budding Yeast," *Cell*, vol. 147, no. 5, pp. 1186–1196, 2011, doi: 10.1016/j.cell.2011.11.002.
- [311] B. Liu et al., "The Polarisome Is Required for Segregation and Retrograde Transport of Protein Aggregates," *Cell*, vol. 140, no. 2, pp. 257–267, 2010, doi: 10.1016/j.cell.2009.12.031.
- [312] T. Nyström, J. Yang, and M. Molin, "Peroxiredoxins, gerontogenes linking aging to genome instability and cancer," *Gene Dev*, vol. 26, no. 18, pp. 2001–2008, 2012, doi: 10.1101/gad.200006.112.
- [313] D. A. Knorre et al., "Sir2-dependent daughter-to-mother transport of the damaged proteins in yeast is required to prevent high stress sensitivity of the daughters," *Cell Cycle*, vol. 9, no. 22, pp. 4501–4505, 2010, doi: 10.4161/cc.9.22.13683.
- [314] P. Tessarz, M. Schwarz, A. Mogk, and B. Bukau, "The Yeast AAA+ Chaperone Hsp104 Is Part of a Network That Links the Actin Cytoskeleton with the Inheritance of Damaged Proteins," *Mol Cell Biol*, vol. 29, no. 13, pp. 3738–3745, 2009, doi: 10.1128/mcb.00201-09.
- [315] C. Paoletti, S. Quintin, A. Matifas, and G. Charvin, "Kinetics of Formation and Asymmetrical Distribution of Hsp104-Bound Protein Aggregates in Yeast," *Biophys J*, vol. 110, no. 7, pp. 1605–1614, 2016, doi: 10.1016/j.bpj.2016.02.034.
- [316] D. F. Moreno, K. Jenkins, S. Morlot, G. Charvin, A. Csikasz-Nagy, and M. Aldea, "Proteostasis collapse, a hallmark of aging, hinders the chaperone-Start network and arrests cells in G1," *Elife*, vol. 8, p. e48240, 2019, doi: 10.7554/elife.48240.
- [317] U. Kruegel et al., "Elevated Proteasome Capacity Extends Replicative Lifespan in

- Saccharomyces cerevisiae*," *Plos Genet*, vol. 7, no. 9, p. e1002253, 2011, doi: 10.1371/journal.pgen.1002253.
- [318] D. G. Hendrickson et al., "A new experimental platform facilitates assessment of the transcriptional and chromatin landscapes of aging yeast," *Elife*, vol. 7, p. e39911, 2018, doi: 10.7554/elife.39911.
- [319] K. K. Steffen et al., "Yeast Life Span Extension by Depletion of 60S Ribosomal Subunits Is Mediated by Gcn4," *Cell*, vol. 133, no. 2, pp. 292–302, 2008, doi: 10.1016/j.cell.2008.02.037.
- [320] F. Capuano, M. Mülleder, R. Kok, H. J. Blom, and M. Ralser, "Cytosine DNA Methylation Is Found in *Drosophila melanogaster* but Absent in *Saccharomyces cerevisiae*, *Schizosaccharomyces pombe*, and Other Yeast Species," *Anal Chem*, vol. 86, no. 8, pp. 3697–3702, 2014, doi: 10.1021/ac500447w.
- [321] W. Dang et al., "Histone H4 lysine 16 acetylation regulates cellular lifespan," *Nature*, vol. 459, no. 7248, pp. 802–807, 2009, doi: 10.1038/nature08085.
- [322] M. Kaerberlein, M. McVey, and L. Guarente, "The SIR2/3/4 complex and SIR2 alone promote longevity in *Saccharomyces cerevisiae* by two different mechanisms," *Gene Dev*, vol. 13, no. 19, pp. 2570–2580, 1999, doi: 10.1101/gad.13.19.2570.
- [323] M. A. McCormick et al., "The SAGA Histone Deubiquitinase Module Controls Yeast Replicative Lifespan via Sir2 Interaction," *Cell Reports*, vol. 8, no. 2, pp. 477–486, 2014, doi: 10.1016/j.celrep.2014.06.037.
- [324] S. Giavara et al., "Yeast Nhp6A/B and Mammalian Hmgb1 Facilitate the Maintenance of Genome Stability," *Curr Biol*, vol. 15, no. 1, pp. 68–72, 2005, doi: 10.1016/j.cub.2004.12.065.
- [325] R. Yu, L. Sun, Y. Sun, X. Han, L. Qin, and W. Dang, "Cellular response to moderate chromatin architectural defects promotes longevity," *Sci Adv*, vol. 5, no. 7, p. eaav1165, 2019, doi: 10.1126/sciadv.aav1165.
- [326] Z. Hu et al., "Nucleosome loss leads to global transcriptional up-regulation and genomic instability during yeast aging," *Gene Dev*, vol. 28, no. 4, pp. 396–408, 2014, doi: 10.1101/gad.233221.113.
- [327] W. Dang et al., "Inactivation of Yeast Isw2 Chromatin Remodeling Enzyme Mimics Longevity Effect of Calorie Restriction via Induction of Genotoxic Stress Response," *Cell Metab*, vol. 19, no. 6, pp. 952–966, 2014, doi: 10.1016/j.cmet.2014.04.004.
- [328] Y. Li et al., "Multigenerational silencing dynamics control cell aging," *Proc National Acad Sci*, vol. 114, no. 42, pp. 11253–11258, 2017, doi: 10.1073/pnas.1703379114.
- [329] K. Saka, S. Ide, A. R. D. Ganley, and T. Kobayashi, "Cellular Senescence in Yeast Is Regulated by rDNA Noncoding Transcription," *Curr Biol*, vol. 23, no. 18, pp. 1794–1798, 2013, doi: 10.1016/j.cub.2013.07.048.
- [330] S. Pal, S. D. Postnikoff, M. Chavez, and J. K. Tyler, "Impaired cohesion and homologous recombination during replicative aging in budding yeast," *Sci Adv*, vol. 4, no. 2, p. eaq0236, 2018, doi: 10.1126/sciadv.aq0236.
- [331] S. S. Lin, J. K. Manchester, and J. I. Gordon, "Enhanced Gluconeogenesis and Increased Energy Storage as Hallmarks of Aging in *Saccharomyces cerevisiae* * 210," *J Biol Chem*, vol. 276, no. 38, pp. 36000–36007, 2001, doi: 10.1074/jbc.m103509200.
- [332] G. Yiu et al., "Pathways Change in Expression During Replicative Aging in *Saccharomyces cerevisiae*," *Journals Gerontology Ser*, vol. 63, no. 1, pp. 21–34, 2008, doi: 10.1093/gerona/63.1.21.
- [333] Y. Kamei, Y. Tamada, Y. Nakayama, E. Fukusaki, and Y. Mukai, "Changes in Transcription and Metabolism During the Early Stage of Replicative Cellular Senescence in Budding Yeast*," *J Biol Chem*, vol. 289, no. 46, pp. 32081–32093, 2014, doi: 10.1074/jbc.m114.600528.
- [334] S.-J. Lin, P.-A. Defossez, and L. Guarente, "Requirement of NAD and SIR2 for Life-Span Extension by Calorie Restriction in *Saccharomyces cerevisiae*," *Science*, vol. 289, no.

- 5487, pp. 2126–2128, 2000, doi: 10.1126/science.289.5487.2126.
- [335] D. H. E. W. Huberts et al., “Calorie restriction does not elicit a robust extension of replicative lifespan in *Saccharomyces cerevisiae*,” *Proc National Acad Sci*, vol. 111, no. 32, pp. 11727–11731, 2014, doi: 10.1073/pnas.1410024111.
- [336] C. V. Jack, C. Cruz, R. M. Hull, M. A. Keller, M. Ralser, and J. Houseley, “Regulation of ribosomal DNA amplification by the TOR pathway,” *Proc National Acad Sci*, vol. 112, no. 31, pp. 9674–9679, 2015, doi: 10.1073/pnas.1505015112.
- [337] F. R. Neumann and P. Nurse, “Nuclear size control in fission yeast,” *J Cell Biology*, vol. 179, no. 4, pp. 593–600, 2007, doi: 10.1083/jcb.200708054.
- [338] P. Jorgensen, N. P. Edgington, B. L. Schneider, I. Rupeš, M. Tyers, and B. Futcher, “The Size of the Nucleus Increases as Yeast Cells Grow,” *Mol Biol Cell*, vol. 18, no. 9, pp. 3523–3532, 2007, doi: 10.1091/mbc.e06-10-0973.
- [339] D. L. Levy and R. Heald, “Nuclear Size Is Regulated by Importin α and Ntf2 in *Xenopus*,” *Cell*, vol. 143, no. 2, pp. 288–298, 2010, doi: 10.1016/j.cell.2010.09.012.
- [340] K. Kume, H. Cantwell, F. R. Neumann, A. W. Jones, A. P. Snijders, and P. Nurse, “A systematic genomic screen implicates nucleocytoplasmic transport and membrane growth in nuclear size control,” *Plos Genet*, vol. 13, no. 5, p. e1006767, 2017, doi: 10.1371/journal.pgen.1006767.
- [341] I. L. Rempel et al., “Age-dependent deterioration of nuclear pore assembly in mitotic cells decreases transport dynamics,” *Elife*, vol. 8, p. e48186, 2019, doi: 10.7554/elife.48186.
- [342] D. H. Lin and A. Hoelz, “Infographic: The Nuclear Pore Complex,” 2016. <https://www.the-scientist.com/infographics/infographic-the-nuclear-pore-complex-32456> (accessed 2021).
- [343] C. W. Akey et al., “Comprehensive Structure and Functional Adaptations of the Yeast Nuclear Pore Complex,” *Biorxiv*, p. 2021.10.29.466335, 2021, doi: 10.1101/2021.10.29.466335.
- [344] A. Taddei et al., “Nuclear pore association confers optimal expression levels for an inducible yeast gene,” *Nature*, vol. 441, no. 7094, pp. 774–778, 2006, doi: 10.1038/nature04845.
- [345] R. Reed, “Coupling transcription, splicing and mRNA export,” *Curr Opin Cell Biol*, vol. 15, no. 3, pp. 326–331, 2003, doi: 10.1016/s0955-0674(03)00048-6.
- [346] K. Sträßer et al., “TREX is a conserved complex coupling transcription with messenger RNA export,” *Nature*, vol. 417, no. 6886, pp. 304–308, 2002, doi: 10.1038/nature746.
- [347] V. Galy, O. Gadal, M. Fromont-Racine, A. Romano, A. Jacquier, and U. Nehrbass, “Nuclear Retention of Unspliced mRNAs in Yeast Is Mediated by Perinuclear Mlp1,” *Cell*, vol. 116, no. 1, pp. 63–73, 2004, doi: 10.1016/s0092-8674(03)01026-2.
- [348] B. Khadaroo et al., “The DNA damage response at eroded telomeres and tethering to the nuclear pore complex,” *Nat Cell Biol*, vol. 11, no. 8, pp. 980–987, 2009, doi: 10.1038/ncb1910.
- [349] C. Lemaître et al., “The nucleoporin 153, a novel factor in double-strand break repair and DNA damage response,” *Oncogene*, vol. 31, no. 45, pp. 4803–4809, 2012, doi: 10.1038/onc.2011.638.
- [350] P. Heun, T. Laroche, K. Shimada, P. Furrer, and S. M. Gasser, “Chromosome Dynamics in the Yeast Interphase Nucleus,” *Science*, vol. 294, no. 5549, pp. 2181–2186, 2001, doi: 10.1126/science.1065366.
- [351] C. Horigome, E. Unozawa, T. Ooki, and T. Kobayashi, “Ribosomal RNA gene repeats associate with the nuclear pore complex for maintenance after DNA damage,” *Plos Genet*, vol. 15, no. 4, p. e1008103, 2019, doi: 10.1371/journal.pgen.1008103.
- [352] M. Gomar-Alba and M. Mendoza, “Modulation of Cell Identity by Modification of Nuclear Pore Complexes,” *Frontiers Genetics*, vol. 10, p. 1301, 2020, doi: 10.3389/fgene.2019.01301.
- [353] A. Kumar et al., “Daughter-cell-specific modulation of nuclear pore complexes

- controls cell cycle entry during asymmetric division," *Nat Cell Biol*, vol. 20, no. 4, pp. 432–442, 2018, doi: 10.1038/s41556-018-0056-9.
- [354] Z. Shcheprova, S. Baldi, S. B. Frei, G. Gonnet, and Y. Barral, "A mechanism for asymmetric segregation of age during yeast budding," *Nature*, vol. 454, no. 7205, pp. 728–734, 2008, doi: 10.1038/nature07212.
- [355] B. M. Webster, P. Colombi, J. Jäger, and C. P. Lusk, "Surveillance of Nuclear Pore Complex Assembly by ESCRT-III/Vps4," *Cell*, vol. 159, no. 2, pp. 388–401, 2014, doi: 10.1016/j.cell.2014.09.012.
- [356] A. Denoth-Lippuner, M. K. Krzyzanowski, C. Stober, and Y. Barral, "Role of SAGA in the asymmetric segregation of DNA circles during yeast ageing," *Elife*, vol. 3, p. e03790, 2014, doi: 10.7554/elife.03790.
- [357] I. L. Rempel, A. Steen, and L. M. Veenhoff, "Poor old pores—The challenge of making and maintaining nuclear pore complexes in aging," *Febs J*, vol. 287, no. 6, pp. 1058–1075, 2020, doi: 10.1111/febs.15205.
- [358] A. C. Meinema, T. Aspert, S. S. Lee, G. Charvin, and Y. Barral, "Specialization of chromatin-bound nuclear pore complexes promotes yeast aging," *Biorxiv*, p. 2021.06.28.450139, 2021, doi: 10.1101/2021.06.28.450139.
- [359] A. Khmelinskii et al., "Tandem fluorescent protein timers for in vivo analysis of protein dynamics," *Nat Biotechnol*, vol. 30, no. 7, pp. 708–714, 2012, doi: 10.1038/nbt.2281.
- [360] C. L. Lord, B. L. Timney, M. P. Rout, and S. R. Wentz, "Altering nuclear pore complex function impacts longevity and mitochondrial function in *S. cerevisiae* NPCs and nuclear transport regulate longevity," *J Cell Biology*, vol. 208, no. 6, pp. 729–744, 2015, doi: 10.1083/jcb.201412024.
- [361] C. L. Lord, O. Ospovat, and S. R. Wentz, "Nup100 regulates *Saccharomyces cerevisiae* replicative life span by mediating the nuclear export of specific tRNAs," *Rna*, vol. 23, no. 3, pp. 365–377, 2017, doi: 10.1261/rna.057612.116.
- [362] M. A. D'Angelo, M. Raices, S. H. Panowski, and M. W. Hetzer, "Age-Dependent Deterioration of Nuclear Pore Complexes Causes a Loss of Nuclear Integrity in Postmitotic Cells," *Cell*, vol. 136, no. 2, pp. 284–295, 2009, doi: 10.1016/j.cell.2008.11.037.
- [363] A. Ghavami, L. M. Veenhoff, E. van der Giessen, and P. R. Onck, "Probing the Disordered Domain of the Nuclear Pore Complex through Coarse-Grained Molecular Dynamics Simulations," *Biophys J*, vol. 107, no. 6, pp. 1393–1402, 2014, doi: 10.1016/j.bpj.2014.07.060.
- [364] J. Venema and D. Tollervy, "Ribosome synthesis in *Saccharomyces cerevisiae*," *Annu Rev Genet*, vol. 33, no. 1, pp. 261–311, 1999, doi: 10.1146/annurev.genet.33.1.261.
- [365] J. L. Woolford and S. J. Baserga, "Ribosome Biogenesis in the Yeast *Saccharomyces cerevisiae*," *Genetics*, vol. 195, no. 3, pp. 643–681, 2013, doi: 10.1534/genetics.113.153197.
- [366] T. Kobayashi, "How does genome instability affect lifespan?," *Genes Cells*, vol. 16, no. 6, pp. 617–624, 2011, doi: 10.1111/j.1365-2443.2011.01519.x.
- [367] E. Matos-Perdomo and F. Machín, "Nucleolar and Ribosomal DNA Structure under Stress: Yeast Lessons for Aging and Cancer," *Cells*, vol. 8, no. 8, p. 779, 2019, doi: 10.3390/cells8080779.
- [368] D. A. Sinclair, K. Mills, and L. Guarente, "Accelerated Aging and Nucleolar Fragmentation in Yeast *sgs1* Mutants," *Science*, vol. 277, no. 5330, pp. 1313–1316, 1997, doi: 10.1126/science.277.5330.1313.
- [369] V. Tiku et al., "Small nucleoli are a cellular hallmark of longevity," *Nat Commun*, vol. 8, no. 1, p. 16083, 2017, doi: 10.1038/ncomms16083.
- [370] V. Tiku and A. Antebi, "Nucleolar Function in Lifespan Regulation," *Trends Cell Biol*, vol. 28, no. 8, pp. 662–672, 2018, doi: 10.1016/j.tcb.2018.03.007.
- [371] S. Hamperl, M. Wittner, V. Babl, J. Perez-Fernandez, H. Tschochner, and J. Griesenbeck, "Chromatin states at ribosomal DNA loci," *Biochimica Et Biophysica Acta Bba*

- *Gene Regul Mech*, vol. 1829, no. 3–4, pp. 405–417, 2013, doi: 10.1016/j.bbagrm.2012.12.007.
- [372] J. O. Nelson, G. J. Watase, N. Warsinger-Pepe, and Y. M. Yamashita, “Mechanisms of rDNA Copy Number Maintenance,” *Trends Genet*, vol. 35, no. 10, pp. 734–742, 2019, doi: 10.1016/j.tig.2019.07.006.
- [373] T. Kobayashi, “Regulation of ribosomal RNA gene copy number and its role in modulating genome integrity and evolutionary adaptability in yeast,” *Cell Mol Life Sci*, vol. 68, no. 8, pp. 1395–1403, 2011, doi: 10.1007/s00018-010-0613-2.
- [374] T. Kobayashi and M. Sasaki, “Ribosomal DNA stability is supported by many ‘buffer genes’—introduction to the Yeast rDNA Stability Database,” *Fems Yeast Res*, vol. 17, no. 1, p. fox001, 2017, doi: 10.1093/femsyr/fox001.
- [375] J. R. Warner, “The economics of ribosome biosynthesis in yeast,” *Trends Biochem Sci*, vol. 24, no. 11, pp. 437–440, 1999, doi: 10.1016/s0968-0004(99)01460-7.
- [376] J. E. Pérez-Ortín, V. Tordera, and S. Chávez, “Homeostasis in the Central Dogma of molecular biology: the importance of mRNA instability,” *Rna Biol*, vol. 16, no. 12, pp. 1–8, 2019, doi: 10.1080/15476286.2019.1655352.
- [377] I. Grummt and C. S. Pikaard, “Epigenetic silencing of RNA polymerase I transcription,” *Nat Rev Mol Cell Bio*, vol. 4, no. 8, pp. 641–649, 2003, doi: 10.1038/nrm1171.
- [378] A. Mansisidor et al., “Genomic Copy-Number Loss Is Rescued by Self-Limiting Production of DNA Circles,” *Mol Cell*, vol. 72, no. 3, pp. 583–593.e4, 2018, doi: 10.1016/j.molcel.2018.08.036.
- [379] R. Dammann, R. Lucchini, T. Koller, and J. M. Sogo, “Chromatin structures and transcription of rDNA in yeast *Saccharomyces cerevisiae*,” *Nucleic Acids Res*, vol. 21, no. 10, pp. 2331–2338, 1993, doi: 10.1093/nar/21.10.2331.
- [380] M. Toussaint, G. Levasseur, M. Tremblay, M. Paquette, and A. Conconi, “Psoralen photocrosslinking, a tool to study the chromatin structure of RNA polymerase I - transcribed ribosomal genes,” *Biochem Cell Biol*, vol. 83, no. 4, pp. 449–459, 2005, doi: 10.1139/o05-141.
- [381] S. L. French, Y. N. Osheim, F. Cioci, M. Nomura, and A. L. Beyer, “In Exponentially Growing *Saccharomyces cerevisiae* Cells, rRNA Synthesis Is Determined by the Summed RNA Polymerase I Loading Rate Rather than by the Number of Active Genes,” *Mol Cell Biol*, vol. 23, no. 5, pp. 1558–1568, 2003, doi: 10.1128/mcb.23.5.1558-1568.2003.
- [382] D. R. Kief and J. R. Warner, “Hierarchy of elements regulating synthesis of ribosomal proteins in *Saccharomyces cerevisiae*,” *Mol Cell Biol*, vol. 1, no. 11, pp. 1016–1023, 1981, doi: 10.1128/mcb.1.11.1016.
- [383] D. R. Kief and J. R. Warner, “Coordinate control of syntheses of ribosomal ribonucleic acid and ribosomal proteins during nutritional shift-up in *Saccharomyces cerevisiae*,” *Mol Cell Biol*, vol. 1, no. 11, pp. 1007–1015, 1981, doi: 10.1128/mcb.1.11.1007.
- [384] M. Oakes, I. Siddiqi, L. Vu, J. Aris, and M. Nomura, “Transcription Factor UAF, Expansion and Contraction of Ribosomal DNA (rDNA) Repeats, and RNA Polymerase Switch in Transcription of Yeast rDNA,” *Mol Cell Biol*, vol. 19, no. 12, pp. 8559–8569, 1999, doi: 10.1128/mcb.19.12.8559.
- [385] H. Li, C. K. Tsang, M. Watkins, P. G. Bertram, and X. F. S. Zheng, “Nutrient regulates Tor1 nuclear localization and association with rDNA promoter,” *Nature*, vol. 442, no. 7106, pp. 1058–1061, 2006, doi: 10.1038/nature05020.
- [386] C. W. Ha and W.-K. Huh, “Rapamycin increases rDNA stability by enhancing association of Sir2 with rDNA in *Saccharomyces cerevisiae*,” *Nucleic Acids Res*, vol. 39, no. 4, pp. 1336–1350, 2011, doi: 10.1093/nar/gkq895.
- [387] Y. Wei, C. K. Tsang, and X. F. S. Zheng, “Mechanisms of regulation of RNA polymerase III-dependent transcription by TORC1,” *Embo J*, vol. 28, no. 15, pp. 2220–2230, 2009, doi: 10.1038/emboj.2009.179.
- [388] T. Kobayashi and T. Horiuchi, “A yeast gene product, Fob1 protein, required for both

- replication fork blocking and recombinational hotspot activities," *Genes Cells*, vol. 1, no. 5, pp. 465–474, 1996, doi: 10.1046/j.1365-2443.1996.d01-256.x.
- [389] J. Huang and D. Moazed, "Association of the RENT complex with nontranscribed and coding regions of rDNA and a regional requirement for the replication fork block protein Fob1 in rDNA silencing," *Gene Dev*, vol. 17, no. 17, pp. 2162–2176, 2003, doi: 10.1101/gad.1108403.
- [390] T. Kobayashi, "The Replication Fork Barrier Site Forms a Unique Structure with Fob1p and Inhibits the Replication Fork," *Mol Cell Biol*, vol. 23, no. 24, pp. 9178–9188, 2003, doi: 10.1128/mcb.23.24.9178-9188.2003.
- [391] A. R. D. Ganley, K. Hayashi, T. Horiuchi, and T. Kobayashi, "Identifying gene-independent noncoding functional elements in the yeast ribosomal DNA by phylogenetic footprinting," *P Natl Acad Sci Usa*, vol. 102, no. 33, pp. 11787–11792, 2005, doi: 10.1073/pnas.0504905102.
- [392] C. Li, J. E. Mueller, and M. Bryk, "Sir2 Represses Endogenous Polymerase II Transcription Units in the Ribosomal DNA Nontranscribed Spacer," *Mol Biol Cell*, vol. 17, no. 9, pp. 3848–3859, 2006, doi: 10.1091/mbc.e06-03-0205.
- [393] L. Vasiljeva, M. Kim, N. Terzi, L. M. Soares, and S. Buratowski, "Transcription Termination and RNA Degradation Contribute to Silencing of RNA Polymerase II Transcription within Heterochromatin," *Mol Cell*, vol. 29, no. 3, pp. 313–323, 2008, doi: 10.1016/j.molcel.2008.01.011.
- [394] E. Cesarini, F. R. Mariotti, F. Cioci, and G. Camilloni, "RNA Polymerase I Transcription Silences Noncoding RNAs at the Ribosomal DNA Locus in *Saccharomyces cerevisiae* ▽," *Eukaryot Cell*, vol. 9, no. 2, pp. 325–335, 2010, doi: 10.1128/ec.00280-09.
- [395] J. S. Smith and J. D. Boeke, "An unusual form of transcriptional silencing in yeast ribosomal DNA," *Gene Dev*, vol. 11, no. 2, pp. 241–254, 1997, doi: 10.1101/gad.11.2.241.
- [396] C. M. Armstrong, M. Kaeberlein, S. I. Imai, and L. Guarente, "Mutations in *Saccharomyces cerevisiae* Gene SIR2 Can Have Differential Effects on In Vivo Silencing Phenotypes and In Vitro Histone Deacetylation Activity," *Mol Biol Cell*, vol. 13, no. 4, pp. 1427–1438, 2002, doi: 10.1091/mbc.01-10-0482.
- [397] J. J. Sandmeier et al., "RPD3 is required for the inactivation of yeast ribosomal DNA genes in stationary phase," *Embo J*, vol. 21, no. 18, pp. 4959–4968, 2002, doi: 10.1093/emboj/cdf498.
- [398] S. W. Buck, J. J. Sandmeier, and J. S. Smith, "RNA Polymerase I Propagates Unidirectional Spreading of rDNA Silent Chromatin," *Cell*, vol. 111, no. 7, pp. 1003–1014, 2002, doi: 10.1016/s0092-8674(02)01193-5.
- [399] F. Cioci, L. Vu, K. Eliason, M. Oakes, I. N. Siddiqi, and M. Nomura, "Silencing in Yeast rDNA Chromatin Reciprocal Relationship in Gene Expression between RNA Polymerase I and II," *Mol Cell*, vol. 12, no. 1, pp. 135–145, 2003, doi: 10.1016/s1097-2765(03)00262-4.
- [400] M. R. Gartenberg and J. S. Smith, "The Nuts and Bolts of Transcriptionally Silent Chromatin in *Saccharomyces cerevisiae*," *Genetics*, vol. 203, no. 4, pp. 1563–1599, 2016, doi: 10.1534/genetics.112.145243.
- [401] H. Chen, M. Fan, L. M. Pfeffer, and R. N. Larabee, "The histone H3 lysine 56 acetylation pathway is regulated by target of rapamycin (TOR) signaling and functions directly in ribosomal RNA biogenesis," *Nucleic Acids Res*, vol. 40, no. 14, pp. 6534–6546, 2012, doi: 10.1093/nar/gks345.
- [402] P. Tessarz et al., "Glutamine methylation in Histone H2A is an RNA Polymerase I dedicated modification," *Nature*, vol. 505, no. 7484, pp. 564–568, 2014, doi: 10.1038/nature12819.
- [403] R. Srivastava, R. Srivastava, and S. H. Ahn, "The Epigenetic Pathways to Ribosomal DNA Silencing," *Microbiol Mol Biol R*, vol. 80, no. 3, pp. 545–563, 2016, doi: 10.1128/mmbr.00005-16.
- [404] R. T. Yamamoto, Y. Nogi, J. A. Dodd, and M. Nomura, "RRN3 gene of *Saccharomyces*

- cerevisiae* encodes an essential RNA polymerase I transcription factor which interacts with the polymerase independently of DNA template.," *Embo J*, vol. 15, no. 15, pp. 3964–73, 1996.
- [405] G. Peyroche et al., "The recruitment of RNA polymerase I on rDNA is mediated by the interaction of the A43 subunit with Rrn3," *Embo J*, vol. 19, no. 20, pp. 5473–5482, 2000, doi: 10.1093/emboj/19.20.5473.
- [406] C. Blattner et al., "Molecular basis of Rrn3-regulated RNA polymerase I initiation and cell growth," *Gene Dev*, vol. 25, no. 19, pp. 2093–2105, 2011, doi: 10.1101/gad.17363311.
- [407] K. Hannig et al., "The C-terminal region of Net1 is an activator of RNA polymerase I transcription with conserved features from yeast to human," *Plos Genet*, vol. 15, no. 2, p. e1008006, 2019, doi: 10.1371/journal.pgen.1008006.
- [408] T. Kobayashi, "Strategies to maintain the stability of the ribosomal RNA gene repeats," *Genes Genet Syst*, vol. 81, no. 3, pp. 155–161, 2006, doi: 10.1266/ggs.81.155.
- [409] Y. Takeuchi, T. Horiuchi, and T. Kobayashi, "Transcription-dependent recombination and the role of fork collision in yeast rDNA," *Gene Dev*, vol. 17, no. 12, pp. 1497–1506, 2003, doi: 10.1101/gad.1085403.
- [410] T. Kobayashi, D. J. Heck, M. Nomura, and T. Horiuchi, "Expansion and contraction of ribosomal DNA repeats in *Saccharomyces cerevisiae*: requirement of replication fork blocking (Fob1) protein and the role of RNA polymerase I," *Gene Dev*, vol. 12, no. 24, pp. 3821–3830, 1998, doi: 10.1101/gad.12.24.3821.
- [411] J. W. Szostak and R. Wu, "Unequal crossing over in the ribosomal DNA of *Saccharomyces cerevisiae*," *Nature*, vol. 284, no. 5755, pp. 426–430, 1980, doi: 10.1038/284426a0.
- [412] S. Gangloff, H. Zou, and R. Rothstein, "Gene conversion plays the major role in controlling the stability of large tandem repeats in yeast.," *Embo J*, vol. 15, no. 7, pp. 1715–25, 1996.
- [413] S. Ide, K. Saka, and T. Kobayashi, "Rtt109 Prevents Hyper-Amplification of Ribosomal RNA Genes through Histone Modification in Budding Yeast," *Plos Genet*, vol. 9, no. 4, p. e1003410, 2013, doi: 10.1371/journal.pgen.1003410.
- [414] T. Iida and T. Kobayashi, "How do cells count multi-copy genes?: 'Musical Chair' model for preserving the number of rDNA copies," *Curr Genet*, vol. 65, no. 4, pp. 883–885, 2019, doi: 10.1007/s00294-019-00956-0.
- [415] T. Iida and T. Kobayashi, "RNA Polymerase I Activators Count and Adjust Ribosomal RNA Gene Copy Number," *Mol Cell*, vol. 73, no. 4, pp. 645–654.e13, 2019, doi: 10.1016/j.molcel.2018.11.029.
- [416] K. Saka, A. Takahashi, M. Sasaki, and T. Kobayashi, "More than 10% of yeast genes are related to genome stability and influence cellular senescence via rDNA maintenance," *Nucleic Acids Res*, vol. 44, no. 9, pp. 4211–4221, 2016, doi: 10.1093/nar/gkw110.
- [417] A. R. D. Ganley, S. Ide, K. Saka, and T. Kobayashi, "The Effect of Replication Initiation on Gene Amplification in the rDNA and Its Relationship to Aging," *Mol Cell*, vol. 35, no. 5, pp. 683–693, 2009, doi: 10.1016/j.molcel.2009.07.012.
- [418] T. Kobayashi, T. Horiuchi, P. Tongaonkar, L. Vu, and M. Nomura, "SIR2 Regulates Recombination between Different rDNA Repeats, but Not Recombination within Individual rRNA Genes in Yeast," *Cell*, vol. 117, no. 4, pp. 441–453, 2004, doi: 10.1016/s0092-8674(04)00414-3.
- [419] S. Gottlieb and R. E. Esposito, "A new role for a yeast transcriptional silencer gene, SIR2, in regulation of recombination in ribosomal DNA," *Cell*, vol. 56, no. 5, pp. 771–776, 1989, doi: 10.1016/0092-8674(89)90681-8.
- [420] T. Kobayashi and A. R. D. Ganley, "Recombination Regulation by Transcription-Induced Cohesin Dissociation in rDNA Repeats," *Science*, vol. 309, no. 5740, pp. 1581–1584, 2005, doi: 10.1126/science.1116102.
- [421] T. Kobayashi, "A new role of the rDNA and nucleolus in the nucleus—rDNA instability

- maintains genome integrity," *Bioessays*, vol. 30, no. 3, pp. 267–272, 2008, doi: 10.1002/bies.20723.
- [422] A. R. D. Ganley and T. Kobayashi, "Ribosomal DNA and cellular senescence: new evidence supporting the connection between rDNA and aging," *Fems Yeast Res*, vol. 14, no. 1, pp. 49–59, 2014, doi: 10.1111/1567-1364.12133.
- [423] E. Cesarini, A. D'Alfonso, and G. Camilloni, "H4K16 acetylation affects recombination and ncRNA transcription at rDNA in *Saccharomyces cerevisiae*," *Mol Biol Cell*, vol. 23, no. 14, pp. 2770–2781, 2012, doi: 10.1091/mbc.e12-02-0095.
- [424] D. A. Sinclair and L. Guarente, "Extrachromosomal rDNA Circles— A Cause of Aging in Yeast," *Cell*, vol. 91, no. 7, pp. 1033–1042, 1997, doi: 10.1016/s0092-8674(00)80493-6.
- [425] P.-A. Defossez et al., "Elimination of Replication Block Protein Fob1 Extends the Life Span of Yeast Mother Cells," *Mol Cell*, vol. 3, no. 4, pp. 447–455, 1999, doi: 10.1016/s1097-2765(00)80472-4.
- [426] C. S. Gillespie, C. J. Proctor, R. J. Boys, D. P. Shanley, D. J. Wilkinson, and T. B. L. Kirkwood, "A mathematical model of ageing in yeast," *J Theor Biol*, vol. 229, no. 2, pp. 189–196, 2004, doi: 10.1016/j.jtbi.2004.03.015.
- [427] L. R. Gehlen, S. Nagai, K. Shimada, P. Meister, A. Taddei, and S. M. Gasser, "Nuclear Geometry and Rapid Mitosis Ensure Asymmetric Episome Segregation in Yeast," *Curr Biol*, vol. 21, no. 1, pp. 25–33, 2011, doi: 10.1016/j.cub.2010.12.016.
- [428] B. Boettcher, T. T. Marquez-Lago, M. Bayer, E. L. Weiss, and Y. Barral, "Nuclear envelope morphology constrains diffusion and promotes asymmetric protein segregation in closed mitosis," *J Cell Biol*, vol. 197, no. 7, pp. 921–937, 2012, doi: 10.1083/jcb.201112117.
- [429] A. Khmelinskii, M. Meurer, M. Knop, and E. Schiebel, "Artificial tethering to nuclear pores promotes partitioning of extrachromosomal DNA during yeast asymmetric cell division," *Curr Biol*, vol. 21, no. 1, pp. R17–R18, 2011, doi: 10.1016/j.cub.2010.11.034.
- [430] A. W. Murray and J. W. Szostak, "Pedigree analysis of plasmid segregation in yeast," *Cell*, vol. 34, no. 3, pp. 961–970, 1983, doi: 10.1016/0092-8674(83)90553-6.
- [431] A. B. Futcher and B. S. Cox, "Copy number and the stability of 2-micron circle-based artificial plasmids of *Saccharomyces cerevisiae*," *J Bacteriol*, vol. 157, no. 1, pp. 283–90, 1984.
- [432] M. C. Espinosa, M. A. Rehman, P. Chisamore-Robert, D. Jeffery, and K. Yankulov, "GCN5 Is a Positive Regulator of Origins of DNA Replication in *Saccharomyces cerevisiae*," *Plos One*, vol. 5, no. 1, p. e8964, 2010, doi: 10.1371/journal.pone.0008964.
- [433] A. A. Falcón and J. P. Aris, "Plasmid Accumulation Reduces Life Span in *Saccharomyces cerevisiae*," *J Biol Chem*, vol. 278, no. 43, pp. 41607–41617, 2003, doi: 10.1074/jbc.m307025200.
- [434] R. Sweeney and V. A. Zakian, "Extrachromosomal elements cause a reduced division potential in *nib 1* strains of *Saccharomyces cerevisiae*," *Genetics*, vol. 122, no. 4, pp. 749–757, 1989, doi: 10.1093/genetics/122.4.749.
- [435] H. Wang, L. B. Carey, Y. Cai, H. Wijnen, and B. Futcher, "Recruitment of Cln3 Cyclin to Promoters Controls Cell Cycle Entry via Histone Deacetylase and Other Targets," *Plos Biol*, vol. 7, no. 9, p. e1000189, 2009, doi: 10.1371/journal.pbio.1000189.
- [436] P. Bensidoun, T. Reiter, B. Montpetit, D. Zenklusen, and M. Oeffinger, "Nuclear mRNA metabolism drives selective basket assembly on a subset of nuclear pores in budding yeast," *Biorxiv*, p. 2021.11.07.467636, 2021, doi: 10.1101/2021.11.07.467636.
- [437] C. L. Woldringh, K. Fluiter, and P. G. Huls, "Production of senescent cells of *Saccharomyces cerevisiae* by centrifugal elutriation," *Yeast*, vol. 11, no. 4, pp. 361–369, 1995, doi: 10.1002/yea.320110409.
- [438] I. Lesur and J. L. Campbell, "The Transcriptome of Prematurely Aging Yeast Cells Is Similar to That of Telomerase-deficient Cells," *Mol Biol Cell*, vol. 15, no. 3, pp. 1297–1312, 2004, doi: 10.1091/mbc.e03-10-0742.

- [439] D. L. Lindstrom and D. E. Gottschling, "The Mother Enrichment Program: A Genetic System for Facile Replicative Life Span Analysis in *Saccharomyces cerevisiae*," *Genetics*, vol. 183, no. 2, pp. 413–422, 2009, doi: 10.1534/genetics.109.106229.
- [440] B. C.E., "The Molecular Biology of the Yeast *Saccharomyces*: Metabolism and Gene Expression," *Cold Spring Harbor Laboratory Press*, 1982.
- [441] E. A. Sarnoski, P. Liu, and M. Acar, "A High-Throughput Screen for Yeast Replicative Lifespan Identifies Lifespan-Extending Compounds," *Cell Reports*, vol. 21, no. 9, pp. 2639–2646, 2017, doi: 10.1016/j.celrep.2017.11.002.
- [442] T. Chen et al., "A drug-compatible and temperature-controlled microfluidic device for live-cell imaging," *Open Biol*, vol. 6, no. 8, p. 160156, 2016, doi: 10.1098/rsob.160156.
- [443] R. B. Kopito and E. Levine, "Durable spatiotemporal surveillance of *Caenorhabditis elegans* response to environmental cues," *Lab Chip*, vol. 14, no. 4, pp. 764–770, 2013, doi: 10.1039/c3lc51061a.
- [444] R. Gómez-Sjöberg, A. A. Leyrat, D. M. Pirone, C. S. Chen, and S. R. Quake, "Versatile, Fully Automated, Microfluidic Cell Culture System," *Anal Chem*, vol. 79, no. 22, pp. 8557–8563, 2007, doi: 10.1021/ac071311w.
- [445] A. M. Taylor, D. C. Dieterich, H. T. Ito, S. A. Kim, and E. M. Schuman, "Microfluidic Local Perfusion Chambers for the Visualization and Manipulation of Synapses," *Neuron*, vol. 66, no. 1, pp. 57–68, 2010, doi: 10.1016/j.neuron.2010.03.022.
- [446] D. Qin, Y. Xia, and G. M. Whitesides, "Soft lithography for micro- and nanoscale patterning," *Nat Protoc*, vol. 5, no. 3, pp. 491–502, 2010, doi: 10.1038/nprot.2009.234.
- [447] R. O’Laughlin et al., "Advances in quantitative biology methods for studying replicative aging in *Saccharomyces cerevisiae*," *Transl Medicine Aging*, 2019, doi: 10.1016/j.tma.2019.09.002.
- [448] M. M. Crane, I. B. N. Clark, E. Bakker, S. Smith, and P. S. Swain, "A Microfluidic System for Studying Ageing and Dynamic Single-Cell Responses in Budding Yeast," *Plos One*, vol. 9, no. 6, p. e100042, 2014, doi: 10.1371/journal.pone.0100042.
- [449] P. Liu, T. Z. Young, and M. Acar, "Yeast Replicator: A High-Throughput Multiplexed Microfluidics Platform for Automated Measurements of Single-Cell Aging," *Cell Reports*, vol. 13, no. 3, pp. 634–644, 2015, doi: 10.1016/j.celrep.2015.09.012.
- [450] J. Ryley and O. M. Pereira-Smith, "Microfluidics device for single cell gene expression analysis in *Saccharomyces cerevisiae*," *Yeast*, vol. 23, no. 14–15, pp. 1065–1073, 2006, doi: 10.1002/yea.1412.
- [451] S. Beucher, "The Watershed Transformation Applied to Image Segmentation," *Scanning Microscopy*, vol. 6, 1992.
- [452] E. Bakker, P. S. Swain, and M. M. Crane, "Morphologically constrained and data informed cell segmentation of budding yeast," *Bioinformatics*, vol. 34, no. 1, pp. 88–96, 2017, doi: 10.1093/bioinformatics/btx550.
- [453] N. E. Wood and A. Doncic, "A fully-automated, robust, and versatile algorithm for long-term budding yeast segmentation and tracking," *Plos One*, vol. 14, no. 3, p. e0206395, 2019, doi: 10.1371/journal.pone.0206395.
- [453b] K. W. Eliceiri et al., "Biological imaging software tools," *Nat Methods*, vol. 9, no. 7, pp. 697–710, 2012, doi: 10.1038/nmeth.2084.
- [454] I. Walsh et al., "DOME: recommendations for supervised machine learning validation in biology," *Nat Methods*, vol. 18, no. 10, pp. 1122–1127, 2021, doi: 10.1038/s41592-021-01205-4.
- [455] M. Weigert et al., "Content-aware image restoration: pushing the limits of fluorescence microscopy," *Nat Methods*, vol. 15, no. 12, pp. 1090–1097, 2018, doi: 10.1038/s41592-018-0216-7.
- [456] M. Priesnner, et al., and R. Laine, "Content-aware frame interpolation (CAFI): Deep Learning-based temporal super-resolution for fast bioimaging," *bioRxiv*, 2021, doi: 10.1101/2021.11.02.466664.

- [457] J. Jumper et al., "Highly accurate protein structure prediction with AlphaFold," *Nature*, vol. 596, no. 7873, pp. 583–589, 2021, doi: 10.1038/s41586-021-03819-2.
- [458] S. Berg et al., "ilastik: interactive machine learning for (bio)image analysis," *Nat Methods*, vol. 16, no. 12, pp. 1226–1232, 2019, doi: 10.1038/s41592-019-0582-9.
- [459] Y. LeCun and Y. Bengio, "Convolutional networks for images, speech, and time series," *The handbook of brain theory and neural networks*, 1995.
- [460] O. Ronneberger, P. Fischer, and T. Brox, "U-Net: Convolutional Networks for Biomedical Image Segmentation," *Arxiv*, 2015.
- [461] C. Stringer, T. Wang, M. Michaelos, and M. Pachitariu, "Cellpose: a generalist algorithm for cellular segmentation," *Nat Methods*, vol. 18, no. 1, pp. 100–106, 2021, doi: 10.1038/s41592-020-01018-x.
- [462] U. Schmidt, M. Weigert, C. Broaddus, and G. Myers, "Cell Detection with Star-convex Polygons," *Arxiv*, 2018, doi: 10.1007/978-3-030-00934-2_30.
- [463] N. Dietler et al., "A convolutional neural network segments yeast microscopy images with high accuracy," *Nat Commun*, vol. 11, no. 1, p. 5723, 2020, doi: 10.1038/s41467-020-19557-4.
- [464] D. Salem, Y. Li, P. Xi, H. Phenix, M. Cuperlovic-Culf, and M. Kærn, "YeastNet: Deep-Learning-Enabled Accurate Segmentation of Budding Yeast Cells in Bright-Field Microscopy," *Appl Sci*, vol. 11, no. 6, p. 2692, 2021, doi: 10.3390/app11062692.
- [465] A. X. Lu, T. Zarin, I. S. Hsu, and A. M. Moses, "YeastSpotter: Accurate and parameter-free web segmentation for microscopy images of yeast cells," *Bioinformatics*, vol. 35, no. 21, pp. 4525–4527, 2019, doi: 10.1093/bioinformatics/btz402.
- [466] D. Bunk, J. Moriasy, F. Thoma, C. Jakubke, C. Osman, and D. Hörl, "YeastMate: Neural network-assisted segmentation of mating and budding events in *S. cerevisiae*," 2021, doi: 10.1101/2021.10.13.464238.
- [467] T. Prangemeier, C. Reich, and H. Koepl, "Attention-Based Transformers for Instance Segmentation of Cells in Microstructures," *Arxiv*, 2020, doi: 10.1109/bibm49941.2020.9313305.
- [468] T. Prangemeier, C. Wildner, A. O. Françani, C. Reich, and H. Koepl, "Multiclass Yeast Segmentation in Microstructured Environments with Deep Learning," *Arxiv*, 2020, doi: 10.1109/cibcb48159.2020.9277693.
- [469] J.-Y. Tinevez et al., "TrackMate: An open and extensible platform for single-particle tracking," *Methods*, vol. 115, pp. 80–90, 2017, doi: 10.1016/j.ymeth.2016.09.016.
- [470] J.-B. Lugagne, H. Lin, and M. J. Dunlop, "DeLTA: Automated cell segmentation, tracking, and lineage reconstruction using deep learning," *Plos Comput Biol*, vol. 16, no. 4, p. e1007673, 2020, doi: 10.1371/journal.pcbi.1007673.
- [471] S. Hochreiter and J. Schmidhuber, "Long Short-Term Memory," *Neural Comput*, vol. 9, no. 8, pp. 1735–1780, 1997, doi: 10.1162/neco.1997.9.8.1735.
- [472] P. B. Dennis, S. Fumagalli, and G. Thomas, "Target of rapamycin (TOR): balancing the opposing forces of protein synthesis and degradation," *Curr Opin Genet Dev*, vol. 9, no. 1, pp. 49–54, 1999, doi: 10.1016/s0959-437x(99)80007-0.
- [473] S.-B. Qian, X. Zhang, J. Sun, J. R. Bennink, J. W. Yewdell, and C. Patterson, "mTORC1 Links Protein Quality and Quantity Control by Sensing Chaperone Availability*," *J Biol Chem*, vol. 285, no. 35, pp. 27385–27395, 2010, doi: 10.1074/jbc.m110.120295.
- [474] M. Perić et al., "TORC1-mediated sensing of chaperone activity alters glucose metabolism and extends lifespan," *Aging Cell*, vol. 16, no. 5, pp. 994–1005, 2017, doi: 10.1111/accel.12623.
- [475] R. Hatakeyama et al., "Spatially Distinct Pools of TORC1 Balance Protein Homeostasis," *Mol Cell*, vol. 73, no. 2, pp. 325–338.e8, 2019, doi: 10.1016/j.molcel.2018.10.040.
- [476] M. N. Devare, Y. H. Kim, J. Jung, W. K. Kang, K. Kwon, and J. Kim, "TORC1 signaling regulates cytoplasmic pH through Sir2 in yeast," *Aging Cell*, vol. 19, no. 6, p. e13151, 2020,

doi: 10.1111/accel.13151.

[477] A. Caballero et al., "Absence of Mitochondrial Translation Control Proteins Extends Life Span by Activating Sirtuin-Dependent Silencing," *Mol Cell*, vol. 42, no. 3, pp. 390–400, 2011, doi: 10.1016/j.molcel.2011.03.021.

[478] I. Orlandi, M. Bettiga, L. Alberghina, T. Nyström, and M. Vai, "Sir2-dependent asymmetric segregation of damaged proteins in ubp10 null mutants is independent of genomic silencing," *Biochimica Et Biophysica Acta Bba - Mol Cell Res*, vol. 1803, no. 5, pp. 630–638, 2010, doi: 10.1016/j.bbamcr.2010.02.009.

[479] B. Sampaio-Marques et al., "SNCA (α -synuclein)-induced toxicity in yeast cells is dependent on Sir2-mediated mitophagy," *Autophagy*, vol. 8, no. 10, pp. 79–78, 2012, doi: 10.4161/auto.21275.

[480] J. Song et al., "Essential Genetic Interactors of SIR2 Required for Spatial Sequestration and Asymmetrical Inheritance of Protein Aggregates," *Plos Genet*, vol. 10, no. 7, p. e1004539, 2014, doi: 10.1371/journal.pgen.1004539.

[481] M. Kaerberlein, K. T. Kirkland, S. Fields, and B. K. Kennedy, "Sir2-Independent Life Span Extension by Calorie Restriction in Yeast," *Plos Biol*, vol. 2, no. 9, p. e296, 2004, doi: 10.1371/journal.pbio.0020296.

[482] D. Koshland, J. C. Kent, and L. H. Hartwell, "Genetic analysis of the mitotic transmission of minichromosomes," *Cell*, vol. 40, no. 2, pp. 393–403, 1985, doi: 10.1016/0092-8674(85)90153-9.

[483] I. Prada-Luengo et al., "Replicative aging is associated with loss of genetic heterogeneity from extrachromosomal circular DNA in *Saccharomyces cerevisiae*," *Nucleic Acids Res*, vol. 48, no. 14, pp. gkaa545–, 2020, doi: 10.1093/nar/gkaa545.

[484] S. Baldi, A. Bolognesi, A. C. Meinema, and Y. Barral, "Heat stress promotes longevity in budding yeast by relaxing the confinement of age-promoting factors in the mother cell," *Elife*, vol. 6, p. e28329, 2017, doi: 10.7554/elife.28329.

[485] A. Mena et al., "Asymmetric cell division requires specific mechanisms for adjusting global transcription," *Nucleic Acids Res*, vol. 45, no. 21, pp. 12401–12412, 2017, doi: 10.1093/nar/gkx974.

[486] M. Niepel et al., "The nuclear basket proteins Mlp1p and Mlp2p are part of a dynamic interactome including Esc1p and the proteasome," *Mol Biol Cell*, vol. 24, no. 24, pp. 3920–3938, 2013, doi: 10.1091/mbc.e13-07-0412.

[487] J. Miné-Hattab and A. Taddei, "Physical principles and functional consequences of nuclear compartmentalization in budding yeast," *Curr Opin Cell Biol*, vol. 58, pp. 105–113, 2019, doi: 10.1016/j.ceb.2019.02.005.

[488] L. E. Orgel and F. H. C. Crick, "Selfish DNA: the ultimate parasite," *Nature*, vol. 284, no. 5757, pp. 604–607, 1980, doi: 10.1038/284604a0.

[489] T. Cavalier-Smith, "Skeletal DNA and the Evolution of Genome Size," *Annu Rev Biophys Bio*, vol. 11, no. 1, pp. 273–302, 1982, doi: 10.1146/annurev.bb.11.060182.001421.

[490] T. R. Gregory, "The Evolution of the Genome," *Part C-value Enigma*, no. Adv Enzymol161955, pp. 3–87, 2005, doi: 10.1016/b978-012301463-4/50003-6.

[491] M. P. Swaffer et al., "Transcriptional and chromatin-based partitioning mechanisms uncouple protein scaling from cell size," *Mol Cell*, 2021, doi: 10.1016/j.molcel.2021.10.007.

[492] Z. Liao, W. Jiang, L. Ye, T. Li, X. Yu, and L. Liu, "Classification of extrachromosomal circular DNA with a focus on the role of extrachromosomal DNA (ecDNA) in tumor heterogeneity and progression," *Biochimica Et Biophysica Acta Bba - Rev Cancer*, vol. 1874, no. 1, p. 188392, 2020, doi: 10.1016/j.bbcan.2020.188392.

[493] H. D. Møller et al., "Circular DNA elements of chromosomal origin are common in healthy human somatic tissue," *Nat Commun*, vol. 9, no. 1, p. 1069, 2018, doi: 10.1038/s41467-018-03369-8.

[494] R. P. Koche et al., "Extrachromosomal circular DNA drives oncogenic genome

- remodeling in neuroblastoma," *Nat Genet*, vol. 52, no. 1, pp. 29–34, 2020, doi: 10.1038/s41588-019-0547-z.
- [495] R. G. W. Verhaak, V. Bafna, and P. S. Mischel, "Extrachromosomal oncogene amplification in tumour pathogenesis and evolution," *Nat Rev Cancer*, vol. 19, no. 5, pp. 283–288, 2019, doi: 10.1038/s41568-019-0128-6.
- [496] R. M. Hull, M. King, G. Pizza, F. Krueger, X. Vergara, and J. Houseley, "Transcription-induced formation of extrachromosomal DNA during yeast ageing," *Plos Biol*, vol. 17, no. 12, p. e3000471, 2019, doi: 10.1371/journal.pbio.3000471.
- [497] R. M. Hull and J. Houseley, "The adaptive potential of circular DNA accumulation in ageing cells," *Curr Genet*, vol. 66, no. 5, pp. 889–894, 2020, doi: 10.1007/s00294-020-01069-9.
- [498] Q. Ain, C. Schmeer, D. Wengerodt, O. W. Witte, and A. Kretz, "Extrachromosomal Circular DNA: Current Knowledge and Implications for CNS Aging and Neurodegeneration," *Int J Mol Sci*, vol. 21, no. 7, p. 2477, 2020, doi: 10.3390/ijms21072477.
- [499] B. Xu et al., "Ribosomal DNA copy number loss and sequence variation in cancer," *Plos Genet*, vol. 13, no. 6, p. e1006771, 2017, doi: 10.1371/journal.pgen.1006771.
- [500] R. Ren et al., "Visualization of aging-associated chromatin alterations with an engineered TALE system," *Cell Res*, vol. 27, no. 4, pp. 483–504, 2017, doi: 10.1038/cr.2017.18.
- [501] M. Wang and B. Lemos, "Ribosomal DNA harbors an evolutionarily conserved clock of biological aging," *Genome Res*, vol. 29, no. 3, pp. 325–333, 2019, doi: 10.1101/gr.241745.118.
- [502] K. Nishimura et al., "Perturbation of Ribosome Biogenesis Drives Cells into Senescence through 5S RNP-Mediated p53 Activation," *Cell Reports*, vol. 10, no. 8, pp. 1310–1323, 2015, doi: 10.1016/j.celrep.2015.01.055.
- [503] F. Lessard et al., "Senescence-associated ribosome biogenesis defects contributes to cell cycle arrest through the Rb pathway," *Nat Cell Biol*, vol. 20, no. 7, pp. 789–799, 2018, doi: 10.1038/s41556-018-0127-y.
- [504] E. Zlotorynski, "Live longer with small nucleoli," *Nat Rev Mol Cell Bio*, vol. 18, no. 11, pp. 651–651, 2017, doi: 10.1038/nrm.2017.100.
- [505] C. K. Tsang, P. G. Bertram, W. Ai, R. Drenan, and X. F. S. Zheng, "Chromatin-mediated regulation of nucleolar structure and RNA Pol I localization by TOR," *Embo J*, vol. 22, no. 22, pp. 6045–6056, 2003, doi: 10.1093/emboj/cdg578.
- [506] M. M. Crane and M. Kaeberlein, "The paths of mortality: How understanding the biology of aging can help explain systems behavior of single cells," *Curr Opin Syst Biology*, vol. 8, pp. 25–31, 2018, doi: 10.1016/j.coisb.2017.11.010.
- [507] M. M. Crane, K. L. Chen, B. W. Blue, and M. Kaeberlein, "Trajectories of Aging: How Systems Biology in Yeast Can Illuminate Mechanisms of Personalized Aging," *Proteomics*, vol. 20, no. 5–6, p. 1800420, 2020, doi: 10.1002/pmic.201800420.
- [508] M. Morawska and H. D. Ulrich, "An expanded tool kit for the auxin-inducible degron system in budding yeast," *Yeast Chichester Engl*, vol. 30, no. 9, pp. 341–351, 2013, doi: 10.1002/yea.296

Chapter 2: Monitoring single-cell dynamics of entry into quiescence during an unperturbed life-cycle

This work is the result of a side-project in close collaboration with Basile Jacquelin (another PhD student from the lab). It was recently published in Elife. I will shortly introduce the background and the result part will consist in the published paper.

The chapter ends with a short discussion.

Introduction

1. General concepts of quiescence

Microorganisms are tightly controlling their proliferation in response to nutrient availability from their immediate environment. In fact, in their natural habitat they spend most of the time under nutrient depletion [1,2]. Therefore, prokaryotic and eukaryotic microbes have evolved complex programs to maintain viability in the absence of metabolizable carbon, nitrogen, or amino acids, in order to be able to proliferate again when these nutrients are available again. For example, starved diploid budding yeast can perform meiosis and form spores that can survive for extended periods [3]. Similarly, cells can enter **quiescence, defined as a reversible nonproliferating state** [1]. In this state, microbial cells can survive for many years without nutrients and tolerate stresses several orders of magnitude higher than what would kill them in a proliferative state.

Quiescence also occurs in mammal cells, especially in stem cells, when no proliferation is needed [4,5]. It is also a property of certain cancer cells which allows them to survive chemotherapies [6].

Of note, the molecular pathways involved in the entry into quiescence are partially conserved across eukaryotes (notably driven by the TOR and PKA metabolic pathways) [7].

Overall, and similarly to replicative aging, budding yeast is a relevant organism to study quiescence.

2. The molecular pathways of entry into quiescence

Originally, cells were thought to be able to enter quiescence only by exiting the cell cycle from the G1 phase, which is why quiescence is sometimes termed G0 phase (Figure 75) [8].

In line with that, many genes blocking the G1/S transition are repressed during the entry into quiescence [9,10]. However, later studies established that *S. cerevisiae*, *Cryptococcus neoformans*, and *Tetrahymena pyriformis* could enter quiescence in G2 [2,11]. Therefore, cells could prefer to stay in G1 before entering quiescence when the nutrients start waning, but being in G1 is not necessary to enter it.

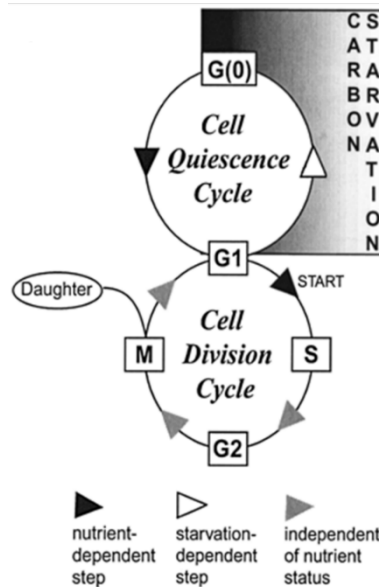


Figure 75: Relation between the cell cycle and quiescence, as historically stated (From [1]).

The molecular pathways driving the transition to quiescence are partially known and rely on TORC1 and PKA (major nutrient sensing and metabolic pathways, see p.44). Their repression leads to the transcription and activation of several hub repressor genes such as Rim15, Xbp1, and Stp3. Rim15 induces the general stress response, indirectly inhibits Pol II transcription, and promotes glycogen and trehalose storage (important for longevity in quiescence, as discussed later) [12–14]. Similarly, Xbp1 represses 800 genes, and Stb3 represses ribosomal protein transcripts.

Overall, quiescence is regulated molecularly with specifically dedicated programs. However, these molecular pathways are not the only layer of control.

3. Structural rearrangements in quiescence

Indeed, the entry into quiescence is also characterized by a wide reorganization of cellular structures, presumed to be involved in the long-term viability in this state [2] (Figure 76).

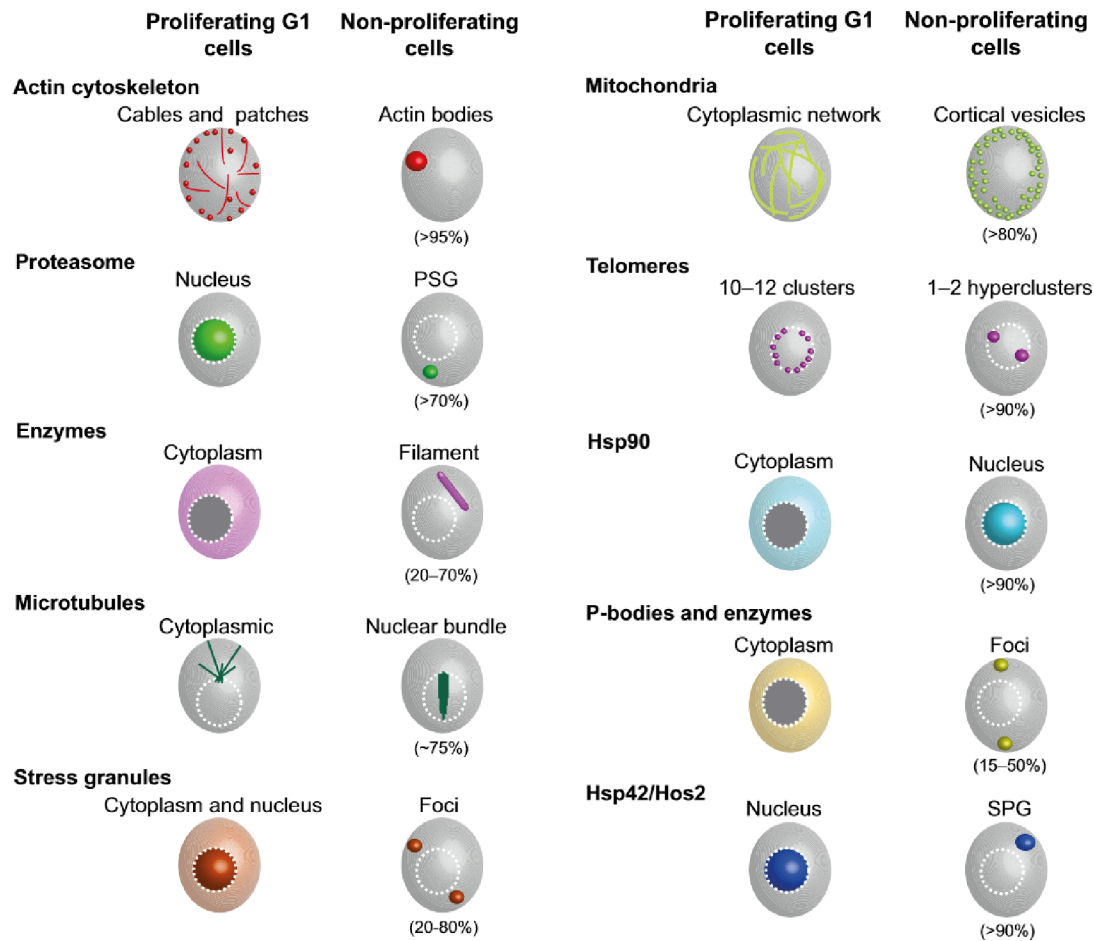


Figure 76: Cellular and organellar reorganizations upon proliferation cessation in budding yeast. The percentages indicate the number of cells displaying these changes in the population among all other possible forms (From [2]).

The following subsections will briefly present some of these changes.

3.1. Cytoskeleton

The cytoskeleton is the central controller of the dynamical mechanical properties of cells and is involved in intracellular transports, polarized growth, and material segregation during division [15]. Upon nutrient depletion and proliferation arrest, it is remodeled with the actin network transitioning into single bodies (called actin bodies) [16], and microtubules forming a single tubular structure called nuclear bundle [17] (Figure 76). Importantly, these quiescence-specific structures are reversible and return to their functional state when nutrients are available again, suggesting that they act as a storage compartment to efficiently re-enter proliferation.

3.2. Mitochondrial network and respiration

As seen previously (Chapter I, p.36), mitochondria are an important metabolic hub and are necessary for respiration. In response to abrupt starvation, cells need to have a flux in the respiration metabolism in order to survive [18]. Besides, the mitochondrial network (which directly depends on the mitochondrial activity) is also remodeled during quiescence, going from a tubular network during proliferation to small vesicles (Figure 76). Importantly, cells that do not display this remodeling do not survive longer than a few days (discussed later) [19]. Overall, this suggests that respiration and mitochondrial reorganization play a critical role in the establishment of a "healthy" quiescent state.

3.3. Proteasome

As discussed in Chapter I (p.42), the proteasome is a group of enzymatic complexes which control the proteostasis and the degradation of damaged proteins [20]. During the entry into quiescence, the proteasome is relocalized from the nucleus to the cytoplasm and forms Proteasome Storage Granules (PSG) [21] (Figure 77). This sequestering protects the proteasome from autophagic degradation occurring upon carbon starvation [22], and could explain why the cells have evolved to form these structures during the entry into quiescence. Like precedently, this structure is reversible since the PSG can rapidly be transformed into a functional proteasome upon nutrient availability [21].

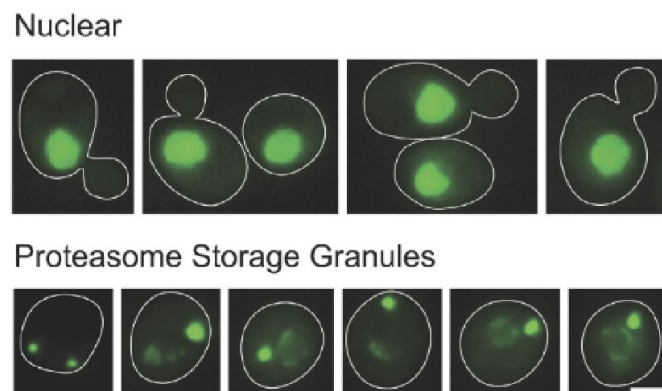


Figure 77: Images from the different types of organizations the proteasome can adopt. Most of the cells display a « nuclear » proteasome during proliferation, and a PSG during proliferation arrest (From [21]).

3.4. Phase transition of the cytoplasm

Beyond cellular structures, the whole cytoplasm organization could be modified in quiescence. In fact, it was shown that the cytoplasm of the cell was transitioning from a liquid-like state to a gel-like state upon starvation, not only in budding yeast but also in fission yeast and bacteria [23–26]. This state is caused by a decrease in metabolic activity and is associated

with reduced mobility of cytoplasmic particles above a certain size, as well as an increase in molecular crowding (Figure 78). Two biophysical phenomena can explain this phenomenon: the decrease in cell volume during nutrient stress [23] and the acidification of the cytosol [24]. Indeed, the cytosolic pH is mainly controlled by ATP-dependent proton pumps (such as Pma1) [27] and since ATP levels drop upon starvation [18], the cytosol becomes acid [24]. In turn, a low pH can induce the aggregation of several proteins such as metabolic enzymes [24,28], proteasomal proteins [29], stress granules, and P-bodies [30–32].

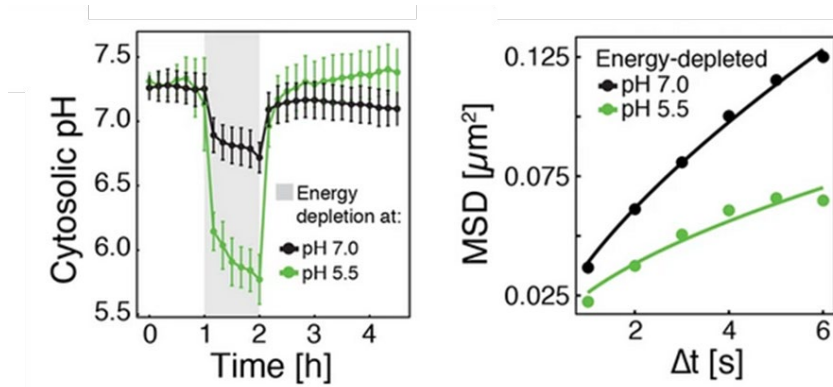


Figure 78: Link between energy, pH, and cytosolic physical state. (Left) : Cytosolic pH vs. Time. The gray area indicates an induced energy depletion, in a media of pH 7.0 (black) or 5.5 (green). When cells are depleted from energy, intracellular pH becomes close to extracellular pH. (Right) : Mean Square Displacement of a given fluorescent particle in energy-depleted cells in different pH. The mobility is decreased in low-pH cytosols (From [24]).

If the transition of the cytosol into a gel-like state is the result of a global aggregation of proteins or just an independent effect of a drop of pH and volume decrease, is still debated. Nonetheless, the aggregation of the proteins described previously participates in the cellular fitness in starvation and quiescence [22,24,30,31].

Furthermore, the phase transition of proteins is also known to depend on their concentration [30,54–56], and a reduction in volume during starvation could help achieve a gel-like state. More generally, this state is also thought to confer stress resistance properties and protect the proteins and structures by reducing their interactions [30].

Overall, in the absence of nutrients, protein aggregation and the phase transition of the cytosol are driven by a drop of pH, and are an efficient and energy-free mechanism for the cell to keep its integrity.

4. Quiescence and life-cycle of budding yeast

4.1. The life-cycle of budding yeast

In most ecological niches, yeast experience different metabolic phases where they catabolize several carbon sources. For example, in the wine-making process, they start by fermenting the sugars from the media until their exhaustion. Then, after a diauxic shift period, they can proliferate again by respiring the ethanol produced during the fermentative phase. Finally, when all the carbon sources are exhausted, the population reaches the stationary phase and cells enter quiescence (Figure 79). Hence, quiescence in the wild rarely happens after a sharp nutrient depletion, but rather after a dynamic change of environments.

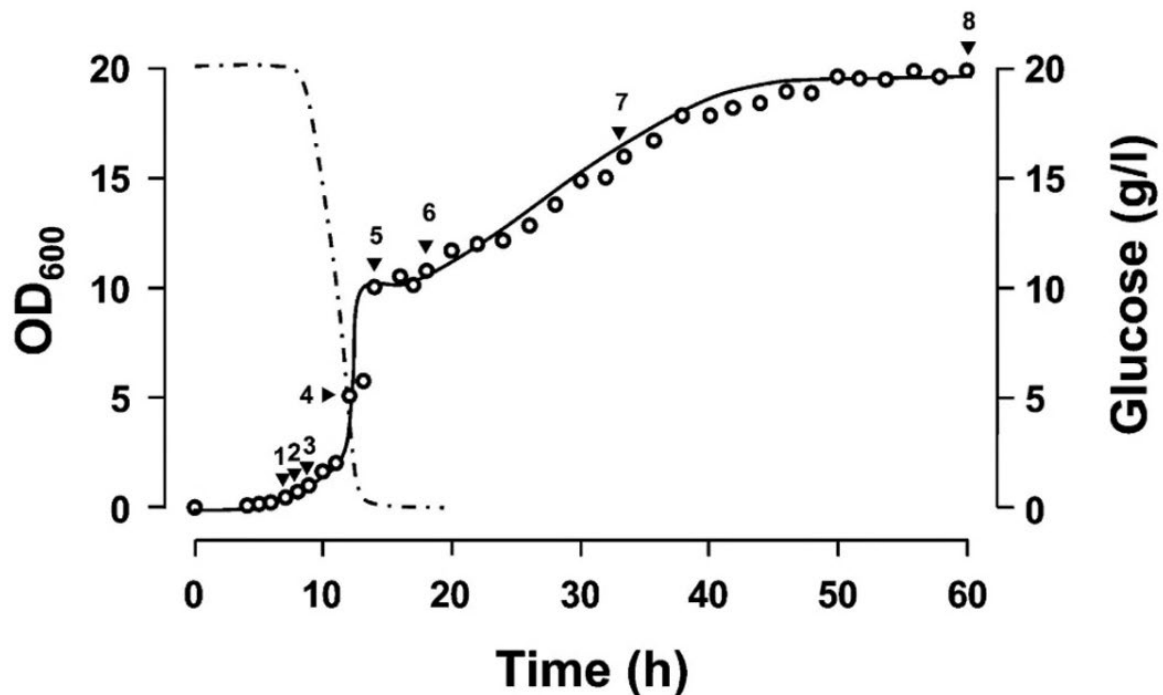


Figure 79: Optical density (i.e., indirect measurement of the cell concentration)(solid line and dots) and glucose concentration (dashed line) vs. Time of a population of cells put in a glucose-based media. The points 1-5 represent the **fermentative phase**, 5-6 the **diauxic shift**, 6-7.5 the **respirative phase**, and from 7.5, the **stationary phase** (From [33]).

4.2. Quiescence: one unique cellular state?

Do cells from an isogenic population reach the same quiescent state after this dynamic change of environment? In other words, is there a single genetically encoded quiescent state and if not, what factors determine the population's heterogeneity?

If the different hallmarks presented previously are happening in most cells, there is always a subpopulation not displaying them, or displaying another form of hallmark (see % in Figure 76). In line with that, two subpopulations were identified based on more general markers such as cell density [34]. The population with the lowest density was called 'non-quiescent' because its viability was null after 21 days of culture, while the other was called quiescent.

Further study identified the 'non-quiescent' cells as cells that could not respire during the respiration phase [19,35] and show a globularization of their mitochondrial network in respiratory phase (instead of fragmentation). They have been termed senescent cells and represent the same population as the 'non-quiescent' cells.

In agreement with this, cells with a null respiratory capacity (*ρ0* cells) rapidly die upon stationary phase. Interestingly, the longevity of these cells can be rescued when adding trehalose to the media [36], a sugar that is normally produced and stored in the cells during respiration.

Hence, to respire or not during the respiratory phase of the culture can lead to a different final state once in stationary phase.

Besides, the appearance of these two populations during the respiratory phase has been recently proposed as a bet-hedging strategy for the cells to adapt to environmental instability [37]. In this study, they performed an abrupt switch between a fermentative and a respiratory media, and found that the cells that could not respire after the switch were growing slightly faster than the cells that could do the metabolic switch. However, how one cell decides to be of one or the other type is unclear.

More generally, it is known that how yeast and other microorganisms respond to their environment is dependent on their history ('termed history-dependent behavior') [38]. Along the same line, cells can anticipate and predict future environmental changes in the context of the standard life-cycle (fermentative phase → respiratory phase → stationary phase). It was indeed shown that exposition to ethanol during the fermentative phase was protective against ROS produced during the respiratory phase [39].

Thus, the quiescence state is most likely shaped by the previous experiences of the cell (for example, respiration).

As an illustration, cells can reach a different quiescent state depending on the type of nutrient depletion they experience (glucose, nitrogen, or phosphate), although several properties such as stress tolerance and increase in cell wall thickness were common [40].

Overall, this suggests that quiescence is not a unique and well-defined state, and is strongly influenced by what the cell experienced in its life. In the context of the standard life-cycle, to respire or not is identified as a source of heterogeneity later on in quiescence. Yet, what determines if a cell will respire during the respirative phase is unclear, nor if the subpopulations pre-exist before respiration.

4.3. Assessing quiescence

One way of assessing the state of quiescence in which the cells are is by putting them in a glucose-based media, let them grow until the stationary phase, and measure how long they remain viable (Chronological Lifespan) (often done using Colony Formation Units (CFU) as a readout (see p.25) (Figure 80, 'Q cells')). Similarly, extracting a fraction of the cells at given timepoints to observe specific markers (see introduction) can also be informative. The caveat of this approach is the absence of information at the single-cell level. In particular, the history of the cell that recreate a colony, or that is being observed, is entirely unknown.

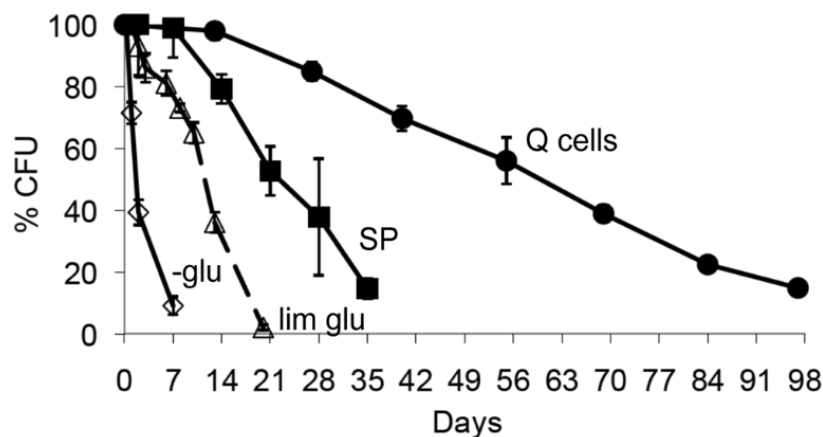


Figure 80: CFU of cells experiencing different environmental conditions? (Q): a normal life-cycle without any perturbation. (SP): cells left until the stationary phase before being put into water. (lim glu): Cells grown in a media with 0.8% glucose before being transferred to a media with 0% glucose (starvation). (-glu): Cells grown in a media with 2% glucose before being transferred to a media with 0% glucose. (From [41])

Another approach consists of observing single-cells longitudinally in microfluidics, by doing synthetic nutrient starvation such as switching from a rich media to a glucose-depleted one. Yet, such treatment ignores the complex dynamical processes that the cell put in place during evolution (see previous section). In support of that, cells experiencing an abrupt nutrient depletion can only survive a few days, while cells that underwent an entire life-cycle and were left in their media, can survive more than 100 days. This suggests that the conditions of growth can impact the quiescent state of the cells (as intuited in the previous section) [41] (Figure 80).

Summary and motivations

Quiescence defines a reversible proliferative arrest accompanied by several molecular processes and a massive reorganization of many cellular structures. However, it does not represent a unique and well-defined state. Even an isogenic population cultured in the same environment will reach heterogeneous states. Besides, the state of quiescence is highly dependent on the cell's past experiences.

In particular, in the context of the yeast life-cycle, respiration seems a source of heterogeneity later on in stationary phase, leading to a quiescent and a 'non-quiescent' (also called senescent) population.

Relative to the methodology, populational assays lead to averaging biases of these heterogeneous populations and fail to capture the history of single-cells (similarly to traditional methods used in replicative aging). When they manage to do it, they ignore the dynamic environments for which the cells have evolved specific ordered responses.

To our knowledge, there is no available method to track single-cells longitudinally while experiencing their natural life-cycle.

Therefore, the objectives of this project were to:

- a) Develop a methodology to track single-cells experiencing all the phases from the yeast life-cycle, from the fermentation to the entry into quiescence and the survival once in quiescence.
- b) Understand the source of heterogeneities and better characterize the 'non-quiescent' population:

What is the source of this non-quiescent population?

Can we predict which cells will become 'non-quiescent' before stationary phase by looking at their history?

Do these cells enter some kind of quiescence before losing viability, or do they die directly?

Results

The result part is composed of a published paper, but a small paragraph will introduce the details of one key component from the methodological pipeline (that is not detailed in the paper).

As described later in the paper (Figure 1), we plugged a culture of cells to an observation microfluidic device to follow single cells throughout the life-cycle. Consequently, the cells present in the observation chambers can experience the same media as the cells in the batch culture. Yet, the concentration of cells is so high in the late stages of the life-cycle ($5 \cdot 10^8$ cells/mL) that a filtration device is needed between the culture and the observation chamber to avoid unwanted cells colonizing it.

Beyond being used to trap cells, microfluidic devices can also be serve to focus particles in a thin streamline. For that, several solutions exist. If of adequate dimensions, a rectangular channel will focus particles above a certain size, along its outer walls [42] (Figure 81, top middle). That is due to an inertial force, called lift force, which is a result of a shear force induced by the flow (due to the parabolic nature of the velocity, since microfluidic flows are mostly Poiseuille flows), and a lift force exerted by the walls (said simply).

From that, adding curvatures to the channels adds other inertial forces such as the Dean force (a drag force with a vortices profil), which focuses the particles onto a unique wall (Figure 81, right)⁴.

Among these channel types, we can cite "bumpy" channels [43], asymmetrically curved channels [44], or spirals [45].

Therefore, by tweaking the dimensions of these channels, it is possible to split a mixed group of objects of different sizes⁵ into ordered focused streams [46].

⁴ The physics of inertial microfluidics will not be further detailed here for the sake of conciseness (more details: [51]).

⁵ Of note, it is also possible to sort particles by shape [48] using the same principle.

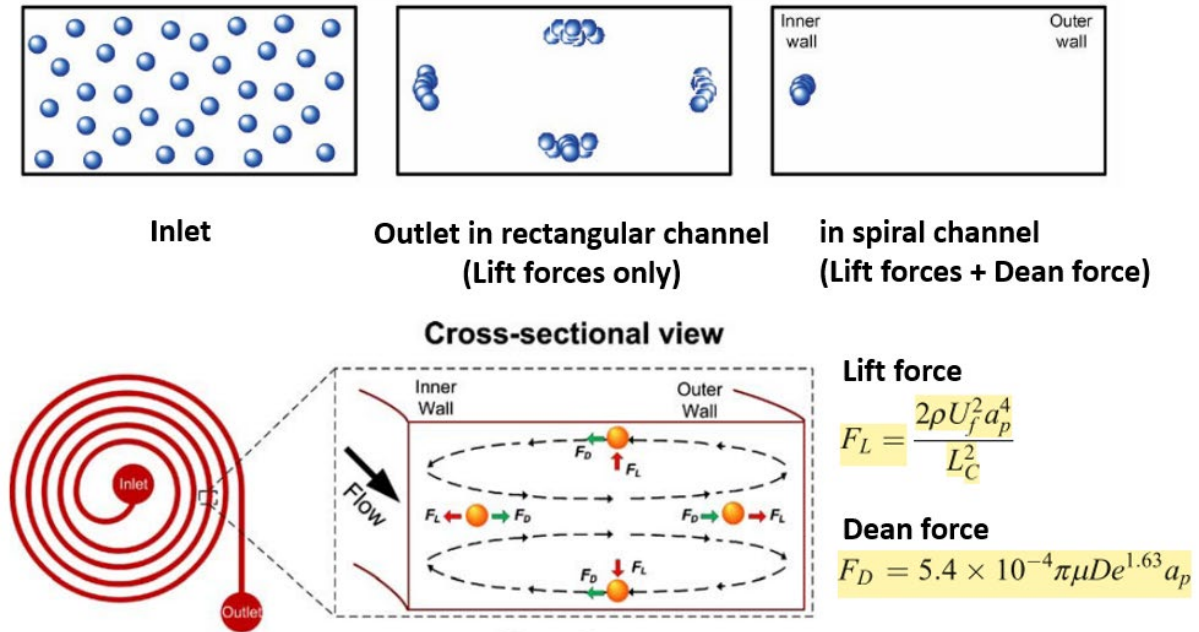


Figure 81: Schematics of the principle of inertial separation. (Top) : Cross-section of a channel, with blue dots representing particles, at the channel's inlet (left), at the outlet of a rectangular channel (middle), or at the outlet of a spiral channel. (Bottom) : A spiral device (left) and a close up on its cross-section indicating the different non-negligible forces at stake (middle). The expression of the forces is indicated on the right, with a_p the size of the particle, ρ the density of the fluid, U_f the average fluid velocity, L_C the narrowest dimension of the channel, μ the viscosity of the fluid, and De the Dean number, which depends on the channel dimensions and the Reynolds number (Adapted from [47]).

This type of particle separation is used, for example, to separate the different types of blood cells from a sample [49,50]. Yet, if the threshold side is well adapted, one can separate particles (like cells) from the media. Hence, among the different device types, we found that the spiral-like was the best compromise between continuous filtration of particles above $3\mu\text{m}$ and hydrodynamic resistivity, and can achieve a 99% filtration efficiency.

Monitoring single-cell dynamics of entry into quiescence during an unperturbed life cycle

Basile Jacquél^{1,2,3,4†}, Théo Aspert^{1,2,3,4†}, Damien Laporte⁵, Isabelle Sagot⁵, Gilles Charvin^{1,2,3,4*}

¹Department of Developmental Biology and Stem Cells, Institut de Génétique et de Biologie Moléculaire et Cellulaire, Illkirch, France; ²Centre National de la Recherche Scientifique, Illkirch, France; ³Institut National de la Santé et de la Recherche Médicale, Illkirch, France; ⁴Université de Strasbourg, Illkirch, France; ⁵Institut de Biochimie et Génétique Cellulaires, UMR 5095 CNRS - Université de Bordeaux, Bordeaux, France, Bordeaux, France

Abstract The life cycle of microorganisms is associated with dynamic metabolic transitions and complex cellular responses. In yeast, how metabolic signals control the progressive choreography of structural reorganizations observed in quiescent cells during a natural life cycle remains unclear. We have developed an integrated microfluidic device to address this question, enabling continuous single-cell tracking in a batch culture experiencing unperturbed nutrient exhaustion to unravel the coordination between metabolic and structural transitions within cells. Our technique reveals an abrupt fate divergence in the population, whereby a fraction of cells is unable to transition to respiratory metabolism and undergoes a reversible entry into a quiescence-like state leading to premature cell death. Further observations reveal that nonmonotonous internal pH fluctuations in respiration-competent cells orchestrate the successive waves of protein superassemblies formation that accompany the entry into a *bona fide* quiescent state. This ultimately leads to an abrupt cytosolic glass transition that occurs stochastically long after proliferation cessation. This new experimental framework provides a unique way to track single-cell fate dynamics over a long timescale in a population of cells that continuously modify their ecological niche.

***For correspondence:**
charvin@igbmc.fr

[†]These authors contributed equally to this work

Competing interest: The authors declare that no competing interests exist.

Funding: See page 13

Received: 19 August 2021

Accepted: 15 October 2021

Published: 16 November 2021

Reviewing Editor: Bavesh D Kana, University of the Witwatersrand, South Africa

© Copyright Jacquél et al. This article is distributed under the terms of the [Creative Commons Attribution License](#), which permits unrestricted use and redistribution provided that the original author and source are credited.

Editor's evaluation

The cell fate program that is set in motion as yeast cells transition from fermentation to respiration is still not well understood. The development of the microfluidic platform described in this manuscript could make a significant contribution to understanding the succession of metabolic and structural changes occurring during this transition. The application of single cell tracking to monitor the temporal program of these changes represents a major technical advance that will be of general interest to researchers interested in defining the developmental programs that contribute to cellular quiescence and longevity.

Introduction

Microorganisms have evolved plastic growth control mechanisms that ensure adaptation to dynamical environmental changes, including those that arise from their proliferation (such as nutrients limitations and cellular secretion in the medium). During its natural life cycle, budding yeast may undergo several metabolic transitions from fermentation to respiration, followed by entry into a reversible state of

proliferation arrest known as quiescence (*De Virgilio, 2012; Gray et al., 2004; Sun and Gresham, 2021; Miles et al., 2021*). Despite quiescence being an essential part of the microorganism life cycle that ensures cell survival over prolonged periods (*Fontana et al., 2010*), it has received little attention compared to the analysis of biological processes in proliferative contexts.

Quiescent cells strongly differ from proliferating cells in terms of metabolic activity and gene expression (*Gray et al., 2004; Miles et al., 2013*). They also display a large body of structural rearrangements in the cytoskeleton, mitochondria, nuclear organization, and the appearance of protein superassemblies, clusters, and aggregates (*Sagot and Laporte, 2019; Sun and Gresham, 2021*). So far, the complex and entangled regulatory processes controlling this particular state's establishment remain poorly understood. In particular, the detailed sequence of events describing how the dynamics of metabolic cues during the natural life cycle drive the entry into quiescence is still missing.

Also, an essential feature of microbial ecosystems in the stationary phase (SP) is the existence of phenotypic variability (*Campbell et al., 2016; Avery, 2006; Holland et al., 2014; Labhsetwar et al., 2013; Ackermann, 2015; Bagamery et al., 2020; Solopova et al., 2014*) and history-dependent behaviors that lead to fate divergences (*Balaban et al., 2004; Cerulus et al., 2018*). In quiescence, the coexistence of heterogeneous cell populations has been previously reported (*Allen et al., 2006; Laporte et al., 2018a*). Nevertheless, how phenotypic diversity emerges in a clonal population during a natural life cycle remains elusive (*Figure 1—figure supplement 1A*). Bridging this gap requires performing longitudinal tracking of individual cells over time. However, an important technical obstacle is that it must be done in population-scale growth experiments to allow cell proliferation to have a collective impact on the environment.

Previous work has used an abrupt transition to glucose starvation to study how cells reorganize upon entry into the SP in various biological contexts (*Munder et al., 2016; Bagamery et al., 2020*). While this experimental framework may be helpful for studying standard properties of cells undergoing proliferation arrest, the results cannot be transposed to the context of entering quiescence during an undisturbed life cycle, in which cells undergo a sequence of metabolic transitions and feed-back continuously into the composition of their environment. Indeed, an essential condition to reach a *bona fide* quiescence state (i.e., the ability to recover proliferation after prolonged arrest) is that cells must experience a respiration phase (RP) to accumulate carbohydrates, which does not occur upon abrupt glucose starvation (*Ocampo et al., 2012; Li et al., 2013*). In addition, different nutrient limitations lead to distinct quiescent states (*Klosinska et al., 2011*). Therefore, it is essential to develop novel methods that capture the true dynamics of cell transitions as they may occur in their ecological niche (*Miles et al., 2021*).

Here, we report the development of a microfluidic platform for single-cell ecology, allowing continuous tracking of individual cells' fate during an unperturbed full life cycle (up to 10 days). Using a fluorescent reporter of internal pH (*Mouton et al., 2020; Miesenböck et al., 1998; Dechant et al., 2010; Munder et al., 2016*), we observe that the diauxic shift (DS) witnesses a cell fate divergence, where a minority of cells experience a metabolic crash similar to that observed upon an abrupt starvation (*Bagamery et al., 2020*). Interestingly, our long-term tracking capabilities further reveal that these cells experience a premature yet reversible induction of cellular reorganizations that coincide with limited survival. In contrast, respiration-competent cells experience fluctuations in internal pH in sync with metabolic transitions that drive successive waves of cellular reorganizations and a stochastic switch to a glass transition of the cytoplasm long after proliferation cessation. Altogether, our analysis reveals how metabolic changes encountered by yeast cells during an unperturbed life cycle coordinate the temporal control of complex cellular reorganizations.

Results

To track individual cell behavior during an unperturbed life cycle, we set up a device composed of a 25 ml liquid yeast culture (YPD medium) connected to a microfluidic device for single-cell observation (*Figure 1A, Figure 1—figure supplement 1B and C, 1F*). Thanks to a closed recirculation loop, individual cells trapped in the microfluidic device could be imaged over time while experiencing the same environmental changes as the population liquid culture. To prevent clogging in the microfluidic device due to the high cell density in the culture (up to 10^9 cells/ml), we designed a filtration device based on inertial differential migration (*Kuntaegowdanahalli and Papautsky, 2008*). Using this technique, cells were rerouted back to the liquid culture before entering the microfluidic device (*Figure 1A*).

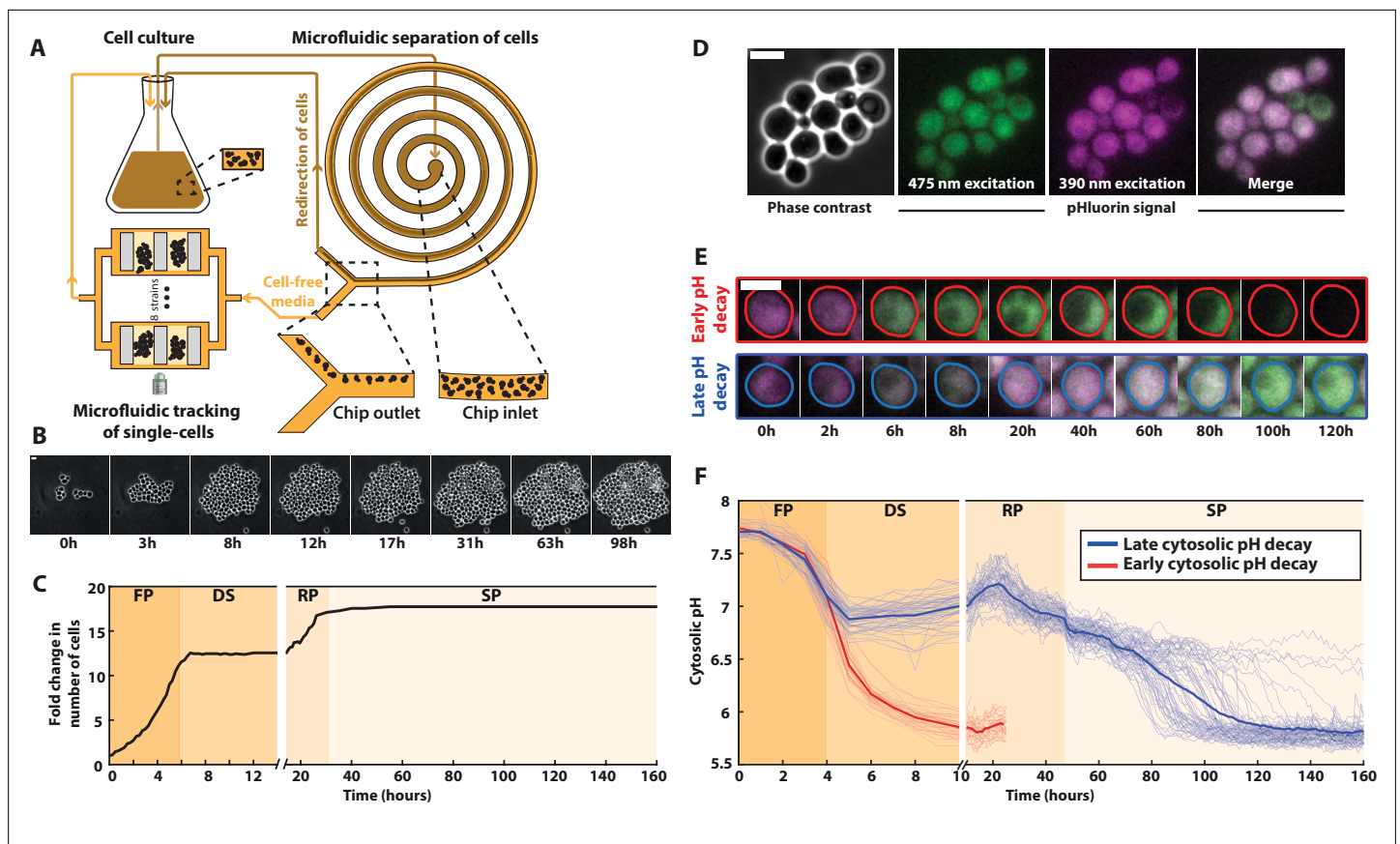


Figure 1. A microfluidic platform for single-cell tracking during the yeast proliferation cycle. **(A)** Schematics of the experimental setup, representing the liquid culture flask, the observation microfluidic device with trapped cells, and the microfluidic filtering device designed to redirect the cells back to the liquid culture while recirculating the medium of the liquid culture to the observation microfluidic chamber. **(B)** Sequence of phase-contrast images of cells growing in the microfluidic device. Scale bar = 5 μm . **(C)** Fold increase in cell number over an entire life cycle for the microcolony displayed in B; each shaded area represents a distinct proliferation phase, which was determined using piecewise linear fitting to cell proliferation data (see Materials and methods and **Figure 1—figure supplement 1G** for details): fermentation phase (FP), diauxic shift (DS), respiration phase (RP), and stationary phase (SP). **(D)** Cluster of cells showing typical phase-contrast, fluorescence, and overlay images using the cytosolic pH sensor pHluorin. **(E)** Typical sequences of overlaid fluorescence images obtained with the pHluorin sensor at indicated time points. Colored lines indicate cell contours. **(F)** Quantification of the absolute cytosolic pH as a function of time; each line represents an individual cell, while the bold line indicates the average among cells with either an early (red lines, $N = 32$ cells displayed) or late (blue line, $N = 64$ cells displayed) decaying pH.

The online version of this article includes the following video and figure supplement(s) for figure 1:

Source data 1. Spreadsheet containing the numerical values used to plot panels 1C and D.

Figure supplement 1. Design and calibration of the experimental setup.

Figure supplement 2. Population measurements of cell growth during an entire life cycle.

Figure supplement 3. Single-cell dynamics of entry into stationary phase in BY versus W303 strains.

Figure 1—video 1. Top: phase-contrast video of a microcolony growing in the observation device during the life cycle of the culture.

<https://elifesciences.org/articles/73186/figures#fig1video1>

Figure 1—video 2. Top: phase-contrast (left) and pHluorin (right, channels 1 and 2 merged as in Figure 1) video of a microcolony growing in the observation device during the life cycle of the culture.

<https://elifesciences.org/articles/73186/figures#fig1video2>

Optical density (OD) and fluorescence measurements revealed a filtration efficiency superior to 99%, reducing the concentration of cells entering the device by two orders of magnitude (**Figure 1—figure supplement 1–S1E**), and allowing us to image the cells over up to 10 days. We also checked that the same filtration device could sort *S. pombe* cells with 92% efficiency, thus highlighting the versatility of the methodology.

Using this methodology, we successfully recapitulated the successive proliferation phases occurring at the population level upon carbon source exhaustion with single-cell resolution (**Richards, 1928**), namely: a rapid exponential growth (doubling time = 84 ± 12 min) corresponding to glucose fermentation (referred to as the fermentation phase or FP in the following, from $t = 0$ to $t = 5.5$ hr), followed by a sharp growth arrest, or DS (from $t = 5.5$ to $t = 13.9$ hr); then, the resumption of a slow proliferative regime (doubling time = 307 ± 52 min) which is associated with the use of ethanol as a carbon source for a respiratory metabolism (RP, from $t = 13.9$ to $t = 31.6$ hr) and a final cell proliferation cessation occurring upon carbon source exhaustion, leading to SP, see **Figure 1B, C** and **Figure 1—video 1**. **Figure 1—source data 1**. To make sure that this growth pattern was not specific to the BY strain used for this experiment, we also made population growth measurements in various prototrophic and auxotrophic strains, and obtained similar results (**Figure 1—figure supplement 2**). To quantify the data further, the transition times between each metabolic phase were determined using piecewise exponential fits (**Figure 1—figure supplement 1 S1G**). By refeeding the cells with fresh YPD medium after 10 days, we observed that up to ~80 % of them reentered the cell cycle within 5 hr (**Figure 1—figure supplement 1 S1H**). This result confirmed the reversibility of cell proliferation arrest and testified that cells establish *bona fide* quiescence in our growth conditions (**Laporte et al., 2018b**).

A drop in medium pH has long been reported to coincide with the resources' exhaustion during microbial growth (**Burtner et al., 2009**). Yet, how internal pH evolves over an entire life cycle has never been investigated. To address this, we used the ratiometric fluorescent probe of cytosolic pH, pHluorin (**Figure 1D**, **Miesenböck et al., 1998**; **Mouton et al., 2020**), which was calibrated to display the actual internal pH (**Figure 1D–F** and **Figure 1—figure supplement 1–S1I**). Using this readout, we observed that the pH, which was initially around 7.7, started to decline synchronously in all cells during the F phase (**Figure 1E, F** and **Figure 1—video 2**). At the onset of the DS, most cells (88%, $N = 466$) abruptly reached a plateau (pH ~6.9, blue lines on **Figure 1F**) followed by a slight pH increase (up to pH ~7.2) that coincided with entry into a respiratory metabolism. In contrast, a minority (12%, $N = 466$) of cells (**Figure 1E** and red lines on **Figure 1F**) experienced a further drop in pH down to about 5.8 during the DS. In this subpopulation, the fluorescence signal progressively disappeared, precluding monitoring the internal pH for more than 20 hr in a reliable manner.

In cells with high internal pH during the DS, the pH gradually declined after reaching a local maximum during the R phase. These cells then experienced a sharp pH drop down to about 5.8, which occurred at very heterogeneous times during the SP, unlike the cells with an early pH drop. Altogether, these observations revealed unprecedented dynamics of internal pH during the yeast life cycle: pH variations appeared to be in sync with the sequence of proliferation phases, suggesting that internal pH is a crucial marker of the cells' metabolic status during their life cycle.

These continuous pH measurements also unraveled a divergence in cell fate at the DS, leading to the early emergence of heterogeneity within the population, in line with previous observations made upon abrupt starvation (**Bagamery et al., 2020**). This phenomenon was also observed in a W303 strain (**Figure 1—figure supplement 3**). Recent studies have shown that the activation of respiration was a crucial metabolic response to survive glucose deprivation (**Weber et al., 2020**), enabling carbohydrate storage (**Ocampo et al., 2012**) and long-term viability (**Laporte et al., 2018a**). Interestingly, it was shown that a respiration defect was naturally observed in about 10 % of cells upon proliferation cessation following glucose exhaustion (**Laporte et al., 2018a**). Hence to further characterize whether differences in metabolic status drove the emergence of divergent cell fates at the DS, first, we quantified cellular proliferation over time using single-cell area measurements. We found that cells with a late pH drop resumed growth and roughly doubled their biomass during the R phase (blue lines on **Figure 2A** and **Figure 2—source data 1**) in agreement with **Figure 1C**.

In contrast, cells that experienced an early pH drop (red lines on **Figure 2A**) did not recover during the R phase, suggesting that they could not transition to respiratory metabolism. Indeed, these cells did not resume growth when adding lactate (i.e., a nonfermentable carbon source) to the medium neither (**Figure 2—figure supplement 1A**). However, most of them were still viable after 3 days in SP, even though their survival declined faster than adapting cells (**Figure 2B**).

Second, to assess cellular respiratory function, we used the mitochondrial *Ilv3*-mCherry marker (**Laporte et al., 2018a**). Whereas the mitochondrial network architecture appeared similar (i.e., tubular) in all cells before the DS, proliferating cells in the R phase displayed a fragmented mitochondria phenotype typical of respiring cells (blue cell, **Figure 2C**). In contrast, nonproliferating

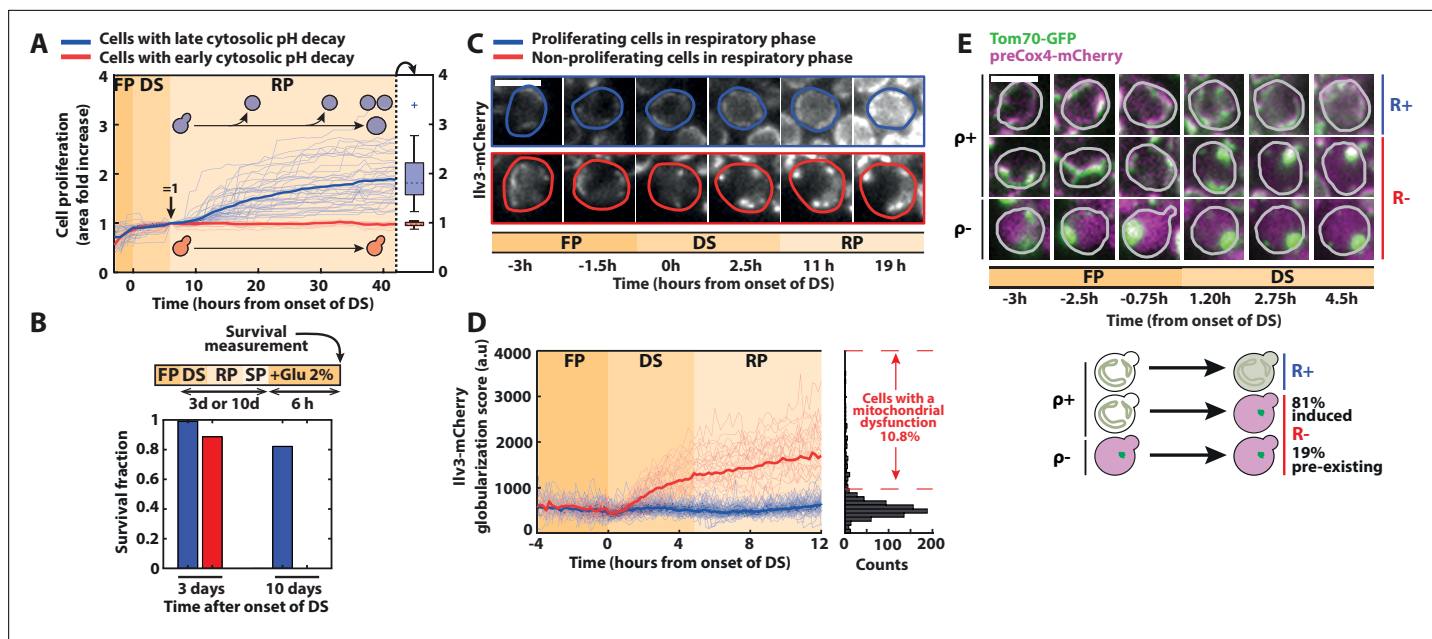


Figure 2. Divergent cell fates induced by a metabolic challenge at the diauxic shift (DS). **(A)** Quantification of single-cell growth during F, DS, and R phases, as defined in **Figure 1**. Each line represents the fold area increase (including buds) of single cells over time, normalized by cell area at the end of the DS ($N = 50$). The bold lines represent the averages over all the cells that experience fast (red) and slow (blue) pH decay, respectively. Right: box plot indicating the fold increase in cellular area in each subpopulation during the R phase ($N = 40$ for the slow pH decay population, $N = 10$ for the fast pH decay population). **(B)** Fraction of surviving cells among adapting (blue bars) and nonadapting (red bars) cells, measured by quantifying the cells' ability to resume growth 6 hr after reintroduction of fresh medium (2 % glucose) at 3 ($N = 53$ for red bars, $N = 221$ for blue bars) or 10 days ($N = 114$ for red bars, $N = 403$ for blue bars) after the DS. Scale bar = 5 μm . **(C)** Representative sequence of fluorescence images obtained with the Ilv3-mCherry mitochondrial marker at the indicated time points for the different classes of cells, as indicated by the colored contour. **(D)** Single-cell quantification of a globularization score (see Materials and methods) from fluorescence images over time for both adapting (blue line; $N = 81$) and nonadapting cells (red line; $N = 28$). The bold lines represent averages within each subpopulation. Right: histogram of globularization score for each cell ($N = 720$). **(E)** Preexisting versus newly occurring respiratory defects in cells experiencing the DS. Sequence of fluorescent images (overlay of preCox4-mCherry and Tom70-GFP) at indicated times. Scale bar = 5 μm . Each line represents a different type of cell fates (top: $\rho + R+$; middle: $\rho + R-$; bottom: $\rho - R-$). Schematics: representation of the different cell fates based on the fluorescence patterns of preCox4-mCherry and Tom70-GFP, with the quantification of the fraction of each subpopulation ($N = 701$).

The online version of this article includes the following video and figure supplement(s) for figure 2:

Source data 1. Spreadsheet containing the numerical values used to plot panels 2A and D.

Figure supplement 1 Complementary analyses of the divergent cell fate at the diauxic shift.

Figure 2—video 1. Phase-contrast (left) and Ilv3-mCherry (right) video of a microcolony growing in the observation device during the life cycle of the culture.

<https://elifesciences.org/articles/73186/figures#fig2video1>

cells underwent a globularization of their mitochondrial network (red cell, **Figure 2C** and **Figure 2—video 1**). We further quantified the mitochondrial network's reorganization dynamics by computing a custom aggregation index that discriminates globularized versus tubular and fragmented mitochondria (**Figure 2D** and **Figure 2—source data 1**, see Materials and methods for details). Based on the clear distinction in the aggregation index between adapting and nonadapting cells, we measured that about ~10 % of the cells could not transition to a respiratory metabolism (at $t = 12$ hr post-DS, **Figure 2D**), in agreement with previous findings (Laporte et al., 2018a). Importantly, this quantification revealed that the mitochondrial globularization in nonadapting cells was temporally closely associated with the DS since it started as early as 1h20 ($p < 0.05$) after its onset (**Figure 2C,D**). Altogether, these results demonstrate that proliferating and nonproliferating cells experienced divergent cell fates at the DS based on their ability to switch to respiration; hence, they were referred to as respiration positive ($R+$) and negative ($R-$), respectively. Also, these results suggest that the inability of $R-$ cells to activate a respiratory metabolism was either triggered by this metabolic challenge or, alternatively, preexisted the DS, knowing that respiratory deficient cells (i.e., $\rho -$ cells) are common in

the BY background (yet less so in W303 strains) due to the genetic instability of mitochondrial DNA (Dimitrov *et al.*, 2009).

To discriminate between these two hypotheses, we used the mitochondrial localization marker Tom70-GFP (Tom70 is a protein of the outer mitochondrial membrane) and a preCox4-mCherry fusion (preCox4 is a nuclear-encoded mitochondrial protein that is imported only in functional mitochondria Veatch *et al.*, 2009), to assess the cells' ability to respire (Fehrmann *et al.*, 2013). Using these markers, we first checked that all R+ cells maintained a functional preCox4-mCherry import from fermentation to respiration (i.e., they were ρ + cells, Figure 2E). Then, we observed that among the R− cells, only a minority (i.e., 19%) had a dysfunctional mitochondrial import before the DS, indicating that they had a preexisting respiratory deficiency (see ρ − cells in Figure 2E). In contrast, the vast majority of R− cells (81%) transitioned from ρ + to ρ − during the DS. This result demonstrates that the respiration defect observed in R− cells occurred concomitantly with the environmental switch and was therefore not due to a preexisting condition. Also, we showed that the progeny quite faithfully inherited it (inheritance index = 0.52, i.e., is smaller than 1, see Figure 2—figure supplement 1B and Material and methods for details). Altogether, these observations supported a scenario in which a fate divergence occurred early at the onset of the DS, where R+ cells quickly switched to a respiratory metabolism, while R− cells failed to do so.

As numerous cellular reorganizations occur during entry into quiescence (Sagot and Laporte, 2019), we sought to quantitatively determine how they are coordinated with metabolic transitions during the life cycle. Indeed, the metabolism controls internal cellular pH, which in turn can induce significant physicochemical changes in the proteome, such as protein aggregation and phase transition (Munder *et al.*, 2016; Dechant *et al.*, 2010). To do this, we monitored the dynamics of formation of supramolecular bodies associated with quiescence or the response to starvation: P-bodies formation (using the Dhh1-GFP fusion Beckham *et al.*, 2008; Balagopal and Parker, 2009; Mugler *et al.*, 2016), metabolic or regulatory enzymes prone to aggregation (Gln1-GFP and Cdc28-GFP) (Narayanaswamy *et al.*, 2009; Petrovska *et al.*, 2014; Shah *et al.*, 2014), actin bodies formation (Abp1-GFP) (Sagot *et al.*, 2006), and proteasome storage granules (PSGs, using the Scl1-GFP fusion) (Laporte *et al.*, 2008; Peters *et al.*, 2013).

We found that the cellular reorganizations were highly coordinated with the sequence of metabolic phases and the cellular proliferation status (Figure 3A and Figure 3—source data 1): in R+ cells, Dhh1-GFP and Gln1-GFP (Figure 3—video 1) foci appeared at the onset of the DS, then were partially dissolved during the R phase, and reappeared upon entry into SP. Other hallmarks of proliferation cessation, such as actin bodies, PSGs, and other protein foci (Cdc28-GFP), showed up only at the end of the R phase. Importantly, we observed that R− cells also experienced a consistent formation of fluorescent foci for the markers that we monitored, yet, unlike R+ cells, they all appeared during the DS. In addition, all these foci ultimately disappeared, presumably as a consequence of the premature cell death observed in this subpopulation.

By overlapping the dynamics of fluorescence foci formation with that of internal pH (from Figure 1F), we noticed that the formation of bodies overall coincided with variation in absolute pH level in both R+ and R− cells, even though it appeared at different timescales. This finding is compatible with the hypothesis that the drop in internal pH – which reflects a decrease in metabolic activity – actually drives successive waves of body formation and the appearance of quiescence hallmarks. Indeed, upon the DS, a pH decrease down to ~7 would trigger the formation of Gln1 and Dhh1 foci in both R+ and R− cells. In R+ cells, the rise of the pH associated with proliferation resumption in the R phase would induce the disassembly of these structures until the pH reaches 7 again, after carbon source exhaustion in SP. In both R+ and R−, actin bodies, PSG, and Cdc28 foci would form only when the intracellular pH reaches 6.

To further check this hypothesis, since energy depletion was shown to induce a global modification of the cytoplasm to a glassy state (Munder *et al.*, 2016), we sought to observe these transitions by monitoring the frame-to-frame displacement of Gln1-GFP foci over time (Figure 3B, Munder *et al.*, 2016). This marker was chosen because foci are already present at the DS. We found that the mobility of Gln1-GFP foci decreased sharply in R− cells during the DS (Figure 3—video 1) and much later in R+ cells, consistently with the differences observed regarding the times of pH drops in both populations (Figure 3C). To better establish the links between pH and mobility, we exploited the fact that lipid droplets (LDs) could be conveniently observed using phase-contrast images (Heimlicher

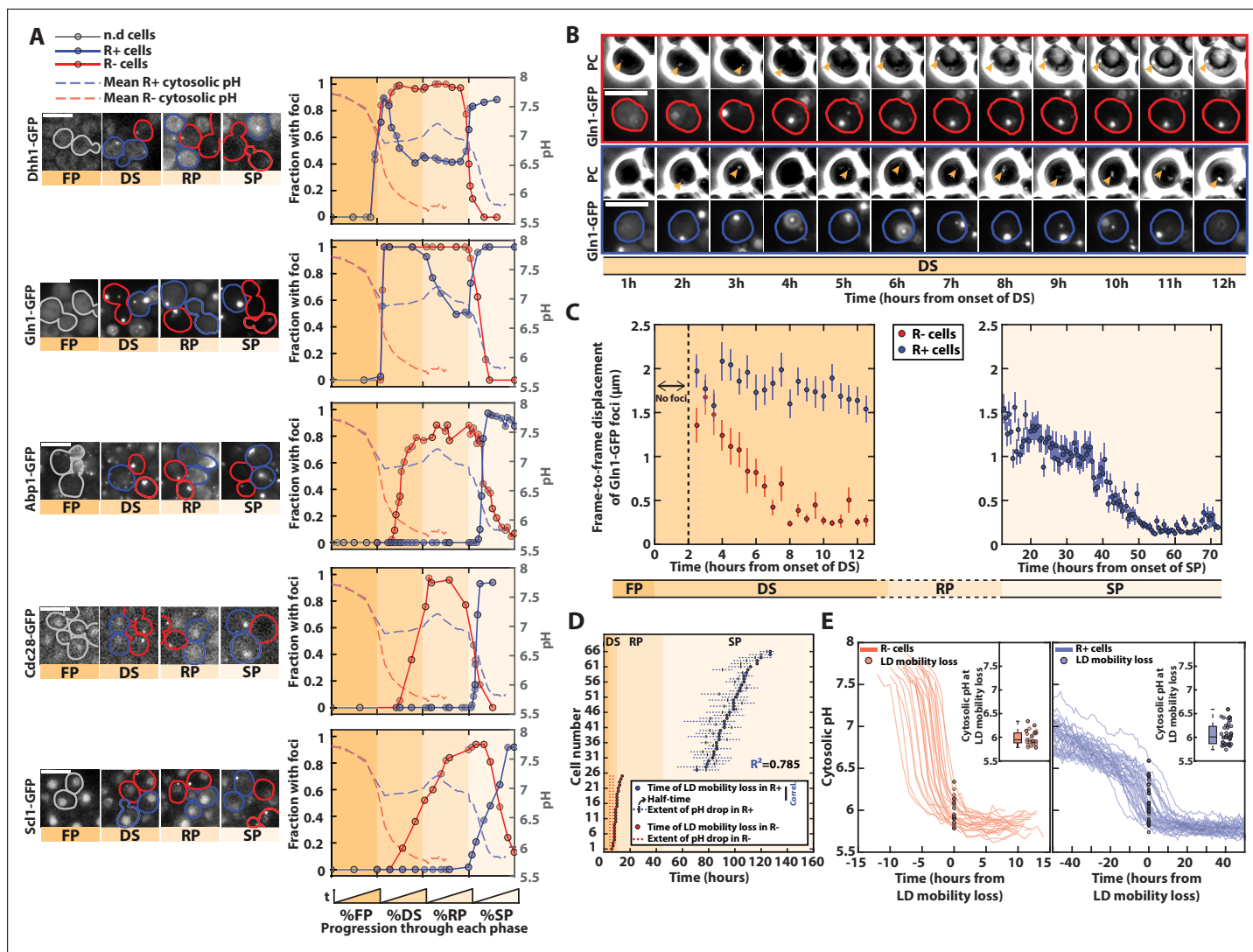


Figure 3. pH-driven phase transition to a gel-like state upon proliferation cessation. **(A)** Observation and quantification of fluorescent foci formation for the indicated fusion proteins (Dhh1-GFP, Gln1-GFP, Abp1-GFP, Cdc28-GFP, and Scl1-GFP). Left: each strip of fluorescence images displays unrelated cells at different phases during entry into stationary phase (SP). Colored contours indicate cells of interest (red for R- cells, blue for R+ cells, gray before the diauxic shift [DS]). Right: quantification of the fraction of cells with foci for each indicated fluorescent marker, as a function of the normalized time spent in each phase. Each solid colored line represents an indicated subpopulation of cells. The dashed colored lines represent the evolution of pH over time, based on data obtained in **Figure 1**; $N > 25$ cells for each marker. Scale bar = 5 μ m. **(B)** Mobility of Gln1-GFP fluorescent foci and observation of lipid droplets (LDs). Sequence of phase-contrast and Gln1-GFP fluorescence images at indicated time points. The colored contours indicate the cells of interest (red and blue for R- and R+ cells, respectively). The orange arrowheads on the phase-contrast images indicated the LD. Scale bar = 5 μ m. **(C)** Mobility of Gln1-GFP fluorescent foci. Quantification of average frame-by-frame displacement of Gln1-GFP foci for R+ and R- cells (blue and red points, respectively) starting after the appearance of foci ($t > 2$ hr after the onset of DS). Error bars represent the standard error on mean ($N = 51$ for R- and $N = 110$ for R+). The right plot only features R+ cells, since Gln1-GFP foci are no longer present in the SP phase in R- cells ($N = 28$). **(D)** Temporal link between the drop in internal pH and the time of mobility loss of LD ($N = 25$ for R- and $N = 43$ for R+). Each line corresponds to a single cell and represents the extent of pH drop (see Material and methods for details). Half-times of these drops are represented by a small vertical bar. The time of LD mobility loss is displayed as a dot. Of note, two cells did not display a pH drop, nor an LD mobility loss, hence they are not displayed on the plot. **(E)** Measurement of internal pH at the time of LD mobility loss. Overlay of internal pH in single cells obtained after synchronizing all traces with respect to the time of LD mobility loss, for R- (left) and R+ cells (right). Each dot represents the pH at the time of mobility loss in each cell ($N = 25$ for R- and $N = 43$ for R+). Inset: box plot showing the distribution of pH values of every single cell at the time of LD mobility loss.

The online version of this article includes the following video and figure supplement(s) for figure 3:

Source data 1. Spreadsheet containing the numerical values used to plot panel 3A.

Source data 2. Spreadsheet containing the numerical values used to plot panels 3D and E for R+ cells.

Figure 3 continued on next page

Figure 3 continued

Source data 3. Spreadsheet containing the numerical values used to plot panels 3D and E for R[−] cells.

Figure supplement 1 Coincidence of lipid droplets and Gln1-GFP foci mobility.

Figure 3—video 1. Phase-contrast (left) and Gln1-GFP (right) video of a microcolony growing in the observation device from fermentation phase to respiration phase.

<https://elifesciences.org/articles/73186/figures#fig3video1>

et al., 2019). Similarly, the time of loss of LDs mobility correlated very well with that of Gln1-GFP foci (**Figure 3—figure supplement 1A**). By quantifying both the time of loss of LD mobility and the dynamics of pH drop in single cells, we observed that both events were tightly correlated in all cells, despite the large cell-to-cell heterogeneity in the time of pH drop in R⁺ cells (**Figure 3D**, **Figure 3—figure supplement 1B**, **Figure 3—source data 2** and **Figure 3—source data 3**). Also, after synchronizing all single-cell trajectories from the time of loss of LD mobility, we showed that the mobility loss of the cytoplasm occurred at a similar pH ~6 in both R⁺ and R[−] cells (**Figure 3E**, **Figure 3—source data 2** and **Figure 3—source data 3**). Therefore, these observations suggest that the internal pH, which displays a very dynamic behavior during the yeast life cycle, induces waves of cellular structural remodeling that ultimately triggers a global transition of the cytoplasm to a gel-like state. This model is further supported by the concomitance between the premature pH drop and the phase transition in respiratory deficient (R[−]) cells. Altogether, it suggests that, upon nutrient exhaustion, cells undergo stereotypical pH-dependent structural reorganizations, no matter their respiratory status. R[−] cells' inability to switch to respiration, which ultimately compromises the long-term viability in this subpopulation (*Ocampo et al., 2012; Weber et al., 2020*), makes this transition precocious, and explains the divergent cell fates in the population at the DS.

Discussion

In this study, we have developed a new microfluidic platform that allows us to monitor a full cell proliferation cycle in liquid culture with single-cell resolution. Individual cell tracking and quantitative fluorescence measurements provide a unique dynamic assessment of the successive metabolic transitions from fermentation to the SP observed in a liquid culture submitted to nutrients exhaustion. In contrast to most previous studies that used abrupt environmental switches to investigate the metabolic response to starvation, our methodology recapitulates the unperturbed dynamics of nutrients experienced by cells during a life cycle in laboratory conditions. We envision that this methodology could be further applied to other contexts in which collective cell behavior impacts the environment, which in turn shapes individual cellular responses – for example, metabolic oscillations (*Tu et al., 2005*) and cooperative behaviors (*Dal Co et al., 2020; Campbell et al., 2015*).

Continuous monitoring of cell growth and mitochondrial markers revealed a clear divergence in cell fate, where a minority of them failed to establish a respiratory metabolism, in line with recent observations obtained using an abrupt medium change (*Bagamery et al., 2020*). The dramatic drop in internal pH upon proliferation cessation in R[−] cells at the DS suggests that the failure to transition to respiration induces a major loss of energy homeostasis in this subpopulation, that may, in turn, compromise long-term viability (*Ocampo et al., 2012; Weber et al., 2020*). By and large, this phenomenon could not be explained by preexisting phenotypic differences in the population during the FP (*Bagamery et al., 2020*) but rather appeared to be triggered by the metabolic challenge associated with the exhaustion of glucose.

Previous studies have unraveled how changes in cytosolic pH – including upon nutrient exhaustion – control protein supramolecular assemblies (*Peters et al., 2013; Petrovska et al., 2014*). Our analysis shows that nonmonotonous fluctuations in pH level occur in sync with metabolic transitions during an unperturbed life cycle. Further, it reveals that successive pH drops are closely temporally related to the formation of many protein bodies and granules, despite the large cell-to-cell temporal variability associated with the onset of these events. Interestingly, since the structural reorganization of many protein complexes is one of the well-described hallmarks of quiescence (*Sagot and Laporte, 2019*), our observations thus suggest that internal pH acts as a key controller that drives waves of structural changes at well-defined pH levels during entry into quiescence. That R[−] cells display foci formation

similarly as the R+ cells provide further support to a model of stereotypical structural reorganizations driven by energy depletion and transduced by internal pH level.

In addition to monitoring the superassembly of specific markers, we showed that the transition to SP is accompanied by a transition of the cytoplasm to a glassy-like phase, hence transposing previous observations (Parry et al., 2014; Joyner et al., 2016; Munder et al., 2016) to the context of an unperturbed life cycle in budding yeast (Heimlicher et al., 2019). Importantly, the appearance of the glassy-like state occurs right at the DS in the R– cells and is significantly delayed and variable in time in R+ cells. We propose that the start of respiration upon glucose exhaustion prevents a precocious glass transition, which might be detrimental to cell viability if it occurs in an uncoordinated manner with other cellular reorganizations processes (e.g., energy storage)(Ocampo et al., 2012; Weber et al., 2020).

The abrupt and concomitant transition of all cells during the DS shows how the rapid evolution of the environment at this precise moment drives cell behavior in a deterministic manner, in the same way as during abrupt starvation (Bagamery et al., 2020; Munder et al., 2016). Conversely, the remarkable cell-to-cell temporal heterogeneity during the transition to a glassy state in R+ cells suggests that the cells have a developmental program whose progression is partly stochastic, that is, not entirely determined by the external environment. This last observation further supports that it is impossible to follow the process of entry into quiescence faithfully by imposing the dynamics of environmental changes (Miles et al., 2021) or based on population measurements only. Further studies using our methodology may allow us to discover how the succession of the different key steps of this developmental process contributes to establishing the specific physiological properties of quiescent cells (e.g., long-term survival and stress tolerance).

Materials and methods

Key resources table

Reagent type (species) or resource	Designation	Source or reference	Identifiers	Additional information
Strain, strain background (S. cerevisiae, BY, mat a)	WT	Euroscarf; PMID:9483801		
Strain, strain background (S. cerevisiae, BY, mat a)	BJQ-3	Thermo Fisher; PMID:14562095		
Strain, strain background (S. cerevisiae, BY, mat a)	BJQ-7	Thermo Fisher; PMID:14562095		
Strain, strain background (S. cerevisiae, BY, mat a)	BJQ-28	Thermo Fisher; PMID:14562095		
Strain, strain background (S. cerevisiae, BY, mat a)	BJQ-23	Thermo Fisher; PMID:14562095		
Strain, strain background (S. cerevisiae, BY, mat a)	BJQ3-3	Thermo Fisher; PMID:14562095		
Strain, strain background (S. cerevisiae, BY, mat a)	Y10794	Sagot Lab; PMID:18504300		
Strain, strain background (S. cerevisiae, BY, mat a)	YSF120-9D	Charvin Lab; PMID:24332850		
Strain, strain background (S. cerevisiae, BY, mat a)	SMY12	Veenhoff lab; PMID:32990592		
Strain, strain background (S. cerevisiae, BY, mat a)	BJ2-44	Thermo Fisher; PMID:14562095		
Strain, strain background (S. cerevisiae, BY, mat alpha)	Y11453	This paper		Results from a cross between Y11314 (Daignan-Fornier lab) and Y11453
Strain, strain background (S. cerevisiae, S288C, mat alpha)	Y2658	Daignan-Fornier Lab; PMID:19795422		
Strain, strain background (S. cerevisiae, FY, mat a)	Y2438	Daignan-Fornier Lab; PMID:7762301		

Continued on next page

Continued

Reagent type (species) or resource	Designation	Source or reference	Identifiers	Additional information
Strain, strain background (<i>S. cerevisiae</i> , FY, mat a)	Y2439	Daignan-Fornier Lab; PMID:7762301		
Strain, strain background (<i>S. cerevisiae</i> , FY, mat a/alpha)	Y12322	This paper		Results from a cross between Y2438 and Y2439
Strain, strain background (<i>S. cerevisiae</i> , FY, mat a)	Y5738	Sagot Lab; PMID:30299253		
Strain, strain background (<i>S. cerevisiae</i> , W303, mat a)	Y8037	Sagot Lab; PMID:24338369		
Strain, strain background (<i>S. cerevisiae</i> , BY, mat a)	Y6735	Sagot Lab; PMID:24338369		
Strain, strain background (<i>S. cerevisiae</i> , W303, mat alpha)	BJQ-11	Alberti Lab; PMID: PMID:27003292		

Strains

All strains used in this study are congenic to BY4741 (see *Supplementary file 1* for details), unless specified otherwise (*Figure 1—figure supplement 2* and *Figure 1—figure supplement 3*).

Cell culture

Freshly thawed cells were grown overnight. In the morning, 2 ml of the culture was inoculated into a 25 ml flask containing fresh YPD medium. After 5 hr, 2 ml of culture was used to load the cells into the microfluidic device, and the rest was used as circulating media for the experiment. This 5 hr delay was chosen so that cells only spend two to three divisions in a FP to limit the number of cells in the microfluidic device at the DS.

Microfluidics and microfabrication

Microfabrication

Microfluidic chips were generated using custom-made microfluidic master molds. The master molds were made using standard soft-photolithography processes using SU-8 2025 photoresist (Microchem, USA). The designs (which are available for download on github: https://github.com/TAspert/Continuous_filtration (Aspert, 2021) copy archived at [swih:1:rev:8476f782bf6ff8ff2a9c78172cc8f072cc73916](https://www.swh.io/rev/8476f782bf6ff8ff2a9c78172cc8f072cc73916)) were made on AutoCAD (Autodesk, USA) to produce chrome photomasks (jd-photodata, UK). The observation device was taken from a previous study (Goulev et al., 2017).

The mold of the dust filter chip (see below for details) was made by spin coating a 25 µm layer of SU-8 2025 photoresist on a 3" wafer (Neyco, FRANCE) at 2700 rpm for 30 s. Then, we used a soft bake of 7 min at 95 °C on heating plates (VWR) followed by exposure to 365 nm UVs at 160 mJ/cm² with a mask aligner (UV-KUB3 Kioé, FRANCE). Finally, a postexposure bake identical to the soft bake was performed before development using SU-8 developer (Microchem, USA).

The mold for the spiral-shaped cell filter device (see below for details) was obtained by spinning SU-8 2025 at 1750 rpm to achieve a 50 µm deposit. Bakes were 6 min long at 95 °C and UV exposure was done at 180 mJ/cm². A hard bake at 150 °C for 15 min was then performed to anneal potential cracks and to stabilize the resist.

Finally, the master molds were treated with chlorotrimethylsilane to passivate the surface.

Microfluidic chip fabrication

The microfluidic devices were fabricated by pouring polydimethylsiloxane (PDMS, Sylgard 184, Dow Chemical, USA) with its curing agent (10:1 mixing ratio) on the different molds. The chips were punched with a 1 mm biopsy tool (Kai medical, Japan) and covalently bound to a 24 × 50 mm coverslip using plasma surface activation (Diener, Germany). The assembled chips were then baked for 1 hr at 60 °C to consolidate covalent bonds between glass and PDMS. Then, the dust filter chip was connected to the spiral cell filter which was in turn connected to the observation chip. All the connections used 1 mm (outside diameter) Polytetrafluoroethylene (PTFE)tubing (Adtech Polymer Engineering, UK).

All medium flows were driven using a peristaltic pump (Ismatec, Switzerland) at a 100 $\mu\text{l}/\text{min}$ rate. The system was connected to the tank of media and cells described in the previous section. The observation chip was loaded with the cells of interest using a 5 ml syringe and a 23 G needle. Last, we plugged the cell outlet of the spiral and the observation chip outlet into the tank so the system is closed and without loss of media or cells.

Microfluidic cell filter and dust filter

The spiral-shaped microfluidic device (*Kuntaegowdanahalli and Papautsky, 2008*) was designed to filter out cells coming from the liquid culture to prevent clogging in the observation device (**Figure 1—figure supplement 1C**). The dimensions of the cell filter (i.e., a channel of 100 μm width and 50 μm height, defining a spiral of five loops separated by 900 μm) were set to maximize the separation of haploid yeast cells, that is, ~ 5 μm particles, according to the following principle: particles in a spiral microfluidic channel with a rectangular section are submitted to several inertial forces that depend on their size and are either directed towards the center of the channel or the walls. Therefore, particles of similar diameters reach an equilibrium position and tend to focus on a single line, allowing their separation from the rest of the fluid by splitting the output channel in two different outlets. A similar filter could be used with other microorganisms by adapting the dimensions.

We also added a particle filter before the spiral to avoid any clogging of the spiral because of dust particles or debris (**Figure 1—figure supplement 1B**).

To measure the filtration efficiency of the cell filter, the cell concentration of the inlet and the two outlets was measured at four different time points (0, 24, 48, and 120 hr) using a turbidity measurement (OD 660 nm, Fisherbrand). Another independent measurement was done using Green Fluorescent Protein (GFP) fluorescent yeast cells and measuring the fluorescence along the section of the device (See **Figure 1—figure supplement 1**). The filtration efficiency was equal to 99 % in both measurements, independently of the inlet cell concentration.

Microscopy

For all experiments except pH measurements, cells in the observation device were imaged using an inverted widefield microscope (Zeiss Axio Observer Z1). Fluorescence illumination was achieved using LED lights (precisExcite, CoolLed) and the light was collected using a $\times 63$ (N.A. 1.4) objective and an EM-CCD Luca-R camera (Andor). Standard GFP and mCherry filters were used.

For experiments using the pHluorin cytosolic pH probe, a Nikon Ti-E microscope was used along with a LED light (Lumencor) fluorescence illumination system. The fluorescence was measured using two excitation wavelengths using a standard roGFP2 filter set (AHF, peak excitation wavelengths 390 /18 and 475/28 nm, beamsplitter 495 nm, and emission filter 525/50 nm). Emitted light was collected using a $\times 60$ N.A. 1.4 objective and a CMOS camera (Hamamatsu Orca Flash 4.0).

We used motorized stages to follow up to 64 positions in parallel throughout the experiment. Single plane images were acquired every 15, 30, 60, or 240 min depending on the phase of the culture (high sampling rate during FP versus lower acquisition frequency in SP) to limit photodamage.

Image processing and data quantification

Calibration of the cytosolic pH probe

To calibrate the probe, 2 ml of exponentially growing culture (0.5 OD600) were centrifuged and resuspended in 200 μl calibration buffer (50 mM 2-(N-morpholino)ethanesulfonic acid (MES), 50 mM 4-(2-hydroxyethyl)-1-piperazineethanesulfonic acid (HEPES), 50 mM KCl, 50 mM NaCl, and 200 mM $\text{NH}_4\text{CH}_3\text{CO}_2$) at various pH from 5 to 8, and supplemented with 75 μM monensin, 10 μM nigericin, 10 mM 2-deoxyglucose, and 10 mM NaN_3 , as described previously (*Mouton et al., 2020*). The cells were incubated in this buffer for 30 min and then imaged in the microfluidic device to perform a ratiometric fluorescence measurement (**Figure 1—figure supplement 1I**).

Image processing

The raw images were processed using Matlab-based software (PhyloCell) and custom additional routines (*Fehrmann et al., 2013; Paoletti et al., 2016*). This software has a complete graphical interface for cell segmentation (based on a watershed algorithm), tracking (assignment cost minimization), and fluorescence signal quantification. The software can be downloaded online (<https://github.com/>

[gcharvin/phyloCell](https://doi.org/105281/zenodo5592983) Charvin, 2021). Raw data related to **Figure 1** can be found online: <https://doi.org/105281/zenodo5592983>.

Data replicates

All measurements reported in this study are based on at least two replicates.

Quantification of growth rate

The growth rate of the cells was computed using the evolution of the area of segmented cells (and buds) over time.

Identification of growth phases

To determine the limit between successive growth phases, we used a piecewise linear fit to the evolution of the total number of cells with time (D'Errico, 2017). The time point of the intersection between two pieces of the piecewise linear fit was defined as the time of transition between the two corresponding phases (Figure 1—figure supplement 1G).

Globularization score

The Ilv3-mCherry globularization score was measured in each cell by calculating the mean intensity of the five brightest pixels of the cell minus that of the other pixels, as previously described (Cai et al., 2008).

Inheritance of the respiration defect

To quantify the inheritance of the respiration defect, we measured the average standard deviation of the respiration status (after assigning a value of 0 if the cells are unable to respire and one if they are respiration competent) within individual microcolonies of cells (microcolony size from 10 to 20 cells). We then obtained an 'inheritance index' by normalizing this value to the standard deviation obtained after taking all cells into account (i.e., with no distinction about their belonging to a given microcolony). Hence this index equals 1 when the respiration defect appears at random in lineages and 0 if the transmission of the phenotype is fully inheritable.

Quantification of fluorescence foci

The fraction of cells displaying foci of GFP was manually scored at different time points using the ImageJ Cell Counter plugin.

Mobility of fluorescent foci

The fluorescent foci in each cell were detected using the centroid position of the five brightest pixels. The frame-to-frame displacement of the foci was computed by iterating this procedure over all the frames and then averaged over a population of cells.

Time of foci mobility loss and LDs

The time of mobility loss was determined by visual inspection of successive images due to the low signal-to-noise ratio in the image.

Extend of pH drop

The start and end of the pH drops were determined using a piecewise linear adjustment, similar to what was used to determine the transition between metabolic phases.

Acknowledgements

We thank Sara Mouton and Liesbeth Veenhoff for discussions and for sharing the pHluorin strain ahead of their publication, Audrey Matifas for constant technical support throughout this work, Titus Franzmann for fruitful discussions, Sophie Quintin and Sandrine Morlot for careful reading of the manuscript. We thank Denis Fumagalli at the Mediaprep facility. This work was supported by the Fondation pour la Recherche Médicale (FRM, BJ, and GC), the Agence Nationale pour la Recherche (TA and

GC), the grant ANR-10-LABX-0030-INRT, a French State fund managed by the Agence Nationale de la Recherche under the frame program Investissements d'Avenir ANR-10-IDEX-0002-02.

Additional information

Funding

Funder	Grant reference number	Author
Fondation pour la Recherche Médicale		Basile Jacquél Gilles Charvin
Agence Nationale de la Recherche		Théo Aspert Gilles Charvin

The funders had no role in study design, data collection and interpretation, or the decision to submit the work for publication.

Author contributions

Basile Jacquél, Conceptualization, Data curation, Formal analysis, Investigation, Methodology, Software, Validation, Writing – original draft, Writing – review and editing; Théo Aspert, Conceptualization, Data curation, Formal analysis, Investigation, Methodology, Resources, Software, Validation, Writing – original draft, Writing – review and editing; Damien Laporte, Conceptualization, Investigation, Methodology, Resources, Writing – review and editing; Isabelle Sagot, Conceptualization, Methodology, Supervision, Writing – review and editing; Gilles Charvin, Conceptualization, Formal analysis, Project administration, Software, Writing – original draft, Writing – review and editing

Author ORCIDs

Basile Jacquél  <http://orcid.org/0000-0002-5670-4635>

Théo Aspert  <http://orcid.org/0000-0003-2957-0683>

Damien Laporte  <http://orcid.org/0000-0002-1556-5253>

Isabelle Sagot  <http://orcid.org/0000-0003-2158-1783>

Gilles Charvin  <http://orcid.org/0000-0002-6852-6952>

Decision letter and Author response

Decision letter <https://doi.org/10.7554/eLife.73186.sa1>

Author response <https://doi.org/10.7554/eLife.73186.sa2>

Additional files

Supplementary files

- Transparent reporting form
- Supplementary file 1. Strain table.

Data availability

The CAD file used to generate the microfluidic device is available on a github repository (https://github.com/TAspert/Continuous_filtration copy archived at <https://archive.softwareheritage.org/swh:1:rev:8476f782bf6ff8fff2a9c78172cc8f072cc73916>). The source data used to make the panels (excluding raw image files) are included for each figure. Due to size constraints representative raw image data for Figure 1 is available at Zenodo (<https://doi.org/10.5281/zenodo.5592983>) and the remaining raw image data, including files for Figures 2 and 3, are available on request from the corresponding author.

The following dataset was generated:

Author(s)	Year	Dataset title	Dataset URL	Database and Identifier
Aspert T, Jacquelin B, Charvin G	2021	Dataset pHluorin cells experiencing entry into quiescence	https://doi.org/10.5281/zenodo.5592983	Zenodo, 10.5281/zenodo.5592983

References

- Ackermann M.** 2015. A Functional Perspective on Phenotypic Heterogeneity in Microorganisms. *Nature Reviews. Microbiology* **13**: 497–508. DOI: <https://doi.org/10.1038/nrmicro3491>, PMID: 26145732
- Allen C, Büttner S, Aragon AD, Thomas JA, Meirelles O, Jaetao JE, Benn D, Ruby SW, Veenhuis M, Madeo F, Werner-Washburne M.** 2006. Isolation of Quiescent and Nonquiescent Cells from Yeast Stationary-Phase Cultures. *The Journal of Cell Biology* **174**: 89–100. DOI: <https://doi.org/10.1083/jcb.200604072>, PMID: 16818721
- Aspert T.** 2021. Continuous_filtration. swl:1:rev:8476f782bf6ff8ff2a9c78172cc8f072cc73916. Software Heritage. https://archive.softwareheritage.org/swl:1:dir:f70d29e8731b95621060c830deec70b51b19d103;origin=https://github.com/TAspert/Continuous_filtration;visit=swl:1:snp:d4369ff4d7cd8d27fc22e10bbaed4a73115bf35c;anchor=swl:1:rev:8476f782bf6ff8ff2a9c78172cc8f072cc73916
- Avery SV.** 2006. Microbial Cell Individuality and the Underlying Sources of Heterogeneity. *Nature Reviews. Microbiology* **4**: 577–587. DOI: <https://doi.org/10.1038/nrmicro1460>, PMID: 16845428
- Bagamery LE, Justman QA, Garner EC, Murray AW.** 2020. A Putative Bet-Hedging Strategy Buffers Budding Yeast against Environmental Instability. *Current Biology* **30**: 4563–4578. DOI: <https://doi.org/10.1016/j.cub.2020.08.092>
- Balaban NQ, Merrin J, Chait R, Kowalik L, Leibler S.** 2004. Bacterial Persistence as a Phenotypic Switch. *Science* **305**: 1622–1625. DOI: <https://doi.org/10.1126/science.1099390>, PMID: 15308767
- Balagopal V, Parker R.** 2009. Stm1 Modulates mRNA Decay and Dhh1 Function in *Saccharomyces cerevisiae*. *Genetics* **181**: 93–103. DOI: <https://doi.org/10.1534/genetics.108.092601>, PMID: 19015546
- Beckham C, Hilliker A, Cziko A-M, Noueiry A, Ramaswami M, Parker R.** 2008. The DEAD-Box RNA Helicase Ded1p Affects and Accumulates in *Saccharomyces cerevisiae* P-Bodies. *Molecular Biology of the Cell* **19**: 984–993. DOI: <https://doi.org/10.1091/mbc.e07-09-0954>, PMID: 18162578
- Burtner CR, Murakami CJ, Kennedy BK, Kaeblerlein M.** 2009. A Molecular Mechanism of Chronological Aging in Yeast. *Cell Cycle* **8**: 1256–1270. DOI: <https://doi.org/10.4161/cc.8.8.8287>, PMID: 19305133
- Cai L, Dalal CK, Elowitz MB.** 2008. Frequency-Modulated Nuclear Localization Bursts Coordinate Gene Regulation. *Nature* **455**: 485–490. DOI: <https://doi.org/10.1038/nature07292>, PMID: 18818649
- Campbell K, Vowinkel J, Müllerer M, Malmshiemer S, Lawrence N, Calvani E, Miller-Fleming L.** 2015. Self-Establishing Communities Enable Cooperative Metabolite Exchange in a Eukaryote. *eLife* **4**: e09943. DOI: <https://doi.org/10.7554/eLife.09943>
- Campbell K, Vowinkel J, Ralser M.** 2016. Cell-to-Cell Heterogeneity Emerges as Consequence of Metabolic Cooperation in a Synthetic Yeast Community. *Biotechnology Journal* **11**: 1169–1178. DOI: <https://doi.org/10.1002/biot.201500301>, PMID: 27312776
- Cerulus B, Jariani A, Perez-Samper G, Vermeersch L, Pietsch JM, Crane MM, New AM.** 2018. Transition between Fermentation and Respiration Determines History-Dependent Behavior in Fluctuating Carbon Sources. *eLife* **7**: e39234. DOI: <https://doi.org/10.7554/eLife.39234>
- Charvin G.** 2021. phyloCell. aec9949. GitHub. <https://github.com/gcharvin/phyloCell>
- Dal Co A, van Vliet S, Kiviet DJ, Schlegel S, Ackermann M.** 2020. Short-Range Interactions Govern the Dynamics and Functions of Microbial Communities. *Nature Ecology & Evolution* **4**: 366–375. DOI: <https://doi.org/10.1038/s41559-019-1080-2>
- De Virgilio C.** 2012. The Essence of Yeast Quiescence. *FEMS Microbiology Reviews* **36**: 306–339. DOI: <https://doi.org/10.1111/j.1574-6976.2011.00287.x>, PMID: 21658086
- Dechant R, Binda M, Lee SS, Pelet S, Winderickx J, Peter M.** 2010. Cytosolic pH Is a Second Messenger for Glucose and Regulates the PKA Pathway through V-ATPase. *The EMBO Journal* **29**: 2515–2526. DOI: <https://doi.org/10.1038/emboj.2010.138>, PMID: 20581803
- Dimitrov LN, Brem RB, Kruglyak L, Gottschling DE.** 2009. Polymorphisms in Multiple Genes Contribute to the Spontaneous Mitochondrial Genome Instability of *Saccharomyces cerevisiae* S288C Strains. *Genetics* **183**: 365–383. DOI: <https://doi.org/10.1534/genetics.109.104497>, PMID: 19581448
- D’Errico J.** 2017. SLM-Shape Language Modeling-File Exchange-MATLAB Central. Version 1.14. <https://www.mathworks.com/matlabcentral/fileexchange/24443-slm-shape-language-modeling>
- Fehrmann S, Paoletti C, Goulev Y, Ungureanu A, Aguilaniu H, Charvin G.** 2013. Aging Yeast Cells Undergo a Sharp Entry into Senescence Unrelated to the Loss of Mitochondrial Membrane Potential. *Cell Reports* **5**: 1589–1599. DOI: <https://doi.org/10.1016/j.celrep.2013.11.013>, PMID: 24332850
- Fontana L, Partridge L, Longo VD.** 2010. Extending Healthy Life Span—from Yeast to Humans. *Science* **328**: 321–326. DOI: <https://doi.org/10.1126/science.1172539>, PMID: 20395504
- Goulev Y, Morlot S, Matifas A, Huang B, Molin M, Toledano MB, Charvin G.** 2017. Nonlinear Feedback Drives Homeostatic Plasticity in H2O2 Stress Response. *eLife* **6**: e23971. DOI: <https://doi.org/10.7554/eLife.23971>

- Gray JV, Petsko GA, Johnston GC, Ringe D, Singer RA, Werner-Washburne M. 2004. "Sleeping beauty": quiescence in *Saccharomyces cerevisiae*. *Microbiology and Molecular Biology Reviews* **68**: 187–206. DOI: <https://doi.org/10.1128/MMBR.68.2.187-206.2004>, PMID: 15187181
- Heimlicher MB, Bächler M, Liu M, Ibeneche-Nnewiwe C, Florin E-L, Hoenger A, Brunner D. 2019. Reversible Solidification of Fission Yeast Cytoplasm after Prolonged Nutrient Starvation. *Journal of Cell Science* **132**: 21. DOI: <https://doi.org/10.1242/jcs.231688>
- Holland SL, Reader T, Dyer PS, Avery SV. 2014. Phenotypic Heterogeneity Is a Selected Trait in Natural Yeast Populations Subject to Environmental Stress. *Environmental Microbiology* **16**: 1729–1740. DOI: <https://doi.org/10.1111/1462-2920.12243>, PMID: 24000788
- Joyner RP, Tang JH, Helenius J, Dultz E, Brune C, Holt LJ, Huet S, Müller DJ, Weis K. 2016. A Glucose-Starvation Response Regulates the Diffusion of Macromolecules. *eLife* **5**: e09376. DOI: <https://doi.org/10.7554/eLife.09376>
- Klosinska MM, Crutchfield CA, Bradley PH, Rabinowitz JD, Broach JR. 2011. Yeast Cells Can Access Distinct Quiescent States. *Genes & Development* **25**: 336–349. DOI: <https://doi.org/10.1101/gad.2011311>
- Kuntaegowdanahalli SS, Papautsky I. 2008. Continuous Particle Separation in Spiral Microchannels Using Dean Flows and Differential Migration. *Lab on a Chip* **8**: 1906–1914. DOI: <https://doi.org/10.1039/b807107a>, PMID: 18941692
- Labhsetwar P, Cole JA, Roberts E, Price ND, Luthy-Schulten ZA. 2013. Heterogeneity in Protein Expression Induces Metabolic Variability in a Modeled *Escherichia coli* Population. *PNAS* **110**: 14006–14011. DOI: <https://doi.org/10.1073/pnas.1222569110>, PMID: 23908403
- Laporte D, Salin B, Daignan-Fornier B, Sagot I. 2008. Reversible Cytoplasmic Localization of the Proteasome in Quiescent Yeast Cells. *The Journal of Cell Biology* **181**: 737–745. DOI: <https://doi.org/10.1083/jcb.200711154>, PMID: 18504300
- Laporte D, Gouleme L, Jimenez L, Khemiri I, Sagot I. 2018a. Mitochondria Reorganization upon Proliferation Arrest Predicts Individual Yeast Cell Fate. *eLife* **7**: e35685. DOI: <https://doi.org/10.7554/eLife.35685>
- Laporte D, Jimenez L, Gouleme L, Sagot I. 2018b. Yeast Quiescence Exit Swiftly Is Influenced by Cell Volume and Chronological Age. *Microbial Cell* **5**: 104–111. DOI: <https://doi.org/10.15698/mic2018.02.615>
- Li L, Miles S, Melville Z, Prasad A, Bradley G, Breeden LL. 2013. Key Events during the Transition from Rapid Growth to Quiescence in Budding Yeast Require Posttranscriptional Regulators. *Molecular Biology of the Cell* **24**: 3697–3709. DOI: <https://doi.org/10.1091/mbc.E13-05-0241>, PMID: 24088570
- Miesenböck G, De Angelis DA, Rothman JE. 1998. Visualizing Secretion and Synaptic Transmission with pH-Sensitive Green Fluorescent Proteins. *Nature* **394**: 192–195. DOI: <https://doi.org/10.1038/28190>, PMID: 9671304
- Miles S, Li L, Davison J, Breeden LL, Andrews BJ. 2013. Xbp1 Directs Global Repression of Budding Yeast Transcription during the Transition to Quiescence and Is Important for the Longevity and Reversibility of the Quiescent State. *PLOS Genetics* **9**: e1003854. DOI: <https://doi.org/10.1371/journal.pgen.1003854>
- Miles S, Bradley GT, Breeden LL. 2021. The Budding Yeast Transition to Quiescence. *Yeast* **38**: 30–38. DOI: <https://doi.org/10.1002/yea.3546>, PMID: 33350501
- Mouton SN, Thaller DJ, Crane MM, Rempel IL, Terpstra OT, Steen A, Kaeberlein M, Boersma AJ, Veenhoff LM. 2020. A Physicochemical Perspective of Aging from Single-Cell Analysis of pH, Macromolecular and Organellar Crowding in Yeast. *eLife* **9**: e54707. DOI: <https://doi.org/10.7554/eLife.54707>
- Mugler CF, Hondele M, Heinrich S, Sachdev R, Vallotton P, Koek AY, Chan LY, Weis K. 2016. ATPase Activity of the DEAD-Box Protein Dhh1 Controls Processing Body Formation. *eLife* **5**: e18746. DOI: <https://doi.org/10.7554/eLife.18746>
- Munder MC, Midtvedt D, Franzmann T, Nüske E, Otto O, Herbig M, Ulbricht E, Müller P, Taubenberger A, Maharana S, Malinowska L, Richter D, Guck J, Zaburdaev V, Alberti S. 2016. A pH-Driven Transition of the Cytoplasm from a Fluid- to a Solid-like State Promotes Entry into Dormancy. *eLife* **5**: e09347. DOI: <https://doi.org/10.7554/eLife.09347>
- Narayanaswamy R, Levy M, Tschansky M, Stovall GM, O'Connell JD, Mirrieles J, Ellington AD, Marcotte EM. 2009. Widespread Reorganization of Metabolic Enzymes into Reversible Assemblies upon Nutrient Starvation. *PNAS* **106**: 10147–10152. DOI: <https://doi.org/10.1073/pnas.0812771106>, PMID: 19502427
- Ocampo A, Liu J, Schroeder EA, Shadel GS, Barrientos A. 2012. Mitochondrial Respiratory Thresholds Regulate Yeast Chronological Life Span and Its Extension by Caloric Restriction. *Cell Metabolism* **16**: 55–67. DOI: <https://doi.org/10.1016/j.cmet.2012.05.013>
- Paoletti C, Quintin S, Matifas A, Charvin G. 2016. Kinetics of Formation and Asymmetrical Distribution of Hsp104-Bound Protein Aggregates in Yeast. *Biophysical Journal* **110**: 1605–1614. DOI: <https://doi.org/10.1016/j.bpj.2016.02.034>, PMID: 27074685
- Parry BR, Surovtsev IV, Cabeen MT, O'Hern CS, Dufresne ER, Jacobs-Wagner C. 2014. The Bacterial Cytoplasm Has Glass-like Properties and Is Fluidized by Metabolic Activity. *Cell* **156**: 183–194. DOI: <https://doi.org/10.1016/j.cell.2013.11.028>, PMID: 24361104
- Peters LZ, Hazan R, Breker M, Schuldiner M, Ben-Aroya S. 2013. Formation and Dissociation of Proteasome Storage Granules Are Regulated by Cytosolic pH. *The Journal of Cell Biology* **201**: 663–671. DOI: <https://doi.org/10.1083/jcb.201211146>, PMID: 23690178
- Petrovskaya I, Nüske E, Munder MC, Kulasegaran G, Malinowska L, Kroschwald S, Richter D, Fahmy K, Gibson K, Verbavatz JM, Alberti S. 2014. Filament Formation by Metabolic Enzymes Is a Specific Adaptation to an Advanced State of Cellular Starvation. *eLife* **3**: e02409. DOI: <https://doi.org/10.7554/eLife.02409>

- Richards OW.** 1928. The Growth of the Yeast *Saccharomyces cerevisiae*. *Annals of Botany* **os-42**: 271–283. DOI: <https://doi.org/10.1093/oxfordjournals.aob.a090112>
- Sagot I,** Pinson B, Salin B, Daignan-Fornier B. 2006. Actin bodies in yeast quiescent cells: an immediately available actin reserve? *Molecular Biology of the Cell* **17**: 4645–4655. DOI: <https://doi.org/10.1091/mbc.e06-04-0282>, PMID: 16914523
- Sagot I,** Laporte D. 2019. The cell biology of quiescent yeast – a diversity of individual scenarios. *Journal of Cell Science* **132**: 1. DOI: <https://doi.org/10.1242/jcs.213025>
- Shah KH,** Nostramo R, Zhang B, Varia SN, Klett BM, Herman PK. 2014. Protein Kinases Are Associated with Multiple, Distinct Cytoplasmic Granules in Quiescent Yeast Cells. *Genetics* **198**: 1495–1512. DOI: <https://doi.org/10.1534/genetics.114.172031>, PMID: 25342717
- Solopova A,** van Gestel J, Weissing FJ, Bachmann H, Teusink B, Kok J, Kuipers OP. 2014. Bet-Hedging during Bacterial Diauxic Shift. *PNAS* **111**: 7427–7432. DOI: <https://doi.org/10.1073/pnas.1320063111>, PMID: 24799698
- Sun S,** Gresham D. 2021. Cellular Quiescence in Budding Yeast. *Yeast* **38**: 12–29. DOI: <https://doi.org/10.1002/yea.3545>, PMID: 33350503
- Tu BP,** Kudlicki A, Rowicka M, McKnight SL. 2005. Logic of the Yeast Metabolic Cycle: Temporal Compartmentalization of Cellular Processes. *Science* **310**: 1152–1158. DOI: <https://doi.org/10.1126/science.1120499>, PMID: 16254148
- Veatch JR,** McMurray MA, Nelson ZW, Gottschling DE. 2009. Mitochondrial Dysfunction Leads to Nuclear Genome Instability via an Iron-Sulfur Cluster Defect. *Cell* **137**: 1247–1258. DOI: <https://doi.org/10.1016/j.cell.2009.04.014>, PMID: 19563757
- Weber CA,** Sekar K, Tang JH, Warmer P, Sauer U, Weis K. 2020. β -Oxidation and Autophagy Are Critical Energy Providers during Acute Glucose Depletion in *Saccharomyces cerevisiae*. *PNAS* **117**: 12239–12248. DOI: <https://doi.org/10.1073/pnas.1913370117>, PMID: 32430326

Figure 1 – Supplement 1

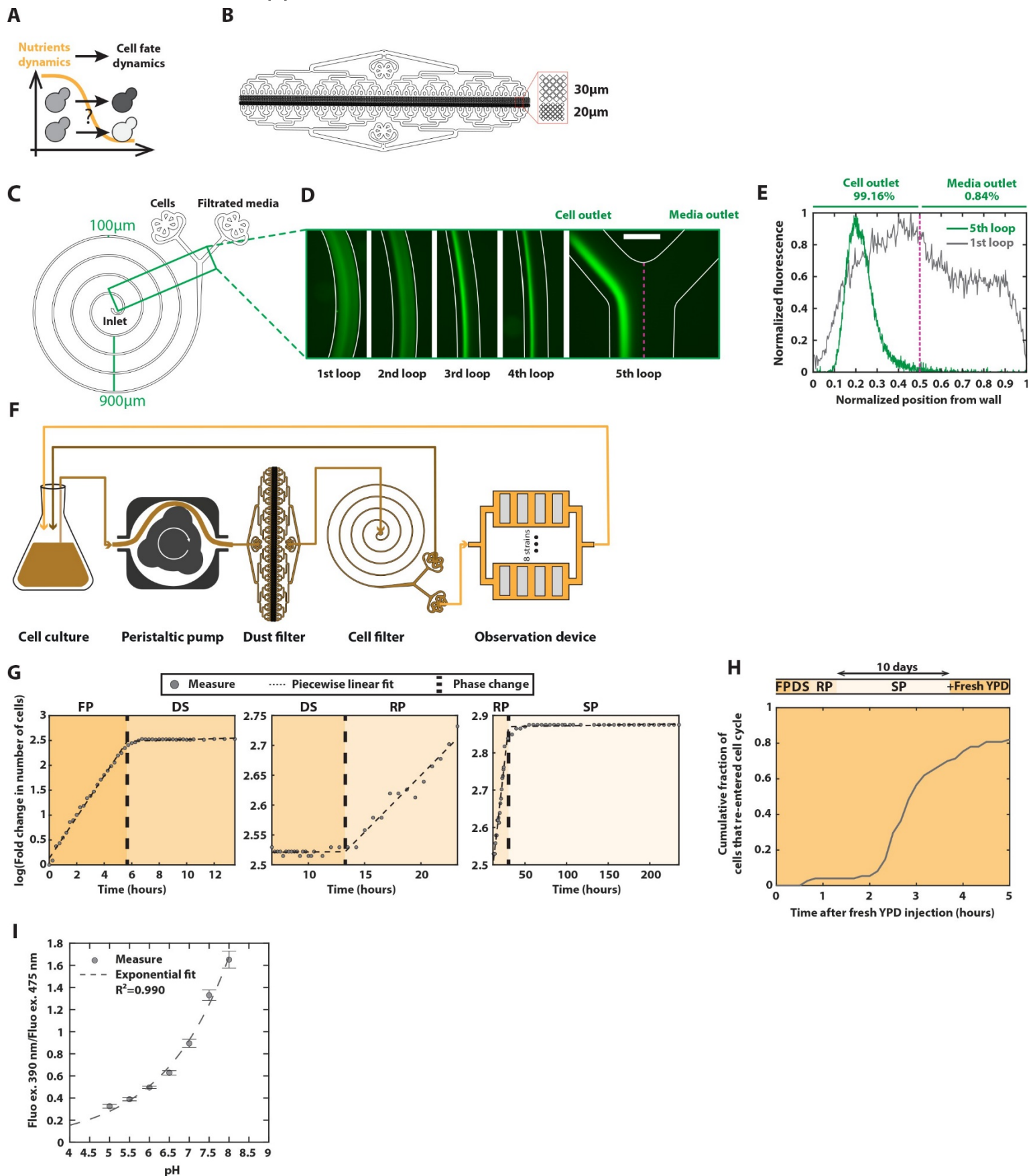


Figure 1 – Supplement 1: Design and calibration of the experimental setup.

(A) Schematics representing the main question addressed in this study, namely how the natural dynamics of environmental changes shapes nonuniform cellular responses and induces distinct cellular fates in a clonal population. (B) Schematics of the dust filter device, including a closeup of the debris retention arrays of 30 and 20 μm size. (C) Schematics of the cell-filtering device, made of a spiraling channel with five loops of 100 μm width, separated by 900 μm . (D) Sample fluorescence images of TDH3-GFP cells at different positions in the filtering device. Each image represents the indicated loop. The magenta dotted line represents the middle of the channel. Scale bar = 150 μm . (E) Fluorescence profile of the first loop (gray) and fifth loop (green) along the channel's cross-section. The value is normalized to the maximum of each condition. In the upper part is displayed the cumulative signal on each side of the channel of the fifth loop. (F) Schematics of the whole closed-loop fluidic platform. The flask is connected to a peristaltic pump, which drives media flows to the dust filter. The dust-free media then flows into the inlet of the spiral. The cell outlet of the spiral is redirected into the flask while the cell-free outlet irrigates the observation device. To close the loop, the outlet of the observation device is connected to the flask. (G) Determination of the culture metabolic phases during the yeast life cycle based on the evolution of cell number over time. A piecewise linear fit on the number of cells defines the limit between fermentation phase (FP) and diauxic shift (DS; left), DS and respiration phase (RP; middle), or RP and stationary phase (SP; right). Gray dots represent the measured number of cells in one microcolony, thin dashed lines represent the line fits and vertical dashed lines the transition time. Each shaded area represents a distinct proliferation phase, as indicated in the legend. (H) Cumulative fraction of cells reentering the cell cycle after 10 days in SP over time, upon refeeding with YPD medium ($N = 60$). (I) Calibration curve of the pHluorin probe. Gray dots represent the ratio of fluorescence collected at 390 nm over the fluorescence collected at 475 nm excitations, error bars represent the standard deviation ($N = 20$). The dashed line corresponds to an exponential fit $f(x) = a \times \exp(b \times x)$ of parameters (with 95 % confidence bounds): $a = 0.01419$ (0.005774, 0.0226) and $b = 0.5967$ (0.5174, 0.6761).

Figure 1 – Supplement 2

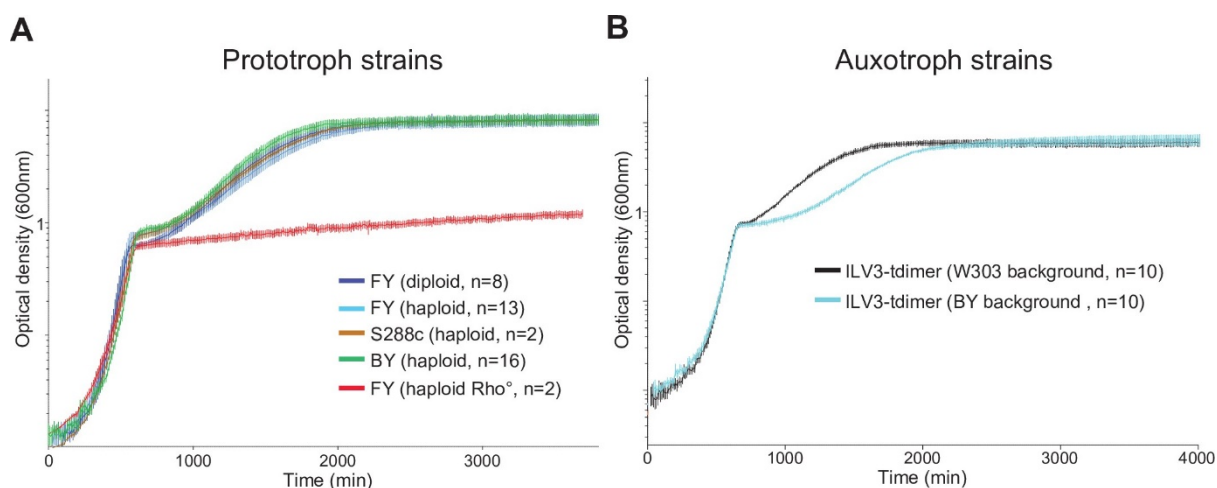
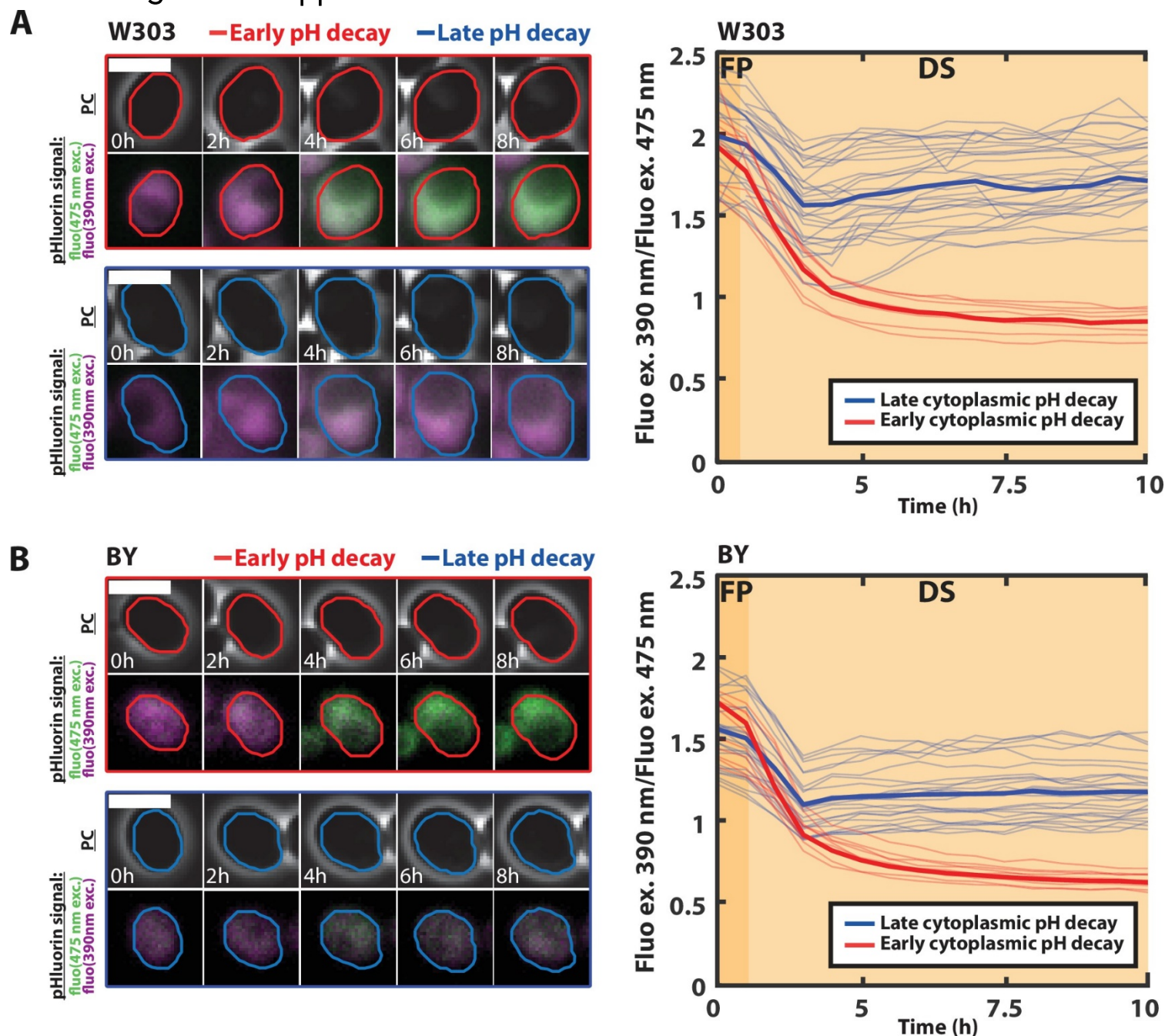


Figure 1 – Supplement 2: Population measurements of cell growth during an entire life cycle.

Growth curves comparison between prototrophs FY, S288c, and BY (**A**) and auxotrophs W303 and BY Ilv3-tetramer expressing strains (**B**). Haploid FY Rho (red curve) is unable to respire and stop proliferating after carbon fermentation. Automated turbidity measurement was done using the Bioscreen C device (Labsystems). Strains were maintained 24 hr in exponential phase in rich medium supplemented with Adenine (YPDA) at 30°C, then inoculated into the microplates at OD_{600m} = 0.01, 150 µl YPDA, 30 °C. Yeasts were grown at continuous agitation, with absorbances reading every 10 min during 3 days.

Figure 1 – Supplement 3



Single-cell dynamics of entry into stationary phase in BY versus W303 strains.

(A) Left: typical sequence of phase-contrast and fluorescence images for W303 cells that display (respectively, do not display) an early cytosolic pH decay upon the diauxic shift (DS; red and blue cell contours, respectively). The fluorescence image displays an overlay of fluorescence images obtained using indicated excitation wavelengths. Right: quantification of the raw (i.e., uncalibrated) ratio of the fluorescence level obtained using indicated excitation wavelength. The colored shading indicates the fermentation phase (FP) and the DS. $N > 30$ cells. (B) Same as A, but using the BY strain as a control. $N > 30$ cells.

Figure 1 – Video 1: (please see

<https://elifesciences.org/articles/73186/figures#fig1video1>)

Top: phase-contrast video of a microcolony growing in the observation device during the life cycle of the culture.

Bottom: fold increase in the number of cells during colony proliferation. The colored progress bar indicates the metabolic phase of the culture as defined in Figure 1. Scale bar: 6.3 μm .

Figure 1 – Video 2: (please see

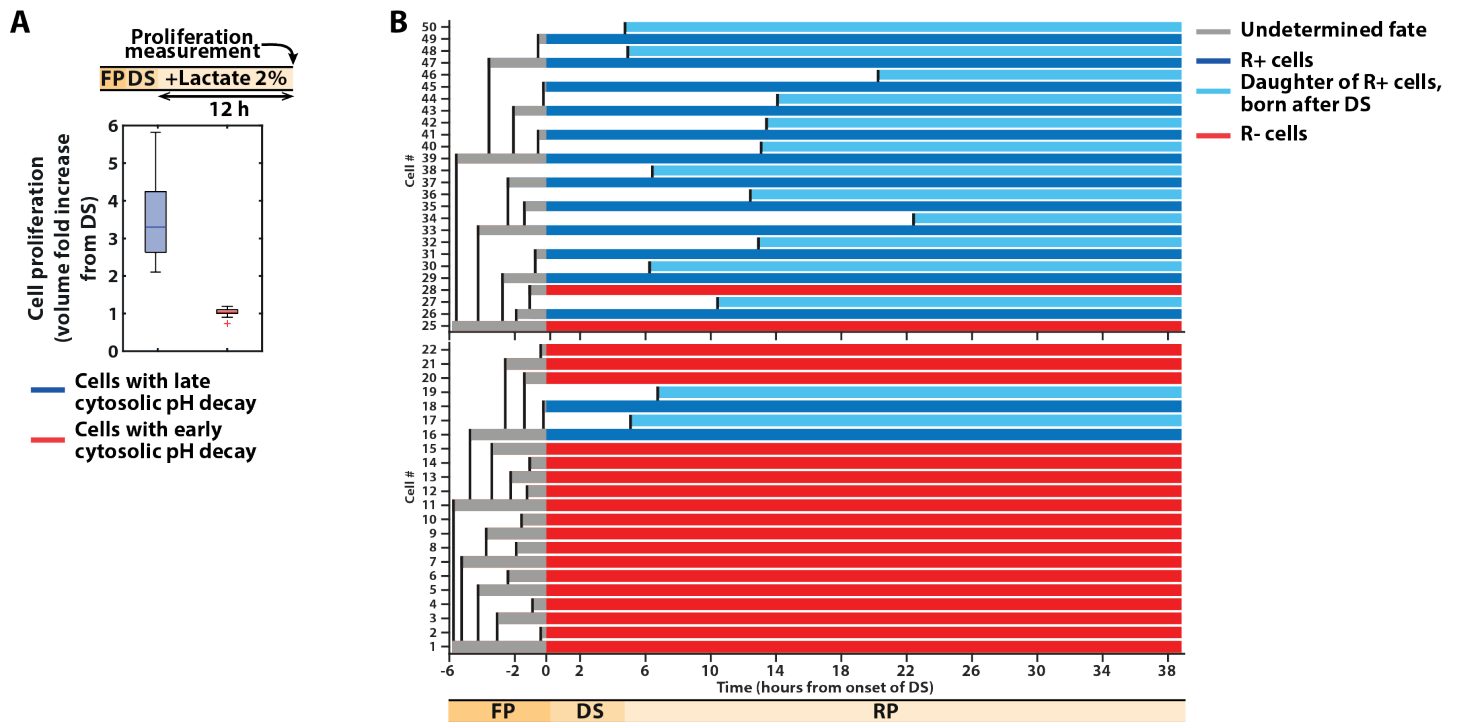
<https://elifesciences.org/articles/73186/figures#fig1video2>)

Top: phase-contrast (left) and pHluorin (right, channels 1 and 2 merged as in Figure 1) video of a microcolony growing in the observation device during the life cycle of the culture.

The colored progress bar indicates the metabolic phase of the culture as defined in Figure 1.

The red and blue contours indicate R⁻ and R⁺ cells, respectively. Scale bar: 10.8 μm . Bottom: quantification of cytosolic pH over time, as described in Figure 1.

Figure 2 – Supplement 1:



Complementary analyses of the divergent cell fate at the diauxic shift.

(A) Proliferation capacity in a respirative media. Box plots indicate the fold increase in cell area from the diauxic shift (DS) in each subpopulation (blue and red lines for cells with a late or early cytoplasmic pH decay, respectively), after a 12 hr exposure to a 2 % lactate respirative media after the DS ($N = 30$ for each box plot). (B) Inheritance of the R+ and R– phenotypes. Sample pedigrees representing two single cells (#1 and #25) and their progeny; each horizontal bar represents a cell. Cells reveal their respiratory status at the DS, hence are displayed in gray before the DS, and red (for R–) or blue (R+) after the DS. Daughters born after DS are represented in light blue. Only the first daughter of mothers born before the DS are represented for clarity.

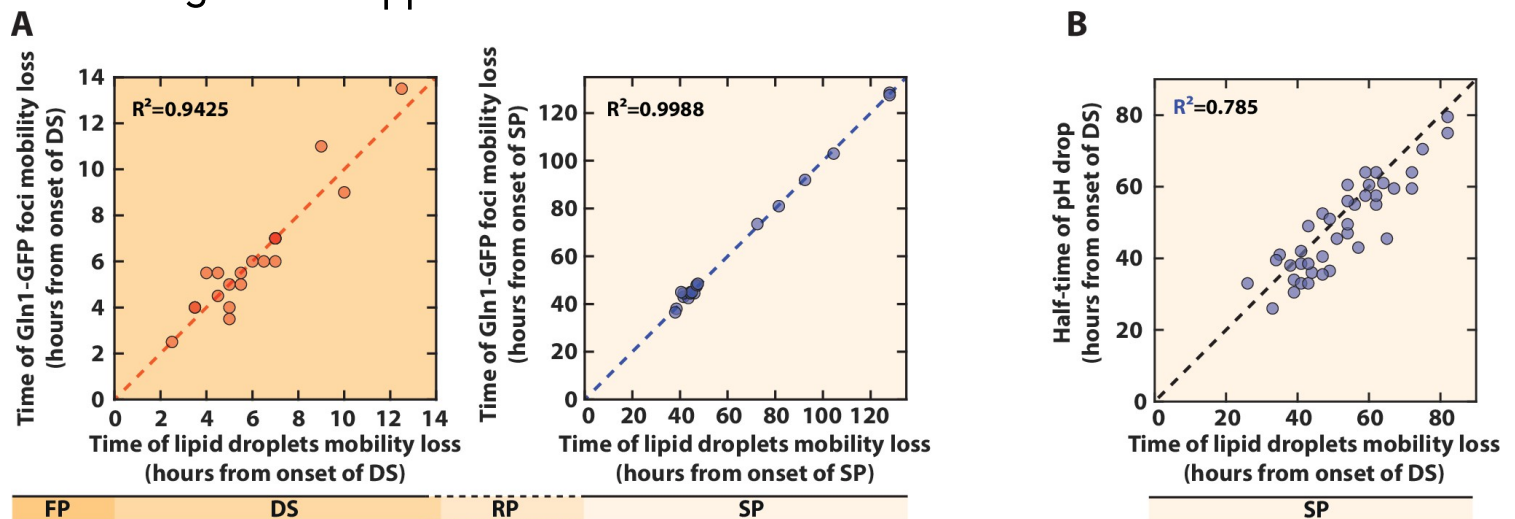
Figure 2 – Video 1: (please see

<https://elifesciences.org/articles/73186/figures#fig2video1>)

Phase-contrast (left) and Ilv3-mCherry (right) video of a microcolony growing in the observation device during the life cycle of the culture.

The colored progress bar indicates the metabolic phase of the culture as defined in [Figure 1](#). The thick red and blue contours indicate original R– and R+ cells, respectively, while the thin red and blue contours indicate the daughters of the original cells. Scale bar: 6.3 μm .

Figure 2 – Supplement 1:



Coincidence of lipid droplets and Gln1-GFP foci mobility.

Correlation of the time of mobility loss of Gln1-GFP foci with that of the lipid droplet (LD) in R- (left plot) or R+ (right plot) cells. The origin of time is set as the proliferation arrest for each type of cells, that is the onset of diauxic shift (DS) and the onset of stationary phase (SP), respectively. The dashed lines represent the diagonal. **(B)** Correlation of the half-time of the pH drop with the time of LD mobility loss in R+ cells. The time origin the onset of SP. The dashed lines represent the diagonal.

Figure 3 – Video 1: (please see

<https://elifesciences.org/articles/73186/figures#fig3video1>)

Phase-contrast (left) and Gln1-GFP (right) video of a microcolony growing in the observation device from fermentation phase to respiration phase.

The colored progress bar indicates the metabolic phase of the culture as defined in [Figure 1](#).

The red and blue contours indicate R- and R+ cells, respectively. Scale bar: 6.3 μm

Discussion

In addition to the paper's discussion:

Our methodology allowed us to follow single-cell throughout the successive phase and capture their entry into quiescence. With that, we were able to answer the following question:

What is the source of this senescent population? The inability to activate the respirative metabolism **at the diauxic shift**, that is why we call them R- cells.

Do these cells enter some kind of quiescence before losing viability? They have been described as senescent or non-quiescent because of their short viability and because they lose quiescence markers after their death. Our data show that these cells display all the markers seen in *bona fide* quiescent cells, and that the R- cells can re-enter the cell cycle during a few days after proliferation arrest. Therefore, if these cells are unable to sustain quiescence, they can enter it. Hence, in the strict sense of the term, they are quiescent cells. The fact that they die rapidly is (at least partly) linked to their inability to form trehalose and glycogen storages [52] [36], two well-known byproducts of respiration. The R- cells are probably close to cells abruptly switched from a glucose media to glucose depleted media (See "SP" on Figure 78, p.186).

Yet, if trehalose supplementation during fermentation can restore longevity in non-respirative cells [36], it cannot do so after an abrupt starvation [53]. This suggests that other processes linked to the dynamics of the media (like a prolonged exposure to ethanol during fermentation) are necessary to achieve a prolonged quiescence.

Can we predict which cells will become R- before quiescence by looking at their history? A part is predictable and due to the loss of mtDNA ($\rho 0$ cells), but unexpectedly, it does not represent the majority of the R- cells. In line with that, we performed the experiment in another background known to have very few $\rho 0$ cells, and also observed R- cells (Figure 1 – Suppl 3). Characterizing these cells in detail and understanding why they experience this metabolic crash is made possible with this new methodology and is an interesting perspective.

Do we observe gelification of the cytosol like in abrupt energy depletion experiments? Yes, to our knowledge, this is the first evidence that the cytosol of cells undergoes a gel-like transition during quiescence in physiological conditions. Even if this was expected since it is the case after abrupt transitions [24,25], these experiments require drugs to completely abolish the glycolysis, and the phase transition is not observed with a simple glucose depletion.

Yet, if our data about the phase transition are weak (based on the decreased mobility of particles), they are strongly supported by in-vitro experiments that can reproduce protein phase transition by decreasing the pH of the solution [30,54–56]. Besides, *S. pombe* cells submitted to abrupt starvation with drugs remain cylindrical after cell wall removal, suggesting a gel-like state of the cytosol [25].

Interestingly, we observe this gelification occurs several days after proliferation arrest, while abruptly arrested cells only take a few minutes to display it. The mechanism behind that is also likely to explain the vast heterogeneity regarding the time of freezing in R+ cells during quiescence.

Overall, this method opens new opportunities to track single-cell and link their history with their phenotype, not only in the field of quiescence but also collective oscillatory behaviors, cellular cooperation, or antibiotics collective response.

References Chapter II

- [1] J.V. Gray, G.A. Petsko, G.C. Johnston, D. Ringe, R.A. Singer, M. Werner-Washburne, "Sleeping Beauty": Quiescence in *Saccharomyces cerevisiae*†, *Microbiol Mol Biol R.* 68 (2004) 187–206. <https://doi.org/10.1128/membr.68.2.187-206.2004>.
- [2] I. Sagot, D. Laporte, The cell biology of quiescent yeast – a diversity of individual scenarios, *J Cell Sci.* 132 (2019) jcs213025. <https://doi.org/10.1242/jcs.213025>.
- [3] A.M. Neiman, Sporulation in the Budding Yeast *Saccharomyces cerevisiae*, *Genetics.* 189 (2011) 737–765. <https://doi.org/10.1534/genetics.111.127126>.
- [4] N. Urbán, I.M. Blomfield, F. Guillemot, Quiescence of Adult Mammalian Neural Stem Cells: A Highly Regulated Rest, *Neuron.* 104 (2019) 834–848. <https://doi.org/10.1016/j.neuron.2019.09.026>.
- [5] G. Yao, Modelling mammalian cellular quiescence, *Interface Focus.* 4 (2014) 20130074. <https://doi.org/10.1098/rsfs.2013.0074>.
- [6] W. Chen, J. Dong, J. Haiech, M.-C. Kilhoffer, M. Zeniou, Cancer Stem Cell Quiescence and Plasticity as Major Challenges in Cancer Therapy, *Stem Cells Int.* 2016 (2016) 1740936. <https://doi.org/10.1155/2016/1740936>.
- [7] C.D. Virgilio, The essence of yeast quiescence, *Fems Microbiol Rev.* 36 (2012) 306–339. <https://doi.org/10.1111/j.1574-6976.2011.00287.x>.
- [8] J.R. Pringle, L.H. Hartwell, The *Saccharomyces cerevisiae* cell cycle, *Mol. Biol.* (1981) 97–142.
- [9] S. Miles, L. Li, J. Davison, L.L. Breeden, Xbp1 Directs Global Repression of Budding Yeast Transcription during the Transition to Quiescence and Is Important for the Longevity and Reversibility of the Quiescent State, *Plos Genet.* 9 (2013) e1003854. <https://doi.org/10.1371/journal.pgen.1003854>.
- [10] M. Moreno-Torres, M. Jaquenoud, C.D. Virgilio, TORC1 controls G1–S cell cycle transition in yeast via Mpk1 and the greatwall kinase pathway, *Nat Commun.* 6 (2015) 8256. <https://doi.org/10.1038/ncomms9256>.
- [11] D. Laporte, A. Lebaudy, A. Sahin, B. Pinson, J. Ceschin, B. Daignan-Fornier, I. Sagot, Metabolic status rather than cell cycle signals control quiescence entry and exit, *J Cell Biology.* 192 (2011) 949–957. <https://doi.org/10.1083/jcb.201009028>.
- [12] E. Boy-Marcotte, M. Perrot, F. Bussereau, H. Boucherie, M. Jacquet, Msn2p and Msn4p Control a Large Number of Genes Induced at the Diauxic Transition Which Are Repressed by Cyclic AMP in *Saccharomyces cerevisiae*, *J Bacteriol.* 180 (1998) 1044–1052. <https://doi.org/10.1128/jb.180.5.1044-1052.1998>.
- [13] O. Kandror, N. Bretschneider, E. Kreydin, D. Cavalieri, A.L. Goldberg, Yeast Adapt to Near-Freezing Temperatures by STRE/Msn2,4-Dependent Induction of Trehalose Synthesis and Certain Molecular Chaperones, *Mol Cell.* 13 (2004) 771–781. [https://doi.org/10.1016/s1097-2765\(04\)00148-0](https://doi.org/10.1016/s1097-2765(04)00148-0).
- [14] V. Pfanzagl, W. Görner, M. Radolf, A. Parich, R. Schuhmacher, J. Strauss, W. Reiter, C. Schüller, A constitutive active allele of the transcription factor Msn2 mimicking low PKA activity dictates metabolic remodeling in yeast, *Mol Biol Cell.* 29 (2018) 2848–2862. <https://doi.org/10.1091/mbc.e18-06-0389>.

- [15] D.A. Fletcher, R.D. Mullins, Cell mechanics and the cytoskeleton, *Nature*. 463 (2010) 485–492. <https://doi.org/10.1038/nature08908>.
- [16] I. Sagot, B. Pinson, B. Salin, B. Daignan-Fornier, Actin Bodies in Yeast Quiescent Cells: An Immediately Available Actin Reserve?, *Mol Biol Cell*. 17 (2006) 4645–4655. <https://doi.org/10.1091/mbc.e06-04-0282>.
- [17] D. Laporte, F. Courtout, B. Salin, J. Ceschin, I. Sagot, An array of nuclear microtubules reorganizes the budding yeast nucleus during quiescence, *J Cell Biol*. 203 (2013) 585–594. <https://doi.org/10.1083/jcb.201306075>.
- [18] C.A. Weber, K. Sekar, J.H. Tang, P. Warmer, U. Sauer, K. Weis, β -Oxidation and autophagy are critical energy providers during acute glucose depletion in *Saccharomyces cerevisiae*, *Proc National Acad Sci*. 117 (2020) 12239–12248. <https://doi.org/10.1073/pnas.1913370117>.
- [19] D. Laporte, L. Gouleme, L. Jimenez, I. Khemiri, I. Sagot, Mitochondria reorganization upon proliferation arrest predicts individual yeast cell fate, *Elife*. 7 (2018) e35685. <https://doi.org/10.7554/elife.35685>.
- [20] K. Tanaka, The proteasome: Overview of structure and functions, *Proc Jpn Acad Ser B*. 85 (2009) 12–36. <https://doi.org/10.2183/pjab.85.12>.
- [21] D. Laporte, B. Salin, B. Daignan-Fornier, I. Sagot, Reversible cytoplasmic localization of the proteasome in quiescent yeast cells, *J Cell Biology*. 181 (2008) 737–745. <https://doi.org/10.1083/jcb.200711154>.
- [22] R.S. Marshall, R.D. Vierstra, Proteasome storage granules protect proteasomes from autophagic degradation upon carbon starvation, *Elife*. 7 (2018) e34532. <https://doi.org/10.7554/elife.34532>.
- [23] R.P. Joyner, J.H. Tang, J. Helenius, E. Dultz, C. Brune, L.J. Holt, S. Huet, D.J. Müller, K. Weis, A glucose-starvation response regulates the diffusion of macromolecules, *Elife*. 5 (2016) e09376. <https://doi.org/10.7554/elife.09376>.
- [24] M.C. Munder, D. Midtvedt, T. Franzmann, E. Nüske, O. Otto, M. Herbig, E. Ulbricht, P. Müller, A. Taubenberger, S. Maharana, L. Malinowska, D. Richter, J. Guck, V. Zaburdaev, S. Alberti, A pH-driven transition of the cytoplasm from a fluid- to a solid-like state promotes entry into dormancy, *Elife*. 5 (2016) e09347. <https://doi.org/10.7554/elife.09347>.
- [25] M.B. Heimlicher, M. Bächler, M. Liu, C. Ibeneche-Nnewiwe, E.-L. Florin, A. Hoenger, D. Brunner, Reversible solidification of fission yeast cytoplasm after prolonged nutrient starvation, *J Cell Sci*. 132 (2019) jcs231688. <https://doi.org/10.1242/jcs.231688>.
- [26] B.R. Parry, I.V. Surovtsev, M.T. Cabeen, C.S. O’Hern, E.R. Dufresne, C. Jacobs-Wagner, The Bacterial Cytoplasm Has Glass-like Properties and Is Fluidized by Metabolic Activity, *Cell*. 156 (2014) 183–194. <https://doi.org/10.1016/j.cell.2013.11.028>.
- [27] R. Orij, S. Brul, G.J. Smits, Intracellular pH is a tightly controlled signal in yeast, *Biochimica Et Biophysica Acta Bba - Gen Subj*. 1810 (2011) 933–944. <https://doi.org/10.1016/j.bbagen.2011.03.011>.
- [28] I. Petrovska, E. Nüske, M.C. Munder, G. Kulasegaran, L. Malinowska, S. Kroschwald, D. Richter, K. Fahmy, K. Gibson, J.-M. Verbavatz, S. Alberti, Filament formation by metabolic enzymes is a specific adaptation to an advanced state of cellular starvation, *Elife*. 3 (2014) e02409. <https://doi.org/10.7554/elife.02409>.

- [29] L.Z. Peters, R. Hazan, M. Breker, M. Schuldiner, S. Ben-Aroya, Formation and dissociation of proteasome storage granules are regulated by cytosolic pH Regulation of PSGs by cytosolic pH, *J Cell Biology*. 201 (2013) 663–671. <https://doi.org/10.1083/jcb.201211146>.
- [30] J.A. Riback, C.D. Katanski, J.L. Kear-Scott, E.V. Pilipenko, A.E. Rojek, T.R. Sosnick, D.A. Drummond, Stress-Triggered Phase Separation Is an Adaptive, Evolutionarily Tuned Response, *Cell*. 168 (2017) 1028–1040.e19. <https://doi.org/10.1016/j.cell.2017.02.027>.
- [31] V. Ramachandran, K.H. Shah, P.K. Herman, The cAMP-Dependent Protein Kinase Signaling Pathway Is a Key Regulator of P Body Foci Formation, *Mol Cell*. 43 (2011) 973–981. <https://doi.org/10.1016/j.molcel.2011.06.032>.
- [32] D. Mateju, T.M. Franzmann, A. Patel, A. Kopach, E.E. Boczek, S. Maharana, H.O. Lee, S. Carra, A.A. Hyman, S. Alberti, An aberrant phase transition of stress granules triggered by misfolded protein and prevented by chaperone function, *Embo J*. 36 (2017) 1669–1687. <https://doi.org/10.15252/emboj.201695957>.
- [33] F. Monje-Casas, C. Michan, C. Pueyo, Absolute transcript levels of thioredoxin- and glutathione-dependent redox systems in *Saccharomyces cerevisiae*: response to stress and modulation with growth, *Biochem J*. 383 (2004) 139–147. <https://doi.org/10.1042/bj20040851>.
- [34] C. Allen, S. Büttner, A.D. Aragon, J.A. Thomas, O. Meirelles, J.E. Jaetao, D. Benn, S.W. Ruby, M. Veenhuis, F. Madeo, M. Werner-Washburne, Isolation of quiescent and nonquiescent cells from yeast stationary-phase cultures, *J Cell Biology*. 174 (2006) 89–100. <https://doi.org/10.1083/jcb.200604072>.
- [35] D. Laporte, L. Jimenez, L. Gouleme, I. Sagot, Yeast quiescence exit swiftness is influenced by cell volume and chronological age, *Microb Cell*. 5 (2017) 104. <https://doi.org/10.15698/mic2018.02.615>.
- [36] A. Ocampo, J. Liu, E.A. Schroeder, G.S. Shadel, A. Barrientos, Mitochondrial Respiratory Thresholds Regulate Yeast Chronological Life Span and its Extension by Caloric Restriction, *Cell Metab*. 16 (2012) 55–67. <https://doi.org/10.1016/j.cmet.2012.05.013>.
- [37] L.E. Bagamery, Q.A. Justman, E.C. Garner, A.W. Murray, A Putative Bet-Hedging Strategy Buffers Budding Yeast against Environmental Instability, *Curr Biol*. 30 (2020) 4563–4578.e4. <https://doi.org/10.1016/j.cub.2020.08.092>.
- [38] B. Cerulus, A. Jariani, G. Perez-Samper, L. Vermeersch, J.M. Pietsch, M.M. Crane, A.M. New, B. Gallone, M. Roncoroni, M.C. Dzialo, S.K. Govers, J.O. Hendrickx, E. Galle, M. Coomans, P. Berden, S. Verbandt, P.S. Swain, K.J. Verstrepen, Transition between fermentation and respiration determines history-dependent behavior in fluctuating carbon sources, *Elife*. 7 (2018) e39234. <https://doi.org/10.7554/elife.39234>.
- [39] A. Mitchell, G.H. Romano, B. Groisman, A. Yona, E. Dekel, M. Kupiec, O. Dahan, Y. Pilpel, Adaptive prediction of environmental changes by microorganisms, *Nature*. 460 (2009) 220–224. <https://doi.org/10.1038/nature08112>.
- [40] M.M. Klosinska, C.A. Crutchfield, P.H. Bradley, J.D. Rabinowitz, J.R. Broach, Yeast cells can access distinct quiescent states, *Gene Dev*. 25 (2011) 336–349. <https://doi.org/10.1101/gad.2011311>.
- [41] L. Li, S. Miles, Z. Melville, A. Prasad, G. Bradley, L.L. Breeden, Key events during the transition from rapid growth to quiescence in budding yeast require posttranscriptional regulators, *Mol Biol Cell*. 24 (2013) 3697–3709. <https://doi.org/10.1091/mbc.e13-05-0241>.

-
- [42] D.D. Carlo, Inertial microfluidics, *Lab Chip*. 9 (2009) 3038–3046. <https://doi.org/10.1039/b912547g>.
- [43] D.D. Carlo, D. Irimia, R.G. Tompkins, M. Toner, Continuous inertial focusing, ordering, and separation of particles in microchannels, *Proc National Acad Sci*. 104 (2007) 18892–18897. <https://doi.org/10.1073/pnas.0704958104>.
- [44] D.R. Gossett, D.D. Carlo, Particle Focusing Mechanisms in Curving Confined Flows, *Anal Chem*. 81 (2009) 8459–8465. <https://doi.org/10.1021/ac901306y>.
- [45] A.A.S. Bhagat, S.S. Kuntaegowdanahalli, I. Papautsky, Enhanced particle filtration in straight microchannels using shear-modulated inertial migration, *Phys Fluids*. 20 (2008) 101702. <https://doi.org/10.1063/1.2998844>.
- [46] S.S. Kuntaegowdanahalli, A.A.S. Bhagat, G. Kumar, I. Papautsky, Inertial microfluidics for continuous particle separation in spiral microchannels, *Lab Chip*. 9 (2009) 2973–2980. <https://doi.org/10.1039/b908271a>.
- [47] A.A.S. Bhagat, S.S. Kuntaegowdanahalli, I. Papautsky, Continuous particle separation in spiral microchannels using dean flows and differential migration, *Lab Chip*. 8 (2008) 1906–1914. <https://doi.org/10.1039/b807107a>.
- [48] M. Masaeli, E. Sollier, H. Amini, W. Mao, K. Camacho, N. Doshi, S. Mitragotri, A. Alexeev, D.D. Carlo, Continuous Inertial Focusing and Separation of Particles by Shape, *Phys Rev X*. 2 (2012) 031017. <https://doi.org/10.1103/physrevx.2.031017>.
- [49] E. Guzniczak, O. Otto, G. Whyte, T. Chandra, N.A. Robertson, N. Willoughby, M. Jimenez, H. Bridle, Purifying stem cell-derived red blood cells: a high-throughput label-free downstream processing strategy based on microfluidic spiral inertial separation and membrane filtration, *Biotechnol Bioeng*. 117 (2020) 2032–2045. <https://doi.org/10.1002/bit.27319>.
- [50] A.J. Mach, D.D. Carlo, Continuous scalable blood filtration device using inertial microfluidics, *Biotechnol Bioeng*. 107 (2010) 302–311. <https://doi.org/10.1002/bit.22833>.
- [51] H. Amini, W. Lee, D.D. Carlo, Inertial microfluidic physics, *Lab Chip*. 14 (2014) 2739–2761. <https://doi.org/10.1039/c4lc00128a>.
- [52] L. Shi, B.M. Sutter, X. Ye, B.P. Tu, Trehalose Is a Key Determinant of the Quiescent Metabolic State That Fuels Cell Cycle Progression upon Return to Growth, *Mol Biol Cell*. 21 (2010) 1982–1990. <https://doi.org/10.1091/mbc.e10-01-0056>.
- [53] S. Miles, G.T. Bradley, L.L. Breeden, The budding yeast transition to quiescence, *Yeast*. 38 (2021) 30–38. <https://doi.org/10.1002/yea.3546>.
- [54] S. Alberti, A. Gladfelter, T. Mittag, Considerations and Challenges in Studying Liquid-Liquid Phase Separation and Biomolecular Condensates, *Cell*. 176 (2019) 419–434. <https://doi.org/10.1016/j.cell.2018.12.035>.
- [55] T.M. Franzmann, M. Jahnel, A. Pozniakovsky, J. Mahamid, A.S. Holehouse, E. Nüske, D. Richter, W. Baumeister, S.W. Grill, R.V. Pappu, A.A. Hyman, S. Alberti, Phase separation of a yeast prion protein promotes cellular fitness, *Science*. 359 (2018) eaao5654. <https://doi.org/10.1126/science.aao5654>.
- [56] O. Adame-Arana, C.A. Weber, V. Zaburdaev, J. Prost, F. Jülicher, Liquid Phase Separation Controlled by pH, *Biophys J*. 119 (2020) 1590–1605. <https://doi.org/10.1016/j.bpj.2020.07.044>.

Appendixes

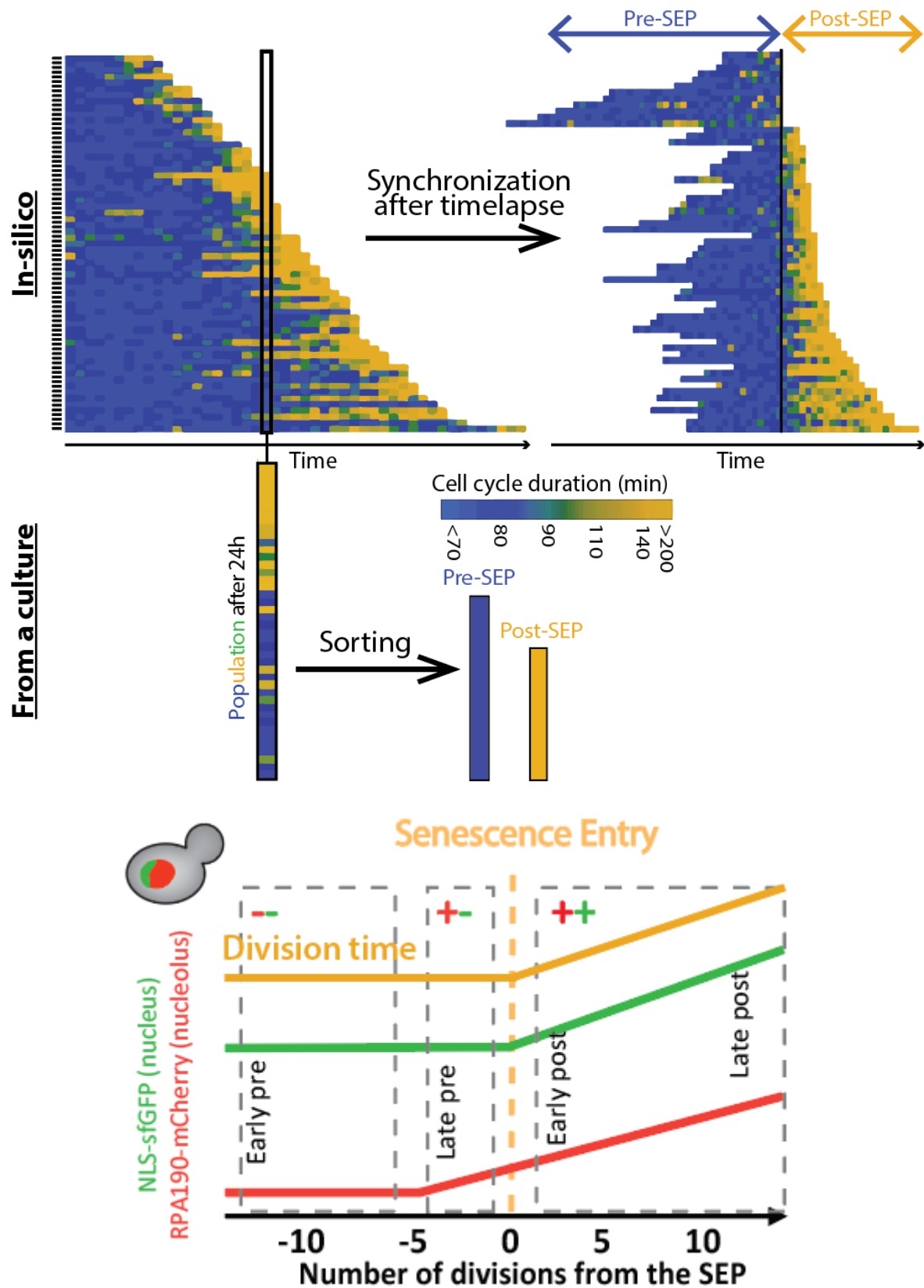
Appendix 1: Microfluidic enrichment of old cells and sorting according to their senescent state

Single-cell timelapse approaches are powerful but limited to fluorescent reporters and can hardly probe complex signals such as chromatin state, protein-DNA interactions. Besides, they are limited to a candidate approach and do not allow genome/proteome-wide analysis.

On the other hand, when working with standard enrichment methods, the fact that cells do not age in the same way or at the same pace is not considered. Therefore, since the hallmarks of aging appear at different times from one cell to another, assaying a desynchronized population opacifies the dynamics of the hallmarks themselves as well as their in-between temporal (thus causal) links (discussed p.67) (Figure 44).. Among them, some might be triggering aging, while some *Page left blank on purpose* others might just be a byproduct (see main text).

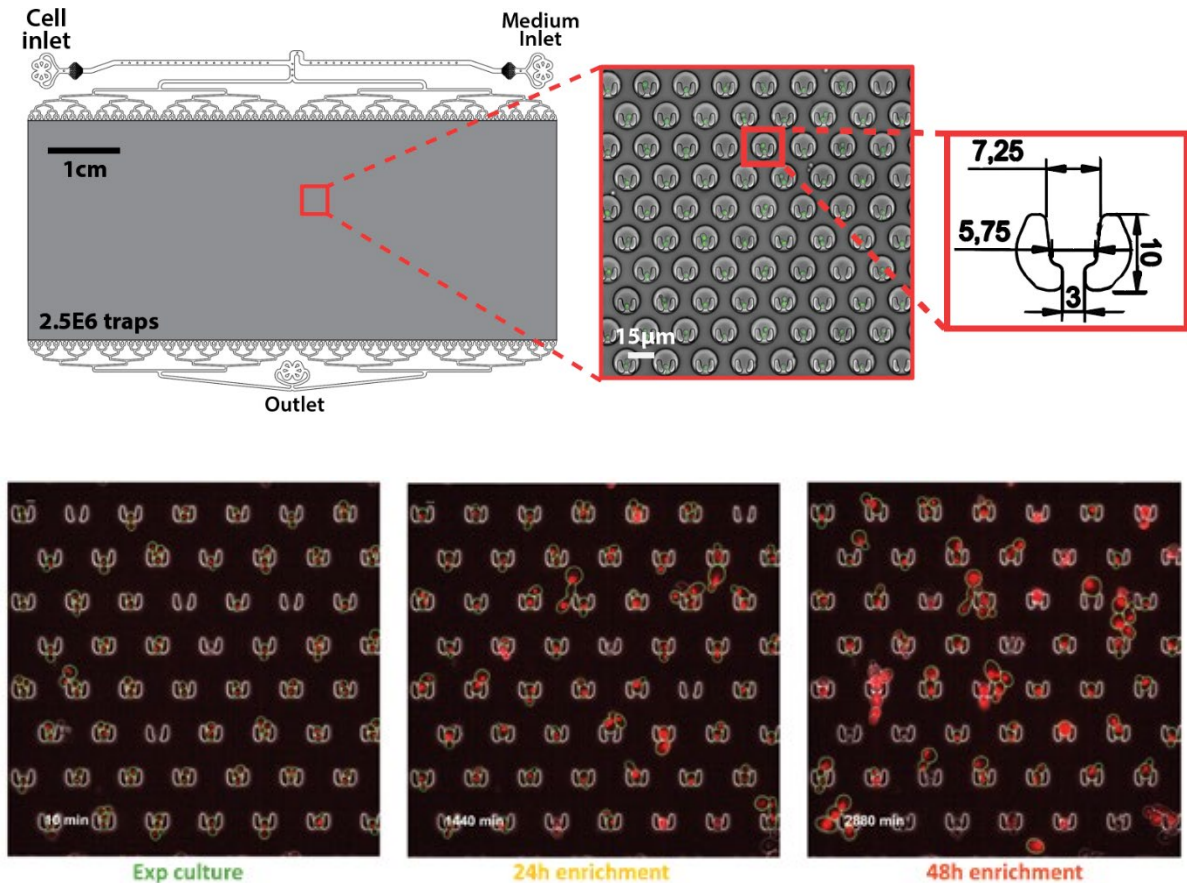
Therefore, some kind of sorting must be done before performing population assays in order to reduce the impact of the averaging bias.

As presented in the main text (p.86), most cells follow a stereotyped path of aging in which they experience a cell-cycle slowdown (Senescence Entry Point, SEP). This slowdown strongly correlates with an increase in the karyoplasmic ratio and is preceded by an increase in nucleolus size. The SEP occurs at very different ages from one cell to another, but using these two markers could help sort the cells in pre-SEP and post-SEP categories (Appendix figure 1).



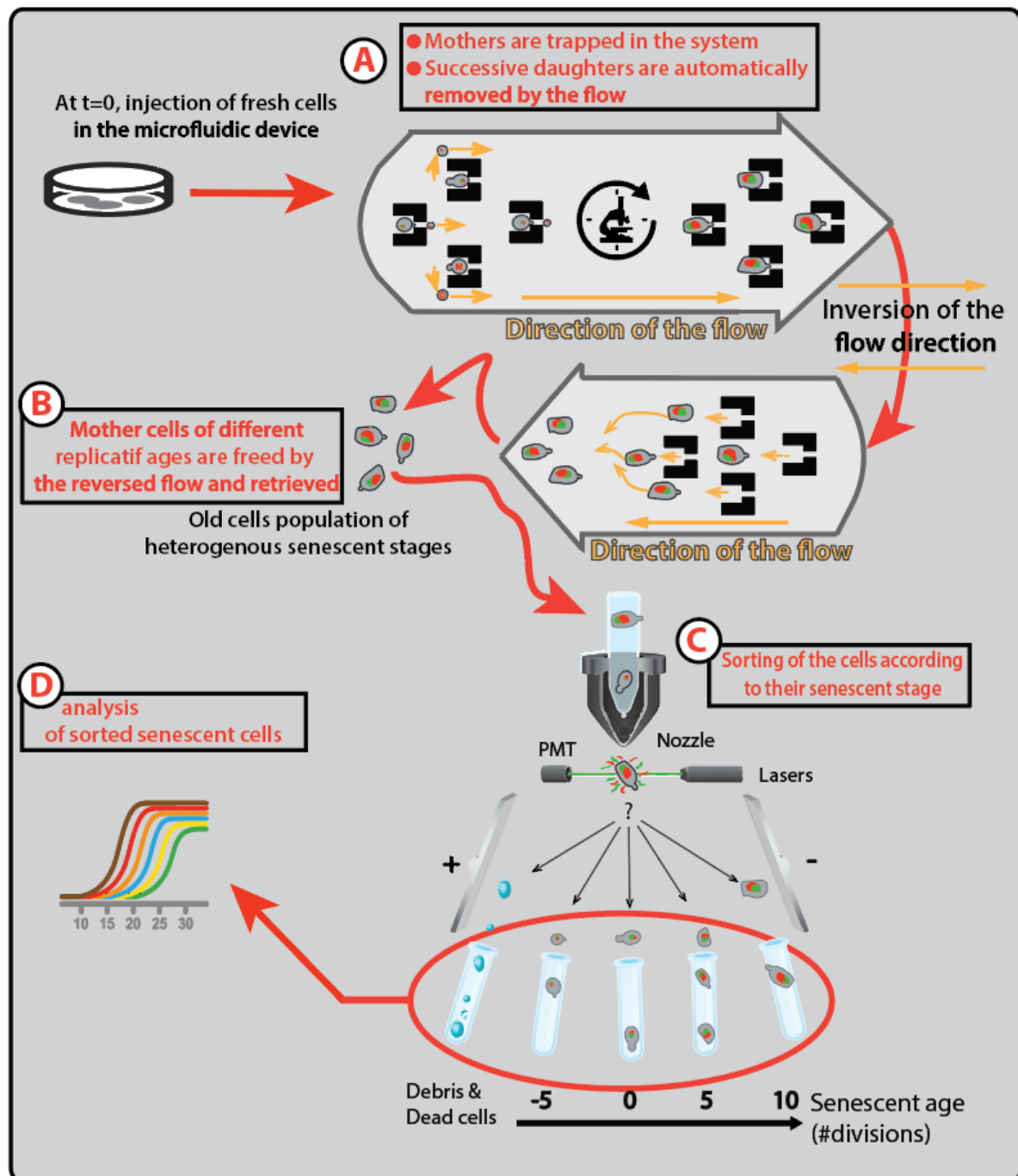
Appendix figure 1: (Top) Division duration of a population aligned to birth (left) and to the SEP (right) after a timelapse. (Middle): Harvesting a culture of old cells at a given time gives a heterogeneous population made of pre-SEP and post-SEP cells, that needs to be sorted. (Bottom): Sorting cells regarding their SEP state is possible without knowing their history, by using fluorescent markers.

To enrich a population with old cells, I developed a microfluidic device based on microtraps similar to what is presented in the main text (p.89). Indeed, an array of 2 million U-shaped traps (improved from [3], [4]) can trap mother cells that are maintained against the structure by a constant flow of media. Hence, the progeny of the trapped mothers is automatically dissected and flushed away (Appendix figure 2).



Appendix figure 2: (Top): Schematics and image of the microfluidic device used for old mothers enrichment. (Bottom): Typical images (Phase contrast + mCherry) of the chip after injection (left), after 24h (center), or after 48h (right). Old cells are larger and their NLS-mCherry signal is stronger.

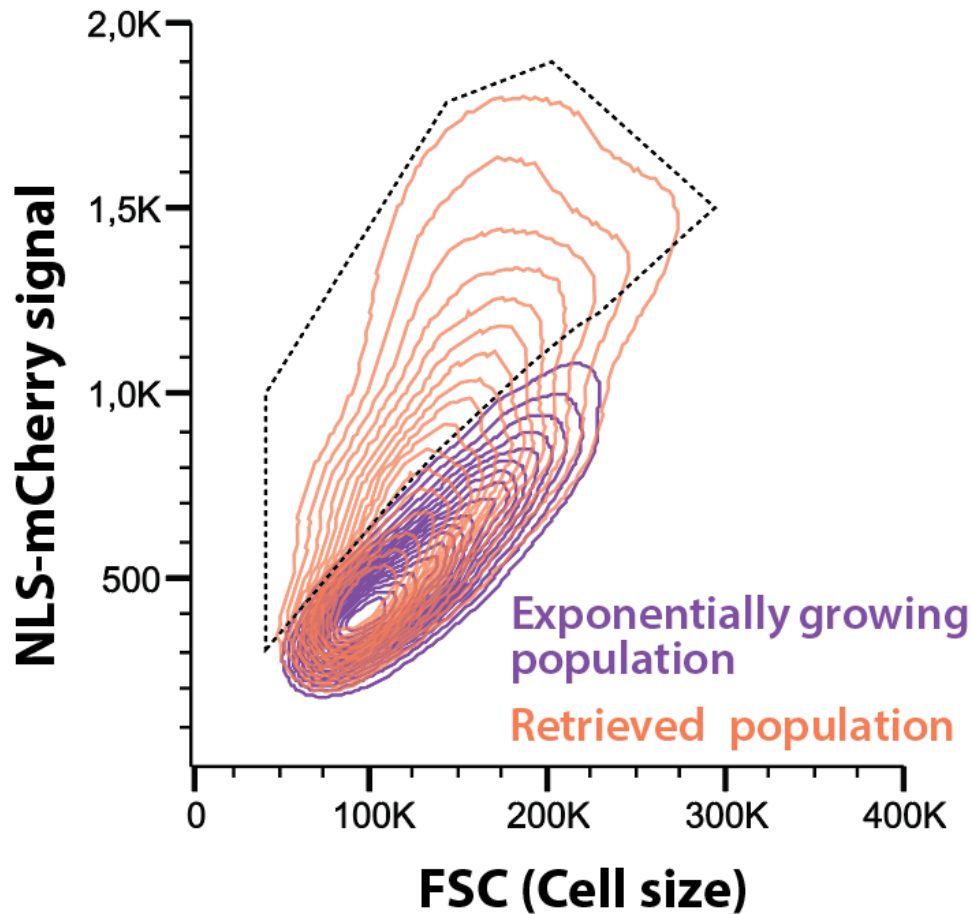
Importantly, the trapping is reversible and cells can be freed from the traps by applying a flow in the opposite direction, with an efficiency of $97 \pm 0.5\%$ ($N=3$ replicates of 500 cells, by counting the number of cells remaining of the traps after the retrieval). The fluorescence and size of these cells can then be measured by flow cytometry, and cells of interest can be sorted out based on the cytometric signals (Appendix figure 3).



Appendix figure 3: Summary of the method to enrich a population with old individuals and sort them according to their senescence status. (A) Using a microfluidic device, one can trap and age mother cells inside specific structures that automatically remove the progeny. (B) Reverting the flow allows retrieval of the old cells. (C) FACS is used to discriminate cells according to their senescent stage. (D) Subsequent analysis can be performed on the different categories

Doing that after 24h enrichment with a strain harboring a nuclear marker (NLS-mCherry) shows that 35% of the 2 million retrieved cells have a fluorescent signal higher than the one from exponential culture (Appendix figure 4). However, we could still observe a population of small cells with a small nuclear signal, which is probably daughters born during the

harvesting. By selecting cells from different gatings relative to their size and fluorescence, we could obtain subpopulations with different post-SEP/pre-SEP ratios.



Appendix figure 4: NLS-mCherry signal against forward scatter signal from the cytometric profile of exponentially growing culture (purple) and of the retrieved population after 24h of enrichment (orange).

These preliminary results suggest that it is possible to enrich a population with old cells and sort them according to their senescence status. However, controls have to be done to validate the method. In particular, it is possible to reinject the sorted subpopulations in the microfluidic device in order to measure their cell cycle duration, size, and nucleus size, as well as their remaining replicative lifespan.

Therefore, to estimate the stringency of the sorting, measuring the age distribution of the different subpopulations (by counting the bud scars), but also the fraction of pre- and post-SEP cells will need to be done.

Why use microfluidics over already existing enrichment techniques? If the yield is two orders of magnitude lower than standard techniques, microfluidics allows the tracking of the cells

before harvesting them to correlate longitudinal signals with the subsequent readouts (such as transcriptomic profiles). Besides, cells can be cultured in changing environments (for instance, temporal patterns such as steps, ramps, or PWM of a given stress), which is difficult to do with the current methods.

As a perspective, the sorting could be refined using a nucleolar marker to differentiate between an “early pre-SEP” and a “late-pre-SEP” population (Appendix figure 1). Besides, the whole pipeline could be integrated into a single microfluidic device using droplet-based microfluidic sorting of single-cells [5–7].

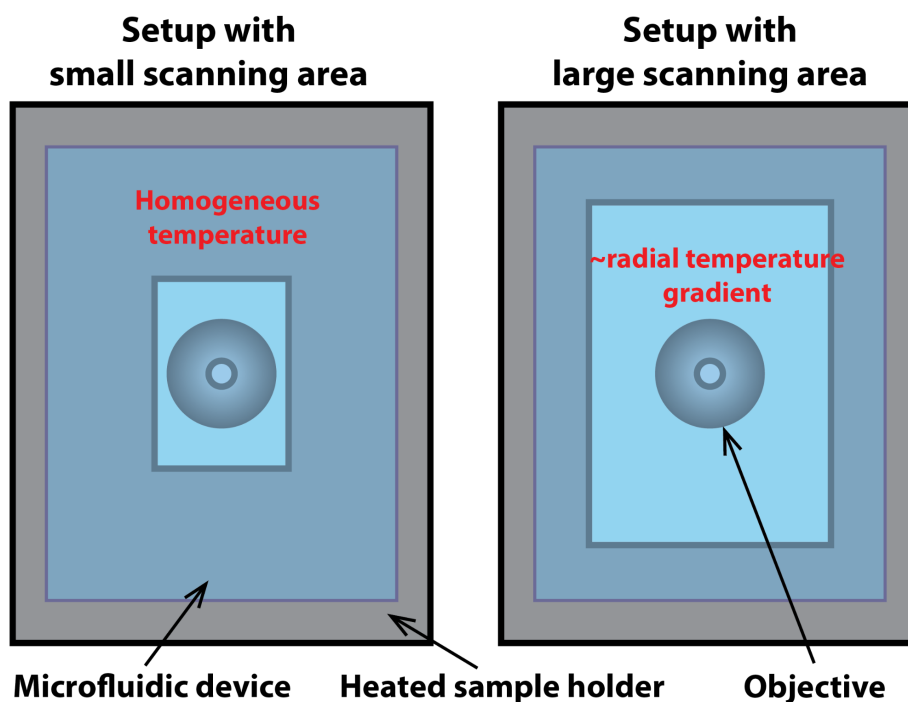
References

- [1] S. Fehrmann, C. Paoletti, Y. Goulev, A. Ungureanu, H. Aguilaniu, and G. Charvin, “Aging Yeast Cells Undergo a Sharp Entry into Senescence Unrelated to the Loss of Mitochondrial Membrane Potential,” *Cell Reports*, vol. 5, no. 6, pp. 1589–1599, 2013, doi: 10.1016/j.celrep.2013.11.013.
- [2] S. Morlot, J. Song, I. Léger-Silvestre, A. Matifas, O. Gadai, and G. Charvin, “Excessive rDNA Transcription Drives the Disruption in Nuclear Homeostasis during Entry into Senescence in Budding Yeast,” *Cell Reports*, vol. 28, no. 2, pp. 408–422.e4, 2019, doi: 10.1016/j.celrep.2019.06.032.
- [3] M. M. Crane, I. B. N. Clark, E. Bakker, S. Smith, and P. S. Swain, “A Microfluidic System for Studying Ageing and Dynamic Single-Cell Responses in Budding Yeast,” *Plos One*, vol. 9, no. 6, p. e100042, 2014, doi: 10.1371/journal.pone.0100042.
- [4] M. C. Jo, W. Liu, L. Gu, W. Dang, and L. Qin, “High-throughput analysis of yeast replicative aging using a microfluidic system,” *Proc National Acad Sci*, vol. 112, no. 30, pp. 9364–9369, 2015, doi: 10.1073/pnas.1510328112.
- [5] J.-C. Baret *et al.*, “Fluorescence-activated droplet sorting (FADS): efficient microfluidic cell sorting based on enzymatic activity,” *Lab Chip*, vol. 9, no. 13, pp. 1850–1858, 2009, doi: 10.1039/b902504a.
- [6] L. Mazutis, J. Gilbert, W. L. Ung, D. A. Weitz, A. D. Griffiths, and J. A. Heyman, “Single-cell analysis and sorting using droplet-based microfluidics,” *Nat Protoc*, vol. 8, no. 5, pp. 870–891, 2013, doi: 10.1038/nprot.2013.046.
- [7] A. Fallah-Araghi, J.-C. Baret, M. Ryckelynck, and A. D. Griffiths, “A completely in vitro ultrahigh-throughput droplet-based microfluidic screening system for protein engineering and directed evolution,” *Lab Chip*, vol. 12, no. 5, pp. 882–891, 2012, doi: 10.1039/c2lc21035e.

Appendix 2: Versatile heating system for long-term microfluidic culture

Culturing cells during their replicative lifespan requires a constant temperature to avoid potential unwanted effects and ensure reproducibility. Besides, a stable temperature ensures focus stability during timelapses.

Traditional systems for temperature control in microfluidic are based on heating the plate holding the microfluidic device. This is efficient when the contact surface between the chip and the holder is high. However, for high-throughput applications, this surface has to be minimized in order to increase the area of the device that can be imaged. This leads to high-temperature heterogeneities (up to 3°K) between the device's center and edges (Appendix figure 5).



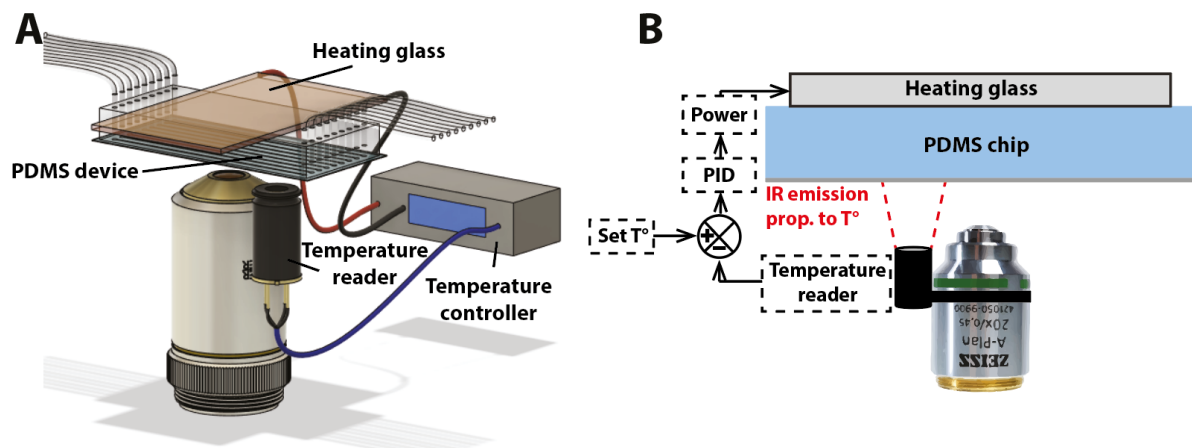
Appendix figure 5: Schematics representing the different contact area between the microfluidic device and the heated sample holder. A setup with a high contact area as a small scanning area (left) and vice-versa (right).

Other ways of controlling the temperature of a microfluidic device involve using heated fluids, which are very efficient and allow high-speed temperature switches (of the scale of the second) but require specific secondary channels for each device.

It is also possible to homogeneously control the temperature of the microfluidic device by putting the microscope in an incubator, but this solution requires a lot of space and a complex setup.

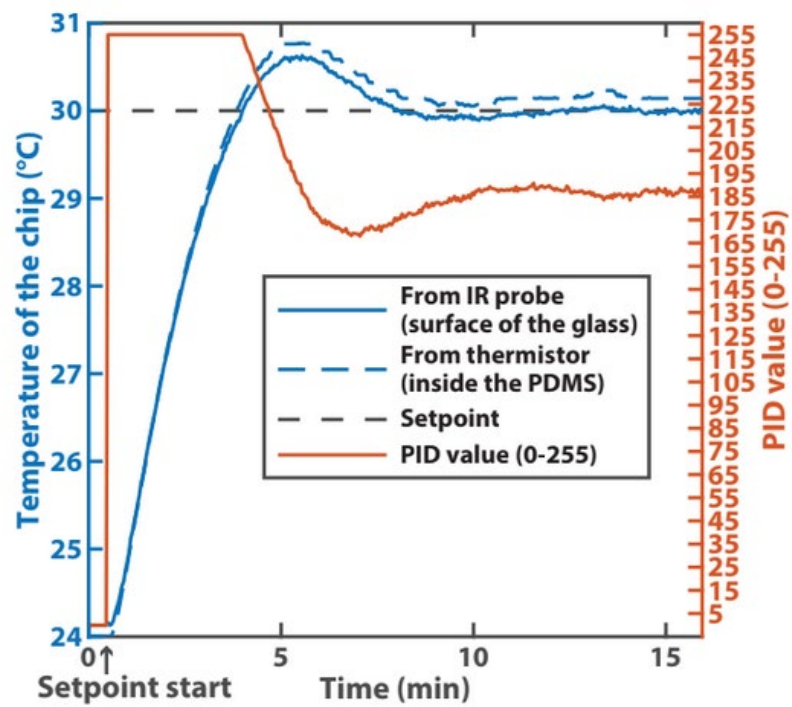
Therefore, no simple and versatile system can heat a microfluidic device on a large optical opening sample holder. Hence, I developed a portable heating system based on a heating glass in contact with the device from the top face.

With that, the heating is homogeneous and adaptable to any device. To control the temperature precisely, a probe based on the infrared emission measures the temperature of the glass slide on which the cells are. Interestingly, the PDMS and the glass slide are opaque to infrared light, so all the infrared incoming to the probe is emitted by the glass surface. Confirming that, a thermistor probe casted into the PDMS gives a very similar temperature to that of the infrared probe (Appendix figure 6). Finally, an Arduino chip with a custom program enslaves the temperature to the given setpoint using a Proportional Integral Derivative (PID) controller.



Appendix figure 6: Schematics of the heating system in 3D (A) and in 2D (B).

With this system, one can achieve stable temperature control, reaching a steady-state in 5min (Appendix figure 7) and with a maximal spatial temperature variation of 0.3°K (data not shown). Although it is not suitable to make fast temperature switches (for example, to apply a heatshock), it is applicable to any microfluidic device and costs less than 75€.



Appendix figure 7: Temperature of the chip (blue curve) measured with the infrared probe (solid line) or with a thermistor casted inside the chip (dotted line). The setpoint is represented with the black dotted line and the startpoint is indicated by the black arrow. The orange line indicates the value of the PID controller.

Appendix 3: (Collaboration) Specialization of chromatin-bound nuclear pore complexes promotes yeast aging

This paper is the result of a collaboration with the Barral lab (ETH Zurich), to which I sent my microfluidic devices for them to perform aging experiments. The message of the paper is in line with the rest of the thesis since it describes how ERCs can be toxic to the cell. (See paper next page)

Specialization of chromatin-bound nuclear pore complexes promotes yeast aging

Anne C. Meinema¹, Theo Aspert², Sung Sik Lee¹, Gilles Charvin², Yves Barral^{1*}

1) Institute of Biochemistry, Department of Biology, ETH Zürich, Zürich, Switzerland.

2) Institute of Genetics and Molecular and Cellular Biology, Illkirch, France.

3) Institute of Molecular and Systems Biology, ETH Zürich, Zürich, Switzerland.

The nuclear pore complex (NPC) mediates nearly all exchanges between nucleus and cytoplasm, and changes composition in many species as the organism ages. However, how these changes arise and whether they contribute themselves to aging is poorly understood. We show that in replicatively aging yeast cells attachment of DNA circles to NPCs drives the displacement of the NPCs' nuclear basket and cytoplasmic complexes. Remodeling of the NPC resulted from the regulation of basket components by SAGA, rather than from damages. These changes affected NPC interaction with mRNA export factors, without affecting the residence of import factors or engaging the NPC quality control machinery. Mutations preventing NPC remodeling extended the replicative lifespan of the cells. Thus, our data indicate that DNA circles accumulating in the mother cell drive aging at least in part by triggering NPC specialization. We suggest that antagonistic pleiotropic effects of NPC specialization are key drivers of aging.

Keywords:

Aging; DNA circles; NPC; nuclear basket;

* Correspondence: yves.barral@bc.biol.ethz.ch

1 Introduction

2 Nuclear pore complexes (NPCs), which mediate transport of cargos between the nucleus and the
 3 cytoplasm, undergo substantial changes during aging from yeast to mammals (Rempel et al., 2020).
 4 In post-mitotic cells such as neurons, core NPC components are very stable, tend to become oxidized
 5 over time and progressively lose functionality (Savas et al., 2012; Toyama et al., 2013). Accordingly,
 6 in the neurons of old rats NPCs become increasingly leaky with age, affecting the proper retention of
 7 nucleoplasmic proteins in the nucleus (D'Angelo et al., 2009). On the opposite, yeast NPCs are
 8 targeted by a quality control machinery that removes damaged or misassembled NPCs (Webster et
 9 al., 2014). Accordingly, no oxidized NPCs are observed in replicative aging yeast cells (Rempel et al.,
 10 2019). Still, proteomics analysis of the old yeast cells indicate that they progressively change
 11 composition, losing their nuclear basket and cytoplasmic complexes (Janssens et al., 2015; Rempel et
 12 al., 2019). Similar changes are observed in the liver of aging rats (Ori et al., 2015; Rempel et al.,
 13 2020). However, little is known about the underlying mechanisms and whether this process is
 14 simply a consequence or contributes to aging. Particularly, the NPC changes observed in replicative
 15 aging yeast cells did not lead to leakage but rather to a more stringent compartmentalization of the
 16 tested cargos (Morlot et al., 2019; Rempel et al., 2019). Given the pivotal role of NPCs in a wide
 17 variety of cellular processes beyond nucleocytoplasmic exchange, from the regulation of gene
 18 expression to DNA repair, it is plausible that defects in NPC function could affect cellular physiology
 19 and contribute to the ageing process. However, a clear view of how age affects NPCs and their
 20 functionality has been lacking so far, precluding a robust understanding of whether and how NPCs
 21 indeed contribute to the aging process.

22 The budding yeast *Saccharomyces cerevisiae* undergoes both post mitotic and replicative aging
 23 (Longo et al., 2012). In the first case, also called chronological aging, starved yeast cells progressively
 24 lose viability, with their mortality increasing exponentially with time (Fabrizio and Longo, 2003). In
 25 the second case, cells that proliferate in rich nutrient conditions divide asymmetrically through the
 26 budding of rejuvenated daughters off the surface of their aging mother cell, which retain and
 27 accumulate diverse aging factors (Mortimer and Johnston, 1959; reviewed in Denoth Lippuner et al.,
 28 2014). After undergoing 20-30 divisions and generating as many daughter cells, these mother cells
 29 stop dividing and ultimately die. Although a number of the involved aging factors and some of the
 30 mechanisms of their retention in the mother cell have been characterized, little is known about how
 31 they affect the viability of old mother cells.

32 Extrachromosomal DNA circles (ERCs, (Denoth Lippuner et al., 2014; Morlot et al., 2019; Sinclair and
 33 Guarente, 1997)), which are generated in virtually all mother cells at some point in their lifespan
 34 through excision of one or more rDNA repeat(s) from the rDNA locus, are a particularly prominent
 35 aging factor. These episomes lack a centromere and are very efficiently retained in the mother cell
 36 at mitosis. As they replicate once per division cycle, they accumulate exponentially in the nucleus of
 37 the old mother cell over time. At the end of their life, the mother cell may contain up to thousand
 38 ERCs, which represent about as much DNA as the rest of the genome (Denoth-Lippuner et al., 2014;
 39 Morlot et al., 2019). Several lines of evidence establish that ERCs accumulation promote aging of
 40 the cell. Mutants that form ERCs at a reduced rate, such as the *fob1Δ* mutant cells, show an
 41 extended replicative lifespan (RLS; (Defossez et al., 1999). In reverse, cells in which recombination in
 42 the rDNA is derepressed, such as cells lacking the sirtuin Sir2, show a higher rate of ERC formation,
 43 accumulate them faster and are short-lived (Kaeberlein et al., 1999). Finally, artificially introducing
 44 an ERC (Sinclair and Guarente, 1997) or any other replicating DNA circle in a young cell (Denoth-
 45 Lippuner et al., 2014) causes premature aging. However, how ERCs promote aging is not known.

The tight retention of the ERCs in the mother cell depends on their attachment to NPCs at the nuclear periphery (Denoth-Lippuner et al., 2014). Attachment is mediated by the SAGA complex, a large multi-subunit complex harboring acetyl-transferase activity (provided by Gcn5) and which binds both NPCs, via the SAGA subunit Sgf73 and the stable nucleoporin Nup1 (Jani et al., 2014; Köhler et al., 2008) and chromatin (Durand et al., 2014; Wang et al., 2020). Since yeast cells undergo a closed mitosis and NPCs remain intact through mitosis, attachment of the DNA circles to NPCs leads to the retention of both in the mother cell. Retention is facilitated by the presence of a ceramide-based, lateral diffusion barrier in the outer-membrane of the nuclear envelope (Baldi et al., 2017; Clay et al., 2014; Denoth-Lippuner et al., 2014; Megyeri et al., 2019; Prasad et al., 2020; Shcheprova et al., 2008). Accordingly, cells that fail to attach ERCs to NPCs (such as the cells lacking the SAGA subunits Sgf73 and Gcn5) or fail to assemble the diffusion barrier (in cells lacking the barrier protein Bud6) cannot tightly confine the ERCs to the mother cell anymore and do not accumulate them over time. Providing further evidence for ERCs promoting cellular aging, these cells and the mutant strains unable to form a lateral diffusion barrier in the nuclear envelope (such as the cells lacking the ceramide synthase Lag1, the sphinganine C4-hydroxylase Sur2) show a dramatically increased longevity (Clay et al., 2014; D'Mello et al., 1994; Denoth Lippuner et al., 2014; Megyeri et al., 2019; Shcheprova et al., 2008). Interestingly, because ERCs and NPCs are retained together in the mother cell during cell division, aging wild type cells also accumulate NPCs and this accumulation is relaxed in cells lacking either of the Fob1, Sgf73 or Bud6 proteins (Denoth-Lippuner et al., 2014). Thus, these accumulating NPCs may contribute to the mechanisms by which ERCs promote aging of the cell.

The nuclear pore complex is a ~100 megadalton entity comprising repetitions of more than 30 different subunits, called nucleoporins (short Nups)(Beck and Hurt, 2017; Kim et al., 2018). The core of the NPC is inserted in the nuclear envelope and stabilized by protein rings at its periphery. The center is filled by so-called FG-Nups, which both form a barrier to passive diffusion through the pore and facilitate the passage of transport intermediates across the NPC. On their cytoplasmic face, NPCs are decorated by a complex of cytoplasmic Nups which have been also described as fibrils or filaments (Fernandez-Martinez et al., 2016; Strambio-De-Castillia et al., 2010)(Fig. 1A). On their nucleoplasmic side, they assemble the so-called nuclear basket formed mainly of the extended protein TPR, known as Mlp1 and Mlp2 in yeast (Strambio-de-Castillia et al., 1999). Diverse studies have involved the basket in controlling the interaction of chromatin with the NPC (Niepel et al., 2013). However, whether and how DNA circle attachment to NPCs affects these NPCs is not known. Therefore, we have investigated here whether the anchorage of DNA circles to NPCs affects their composition during replicative aging and whether this has an effect on cellular viability.

Results and discussion

Circle-bound NPCs lack the nuclear basket

In order to study whether the anchorage of DNA circles to NPCs affects the NPCs' composition, we took advantage of an engineered reporter DNA circle, which we have previously characterized (Baldi et al., 2017; Denoth-Lippuner et al., 2014; Shcheprova et al., 2008). The non-centromeric reporter DNA circle can be generated in vivo in a controlled manner. This circle is formed upon the induced excision of the centromere from a circular mini-chromosome and carries an array of 256 TetO repeats (Megee and Koshland, 1999). Hence, it is visible as a fluorescent dot in cells expressing TetR fused to a fluorescent protein (Fig. 1B, see methods and (Denoth-Lippuner et al., 2014). This circle

replicates in S-phase and remains confined in the mother cell upon cell division, where it accumulates as the cell ages through successive rounds of cell division. Within 8-10 division cycles, the accumulating DNA circles cluster together to form a bright patch at the nuclear periphery. The attached NPCs accumulate with them in the nuclear envelope adjacent to the cluster (Denoth-Lippuner et al., 2014). Upon fusion of GFP to core nucleoporins, these NPCs are visible as a cap of enhanced fluorescence density (Fig. 1C, Figure 1-supplement 1A), different from young cells without accumulation of DNA circles, where nucleoporins are rather homogeneously distributed in the nuclear envelope (Figure 1-supplement 1B). In the few cells that accumulate the circle in the population, this system conveniently allows imaging circle-bound NPCs at single cell level, to discriminate them from unbound NPCs in the remainder of the same nuclear envelope.

Thus, we used this engineered DNA circle to quantify the local enrichment of single nucleoporins in the NPC cap compared to the rest of the nuclear envelope, to study the composition of DNA circle bound NPCs. We tagged 17 nucleoporins with GFP, representative of different NPC subcomplexes, in cells where the DNA circle cluster was labelled in red, owing to the expression of TetR-mCherry (Fig. 1B, C). In these images, all the stable core Nups, i.e. the scaffold components (outer ring: Nup84, Nup133; inter ring: Nup170, Nup96) and the components of the transport channel (FG-Nups: Nup53, Nup59) accumulated in the cap to similar extents. Quantification of their indicated a median of 2.4-fold enrichment, compared to their localization elsewhere in the nuclear envelope; Fig. 1D, E). All tested core nucleoporins showed the same enrichment in the cap covering the DNA circles, indicating that the circles bind intact NPC cores. The enrichment level of core Nups in the cap served therefore as reference to determine whether peripheral Nups were stoichiometrically associated with core NPCs bound to circles or depleted from those pores.

In striking contrast to core Nups, most peripheral subunits on both sides of the NPC were found to not accumulate in the cap. Four out of the five components of the nuclear basket and four out of the six components of the cytoplasmic complexes were excluded from the cap (Fig. 1C, E). Only Nup1, a stable nucleoporin at the nuclear side, and Nup159 and Nup83, which form the docking site for the cytoplasmic complexes at the cytoplasmic side of NPCs, accumulated together with core Nups. The basket components Mlp1 and 2, Nup60 and Nup2, and the subunits at the cytoplasmic side Nup116, Nup42, Gle1 and Gle2 were extensively excluded from the cap. The exclusion was the strongest for the basket proteins Mlp1 and Mlp2 (Fig. 1E), similarly to what is observed in the vicinity of the nucleolus (Galy et al., 2004), although the cluster of circles and the nucleolus do not overlap (Denoth-Lippuner et al., 2014). Altogether, these quantifications indicate that relative to the unbound NPCs, the circle-bound NPCs were specifically stripped of their nuclear basket and cytoplasmic complexes.

This picture is highly reminiscent of recent proteomics data indicating that Nup116, Nup2 and Nup60 are extensively lost from old yeast cells (Rempel et al., 2019). This study also identified Nsp1, a component of both the core and the cytoplasmic complex of the NPC (Bailer et al., 2001), as being lost with age. Because tagged Nsp1 is partially defective (Rajoo et al., 2018), we did not characterize its distribution. Thus, our results support previous observations indicating that old cells lose specific parts of the NPC, and suggest that this loss is driven by the attachment of DNA circles to the affected NPCs. Since Mlp1 and Mlp2 are required for DNA attachment to NPCs (Texari et al., 2013), including the attachment of DNA circles (Shcheprova et al., 2008), these proteins might mediate the recruitment of the DNA to NPCs but be subsequently displaced from them. Furthermore, our observations suggest that the loss of NPC components is not limited to those picked up by mass spectrometry but can be extended to nearly the entire basket and cytoplasmic complexes, including

Mlp1 and Mlp2, Nup42, Gle1 and Gle2. Indeed, proteomic studies do not have the subcellular resolution obtained with our approach.

The basket and cytoplasmic complexes are displaced from NPCs in wild type cells aging under physiological conditions.

To evaluate whether remodeling of the circle-bound NPCs was indeed reflecting what happens in cells undergoing unperturbed aging, we next asked whether the basket and cytoplasmic complexes dissociates from NPCs of old cells not carrying our reporter circles. For some reason, accumulating ERCs are rather dispersed throughout the nuclear periphery and form clusters only episodically, such that NPC caps are less prominently observed in these cells. Clustering of the reporter circle might be stabilized by the fluorescent label (mCherry still has a low affinity for itself) or ERCs have means to escape clustering. In order to study if NPC remodeling happens under these conditions, we co-labelled pairs of Nups with distinct fluorophores and characterized their co-incorporation into NPCs by analyzing the spatial correlation of their fluorescence in the nuclear periphery as the cells aged (Fig. 2A). Indeed, the signals of the two labelled Nups should correlate well with each other as long as both colocalize to NPCs, and poorly if any one of them is displaced from NPCs (Fig. 2A).

In order to acquire images of old mother cells, the labelled cells were loaded on a microfluidic chip (Jo et al., 2015) and imaged for 26 hours (21 divisions in average). A continuous flow of fresh medium provided nutrients to the trapped mother cells and flushed their daughter cells out, allowing the continuous imaging of the isolated mother cells. Bright field images were taken every 15 minutes to monitor budding events and record the replicative age of each cell. Fluorescence images were acquired after 2 and 26 hours (i.e. on average 2 and 21 divisions, respectively, Fig. 2B) and the degree of colocalization between two Nups was quantified at these two time points (Fig. 2C).

Analysis of the Pearson correlation between the signals of two core nucleoporins, namely Nup159 (labelled with mCherry) and Nup170 (labelled with GFP), showed that it was high in young cells and remained similarly high in old yeast mother cells (average correlation = 0.79 ± 0.02 , $n=30$ and 0.78 ± 0.03 , $n=33$, respectively; Fig. 2C). Thus, these two proteins remain indeed stable at NPCs of old cells. In contrast, the basket proteins Nup60 and Mlp1 and the cytoplasmic protein Gle1 (labelled with GFP) colocalized less extensively with Nup159 already in young cells (average correlation = 0.68 ± 0.04 , $n=32$; 0.61 ± 0.04 , $n=31$ and 0.62 ± 0.05 , $n=32$ respectively), consistent with these proteins being more mobile and transiently associated with NPCs (Denning et al., 2001; Denoth-Lippuner et al., 2014; Dilworth et al., 2001; Niepel et al., 2013). More importantly, the correlation substantially dropped further in old cells (average correlation 0.35 ± 0.05 , $n=33$; 0.31 ± 0.06 , $n=37$ and 0.24 ± 0.06 , $n=35$ respectively; $p < 10^{-4}$; Fig. 2C). A similar drop of correlation was observed when comparing the signals of Mlp1-GFP and Nup82-mCherry (Fig. 2D, E), indicating that this correlation drop did not depend on the core Nup used as reference. Thus, the basket and cytoplasmic complexes are indeed displaced from a substantial fraction of the NPCs in old cells, upon unperturbed aging.

The ERCs mediate the displacement of the basket from NPCs of old mother cells

To determine whether this remodeling of the NPC upon aging is driven by the accumulation and attachment of endogenous DNA circles, we first asked whether delaying ERC accumulation also delayed the removal of the basket from NPCs. Thus, we deleted the *FOB1* gene, which promotes ERC formation, and tested whether this restored the presence of the basket components Nup60 and Mlp1 at NPCs of old mutant cells (Fig. 3A). Strikingly, no significant dissociation of the basket from NPCs was observed in old *fob1Δ* mutant cells compared to wild type at the same age (same number

of divisions) or to young *fob1Δ* mutant cells (Fig. 3A). Moreover, deleting the *SGF73* gene, which docks SAGA to NPCs and mediates circle anchorage to nuclear pores, also restored the localization of the basket to NPCs in aged cells (Fig. 3B). Thus, ERC presence and attachment is required for the basket to be displaced from NPCs.

Finally, as ERC anchorage displaces the basket from a substantial fraction of the NPCs in old wild type mother cells, their daughters, which do not inherit ERCs are expected to rapidly restore the proper localization of the basket proteins. Indeed, when comparing signal correlation between the basket proteins Nup60 or Mlp1, with the core Nup, Nup159, colocalization between basket and core nucleoporins was extensive in the rejuvenated daughter cells of old mothers, similar to what is observed in both the young mothers and their daughters (Fig. 3C, D). The correlation between basket and core Nups was only reduced in aged mothers. Altogether, we conclude that the formation of ERCs and their attachment to NPCs drives the displacement of the nuclear basket from pores. ERC accumulation is a direct cause for the displacement and loss of the nuclear basket from NPCs in physiologically aging yeast cell. This event probably mediates the subsequent displacement and loss of the cytoplasmic complexes (see below).

The cells do not recognize remodeled NPCs as defective

Several studies have indicated that NPCs can deteriorate with time and established the existence of a machinery dedicated to removing damaged or misassembled NPCs. This quality control system recruits the ESCRT III machinery, including the adaptor protein Chm7, to defective NPCs and mediates their removal from the nuclear envelope (Rempel et al., 2019; Webster et al., 2016). Thus, we next asked whether the attachment of DNA circles and basket removal induces a defect that would be recognized as damage by the cell. To address this question, we investigated whether the circle-bound NPCs recruit Chm7 more frequently than bulk NPCs. We recorded the localization of Chm7, tagged with GFP, in cells loaded with DNA circles and asked whether it accumulated in the cap (Fig. 4A). The cells containing a cluster of DNA circles were categorized in the following classes: 1) the cells showing at least one Chm7 focus in the NPC-cap, 2) those showing a Chm7 focus somewhere else in the nuclear envelope and 3) those showing no visible Chm7 foci in the nuclear envelope (Fig. 4A). Interestingly, most cells formed either no Chm7 focus at the nuclear periphery (category 3, 41% of cells, $n = 190$ cells with circle cluster) or the focus formed was not associated with the cluster of DNA circles (category 2, 23% of the cells). Only about a third of the cells (category 1, 36%) formed a Chm7 focus adjacent to the circle-cluster, i.e. where the NPC-cap is located. Note that these Chm7-labeled foci are much smaller than the NPC-cap (Fig. 1C, 4A), indicating that if any, only few of the NPCs in the cap are targeted by this machinery. Importantly, based on fluorescence intensity measurements using Nup84-GFP in DNA circle loaded cells (Fig. 1C), we estimate that about 45% (+/- 12%, $n = 10$) of the NPCs is sequestered in the NPC-cap at that stage. Thus, this analysis did not reveal any substantial enrichment of Chm7 overlapping with the clusters of DNA circle; the occurrence of Chm7 in the NPC cap seemed to be rather coincidental. We concluded that the circle-bound NPCs are not detected as defective by the cell more or less than the other NPCs in the rest of the nuclear envelope.

The remodeled NPCs are not particularly old

Since the anchorage of a DNA circle to an NPC causes its retention in the mother cell, we next wondered whether this could cause the progressive accumulation of older NPCs in aged mother cells. To test this possibility, we measured the relative age of NPCs in old mothers and their daughter cells using the tandem fluorescent protein timer, consisting of mCherry (mCh) and superfolder GFP (sfGFP) (Khmelniskii et al., 2012). Due to different maturation kinetics between the

two fluorophores, a newly synthesized protein appears first in the green channel before acquiring the red fluorescence over time. As the turnover rate of Nup170 is very low in NPCs (D'Angelo et al., 2009), older pores with tagged Nup170 are expected to emit more red fluorescence than green in comparison to newly assembled pores. To see if old mothers are enriched in red-shifted old pores, we loaded the cells expressing Nup170-mCh-sfGFP on the microfluidic chip and imaged them as above (Fig. 2B) as the cells aged (Jo et al., 2015). The fluorescence channels were recorded after 2 and 26h. We did observe a tendency for young cells to put slightly more red shifted NPCs in the bud than in the mother cell (Fig. 4B, not statistically significant, $n=31$ mother-bud pairs), as was shown before (Khmelniskii et al., 2012). Over time we observed a highly significant increase of the red fluorescence signal relative to the green signal in old compared to young cells ($n=29$ old cells, $p<0.001$), indicating that old cells actually accumulate old pores over time. Although we observed a trend for the NPCs of the daughters of old mother cells to be slightly younger, indicative for some retention of old pores in the mother cell, this difference was not significant in our analysis (Fig. 4B).

Thus, together these data make three points. First, the data support earlier findings indicating that pre-existing NPCs in young cells are not particularly retained in the mother cell and even that their segregation might be biased towards the daughter cell (Khmelniskii et al., 2012). Second, the data establish that over time the mother cell does accumulate older NPCs, possibly with the accumulation of ERCs. Third, these older NPCs are however not tightly retained in the old mother cell. As circle-bound NPCs are retained in the mother cell (Fig. 3C, D, (Denoth-Lippuner et al., 2014)), these findings suggest that old NPCs do exchange the circles with younger ones. This conclusion is in agreement with the results from photobleaching experiments previously reported (Denoth-Lippuner et al., 2014), indicating that although NPC exchange is slow between the cap and the rest of the nuclear envelope, it does happen. Thus, we concluded that although circle-bound NPCs accumulating in mother cells are rather old in average, they are not significantly older than those of the rejuvenated daughter cells. Thus, together our data do not support the notion that the age of the old mother NPCs drives their remodeling.

Nucleoporin acetylation promotes NPC remodeling

Since DNA circles attach to NPCs via the SAGA complex, we next wondered whether basket removal could be driven by their SAGA-dependent acetylation. Indeed, three of the four basket proteins displaced from NPCs upon circle attachment are acetylated *in vivo*, and the acetylation of Nup60 and Nup2 is mediated at least in part by SAGA (Downey et al., 2015; Henriksen et al., 2012). Testing whether removing SAGA activity altogether restored the recruitment of the basket proteins was not possible in our "cap" assay since knocking out its catalytic subunit, encoded by *GCN5*, abolished circle clustering and cap formation (Fig. 5A), consistent with SAGA and its acetyl-transferase activity mediating circle anchorage to NPCs (Denoth-Lippuner et al., 2014).

Thus, instead of inactivating SAGA we asked whether acetylation of the basket proteins contributes to displacing them from pores. Nup60 is prominently acetylated on lysine 467 (Choudhary et al., 2014, 2009). Therefore, we asked as a proof of principle whether preventing this modification by substituting lysine-467 by arginine was sufficient to abrogate the exclusion of Nup60 from the cap (Fig. 1C, E). Strikingly, not only Nup60-K467R now accumulated in the cap nearly as much as core nucleoporins, but the cells expressing this protein also restored the localization of the cytoplasmic complexes (Nup116, Nup42, Gle1 and Gle2) to cap NPCs (Fig. 5B, C). In contrast, the basket component Mlp1 remained displaced, indicating that the anchorage of DNA circles might also lead to other modifications in different basket proteins, independently of that of Nup60 at lysine-467. Thus, we concluded that the acetylation of Nup60 on K467 upon circle attachment drives Nup60's displacement from NPCs and subsequently that of the cytoplasmic complexes as well. How Nup60's

presence at the nuclear pore regulates the recruitment or stabilization of the cytoplasmic complexes on NPCs is not known at this stage. Possibly a signal is transduced from the nuclear to the cytoplasmic side of the NPC, or the clustering of the pores could drive the displacement of the cytoplasmic complexes. Furthermore, additional events displace the Mlp1/2 proteins as well, possibly also through their own acetylation or that of Nup2.

Thus, altogether we found no indication for the anchorage of DNA circles causing NPC deterioration. Rather, our data indicate that circle anchorage promotes the displacement of the nuclear basket through post-translational modifications, and that this in turn causes the detachment of the cytoplasmic complexes. Considering the fact that Nup60 acetylation contributes to the regulation of gene expression (Kumar et al., 2018), and that the residence of the basket to NPCs is dynamic also in young cells, the removal of the basket upon circle attachment might reflect a common physiological process taking place each time chromatin interact in a SAGA-dependent manner with interphase NPCs. The fact that DNA circles remain attached to NPCs during mitosis, whereas chromosomes detach from the nuclear periphery at that stage (Kanoh, 2013), might be caused by their inability to undergo condensation and recruit the deacetylase Hst2 (Kruitwagen et al., 2018). Further studies will be needed to determine the role of acetylating other Nups beyond Nup60 in basket displacement, circle anchorage and aging, and whether Hst2 reverts the acetylation of these proteins at chromosome-attached NPCs during mitosis.

Basket displacement promotes aging

Thus, together our results indicate that DNA circles modulate the organization of NPCs as they attach to them, leading to the accumulation of remodeled NPCs as circles accumulate and the cell progresses in replicative aging. Therefore, we wondered whether the effect of DNA circles on NPC organization is at least a part of the mechanisms by which ERCs promote cellular aging. Thus, we next investigated whether interfering with NPC remodeling has an impact on the lifespan of the cells. We took advantage of a new microfluidic chip design, that could retain more efficiently cells during their entire lifespan (i.e. >95% of the cells were kept until cell death (Fig. 6A, B), see methods). When monitoring wild type cells in this setup, their replicative life span was reproducibly of 18 generations (Fig. 6C). Although this lifespan is relatively low, it is within the range of RLSs reported for wild type cells measured on different microfluidic platforms (Chen et al., 2017; Janssens and Veenhoff, 2016). Interestingly, mutant cells with pores lacking the central basket component Nup60 aged rapidly (median life span of 13 divisions), while the *nup60-K467R* mutant cells already showed an extended longevity (20 divisions, Fig. 6C), despite the proteins Mlp1 and Mlp2 remaining displaced in these cells. Thus, our observations support the idea that displacement of the basket by SAGA promotes aging, while basket stabilization fosters longevity. Together our data indicate that the remodeling of NPCs upon DNA circle attachment to them is one causal element for how ERC accumulation limits the longevity of yeast mother cells.

Strikingly, the displacement of the basket from NPCs is highly reminiscent of what has been already described for the NPCs adjacent to the nucleolus in yeast. Indeed, the yeast nucleolus adheres to the nuclear envelope and the NPCs bordering the nucleolus lack Mlp1/2 (Galy et al., 2004). The functional relevance of this observation is unknown but has suggested that these NPCs might be functionally specialized. Thus, we suggest that the accumulation of basket-less NPCs with age does not reflect an accumulation of defective NPCs per-se, but rather leads to an imbalance of specialized over non-specialized NPCs in old cells (Fig. 6D).

mRNA export and mRNA surveillance factors are specifically displaced from circle-bound NPCs

Thus, we reasoned that NPC specialization might have some regulatory effect on their function. Nuclear pore complexes mediate the transport of cargos between nucleoplasm and cytoplasm and therefore transport factors transiently localize to NPCs in young and healthy cells (Derrer et al., 2019; Kumar et al., 2002). Any effect of NPC remodeling on the localization of these factors to NPCs may reflect changes in their dynamics within NPCs and hence, on NPC functionality. Therefore, we characterized how circle anchorage affected the recruitment of transport factors and other associated proteins to NPCs. We labeled a broad panel of transport and associated factors with GFP and quantified their nuclear localization in respect to the DNA circle cluster, as in Fig. 1. Only the factors showing a clear (transient) localization to the nuclear envelope of young wild type cells were characterized. Consistent with circle-bound NPCs lacking a basket, the two basket-associated proteins Esc1 and Ulp1 (both involved in telomeric silencing and mRNA surveillance, (Bonnet et al., 2015)) were excluded from NPC caps (Fig. 7A, B). In striking contrast, none of the 10 importins tested were displaced from the cap (Fig. 7B). Likewise, the exportins Xpo1 (Crm1), Msn5 and Los1, which ensure the export of proteins and tRNAs, accumulated with the cap to similar extent as the core Nups. Since nearly all these proteins accumulated to the same extent as core NPCs in the cap compared to elsewhere in the nuclear envelope, we concluded that basket-less pores interact with them with similar dynamics as bulk NPCs. Two importins were in average significantly further enriched at the cap, namely Srp1/Kap60 and Kap123. This may indicate either that these two nucleoporins shuttle more intensely through basket-less NPCs, or that they linger longer in them. Strikingly, Kap123 mediates the nuclear import of ribosomal proteins, promoting their subsequent assembly into ribosomes, and the import of histones H3 and H4. Both ribosome and nucleosome assembly have been shown to become reduced in aged yeast cells (reviewed in (Matos-Perdomo and Machín, 2019)).

More strikingly, 5 exportins were specifically depleted from the cap (Fig. 7B), indicating that their interaction with core NPCs was substantially decreased. Interestingly, all of these exportins are involved in mRNA export. Thus, all seven proteins that we find to be excluded from the cap are involved in this process (Bonnet et al., 2015; Iglesias et al., 2010; Stewart, 2010). We postulate that circle-bound NPCs are specifically inhibited for their function in mRNA export.

Conclusion

In summary, our data indicate that old yeast cells accumulate an increasing proportion of NPCs depleted of the nuclear basket and cytoplasmic complexes and that may have a reduced capacity for mRNA export. Once the proportion of basket-associated NPCs goes below some threshold, the resulting imbalance become deleterious for the cell. Importantly, our study establishes that the stoichiometry changes observed with age are not due to NPC deterioration but rather to their specialization as they become increasingly decorated with DNA circles, mainly ERCs. The function of this specialization is not known but observed also in young cells, for example near the nucleolus. Whether nucleolus-associated NPCs are depleted of other factors, such as the cytoplasmic complexes, has not been reported but our study suggests that it might be the case. Furthermore, the dissociation of the basket from NPCs appears to have broad functions beyond nucleolar NPCs in young cells since the acetylation of Nup60 is involved in the regulation of diverse loci on chromosomes, such as the activation of cell cycle genes (Kumar et al., 2018), and the SAGA complex is involved in the rapid activation of many genes in response to environmental changes such as heat shock, inositol starvation or changes in the available carbon source (Huisinga and Pugh, 2004; Kremer and Gross, 2009). In many of these instances, SAGA-dependent regulation involves the recruitment of the target locus to the nuclear periphery and their anchorage to NPCs. Thus, the modifications observed at circle-bound NPCs reflect physiological changes that are common in

1 young cells and amplified through ERC accumulation in old cells. Future studies will require to
2 determine how this imbalance affects cellular viability.

3 The notion that the age-dependent remodeling of NPC is not due to damages but to regulatory steps
4 has consequences for our understanding of the evolution of aging. Indeed, a leading theory for the
5 apparition of the aging process in evolution is that it is the result of traits and processes that are
6 selected for their selective advantage early in life, despite of deleterious effects later-on (Kirkwood
7 and Rose, 1991). Antagonistic pleiotropy has been difficult to document beyond the well accepted
8 idea that sparing on quality control and damage-repair liberates resources for the generation of
9 progeny early in life, at the expense of longevity (Ackermann et al., 2007; Austad and Hoffman,
10 2018; Williams, 1957). The case of NPCs and their role in SAGA-dependent gene regulation might
11 depart from this notion by suggesting that the trade-off here is not a matter of quality control but of
12 adaptability. Indeed our data suggest that the remodeling of NPCs with age is a secondary
13 consequence of the role of chromatin-NPC interaction in the rapid and strongly response of cells to
14 environmental challenges. The mechanistic relevance of these interactions during gene regulation,
15 sometimes referred as gene gating, as well as their effects on NPC activity and possibly other
16 processes at NPCs, such as DNA repair (Strambio-De-Castillia et al., 2010), are not yet fully
17 understood but their characterization is likely to shed light into why and how aging has emerged, at
18 least in yeast. Furthermore, our study indicate that aged cells may offer a model of choice for
19 studying how NPC specialization affects their function.

20 There is currently no evidence for DNA circles contributing to aging in other organisms but there is
21 strong evidence that chromatin interaction with the nuclear periphery is affected by age in many cell
22 types. Most remarkably, progerin, a progeriatric isoform of Lamin A and causing the Hutchinson-
23 Gilford progeria syndrome in humans, affects the recruitment of heterochromatin to the nuclear
24 periphery, and displaces Nup153 and TPR (the mammalian homologs of Nup60 and Mlp1/2) from
25 the nuclear periphery (Balmus et al., 2018; Cobb et al., 2016; Kelley et al., 2011; Larrieu et al., 2018).
26 Thus, we suspect that the effects of aging on NPCs and the role of NPCs in aging might be strikingly
27 similar between yeast and mammals.

Materials and methods

- Strains and plasmid

All the yeast strains and plasmids used in this study are listed in table S1 and are isogenic to S288C. GFP-tag and knock-out strains were generated using classical genetic approaches (Janke et al., 2004)). All cultures were grown using standard conditions, in synthetic drop-out medium (SD-medium; ForMedium, Norfolk, UK) or indicated otherwise, at 30°C.

The non-chromosomal DNA circle was obtained from the Megee lab (Megee and Koshland, 1999) and contains an array of 256 TetO repeats, the centromere is flanked by target site for the R-recombinase; the β -estradiol-inducible expression recombinase (from the genome) drives the excision of the centromere and converts the minichromosome into a non-chromosomal DNA circle ((Baldi et al., 2017; Denoth-Lippuner et al., 2014; Shcheprova et al., 2008). TetR-NLS-mCherry is genetically expressed and labels the TetO repeats; the NLS (nuclear localization signal) ensures its accumulation in the nucleus.

The nup60-K468R strain was generated with a one-step CRISPR-Cas9 method, based on (Laughery et al., 2015). The gRNA was designed with an online tool to identify an optimal guide RNA (gRNA) target site in Nup60 (<http://wyrickbioinfo2.smb.wsu.edu/crispr.html>). The donor DNA with the Nup60K467R mutation and the gRNA-encoded DNA were ordered as single stranded oligo's (Microsynth AG, Balgach, Switzerland) and annealed. The gRNA-encoded DNA was recombined into the Cas9 expression vector pML104_Cas9_HygR in a one-step approach, to induce the Nup60K467R mutation simultaneously: Swal-linearized vector, the gRNA-encoded double stranded oligo's and the donor DNA were transformed all at once into a wild type yeast strain and plated on hygromycin selection medium. The expression vector with gRNA (pML104_Cas9_HygR_Nup60) was rescued from cell material, propagated in bacteria and confirmed by digest analysis and sequencing. Genomic DNA was extracted from single yeast clones and the presence of the point mutation was confirmed by sequencing. Positive clones were propagated on YPD to get rid of the expression vector.

- Microscopy

For fluorescent microscopy, yeast cells were precultured for minimally 24h in synthetic drop-out medium. 1 ml of cells from exponential growing cultures with OD<1 were concentrated by centrifugation at 1.000xG, resuspended in ~5 ul of low fluorescent SD-medium, spotted on a round coverslip and immobilized with a SD/agar patch. The cells were imaged in z-stacks of 6 slices with 0.5 μ m spacing, with a 100x/1.4 NA objective on a DeltaVision microscope (Applied Precision) equipped with a CCD HQ2 camera (Roper), 250W Xenon lamps, Softworx software (Applied Precision) and a temperature chamber set to 30°C.

To accumulated DNA circles in the nuclei of aging mother cells, yeast cells were pre-cultured for 24h in SD-URA at 30°C and then shifted to SD-LEU medium supplemented with 1 μ M β -Estradiol (Sigma-Aldrich, St. Louis, MO), incubated for 16-18h at room temperature. The β -Estradiol induced expression of the recombinase and the excision of the centromere, see:(Denoth-Lippuner et al., 2014). To visualize DNA clusters, we use specifically 1x1 binning and made short time-lapse movies of 15 min, intervals for 5 min.

- Aging microfluidic platform

Nucleoporin colocalization and the tandem fluorescent protein timer analysis during aging were investigated using the high-throughput yeast aging analysis (HYAA) microfluidics dissection platform (Jo et al., 2015). The PDMS (polydimethylsiloxane) microchannel is made by soft-lithography and

bonded on the 30 mm micro-well cover glass in the 55 mm glass bottom dish (Cellvis, CA, USA). For the lifespan analyses, a chip with a new cell trapping design was used (Fig. 6A, B), to ensure excellent retention of old cells (see below).

To start the experiment, yeast cells were pre-cultured for 24h in SD-full supplemented with 0.1% Albumin Bovine Serum (protease free BSA; Acros Organics, Geel, Belgium). Young cells from a exponentially growing culture were captured in the traps of the microfluidic chip; the chip was continuously flushed with fresh medium at a constant flow of 10 μ l/min, using a Harvard PHD Ultra syringe pump (Harvard Apparatus, Holiston, MA, USA) with two or four 60mL BD syringes, with inner diameter 26.7 mm (Becton Dickinson, Franklin Lakes, NJ, USA). Bright field images were recorded every 15 min. throughout the duration of the entire experiment. To measure the nucleoporin colocalization or pre-mRNA translation, fluorescent images only after 2h, 12h, 26h or/and 50h. For imaging we used an epi-fluorescent microscope (TiE, Nikon Instruments, Tokyo, Japan) controlled by Micro-Manager 1.4.23 software (μ Manager, PMID 25606571), with a Plan Apo 60x 1.4 NA objective. For fluorescence illumination of the GFP and mCherry labeled proteins, a Lumencor Spectra-X LED Light Engine was used. Stacks of 7 slices with 0.3 μ m spacing were recorded during. The age of the cell was defined by the number of daughter cells that emerged during the budding cycles.

For the nucleoporin correlation analysis, a cell of interest was manually selected if it stays in the focal plane in the bright field channel. Its age was determined and a segmented line was drawn through the nuclear envelope in an image in the focal plane, using Fiji/ImageJ 1.51n (Schindelin et al., 2012), and the intensity profiles were recorded for both fluorescence channels. The Pearson correlation between the intensity profiles was calculated and plotted in R (R Development Core Team, 2011).

For the tandem fluorescent protein timer analysis, late mitotic cells were selected after 2h and 26h incubation in the chip. Its age was determined and a segmented line was drawn through the nuclear envelope in an image in the focal plane, as described above. The average background corrected intensity for GFP and mCherry was calculated and plotted in R.

To obtain a reliable lifespan curves, the majority of the cells should be retained until cell death to prevent biasing the data. Although different microfluidic dissection platforms have been developed, it is still a challenge to reach high enough retention efficiency in the microfluidics chip for life span analysis. Here we used an improved design of yeast cell traps, having small “claws” at both sides, preventing the escape of bigger cells at higher age (Fig. 6A, B). This allowed us to retain >95% of the cells during their full lifetime. Only bright field images were recorded every 15 min. throughout the entire experiment of 70-80 hours. All cells in a field of view were analyzed, the replicative lifespan was determined for each single cell by counting the budding cycles before cell death.

Acknowledgements

We thank Joachim Hehl, Tobias Schwartz and the light microscopy center of ETH Zürich (ScopeM) for microscopy support; Rodrigo Merayo Martínez, Irina Remple and Liesbeth Veenhoff for their help with running the microfluidic chips. We acknowledge financial support by Swiss National Science Foundation (grant 31003A-105904 to Y.B.).

References

- Ackermann M, Schauer A, Stearns SC, Jenal U. 2007. Experimental evolution of aging in a bacterium. *BMC Evol Biol* **7**:1–10. doi:10.1186/1471-2148-7-126
- Austad SN, Hoffman JM. 2018. Is antagonistic pleiotropy ubiquitous in aging biology? *Evol Med Public Heal* **2018**:287–294. doi:10.1093/emph/eoy033
- Bailer SM, Balduf C, Hurt E. 2001. The Nsp1p Carboxy-Terminal Domain Is Organized into Functionally Distinct Coiled-Coil Regions Required for Assembly of Nucleoporin Subcomplexes and Nucleocytoplasmic Transport. *Mol Cell Biol* **21**:7944–7955. doi:10.1128/mcb.21.23.7944-7955.2001
- Baldi S, Bolognesi A, Meinema AC, Barral Y. 2017. Heat stress promotes longevity in budding yeast by relaxing the confinement of age-promoting factors in the mother cell. *Elife* **6**:1–26. doi:10.7554/eLife.28329
- Balmus G, Larrieu D, Barros AC, Collins C, Abrudan M, Demir M, Geisler NJ, Lelliott CJ, White JK, Karp NA, Atkinson J, Kirton A, Jacobsen M, Clift D, Rodriguez R, Shannon C, Sanderson M, Gates A, Dench J, Vancollie V, McCarthy C, Pearson S, Cambridge E, Isherwood C, Wilson H, Grau E, Galli A, Hooks YE, Tudor CL, Green AL, Kussy FL, Tuck EJ, Siragher EJ, McLaren RSB, Swiatkowska A, Caetano SS, Mazzeo CI, Dabrowska MH, Maguire SA, Lafont DT, Anthony LFE, Sumowski MT, Bussell J, Sinclair C, Brown E, Doe B, Wardle-Jones H, Griggs N, Woods M, Kundi H, McConnell G, Doran J, Griffiths MND, Kipp C, Holroyd SA, Gannon DJ, Alcantara R, Ramirez-Solis R, Bottomley J, Ingle C, Ross V, Barrett D, Sethi D, Gleeson D, Burvill J, Platte R, Ryder E, Sins E, Miklejewska E, Von Schiller D, Duddy G, Urbanova J, Boroviak K, Imran M, Reddy SK, Adams DJ, Jackson SP. 2018. Targeting of NAT10 enhances healthspan in a mouse model of human accelerated aging syndrome. *Nat Commun* **9**. doi:10.1038/s41467-018-03770-3
- Beck M, Hurt E. 2017. The nuclear pore complex: Understanding its function through structural insight. *Nat Rev Mol Cell Biol*. doi:10.1038/nrm.2016.147
- Bonnet A, Bretes H, Palancade B. 2015. Nuclear pore components affect distinct stages of intron-containing gene expression. *Nucleic Acids Res* **43**:1–13. doi:10.1093/nar/gkv280
- Chen KL, Crane MM, Kaeberlein M. 2017. Microfluidic technologies for yeast replicative lifespan studies. *Mech Ageing Dev*. doi:10.1016/j.mad.2016.03.009
- Choudhary C, Kumar C, Gnad F, Nielsen ML, Rehman M, Walther TC, Olsen J V, Mann M. 2009. Lysine acetylation targets protein complexes and co-regulates major cellular functions. *Science* **325**:834–840. doi:10.1126/science.1175371
- Choudhary C, Weinert BT, Nishida Y, Verdin E, Mann M. 2014. The growing landscape of lysine acetylation links metabolism and cell signalling. *Nat Rev Mol Cell Biol* **15**:536–50. doi:10.1038/nrm3841
- Clay L, Caudron F, Denoth-lippuner A, Boettcher B, Frei SB, Snapp EL, Barral Y. 2014. A sphingolipid-dependent diffusion barrier confines ER stress to the yeast mother cell 1–23. doi:10.7554/eLife.01883
- Cobb AM, Larrieu D, Warren DT, Liu Y, Srivastava S, Smith AJO, Bowater RP, Jackson SP, Shanahan CM. 2016. Prelamin A impairs 53BP1 nuclear entry by mislocalizing NUP153 and disrupting the Ran gradient. *Aging Cell* **15**:1039–1050. doi:10.1111/ace.12506
- D’Angelo M a, Raices M, Panowski SH, Hetzer MW. 2009. Age-dependent deterioration of nuclear

- 1 pore complexes causes a loss of nuclear integrity in postmitotic cells. *Cell* **136**:284–95.
2 doi:10.1016/j.cell.2008.11.037
- 3 D’Mello NP, Childress AM, Franklin DS, Kale SP, Pinswasdi C, Jazwinski SM. 1994. Cloning and
4 characterization of LAG1, a longevity-assurance gene in yeast. *J Biol Chem* **269**:15451–15459.
5 doi:10.1016/s0021-9258(17)40700-9
- 6 Defossez PA, Prusty R, Kaeberlein M, Lin SJ, Ferrigno P, Silver PA, Keil RL, Guarente L. 1999.
7 Elimination of replication block protein Fob1 extends the life span of yeast mother cells. *Mol*
8 *Cell* **3**:447–455. doi:10.1016/S1097-2765(00)80472-4
- 9 Denning D, Mykytka B, Allen NPC, Huang L, Burlingame A, Rexach M. 2001. The nucleoporin Nup60p
10 functions as a Gsp1p-GTP-sensitive tether for Nup2p at the nuclear pore complex. *J Cell Biol*
11 **154**:937–950. doi:10.1083/jcb.200101007
- 12 Denoth-Lippuner A, Krzyzanowski MK, Stober C, Barral Y. 2014. Role of SAGA in the asymmetric
13 segregation of DNA circles during yeast ageing. *Elife* **2014**:1–33. doi:10.7554/eLife.03790.001
- 14 Denoth Lippuner A, Julou T, Barral Y. 2014. Budding yeast as a model organism to study the effects
15 of age. *FEMS Microbiol Rev* **38**:300–25. doi:10.1111/1574-6976.12060
- 16 Derrer CP, Mancini R, Vallotton P, Huet S, Weis K, Dultz E. 2019. The RNA export factor Mex67
17 functions as a mobile nucleoporin. *J Cell Biol* **218**:3967–3976. doi:10.1083/JCB.201909028
- 18 Dilworth DJ, Suprpto A, Padovan JC, Chait BT, Wozniak RW, Rout MP, Aitchison JD. 2001. Nup2p
19 dynamically associates with the distal regions of the yeast nuclear pore complex. *J Cell Biol*
20 **153**:1465–78.
- 21 Downey M, Johnson JR, Davey NE, Newton BW, Johnson TL, Galaang S, Seller CA, Krogan N, Toczyski
22 DP. 2015. Acetylome profiling reveals overlap in the regulation of diverse processes by sirtuins,
23 Gcn5, and esa1. *Mol Cell Proteomics* **14**:162–176. doi:10.1074/mcp.M114.043141
- 24 Durand A, Bonnet J, Fournier M, Chavant V, Schultz P. 2014. Mapping the deubiquitination module
25 within the saga complex. *Structure* **22**:1553–1559. doi:10.1016/j.str.2014.07.017
- 26 Fabrizio P, Longo VD. 2003. The chronological life span of *Saccharomyces cerevisiae*. *Aging Cell*.
27 doi:10.1046/j.1474-9728.2003.00033.x
- 28 Fernandez-Martinez J, Kim SJ, Shi Y, Upla P, Pellarin R, Gagnon M, Chemmama IE, Wang J, Nudelman
29 I, Zhang W, Williams R, Rice WJ, Stokes DL, Zenklusen D, Chait BT, Sali A, Rout MP. 2016.
30 Structure and Function of the Nuclear Pore Complex Cytoplasmic mRNA Export Platform. *Cell*
31 **167**:1215–1228.e25. doi:10.1016/j.cell.2016.10.028
- 32 Galy V, Gadal O, Fromont-Racine M, Romano A, Jacquier A, Nehrbass U. 2004. Nuclear retention of
33 unspliced mRNAs in yeast is mediated by perinuclear Mlp1. *Cell* **116**:63–73.
- 34 Henriksen P, Wagner S a., Weinert BT, Sharma S, Bacinskaja G, Rehman M, Juffer a. H, Walther TC,
35 Lisby M, Choudhary C. 2012. Proteome-wide analysis of lysine acetylation suggests its broad
36 regulatory scope in *Saccharomyces cerevisiae*. *Mol Cell Proteomics* **11**:1510–22.
37 doi:10.1074/mcp.M112.017251
- 38 Huisinga KL, Pugh BF. 2004. A genome-wide housekeeping role for TFIID and a highly regulated
39 stress-related role for SAGA in *Saccharomyces cerevisiae*. *Mol Cell* **13**:573–585.
40 doi:10.1016/S1097-2765(04)00087-5
- 41 Iglesias N, Tutucci E, Gwizdek C, Vinciguerra P, Von Dach E, Corbett AH, Dargemont C, Stutz F. 2010.
42 Ubiquitin-mediated mRNP dynamics and surveillance prior to budding yeast mRNA export.
43 *Genes Dev* **24**:1927–1938. doi:10.1101/gad.583310

- 1 Jani D, Valkov E, Stewart M. 2014. Structural basis for binding the TREX2 complex to nuclear pores,
2 GAL1 localisation and mRNA export. *Nucleic Acids Res* **42**:6686–6697. doi:10.1093/nar/gku252
- 3 Janke C, Magiera MM, Rathfelder N, Taxis C, Reber S, Maekawa H, Moreno-Borchart A, Doenges G,
4 Schwob E, Schiebel E, Knop M. 2004. A versatile toolbox for PCR-based tagging of yeast genes:
5 new fluorescent proteins, more markers and promoter substitution cassettes. *Yeast* **21**:947–62.
6 doi:10.1002/yea.1142
- 7 Janssens GE, Meinema AC, González J, Wolters JC, Schmidt A, Guryev V, Bischoff R, Wit EC, Veenhoff
8 LM, Heinemann M. 2015. Protein biogenesis machinery is a driver of replicative aging in yeast.
9 *Elife* **4**. doi:10.7554/eLife.08527
- 10 Janssens GE, Veenhoff LM. 2016. The Natural Variation in Lifespans of Single Yeast Cells Is Related to
11 Variation in Cell Size, Ribosomal Protein, and Division Time. *PLoS One* **11**:e0167394.
12 doi:10.1371/journal.pone.0167394
- 13 Jo MC, Liu W, Gu L, Dang W, Qin L. 2015. High-throughput analysis of yeast replicative aging using a
14 microfluidic system. *Proc Natl Acad Sci U S A* **112**:9364–9. doi:10.1073/pnas.1510328112
- 15 Kaeberlein M, McVey M, Guarente L. 1999. The SIR2/3/4 complex and SIR2 alone promote longevity
16 in *Saccharomyces cerevisiae* by two different mechanisms. *Genes Dev* **13**:2570–2580.
17 doi:10.1101/gad.13.19.2570
- 18 Kanoh J. 2013. Release of chromosomes from the nuclear envelope: A universal mechanism for
19 eukaryotic mitosis? *Nucl (United States)* **4**:100–104. doi:10.4161/nucl.23984
- 20 Kelley JB, Datta S, Snow CJ, Chatterjee M, Ni L, Spencer A, Yang C-S, Cubeñas-Potts C, Matunis MJ,
21 Paschal BM. 2011. The defective nuclear lamina in Hutchinson-gilford progeria syndrome
22 disrupts the nucleocytoplasmic Ran gradient and inhibits nuclear localization of Ubc9. *Mol Cell*
23 *Biol* **31**:3378–95. doi:10.1128/MCB.05087-11
- 24 Khmelinskii, Keller, Bartosik, Meurer, Barry, Mardin, Kaufmann, Trautmann, Wachsmuth, Pereira,
25 Huber, Schiebel, Knop. 2012. Tandem fluorescent protein timers for in vivo analysis of protein
26 dynamics. *Nat Biotechnol* **30**:708–14. doi:10.1038/nbt.2281
- 27 Kim SJ, Fernandez-Martinez J, Nudelman I, Shi Y, Zhang W, Raveh B, Herricks T, Slaughter BD, Hogan
28 JA, Upla P, Chemmama IE, Pellarin R, Echeverria I, Shivaraju M, Chaudhury AS, Wang J, Williams
29 R, Unruh JR, Greenberg CH, Jacobs EY, Yu Z, De La Cruz MJ, Mironska R, Stokes DL, Aitchison JD,
30 Jarrold MF, Gerton JL, Ludtke SJ, Akey CW, Chait BT, Sali A, Rout MP. 2018. Integrative
31 structure and functional anatomy of a nuclear pore complex. *Nature* **555**:475–482.
32 doi:10.1038/nature26003
- 33 Kirkwood TBL, Rose MR. 1991. Evolution of senescence: late survival sacrificed for reproduction.
34 *Philos Trans - R Soc London, B* **332**:15–24. doi:10.1098/rstb.1991.0028
- 35 Köhler A, Schneider M, Cabal GG, Nehrbass U, Hurt E. 2008. Yeast Ataxin-7 links histone
36 deubiquitination with gene gating and mRNA export. *Nat Cell Biol* **10**:707–715.
37 doi:10.1038/ncb1733
- 38 Kremer SB, Gross DS. 2009. SAGA and Rpd3 chromatin modification complexes dynamically regulate
39 heat shock gene structure and expression. *J Biol Chem* **284**:32914–32931.
40 doi:10.1074/jbc.M109.058610
- 41 Kruitwagen T, Chymkowitch P, Denoth-Lippuner A, Enserink J, Barral Y. 2018. Centromeres License
42 the Mitotic Condensation of Yeast Chromosome Arms. *Cell* **175**:780-795.e15.
43 doi:10.1016/j.cell.2018.09.012

- 1 Kumar A, Agarwal S, Heyman JA, Matson S, Heidtman M, Piccirillo S, Umansky L, Drawid A, Jansen R,
2 Liu Y, Cheung KH, Miller P, Gerstein M, Shirleen Roeder G, Snyder M. 2002. Subcellular
3 localization of the yeast proteome. *Genes Dev* **16**:707–719. doi:10.1101/gad.970902
- 4 Kumar A, Sharma P, Gomar-Alba M, Shcheprova Z, Daulny A, Sanmartín T, Matucci I, Funaya C, Beato
5 M, Mendoza M. 2018. Daughter-cell-specific modulation of nuclear pore complexes controls
6 cell cycle entry during asymmetric division. *Nat Cell Biol* **20**:432–442. doi:10.1038/s41556-018-
7 0056-9
- 8 Larrieu D, Vire E, Robson S, Breusegem SY, Kouzarides T, Jackson SP. 2018. Inhibition of the
9 acetyltransferase NAT10 normalizes progeric and aging cells by rebalancing the Transportin-1
10 nuclear import pathway. *Sci Signal* **11**:5401. doi:10.1126/scisignal.aar5401
- 11 Laughery MF, Hunter T, Brown A, Hoopes J, Ostbye T, Shumaker T, Wyrick JJ. 2015. New vectors for
12 simple and streamlined CRISPR-Cas9 genome editing in *Saccharomyces cerevisiae*. *Yeast*
13 **32**:711–720. doi:10.1002/yea.3098
- 14 Longo VD, Shadel GS, Kaeberlein M, Kennedy B. 2012. Replicative and chronological aging in
15 *Saccharomyces cerevisiae*. *Cell Metab* **16**:18–31. doi:10.1016/j.cmet.2012.06.002
- 16 Matos-Perdomo E, Machín F. 2019. Nucleolar and Ribosomal DNA Structure under Stress: Yeast
17 Lessons for Aging and Cancer. *Cells* **8**:779. doi:10.3390/cells8080779
- 18 Megee PC, Koshland D. 1999. A functional assay for centromere-associated sister chromatid
19 cohesion. *Science* **285**:254–257.
- 20 Megyeri M, Prasad R, Volpert G, Sliwa-Gonzalez A, Haribowo AG, Aguilera-Romero A, Riezman H,
21 Barral Y, Futerman AH, Schuldiner M. 2019. Yeast ceramide synthases, Lag1 and Lac1, have
22 distinct substrate specificity. *J Cell Sci* **132**. doi:10.1242/jcs.228411
- 23 Morlot S, Song J, Léger-Silvestre I, Matifas A, Gadad O, Charvin G. 2019. Excessive rDNA Transcription
24 Drives the Disruption in Nuclear Homeostasis during Entry into Senescence in Budding Yeast.
25 *Cell Rep* **28**:408–422.e4. doi:10.1016/j.celrep.2019.06.032
- 26 Mortimer RK, Johnston JR. 1959. Life Span of Individual Yeast Cells. *Nature* **183**:1751–1752.
27 doi:10.1038/1831751a0
- 28 Niepel M, Molloy KR, Williams R, Farrar JC, Meinema AC, Vecchiotti N, Cristea IM, Chait BT, Rout MP,
29 Strambio-De-Castillia C. 2013. The nuclear basket proteins Mlp1p and Mlp2p are part of a
30 dynamic interactome including Esc1p and the proteasome. *Mol Biol Cell* **24**:3920–3938.
31 doi:10.1091/mbc.E13-07-0412
- 32 Ori A, Toyama BH, Harris MS, Bock T, Iskar M, Bork P, Ingolia NT, Hetzer MW, Beck M. 2015.
33 Integrated Transcriptome and Proteome Analyses Reveal Organ-Specific Proteome
34 Deterioration in Old Rats. *Cell Syst* **1**:224–237. doi:10.1016/j.cels.2015.08.012
- 35 Prasad R, Sliwa-Gonzalez A, Barral Y. 2020. Mapping bilayer thickness in the ER membrane. *Sci Adv* **6**.
36 doi:10.1126/sciadv.aba5130
- 37 R Development Core Team R. 2011. R: A Language and Environment for Statistical Computing. *R*
38 *Found Stat Comput*, R Foundation for Statistical Computing. doi:10.1007/978-3-540-74686-7
- 39 Rajoo S, Vallotton P, Onischenko E, Weis K. 2018. Stoichiometry and compositional plasticity of the
40 yeast nuclear pore complex revealed by quantitative fluorescence microscopy. *Proc Natl Acad*
41 *Sci U S A* **115**:E3969–E3977. doi:10.1073/pnas.1719398115
- 42 Rempel IL, Crane MM, Thaller DJ, Mishra A, Jansen DPM, Janssens G, Popken P, Akşit A, Kaeberlein
43 M, van der Giessen E, Steen A, Onck PR, Lusk CP, Veenhoff LM. 2019. Age-dependent

- deterioration of nuclear pore assembly in mitotic cells decreases transport dynamics. *Elife* **8**. doi:10.7554/eLife.48186
- Rempel IL, Steen A, Veenhoff LM. 2020. Poor old pores—The challenge of making and maintaining nuclear pore complexes in aging. *FEBS J*. doi:10.1111/febs.15205
- Savas JN, Toyama BH, Xu T, Yates JR, Hetzer MW. 2012. Extremely long-lived nuclear pore proteins in the rat brain. *Science (80-)*. doi:10.1126/science.1217421
- Schindelin J, Arganda-Carreras I, Frise E, Kaynig V, Longair M, Pietzsch T, Preibisch S, Rueden C, Saalfeld S, Schmid B, Tinevez J-Y, White DJ, Hartenstein V, Eliceiri K, Tomancak P, Cardona A. 2012. Fiji: an open-source platform for biological-image analysis. *Nat Methods* **9**:676–682. doi:10.1038/nmeth.2019
- Shcheprova Z, Baldi S, Frei SB, Gonnet G, Barral Y. 2008. A mechanism for asymmetric segregation of age during yeast budding. *Nature* **454**:728–734. doi:10.1038/nature07212
- Sinclair DA, Guarente L. 1997. Extrachromosomal rDNA circles—a cause of aging in yeast. *Cell* **91**:1033–42.
- Stewart M. 2010. Nuclear export of mRNA. *Trends Biochem Sci*. doi:10.1016/j.tibs.2010.07.001
- Strambio-de-Castillia C, Blobel G, Rout MP. 1999. Proteins connecting the nuclear pore complex with the nuclear interior. *J Cell Biol* **144**:839–55.
- Strambio-De-Castillia C, Niepel M, Rout MP. 2010. The nuclear pore complex: bridging nuclear transport and gene regulation. *Nat Rev Mol Cell Biol* **11**:490–501. doi:10.1038/nrm2928
- Texari L, Dieppo G, Vinciguerra P, Contreras MP, Groner A, Letourneau A, Stutz F. 2013. The nuclear pore regulates GAL1 gene transcription by controlling the localization of the SUMO protease Ulp1. *Mol Cell* **51**:807–18. doi:10.1016/j.molcel.2013.08.047
- Toyama BH, Savas JN, Park SK, Harris MS, Ingolia NT, Yates JR, Hetzer MW. 2013. Identification of Long-Lived Proteins Reveals Exceptional Stability of Essential Cellular Structures. *Cell* **154**:971–982. doi:10.1016/j.cell.2013.07.037
- Wang H, Dienemann C, Stützer A, Urlaub H, Cheung ACM, Cramer P. 2020. Structure of the transcription coactivator SAGA. *Nature* **577**:717–720. doi:10.1038/s41586-020-1933-5
- Webster BM, Colombi P, Jäger J, Lusk CP. 2014. Surveillance of nuclear pore complex assembly by ESCRT-III/Vps4. *Cell* **159**:388–401. doi:10.1016/j.cell.2014.09.012
- Webster BM, Thaller DJ, Jäger J, Ochmann SE, Borah S, Lusk CP. 2016. Chm7 and Heh1 collaborate to link nuclear pore complex quality control with nuclear envelope sealing. *EMBO J* **35**:2447–2467. doi:10.15252/embj.201694574
- Williams GC. 1957. Pleiotropy, Natural Selection, and the Evolution of Senescence. *Evolution (N Y)* **11**:398. doi:10.2307/2406060

Figures

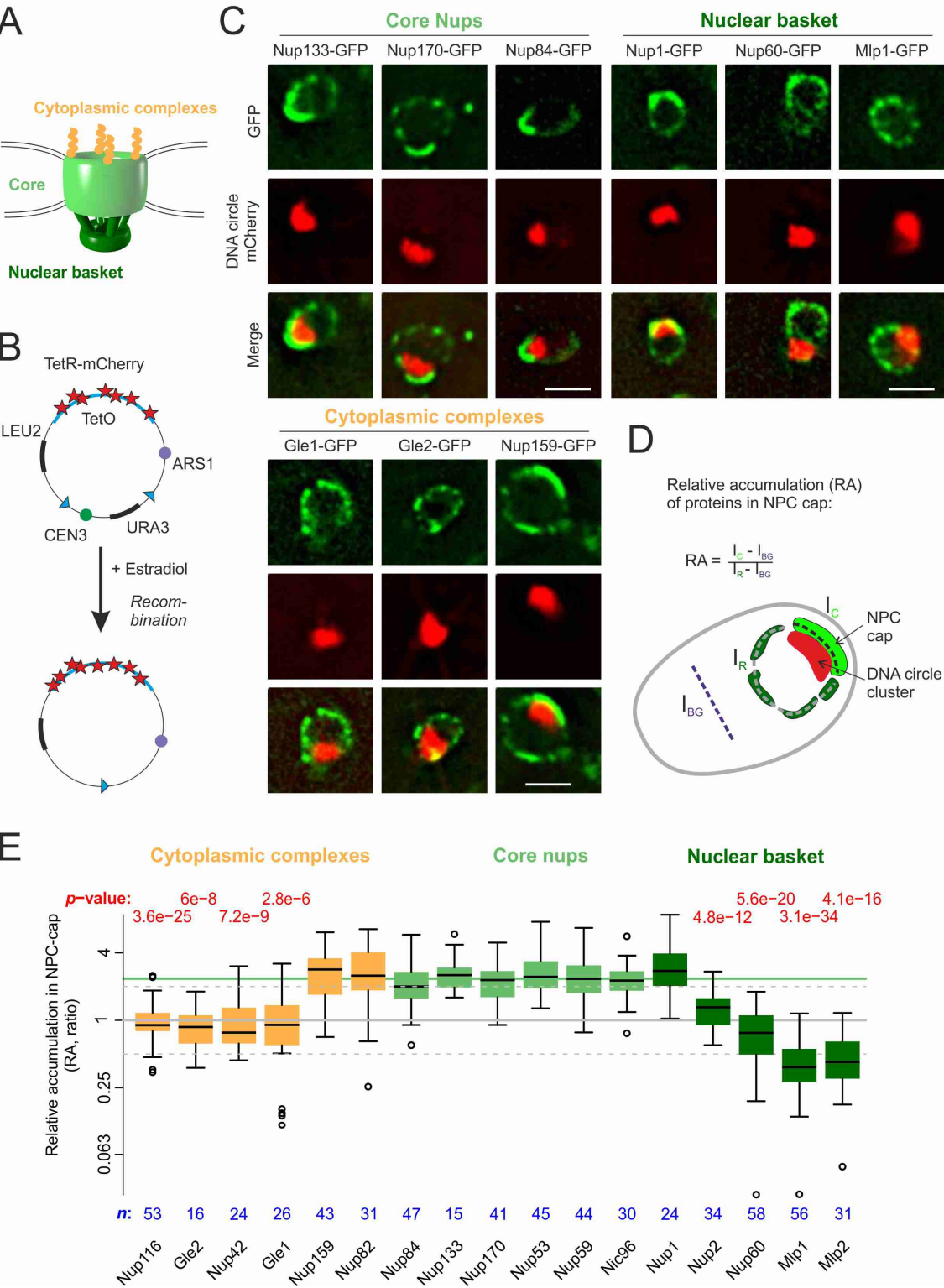
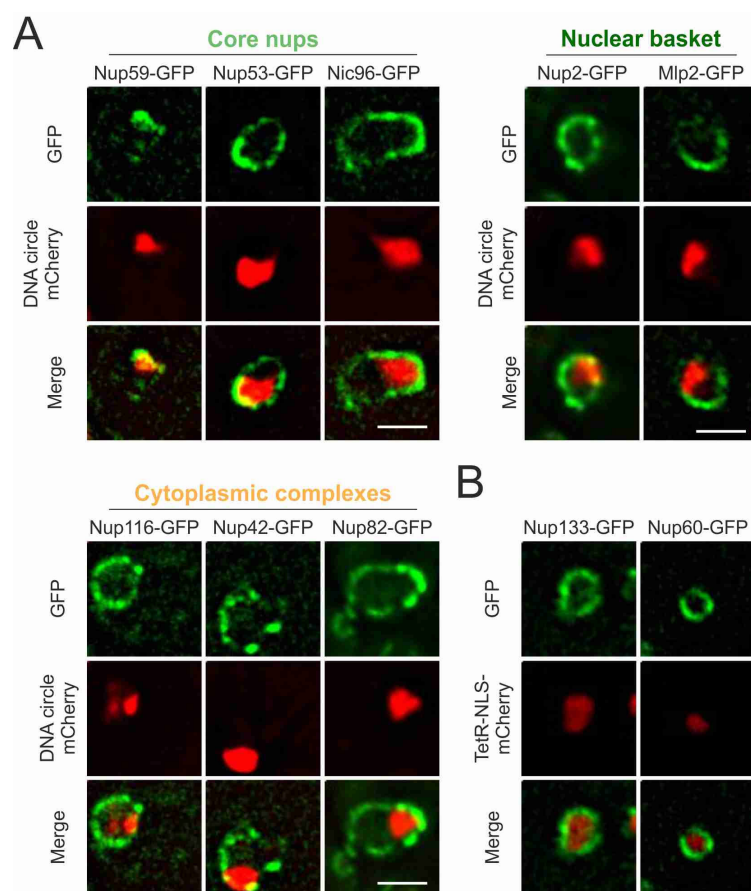


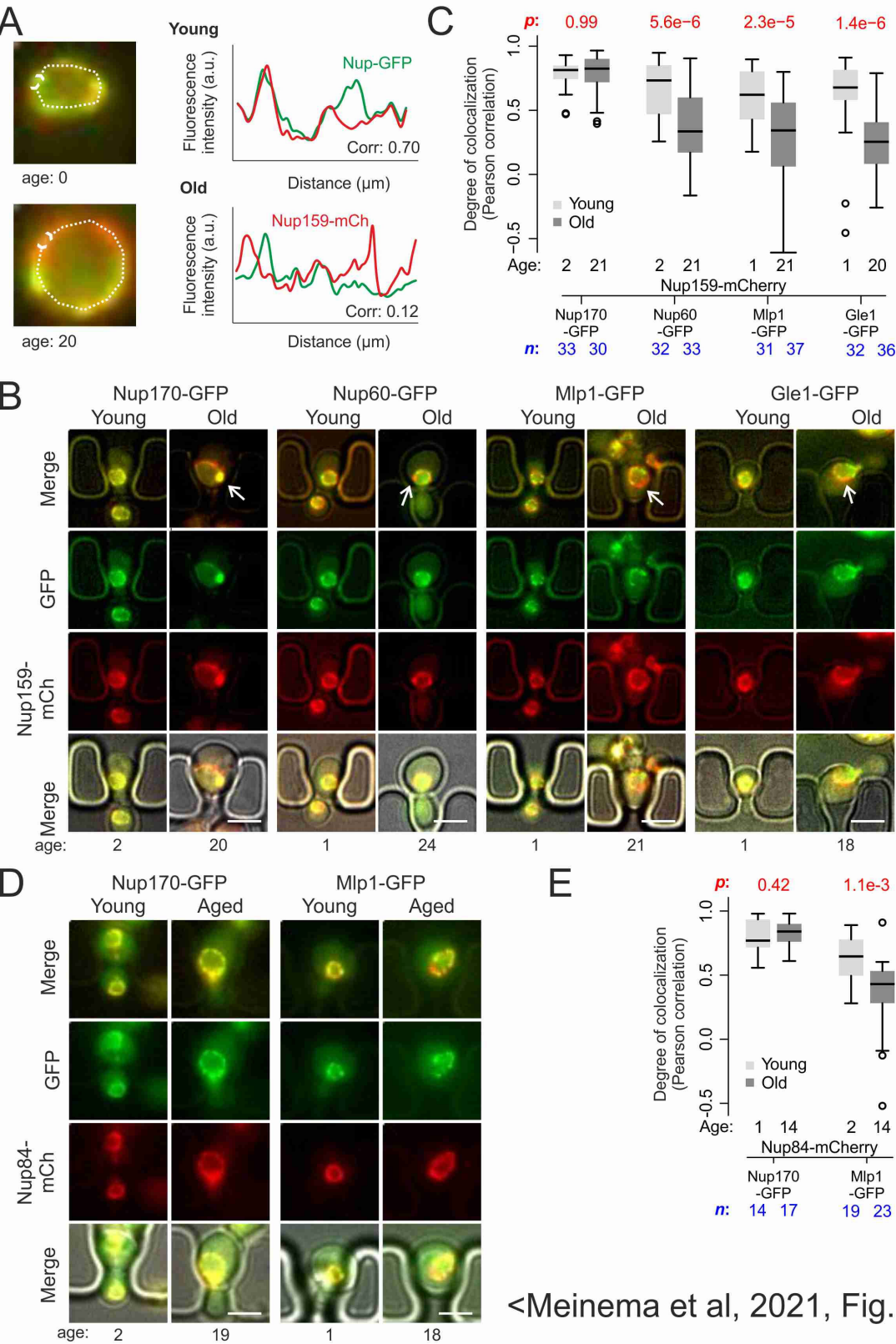
Figure 1. DNA circle anchored NPCs lack the peripheral subunits. (A) Cartoon of the NPC, showing the scaffold core, cytoplasmic complexes and nuclear basket. (B) Cartoon of an engineered DNA circle with excisable centromere (CEN3) and TetR-mCherry decorated TetO repeats. The circle contains an autonomous replication sequence (ARS1) and selection markers (LEU2, URA3). (C) Fluorescent images of nuclei in yeast cells with accumulated DNA circles; the DNA circle clusters are labeled with TetR-NLS-mCherry (red) and different nucleoporins labeled with GFP (green). Scale bar

is 2 μm . More images in Figure 1 – figure supplement 1. (D) Cartoon exemplifying the quantification of protein accumulation around the DNA cluster. The NPC cap was selected by a line scan through the nuclear envelope adjacent to the DNA circle cluster. The relative accumulation (RA) is defined as the ratio of background corrected GFP intensity in the NPC cap ($I_c - I_{BG}$) over that in the rest of the nucleus ($I_R - I_{BG}$). (E) Quantification of GFP-labeled nucleoporin accumulation in the NPC cap localized at the DNA circle cluster. The relative fluorescence intensity in the NPC cap is plotted on a log₂-scale. The median accumulation of the core nucleoporins is indicated (green line). *p*-value stands for student's t-test between the specific nucleoporin and pooled data of all core nups together, no *p*-value is indicated if the difference is not significant; the sample size per strain is indicated (n).



<Meinema et al, 2021, Fig. 1 - supplement 1>

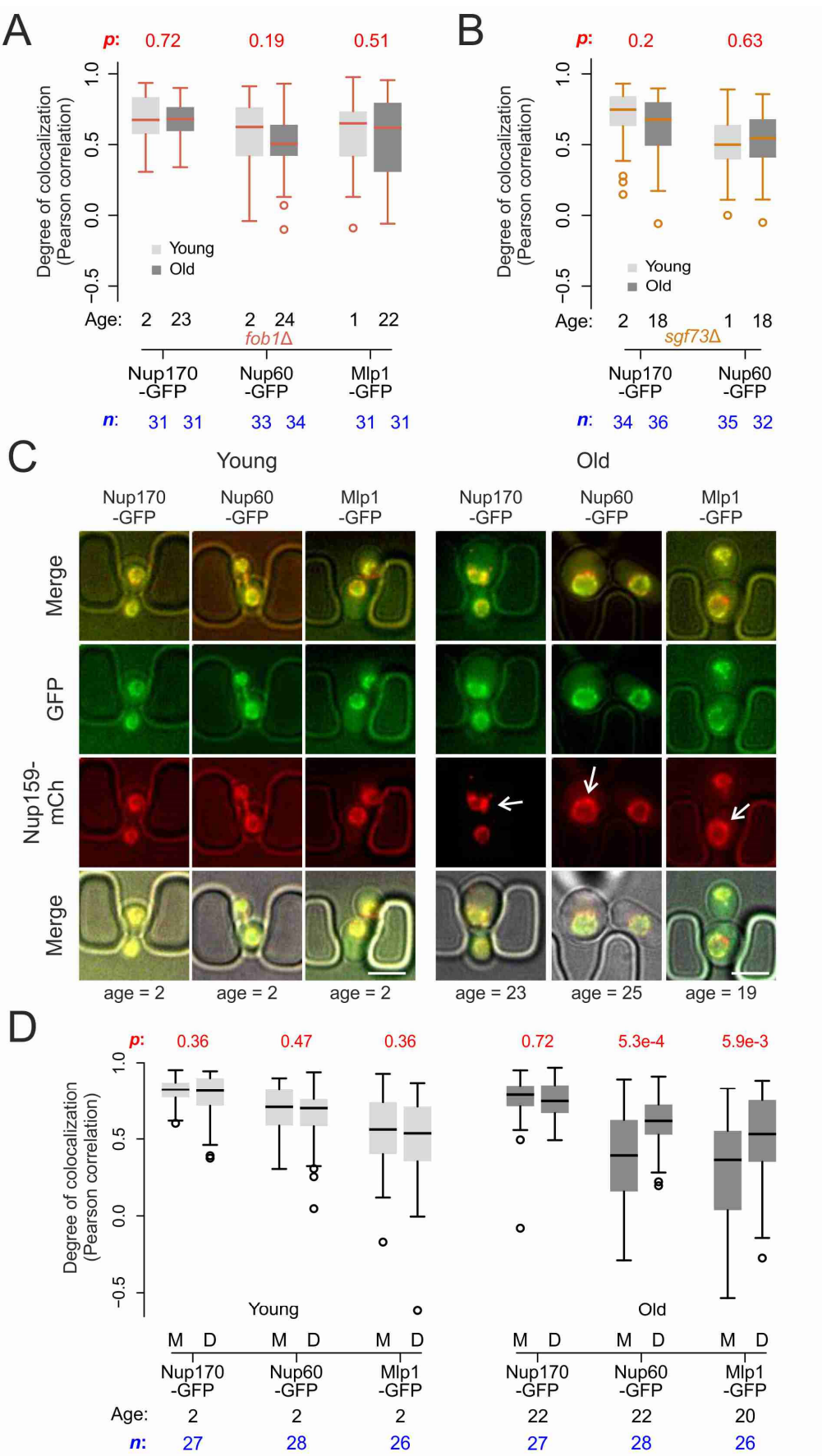
Figure 1-supplement 1. DNA circle anchored NPCs lack the peripheral subunits, Related to figure 1. (A) Additional example images of all strains as quantified in Figure 1E. The DNA circle clusters are labeled with TetR-NLS-mCherry (red) and different nucleoporins with GFP (green). Scale bar is 2 μm . (B) Example images of nuclei in young yeast cells prior to DNA circle accumulation; with nucleoporins labeled with GFP and soluble TetR-NLS-mCherry. Without Tet-O containing DNA circles, TetR-NLS-mCherry is homogenously distributed in the nucleoplasm and the localization of both core subunits (Nup133-GFP) and basket subunits (Nup60-GFP) is rather homogenously distributed throughout the nuclear envelope.



<Meinema et al, 2021, Fig. 2>

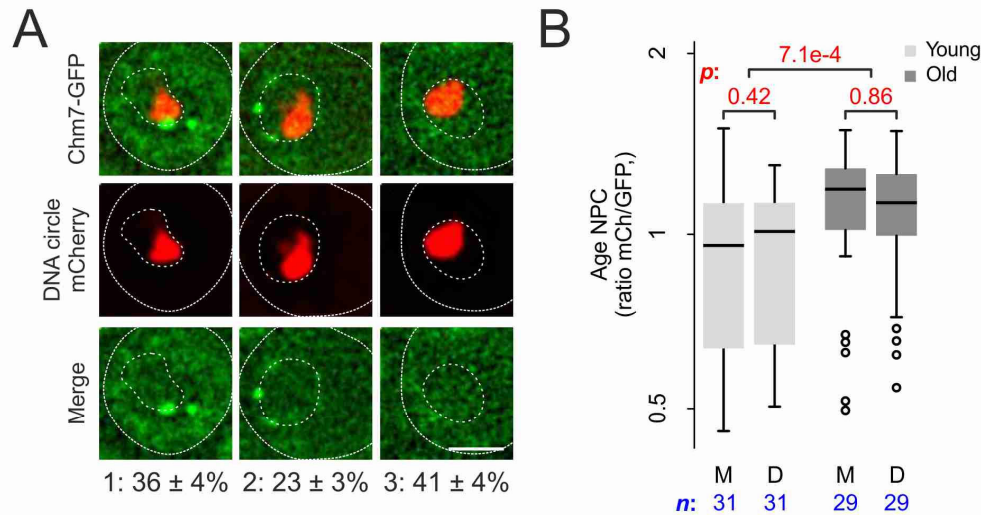
Figure 2. Peripheral subunits of NPC displaced in wild type aged cells. (A) To quantify the degree of nucleoporin colocalization, a line was drawn through the nuclear envelope in a focal image of a young (top) and aged (bottom) nucleus of cells co-expressing GFP-tagged Nup GFP (e.g. Nup60-GFP) and a mCherry-tagged Nup as a reference (e.g. Nup159-mCherry, see material and methods). The

1 Pearson correlation between the two intensity profiles is calculated, and used as a measure for
2 nucleoporin colocalization. (B) Fluorescent images of young and old cells in the yeast aging chip, with
3 nucleoporins labeled with GFP (green) and the reference Nup159 with mCherry (red). The age of
4 each cell is indicated. Scale bars are 5 μm . (C) Quantification of the degree of colocalization between
5 target and reference nucleoporin is plotted for young and old wt. The p -value stands for the
6 student's t-test between young and old cells. The sample size (n) and the median age is indicated.
7 (D) Fluorescent images of young and aged cells in the yeast aging chip, as in A, but with Nup84-
8 mCherry as a reference nucleoporin. Scale bars are 5 μm . (E) Quantification of the co-localization
9 between nucleoporins in young and old cells, as in D, but with Nup84-mCherry as a reference.



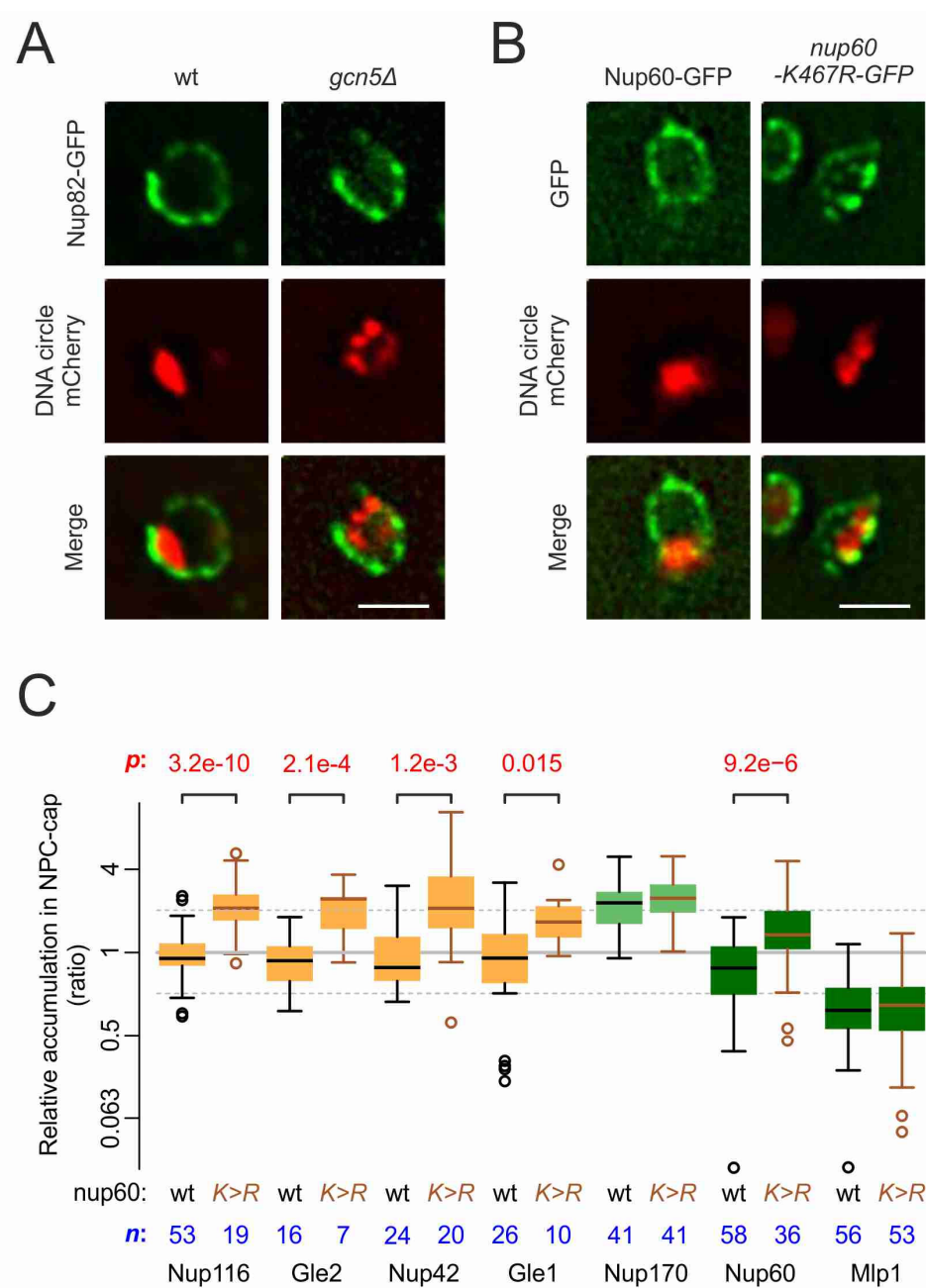
<Meinema et al, 2021, Fig. 3>

Figure 3. Endogenous DNA circles drive nuclear basket displacement in wild type aged cells. (A) Quantification of the degree of colocalization between target and reference nucleoporin is plotted for young and old wt, as was done in Fig. 2C, but in *fob1Δ* cells. The sample size (*n*) and the median age is indicated. The *p*-value stands for the student's t-test between young and old cells. (B) Same as A, but in *sgf73Δ* cells. (C) Fluorescent images of young and old mitotic cells in the yeast aging chip. Scale bars are 5 μm. (D) Same as in Fig. 2C, but comparing nucleoporin colocalization in young and old mother (M) with their corresponding daughter (D) cell. The *p*-value stands for the student's t-test between mother and daughter cell. The sample size (*n*) and the median age is indicated.



<Meinema et al, 2021, Fig. 4>

Figure 4. DNA circle anchored NPCs are not recognized as defective. (A) Fluorescent images of nuclei in yeast cell with accumulated DNA circles labeled with TetR-mCherry and Chm7-GFP. Occurrence of Chm7-GFP localization is categorized 1) at least one Chm7 focus in the NPC-cap, 2) a Chm7 focus somewhere else in the nuclear envelop and 3) no visible Chm7 foci. The standard error of the mean is indicated, *n* = 190. (B) The relative age of the NPC plotted as the intensity ratio between mCherry and GFP of Nup170 tagged with a fluorescent timer (Nup170-mCherry-sfGFP), measured in young and old mother (M) versus daughter cells (D).



<Meinema et al, 2021, Fig. 5>

Figure 5. Basket displacement is post-transcriptional regulated. (A) Example images of nuclei in yeast cells with accumulated DNA circles and Nup82-GFP in wt and *gcn5Δ* cells. The DNA circle clusters are labeled with TetR-mCherry (red). Scale bar is 2 μ m. Same as A, but with Nup60-GFP and *nup60-K467R-GFP*. (C) Quantification of GFP-labeled nucleoporin accumulation in the cap, in *nup60-K467R* (brown lines), compared to wt (black lines) on a log2-scale, as in Fig. 2B. Wt data is a copy from Fig. 2B. The *p*-value stands for the student's t-test between accumulation ratio of a specific nucleoporin in wt and *nup60-K467R*, no *p*-value is indicated if the difference is not significant. The sample size (*n*) is indicated.

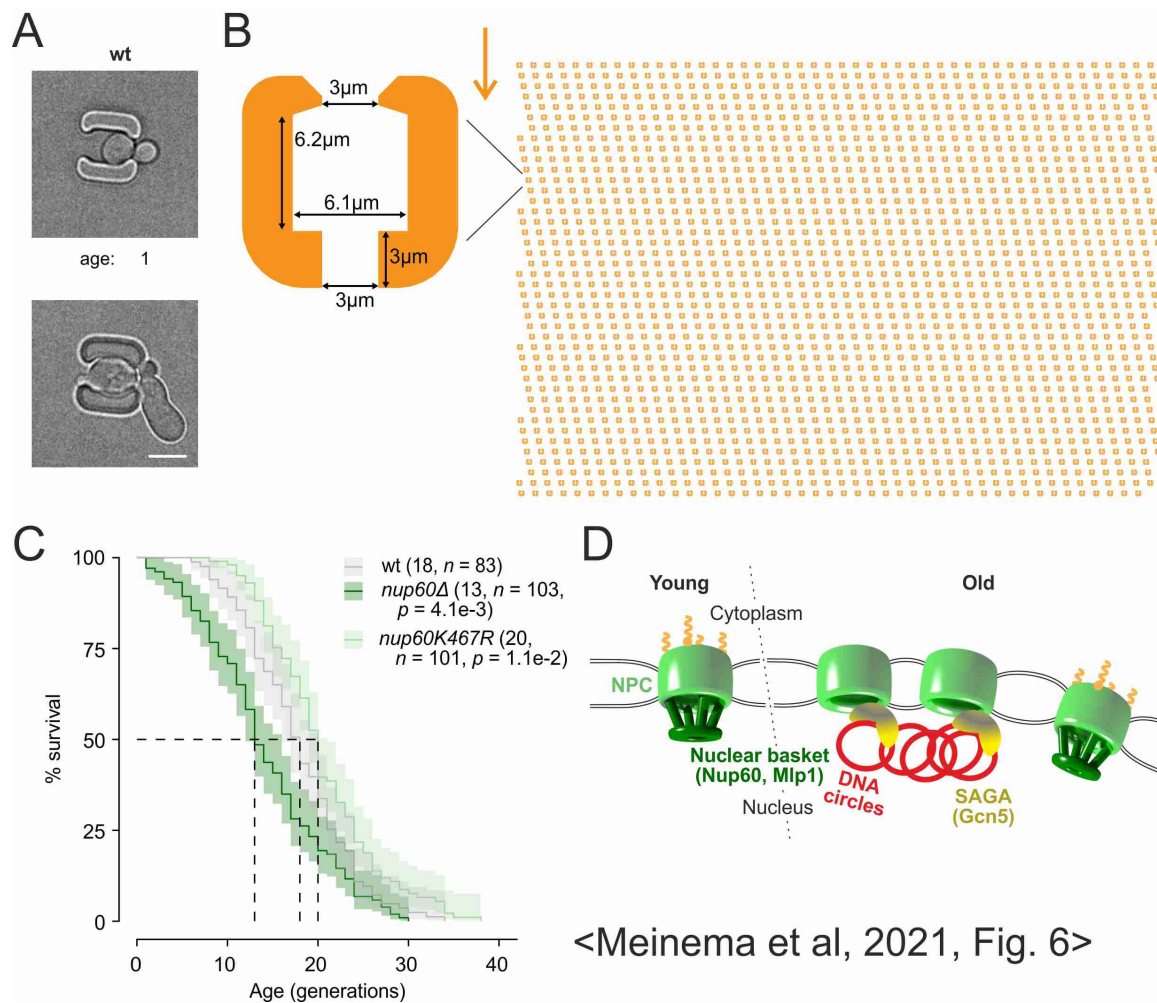
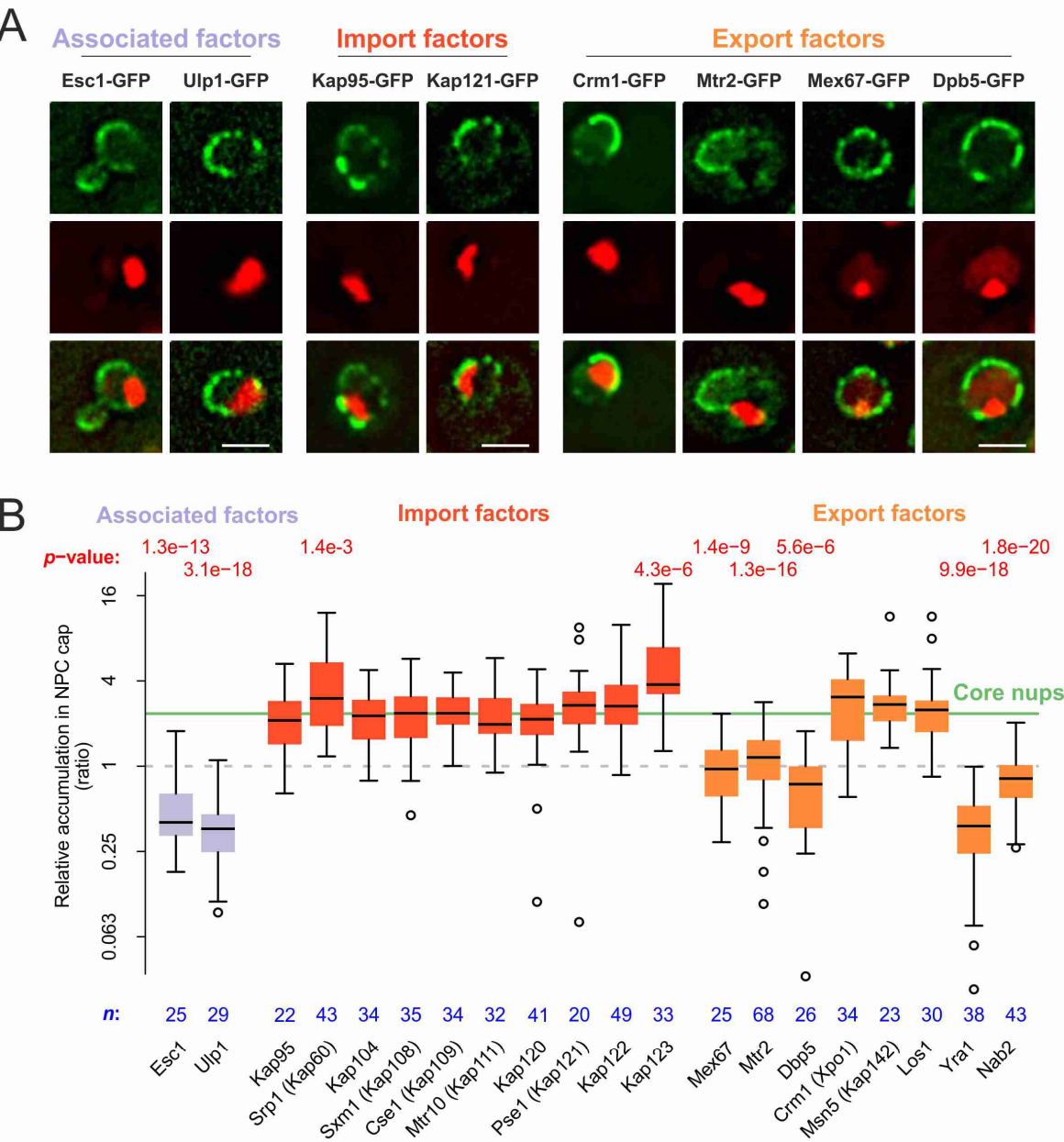


Figure 6. Basket displacement promotes aging (A) Example images of the same young and old wt cell in a trap of the yeast aging chip. The age of the cell is indicated, scale bar is 5 μm. (B) The design of the array with improved traps in the aging chip. One single trap is highlighted to show its dimensions. The arrow shows the direction of the medium flow. (C) The lifespan curve for *nup60Δ* and *nup60-K467R* compared to a wt strain, plotted with 95% confidence interval limits. The p -value stands for Log-Rank test between *nup60Δ* or *nup60-K467R* with the wt strain. (D) Model depicting that DNA circle accumulation affects the organization of the NPC via a SAGA-mediated basket displacement.



<Meinema et al, 2021, Fig. 7>

Figure 7. mRNA export and surveillance factors are displaced from circle-bound NPCs. (A) Fluorescent images of nuclei in aged yeast cells, where the DNA circle clusters are labeled with TetR-NLS-mCherry (red) and transport factors with GFP (green). Scale bar is 2 μ m. (B) Quantification of factor recruitment in the NPC cap adjacent to the DNA circle cluster, as in Fig. 2B. The protein accumulation is plotted for associated factors (grey), import factors (red) and export factors (orange), and is compared to accumulation of the pooled NPC core subunits NPC (green line, duplicated from Fig. 2B), no *p*-value is indicated if the difference is not significant. The sample size (*n*) is indicated.

Appendix 4: Distinct mechanisms underlie H₂O₂ sensing in *C. elegans* head and tail

This paper is the result of an intra-lab collaboration with Sophie Quintin. Here, I developed a microfluidic device to trap *C. elegans* worms in order to observe their response to oxidative stress using timelapse microscopy.

(See paper next page)

Distinct mechanisms underlie H₂O₂ sensing in *C. elegans* head and tail

Sophie Quintin^{1234*}, Théo Aspert¹²³⁴, Tao Ye¹²³⁴ and Gilles Charvin¹²³⁴

* corresponding author (quintin@igbmc.fr)

1) Department of Developmental Biology and Stem Cells, Institut de Génétique et de Biologie Moléculaire et Cellulaire, Illkirch, France

2) Centre National de la Recherche Scientifique, UMR7104, Illkirch, France

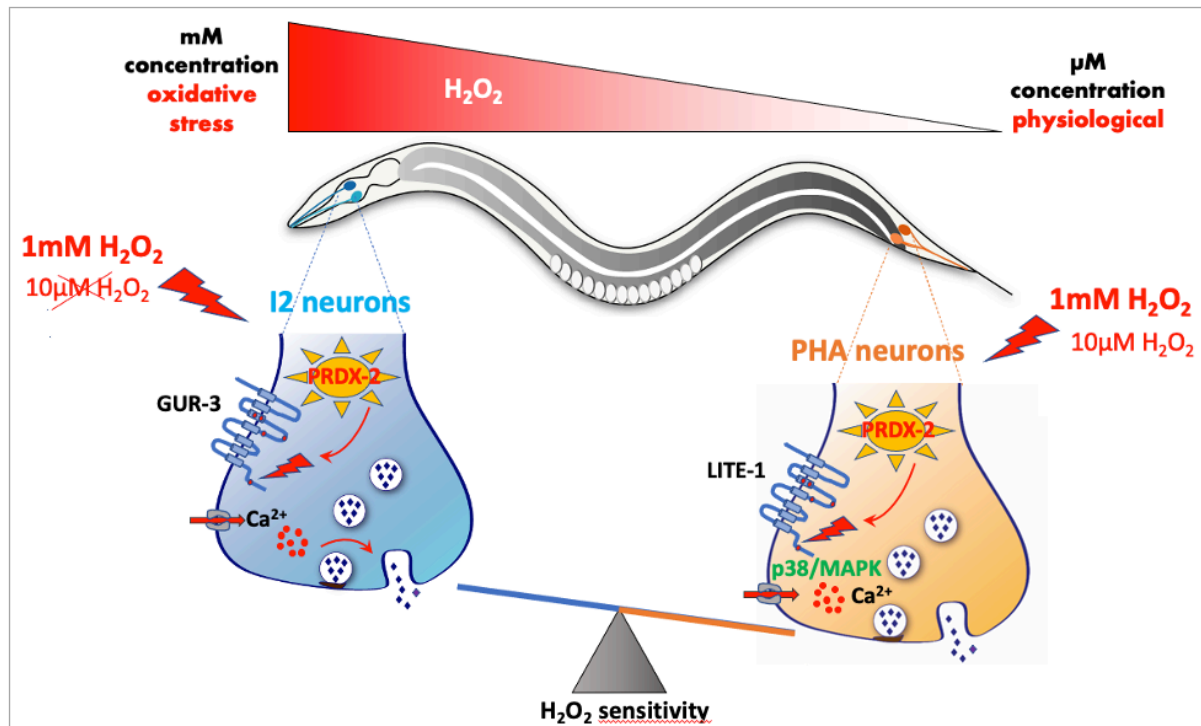
3) Institut National de la Santé et de la Recherche Médicale, U964, Illkirch, France

4) Université de Strasbourg, Illkirch, France

Abstract

Environmental oxidative stress threatens cellular integrity and should therefore be avoided by living organisms. Yet, relatively little is known about environmental oxidative stress perception. Here, using microfluidics, we showed that like I2 pharyngeal neurons, the tail phasmid PHA neurons function as oxidative stress sensing neurons in *C. elegans*, but display different responses to H₂O₂ and light. We uncovered that different but related receptors, GUR-3 and LITE-1, mediate H₂O₂ signaling in I2 and PHA neurons. Still, the peroxiredoxin PRDX-2 is essential for both, and might promote H₂O₂-mediated receptor activation. Our work demonstrates that *C. elegans* can sense a broad range of oxidative stressors using partially distinct H₂O₂ signaling pathways in head and tail sensillae, and paves the way for further understanding of how the integration of these inputs translates into the appropriate behavior.

Graphical abstract



Introduction

Reactive oxygen species (ROS) are well-known to exert a dual effect, promoting aging and pathological conditions on the one hand and increasing organism resistance and longevity on the other hand (Davalli et al., 2016). Neurons are easily exposed to ROS, and many neurodegenerative diseases have been associated with oxidative stress (Cobb and Cole, 2015). However, exposure of *C. elegans* nematodes to a mild oxidative stress has been reported to be beneficial for neuron sensory function: micromolar doses of the ROS-inducing agent paraquat or of hydrogen peroxide (H_2O_2) improve the sensitivity in ASH polymodal neurons (Gourgou and Chronis, 2016; Li et al., 2016), whereas millimolar doses of H_2O_2 reduce neuron response (Li et al., 2016), likely inducing oxidative stress. Therefore, it is essential for nematodes to detect a broad range of H_2O_2 concentrations to preserve their cellular integrity.

Although the cellular response to oxidative stress has been extensively characterized (reviewed in (Blackwell et al., 2015)), little is known on how oxidants are actually perceived and which underlying molecular pathways are involved. Recent studies indicate that light and H_2O_2 sensing are tightly connected in yeast (Bodvard et al., 2017) and in nematodes (Bhatla and Horvitz, 2015). While it has been demonstrated that light is converted into an H_2O_2 signal in yeast (Bodvard et al., 2017), this question remains unanswered in nematodes. Notably, *C. elegans* can detect both H_2O_2 and light via the I2 pharyngeal neurons and responds to these stimuli by inhibition of feeding or by an avoidance behavior (Bhatla and Horvitz, 2015). Initially described as interneurons, the I2 neurons proved to be primary sensory neurons exposed to the environment, and were shown to be highly specialized in oxidative stress sensing (Bhatla and Horvitz, 2015), and were recently shown to respond moderately to salt or odor (Yemini et al., 2021). However, although detection of a large spectrum of H_2O_2 is critical for nematodes, the range of H_2O_2 concentrations detected by I2 neurons has not been investigated, and the molecular mechanisms involved in H_2O_2 signaling are not well defined.

In addition, the nematode also possesses tail sensory neurons specialized in chemorepulsion, called phasmids (PHAs and PHBs) (reviewed in (Goodman and Sengupta, 2019)). In contrast to I2 neurons, these tail neurons can respond to many noxious stimuli (Zou et al., 2017) and trigger avoidance (Hilliard et al., 2002), but whether PHA neurons can sense H_2O_2 or light remains an open question.

H_2O_2 sensing in I2 neurons requires the function of the peroxiredoxin PRDX-2 (Bhatla and Horvitz 2015), a highly conserved antioxidant enzyme whose role remains unclear. Peroxiredoxins (Prxs) belong to a family of thiol peroxidases which can reduce H_2O_2 in cells following the oxidation of one or two cysteines in their catalytic domain, and they are highly abundant from yeast (Breker et al., 2013; Ho et al., 2018) to human cells, in which they represent approximately 1% of the total dry cellular mass (Chae et al., 1999; Low et al., 2007). Oxidised Prxs are recycled in the reduced, active form, by thioredoxin (Hall et al., 2009). At high H_2O_2 concentrations, Prxs become hyperoxidized, a form that has been shown to function as a molecular chaperone (Jang et al., 2004; Moon et al., 2005). Similarly, thioredoxins have been shown to have redox-independent function (McCallum et al., 2016; Sanzo-Machuca et al., 2019). As pivotal antioxidants, Prxs dysfunction has been associated with several pathologies (Park et al., 2016), including cancer (Ding et al., 2017). In budding yeast, the

peroxiredoxin Tsa1 has a major role in maintaining the redox balance, and is massively induced upon oxidative stress as a direct target of the H₂O₂-sensing transcription factor Yap1 (Goulev et al., 2017; Lee et al., 1999). In *C. elegans*, among three genes encoding peroxiredoxins, PRDX-2 is the only one whose depletion induces a phenotype and is considered as the major peroxiredoxin (Isermann et al., 2004; Oláhová et al., 2008). PRDX-2 is expressed in many cell types including neurons, gut (Hirani et al., 2013; Isermann et al., 2004; Oláhová et al., 2008), muscle and epithelial cells (Bhatla and Horvitz, 2015). Although a global induction of *prdx-2* mRNA expression has been reported upon treatment with the strong tBOOH oxidant (Isermann et al., 2004), cells in which PRDX-2 expression is induced remain to be identified. Likewise, the question of a tissue-specific regulation of PRDX-2 by SKN-1, the closest ortholog of Yap1, has not been addressed.

Importantly, beyond their peroxidase activity, Prxs have long been proposed to act as intracellular H₂O₂ sensors, which influence cellular signaling (Ledgerwood et al., 2017; Rhee and Woo, 2011; Veal et al., 2007). For example, the p38/MAPK signaling pathway, which controls adaptive mechanisms and/or cell fate decisions, is activated by H₂O₂ through Prxs in an evolutionary conserved manner (Barata and Dick, 2020; Jarvis et al., 2012). Like in mammalian or in drosophila cells, several studies in *C. elegans* indicate that PRDX-2 would relay H₂O₂ signaling, activating the downstream p38/PMK-1 pathway (Gomes et al., 2016; Haes et al., 2014; Li et al., 2016). Notably, low doses of H₂O₂ potentiate the sensory response of ASH sensory neurons to glycerol through activation of the PRDX-2/p38/PMK-1 cascade (Li et al., 2016). Yet, whether this cascade is at play in I2 neurons to influence H₂O₂ perception has not been analyzed.

Here, we undertook a subcellular analysis of the peroxiredoxin PRDX-2 in *C. elegans*, focusing on its requirement in neuronal H₂O₂ sensing. Using a CRISPR knock-in line, we showed that PRDX-2 is present in many cells, among which several pairs of neurons: I2s in the head, PHAs in the tail and CANs in the body. Interestingly, upon an H₂O₂ challenge, an upregulation of PRDX-2 is observed only in the anterior gut and in the excretory pore, but not in neurons, suggesting that PRDX-2 might fulfill different functions, depending on the cell type where it is expressed. Using a microfluidic-based approach and real-time calcium imaging, we show that PHA neurons also respond to H₂O₂, with an even higher sensitivity than I2 neurons. Although H₂O₂ perception depends on *prdx-2* function in both pairs of neurons, we uncovered that it relies on different gustatory receptors and downstream transducers: while dispensable in I2 neurons, the p38/MAPK kinase contributes to the hypersensitivity of PHA neurons to H₂O₂. Interestingly, we uncovered that H₂O₂ sensing requires the same receptors as light sensing, and that PHA neurons respond to light —establishing a parallel between PHA and photosensory ASH neurons. Based on our work and on previous studies, we propose a molecular model of how H₂O₂ could trigger neuronal activation in I2 and PHA through a peroxiredoxin-mediated redox relay. Taken together, our data suggest that *C. elegans* can sense a broad range of oxidative stress using partially distinct H₂O₂ signaling pathways acting in head and tail sensillae.

Results

Expression pattern of *prdx-2* and its evolution upon H_2O_2 treatment

In budding yeast, the peroxiredoxin Tsa1 is massively induced upon H_2O_2 treatment (Goulev et al., 2017; Lee et al., 1999). To gain insight into the tissue-specific expression of PRDX-2 upon oxidative stress, we first used the PRDX-2 reporter line generated by (Hirani et al., 2013). However, the level of expression of this strain varies a lot, and transgenics show many fluorescent aggregates (Hirani et al., 2013; sup. Fig. 1), likely associated with transgene overexpression. Consistently, the strain displays a much stronger resistance to oxidative stress than wild-type animals (sup. Fig. 1), suggesting that overexpressed PRDX-2 construct induces a higher H_2O_2 scavenging capacity in transgenics. Furthermore, it was impossible to identify PRDX-2-expressing cells in this strain, preventing the use of this strain in our study. For these reasons, we created a GFP knock-in line of PRDX-2, using the CRISPR-Cas9 technique (Dickinson et al., 2013). A C-terminus GFP fusion targeting all PRDX-2 isoforms, comprising a linker, was engineered and inserted at the *prdx-2* locus (Fig. 1A). Three independent knock-in lines were obtained, sharing an identical expression pattern (Fig. 1B).

In the PRDX-2::GFP knock-in line, we detected a broad expression of PRDX-2 in various cell types, including the proximal and distal gut, muscles (body wall, vulval and pharyngeal), epithelial cells (vulva, nose tip, hypodermis) and I2 neurons (Fig. 1B), consistent with previous reports (Bhatla and Horvitz, 2015; Isermann et al., 2004; Oláhová et al., 2008). In addition, we observed for the first time PRDX-2 expression in the excretory pore cell (EPC), and in two other pairs of neurons; the tail phasmids (PHA/PHB) and the excretory canal-associated neurons (CANs), located close to the vulva (Fig. 1B). Consistent with this, a high number of *prdx-2* transcripts was detected in CANs and in the EPC (Cao et al., 2017). Therefore, we hypothesized that the knock-in line faithfully reflects the endogenous PRDX-2 expression, and characterized it further.

PRDX-2 expression is induced in the anterior gut upon H_2O_2 treatment, but not in I2 neurons

We noticed that many PRDX-2-expressing cells are directly in contact with the environment, such as the EPC, the tip of the nose, the vulva, and neurons, which all possess terminations exposed outside. This pattern is strikingly reminiscent of that detected in animals carrying the *HyPer* H_2O_2 biosensor after H_2O_2 exposure (Back et al., 2012). Thus, PRDX-2 is expressed in cells in which environmental H_2O_2 penetrates more easily, suggesting a protective role of PRDX-2 in these cells as a peroxidase. Therefore, in the following, we wondered whether all PRDX-2-expressing cells respond similarly to H_2O_2 -induced oxidative stress.

To determine whether PRDX-2 expression changes upon oxidative stress, we exposed animals to different doses of H_2O_2 , and PRDX-2::GFP expression was quantified in different cells after spinning-disc confocal acquisitions. A higher PRDX-2 expression was detected in the anterior gut two hours after a 10mM H_2O_2 treatment, but not after a 1mM H_2O_2 treatment (Fig. 1C,E). The higher fluorescence was due to PRDX-2::GFP as H_2O_2 -treated controls did not show a higher gut autofluorescence (sup. Fig. 2). Similarly, PRDX-2 expression was only induced in the EPC at the high dose of 10mM H_2O_2 (Fig. 1F, sup. Fig. 2). Thus, our data indicate

a dose-dependent PRDX-2 induction —as it occurs at 10mM but not at 1mM. The origin of this difference could arise from the animal behavioral response: at 1mM H₂O₂ the pharyngeal pumping is strongly inhibited to prevent ingestion (Bhatla and Horvitz, 2015), thereby exposure of gut cells to H₂O₂. This could explain the absence of PRDX-2 induction at 1mM in the gut and the unchanged level of *prdx-2* mRNA reported by Isermann et al. (2004) after 1mM H₂O₂ treatment. In contrast, at 10mM H₂O₂, the nematode should retract back (avoidance response, Bhatla and Horvitz 2015); but here, as animals are trapped in wells and cannot escape, they likely swallow a certain amount of H₂O₂, exposing the foregut to a severe oxidative stress that could in turn trigger PRDX-2 induction. A 10mM H₂O₂ treatment of 30min has been shown to induce hyperoxidation of over 50% total PRDX-2 in wild-type lysed worms (Thamsen et al., 2011) and this form persists after a 4h recovery period (Oláhová et al., 2008). Still, the induction we observed suggests that PRDX-2 could scavenge H₂O₂ in the EPC and in the foregut, to exert a protective role.

Among PRDX-2-expressing neurons, the I2 pair shows the highest expression and possesses terminations exposed to the outside (Bhatla et al., 2015). Therefore, we focused on I2 neurons to investigate whether the neuronal level of PRDX-2 is affected upon H₂O₂ treatment. However, at both concentrations tested (1 and 10mM), the level of PRDX-2 in I2 neurons constantly remained unchanged after H₂O₂ treatment (Fig. 1D,F, sup. Fig. 2).

Thus, we observed an upregulation in the anterior gut and in the EPC following an acute oxidative stress, but not in neurons. As Prxs belong to a homeostatic system, an upregulation was shown to be associated with a detoxification function (Goulev et al., 2007). Therefore, these data suggest that PRDX-2 might fulfill a peroxidase function in the foregut and in the EPC to protect the animal against environmental aggressions, consistent with the reported protective role of intestinal PRDX-2 (Oláhová et al., 2008). In contrast, no upregulation of PRDX-2 has been observed in I2 neurons upon oxidative stress, suggesting that PRDX-2 would instead act in H₂O₂ sensing and/or signaling, as proposed (Isermann et al., 2004; Bhatla and Horvitz, 2015). We conclude that the responses of PRDX-2 to oxidative stress are cellular context-dependent.

SKN-1 controls expression of PRDX-2 in the gut, but not in neurons

This prompted us to test whether PRDX-2 expression could rely on different subcellular regulations. By analogy with yeast, we wondered whether PRDX-2 would be controlled by the Yap1 nematode orthologue SKN-1 (Blackwell et al., 2015) in cells where PRDX-2 is induced upon oxidative stress, and asked whether such regulation occurs in other cells. We sought to test this hypothesis by inactivating the function of SKN-1 in the PRDX-2::GFP knock-in line. We first used the *skn-1(zj15)* allele, which inactivates specifically the gut-specific isoforms, leaving neuronal isoforms unaffected (Tang et al., 2016). In this mutant, the basal expression level of PRDX-2 is reduced in the foregut, but a weak induction persists after a 10mM H₂O₂ treatment (Fig. 2C), suggesting that the neuronal isoforms could mediate this effect. Consistent with this, the RNAi-mediated knock-down of all *skn-1* isoforms also triggered a reduction of PRDX-2::GFP signal in the anterior gut and an absence of induction upon H₂O₂ treatment (Fig. 2B,D). This result indicates that SKN-1 activity is essential to regulate PRDX-2 expression in the anterior gut, both at the basal level and under oxidative stress. In agreement with this, SKN-1 was found to bind to the *prdx-2* promoter in chromatin immunoprecipitation experiments coupled with high-throughput DNA sequencing (ChIP-seq) (Niu et al., 2011) (Fig. 2E).

In contrast, in I2 neurons, no change in the PRDX-2 level was detected at the basal level or after H₂O₂ treatment compared to controls, neither in *skn-1(zj15)* mutants nor in *skn-1(RNAi)* animals (sup. Fig. 2). With the limitation that RNAi efficiency may be lower in neurons (Calixto et al. 2010), we suggest that additional transcription factor(s) might regulate *prdx-2* expression in these neurons. Consistently, multiple transcription factors were reported to bind to the *prdx-2* promoter by ChIP-seq (Niu et al., 2011) (Fig. 2E).

We conclude that *skn-1* accomplishes a cell autonomous regulation of *prdx-2* in the intestine, but this regulation may not occur in neurons, where PRDX-2 is expressed. Taken together, our data suggest that PRDX-2 might exert a different function depending on the cell type: H₂O₂ detoxification in the foregut, triggered by SKN-1, vs. H₂O₂ perception or signaling in I2 neurons.

PHA neurons respond to H₂O₂ in a prdx-2-dependent manner

As PRDX-2 is expressed in other neurons than I2s, we asked whether PRDX-2 endows these neurons with oxidative stress sensing properties. We focused on PHA tail neurons, as they belong to the phasmod sensory sensilla and respond to many noxious stimuli (Zou et al., 2017). We monitored PHA neuron activation by imaging calcium using the GCaMP3 fluorescent sensor (Tian et al., 2009) expressed under the *flp-15* promoter, specific to I2 and PHA neurons (Kim and Li, 2004).

To image calcium fluxes in neurons, L4 animals were trapped in microfluidic chambers and exposed to H₂O₂ (Fig. 3A, sup. Fig. 3), and their response was followed in 4D spinning-disc ultrafast acquisitions. This experimental setup, combined with semi-automated image analyses to quantify the mean fluorescence in neurons over time, confirmed the activation of I2s upon a 1mM H₂O₂ treatment (Fig. 3B-D, movie 1), similar to that observed upon exposure to H₂O₂ vapor (*ie.* 8.82M, Bhatla and Horvitz, 2015). As PRDX-2 reproducibly shows an asymmetric expression level in I2L and I2R (Fig. 1B,D), each neuron was scored individually to take into account a putative left-right effect. However, this did not impact neuron response as no significant difference in the normalized response of left and right neurons was noticed (Fig. 3B,C,L). Importantly, we observed that PHA neurons respond to 1mM H₂O₂ comparably to I2 neurons (Fig. 3C,D,H, movie 2). We then investigated whether PRDX-2 function was necessary for PHA response, using a strong *prdx-2* loss of function mutant. In agreement with previous work (Bhatla and Horvitz, 2015), I2 neurons in *prdx-2(gk169)* mutants failed to respond to 1mM H₂O₂ (Fig. 3E-H, movie 3). Interestingly, we uncovered that PHA neuron response was severely impaired in *prdx-2* mutants, although not completely abolished as in I2s (Fig. 3E,G,H, movie 4). From these observations, we conclude that both I2s and PHAs responses to oxidative stress require the function of the peroxiredoxin PRDX-2, but the residual response of PHA neurons suggests a lesser requirement of the antioxidant in tail neurons.

I2s and PHAs show differences in H₂O₂ sensitivity and in receptors involved

Given the putative role of PRDX-2 as an H₂O₂ sensor, the fact that there was a slight difference in PRDX-2 activity requirement in I2s and PHAs prompted us to analyze whether the head and tail neurons share the same sensitivity to H₂O₂. We thus tested whether I2 and PHA neurons exhibit a response to the very mild dose of 10μM H₂O₂. Indeed, at this dose, it

has been reported that only a minority of animals ($\approx 35\%$) respond by inhibiting pharyngeal pumping (Bhatla and Horvitz, 2015). In our experiments, whereas I2 neurons failed to be activated in most animals at $10\mu\text{M}$ H_2O_2 (25/29, Fig. 3I,J,L, movie 5), PHA neurons responded in the vast majority of animals (25/27, Fig. 3I, movie 6), in a similar manner than at 1mM H_2O_2 (Fig. 3K,L). We conclude that PHA neurons are more sensitive to low doses of H_2O_2 than I2 neurons.

The difference in sensitivity between I2 and PHA neurons may come from distinct molecular mechanisms. To explore this possibility, we first tested which receptors are required in I2s and in PHAs for H_2O_2 perception. We focused on photoreceptors as photosensation is likely to involve the generation of ROS (Bhatla and Horvitz, 2015; Zhang et al., 2020). In *C. elegans*, light sensing relies on unusual gustatory G-protein-coupled receptors (GPCRs) related to vertebrate photoreceptors: the two nematode closest paralogs LITE-1 and GUR-3 mediate photosensation in ASJ and ASH neurons (Liu et al., 2010; Ward et al., 2008; Zhang et al., 2020), and light and H_2O_2 sensing in I2 neurons (Bhatla and Horvitz, 2015). We investigated whether these two receptors are differentially localized in I2 and PHA neurons. We generated a knock-in GUR-3::GFP line, which revealed that GUR-3 is solely expressed in I2 and I4 photosensory neurons (Fig. 4A), as previously reported using episomal expression (Bhatla and Horvitz, 2015). Such a restricted pattern deeply contrasts with the broad expression domain of LITE-1, which includes phasmid neurons (PHA and PHB), but not I2 neurons, as shown using both translational and transcriptional reporters (Bhatla and Horvitz, 2015).

These differential localizations prompted us to inquire whether mutants in these receptors were still able to trigger a response to 1mM H_2O_2 in I2 and PHA neurons. In *gur-3(ok2245)* mutants, only PHA neurons were able to respond to 1mM H_2O_2 (Fig. 4B,C, sup. Fig. 4, movies 7,8), providing evidence that GUR-3 function is not essential in PHA neurons for H_2O_2 sensing. In contrast, *lite-1(ce314)* mutants showed a reciprocal response, with only I2 neurons activated upon 1mM H_2O_2 exposure (Fig. 4B,C, sup. Fig. 4, movies 9,10). In conclusion, H_2O_2 likely activates I2 neurons via *gur-3* and PHA neurons via its paralog *lite-1*, respectively. Interestingly, these observations might explain the previously reported impaired avoidance response of *lite-1* mutants to 1mM H_2O_2 (Bhatla and Horvitz, 2015), as PHA neurons are involved in escape behavior (Hilliard et al., 2002).

PMK-1 is required for PHAs response to H_2O_2 but seems dispensable in I2s

Since H_2O_2 perception in I2 and PHA neurons involves different receptors and requires the function of PRDX-2 in both cases, we wondered what type of signaling occurs downstream PRDX-2 to trigger neuronal activation upon H_2O_2 stimulation.

As mentioned above, studies in various models have reported that peroxiredoxins can modulate the p38/MAPK signaling pathway to influence cellular decisions, notably in drosophila and mammalian cells (Barata and Dick, 2020). In *C. elegans*, specifically, the activation of this PRDX-2-PMK-1/p38 cascade allows micromolar doses of H_2O_2 to potentiate the ASH neuron sensory behavior to glycerol (Li et al., 2016). Therefore, we tested a potential requirement of the PMK-1/p38 MAPK function in H_2O_2 sensing in I2s and PHAs by analyzing their responses in a *pmk-1* loss-of-function genetic background. As the strongest allele *pmk-*

1(ok811) is a homozygous lethal deletion, we had to use the hypomorphic *pmk-1(km25)* viable mutant, which carries an N-terminal deletion, generating a truncated version of PMK-1 (Mizuno et al., 2004). In *pmk-1(km25)* mutants, while I2 neurons responded to 1mM H₂O₂, PHA neurons showed an attenuated response to 1mM H₂O₂ compared to controls (Fig. 4D,E, movies 11, 12). Therefore, PMK-1 seems dispensable in I2 neurons for 1mM H₂O₂ sensing but plays a role in PHA neurons response.

In ASH neurons, the activation of p38/PMK-1 leads to the phosphorylation of the voltage-gated calcium channel OSM-9; resulting in improved neuronal sensitivity (Li et al., 2016). Given the differential requirement of PMK-1 in I2 and PHA neurons, we then asked whether p38/PMK-1 could promote PHA sensitivity to low doses of H₂O₂, as in ASH neurons. We thus examined PHA neuron response to 10μM H₂O₂ in *pmk-1(km25)* mutants, and found that it was abolished (Fig 4D,F, movies 13,14). We conclude that PMK-1/p38MAPK activity is required for PHA neurons hypersensitivity to H₂O₂, whereas it seems dispensable in I2 neurons.

PHA neurons are photosensory neurons like ASH neurons

Light sensing has been reported for ASJ, ASH and I2 neurons and require either the LITE-1 or the GUR-3 receptor, respectively (Bhatla and Horvitz, 2015; Liu et al., 2010; Ward et al., 2008; Zhang et al., 2020). As PHAs neurons require LITE-1 to respond to H₂O₂ (Fig. 4B,C), we asked whether they could respond to light. To test this, we monitored calcium transients in three neuronal compartments using the GCaMP strain upon stimulating neurons with blue light, as previously done for I2 or ASH neurons (Bhatla and Horvitz, 2015; Zhang et al., 2020). Interestingly, we found that all regions of PHA neurons responded to light, displaying a different response profile than those of I2 neurons (Fig. 4G,H, movies 15,16,17): PHA soma showed a stronger and longer response than I2 soma; PHA posterior neurite responded much slower than in I2 where it exhibits the fastest and strongest response peak, and the anterior neurite also had a slower recovery than in I2. Overall, while I2 neurons exhibit a fast photoresponse within 10-15s, PHA neurons photoresponse requires twice longer to return to steady state (approx. 30s). Strikingly, we noticed that PHA neurons profile is highly reminiscent of that reported in ASH neurons photoresponse (Zhang et al., 2020).

Discussion

H₂O₂ sensing in head and tail neurons relies on different mechanisms

Here, we describe how two pairs of sensory neurons located in the head and the tail of *C. elegans*, namely I2s and PHAs, contribute to exogenous H₂O₂ sensing. Compared to previous reports, our study relies on a PRDX-2::GFP knock-in line more closely reflecting endogenous expression level, in comparison to overexpression often observed with extrachromosomal arrays. While classical methods do not enable precise control of the environment such as application of a stress, we carried out neuron response experiments using the microfluidic technology, allowing live imaging of immobilized animals upon simultaneous exposure to a controlled oxidative stress.

We found that PHA tail neurons can elicit a response to a micromolar range of H_2O_2 , whereas I2 head neurons cannot, suggesting that distinct molecular mechanisms may account for this difference. Accordingly, while the peroxiredoxin PRDX-2 is essential for H_2O_2 sensing in both I2 and PHA neurons, each neuron pair seems to require a different transmembrane receptor to transduce the signal: I2 neurons rely on activity of the gustatory receptor GUR-3, while PHA neurons would require its paralogue LITE-1. Finally, we found that p38/PMK-1 activity would be specifically required in PHA neurons to confer their hypersensitivity to H_2O_2 , but dispensable in I2 neurons.

Overall, our data are consistent with previous findings unveiling the existence of two distinct modes of response to oxidative stress in *C. elegans*: a direct response in peripheral tissues such as the gut, and a neuronally-regulated response relying on synaptic transmission (Rangaraju et al., 2015). Specifically, we uncovered that a harsh oxidative stress (10mM H_2O_2) triggers stress response in the anterior gut and in the EPC (Figs. 1-2) through PRDX-2 induction, while a lower dose of H_2O_2 (1mM) triggers I2 and PHA neuron activation (Fig. 3). Interestingly, both types of response involve the peroxiredoxin PRDX-2, which behaves differently in the two cellular contexts: PRDX-2 was found to be cell-autonomously induced by SKN-1 in the intestine, but likely not in neurons. Therefore, we propose that in the gut PRDX-2 might act as a peroxidase, as proposed (Oláhová et al., 2008), whereas it could function as a H_2O_2 -signaling molecule in neurons, as suggested for I2 neurons (Isermann et al., 2004; Bhatla and Horvitz, 2015). Importantly, H_2O_2 response in I2 and PHA neurons requires the joint function of PRDX-2 and a receptor, as each mutant individually cannot respond (Figs. 3-4). In addition, former rescue experiments indicated that light response in I2 requires the activity of PRDX-2 and GUR-3 in I2 neurons (Bhatla and Horvitz, 2015). Based on all these data and recent studies shedding light on how H_2O_2 is sensed in plant and animal cells (Barata and Dick, 2020; Wu et al., 2020), we propose new hypotheses regarding H_2O_2 signaling in neurons which are depicted in Fig. 5 and described below, to integrate our findings with recent results from the literature.

A presumptive model of H_2O_2 sensing in *C. elegans* neurons

In both I2 and PHA neurons, we favor the hypothesis that cytosolic PRDX-2 rather than the transmembrane receptor would be the neuronal H_2O_2 sensor, based on the following observations: i) in many cases, H_2O_2 signaling is mediated by oxidation of cysteines in redox-regulated proteins (Groitel and Jakob, 2014). Alternatively, redox signaling often relies on a cascade involving peroxiredoxins as a sensor and transducer of H_2O_2 signal (Stöcker et al., 2018). It has been proposed that thiol modifications would be much faster when catalyzed by peroxiredoxins (Flohé, 2016; Netto and Antunes, 2016; Randall et al., 2013), due to their relative abundance and their very high reactivity towards H_2O_2 (Winterbourn and Peskin, 2016). Here, the striking abundance of PRDX-2 in PHA and especially in I2 neurons seen in the GFP-tagged *prdx-2* knock-in line reinforces this idea, as well as the quasi-absence of H_2O_2 response in *prdx-2* mutants. Interestingly, LITE-1-dependent photosensation in ASH neurons requires thioredoxin (Zhang et al., 2020), suggesting redox signal transduction through antioxidants of the peroxiredoxic cycle; and LITE-1-dependent ASJ photosensory neurons also express the TRX-1 thioredoxin (Miranda-Vizueté et al., 2006). Therefore, we propose that H_2O_2 signaling in I2 and PHA would involve a redox signaling cascade through PRDX-2. ii) Concerning receptor topology, GUR-3 and LITE-1 present a relatively small extracellular domain —poorly conserved compared to its intracellular part— devoid of any conserved cysteine.

Remarkably, conserved cysteines between LITE-1 and GUR-3 are only found in the first and third intracellular loops and in the fifth transmembrane domain (Fig. 5A,B). This structure is reminiscent of the vertebrate transmembrane protein GDE2, which is activated intracellularly by the Prdx1 peroxiredoxin to induce motor neuron differentiation (Yan et al., 2009); but it sharply contrasts with that of the recently identified H_2O_2 sensor in plants, the HCPA1 receptor (Wu et al., 2020). HCPA1 possesses a large extracellular domain with many cysteines, which when directly oxidized by H_2O_2 , induces a conformation change, in the receptor, hence HCPA1 activation and subsequent calcium intracellular entry. Here, GUR-3 and LITE-1 receptor topology does not support the hypothesis of a direct oxidation by H_2O_2 on the extracellular domain, but rather suggests intracellular signaling as in the case of GDE2.

Taken together, we thus propose a scenario in which H_2O_2 would diffuse through the neuron plasma membrane and oxidize PRDX-2. Oxidized PRDX-2 or its disulfide form (PRDX-2^{ox/S-S}) would in turn activate GUR-3 in I2s, or LITE-1 in PHAs, through the cysteines of their intracellular domain, *eg.* by inducing a conformation change upon the formation of a disulfide bond or by forming a transient disulfide bond conjugate (Fig. 5A,B). Once GUR-3 or LITE-1 becomes activated by PRDX-2^{ox}, this likely triggers action potentials upon the opening of voltage-gated calcium channels and neurotransmitter release, likely inducing the appropriate behavior (Fig. 5C,D). Interestingly, the voltage-gated calcium channels have been reported to be different in the two neuron pairs: whereas I2 activation depends in part on the voltage-gated calcium channels UNC-2 and UNC-36 (Bhatla et al., 2015); PHA neurons calcium transients rely on both the cyclic nucleotide-gated channel TAX-4 and on OSM-9, the nematode equivalent of vertebrate TRPV5 (i.e., transient receptor potential vanilloid cation channel subfamily V member 5) (Zou et al., 2017). In addition, the other TRPV5 channel subunit OCR-2 may also act in PHAs, as it functions in a cooperative association with OSM-9 (Ohnishi et al., 2020), and OCR-2 is expressed in PHAs (Jose et al., 2007)(sup. Fig. 8). Therefore, although they are closely related and can both sense H_2O_2 and light, GUR-3 and LITE-1 signaling seems to rely on different downstream transducers. Thus, except for the requirement of PRDX-2, which might trigger H_2O_2 -mediated receptor activation, I2 and PHA neurons would use distinct molecular pathways to transduce H_2O_2 response.

A striking parallel between PHA and ASH neurons

Our data uncover a high sensitivity of PHAs to micromolar doses of H_2O_2 that is not seen in I2 neurons, which requires PMK-1/p38 activity. Strikingly, micromolar doses of H_2O_2 increase the sensitivity of ASH neurons to glycerol through the PRDX-2-mediated activation of the PMK-1/p38 pathway (Li et al., 2016), which results in the terminal phosphorylation of the TRPV sensory channel OSM-9, likely increasing its sensitivity (Li et al., 2016). Although our study and the latter do not elucidate how PRDX-2 triggers PMK-1 activation, recent evidence sheds light on this process: in both mammalian and drosophila cells, H_2O_2 induces transient disulfide-linked conjugates between the MAP3K and a typical 2-Cys peroxiredoxin (Barata and Dick, 2020). Similarly, in *C. elegans*, PRDX-2 could activate the MAPKKK NSY-1, as NSY-1 function is required in ASH neuron for H_2O_2 -behavioral induced potentiation (Li et al., 2016), and it may be expressed in PHAs (*unidentified cells of the tail*, *D. Moerman, WormBase*). Based on these observations and on the fact that OSM-9 is expressed (Colbert et al., 1997) and likely required in PHA neurons (Zou et al., 2017), we propose that PMK-1 function might increase PHA neurons' sensitivity to H_2O_2 , potentially through the downstream phosphorylation of

OSM-9, as in ASH neurons (Fig. 5D). These assumptions, which will necessitate further experimental validations, are supported by the observation that ASHL/R and PHAL/R are both descendants of ABplp or ABprp in the nematode cell lineage, and hence may express similar sets of genes following lineage-specific priming (Charest et al., 2020). In addition, the fact that PHA, PHB and ASH were found in the same neuron cluster by (Lorenzo et al., 2020), further suggests that they share similar molecular signatures. To illustrate the parallel between ASH and PHA polymodal nociceptors, we retrieved the set of genes expressed in these neurons from (Lorenzo et al. 2020)'s dataset, and analysed which genes were specifically enriched in these two neurons in comparison to all other neurons (sup. Fig. 8). This analysis revealed that ASH and PHA not only express many genes specific to ciliated neurons, as expected (*eg. che-3, nphp-4, che-11, ifta-1*; C33A12.4 and R102.2, (Kunimoto et al. 2005)) but also a number of common receptors (*eg. ocr-2, osm-9, ida-1, casy-1, ptp-3* or *pdfr-1*) although some of them are more enriched in ASH (*dop-2, nrx-1, snt-5, sue-1*). Intriguingly, their neuropeptide profile appears slightly different for the two neuron pairs (PHA enriched in *flp-7, flp-4, flp-16, nlp-1, ins-18*, while ASH strongly express *flp-13* and *npr* genes), suggesting that beyond their functional similarity, ASH and PHA may trigger different types of intercellular communication. Finally, this analysis highlights that several genes with unknown function are highly enriched in both ASH and PHA (*eg. F27C1.11, W05F2.7, tos-1, cab-1*, sup. Fig. 8), pointing to their potential importance in neuronal function.

Taken together, our analyses highlight the common features shared between PHA and ASH polymodal nociceptive neurons, as formerly noticed (Hilliard et al., 2002), since they both: i) display a higher sensitivity dependent on the PMK-1/p38 pathway (Fig. 4F and (Li et al., 2016)), ii) exhibit a similar profile of response to light (Fig. 4H and (Zhang et al., 2020)), iii) require the photoreceptor LITE-1 for lightsensing (Zhang et al., 2020) or H₂O₂ sensing (Fig 4BC), iv) trigger avoidance (Hilliard et al., 2002), and v) were found in the same class of gene-expressing neurons and therefore share a close molecular signature (Lorenzo et al., 2020), sup. Fig. 8). These observations led us to propose that the nematode might integrate the environmental redox signals from at least three different pairs of neurons (I2, ASH, PHA) in order to trigger an appropriate dose-dependent physiological response. To our knowledge, the sensitivity of PHA neurons to light and to a low H₂O₂ concentration has never been described.

GUR-3 and LITE-1 receptors mediate both light and H₂O₂ sensing

In yeast, light sensing relies on the peroxisomal oxidase Pox1 which triggers light-dependent H₂O₂ formation, the latter being sensed by the Tsa1 peroxiredoxin and transduced to thioredoxin for subsequent signaling (Bodvard et al., 2017). Nematodes, unlike yeast, require a photoreceptor in addition to the antioxidant for lightsensation: GUR-3 in I2 neurons (Bhatla and Horvitz, 2015), and LITE-1 in ASJ and ASH neurons (Liu et al., 2010; Zhang et al., 2020). Here we showed that both I2 and PHA respond to light, but with a different profile. Despite its unusual membrane topology, LITE-1 has been shown to encode a bona fide photoreceptor, whose photoabsorption depends on its conformation (Gong et al., 2017). However, whether light directly activate the neuron photoreceptor or triggers intracellular H₂O₂ release and signaling is still unclear. In agreement with the fact that H₂O₂ inhibits LITE-1 photoabsorption *in vitro* (Gong et al., 2017), it has been shown that a H₂O₂ pretreatment reduces LITE-1-mediated photoresponse in ASH neurons (Zhang et al., 2020). Consistent with

these reports, our data illustrate for the first time that GUR-3 and LITE-1 have a dual function in both light and H₂O₂ sensing and open up the hypothesis that, as in yeast, redox signaling could be involved in transducing the light signal, as for H₂O₂ sensing (Fig. 5). We observed that PHA and ASH neurons exhibit a similar type of response to light (Fig 4H and (Zhang et al., 2020)), which is slower than that observed in I2 neurons (Fig. 4G and Bhatla and Horvitz 2015). Whether this difference depends on the photoreceptor (LITE-1 in PHA and ASH vs GUR-3 in I2), or on its downstream redox signaling cascade, would be worth investigating.

Finally, it is noteworthy that some neurons rely on peroxiredoxin for oxidative stress and/or light sensing, such as I2 or PHA, while others rely on thioredoxin, such as ASJ, or ASH for light sensing. This further underlines the importance of redox signaling relays involving antioxidants of the peroxiredoxin cycle in these photosensory neurons of the nematode.

In conclusion, our work illustrates that nematodes can sense various concentrations of H₂O₂ through sensory neurons located in the head and the tail, using either partially different (I2 and PHA), or similar molecular mechanisms (ASH and PHA). This set of neurons also confer light sensing to the nematode with a distinct speed in the response (fast in I2, slow in PHA and ASH, (Zhang et al., 2020)). While I2 neurons seem more specialized in sensing oxidative stress (Bhatla and Horvitz, 2015; Yemini et al., 2021), PHA and ASH can detect many other stimuli (Zou et al, 2016), but all of them can trigger avoidance. These observations may help uncover whether and how inputs from head and tail oxidative stress sensory neurons integrate to allow nematodes to quickly and appropriately react to a sudden change in the environment.

Experimental procedures

Generation of plasmids and transgenic strains by CRISPR/Cas9-mediated genome editing

C. elegans strains (listed in Table S1) were maintained as described (Brenner, 1974). PRDX-2::GFP knock-in strain was generated by CRISPR/Cas9-mediated genome editing, using a DNA plasmid-based repair template strategy (Dickinson et al., 2013). For both PRDX-2 and GUR-3 knock-ins, a C-terminal GFP fusion was generated, comprising a flexible linker between the coding region and GFP to allow correct folding of the fusion protein. A combined small guide-RNA/repair template plasmid was built using the SAP Trap strategy (Schwartz and Jorgensen, 2016). Phusion DNA polymerase was used to amplify by PCR 5' and 3' *prdx-2* and *gur-3* homology arms (HAs) from N2 genomic DNA, using primers containing SapI restriction sites and silent mutations to prevent Cas9 re-cleavage (primers listed in Supplemental Table 2). After purification, 5' and 3' HAs and sgRNA oligonucleotides were assembled into the destination vector (pMLS256), together with the flexible linker (from pMLS287), GFP and the *unc-119* rescuing element (from pMLS252), in a single SapI restriction-ligation reaction, as described (Schwartz and Jorgensen, 2016). Prior to transformation in DH5 α cells, a sabotage restriction was performed with SpeI to digest empty destination vectors but not the desired assembly constructs, which were subsequently verified by restriction digest analysis and sequencing. All plasmids used for injection were purified using a DNA Miniprep Kit (PureLink, Invitrogen), or a DNA midiprep kit (Macherey Nagel). For PRDX-2::GFP knock-in, a plasmid mix containing combined sgRNA/repair template plasmid (50 ng/ μ l), Cas9-encoding pSJ858 (25ng/ μ l) and co-injection markers (pCFJ90 at 2.5ng/ μ l; pCFJ104 at 5ng/ μ l, and pGH8 at 5ng/ μ l) was injected in the germline of *unc-119(ed3)* animals (Dickinson et al., 2013). For GUR-3::GFP knock-in, an injection mix containing purified Cas9 protein (IDT) associated with tracrRNA and crRNA (guide RNA), GUR-3 repair template, and co-injection markers was injected in *unc-119(ed3)* animals, according to IDT online protocols for *C. elegans*. Plates containing 2/3 injected F0 animals were starved, chunked on fresh plates, for candidates screening (attested by the presence of wild-type non fluorescent animals). Knock-in events were validated by PCR on homozygous lysed worms (QuantaBio AccuStart II GelTrack PCR SuperMix), using primers annealing in the inserted sequence and in an adjacent genomic region not included in the repair template. The PRDX-2::GFP strain was outcrossed 5 times to N2 wild-types.

RNA interference

RNAi experiments were performed by feeding using the Ahringer-MRC feeding library (Kamath et al., 2003). Animals fed with the empty vector L4440 served as a negative control. The efficiency of each RNAi experiment was assessed by adding an internal positive control, *zyg-9(RNAi)*, which induces embryonic lethality.

Spinning-disk confocal microscopy acquisitions and fluorescence intensity measurements

For live imaging, animals were anesthetized in M9 containing 1mM levamisole and mounted between slide and coverslip on 3% agarose pads. Synchronized L4 animals were

treated for 30min in a 96-well flat bottom plate, in 50µl of M9 containing 1mM or 10mM H₂O₂. Treated animals were transferred using a siliconized tip on a freshly seeded plate to recover, and imaged 1h30 to 2h later. Spinning-disk confocal imaging was performed on a system composed of an inverted DMI8 Leica microscope, a Yokogawa CSUW1 head, an Orca Flash 4.0 camera (2048*2018 pixels) piloted by the Metamorph software. Objective used were oil-immersion 40X (HC PL APO, NA 1.3) or 63X (HCX PL APO Lambda blue, NA 1.4). The temperature of the microscopy room was maintained at 20 °C for all experiments. Z-stacks of various body regions were acquired with a constant exposure time and a constant laser power in all experiments. Maximum intensity projections were used to generate the images shown. Fluorescence intensity measurements in int1, I2 and EPC cells were performed using the Fiji software, by manually drawing a region of interest (ROI) around the cell (int1, EPC), or applying a threshold (I2 neurons), background was subtracted and average pixel intensity was quantified.

Microfabrication and microfluidic chip preparation

The microfluidic chip original design was inspired by the the Wormspa (Kopito and Levine, 2014), but pillars distances were adapted to trap L4 animals, and multiple series of traps were included to increase the number of experiments per chip (sup. Fig. 3). A master mold was made by standard soft photolithography processes by spin-coating a 25µm layer of SU-8 2025 (Microchem, USA) photoresist at 2700 rpm for 30sec on a 3" wafer (Neyco, FRANCE). Then, we used a soft bake f 7min at 95°C on hot plates (VWR) followed by a UV 365nm exposure at 160 mJ/cm² with a mask aligner (UV-KUB3 Kloeé®, FRANCE). Finally, a post-exposure baking identical to the soft bake was performed before development with SU-8 developer (Microchem, USA). Then, the wafer was baked at 150°C for 15min to anneal potential cracks and strengthen the adhesion of the resist to the wafer. Finally, the master mold was treated with chlorotrimethylsilane to passivate the surface.

Worm microchannels were cast by curing PDMS (Sylgard 184,10:1 mixing ratio), covalently bound to a 24 × 50 mm coverslip after plasma surface activation (Diener, Germany), and incubated 20min at 60°C for optimal adhesion. The chip was perfused with filtrated M9 solution through the medium inlet using a peristaltic pump (Ismatec), until complete removal of air bubbles. Worm loading was performed with the pump set at a low flow rate (<30 µl/min), through a distinct inlet (sup. Fig. 3): 10-15 young L4 animals (synchronized by bleaching 48h prior to each experiment) were picked in a siliconized Eppendorf tube containing M9, and perfused into the traps. The loaded chip was carried to the microscope while being still connected to the pump by a gravity flow (preventing animals to escape) until the microfluidic chip was installed on the microscope stage.

Calcium imaging

I2 and PHA neuronal response was monitored using the calcium sensor GCaMP3 expressed under the *flp-15* promoter as in (Bhatla and Horvitz, 2015). To image H₂O₂ response, young L4 animals trapped in microfluidic chips were imaged using the confocal spinning disc system described above with the 20X air objective (HC PL APO CS2, NA 0.75). The microfluidic chip allowed the simultaneous recording of up to 3 animals per experiment (sup. Fig. 3). Z-stacks of 10-15 images (10 µm spacing) were acquired every 2s (using the stream Z mode), for

350 time points. Exposure time was 50ms and laser power set on 40%. The device was perfused with M9 medium throughout the experiment using a peristaltic pump set at 80 μ l/min, and H₂O₂ was perfused (at 10 μ M or 1mM in M9) for 100 time points (3min20s) after an initial recording of 35-45 time points. Movies were computationally projected using MetaMorph, and data processing (including movie registration, neuron segmentation and tracking over time) was conducted with a custom-developed Matlab program detailed below and available at <https://github.com/gcharvin/viewworm> (a user guide is provided in supplemental Methods).

To image light response in I2 and PHA neurons, L4 worms were mounted on a slide covered with 3% agarose pads in M9 supplemented with 1mM levamisole. Video-recordings were performed on the spinning-disc microscope using the 40X oil objective. Animals were exposed to blue light (485nm) while their neuronal response was simultaneously recorded in stream mode (10 frames/sec, single Z, 100ms exposure, laser 100%) for 30sec.

Calcium response analyses

For H₂O₂ response analyses, sequences of images were spatially realigned with respect to the first image of the timeseries in order to limit the apparent motion of the worm in the trap and ease the tracking of neurons of interest. This image registration process was performed using standard 2D image cross-correlation by taking the first image as a reference. Then, we used a machine-learning algorithm (based on a decision tree) to segment pixels in the fluorescent images. For this, we took a series of image transforms (gaussian, median, range filters) as descriptors for the classifier, and we trained the model on typically 10 frames before applying the result to the rest of the time series. This segmentation method appeared to be superior to simple image thresholding, which is inadequate when dealing with fluorescent signals that vary both in time and space (the brightness of two neurons is quite different). Next to the segmentation procedure, we tracked the identified neurons using distance minimization, and we quantified the mean fluorescence signal in each neuron over time. Last, fluorescence data corresponding to individual animals were pooled after synchronization from the time of exposure to H₂O₂ and signal normalization. This image analysis pipeline is available at <https://github.com/gcharvin/viewworm> and a tutorial for use is included in supplemental methods. As some movies could not be quantified due to uncontrolled animal movements, a visual classification of neuronal responses (high, moderate, absent) was made by comparison to successfully tracked movies.

For light response analyses in I2 and PHA neurons, the same image processing pipeline as in (Bhatla and Horvitz, 2015) was used, except that ROI were manually drawn in Fiji.

Statistical analyses

P-values were calculated with an unpaired two-tailed Student test; the Welch correction was applied when the two samples had unequal variances. Error bars depict standard deviation in all figures. Statistical analyses were conducted with the GraphPad Prism9 software. The data presented here come from at least three independent experiments. For p values, not significant $p > 0.05$; * $p < 0.05$; ** $p < 0.01$; *** $p < 0.001$; **** $p < 0.0001$.

Acknowledgements

We are grateful to all the staff members of the Imaging Center of the IGBMC, especially Elvire Guiot, Erwan Grandgirard and Bertrand Vernay for assistance in confocal microscopy. We thank Christelle Gally, Basile Jacquiel and Eric Marois for helpful discussions and critical reading of the manuscript, and Sandra Bour for assistance with figure design. We are indebted to the Reymann, Vermot and Jarriault labs for sharing their equipments and reagents. We thank the Horvitz lab, especially Na An, for providing the MT GCaMP strains. We thank WormBase and the *Caenorhabditis* Genetics Center (funded by NIH Office of Research Infrastructure Programs P40 OD010440, University of Minnesota) for providing strains.

Funding

This work was funded by the grant ANR-10-LABX-0030-INRT, a French State fund managed by the Agence Nationale de la Recherche under the frame program Investissements d'Avenir ANR-10-IDEX- 0002-02.

Author contributions

S.Q. designed and conducted the experiments, analyzed data and wrote the manuscript; T.A. designed and printed the microfluidic chip; T. Y. contributed to ChIP seq data analyses; G.C. developed the Matlab pipeline for data analyses.

Conflict of interest

The authors declare no competing interest.

References

- Back, P., De Vos, W.H., Depuydt, G.G., Matthijssens, F., Vanfleteren, J.R., and Braeckman, B.P. (2012). Exploring real-time in vivo redox biology of developing and aging *Caenorhabditis elegans*. *Free Radic. Biol. Med.* 52, 850–859.
- Barata, A.G., and Dick, T.P. (2020). A role for peroxiredoxins in H₂O₂- and MEKK-dependent activation of the p38 signaling pathway. *Redox Biol* 28, 101340.
- Bhatla, N., and Horvitz, H.R. (2015). Light and hydrogen peroxide inhibit *C. elegans* Feeding through gustatory receptor orthologs and pharyngeal neurons. *Neuron* 85, 804–818.
- Bhatla, N., Droste, R., Sando, S.R., Huang, A., and Horvitz, H.R. (2015). Distinct Neural Circuits Control Rhythm Inhibition and Spitting by the Myogenic Pharynx of *C. elegans*. *Curr. Biol.* 25, 2075–2089.
- Blackwell, T.K., Steinbaugh, M.J., Hourihan, J.M., Ewald, C.Y., and Isik, M. (2015). SKN-1/Nrf, stress responses, and aging in *Caenorhabditis elegans*. *Free Radic. Biol. Med.* 88, 290–301.
- Bodvard, K., Peeters, K., Roger, F., Romanov, N., Igbaria, A., Welkenhuysen, N., Palais, G., Reiter, W., Toledano, M.B., Käll, M., et al. (2017). Light-sensing via hydrogen peroxide and a peroxiredoxin. *Nat. Commun.* 8, 14791.
- Breker, M., Gymrek, M., and Schuldiner, M. (2013). A novel single-cell screening platform reveals proteome plasticity during yeast stress responses. *J. Cell Biol.* 200, 839–850.
- Brenner, S. (1974). The genetics of *Caenorhabditis elegans*. *Genetics* 77, 71–94.
- Cao, J., Packer, J.S., Ramani, V., Cusanovich, D.A., Huynh, C., Daza, R., Qiu, X., Lee, C., Furlan, S.N., Steemers, F.J., et al. (2017). Comprehensive single-cell transcriptional profiling of a multicellular organism. *Science* 357, 661–667.
- Chae, H.Z., Kim, H.J., Kang, S.W., and Rhee, S.G. (1999). Characterization of three isoforms of mammalian peroxiredoxin that reduce peroxides in the presence of thioredoxin. *Diabetes Res. Clin. Pract.* 45, 101–112.
- Charest, J., Daniele, T., Wang, J., Bykov, A., Mandlbauer, A., Asparuhova, M., Röhsner, J., Gutiérrez-Pérez, P., and Cochella, L. (2020). Combinatorial Action of Temporally Segregated Transcription Factors. *Dev. Cell* 55, 483–499.e7.
- Cobb, C.A., and Cole, M.P. (2015). Oxidative and nitrative stress in neurodegeneration. *Neurobiol. Dis.* 84, 4–21.
- Colbert, H.A., Smith, T.L., and Bargmann, C.I. (1997). OSM-9, a novel protein with structural similarity to channels, is required for olfaction, mechanosensation, and olfactory adaptation in *Caenorhabditis elegans*. *Journal of Neuroscience*.
- Davalli, P., Mitic, T., Caporali, A., Lauriola, A., and D’Arca, D. (2016). ROS, Cell Senescence, and Novel Molecular Mechanisms in Aging and Age-Related Diseases. *Oxid. Med. Cell. Longev.* 2016, 3565127.

- Dickinson, D.J., Ward, J.D., Reiner, D.J., and Goldstein, B. (2013). Engineering the *Caenorhabditis elegans* genome using Cas9-triggered homologous recombination. *Nat. Methods*.
- Ding, C., Fan, X., and Wu, G. (2017). Peroxiredoxin 1 - an antioxidant enzyme in cancer. *Journal of Cellular and Molecular Medicine* 21, 193–202.
- Flohé, L. (2016). The impact of thiol peroxidases on redox regulation. *Free Radic. Res.* 50, 126–142.
- Gomes, L.C., Odedra, D., Dikic, I., and Pohl, C. (2016). Autophagy and modular restructuring of metabolism control germline tumor differentiation and proliferation in *C. elegans*. *Autophagy* 12, 529–546.
- Gong, J., Yuan, Y., Ward, A., Kang, L., Zhang, B., Wu, Z., Peng, J., Feng, Z., Liu, J., and Xu, X.Z.S. (2017). The *C. elegans* Taste Receptor Homolog LITE-1 Is a Photoreceptor. *Cell* 168, 325.
- Goodman, M.B., and Sengupta, P. (2019). How *Caenorhabditis elegans* Senses Mechanical Stress, Temperature, and Other Physical Stimuli. *Genetics* 212, 25–51.
- Goulev, Y., Morlot, S., Matifas, A., Huang, B., Molin, M., Toledano, M.B., and Charvin, G. (2017). Nonlinear feedback drives homeostatic plasticity in H₂O₂ stress response. *Elife* 6.
- Gourgou, E., and Chronis, N. (2016). Chemically induced oxidative stress affects ASH neuronal function and behavior in *C. elegans*. *Sci. Rep.* 6, 38147.
- Groitel, B., and Jakob, U. (2014). Thiol-based redox switches. *Biochim. Biophys. Acta* 1844, 1335–1343.
- Haes, W.D., De Haes, W., Frooninckx, L., Van Assche, R., Smolders, A., Depuydt, G., Billen, J., Braeckman, B.P., Schoofs, L., and Temmerman, L. (2014). Metformin promotes lifespan through mitohormesis via the peroxiredoxin PRDX-2. *Proceedings of the National Academy of Sciences* 111, E2501–E2509.
- Hall, A., Karplus, P.A., and Poole, L.B. (2009). Typical 2-Cys peroxiredoxins--structures, mechanisms and functions. *FEBS J.* 276, 2469–2477.
- Hilliard, M.A., Bargmann, C.I., and Bazzicalupo, P. (2002). *C. elegans* responds to chemical repellents by integrating sensory inputs from the head and the tail. *Curr. Biol.* 12, 730–734.
- Hirani, N., Westenberg, M., Gami, M.S., Davis, P., Hope, I.A., and Dolphin, C.T. (2013). A simplified counter-selection recombineering protocol for creating fluorescent protein reporter constructs directly from *C. elegans* fosmid genomic clones. *BMC Biotechnol.* 13, 1.
- Ho, B., Baryshnikova, A., and Brown, G.W. (2018). Unification of Protein Abundance Datasets Yields a Quantitative *Saccharomyces cerevisiae* Proteome. *Cell Syst* 6, 192-205.e3.
- Isermann, K., Liebau, E., Roeder, T., and Bruchhaus, I. (2004). A peroxiredoxin specifically expressed in two types of pharyngeal neurons is required for normal growth and egg production in *Caenorhabditis elegans*. *J. Mol. Biol.* 338, 745–755.

Jang, H.H., Lee, K.O., Chi, Y.H., Jung, B.G., Park, S.K., Park, J.H., Lee, J.R., Lee, S.S., Moon, J.C., Yun, J.W., et al. (2004). Two Enzymes in One. *Cell* **117**, 625–635.

Jarvis, R.M., Hughes, S.M., and Ledgerwood, E.C. (2012). Peroxiredoxin 1 functions as a signal peroxidase to receive, transduce, and transmit peroxide signals in mammalian cells. *Free Radic. Biol. Med.* **53**, 1522–1530.

Jose, A.M., Bany, I.A., Chase, D.L., and Koelle, M.R. (2007). A specific subset of transient receptor potential vanilloid-type channel subunits in *Caenorhabditis elegans* endocrine cells function as mixed heteromers to promote neurotransmitter release. *Genetics* **175**, 93–105.

Kamath, R.S., Fraser, A.G., Dong, Y., Poulin, G., Durbin, R., Gotta, M., Kanapin, A., Le Bot, N., Moreno, S., Sohrmann, M., et al. (2003). Systematic functional analysis of the *Caenorhabditis elegans* genome using RNAi. *Nature* **421**, 231–237.

Kim, K., and Li, C. (2004). Expression and regulation of an FMRFamide-related neuropeptide gene family in *Caenorhabditis elegans*. *J. Comp. Neurol.* **475**, 540–550.

Kopito, R.B., and Levine, E. (2014). Durable spatiotemporal surveillance of *Caenorhabditis elegans* response to environmental cues. *Lab Chip* **14**, 764–770.

Kuramochi, M., and Doi, M. (2019). An Excitatory/Inhibitory Switch From Asymmetric Sensory Neurons Defines Postsynaptic Tuning for a Rapid Response to NaCl in *Caenorhabditis elegans*. *Frontiers in Molecular Neuroscience* **11**.

Ledgerwood, E.C., Marshall, J.W.A., and Weijman, J.F. (2017). The role of peroxiredoxin 1 in redox sensing and transducing. *Arch. Biochem. Biophys.* **617**, 60–67.

Lee, J., Godon, C., Lagniel, G., Spector, D., Garin, J., Labarre, J., and Toledano, M.B. (1999). Yap1 and Skn7 control two specialized oxidative stress response regulons in yeast. *J. Biol. Chem.* **274**, 16040–16046.

Li, G., Gong, J., Lei, H., Liu, J., and Shawn Xu, X.Z. (2016). Promotion of behavior and neuronal function by reactive oxygen species in *C. elegans*. *Nature Communications* **7**.

Liu, J., Ward, A., Gao, J., Dong, Y., Nishio, N., Inada, H., Kang, L., Yu, Y., Ma, D., Xu, T., et al. (2010). *C. elegans* phototransduction requires a G protein-dependent cGMP pathway and a taste receptor homolog. *Nature Neuroscience* **13**, 715–722.

Lorenzo, R., Onizuka, M., Defrance, M., and Laurent, P. (2020). Combining single-cell RNA-sequencing with a molecular atlas unveils new markers for *Caenorhabditis elegans* neuron classes. *Nucleic Acids Res.* **48**, 7119–7134.

Low, F.M., Hampton, M.B., Peskin, A.V., and Winterbourn, C.C. (2007). Peroxiredoxin 2 functions as a noncatalytic scavenger of low-level hydrogen peroxide in the erythrocyte. *Blood* **109**, 2611–2617.

McCallum, K.C., Liu, B., Fierro-González, J.C., Swoboda, P., Arur, S., Miranda-Vizueté, A., and Garsin, D.A. (2016). TRX-1 Regulates SKN-1 Nuclear Localization Cell Non-autonomously in *Caenorhabditis elegans*. *Genetics* **203**, 387–402.

- Miranda-Vizueté, A., González, J.C.F., Gahmon, G., Burghoorn, J., Navas, P., and Swoboda, P. (2006). Lifespan decrease in a *Caenorhabditis elegans* mutant lacking TRX-1, a thioredoxin expressed in ASJ sensory neurons. *FEBS Letters* 580, 484–490.
- Mizuno, T., Hisamoto, N., Terada, T., Kondo, T., Adachi, M., Nishida, E., Kim, D.H., Ausubel, F.M., and Matsumoto, K. (2004). The *Caenorhabditis elegans* MAPK phosphatase VHP-1 mediates a novel JNK-like signaling pathway in stress response. *EMBO J.* 23, 2226–2234.
- Moon, J.C., Hah, Y.S., Kim, W.Y., Jung, B.G., and Jang, H.H. (2005). Oxidative stress-dependent structural and functional switching of a human 2-Cys peroxiredoxin isotype II that enhances HeLa cell resistance to H₂O₂-induced cell *Journal of Biological*.
- Netto, L.E.S., and Antunes, F. (2016). The Roles of Peroxiredoxin and Thioredoxin in Hydrogen Peroxide Sensing and in Signal Transduction. *Mol. Cells* 39, 65–71.
- Niu, W., Lu, Z.J., Zhong, M., Sarov, M., Murray, J.I., Brdlik, C.M., Janette, J., Chen, C., Alves, P., Preston, E., et al. (2011). Diverse transcription factor binding features revealed by genome-wide ChIP-seq in *C. elegans*. *Genome Res.* 21, 245–254.
- Ohnishi, K., Saito, S., Miura, T., Ohta, A., Tominaga, M., Sokabe, T., and Kuhara, A. (2020). OSM-9 and OCR-2 TRPV channels are accessory warm receptors in *Caenorhabditis elegans* temperature acclimatisation. *Sci. Rep.* 10, 18566.
- Oláhová, M., Taylor, S.R., Khazaipoul, S., Wang, J., Morgan, B.A., Matsumoto, K., Blackwell, T.K., and Veal, E.A. (2008). A redox-sensitive peroxiredoxin that is important for longevity has tissue- and stress-specific roles in stress resistance. *Proc. Natl. Acad. Sci. U. S. A.* 105, 19839–19844.
- Park, M.H., Jo, M., Kim, Y.R., Lee, C.-K., and Hong, J.T. (2016). Roles of peroxiredoxins in cancer, neurodegenerative diseases and inflammatory diseases. *Pharmacology & Therapeutics* 163, 1–23.
- Randall, L.M., Ferrer-Sueta, G., and Denicola, A. (2013). Peroxiredoxins as preferential targets in H₂O₂-induced signaling. *Methods Enzymol.* 527, 41–63.
- Rangaraju, S., Solis, G.M., Andersson, S.I., Gomez-Amaro, R.L., Kardakaris, R., Broaddus, C.D., Niculescu, A.B., 3rd, and Petrascheck, M. (2015). Atypical antidepressants extend lifespan of *Caenorhabditis elegans* by activation of a non-cell-autonomous stress response. *Aging Cell* 14, 971–981.
- Rhee, S.G., and Woo, H.A. (2011). Multiple Functions of Peroxiredoxins: Peroxidases, Sensors and Regulators of the Intracellular Messenger H₂O₂, and Protein Chaperones. *Antioxid. Redox Signal.* 15, 781–794.
- Sanzo-Machuca, Á., Monje Moreno, J.M., Casado-Navarro, R., Karakuzu, O., Guerrero-Gómez, D., Fierro-González, J.C., Swoboda, P., Muñoz, M.J., Garsin, D.A., Pedrajas, J.R., et al. (2019). Redox-dependent and redox-independent functions of *Caenorhabditis elegans* thioredoxin 1. *Redox Biol* 24, 101178.

- Schwartz, M.L., and Jorgensen, E.M. (2016). SapTrap, a Toolkit for High-Throughput CRISPR/Cas9 Gene Modification in *Caenorhabditis elegans*. *Genetics* 202, 1277–1288.
- Stöcker, S., Maurer, M., Ruppert, T., and Dick, T.P. (2018). A role for 2-Cys peroxiredoxins in facilitating cytosolic protein thiol oxidation. *Nat. Chem. Biol.* 14, 148–155.
- Tang, L., Dodd, W., and Choe, K. (2016). Isolation of a Hypomorphic *skn-1* Allele That Does Not Require a Balancer for Maintenance. *G3 Genes|Genomes|Genetics* 6, 551–558.
- Thamsen, M., Kumsta, C., Li, F., and Jakob, U. (2011). Is Overoxidation of Peroxiredoxin Physiologically Significant? *Antioxidants & Redox Signaling* 14, 725–730.
- Tian, L., Hires, S.A., Mao, T., Huber, D., Chiappe, M.E., Chalasani, S.H., Petreanu, L., Akerboom, J., McKinney, S.A., Schreiter, E.R., et al. (2009). Imaging neural activity in worms, flies and mice with improved GCaMP calcium indicators. *Nat. Methods* 6, 875–881.
- Veal, E.A., Day, A.M., and Morgan, B.A. (2007). Hydrogen peroxide sensing and signaling. *Mol. Cell* 26, 1–14.
- Ward, A., Liu, J., Feng, Z., and Shawn Xu, X.Z. (2008). Light-sensitive neurons and channels mediate phototaxis in *C. elegans*. *Nature Neuroscience* 11, 916–922.
- Winterbourn, C.C., and Peskin, A.V. (2016). Kinetic Approaches to Measuring Peroxiredoxin Reactivity. *Mol. Cells* 39, 26–30.
- Wu, F., Chi, Y., Jiang, Z., Xu, Y., Xie, L., Huang, F., Wan, D., Ni, J., Yuan, F., Wu, X., et al. (2020). Hydrogen peroxide sensor HPCA1 is an LRR receptor kinase in *Arabidopsis*. *Nature* 578, 577–581.
- Yan, Y., Sabharwal, P., Rao, M., and Sockanathan, S. (2009). The antioxidant enzyme Prdx1 controls neuronal differentiation by thiol-redox-dependent activation of GDE2. *Cell* 138, 1209–1221.
- Yemini, E., Lin, A., Nejatbakhsh, A., Varol, E., Sun, R., Mena, G.E., Samuel, A.D.T., Paninski, L., Venkatachalam, V., and Hobert, O. (2021). NeuroPAL: A Multicolor Atlas for Whole-Brain Neuronal Identification in *C. elegans*. *Cell* 184, 272–288.e11.
- Zhang, W., He, F., Ronan, E.A., Liu, H., Gong, J., Liu, J., and Xu, X.Z.S. (2020). Regulation of photosensation by hydrogen peroxide and antioxidants in *C. elegans*. *PLoS Genet.* 16, e1009257.
- Zou, W., Cheng, H., Li, S., Yue, X., Xue, Y., Chen, S., and Kang, L. (2017). Polymodal Responses in *C. elegans* Phasmid Neurons Rely on Multiple Intracellular and Intercellular Signaling Pathways. *Sci. Rep.* 7, 42295.

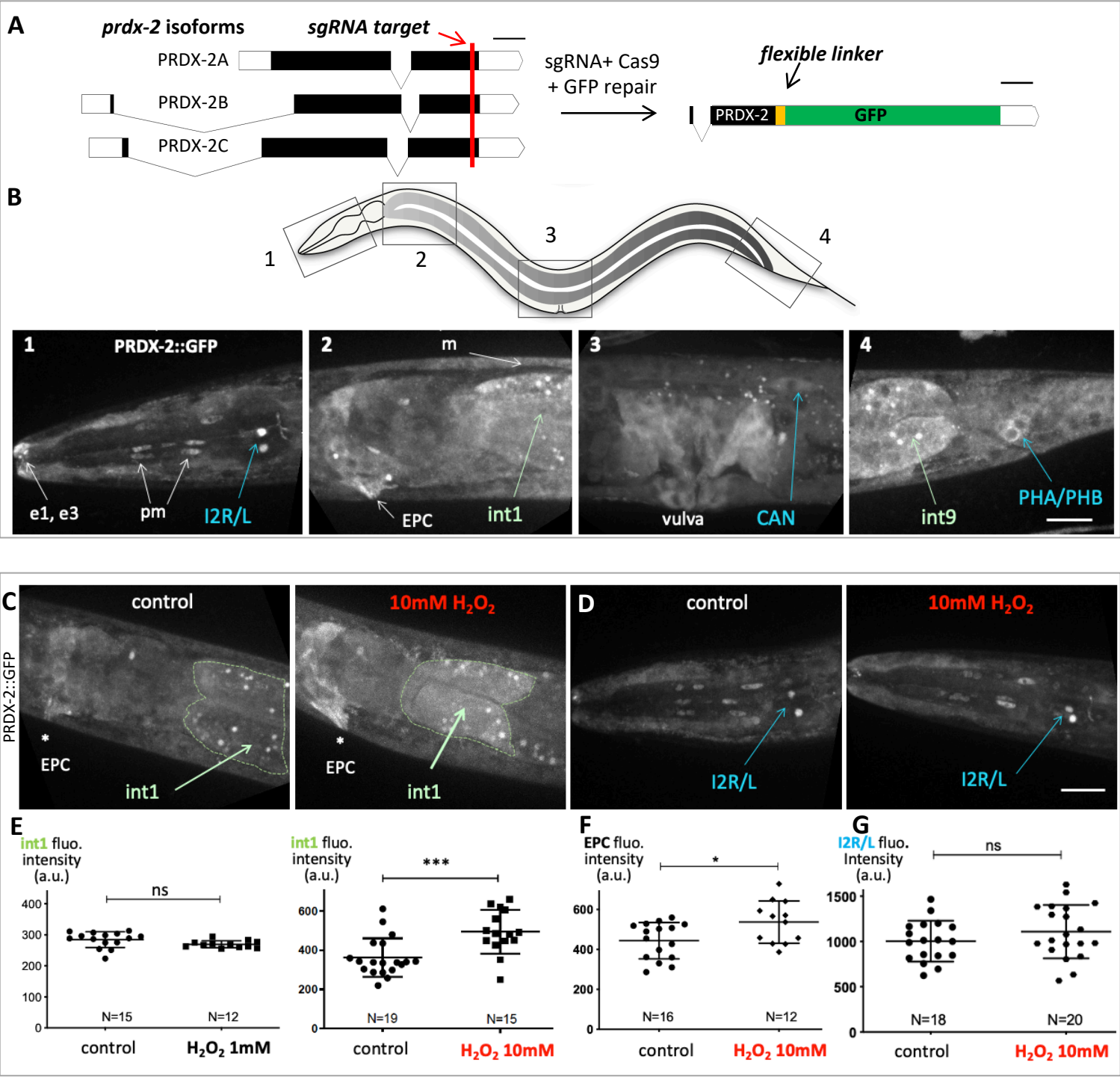


Figure 1

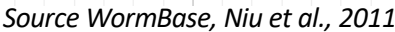


Figure 2

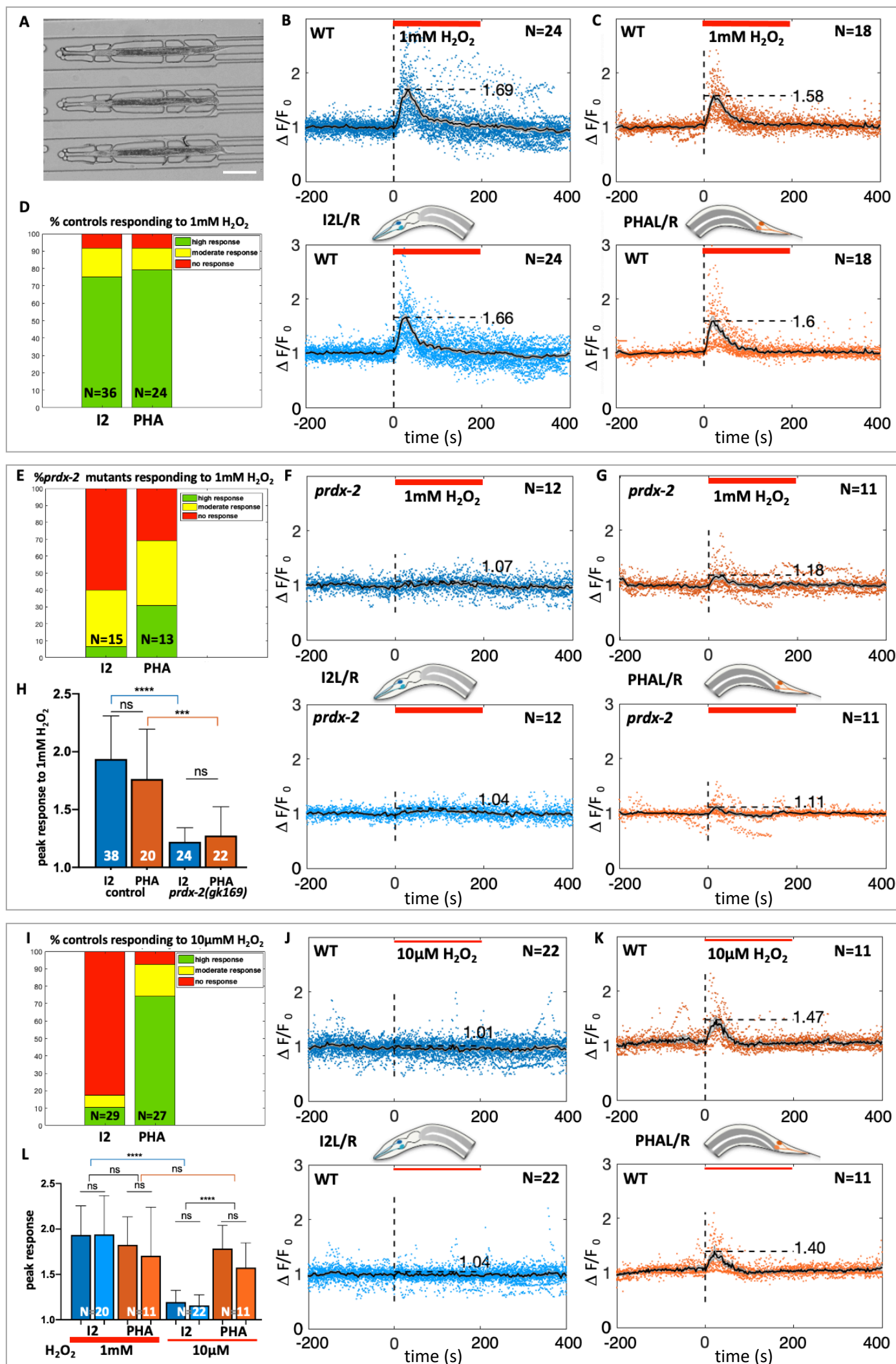


Figure 3

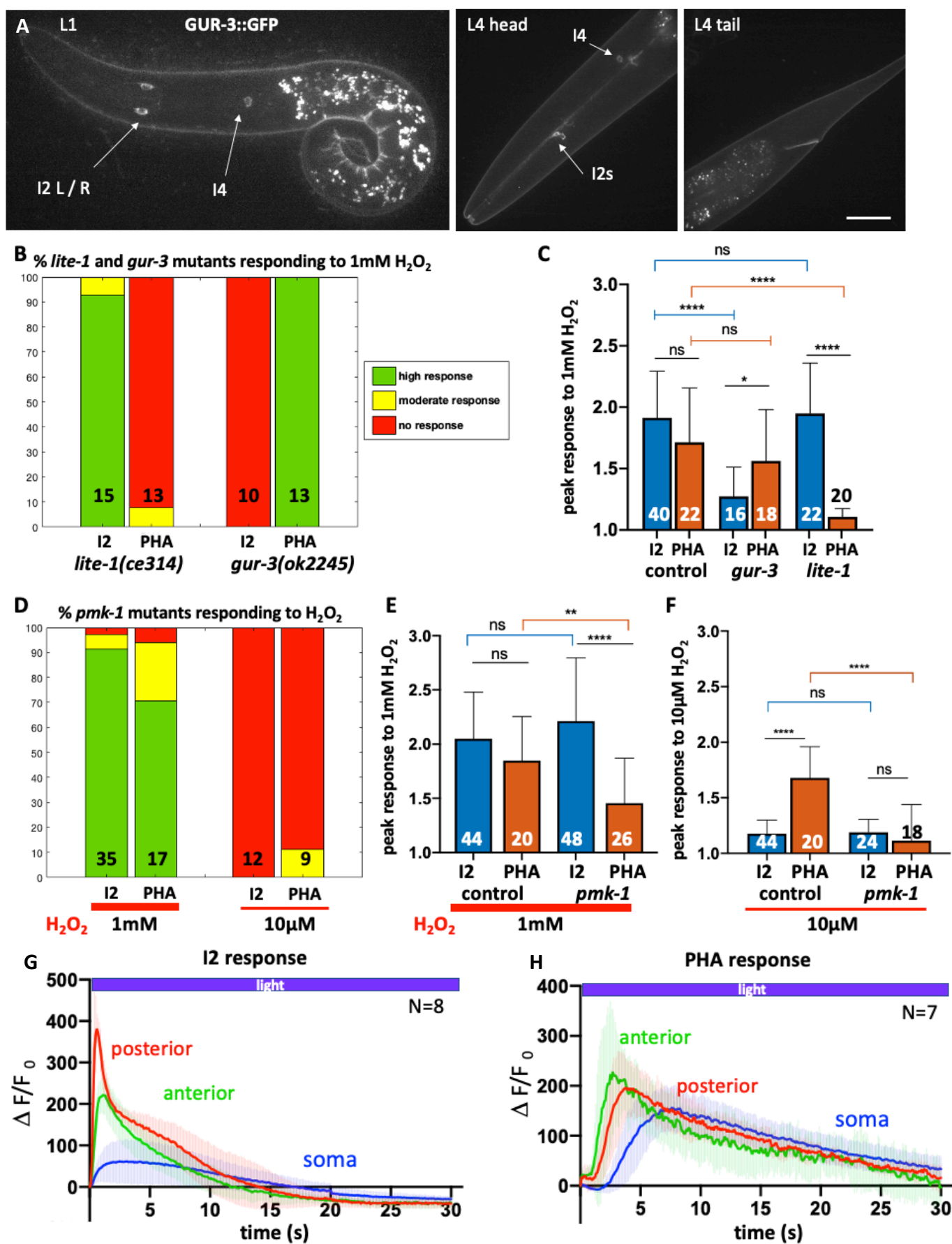


Figure 4

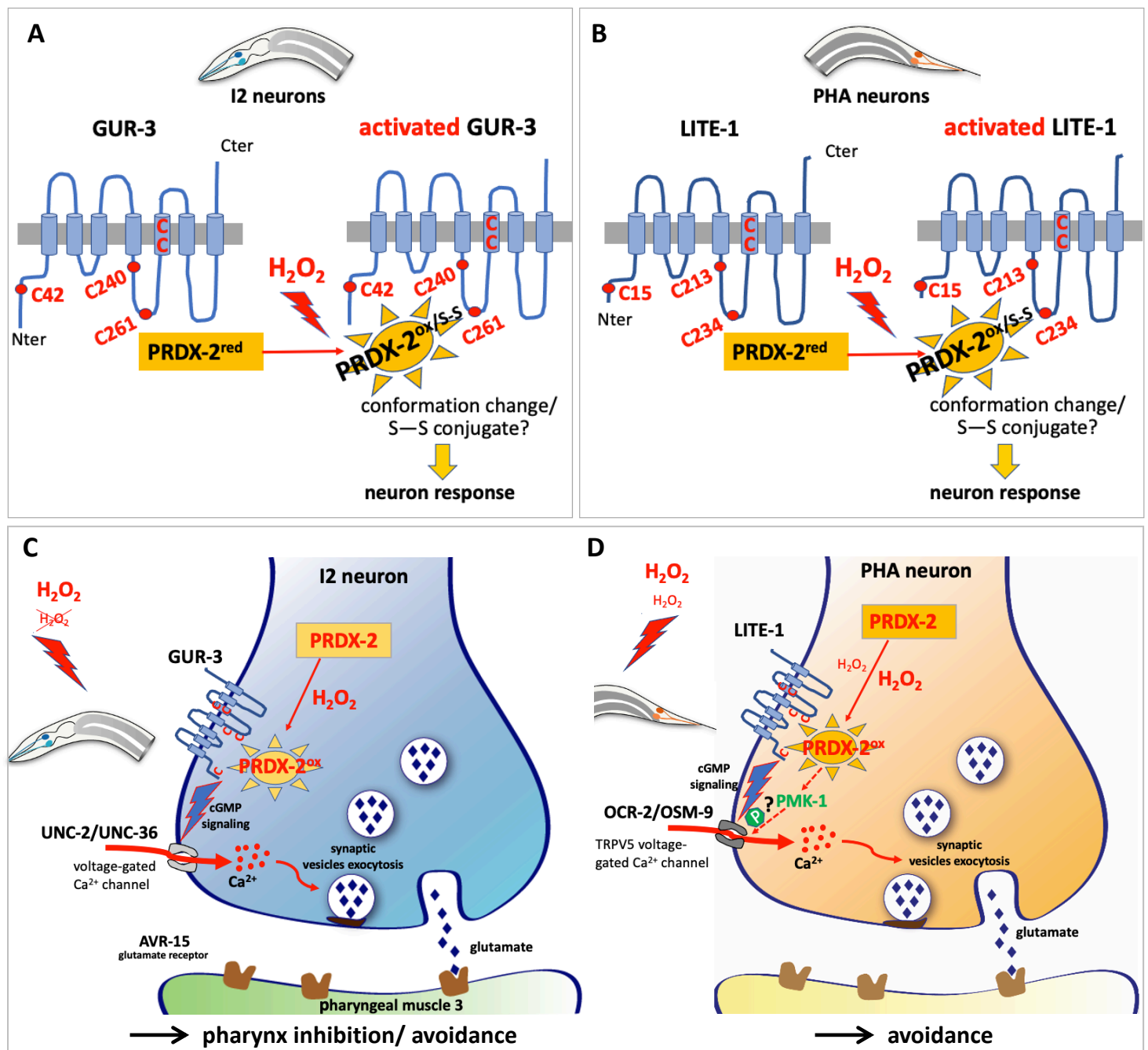


Figure Legends

Figure 1- PRDX-2::GFP knock-in line expression pattern and its evolution upon H₂O₂ treatment

(A)- Sketch depicting the PRDX-2::GFP knock-in strategy using CRISPR Cas9-mediated genome editing. The sgRNA target sequence (shown in red) was chosen a few base pairs upstream PRDX-2 STOP codon, to tag all *prdx-2* isoforms. Black boxes indicate exons, white boxes untranslated regions. Bar, 100 bases pairs. The last exon of the PRDX-2::GFP fusion protein is shown on the right; note the insertion of a flexible linker between PRDX-2 and the GFP, likely allowing its correct folding. After injection, three independent knock-in lines were recovered, sharing the same expression pattern. (B) Spinning-disc confocal projections of a representative PRDX-2::GFP knock-in animal, in 4 body regions (correspondingly boxed in the worm drawing). PRDX-2::GFP expression is observed in the tip of the nose (e3 cell), in pharyngeal muscle cells (pm), in body wall muscles (m), in the excretory pore cell (EPC), in proximal and distal gut cells (int1 and int9), and in several neuron pairs, indicated in blue. Note the different level of PRDX-2 between I2 left and right neurons in panel B1. (C-G) An acute oxidative stress triggers an upregulation of PRDX-2 in the foregut, but not in neurons. (C-D) Spinning-disc confocal projections of control or H₂O₂-treated animals in the foregut (C) or in the head region (D). (E-G) Quantification of fluorescence intensity in controls and in H₂O₂-treated animals in the int1 cell (E), in the EPC (F), and I2 neurons (G). Bars indicate mean and s.d. ns, not significant, $p > 0.05$; * $p < 0.05$; *** $p < 0.001$. Scale bar, 20 μ m.

Figure 2- SKN-1 function is required for PRDX-2 expression in the gut

(A-B)- Spinning-disc confocal projections of head and foregut of PRDX-2::GFP knock-in animals, in control RNAi (A) and in *skn-1(RNAi)* animals (B). The right panel shows the foregut of a 10mM H₂O₂-treated animal in both genotypes. Note the low level of int1 PRDX-2::GFP fluorescence in *skn-1(RNAi)* animal. (C-D) Quantification of the int1 cell fluorescence intensity in control and after a 10mM H₂O₂-treatment, in *skn-1(zj15)* mutants (C) and in *skn-1(RNAi)* animals (D). Bars indicate mean and s.d. ns, not significant, $p > 0.05$; ** $p < 0.01$; *** $p < 0.001$. Scale bar, 20 μ m. (E) Genome Browser from WormBase (release WS283, JBrowse II) showing the peaks detected by ChIP-seq using an anti-GFP antibody (Niu et al., 2011) in *prdx-2* and *pkc-3* promoters, in GFP-tagged transgenic lines of the indicated transcription factors. Top numbers indicate the coordinates on chromosome II. Note the co-regulation of the *prdx-2* and *pkc-3*, which are organized in an operon, indicated by the green bar.

Figure 3- I2 and PHA neurons both respond to 1mM H₂O₂ in a *prdx-2*-dependent manner, but only PHA neurons respond to 10 μ M H₂O₂

(A)- Low-magnification DIC picture of L4 animals trapped in the microfluidic device used in neuron recordings experiments, as in (B,C,F,G,J,K), which indicate I2R/I2L responses (B,F,J) and PHAL/PHAR responses (C,G,K) to a H₂O₂ stimulation at the dose indicated below the red bar. The average curves show the normalized calcium response measured over time (indicated in seconds) using the GCaMP3 sensor expressed in I2 and PHA neurons, for left and right neurons (top and bottom curves). N, number of movies quantified for each genotype, in wild-type (B,C,J,K) and in *prdx-2* mutants (F,G). (D,E,I) Bar graph of the fraction of animals responding to the H₂O₂ stimulation in all experiments, classified as high (green), moderate (yellow) or absent (red) responses (see Methods). N, number of movies analyzed. (H,L) Quantification of the

calcium response to H_2O_2 in I2 and PHA in controls and *prdx-2* mutants at 1mM (H) and in I2LR and PHALR controls, at 1mM and 10 μM (L). The number of movies quantified is indicated on each column. Bars indicate mean and s.d. ns, not significant, $p>0.05$; *** $p<0.001$; **** $p<0.0001$. See also Movies 1-6 and sup. Fig. 5.

Figure 4- The GUR-3 receptor is required in I2 neurons while *lite-1* and *pmk-1* functions are required in PHA response to H_2O_2

(A)- Spinning-disc confocal projections of a representative GUR-3::GFP knock-in animal, at L1 (left) and L4 stages (right). GUR-3::GFP signal is detected in I2 neurons and in a single I4 neurons (head panel), but not in PHA/PHB neurons (tail panel). Bar, 10 μm . (B,D) Bar graph of the fraction of *lite-1* and *gur-3* mutants responding to the H_2O_2 stimulation, classified as high (green), moderate (yellow) or absent (red) responses. N, number of movies analyzed. (C,E,F)- Quantification of the calcium response to 1mM H_2O_2 in I2 and PHA neurons in controls and in *gur-3* and *lite-1* mutants (C), and in *pmk-1* mutants at 1mM (E) and 10 μM H_2O_2 (F). The number of movies quantified is indicated on each column. Bar, s.d.; ns, not significant, $p>0.05$; * $p<0.05$; ** $p<0.01$; **** $p<0.0001$. See also Movies 7-14 and sup. Figs. 6, 7. (G,H)- Blue light triggered different calcium fluxes in I2 and PHA neurons in the three regions analyzed; anterior neurite (green), posterior neurite (red) and soma (blue). Bars indicate s.d. See Movies 15-17.

Figure 5- Model of H_2O_2 sensing in *C. elegans* via I2 and PHA neurons based on this and previous work

(A-B)- A putative PRDX-2 redox relay may trigger H_2O_2 -induced receptor activation. Sketch of GUR-3 (A) and LITE-1 (B) gustatory receptors structure (present in I2 and PHA neurons), showing their 5 conserved cysteines in the intracellular and in the fifth transmembrane domains. In the presence of H_2O_2 , oxidized or disulfide form of PRDX-2 (PRDX-2^{ox/S-S}) could oxidize these cysteines, possibly forming a disulfide conjugate and/or inducing a conformation change which triggers receptor activation. (B)- Hypothetic model of H_2O_2 -induced neuronal activation, based on our data and on previous studies. Schematic drawing of a presynaptic button in I2 (C) and PHA (D) neurons, illustrating the presumptive H_2O_2 -PRDX-2-mediated neuronal activation in both cases. High doses of H_2O_2 (1mM) are sensed by both neurons, but only PHA responds to 10 μM H_2O_2 , as indicated in red. In this presumptive model, H_2O_2 would freely diffuse across the neuron plasma membrane and oxidize PRDX-2, presumably leading to LITE-1 or GUR-3 activation. Receptor activation is likely relayed by cGMP signaling, resulting in the opening of voltage-gated calcium channels (depicted in green) and neurotransmitter release (glutamate in both cases), triggering an adapted response. In PHA neurons, PMK-1/p38MAPK activity is additionally required to promote neuronal response to a low dose of H_2O_2 , potentially through OSM-9 phosphorylation as observed in ASH neurons (Li et al., 2016). See discussion for further details and bibliographic references.

List of supplemental information
Quintin S., Aspert T., Ye T. and Charvin G., 2021

Supplemental Figures

Supplemental Figure 1, related to Fig. 1- The available PRDX-2::GFP transgenic line (CTD1051.3) does not suit to our study.

Supplemental Figure 2, related to Figs. 1, 2- PRDX-2 induction is not observed in I2 neurons upon H₂O₂ treatment.

Supplemental Figure 3, related to Figs. 3, 4- Design of the microfluidic chip used in H₂O₂ neuronal response experiments.

Supplemental Figure 4, related to Fig. 4- *gur-3* and *lite-1* mutant show reciprocal H₂O₂ sensing phenotypes in I2 and PHA neurons.

Supplemental Figure 5, related to Fig. 3- Individual intensity measurements of movies 1-6.

Supplemental Figure 6, related to Fig. 4- Individual intensity measurements of movies 7-10.

Supplemental Figure 7, related to Fig. 4 - Individual intensity measurements of movies 11-14.

Supplemental Figure 8, related to Discussion- PHA and ASH neurons belong to the same neuronal cluster, and share partially overlapping transcriptomic signatures.

Movie list (see Movies legends p.10)

Movie 1- control I2 response to 1mM H₂O₂

Movie 2- control PHA response to 1mM H₂O₂

Movie 3- *prdx-2* mutant I2 response to 1mM H₂O₂

Movie 4- *prdx-2* mutant PHA response to 1mM H₂O₂

Movie 5- control I2 response to 10μM H₂O₂

Movie 6- control PHA response to 10μM H₂O₂

Movie 7- *gur-3* mutant I2 response to 1mM H₂O₂

Movie 8- *gur-3* mutant PHA response to 1mM H₂O₂

Movie 9- *lite-1* mutant I2 response to 1mM H₂O₂

Movie 10- *lite-1* mutant PHA response to 1mM H₂O₂

Movie 11- *pmk-1* mutant I2 response to 1mM H₂O₂

Movie 12- *pmk-1* mutant PHA response to 1mM H₂O₂

Movie 13- *pmk-1* I2 response to 10μM H₂O₂

Movie 14- *pmk-1* PHA response to 10μM H₂O₂

Movie 15- I2 response to light

Movie 16- PHA response to light

Movie 17- I2 and PHA simultaneous responses to light

Supplemental methods

I- Matlab tutorial for analysis of *C. elegans* neuronal activation using a calcium sensor

II-Analysis of single cell transcriptomic data in ASH and PHA neurons (for the generation of the dot plots in supp. Fig. 8)

Supplemental tables

Table S1- List of strains used (p. 15)

Table S2- Sequences of the oligonucleotides used (p. 15-16)

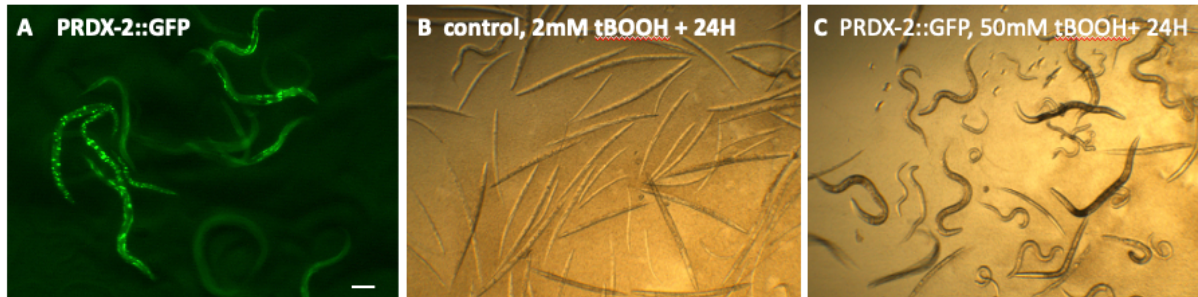
Table S3- Differential analysis of genes expressed in cluster 28 versus all neurons

Table S4- Differential analysis of genes expressed in cluster 28.0 (PHA) versus all neurons

Table S5- Differential analysis of genes expressed in cluster 28.1 (ASH) versus all neurons

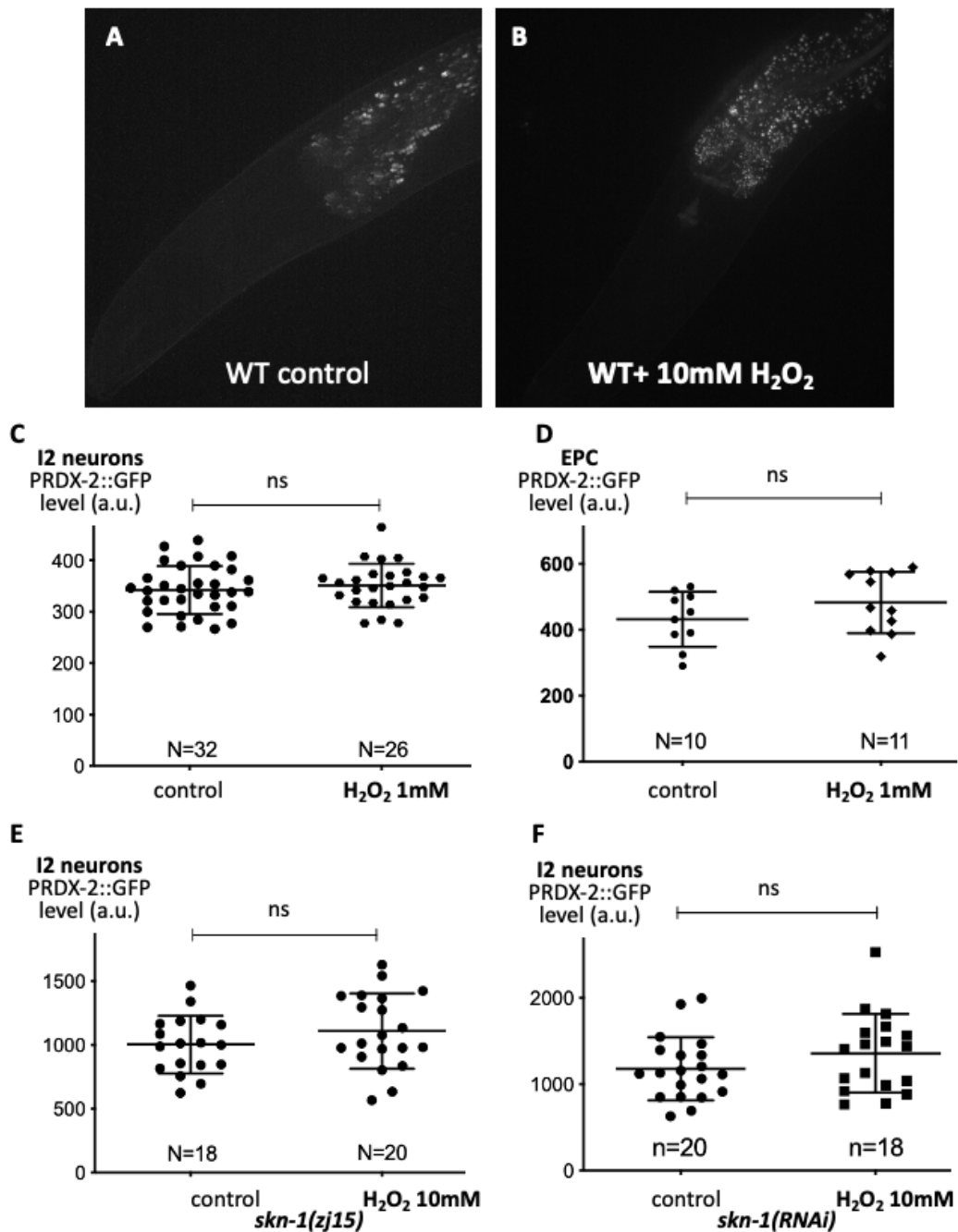
Supplemental References

Supplemental Figures



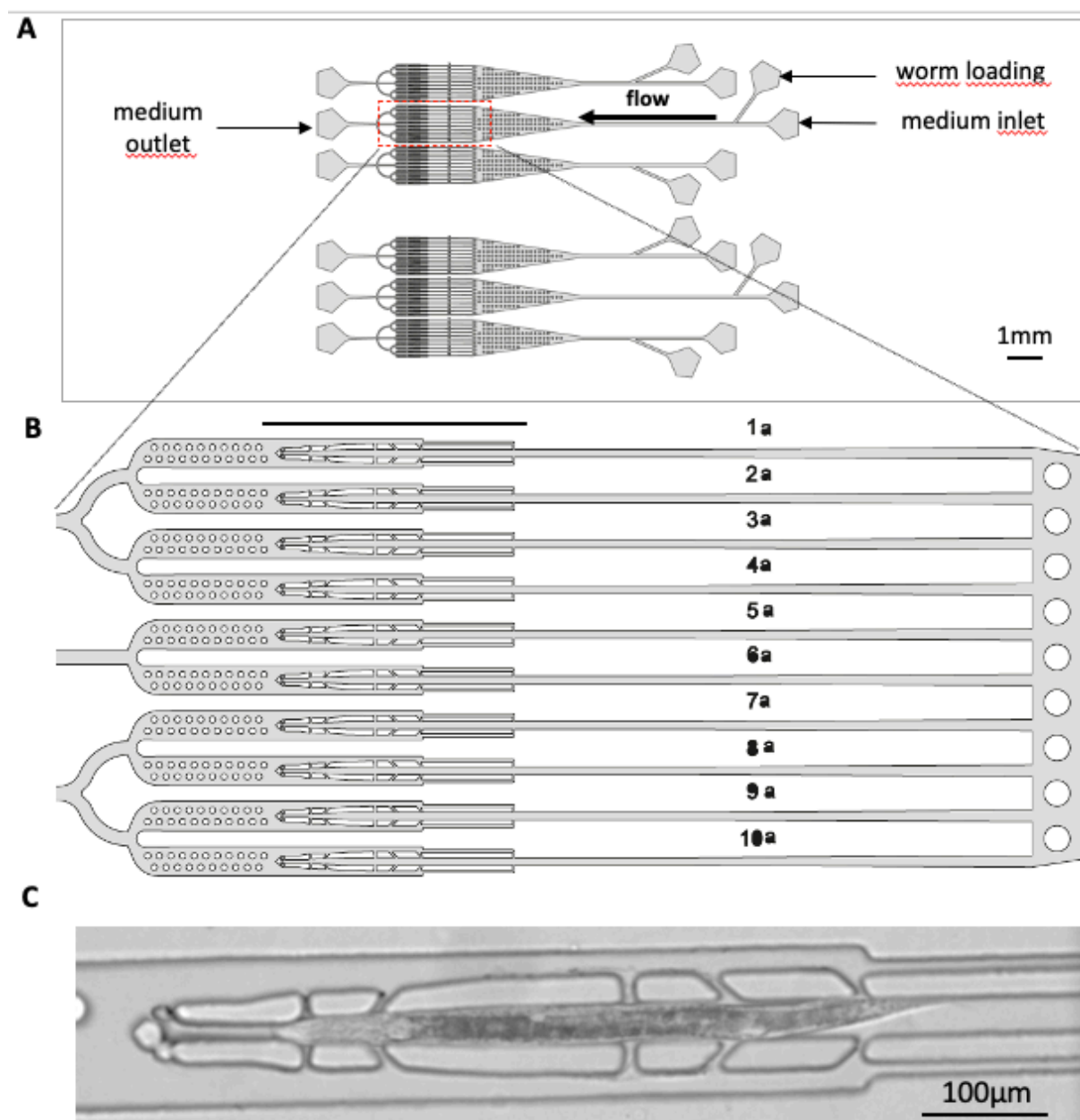
Supplemental Figure 1, related to Fig. 1- The available PRDX-2::GFP transgenic line (CTD1051.3) does not suit to our study.

(A) Low magnification fluorescent image of untreated animals from the CTD1051.3 line showing that transgenics express aggregates of PRDX-2::GFP, a hallmark of overexpression of the fusion protein. Bar, 100 μ m. (B,C) Low magnification images of animals treated in flat bottom wells captured after 24h of treatment in the oxidative stress inducing agent tBOOH. In the control well (A), almost all animals are all dead in 2mM tBOOH, appearing as rods, while CTD1051.3 transgenics survive a 25X higher dose of the drug, indicating their much stronger resistance to oxidative stress.



Supplemental Figure 2, related to Figs. 1, 2- PRDX-2 induction is not observed in I2 neurons upon H₂O₂ treatment.

(A,B)- Wild-type controls do not show a higher gut autofluorescence upon H₂O₂ treatment (N>20). (C,D)- Quantification of the PRDX-2::GFP fluorescence level in I2 neurons and in the excretory pore cell (EPC) in controls upon a 1mM-H₂O₂ treatment. (E,F)- Quantification of the PRDX-2::GFP fluorescence level in I2 neurons in *skn-1(zj15)* mutants and in *skn-1(RNAi)* animals upon a 10mM-H₂O₂ treatment. Bars indicate mean and s.d.; ns, not significant, p>0.05.

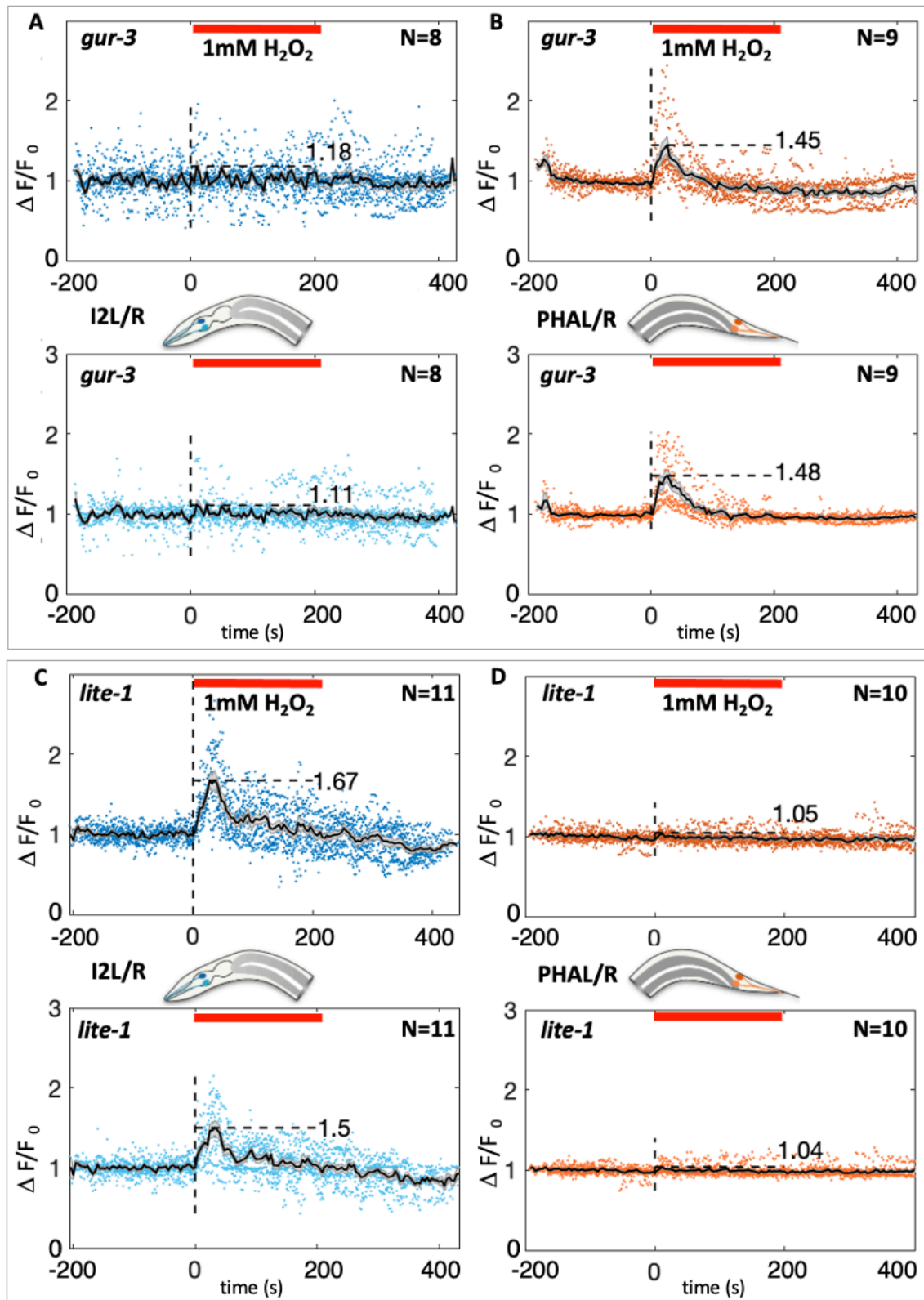


Supplemental Figure 3, related to Figs. 3, 4- Design of the microfluidic chip used in H₂O₂ neuronal response experiments.

A- Global view of the microfluidic chip used in all neuron response experiments, showing the 6 independent series of 10 worm traps. The original file (Autocad format) is available at <https://github.com/gcharvin/viewworm>.

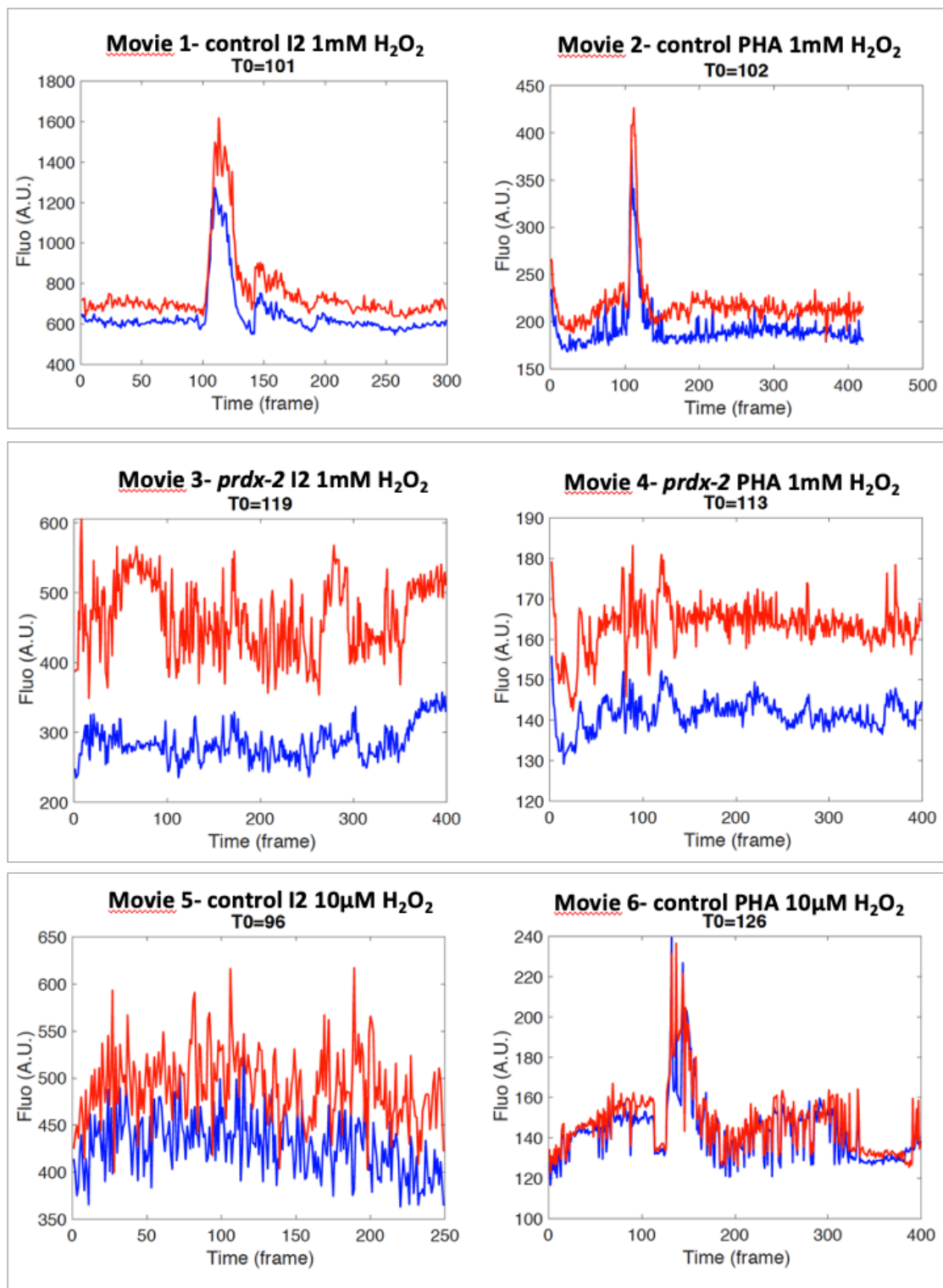
B- Magnification of the worm trap area showing the 10 individual channels (corresponding to the red box in A). Scale bar, 1mm

C- DIC image of an animal trapped (anterior to the left). Occasionally animals were trapped in the opposite orientation, but this did not affect the neuronal response. Scale bar, 100µm.



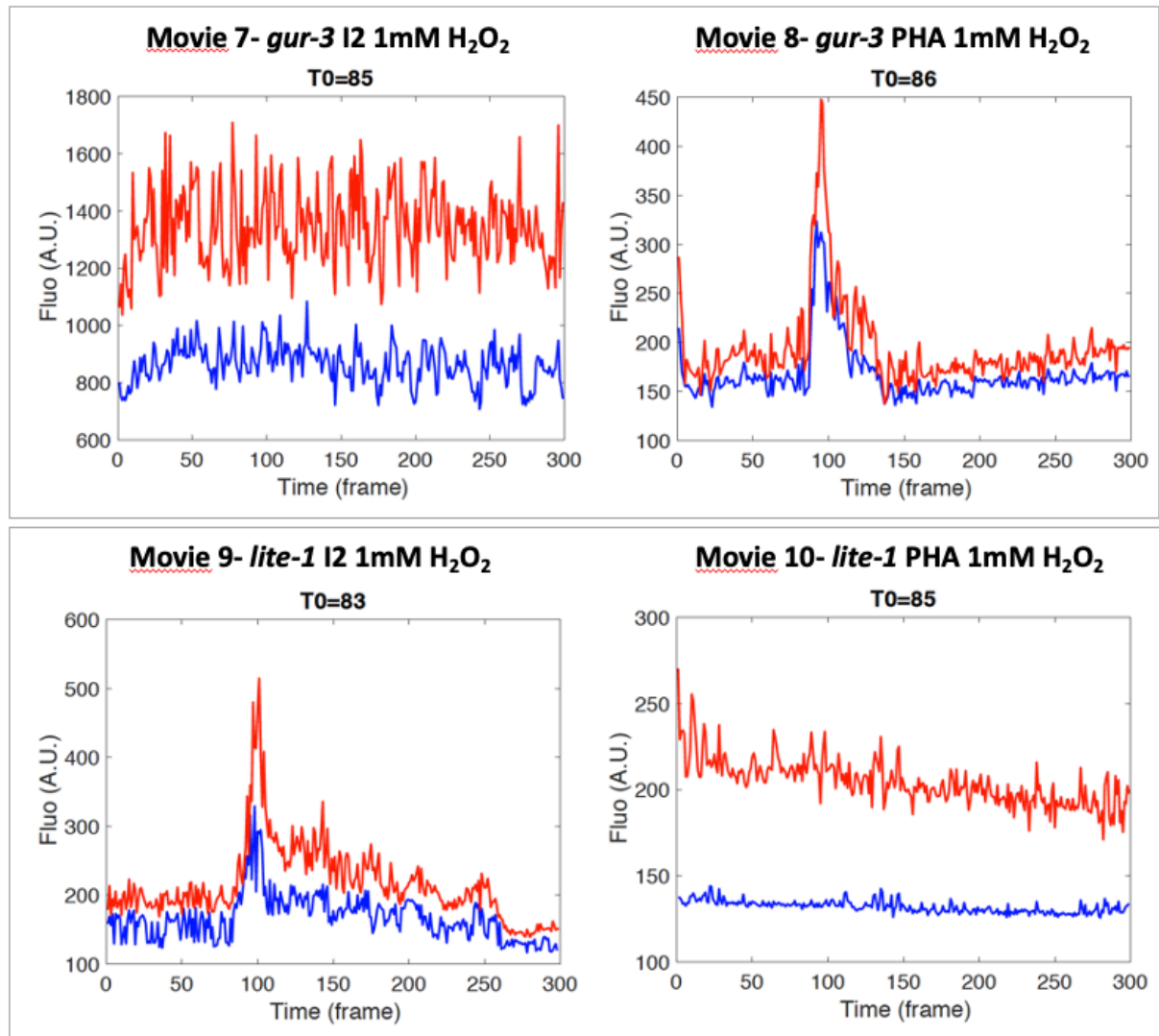
Supplemental Figure 4, related to Fig. 4- *gur-3* and *lite-1* mutants show reciprocal H₂O₂ sensing phenotypes in I2 and PHA neurons.

(A-D) Average curves showing the normalized calcium response to 1mM H₂O₂ measured over time (indicated in seconds) using the GCaMP3 sensor in I2 and PHA neurons, for left and the right neurons (top and bottom curves) in *gur-3(ok2245)* (A,B) or *lite-1(ce314)* mutants (C,D). N, number of movies analyzed for each genotype. See Movies 7-10.



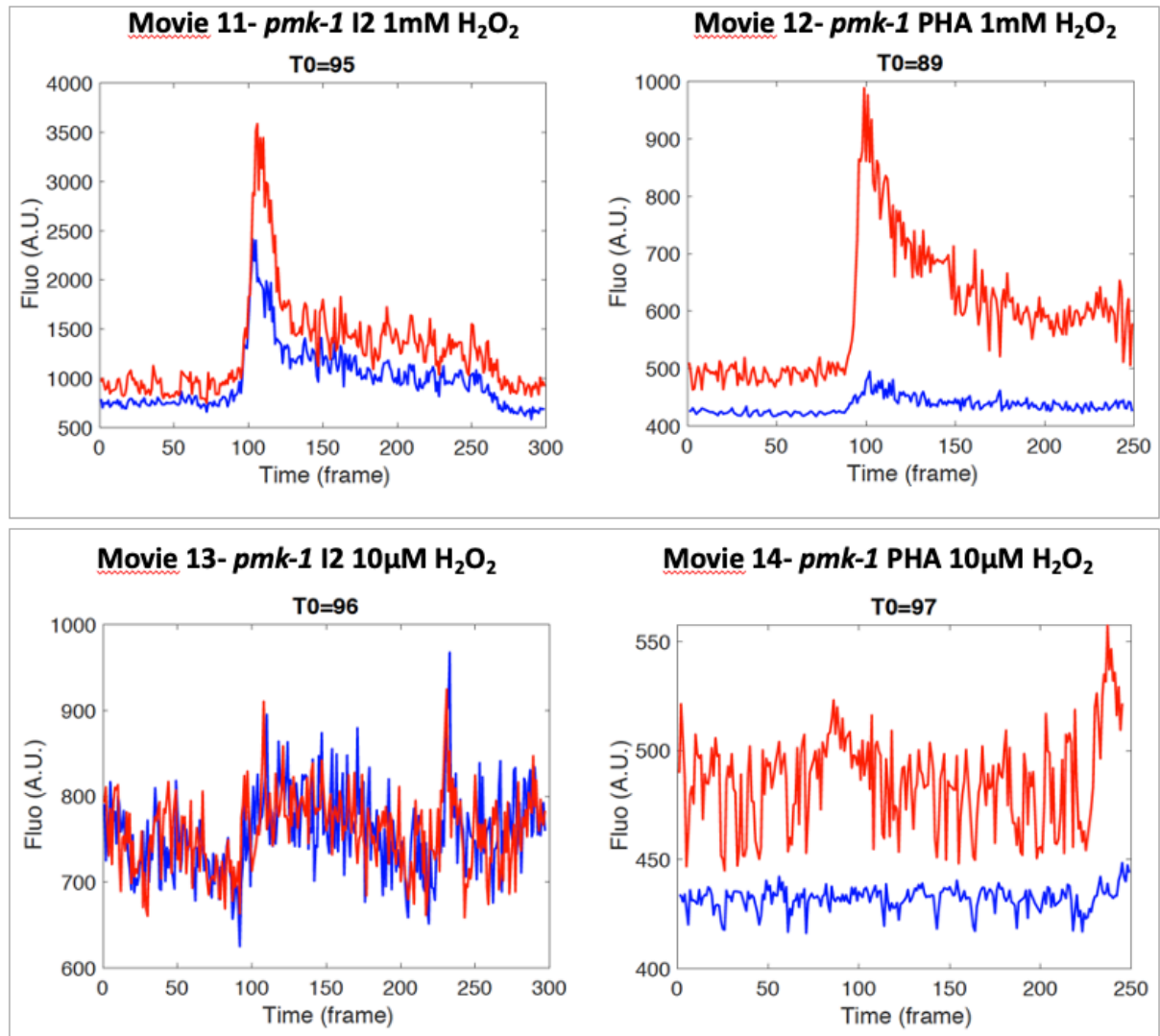
Supplemental Figure 5, related to Fig. 3- Individual intensity measurements of movies 1-6.

The curves represent the mean pixel intensity raw value over time (1 frame=2sec) quantified in I2 and PHA neurons in control and in *prdx-2* mutants (genotypes indicated) upon a 1mM or a 10 μ M H_2O_2 stimulation. Red and blue colors show left and right neurons for I2 (left panel) and PHA (right panel). Note that the colors have been changed in normalized average curves shown in Fig. 3. T_0 indicate the time point at which the H_2O_2 treatment has been applied during 100 frames.



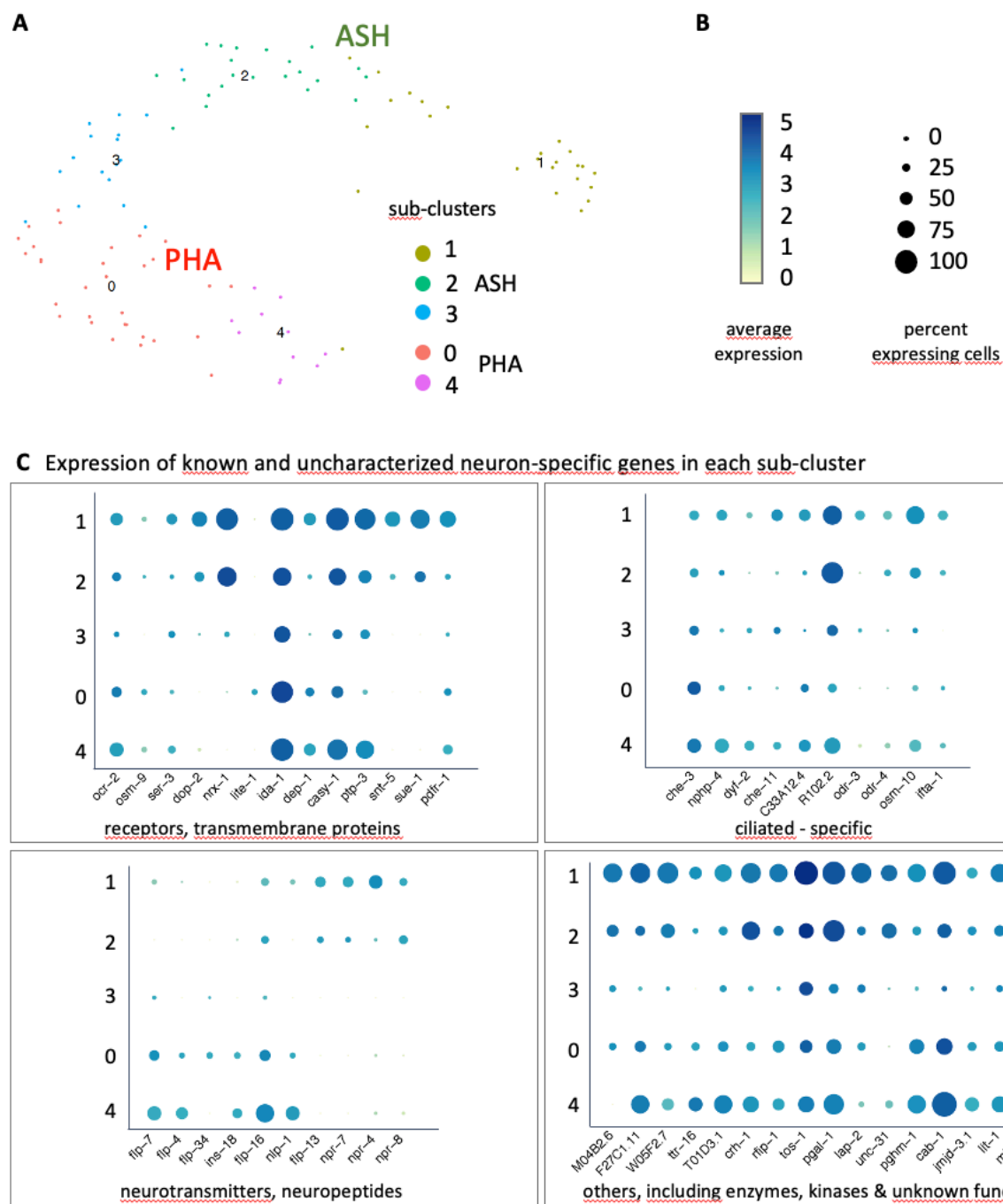
Supplemental Figure 6, related to Fig. 4 and sup. Fig. 4- Individual intensity measurements of movies 7-10.

The curves represent the mean pixel intensity raw value over time (1 frame=2sec) quantified in I2 and PHA neurons in *gur-3* and *lite-1* mutants upon a 1mM H₂O₂ stimulation (starting at T0 and lasting 100 frames). Red and blue colors show left and right neurons for I2 (left panel) and PHA (right panel). Note that the colors have been changed in related normalized average curves shown in sup. Fig. 4.



Supplemental Figure 7, related to Fig. 4, continued- Individual intensity measurements of movies 11-14.

The curves represent the mean pixel intensity raw value over time (1 frame=2sec) quantified in I2 and PHA neurons in *pmk-1* mutants upon a 1mM or a 10μM H₂O₂ stimulation (starting at T0 and lasting 100 frames). Red and blue color show left and right neuron I2 (left panel) and PHA (right panel).



Supplemental Figure 8, related to Discussion- PHA and ASH neurons belong to the same neuronal cluster, and share partially overlapping transcriptomic signatures.

(A)- Uniform Manifold Approximation and Projection (UMAP) projection of parent cluster 28, from (Lorenzo *et al.*, 2020), in which ASH and PHA/PHB nociceptive neurons were found in distinct sub-clusters (Louvain clustering at 8 PCs and at 1.2 resolution).

(B, C)- Dot plot indicating for a selection of genes both the intensity of gene expression and the fraction of expressing cells in each sub-cluster (B), based on single-cell RNA-sequencing data from (Cao *et al.*, 2017). See supplemental Methods, p. 14.

Movie Legends

- Movie 1-** control I2 response to 1mM H₂O₂
- Movie 2-** control PHA response to 1mM H₂O₂
- Movie 3-** *prdx-2* mutant I2 response to 1mM H₂O₂
- Movie 4-** *prdx-2* mutant PHA response to 1mM H₂O₂
- Movie 5-** control I2 response to 10μM H₂O₂
- Movie 6-** control PHA response to 10μM H₂O₂
- Movie 7-** *gur-3* mutant I2 response to 1mM H₂O₂
- Movie 8-** *gur-3* mutant PHA response to 1mM H₂O₂
- Movie 9-** *lite-1* mutant I2 response to 1mM H₂O₂
- Movie 10-** *lite-1* mutant PHA response to 1mM H₂O₂
- Movie 11-** *pmk-1* mutant I2 response to 1mM H₂O₂
- Movie 12-** *pmk-1* mutant PHA response to 1mM H₂O₂
- Movie 13-** *pmk-1* I2 response to 10μM H₂O₂
- Movie 14-** *pmk-1* PHA response to 10μM H₂O₂

Legend of movies 1-14 (related to Figs. 3, 4)

All movies show the neuronal responses to H₂O₂ in I2 and PHA neurons visualized using the GCaMP3 calcium sensor, in animals trapped in microfluidic chambers. All movies shown have been processed for re-alignment to facilitate response visualization (using the Matlab Readworm_PHA code), and accelerated 60 times. See Sup. Figs. 5, 6, 7 for corresponding fluorescence intensity measurements of these movies.

- Movie 15-** I2 response to light
- Movie 16-** PHA response to light
- Movie 17-** I2 and PHA simultaneous responses to light

Legend of movies 15-17 (related to Fig. 4)

Neuronal responses to blue light (485nm) in I2 and PHA neurons visualized with the GCaMP3 calcium sensor. Original movies have been colored artificially (using Fiji ‘glow’ look up table) to highlight fluorescence intensity variations. Note the different pace of response of each neuron especially in the simultaneous recording (movie 17), and the contrast between the quasi instantaneous response of the posterior neurite in I2 neurons (movies 16,17, Fig. 4G) and the strikingly long soma response in PHA (movies 16,17, Fig. 4H). Accelerated 5 times.

Supplemental Methods

I- Matlab tutorial for analysis of *C. elegans* neuronal activation using a calcium sensor

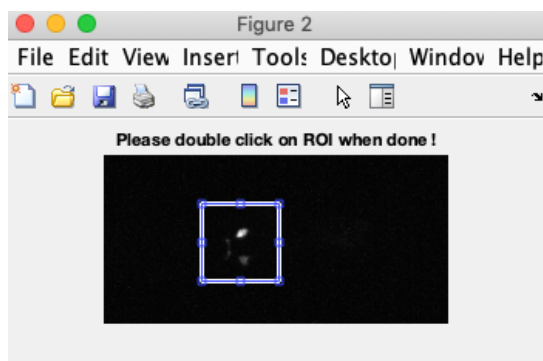
These codes have been created for tracking timelapse recordings of left and right neuronal pairs expressing a calcium sensor such as GCaMP, and available at: <https://github.com/gcharvin/viewworm>. Below are described the sequential functions to run under Matlab to perform movie quantification.

Upon acquisition, movies should be cropped as small as possible to minimize processing time and should be save as .tif files.

Note: we recommend to first make a 4D-projection of the original movie, draw the smallest ROI around the neurons and transfer it to the original movie, to ensure that all frames are properly included in the cropped selection.

1. Movie registration

—> `readworm_PHA('movie_name.tif')`



After ROI selection with the 2 neurons of interest (shown above), the function `readworm_PHA` processes every movie time point and performs the alignment of neurons, generating two files:

`movie-registered.mat`

`movie.mp4`

The mp4 allows the user to quickly verify that the movie has been correctly aligned.

Note: supplemental movies 1-14 were generated using this program.

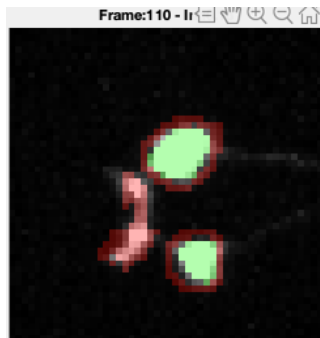
2. Neuron segmentation, selection and tracking

—> `viewworm_2('movie_name')`

The function opens a figure project with several images and buttons. The top left image allows movie traveling in the registered movie for each frame, using the right and left keyboard arrows, or typing directly the frame number in the box at the bottom of the window. To better visualize neurons, the intensity threshold of the image viewer can be adjusted with the top and bottom keyboard arrows.

Using the '**Pixel Train**' button, the user teaches the program which pixels should be selected for neuronal segmentation by painting them in green (left mouse click). The pixels

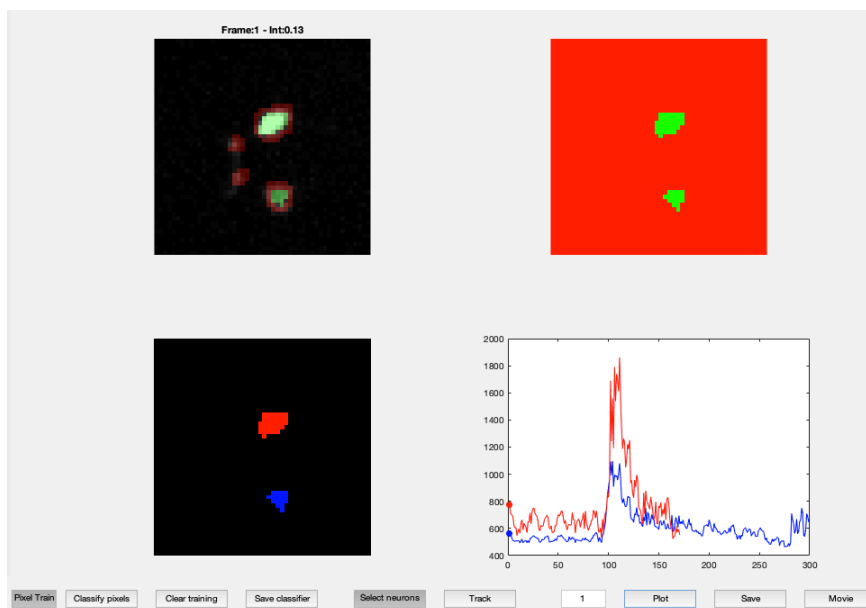
which should not be included for segmentation are painted in red (right mouse click). This needs to be done for several time points to obtain the best segmentation results, especially during the neuronal response. Below is shown an example with the selected neurons in green and the posterior neurite in red (excluded from the analysis), during the response.



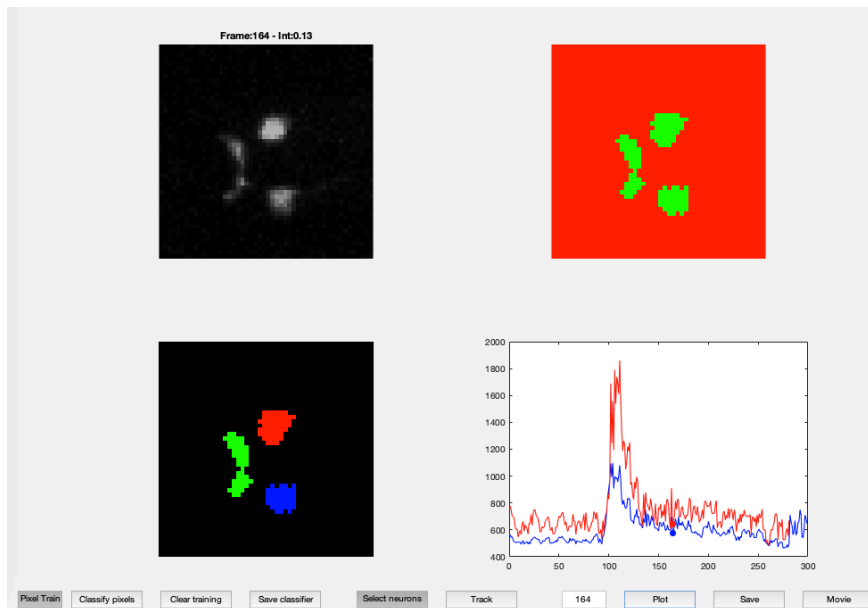
When this teaching has been done as often as needed, the user clicks '**Classify pixels**', leading to the **neuron segmentation** as defined by the user. Then the user defines each neuron in the bottom segmented image, by clicking the '**Select neurons**' button:

- right click—> red selection (left neuron);
- left click —> blue neuron (right neuron);

Upon pressing the '**Track**' button, left and right neurons will be tracked for all movie time points. Upon pressing '**Plot**', the **mean fluorescence intensity** is indicated as a function of time, generating the red and blue curves in the bottom right panel, as shown below.



Important note : this step allows the **correction of tracking errors** at every frame. The quality control is performed by the user by selecting the appropriate neuron and clicking '**Track**' again until all tracking errors are corrected. Below is shown an example of error correction at time point 164 (pixels colored in green are excluded from the quantification in the bottom left box):



When the movie is properly tracked to the end, click '**Save**' button to obtain the .fig files which will be used for subsequent analyses. The user **needs to indicate the T0** in the command window, which corresponds to the time point at which the stress/ stimulus was applied.

Finally click on '**Movie**' to generate an mp4 movie showing the registered, segmented and tracked movies altogether, allowing an assessment of the global quality of the analysis.

Once all movies have been successfully processed, create a folder containing all the individual .fig analyzed files, which will be used for processing the average curve.

3. Average curve processing

—> **averageGCamp2('folder_name')**

In the command window, assign [low, high, offset]=averageGCamp2('folder_name')

—> **processAverage('low,high,offset')**

This function will generate average curves for red and blue neurons, for raw and normalized data.

Finally to retrieve individual intensity mean values at the response peak, run the **ExportSingleWormData** function which will produce an Excel sheet with all individual peak values.

II- Analysis of single cell transcriptomic data in ASH and PHA neurons (for the generation of the dot plots in supp. Fig. 8)

Single-cell RNA-sequencing data was generated by (Cao et al. 2017). Clusters and sub-clusters were defined as described in (Lorenzo et al. 2020), using Louvain clustering at 8 PCs and at 1.2 resolution. The dataset normalization was performed using Seurat v4 (Hao et al. 2021), and visualized using dot plots. We performed differential analyses using the ‘FindMarkers’ function of Seurat v4 to compare cluster 28 versus all neurons (Table S3); cluster 28.0 (PHA) versus all neurons (Table S4); clusters 28.1 (ASH) versus all neurons (Table S5). Selected genes were chosen among the most significantly enriched from these lists.

Supplemental tables

Table S1- List of strains used

N2 wild type, reference strain

CTD1051.3 N2 *whEx127* [fNH059 (PRDX-2::GFP)+pRF4 (*rol-6(su1006)*)] (Hirani et al. 2013)

SXB01 *prdx-2(gch01[PRDX-2::GFP, unc-119(+)]* II; *unc-119(ed3)* III

SXB05 *prdx-2(gch03[PRDX-2::GFP, unc-119(+)]* II; *unc-119(ed3)* III

SXB15 5 times outcrossed SXB01 *prdx-2(gch01[PRDX-2::GFP, unc-119(+)]* II

SXB19 5 times outcrossed SXB05 *prdx-2(gch03[PRDX-2::GFP, unc-119(+)]* II

HT1593 7 times outcrossed *unc-119(ed3)* III (Dickinson et al. 2013)

QV225 *skn-1(zj15)* IV (Tang, Dodd, and Choe 2016)

SXB21 *prdx-2(gch03)* II; *skn-1(zj15)* IV

MT21650 *nIs575[flp-15prom::GCaMP3, lin-15(+)]* III; *lin-15(n765)* X (Bhatla and Horvitz 2015)

MT21570 *nIs575* III; *lite-1(ce314)* *lin-15(n765)* X (Bhatla and Horvitz 2015)

MT21785 *nIs575* III; *gur-3(ok2245)* *lin-15(n765)* X (Bhatla and Horvitz 2015)

KU25 *pmk-1(km25)* IV (Mizuno et al. 2004)

VC289 *prdx-2(gk169)* II (The *C. elegans* Deletion Mutant Consortium et al. 2012)

SXB53 *prdx-2(gk169)* II; *nIs575* III

SXB63 *unc-119(ed3)* III; *gur-3(gch16[GUR-3::GFP, unc-119(+)]* X

SXB67 *nIs575* III; *pmk-1(km25)* IV

All SXB strains were made in the course of this study.

Table S2- Sequences of the oligonucleotides used

All primers listed below are in the 5'-3' orientation.

1°) PRDX-2::GFP knock-in

Introduction of *prdx-2* sgRNA (into pMLS256):

Forward: TTGAGTGCTTCTTGAAGTACTCT

Reverse: AACAGAGTACTTCAAGAAGCACT

PCR amplification of 5' and 3' homology arms (HAs) of *prdx-2* (including a **SapI** restriction site and template-specific **overhangs**):

— 5' HA PCR product (542bp), upstream *prdx-2* stop codon:

Forward: TGTGCTCTTCTTggACCCACTTGACTTCACT

Reverse: gtgGCTCTTTCgCGCGTGCTTCTTAAAGTATTCTTGACTTTCTTTGA (with silent mutations to change the PAM sequence)

— 3' HA PCR product (570bp), starting at *prdx-2* stop codon:

Forward: actGCTCTTTCGggtTAAatgttacctcttaatttcc

Reverse: ttaGCTCTTCTtacatctccgtctctcttaattgatgt

2°) GUR-3::GFP knock-in

Introduction of *gur-3* sgRNA :

Forward: TTGtaagacaattttatTTACAC

Reverse: AACGTGTAAataaaattgtctta

PCR amplification of 5' and 3' HAs of *gur-3* (with **SapI** restriction site and template-specific overhangs):

— 5' HA (614bp), upstream *gur-3* stop codon:

Forward: tga**GCTCTTC**a**TGG**gttatcatttaaccgtgattgcatgca

Reverse: gac**GCTCTTC**t**CGC**CACAGGTGGTTGGACAATGAGCA

— 3' HA (555bp), downstream *gur-3* stop codon:

Forward: tcc**GCTCTTC****GGT**TAAataaaattgtcttaacattttcccatattga

Reverse: ttt**GCTCTTC**g**TAC**tctcgtttaacgatttctcctgtctga

Supplemental References

- Bhatla, Nikhil, and H. Robert Horvitz. 2015. "Light and Hydrogen Peroxide Inhibit C. Elegans Feeding through Gustatory Receptor Orthologs and Pharyngeal Neurons." *Neuron* 85 (4): 804–18.
- Cao, Junyue, Jonathan S. Packer, Vijay Ramani, Darren A. Cusanovich, Chau Huynh, Riza Daza, Xiaojie Qiu, et al. 2017. "Comprehensive Single-Cell Transcriptional Profiling of a Multicellular Organism." *Science* 357 (6352): 661–67.
- Consortium, The C. Elegans Deletion Mutant, and The C. elegans Deletion Mutant Consortium. 2012. "Large-Scale Screening for Targeted Knockouts in the Caenorhabditis Elegans Genome." *G3 Genes|Genomes|Genetics*. <https://doi.org/10.1534/g3.112.003830>.
- Dickinson, D. J., J. D. Ward, D. J. Reiner, and B. Goldstein. 2013. "Engineering the Caenorhabditis Elegans Genome Using Cas9-Triggered Homologous Recombination." *Nature Methods*. <https://www.nature.com/nmeth/journal/v10/n10/abs/nmeth.2641.html>.
- Hao, Yuhan, Stephanie Hao, Erica Andersen-Nissen, William M. Mauck 3rd, Shiwei Zheng, Andrew Butler, Maddie J. Lee, et al. 2021. "Integrated Analysis of Multimodal Single-Cell Data." *Cell* 184 (13): 3573–3587.e29.
- Hirani, Nisha, Marcel Westenberg, Minaxi S. Gami, Paul Davis, Ian A. Hope, and Colin T. Dolphin. 2013. "A Simplified Counter-Selection Recombineering Protocol for Creating Fluorescent Protein Reporter Constructs Directly from C. Elegans Fosmid Genomic Clones." *BMC Biotechnology* 13 (January): 1.
- Lorenzo, Ramiro, Michiho Onizuka, Matthieu Defrance, and Patrick Laurent. 2020. "Combining Single-Cell RNA-Sequencing with a Molecular Atlas Unveils New Markers for Caenorhabditis Elegans Neuron Classes." *Nucleic Acids Research* 48 (13): 7119–34.
- Mizuno, Tomoaki, Naoki Hisamoto, Takashi Terada, Tae Kondo, Makoto Adachi, Eisuke Nishida, Dennis H. Kim, Frederick M. Ausubel, and Kunihiro Matsumoto. 2004. "The Caenorhabditis Elegans MAPK Phosphatase VHP-1 Mediates a Novel JNK-like Signaling Pathway in Stress Response." *The EMBO Journal* 23 (11): 2226–34.
- Tang, Lanlan, William Dodd, and Keith Choe. 2016. "Isolation of a Hypomorphic Skn-1 Allele That Does Not Require a Balancer for Maintenance." *G3 Genes|Genomes|Genetics* 6 (3): 551–58.

Appendix 5: (Collaboration) Self-Learning Microfluidic Platform for Single-Cell Imaging and Classification in Flow

This paper is the result of a collaboration with the Knop lab (Heidelberg). In this study, I participated in the development and fabrication of a microfluidic device for 3D focusing of cells, in order to reproduce a cytometer-like microfluidic device in which the analysis is performed by a machine-learning algorithm.

(See paper next page)

Article

Self-Learning Microfluidic Platform for Single-Cell Imaging and Classification in Flow

Iordania Constantinou ^{1,2,3,†,*} , Michael Jendrusch ^{1,†} , Théo Aspert ^{4,5,6,7}, Frederik Görlitz ¹, André Schulze ¹, Gilles Charvin ^{4,5,6,7} and Michael Knop ^{1,8,*}

¹ Zentrum für Molekulare Biologie der Universität Heidelberg (ZMBH), DKFZ-ZMBH Alliance, Universität Heidelberg, 69120 Heidelberg, Germany; jendrusch@stud.uni-heidelberg.de (M.J.); f.goerlitz@gmx.net (F.G.); a.schulze@zmbh.uni-heidelberg.de (A.S.)

² Institute of Microtechnology, Technische Universität Braunschweig, 38124 Braunschweig, Germany

³ Center of Pharmaceutical Engineering (PVZ), Technische Universität Braunschweig, 38106 Braunschweig, Germany

⁴ Developmental Biology and Stem Cells Department, Institut de Génétique et de Biologie Moléculaire et Cellulaire, 67400 Illkirch-Graffenstaden, France; aspert@igbmc.fr (T.A.); charvin@igbmc.fr (G.C.)

⁵ Centre National de la Recherche Scientifique, 67400 Illkirch-Graffenstaden, France

⁶ Institut National de la Santé et de la Recherche Médicale, 67400 Illkirch-Graffenstaden, France

⁷ Université de Strasbourg, 67400 Illkirch, France

⁸ Cell Morphogenesis and Signal Transduction, German Cancer Research Center (DKFZ), DKFZ-ZMBH Alliance, 69120 Heidelberg, Germany

* Correspondence: i.constantinou@tu-braunschweig.de (I.C.); m.knop@zmbh.uni-heidelberg.de (M.K.); Tel.: +49-0531-391-9769 (I.C.); +49-6221-54-4213 (M.K.)

† These authors contributed equally to this work.

Received: 24 April 2019; Accepted: 6 May 2019; Published: 9 May 2019



Abstract: Single-cell analysis commonly requires the confinement of cell suspensions in an analysis chamber or the precise positioning of single cells in small channels. Hydrodynamic flow focusing has been broadly utilized to achieve stream confinement in microchannels for such applications. As imaging flow cytometry gains popularity, the need for imaging-compatible microfluidic devices that allow for precise confinement of single cells in small volumes becomes increasingly important. At the same time, high-throughput single-cell imaging of cell populations produces vast amounts of complex data, which gives rise to the need for versatile algorithms for image analysis. In this work, we present a microfluidics-based platform for single-cell imaging in-flow and subsequent image analysis using variational autoencoders for unsupervised characterization of cellular mixtures. We use simple and robust Y-shaped microfluidic devices and demonstrate precise 3D particle confinement towards the microscope slide for high-resolution imaging. To demonstrate applicability, we use these devices to confine heterogeneous mixtures of yeast species, brightfield-image them in-flow and demonstrate fully unsupervised, as well as few-shot classification of single-cell images with 88% accuracy.

Keywords: microfluidics; 3D flow focusing; 3D particle focusing; particle/cell imaging; bioMEMS; unsupervised learning; neural networks; variational inference

1. Introduction

Phenotypic profiling of cell populations is routinely performed in research and diagnostic laboratories using flow cytometry [1–3]. Flow cytometry provides cellular analysis at an unparalleled throughput and allows for the screening of diverse samples and the isolation of cell subpopulations for further study. Standard applications of flow cytometry employ multi-channel fluorescence detection

and sample characterization based on light scattering and fluorescence signal intensity, which provide limited spatial resolution [4]. Imaging flow cytometry combines the speed and sample size of flow cytometry with spatial resolution and allows for the acquisition of images and their use for sample characterization and sorting decisions [5]. While imaging flow cytometry gives researchers the opportunity to conduct multiparametric analysis of cell populations based on single-cell images, acquiring high-resolution images at throughputs common in flow cytometry remains challenging. This is primarily due to the difficulty of precisely positioning cells, and the challenges associated with imaging fast moving objects [6].

Recently, there has been a push towards the development of microfluidic-based flow cytometers with the aim to reduce complexity and sample volume and increase accessibility and portability [7,8]. One challenging aspect in the miniaturization of flow cytometers has been the focusing of fast-moving cells in a small, defined volume. Successful 3D hydrodynamic focusing techniques have been demonstrated over the past decade, but many rely on multi-layer structures, incompatible with polydimethylsiloxane (PDMS)-based soft-lithography [9–11]. Additionally, particles in these devices are focused to the center of tall microfluidic channels, tens, or hundreds of micrometers away from the microscope slide which is suboptimal for imaging flow cytometry [12]. For better signal-to-noise ratio, it is preferable that particles are positioned as close to the microscope slide as possible, minimizing background fluorescence. More importantly, when the specimen is located far from the surface of the cover slip the resolution obtained using high numerical aperture (NA) oil objectives is impaired. The use of such objectives is required for sensitive fluorescence detection, but resolution decreases with distance due to optical aberrations arising from a difference in refractive index between the immersion liquid (oil) and the sample (particles in aqueous solution) [13,14]. Moreover, due to the limited depth of field in conventional microscopy, particles in imaging microfluidic cytometers need to be focused in a small volume along the z-axis for high resolution imaging [15].

Microfluidic devices designed for imaging flow cytometry have been demonstrated with partial success. Devices that utilize inertial forces (i.e., inertial lift and Dean forces that arise from fluid and particle inertia) for cell positioning have been a popular alternative to sheath flow-based particle steering. The most prominent examples include curved and spiral microchannels, but successful positioning in such devices demands high flow rates that often compromise image quality [16,17]. While imaging technologies for flow cytometry have been suggested, imaging particles moving at high velocities while processing captured images in parallel still remains challenging [6]. Another popular device design used for imaging applications utilizes channel heights that are comparable in size to the particles being imaged. Such forced confinement works well for bigger cells, like blood cells, but it's prone to clogging, which makes it unsuitable for smaller cells that often tend to aggregate, such as yeast cells [18]. Recently, the first presentation of a microfluidics-based, imaging flow cytometer capable of cell sorting was demonstrated, and it is expected to lead the way for a new field to emerge in microfabrication [19]. Despite the successful demonstration, this system is complicated to set up and operation still requires trained technicians.

Another big challenge associated with high-throughput imaging flow cytometry is the vast amount of complex data collected. As manual analysis of such data sets would be prohibitively slow and laborious, automated image analysis using advanced algorithms is necessary. In the case of standard flow cytometry, event data is low-dimensional and can be analyzed semiautomatically using gating on fluorescence channel intensities and standard non-parametric clustering of gated events [20–22]. Here dimensions correspond to meaningful visual features such as cell shape and cell focal plane. These approaches break down in the face of high-dimensional data due to what is known as the 'curse of dimensionality' [23]. For complex, high-dimensional data such as single-cell images, distance measures become less useful for clustering and values in single dimensions (i.e., pixel values) become less informative for gating purposes [24]. Using hand-crafted sets of image features, more informative low-dimensional representations of images can be extracted [25,26]. Such features could include texture and image moments, or in more specific cases, cell features like elongation and size. However,

these representations are task specific, and may not reflect any kind of biologically relevant properties. To counteract these restrictions, neural networks are becoming popular for the task of learning biologically interpretable classifiers for imaging data based on which different types of cells can be classified [27–29]. However, in order to apply neural networks to a classification problem, the data need to satisfy two main conditions: classes of data need to be known, and data acquisition and annotation should be efficient. For example, neural networks can be trained and applied for the classification of single-cell imaging data with known categorical factors of variation (e.g., species, or protein localization) and easily acquired and annotated training data sets. Successful applications of neural network classifiers include imaging flow cytometry, image activated cell sorting [19], and offline analysis of single-cell imaging data [27,29]. Other classifiers such as support vector machines (SVM) have also been similarly used for the offline analysis of single-cell imaging data [30,31]. However, such approaches become difficult to use when it comes to analyzing complex populations of *a priori* unknown factors of variation, or performing classification tasks using limited training data.

The characterization of a data set without the use of training examples is known as unsupervised learning. As fully unsupervised classification is a hard problem, a variety of methods focus on simplifying this task by learning meaningful low-dimensional representations of high-dimensional data [32]. For that reason, neural networks are not trained directly for classification, but on related tasks, where it is possible to generate training data artificially [33–35]. A more natural approach to imaging data classification is learning to generate realistic image samples from a data set [36–38]. For example, networks can be trained to predict the relationship between rotations, zooms and crops of a given image, or learn to construct realistic images from a low-dimensional representation. This way, the networks learn low-dimensional features relevant to their training data and by extension to downstream classification tasks, without explicitly being trained on annotated examples. Recent approaches further demand low-dimensional representations to be human-interpretable, such that every dimension corresponds to a single factor of variation of the training dataset. For example, training on single cell images should result in a representation, where one dimension corresponds to cell type, another to cell size and yet another to the position of the cell within the image. Such representations are referred to as disentangled representations. Disentangled representations have been shown to be beneficial for classification using very few training examples (few-shot classification) [39]. A subset of unsupervised learning methods known as variational autoencoder (VAE) provide a foundation for learning disentangled representations that are simple to train and implement [40–45]. In particular, FactorVAE and related methods explicitly modify the VAE training process to promote more interpretable representations.

In this report, we attempt to bridge the gap between technology and biology and present a self-learning microfluidic platform for single-cell imaging and classification in flow. To achieve 3D flow and particle focusing, we use a simple microfluidic device, based on a variation of the commonly used three-inlet, Y-shaped microchannel. We utilize a difference in the height between sheath and sample inlet to confine heterogeneous cells in a small controllable volume directly adjacent to the microscope cover slide, which is ideal for high-resolution imaging of cells in flow. Even though the device design is conceptually similar to previous designs [46–48], controlled 3D hydrodynamic flow focusing has never been fully demonstrated in such devices, nor has particle positioning in focused flow streams been investigated. In this study, we fully characterize different device variations using simulations, and experimentally confirm 3D flow focusing using dye solutions. Additionally, we use a novel, neural network-based regression method to directly measure the distribution of microspheres and highly heterogeneous cells within the focused stream. We confine and image mixtures of different yeast species in flow using bright-field illumination and classify them by species by performing fully unsupervised, as well as few-shot cell classification. To our knowledge, this is the first application of unsupervised learning to classification in imaging flow cytometry.

2. Materials and Methods

2.1. Device Design and Fabrication

To achieve sample flow focusing close to the surface of the microscope cover slip we redesigned a simple microfluidic device based on a variation of the commonly used Y-shaped microchannel (Figure 1) [9,46–48]. For the fabrication of the silicon wafer master, we used standard two-layer, SU-8 (MicroChem, Westborough, MA, USA) photolithography [49]. Figure S1a,b show the two layers of photoresist used in the fabrication process. By sequentially combining these two layers, we created a device with three inlets and one outlet, as shown in Figure S1c. The two outer inlets introduce sheath fluids in the device and are taller than the middle inlet, which delivers the sample containing the particles under investigation (i.e., microspheres, cells). The height ratio between the sheath inlets and sample inlet can be controlled by adjusting the height of photoresist and several ratios can be fabricated for testing using the same set of photomasks. Devices for testing were fabricated using single-layer, PDMS-based soft lithography (SYLGARD™ 184 Silicone Elastomer, Dow Chemical, Midland, MI, USA) [50]. Since the difference in inlet height is created at the wafer-level, PDMS devices are fabricated in a single step, with no need of assembling a multi-layer structure.

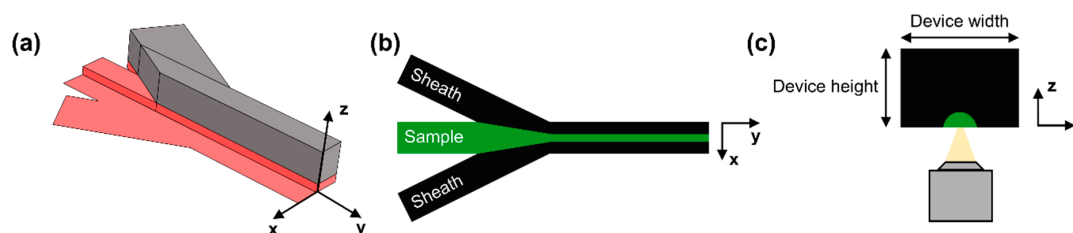


Figure 1. (a) Lengthwise 3D device cross-section showing the difference in height between the sheath and sample inlets. Red color is used to show the bottom layer of photoresist, and also the device footprint. The top layer of photoresist is shown in grey (mirror symmetry across the y-axis applies). The difference in height between the sheath inlet and the sample inlet shown is not drawn to scale and only serves as an example; (b) Device top view showing the flow focusing mechanism, where the black area is occupied by sheath fluid and the green area is occupied by the sample; (c) 2D lengthwise cross-section of the channel (front view) showing sample confinement from both the top and the sides.

2.2. Flow Focusing Principle

A schematic of the full device geometry is shown in Figure 1a. For better visualization of the difference in height between the sheath inlets and the sample inlet, a lengthwise 3D cross section of the device is provided. Any desired height ratio is possible as long as the layer thickness lies within the resolution of the photoresist and the height:width channel aspect ratio remains lower than 1:10 to ensure that channels will not collapse. The flow focusing mechanism behind these devices is shown in Figure 1b (top view; xy-plane) and Figure 1c (cross section; xz-plane). We use a three-inlet, Y-shaped microchannel to introduce the sample along with two sheath flows. The sample enters the device from the middle inlet (shown in green) and is enfolded by two sheath streams (shown in black, Figure 1b). Due to the occurrence of laminar flow in microchannels, the three streams flow parallel to each other without convective mixing [51]. While 2D sample confinement on the xy-plane has been demonstrated in similar devices numerous times [52–54], simultaneous flow confinement along the z-axis (3D flow focusing) has only been briefly investigated [46–48]. One example is a paper by Scott et al., where 2D and 3D flow confinement were achieved in devices of similar geometry, but confinement below the sample inlet height required a geometry modification, a step in the outlet channel after the junction [46]. One other example is a paper by Chung et al. where 3D flow confinement was demonstrated successfully, but control over the degree of confinement also required geometry modifications [48]. Flow focusing along the z-axis is illustrated in Figure 1c. As drawn in the figure, due to the difference in height between the sheath and sample inlet, sheath fluids surround sample

flow from all sides (black color), constraining it in a small volume close to the microscope cover slide. Here, the final volume occupied by the sample stream merely depends on the sheath-to-sample flow rate ratio, with higher sheath flow rate resulting in further sample confinement in both the xy- and xz-planes for any given device height.

2.3. Device Simulations

The device geometry was parameterized within COMSOL Multiphysics®, leaving the channel widths, the sample channel height and the sheath fluid channel height as variables. Two-fold symmetry was exploited by simulating only one half of the device split along the x-axis, applying symmetric boundary conditions where appropriate. Steady-state fluid flow through the device was simulated using the computational fluid dynamics (CFD) module, coupled to the transport of diluted species module for all simulations involving fluorescein. We used the particle tracing module for all simulations involving microparticles. Simulations were conducted under the assumption of laminar flow, with no-slip boundary conditions on all walls. Inlets were subjected to laminar inflow constraints, parameterized by the sample flow rate and the sheath flow rate respectively. The outlet pressure was constrained to zero. Fluid parameters were assigned for liquid water at 293 K. For simulations involving fluorescein, the sample inlet was subjected to a concentration constraint, fixing the concentration of fluorescein at the inlet to its experimental value of 1 mM/mL. All other inlets were subjected to zero concentration constraints. Coupled CFD-transport systems were solved using COMSOL's default solver. Maximum sample (fluorescein) height was calibrated using experimental data for a single set of sample and sheath flow rates, yielding a threshold concentration of fluorescein in the model. Fluorescein heights and widths were predicted by thresholding fluorescein concentration at the outlet. Particles used in tracing simulations were assumed to have a diameter of 6 μm and density 1.002 kg/L, within the range of the parameters of a *Saccharomyces cerevisiae* cell [55]. Particles were subjected to Stokes' drag, neglecting other force contributions. The simulation was initialized with 500 particles uniformly distributed at the sample inlet and traced for 10 ms. Particle positions were registered at the outlet and used to compute the mean particle position and its standard deviation for comparison with experiment.

2.4. Microscopy

To visualize flow focusing and particle confinement in these devices we used confocal microscopy (Leica TCS SP5 confocal microscope). Threshold was determined for the lowest-flowrate image using a modified version of the iterative intermeans algorithm as implemented in ImageJ (default method) [56]. This threshold was kept fixed for thresholding subsequent images. The concentration of microspheres (Fluoresbrite polychromatic red 6.0 micron, Polysciences Inc., Warrington, PA, USA) dispersed in fluorescein solution was 107 particles/ml. For bright-field imaging we used a Nikon Eclipse Ti-U inverted microscope. Images were acquired using a chromatic aberration free infinity (CFI) Plan Apo Lambda 60 \times oil objective (NA 1.4). The calculated lateral resolving power of the objective at 380 nm is 139 nm and the focal depth is 515 nm. A Point Gray Grasshopper (GS3-U3-23S6M-C) camera was used for image acquisition. Images of microspheres in flow were captured at 1330 frames/s and 7- μs exposure times. Images of yeast in flow were captured at 1000 frames/s and 5- μs exposure times.

Stationary images for neural network training were captured at the same conditions. Z-stacks were acquired at 0.25 μm offset between slices. Stacks were segmented automatically using a version of the Multiscale Adaptive Nuclei Analysis (MANA) algorithm adapted to bright-field image stacks [57]. Cell-containing frames were automatically detected by keeping images with maximum patch-wise variance at least twice as high as mean image variance. 128 \times 128-pixel crops were extracted from cell-containing frames by locating the image-patch of maximum variance and cropping a square of 128 \times 128 pixels around the patch center.

2.5. Microsphere Z-Displacement Regression

To determine the offset of each imaged bead from the focal plane, we used neural network-based regression. Z-stacks of static microspheres served as a training set (Supplementary File S1). A neural network was implemented in PyTorch (Figure S2a) [58]. It consisted of three convolutional blocks with leaky rectified linear unit activation [59,60], with batch normalization in every layer but the last. The network was trained on the z-stack data until convergence using the Adam optimizer with mean square error loss and initial learning rate 1×10^{-4} to predict the displacement of bead centers with respect to the focal plane [58,61]. Training images were augmented using random rotations, cropping and addition of Gaussian noise with mean 0 and standard deviation 0.1. Bright-field images of microspheres in flow were evaluated using the network and a z-displacement distribution of microspheres was computed.

2.6. Yeast Cell Z-Distance Regression

To determine the offset between yeast cell images acquired in flow and the focal plane, the strategy used for microspheres (see above) is not easily applicable, since yeast cells exhibit high variability in size and shape. Instead, we used pairs of bright-field cell images captured within the same field of view and at known z-distances from the focal plane. Z-stacks of stationary cells for all yeast species under consideration were acquired with an inter-slice spacing of 0.25 μm . Single-cell stacks were cropped from the acquired fields of view. Image augmentation (rotation, translation, mirroring, addition of noise) was used to yield visually different images at a known z-distance. Using this information, we trained a siamese neural network (Figure S2b) to predict the z-distance between pairs of single-cell images. A siamese neural network yields predictions for inputs relative to a reference by first embedding the reference and inputs using the same neural network module, concatenating the results of the reference-path and target-path, and finally applying a further neural network module for input-reference comparison [62]. This is done to discourage the neural network from learning to compare the input images pixel-by-pixel, instead of on a global scale. The siamese neural network was trained to infer the distance between pairs of z-stack slices for a single cell. Slices were augmented by random rotations, translations, zoom and Gaussian noise with mean 0 and standard deviation 0.1. The network was trained using the Adam optimizer with initial learning rate 1×10^{-4} until convergence [61]. Bright-field images of yeast cells in flow were embedded using the neural network. A well-focused *S. cerevisiae* cell was chosen as a reference for z-distance computation. Z-distances-to-reference were computed for all single-cell images to derive a z-displacement distribution.

2.7. Unsupervised Learning For Cellular Mixtures

To characterize a set of captured single-cell images, we use a probabilistic generative approach. We assume that for single-cell yeast images, x is drawn from a distribution $p_{\theta}(x) = p_{\theta}(x|z)p(z)$ with parameters θ where z are low-dimensional latent variables, $p(z)$ is the prior distribution of latent variables, and $p_{\theta}(x|z)$ is the likelihood of an image x given a latent vector z . Here, $p_{\theta}(x|z)$ is given by a neural network. Following [36], we construct a neural network to give a variational approximation $q_{\theta}(z|x)$ to the true posterior $p(z|x)$ by reparameterization and optimize the variational lower bound to the marginal log-likelihood $\log p(x)$ with respect to all neural network parameters θ (Figure S3). The neural network q_{θ} maps single-cell images to samples from the low-dimensional latent distribution, and can thus be understood as an encoder, embedding data points into latent space. Similarly, p_{θ} can be understood as a decoder, mapping samples from the latent distribution to high-dimensional single-cell images. Optimizing the variational lower bound is then realized as training the encoder and decoder to reconstruct input images well, under the constraint that the latent distribution should be as close as possible to the prior distribution $p(z)$ (Figure S3, purple term). To successfully learn a latent space, where latent dimensions correspond to meaningful visual features (e.g., cell shape, cell focal plane), we follow and implement the FactorVAE term in the variational lower bound promoting

the independence of latent dimensions (Figure S3, red term) [40]. This term penalizes the latent distribution's total correlation (TC) as given by the Kullback–Leibler (KL) divergence of the marginal distribution $q(z)$ and its corresponding factored distribution, which is a product of the distributions for each latent dimension [63]. This forces the latent distribution to be close to a product of independent distributions. Therefore, the neural networks are encouraged to learn a more strongly disentangled latent representation.

For our data set, a variational autoencoder with FactorVAE loss was trained on cell-containing crops (size 128×128 pixels) from continuous-flow imaging [41]. The encoder consisted of six convolutional kernels of size 3×3 with ReLU activation [59], and batch normalization with an increasing number of features (16, 32, 64, 128, 256, 512) [64], followed by reparametrization to yield a sample from a 10-dimensional normal distribution [36,65]. The decoder consisted of transpose convolutions in the reverse order of the encoder, again followed by ReLU activation and batch normalization. The discriminator used for FactorVAE loss computation was a multi-layer perceptron (MLP) with two layers, 64 hidden units and ReLU activation. The networks were trained using the Adam optimizer with initial learning rate 5×10^{-4} , and factor loss balancing parameter $\gamma = 10$ until convergence. K-means clustering as implemented in scikit-learn was applied to the latent space to separate *S. cerevisiae* cells from *S. pombe* cells and compared to ground-truth species labels [66]. Nearest neighbors for sample cells were extracted using euclidean distance in latent space. The latent space was visualized in 2D using t-distributed stochastic neighbor embedding (TSNE) [67].

3. Results and Discussion

3.1. Simulation Results

Our goal is to use these microfluidic devices to deliver and confine yeast cells for in-flow imaging. Since cell diameter for yeast is typically $4\text{--}8\text{ }\mu\text{m}$, we aim to confine sample flow within $10\text{ }\mu\text{m}$ from the microscope cover slide. To optimize our design, we used COMSOL Multiphysics® to simulate the effect of device height and sheath-to-sample flow velocity ratio on the maximum distance between sample and microscope cover slide, referred to here as “sample height”. The results of the parametric sweep are shown in Figure 2a. According to the simulation, any sheath-to-sample flow velocity ratio over 20 (Figure 2a, y-axis) should result in sample height below $10\text{ }\mu\text{m}$ (Figure 2a, color scale, darker green color) relative to the coverslip. This appears to be independent of the height of the device used (Figure 2a, x-axis). To test the simulation results, we fabricated two devices with different heights, the cross sections of which are shown in Figure 2b. The first device has a total height of $60\text{ }\mu\text{m}$ ($10\text{ }\mu\text{m}$ bottom layer height + $50\text{ }\mu\text{m}$ top layer height), and the second device has a height of $120\text{ }\mu\text{m}$ ($10 + 110\text{ }\mu\text{m}$).

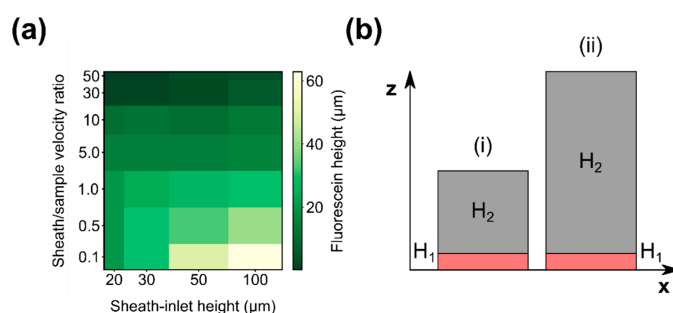


Figure 2. (a) Parametric sweep performed in COMSOL Multiphysics®. Flow velocity ratio (y-axis) refers to the ratio between sheath fluid velocity and sample flow velocity. Device height (x-axis) refers to the total height of the device, assuming a constant sample inlet height of $10\text{ }\mu\text{m}$. Sample height (color scale) refers to the maximum distance between coverslip and sample. Log–log scale has been used to better resolve the areas of interest; (b) Cross sections of two-layer device geometries tested, where H_1 is the height of the bottom layer and H_2 is the height of the top layer: (i) $H_1 = 10\text{ }\mu\text{m}$, $H_2 = 50\text{ }\mu\text{m}$, (ii) $H_1 = 10\text{ }\mu\text{m}$, $H_2 = 110\text{ }\mu\text{m}$ device.

3.2. Sample Confinement Testing Using Fluorescein

To visualize flow focusing in these devices we used confocal microscopy. Fluorescein dissolved in water was introduced through the sample inlet and was kept at a constant flow rate of $0.25 \mu\text{L}/\text{min}$ ($0.87 \text{ mm}/\text{s}$). Water was used as sheath fluid and was introduced through the two taller, outer inlets at increasing flow rates. Figure 3a shows a montage of confocal images (channel cross section) for the device with a height of $60 \mu\text{m}$. As predicted by simulation, for increasing sheath flow rates the volume occupied by fluorescein in the channel is progressively reduced. We observe fluorescein confinement in all directions, seen in the pictures as a reduction in the width and height of the fluorescein cone, also shown as an image overlay in Figure 3b. The reduction in the height of the fluorescein cone corresponds to confinement towards the microscope cover slip. When sheath flow rate is equal to sample flow rate ($0.25 \mu\text{L}/\text{min}$), fluorescein occupies a large fraction of the channel volume (red). With increasing sheath flow rates, the volume occupied by fluorescein shrinks towards the cover slip (black). The highest sheath flow rate achieved without affecting flow equilibrium was $20 \mu\text{L}/\text{min}$, corresponding to a sheath-to-sample flow velocity ratio of 16. This is quantified in Figure 3c in a plot showing the measured fluorescein heights for every sheath flow rate tested. As seen in the graph, experimentally measured fluorescein heights correspond well with the equivalent values obtained from simulations, for sheath flow rates up to $20 \mu\text{L}/\text{min}$. Since our final goal is to use optimized devices for applications in single-cell imaging in flow, sample flow rates were kept low in order to avoid image blur during imaging. For applications in flow cytometry, sample focusing can be optimized at higher flow rates.

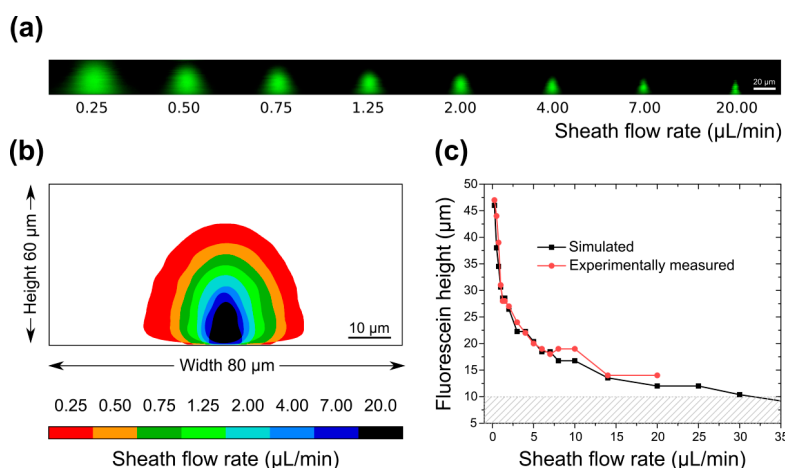


Figure 3. (a) Confocal microscopy images at increasing sheath-to-sample flow velocity ratio for $10 + 50 \mu\text{m}$ device. As sheath flow rate increases, fluorescein is confined both towards the microscope slide (bottom), as well as from the sides. In the z-direction the pixel size is $w = 0.41 \mu\text{m}$, $h = 0.65 \mu\text{m}$; (b) Z-projection of thresholded confocal microscopy images showing fluorescein confinement for increasing sheath flow rate; (c) Simulated (black) and experimentally measured (red) fluorescein heights for constant fluorescein flow rate of $0.25 \mu\text{L}/\text{min}$ and varying sheath flow rates. Shaded area highlights fluorescein height below $10 \mu\text{m}$.

Using these devices, we were not able to experimentally reproduce simulated sheath flow rates over $20 \mu\text{L}/\text{min}$ and fluorescein confinement below $10 \mu\text{m}$ was not achieved (maximum confinement was $\sim 14 \mu\text{m}$). Instead, for sheath flow rates over $20 \mu\text{L}/\text{min}$ ($34.72 \text{ mm}/\text{s}$) we saw fluorescein backflow towards the sample inlet, suggesting a large difference in pressure between the sheath and sample inlets not predicted by the simulation shown in Figure 2a. To predict pressure driven backflow in microchannels using COMSOL Multiphysics®, pressure constraints need to be applied. For all simulations shown in this work, flow velocity constraints that prohibit backflow were applied instead. Indeed, when pressure constraints are applied instead of velocity constraints, we see a negative velocity in the x-direction within the sample channel, which confirms flow towards the sample inlet for sheath

flow rates above 20 $\mu\text{L}/\text{min}$ (Figure S4). These results demonstrate that devices with a height of 60 μm do not fulfill the necessary requirements for sample flow focusing within 10 μm from the coverslip.

To eliminate the problem of sample backflow towards the inlet we next tested devices with a height of 120 μm . An increase in the area of the channel cross-section is expected to alleviate backflow since channel pressure is expected to drop. The logical way to achieve this would be to increase channel height, as opposed to channel width, as we would otherwise lose horizontal focusing. Similar to the previous device, the fluorescein flow rate was kept at 0.25 $\mu\text{L}/\text{min}$ and sheath flow rate was slowly increased from 0.25 $\mu\text{L}/\text{min}$ (0.43 mm/s) to 200 $\mu\text{L}/\text{min}$ (347.22 mm/s). Again, to evaluate fluorescein confinement we used confocal microscopy and the results are shown in Figure 4a. We found that for a 1:1 sheath-to-sample flow rate ratio, fluorescein occupies a large fraction of the channel volume, also shown in red in the image overlay in Figure 4b. With increasing sheath flow rates, we observe continuous fluorescein confinement, seen in the figures as a reduction in the width and height of the fluorescein cone. Quantification of the fluorescein cone height from the images revealed a confinement within a distance of 10 μm from the cover slip at flow rates over 100 $\mu\text{L}/\text{min}$ (173.61 mm/s), shown as the shaded area in the graph in Figure 4c. The distance between the microscope slide and the tip of the fluorescein cone decreased further to a minimum of $\sim 5\mu\text{m}$ when the highest tested flow rate (200 $\mu\text{L}/\text{min}$) was used. At such high sheath flow rates, sample flow begins to become unstable, which results in a change in the observed fluorescein shape, as seen in Figure 4a. Importantly, due to the larger cross-section of this device, flow equilibrium was maintained, and no fluorescein backflow was present even at very high sheath-to-sample flow rate ratios. As seen in the graph, experimentally measured fluorescein heights correspond well with the equivalent simulated heights, and confinement below $\sim 5\mu\text{m}$ was experimentally reproduced. To better visualize confinement, we used COMSOL Multiphysics® to generate animations that show sample flow confinement with increasing sheath flow rates in 2D and 3D, see Supplementary Animation S1 and S2. In summary, devices with a height of 120 μm can robustly confine fluorescein as close as $\sim 5\mu\text{m}$ from the microscope slide.

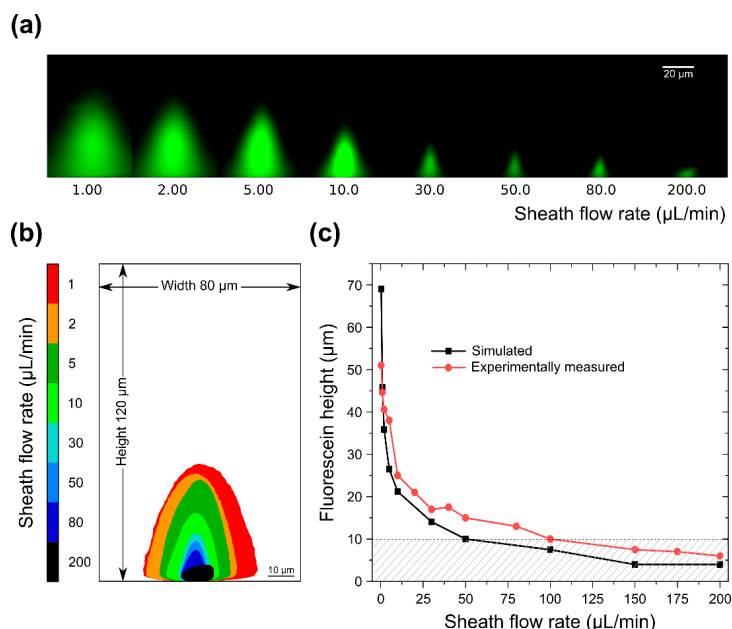


Figure 4. (a) Confocal microscopy images at increasing sheath-to-sample flow velocity ratio for the 120 μm (10 + 110 μm) device. In the z-direction, the pixel size is $w = 0.43\mu\text{m}$, $h = 0.43\mu\text{m}$; (b) Z-projection of thresholded confocal microscopy images showing confinement of the fluorescein cone for increasing sheath flow rate; (c) Simulated and experimentally measured fluorescein heights for constant fluorescein flow rate of 0.25 $\mu\text{L}/\text{min}$ and varying sheath flow rates. Shaded area highlights fluorescein height below 10 μm , which is our target confinement height for live yeast cell in-flow imaging.

Since these devices are optimized for use in single-cell imaging in flow, it is important that flow focusing is maintained for several hundred micrometers after the junction in order to provide enough space for cell detection, cell imaging, and potential integration of cell sorting mechanisms [68]. We therefore investigated four positions within the device with increasing distance from the inlet junction; 100 μm , 500 μm , 1.1 mm, and 2.1 mm. Confocal microscopy images of fluorescein dissolved in water were taken at these positions and are shown in Figure S5i–iv. Flow equilibrium and sample confinement is maintained along the main channel even 2 mm away from the junction ensuring enough space for cell imaging and sorting. Even though the height of the fluorescein cone remains the same along the channel, fluorescein diffuses into the sheath fluid (water), which is to be expected in channels characterized by laminar flows where mass transport by transverse diffusion is the dominant mechanism for mixing [69,70].

3.3. Simulation of Particle Positioning and Validation Using Microspheres

For high-resolution imaging of cells flowing in these devices, it is important to be able to predict how cell position varies along the z-axis according to the flow rates used. To evaluate the equilibrium position of particles flowing in such channels, we first used simulations where we traced 500 microspheres with a diameter of 6 μm uniformly distributed at the sample inlet. We found that at low sheath flow rates, the mean equilibrium position of the microspheres (red squares in Figure 5a) is predicted to be closer to the tip of the fluorescein cone (Figure 5a, black squares) rather than the coverslip. In other words, the center of gravity of the microspheres is predicted to be on average closer to tip of the fluorescein cone than the coverslip. With increasing sheath flow rates (above 100 $\mu\text{L}/\text{min}$) and as the size of the fluorescein cone is decreasing due to flow confinement, the simulations predict that the mean equilibrium position of the microspheres will shift towards the microscope slide, close to the center of the fluorescein cone. This shift in the mean position of microspheres follows a shift in the flow streamlines, which is in turn based on an increase in the shear force exerted by the velocity gradient at higher flow rates (Figures S6 and S7). To validate the results from the simulations, we dispersed red fluorescent microspheres in fluorescein solution and used confocal microscopy to track their location. Due to the limited speed and the line-scanning mode of data acquisition in confocal microscopy, the moving microspheres appear as lines (Figure 5b,c). Even though the confocal microscope image in Figure 5b qualitatively confirms that particles equilibrate on average closer to the tip of the fluorescein cone rather than the base, a quantitative measurement of the position of microspheres is not possible due to limitations of the microscope. Simulations shown in Figure 5c, however, mathematically reproduce the microscopy data shown in Figure 5b. Again, most microspheres are predicted to reach equilibrium closer to the tip of the fluorescein cone (green contour) rather than the cover slip (bottom of the figure). To facilitate comparison between experimental and simulation data we included a juxtaposition of the two as an inset in Figure 5c.

To further quantify the distribution of microsphere positions within the sample phase without line-scanning artefacts, we used bright-field microscopy to image microspheres in flow at a fixed z-position in devices with a height of 120 μm . We set the imaging z-position to match the mean equilibrium z-position of microspheres predicted by simulation. Microspheres were dissolved in water at a concentration of 10^7 particles/ml and were introduced into the device through the sample inlet. To keep the particle velocity within the range we can image without being affected by image blur, we used sample flow rate of 0.1 $\mu\text{L}/\text{min}$ and sheath (water) flow rate of 10 $\mu\text{L}/\text{min}$. These flow rates resulted in microspheres being confined within 16 μm from the coverslip, with a mean equilibrium position at approximately 10 μm away from the coverslip. To automatically and accurately quantify the z-positions of all microspheres imaged in flow with respect to the microscope focal plane and the coverslip, we trained a simple neural network on z-stacks of images acquired from static microspheres (Figure 5d and Supplementary File S2). Details about the network can be found in Section 2.4. The distribution of microspheres within the sample stream is depicted as a histogram in Figure 5e. Microsphere z-displacement is shown relative to the true focal plane (z-displacement = 0), as well as

relative to the microscope slide (z -displacement = 10 μm). Microspheres located within 2 μm from the focal plane, depicted by the shaded area in Figure 5e, account for 68% of all spheres imaged. As we already demonstrated in Figures 3 and 4, further confinement is possible in these devices by increasing the sheath flow rate. It is expected that this will increase the percentage of microspheres located within 2 μm from the focal plane since there will be less space available for them to move. However, increasing the sheath flow rate also increases the velocity of the microspheres, which in turn results in significant motion blur that no longer allows us to quantify the microsphere distribution.

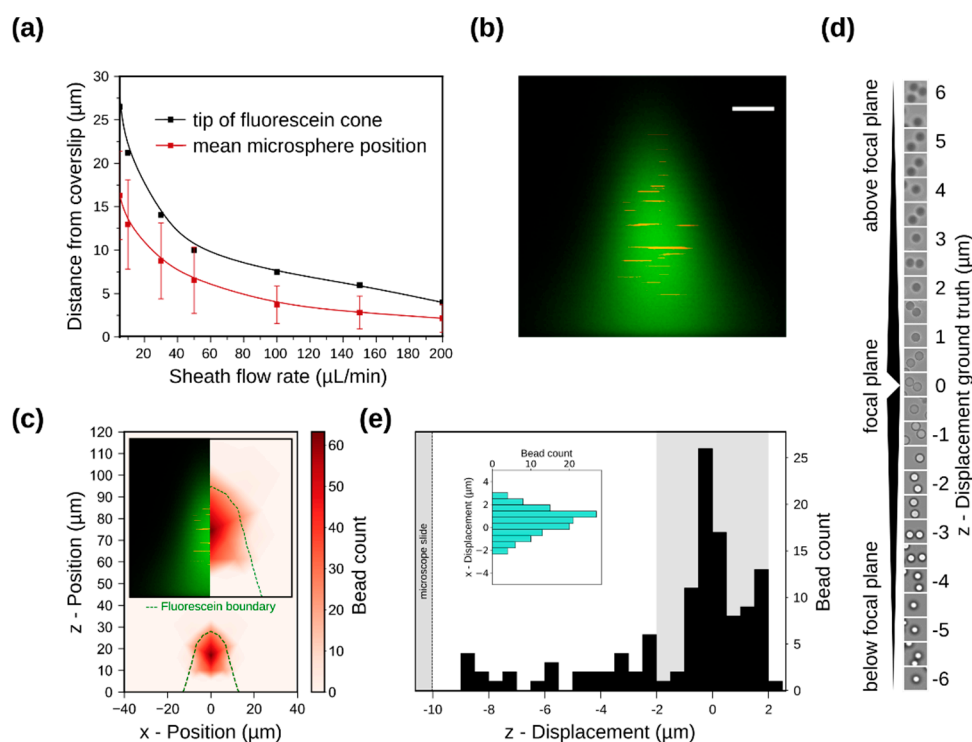


Figure 5. (a) Simulated distance between fluorescein cone tip and microscope slide for increasing sheath flow rates and fluorescein flow rate of 0.25 $\mu\text{L}/\text{min}$ (black). Mean bead equilibrium position (along with standard deviation) with respect to the microscope slide (red); (b) Confocal microscopy image of the cross section of the sample stream (green), sheath fluid (black). Red fluorescent microspheres (diameter $\sim 6 \mu\text{m}$) dispersed in the sample stream appear as lines due to line scanning in confocal microscopy. This image was taken in a device with a height of 120 μm , at a fluorescein flow rate of 0.25 $\mu\text{L}/\text{min}$ (0.43 mm/s) and sheath flow rate of 10 $\mu\text{L}/\text{min}$ (17.36 mm/s). The height of the fluorescein cone in this image is 27 μm , and the scale bar is 6 μm ; (c) Simulation reproducing microscopy data shown in (b). Fluorescein contour shown as green dotted line. Microspheres appear to concentrate closer to the fluorescein cone tip rather than the microscope slide. The insert shows a juxtaposition of the confocal image and the equivalent simulated data. (d) Microsphere images acquired at known distances from the focal plane, used as part of the training set for bead focal plane regression. (e) Histogram of z -displacement of microspheres relative to the focal plane. Bins have a width of 0.5 μm , with the x -axis the displacement relative to the focal plane and the y -axis the bead count for each bin. The shaded region within 2 μm of the focal plane, accounts for 68% of all microspheres. Displacement on the x - y plane is shown in the inset. 87% of sphere centers are located within 2 μm of the stream centerline.

For applications in imaging flow cytometry, it is also important to ensure tight particle focusing on the x - y plane in order to minimize the field-of-view that is imaged and subsequently analyzed. The total width of the sample phase for the flow conditions described above was found to be $\sim 10 \mu\text{m}$. The displacement of bead centers from the stream centerline is provided as the inset in Figure 5e (green histogram). Almost all bead centers (87%) were found to lie within 2 μm from the sample

stream centerline, which confirms excellent focusing along the x-axis and allows for the capturing of small images for fast read-out and processing. Together, our results demonstrate confinement of microspheres in a narrow stream close to the surface of the coverslip, as predicted by the simulations.

3.4. Single-Cell Imaging in Flow

Next, we replaced microspheres with yeast cells of different species, i.e., *S. cerevisiae*, *Sd. ludwigii* and *S. pombe*. Unlike microspheres, each of these species exhibit characteristic cell shapes in the size-range of 3–12 μm . *S. pombe* cells are rod-shaped, *Sd. ludwigii* are lemon shaped, and *S. cerevisiae* cells are round. Furthermore, cell shapes change through the life cycle since *S. pombe* divides by fission, while *Sd. ludwigii* and *S. cerevisiae* cells divide by forming a bud attached to the so-called mother cell. The irregularity in cell shape and sizes imposes limitations on the tools we can use to determine the z-displacement distribution of yeast cells within the focused sample stream in our device. The simple neural network training strategy used for microspheres (Section 2.4, Figure 5d) could not be used in this case due to the lack of homogeneity. Instead, we used pairs of bright-field cell images captured within the same field of view and at known z-distances from the focal plane. Single-cell stacks were cropped from the acquired fields of view and images were augmented to yield visually different images of cells with a known z-distance. Using this information, a siamese neural network was trained to predict the z-distance between pairs of single-cell images (Figure 6a) [62]. More details about yeast cell z-distance regression have been outlined in Section 2.5. To evaluate the learning success of this strategy, we used the trained network to predict the distance between pairs of images taken from a test data set that has not been used for training purposes. As shown in Figure 6b the neuronal network predicted with high accuracy the z-distance in the test data.

To continue with the analysis of cell focusing, we imaged yeast cells in flow under the same conditions described in Section 3.3 for microsphere imaging. Imaging data for all yeast species are given in Supplementary File S3. Some sample yeast images that highlight cell heterogeneity are shown in Figure 6c. We used bright-field microscopy to image cells in flow at a fixed z-position in devices with a height of 120 μm . The focal plane for yeast cells was found to be approximately 16 μm from the coverslip. Using the trained neural network, we determined the position of each imaged cells within the device using well-focused cell images as reference. Similar to what we observed for microspheres in Figure 5e, the z-distribution for all species peaked around the focal plane of the microscope, with a broad tail towards the microscope slide (Figure 6d). When considering cells of all species and sizes, the main peak around the focal plane (z-displacement = 0) contained 51% of imaged cells. The broad tail formed at the bottom of the device, adjacent to the microscope slide can be explained by the broad heterogeneity of the sample, since size and shape distributions are known to influence particle focusing positions in different types of devices [71,72]. Given this information, and in addition to the fact that the tail is much less pronounced when imaging monodisperse microspheres under identical flow conditions in the same devices, we assume that this broad tail is in fact due to cell heterogeneity, examples of which are shown in the inset of Figure 6d. To test this assumption, we limited cell-shape degrees of freedom by considering only *S. cerevisiae* cells in Figure 6e. The distribution now clearly shows two peaks, where the main peak contains 59% of all cells. Closer examination in the composition of the lower peak reveals that 57% of cells are small, single cells and 28% are budding cells. These cases are susceptible to pessimistic neural network predictions. Here, we call a network prediction pessimistic, when the maximum possible z-distance between the imaged cells and the reference cell is predicted. For example, if an input image contains a well-focused mother cell and an out-of-focus daughter cell, the network uses the z-distance between the out-of-focus daughter cell and reference cell, and therefore classifies the entire image as out-of-focus, even though the mother cell is in focus. Examples of these events are shown in the inset of Figure 6e. In total, 85% of lower-peak cells are either differently sized than the main-peak cells, or have pessimistic z-distance predictions. For the purposes of evaluating the cell focusing performance of our device compared to that of microspheres of the same size, we may therefore safely neglect the z-distribution's lower peak. This indicates that

the simple microfluidic devices we developed can be successfully used to also focus cells, allowing for imaging and downstream tasks, such as sample characterization and cell sorting.

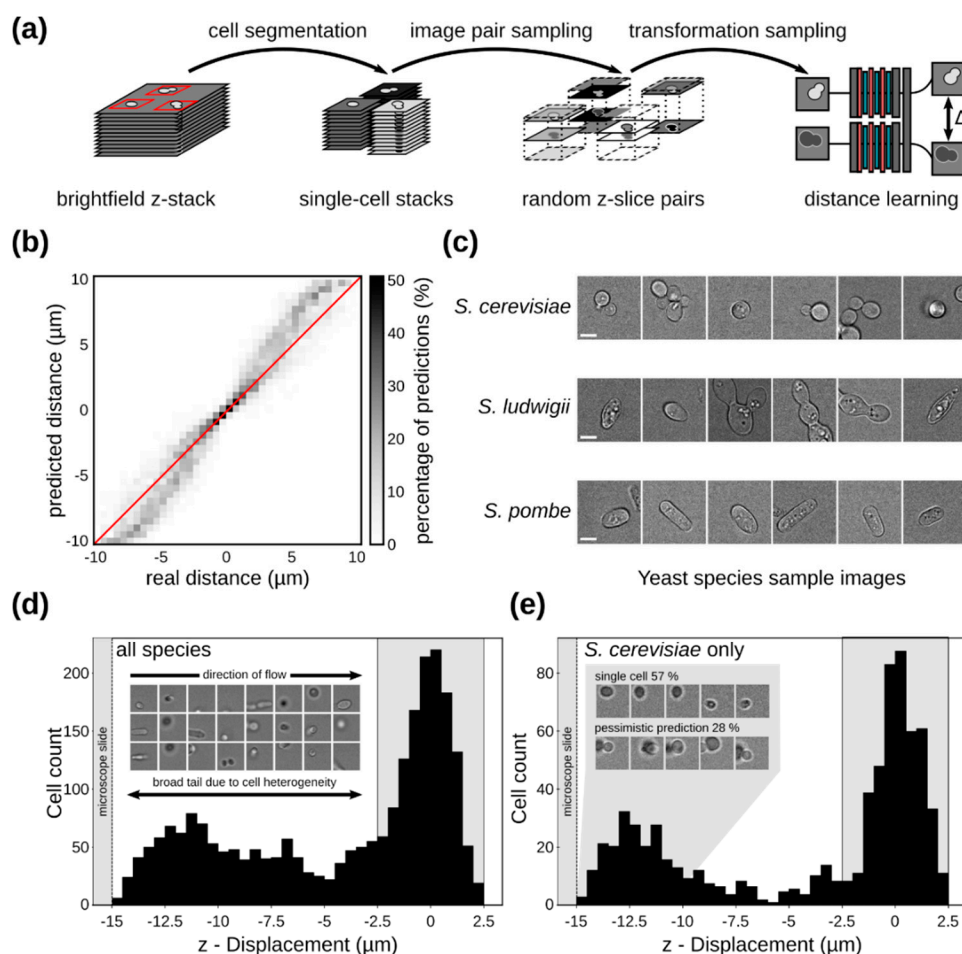


Figure 6. (a) Work flow underlying distance learning for automated z-position determination of flowing cells. Stacks of images of large fields of view containing many cells were recorded on the same microscope used for the imaging of flowing cells, but using an ordinary mounting of the cells. Single-cell stacks were cropped out. Random image pairs with known z-distances taken from single-cell stacks were used after image augmentation to train a Siamese neural network. (b) Predicted and real z-distance in pairs of cells taken from a test set of single cell stacks. (c) Images of the different yeast species used. (c) Example images of *S. cerevisiae*, *S. ludwigii* and *S. pombe* cells. The example cells highlight the high within-species and inter-species heterogeneity of the cells used. Scale bar length corresponds to 5 μm. (d,e) Histogram of z-displacement of flowing yeast cells in the device relative to an in-focus reference cell. Bins have a width of 0.5 μm, with the x-axis the z-displacement relative to the distribution median. Across all yeast species, example images highlighting their heterogeneity are shown. The shaded region within 2.5 μm of the focal plane contains 51% and 60% of imaged cells for all species (d) and *S. cerevisiae* (e) respectively. *S. cerevisiae* examples of non-budding cells and pessimistic predictions in the region below −10 μm are shown, accounting for 85% of the distributions lower peak.

3.5. In-Flow Cell Imaging and Cell Classification

Imaging large cell populations using conventional microscopy requires scanning using large mechanical moving stages. Imaging flow cytometry offers the possibility of imaging many cells while avoiding moving mechanical parts. Moreover, each cell is imaged individually, eliminating the need for retrospective cell segmentation and object identification in large fields of view, which is often a daunting task especially when cells are close together. Microfluidic devices like the one described

in this work offer the possibility for high-throughput imaging and open up applications that also involve rapid, in-line characterization of the investigated sample. To outline possible applications, we took imaging of different yeast species within our devices another step further and concluded this work by devising a flexible framework for efficient, automated imaging data analysis. To this end, we implemented unsupervised machine learning in the form of a VAE to extract phenotypic information from single-cell images without the need for user intervention.

To demonstrate the capabilities of our framework, we trained a VAE with FactorVAE loss on single-cell images (see Section 2.6) and classified yeast cells by species in a fully unsupervised manner. The model consists of an encoder and a decoder. The encoder maps images to 10-dimensional points in latent space, while the decoder generates images from such points. A schematic of the model and objectives involved is shown in Figure 7a. The model is trained to have generated images match input images and produce a latent space, where each dimension corresponds to a meaningful visual characteristic of cells. For example, the cell species should vary along one dimension, while the cell shape should vary along another (for more details, please refer to Section 2.6). Qualitative evaluation of the resulting latent space by nearest neighbor analysis shows that single-cell images at a similar level of focusing and of similar shape are close together in the learned representation. As such, the four nearest neighbors shown in Figure 7b are budding *S. cerevisiae* cells, if the query cell is a budding *S. cerevisiae* cell, and elongated cells, if the query is an elongated cell. This suggests that our VAE has learned a meaningful latent representation, which could be applied to downstream classification tasks.

As our VAE learns visual similarities and differences among imaged cells, a high within-species variance of cells increases the difficulty of distinguishing different species. One factor resulting in high intraspecies variance is a lack of cell focusing. On the other hand, images of similarly sized, well-focused cells reduce intraspecies variance and as a result greatly simplify and improve classification. Our device achieves such improvements by precisely focusing similarly sized cells close to the microscope slide. In addition to particle focusing along the z-axis, our device tends to orient non-spherical particles in the direction of fluid flow, further reducing intraspecies variance. This tendency can be seen in the cells displayed in Figure 7b. Our model learns this regularity of the data and therefore groups similarly oriented cells.

To allow for the automated analysis of data from our devices, the learned representation should capture phenotypic properties necessary for distinguishing single-cell images of different yeast species. We evaluated the suitability of our learned representation for this task of unsupervised classification by using it to distinguish between images of *S. cerevisiae* and *S. pombe* cells captured in-flow in our microfluidic devices. *S. ludwigii* cells were not used for classification since they tend to form aggregates that disrupt flow and clog the microfluidic channels, resulting in few available examples of *S. ludwigii* cells in flow compared to *S. cerevisiae* and *S. pombe*. A qualitative inspection of the latent space labeled by yeast species (Figure 7c, left) reveals a separation between budding and fission yeast cells, with similar subsets of cells forming smaller clusters. Fully unsupervised classification is performed with an accuracy of 74%. Data-points that were wrongly classified (Figure 7c, center) are mostly located in regions where species labels overlap. Some failure cases are shown on the right in Figure 7c. A qualitative inspection of these failure cases reveals small out-of-focus *S. cerevisiae* cells being misclassified as *S. pombe* cells, while round out-of-focus *S. pombe* cells are misclassified as *S. cerevisiae* cells. Both of these are cases of misclassification, where distinguishing between yeast species becomes hard even for human experts. We have therefore achieved fully unsupervised classification of yeast cell by species with an accuracy of 74%. This complements our device with a strong baseline for cell classification without the need for expert intervention.

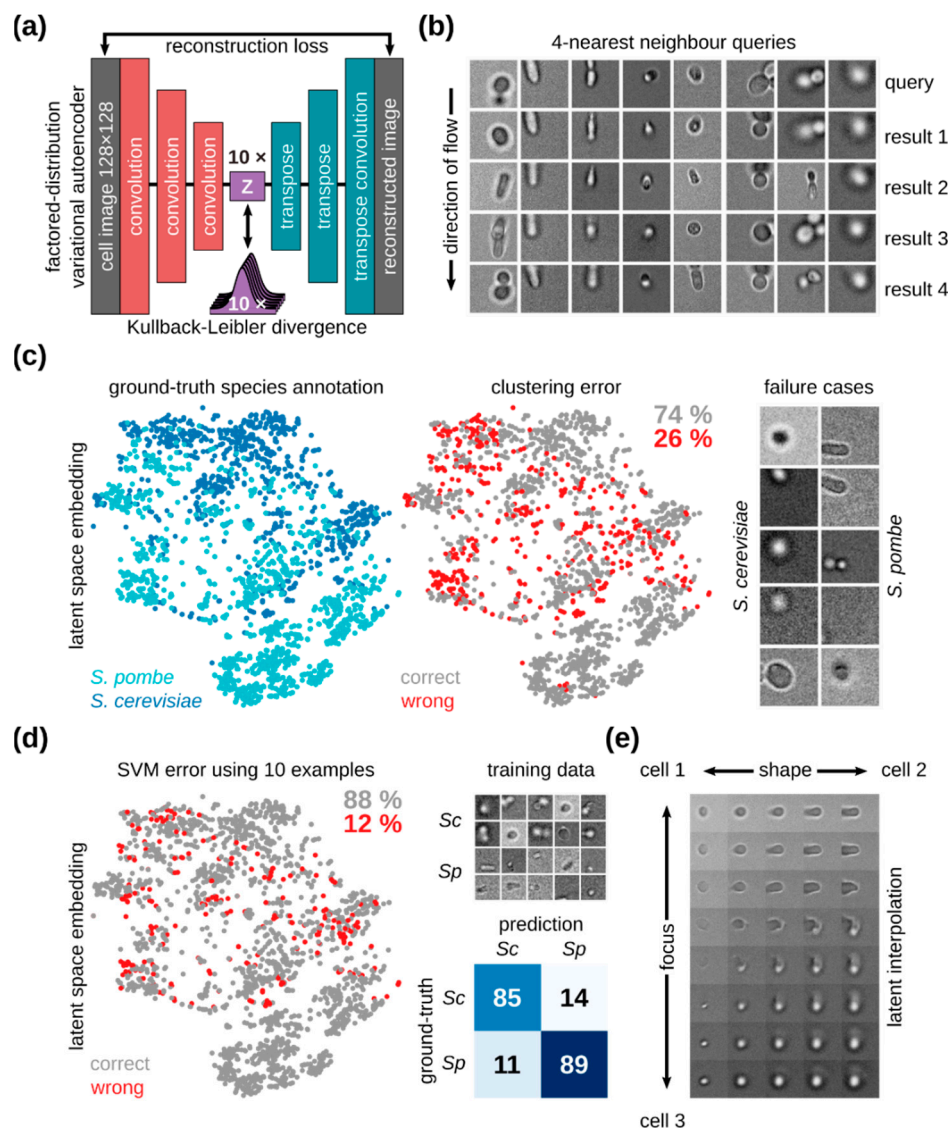


Figure 7. (a) Variational autoencoder (VAE) architecture for unsupervised learning. Cell images are convolutionally embedded into 10-dimensional latent space and reconstructed using same-shaped transpose convolutions. The network is trained to perform image reconstruction and is constrained to produce a disentangled latent space by KL divergence relative to a normal distribution and a penalty on total correlation. (b) Sample nearest neighbor queries for eight query cells. Query results are displayed in the order of increasing distance in latent-space. (c) Assessment of unsupervised classification accuracy. A two-dimensional embedding of data points for *S. cerevisiae* (blue) and *S. pombe* (turquoise) is shown, with ground truth species labels (left), a map of data points wrongly classified (red) by latent space k-means (center), and images of random failure cases for both species (right). Failure cases comprise *S. cerevisiae* cells classified as *S. pombe* cells (left column) and vice versa (right column). k-means on latent space classifies 74% of samples correctly, without the need for supervision. (d) Assessment of few-shot classification accuracy. A map of wrongly classified data points (red) using an support vector machines (SVM) classifier on latent space with 10 training examples per species shows an accuracy of 88% (left). The full training set is displayed for both species (top right), together with a confusion matrix showing the percentage of classifications for the classifier (bottom right). Sc and Sp indicate *S. cerevisiae* and *S. pombe* respectively. (e) Latent space interpretability. A latent space interpolation between three cells is shown, indicating latent space vectors encoding for cell focal plane (focus), as well as cell elongation (shape).

While fully unsupervised classification removes the need for large, hand-annotated training data sets, annotating small amounts of training examples is both feasible and beneficial for classification accuracy. We extend our data analysis setup with few-shot cell classification, to improve accuracy and enable expert-guided adaptation to more fine-grained classification tasks. To this end, we trained an SVM classifier on a representative set of 10 annotated single-cell images per species (Figure 7d, top right). The few-shot classifier increases classification performance to an accuracy of 88%, with negligible training time (Figure 7d). While misclassified data-points occur at similar locations in latent space as for fully unsupervised classification, the number of wrongly classified cells is significantly reduced (Figure 7d, left). The confusion matrix for the SVM classifier (Figure 7d, bottom right) shows that both *S. cerevisiae* and *S. pombe* cells are misclassified as the other with a probability of 11–14%, a vast improvement compared to unsupervised classification. Our integrated platform can therefore perform few-shot classification of yeast cell images captured in-flow in our microfluidic device and achieve 88% success in separating yeast cells by species.

In flow cytometry, it is desirable to gate single-cell events by their properties, e.g., fluorescence intensities. In imaging flow cytometry, such properties correspond to spatially resolved features, such as cell morphology and subcellular protein localization. Ideally, our latent space should capture those properties. Qualitative inspection of the latent space reveals interpretable latent dimensions, which can be linked to biologically meaningful morphological features, such as cell focal plane and elongation. These are visualized in a latent interpolation between cells along these dimensions in Figure 7e. The results in this figure also show that our latent space captures valuable semantic information, which could be used to differentiate between different cell phenotypes based on morphology in bright-field images. These indicate that our combined microfluidic and unsupervised learning platform can be used for the biologically-relevant characterization of complex cellular mixtures with minimal human intervention. The learned semantic latent space captures enough phenotypic features to group cells based on their morphology and extract accurate subpopulation classifiers with very few training examples.

4. Discussion

In this work, we have demonstrated 3D flow focusing in simple microfluidic devices for applications in imaging flow cytometry. The devices used utilize a difference in height between the outer sheath inlets and the middle sample inlet and achieve sample flow confinement within a few micrometers from the microscope slide, which makes them suitable for use with high NA oil objectives. In contrast to most previously demonstrated geometries, our devices maintain a simple, single-layer architecture that makes them accessible to non-expert users. Instructed by simulations, we fabricated and tested two devices with different heights, 60 μm and 120 μm , and found that flow equilibrium between sheath and sample is more stable in taller devices, and sample confinement within 5 μm from the microscope slide was achieved. To evaluate device performance for use in single-cell imaging in flow, we introduced 6- μm polymer microspheres dispersed in fluorescein through the sample inlet and monitored their position using confocal microscopy. Further, we used simulation tools to predict bead equilibrium positions in these devices for different sheath flow rate ratios and the results were confirmed using confocal microscopy. Once the mean microsphere equilibrium positions had been calculated and confirmed, we used bright field microscopy to image fast-moving beads traveling through these devices. We applied a novel, neural network-based approach to determine the distance of spheres to the focal plane. We found that 68% of the microspheres were traveling within 2 μm from the focal plane, thus enabling the acquisition of single plane images across their body. These results were reproduced for yeast cells of multiple species travelling in the same devices, further demonstrating the applicability of such devices in imaging flow cytometry. Our optimized microfluidic device can be used for a range of flow rates (0.1 $\mu\text{L}/\text{min}$ –200 $\mu\text{L}/\text{min}$ have been tested) and a range of particle sizes (3–12 μm tested) without the need for geometry modification, which makes it robust and compatible

with both imaging and non-imaging flow cytometry. Additionally, such devices could be relevant in other applications where hydrodynamic focusing into a small, well-defined volume is required [73].

Furthermore, we applied state-of-the-art unsupervised learning techniques to classify yeast cells by species. This was done in a fully unsupervised manner and also using SVM in a few-shot setting. We learned a semantically meaningful latent representation of yeast cells, with latent vectors representing visually and biologically meaningful features. Our latent representation allowed for the unsupervised distinction between *S. cerevisiae* and *S. pombe* cells with 74% accuracy, increasing to 88% in the 10-shot setting, which proves it suitable for further downstream classification tasks. We also verified via nearest-neighbor analysis, that biologically and visually similar cells are grouped in latent space. In summary, we have presented the first application of unsupervised learning in imaging flow cytometry. Interpretable latent spaces provide biologically meaningful image parameters that could improve image-activated cell sorting and allow for FACS-like gating on imaging data.

Our demonstration only utilized bright field imaging of microspheres and yeast cells. For practical applications, imaging flow cytometry requires the capability to acquire fluorescent images of cells. This requires acquisition speeds that are fast enough to reveal subcellular structures inside the moving cells, ideally in the range of the diffraction limit of a high NA objective (i.e., ~200 nm lateral and ~800 nm vertical resolution when using a 1.4 NA oil objective). This poses several challenges, some of which can be overcome using different techniques already described in the literature [6].

5. Conclusions

In conclusion, we have demonstrated a learning microfluidic platform capable of imaging live cells in flow and classifying acquired images without the need for human supervision. Cell streaming, confinement and imaging are achieved in a simple and versatile microfluidic device. Such devices can confine flow towards the microscope slide in a controlled manner, which makes them especially suitable for applications in single-cell imaging in flow. We have demonstrated that a large range of flow rates and particle sizes can be used without the need for geometry modification, since both tightness of focusing and line of focusing along the z-direction only depends on the flow rate ratio between sheath and sample. In fact, we were able to successfully stream, focus, and image *S. cerevisiae*, *S. ludwigii* and *S. pombe* yeast. This is the first demonstration of controlled 3D flow confinement well below the inlet height in this simplified version of a single layer Y-shaped microfluidic device and the first-time particle and cell positioning in the focused stream are studied. We expect that such a robust device will find applications in the quickly growing fields of imaging flow cytometry and flow cytometry on-chip.

Additionally, we achieved image classification using a powerful unsupervised learning paradigm of disentangling variational autoencoders. Our variational autoencoder embeds single-cell images in an interpretable latent space and allows for both similarity-based queries and classification. The biggest advantage of such classification is that it is completely unsupervised, obviating the need for large hand-annotated training data sets prevalent in neural network-based machine learning. To our knowledge, this is the first application of unsupervised representation learning to imaging flow cytometry. In particular, disentangled representation learning has not been applied to single-cell images before and we expect it will play a big role in gating for image activated cell sorting. In conclusion, we presented a simple and affordable platform for continuous-flow single-cell imaging, large-scale data analysis, and image classification.

Supplementary Materials: The following are available online at <http://www.mdpi.com/2072-666X/10/5/311/s1>, Figure S1: Device fabrication schematic, Figure S2: Schematic of neural network architectures, Figure S3: Schematic of variational autoencoder training, Figure S4: X-direction velocity profile simulation for the 60 μm (10 + 50 μm) device, Figure S5: Flow focusing at four positions within the device with respect to the junction, Figure S6: Qualitative shear force distribution due to xy-velocity gradients in the z direction, Figure S7: Theoretical flow focusing behavior dependent on x-velocity, Supplementary Animation S1, Supplementary Animation S2. Supplementary Files S1–S3 are deposited in the heiDATA Dataverse repository at: <https://doi.org/10.11588/data/L5J7WO>. Source code and neural network weights for all parts of the project are deposited on GitHub at: <https://github.com/mjendrusch/learning-ifc>.

Author Contributions: Conceptualization, I.C., M.J. and M.K.; methodology, I.C., M.J.; experiment design and execution I.C., M.J.; simulations M.J.; machine learning M.J.; photolithography, T.A.; microscopy, I.C., M.J., F.G. and A.S.; writing—original draft preparation, I.C.; writing—review and editing, I.C., M.J. and M.K.; supervision, I.C., G.C. and M.K.

Funding: This research was supported by the state of Baden-Württemberg through bwHPC and the German Research Foundation (DFG), grant number INST 35/1134-1 FUGG and DFG N498/12-1. Iordania Constantinou was supported through a fellowship from the Carl Zeiss Stiftung and by the Ministry of Science and Culture (MWK) of Lower Saxony, Germany through the SMART BIOTECs alliance between the Technische Universität Braunschweig and the Leibniz Universität Hannover. Gilles Charvin was supported by a grant from the Fondation pour la Recherche Médicale, and by a grant ANR-10-LABX-0030-INRT, a French State fund managed by the Agence Nationale de la Recherche under the frame program Investissements d’Avenir ANR-10-IDEX-0002-02.

Acknowledgments: Holger Lorenz and the fluorescence microscopy facility at ZMBH.

Conflicts of Interest: The authors declare no conflicts of interest.

References

1. Gross, H.-J.; Verwer, B.; Houck, D.; Recktenwald, D. Detection of rare cells at a frequency of one per million by flow cytometry. *Cytometry* **1993**, *14*, 519–526. [[CrossRef](#)] [[PubMed](#)]
2. De Rosa, S.C.; Herzenberg, L.A.; Herzenberg, L.A.; Roederer, M. 11-color, 13-parameter flow cytometry: Identification of human naive T cells by phenotype, function, and T-cell receptor diversity. *Nat. Med.* **2001**, *7*, 245–248. [[CrossRef](#)]
3. Sandberg, J.; Werne, B.; Dessing, M.; Lundberg, J. Rapid flow-sorting to simultaneously resolve multiplex massively parallel sequencing products. *Sci. Rep.* **2011**, *1*, 1–7. [[CrossRef](#)]
4. Schonbrun, E.; Gorthi, S.S.; Schaak, D. Microfabricated multiple field of view imaging flow cytometry. *Lab Chip* **2012**, *12*, 268–273. [[CrossRef](#)]
5. Barteneva, N.S.; Fasler-kan, E.; Vorobjev, I.A. Imaging Flow Cytometry: Coping with Heterogeneity in Biological Systems. *J. Histochem. Cytochem.* **2012**, *60*, 723–733. [[CrossRef](#)] [[PubMed](#)]
6. Han, Y.; Gu, Y.; Zhang, A.C.; Lo, Y. Review: Imaging technologies for flow cytometry. *Lab Chip* **2016**, *16*, 4639–4647. [[CrossRef](#)] [[PubMed](#)]
7. Rosenauer, M.; Buchegger, W.; Finoulst, I.; Verhaert, P.; Vellekoop, M. Miniaturized flow cytometer with 3D hydrodynamic particle focusing and integrated optical elements applying silicon photodiodes. *Microfluid. Nanofluid.* **2011**, *10*, 761–771. [[CrossRef](#)]
8. Simonnet, C.; Groisman, A. High-throughput and high-resolution flow cytometry in molded microfluidic devices. *Anal. Chem.* **2006**, *78*, 5653–5663. [[CrossRef](#)]
9. Sundararajan, N.; Pio, M.S.; Lee, L.P.; Berlin, A.A. Three-Dimensional Hydrodynamic Focusing in Polydimethylsiloxane (PDMS) Microchannels. *J. Microelectromech. Syst.* **2004**, *13*, 559–567. [[CrossRef](#)]
10. Chang, C.-C.; Huang, Z.-X.; Yang, R.-J. Three-dimensional hydrodynamic focusing in two-layer polydimethylsiloxane (PDMS) microchannels. *J. Micromech. Microeng.* **2007**, *17*, 1479–1486. [[CrossRef](#)]
11. Wu, T.; Chen, Y.; Park, S.; Hong, J.; Teslaa, T.; Zhong, J.F.; Carlo, D.; Teitell, M.A.; Chiou, P. Pulsed laser triggered high speed microfluidic fluorescence activated cell sorter. *Lab Chip* **2012**, *12*, 1378–1383. [[CrossRef](#)] [[PubMed](#)]
12. Sakuma, S.; Kasai, Y.; Hayakawa, T.; Arai, F. On-chip cell sorting by high-speed local-flow control using dual membrane pumps. *Lab Chip* **2017**, *17*, 2760–2767. [[CrossRef](#)]
13. Mao, X.; Lin, S.C.S.; Dong, C.; Huang, T.J. Single-layer planar on-chip flow cytometer using microfluidic drifting based three-dimensional (3D) hydrodynamic focusing. *Lab Chip* **2009**, *9*, 1583–1589. [[CrossRef](#)]
14. Eluru, G.; Julius, L.A.N.; Gorthi, S.S. Single-layer microfluidic device to realize hydrodynamic 3D flow focusing. *Lab Chip* **2016**, *16*, 4133–4141. [[CrossRef](#)] [[PubMed](#)]
15. Gualda, E.J.; Pereira, H.; Martins, G.G.; Gardner, R.; Moreno, N. Three-dimensional imaging flow cytometry through light-sheet fluorescence microscopy. *Cytom. Part A* **2017**, *91*, 144–151. [[CrossRef](#)]
16. Nawaz, A.A.; Zhang, X.; Mao, X.; Rufo, J.; Lin, S.C.S.; Guo, F.; Zhao, Y.; Lapsley, M.; Li, P.; McCoy, J.P.; et al. Sub-micrometer-precision, three-dimensional (3D) hydrodynamic focusing via “microfluidic drifting”. *Lab Chip Miniaturisation Chem. Biol.* **2014**, *14*, 415–423. [[CrossRef](#)]
17. Paiè, P.; Bragheri, F.; Di Carlo, D.; Osellame, R. Particle focusing by 3D inertial microfluidics. *Microsyste. Nanoeng.* **2017**, *3*, 17027. [[CrossRef](#)]

18. Rane, A.S.; Rutkauskaitė, J.; deMello, A.; Stavrakis, S. High-Throughput Multi-parametric Imaging Flow Cytometry. *Chem* **2017**, *3*, 588–602. [[CrossRef](#)]
19. Nitta, N.; Sugimura, T.; Isozaki, A.; Mikami, H.; Hiraki, K.; Sakuma, S.; Iino, T.; Arai, F.; Endo, T.; Fujiwaki, Y.; et al. Intelligent Image-Activated Cell Sorting. *Cell* **2018**, *175*, 266–276.e13. [[CrossRef](#)]
20. Normolle, D.P.; Donnenberg, V.S.; Donnenberg, A.D. Statistical classification of multivariate flow cytometry data analyzed by manual gating: Stem, progenitor, and epithelial marker expression in nonsmall cell lung cancer and normal lung. *Cytom. Part A* **2013**, *83A*, 150–160. [[CrossRef](#)] [[PubMed](#)]
21. Ye, X.; Ho, J.W.K. Ultrafast clustering of single-cell flow cytometry data using FlowGrid. *BMC Syst. Biol.* **2019**, *13* (Suppl. 2), 35. [[CrossRef](#)]
22. Pouyan, M.B.; Jindal, V.; Birjandtalab, J.; Nourani, M. Single and multi-subject clustering of flow cytometry data for cell-type identification and anomaly detection. *BMC Med. Genom.* **2016**, *9*, 41. [[CrossRef](#)]
23. Kraus, O.Z.; Grys, B.T.; Ba, J.; Chong, Y.T.; Frey, B.J.; Boone, C.; Andrews, B.J.J.; Pärnamaa, T.; Parts, L.; Humeau-Heurtier, A.; et al. The curse of dimensionality. *Mach. Learn.* **2018**, *7*, 18.
24. Köppen, M. The curse of dimensionality. In Proceedings of the 5th Online World Conference on Soft Computing in Industrial Applications, 4–18 September 2000; pp. 4–8.
25. Humeau-Heurtier, A. Texture Feature Extraction Methods: A Survey. *IEEE Access* **2019**, *7*, 8975–9000. [[CrossRef](#)]
26. Carpenter, A.E.; Jones, T.R.; Lamprecht, M.R.; Clarke, C.; Kang, I.H.; Friman, O.; Guertin, D.A.; Chang, J.H.; Lindquist, R.A.; Moffat, J.; et al. CellProfiler: Image analysis software for identifying and quantifying cell phenotypes. *Genome Biol.* **2006**, *7*, R100. [[CrossRef](#)]
27. Kraus, O.Z.; Grys, B.T.; Ba, J.; Chong, Y.; Frey, B.J.; Boone, C.; Andrews, B.J. Automated analysis of high-content microscopy data with deep learning. *Mol. Syst. Biol.* **2017**, *13*, 924. [[CrossRef](#)]
28. Rumetshofer, E.; Hofmarcher, M.; Röhl, C.; Hochreiter, S.; Klambauer, G. Human-level Protein Localization with Convolutional Neural Networks. In Proceedings of the International Conference on Learning Representations, New Orleans, LA, USA, 6–9 May 2019.
29. Pärnamaa, T.; Parts, L. Accurate Classification of Protein Subcellular Localization from High-Throughput Microscopy Images Using Deep Learning. *G3 (Bethesda)* **2017**, *7*, 1385–1392. [[CrossRef](#)]
30. Platt, J. *Sequential Minimal Optimization: A Fast Algorithm for Training Support Vector Machines*; Technical Report MSR-TR-98-14; Microsoft Research: Redmond, WA, USA, 1998.
31. Chong, Y.T.; Koh, J.L.Y.; Friesen, H.; Kaluarachchi Duffy, S.; Cox, M.J.; Moses, A.; Moffat, J.; Boone, C.; Andrews, B.J. Yeast Proteome Dynamics from Single Cell Imaging and Automated Analysis. *Cell* **2015**, *161*, 1413–1424. [[CrossRef](#)] [[PubMed](#)]
32. Bengio, Y. Deep Learning of Representations: Looking Forward. In *Statistical Language and Speech Processing, Lecture Notes in Computer Science*; Dediu, A.-H., Martín-Vide, C., Mitkov, R., Truthe, B., Eds.; Springer: Berlin/Heidelberg, Germany, 2013; pp. 1–27.
33. Gidaris, S.; Singh, P.; Komodakis, N. Unsupervised Representation Learning by Predicting Image Rotations. *arXiv* **2018**, arXiv:1803.07728.
34. Haeusser, P.; Plapp, J.; Golkov, V.; Aljalbout, E.; Cremers, D. Associative Deep Clustering: Training a Classification Network with no Labels. In Proceedings of the German Conference on Pattern Recognition (GCPR), Stuttgart, Germany, 9–12 October 2018.
35. Caron, M.; Bojanowski, P.; Joulin, A.; Douze, M. Deep Clustering for Unsupervised Learning of Visual Features. *arXiv* **2018**, arXiv:1807.05520.
36. Kingma, D.P.; Welling, M. Auto-Encoding Variational Bayes. *arXiv* **2013**, arXiv:1312.6114.
37. Goodfellow, I.J.; Pouget-Abadie, J.; Mirza, M.; Xu, B.; Warde-Farley, D.; Ozair, S.; Courville, A.; Bengio, Y. Generative Adversarial Networks. *arXiv* **2014**, arXiv:1406.2661.
38. Vincent, P.; Larochelle, H.; Lajoie, I.; Bengio, Y.; Manzagol, P.-A. Stacked Denoising Autoencoders: Learning Useful Representations in a Deep Network with a Local Denoising Criterion. *J. Mach. Learn. Res.* **2010**, *11*, 3371–3408.
39. Higgins, I.; Amos, D.; Pfau, D.; Racaniere, S.; Matthey, L.; Rezende, D.; Lerchner, A. Towards a Definition of Disentangled Representations. *arXiv* **2018**, arXiv:1812.02230.
40. Kim, H.; Mnih, A. Disentangling by Factorising. *arXiv* **2018**, arXiv:1802.05983.
41. Kim, M.; Wang, Y.; Sahu, P.; Pavlovic, V. Relevance Factor VAE: Learning and Identifying Disentangled Factors. *arXiv* **2019**, arXiv:1902.01568.

42. Higgins, I.; Matthey, L.; Pal, A.; Burgess, C.; Glorot, X.; Botvinick, M.; Mohamed, S.; Lerchner, A. beta-VAE: Learning Basic Visual Concepts with a Constrained Variational Framework. In Proceedings of the International Conference on Learning Representations, Toulon, France, 24–26 April 2017.
43. Burgess, C.P.; Higgins, I.; Pal, A.; Matthey, L.; Watters, N.; Desjardins, G.; Lerchner, A. Understanding disentangling in β -VAE. *arXiv* **2018**, arXiv:1804.03599.
44. Chen, R.T.Q.; Li, X.; Grosse, R.; Duvenaud, D. Isolating Sources of Disentanglement in Variational Autoencoders. *arXiv* **2018**, arXiv:1802.04942.
45. Mescheder, L.; Geiger, A.; Nowozin, S. Which Training Methods for GANs do actually Converge? *arXiv* **2018**, arXiv:1801.04406.
46. Scott, R.; Sethu, P.; Harnett, C.K. Three-dimensional hydrodynamic focusing in a microfluidic Coulter counter. *Rev. Sci. Instrum.* **2008**, *79*, 46104. [[CrossRef](#)]
47. Hairer, G.; Pär, G.S.; Svasek, P.; Jachimowicz, A.; Vellekoop, M.J. Investigations of micrometer sample stream profiles in a three-dimensional hydrodynamic focusing device. *Sens. Actuators B Chem.* **2008**, *132*, 518–524. [[CrossRef](#)]
48. Chung, S.; Park, S.J.; Kim, J.K.; Chung, C.; Han, D.C.; Chang, J.K. Plastic microchip flow cytometer based on 2- and 3-dimensional hydrodynamic flow focusing. *Microsyst. Technol.* **2003**, *9*, 525–533. [[CrossRef](#)]
49. Lake, M.; Narciso, C.; Cowdrick, K.; Storey, T.; Zhang, S.; Zartman, J.; Hoelzle, D. Microfluidic device design, fabrication, and testing protocols. *Protoc. Exch.* **2015**. [[CrossRef](#)]
50. Qin, D.; Xia, Y.; Whitesides, G.M. Soft lithography for micro- and nanoscale patterning. *Nat. Protoc.* **2010**, *5*, 491. [[CrossRef](#)]
51. Ward, K.; Fan, Z.H. Mixing in microfluidic devices and enhancement methods. *J. Micromech. Microeng.* **2015**, *25*, 094001. [[CrossRef](#)]
52. Tan, J.N.; Neild, A. Microfluidic mixing in a Y-junction open channel. *AIP Adv.* **2012**, *2*, 032160. [[CrossRef](#)]
53. Ushikubo, F.Y.; Birribilli, F.S.; Oliveira, D.R.B.; Cunha, R.L. Y- and T-junction microfluidic devices: Effect of fluids and interface properties and operating conditions. *Microfluid. Nanofluid.* **2014**, *17*, 711–720. [[CrossRef](#)]
54. Watkins, N.; Venkatesan, B.M.; Toner, M.; Rodriguez, W.; Bashir, R. A robust electrical microcytometer with 3-dimensional hydrofocusing. *Lab Chip* **2009**, *9*, 3177–3184. [[CrossRef](#)] [[PubMed](#)]
55. Bryan, A.K.; Goranov, A.; Amon, A.; Manalis, S.R. Measurement of mass, density, and volume during the cell cycle of yeast. *Proc. Natl. Acad. Sci. USA* **2010**, *107*, 999–1004. [[CrossRef](#)]
56. Ridler, T.W.; Calvard, S. Picture Thresholding Using an Iterative Selection Method. *IEEE Trans. Syst. Man Cybern.* **1978**, *8*, 630–632.
57. Salvi, M.; Molinari, F. Multi-tissue and multi-scale approach for nuclei segmentation in H&E stained images. *Biomed. Eng. Online* **2018**, *17*, 89. [[PubMed](#)]
58. Paszke, A.; Chanan, G.; Lin, Z.; Gross, S.; Yang, E.; Antiga, L.; Devito, Z. Automatic differentiation in PyTorch. In Proceedings of the 31st Conference Neural Information Processing, Long Beach, CA, USA, 4–9 December 2017; pp. 1–4.
59. Nair, V.; Hinton, G.E. Rectified Linear Units Improve Restricted Boltzmann Machines. In Proceedings of the 27th International Conference on Machine Learning, Haifa, Israel, 21–24 June 2010; p. 8.
60. Xu, B.; Wang, N.; Chen, T.; Li, M. Empirical Evaluation of Rectified Activations in Convolutional Network. *arXiv* **2015**, arXiv:1505.00853.
61. Kingma, D.P.; Ba, J.L. Adam: A Method for Stochastic Optimization. In Proceedings of the 3rd International Conference for Learning Representations, San Diego, CA, USA, 7–9 May 2015; pp. 1–15.
62. Koch, G.; Zemel, R.; Salakhutdinov, R. Siamese Neural Networks for One-shot Image Recognition. In Proceedings of the 32nd International Conference on Machine Learning, Lille, France, 6–11 July 2015; p. 8.
63. Watanabe, S. Information Theoretical Analysis of Multivariate Correlation. *IBM J. Res. Dev.* **1960**, *4*, 66–82. [[CrossRef](#)]
64. Ioffe, S.; Szegedy, C. Batch Normalization: Accelerating Deep Network Training by Reducing Internal Covariate Shift. *arXiv* **2015**, arXiv:1502.03167.
65. Rezende, D.J.; Mohamed, S.; Wierstra, D. Stochastic Backpropagation and Approximate Inference in Deep Generative Models. *arXiv* **2014**, arXiv:1401.4082.
66. Pedregosa, F.; Varoquaux, G.; Gramfort, A.; Michel, V.; Thirion, B.; Grisel, O.; Blondel, M.; Prettenhofer, P.; Weiss, R.; Dubourg, V.; et al. Scikit-learn: Machine Learning in Python. *J. Mach. Learn. Res.* **2011**, *12*, 2825–2830.

67. Van der Maaten, L.; Hinton, G. Visualizing Data using t-SNE. *J. Mach. Learn. Res.* **2008**, *9*, 2579–2605.
68. Wyatt Shields, C., IV; Reyes, C.D.; López, G.P. Microfluidic cell sorting: A review of the advances in the separation of cells from debulking to rare cell isolation. *Lab Chip* **2015**, *15*, 1230–1249. [[CrossRef](#)]
69. Kuo, J.S.; Chiu, D.T. Controlling Mass Transport in Microfluidic Devices. *Annu. Rev. Anal. Chem.* **2011**, *4*, 275–296. [[CrossRef](#)]
70. Salmon, J.B.; Ajdari, A. Transverse transport of solutes between co-flowing pressure-driven streams for microfluidic studies of diffusion/reaction processes. *J. Appl. Phys.* **2007**, *101*, 074902. [[CrossRef](#)]
71. Kuntaegowdanahalli, S.S.; Bhagat, A.A.; Kumar, G.; Papautsky, I. Inertial microfluidics for continuous particle separation in spiral microchannels. *Lab Chip* **2009**, *9*, 2973–2980. [[CrossRef](#)]
72. Carlo, D. Di Inertial microfluidics. *Lab Chip* **2009**, *9*, 3038–3046. [[CrossRef](#)]
73. Yu, C.; Qian, X.; Chen, Y.; Yu, Q.; Ni, K.; Wang, X. Three-Dimensional Electro-Sonic Flow Focusing Ionization Microfluidic Chip for Mass Spectrometry. *Micromachines* **2015**, *6*, 1890–1902. [[CrossRef](#)]



© 2019 by the authors. Licensee MDPI, Basel, Switzerland. This article is an open access article distributed under the terms and conditions of the Creative Commons Attribution (CC BY) license (<http://creativecommons.org/licenses/by/4.0/>).

Publications (as of December 2021)

[1]. DetecDiv, a deep-learning platform for automated cell division tracking and replicative lifespan analysis

Aspert Théo, Didier Hentsch, Charvin Gilles

bioRxiv, (2021) – DOI: 10.1101/2021.10.05.463175

[2]. Monitoring single-cell dynamics of entry into quiescence during an unperturbed lifecycle

Aspert Théo*, Jacquiel Basile*, Laporte Damien, Sagot Isabelle, Charvin Gilles

* Equally contributed to the work

Elife, 2021;10:e73186 - DOI: 10.7554/eLife.73186

[3]. Distinct mechanisms underlie H₂O₂ sensing in *C. elegans* head and tail

Quintin Sophie, Aspert Théo, Charvin Gilles

bioRxiv, (2021) - DOI: 10.1101/2021.07.26.451501

[4]. Specialization of chromatin-bound nuclear pore complexes promotes yeast aging

Anne C. Meinema, Aspert Théo, Sung Sik Lee, Gilles Charvin, Yves Barral

bioRxiv, (2021) - DOI: 10.1101/2021.06.28.450139

[5]. Self-Learning Microfluidic Platform for Single-Cell Imaging and Classification in Flow

Constantinou I*, Jendrusch M*, Aspert Théo, Görlitz F, Schulze A, Charvin G, Knop M.

* Equally contributed to the work

Micromachines, 10: 311, (2019) - DOI: 10.3390/mi10050311

Résumé long

Chapitre 1: Déchiffrer les dynamiques du vieillissement à l'aide de la microfluidique et de l'apprentissage profond

Introduction générale

Le vieillissement est un phénomène naturel défini par une dégradation des fonctions et une augmentation de la probabilité de mourir avec l'âge. Il implique de nombreux processus biologiques dynamiques et agit à différentes échelles. Ainsi, *Saccharomyces cerevisiae* est l'un des organismes modèles les plus simples pour l'étudier, et notamment pour comprendre pourquoi une cellule meurt après avoir effectué un certain nombre de divisions, phénomène appelé vieillissement réplcatif.

En effet, *S. cerevisiae* est un organisme unicellulaire eucaryote qui se divise asymétriquement : une cellule dite cellule mère donne naissance à une cellule fille à l'issue de la division cellulaire. La cellule mère voit sa probabilité de mourir augmenter avec le nombre de divisions effectuées, tandis que les cellules filles naissent avec un plein potentiel de réplication, c'est-à-dire qu'elles sont réjuvénées.

Lors de cette division, la plupart du contenu de la cellule mère est partagé symétriquement avec la nouvelle cellule, mais certains facteurs sont partagés asymétriquement. Ainsi, le dogme pour expliquer le vieillissement réplcatif est que des facteurs toxiques s'accumuleraient dans la mère avec l'âge réplcatif, et ne seraient pas transmis à la fille.

Dès lors, des dizaines de marqueurs de vieillissement et de gènes de longévité ont été identifiés, comme l'agrégation protéique, la perte de potentiel et de structure mitochondriale, la dérégulation de l'acidité cytosolique et vacuolaire, la dérégulation des ports nucléaires, ou la dérégulation de la transcription de l'AND ribosomique (ADNr).

Partie méthodologique

Introduction

Cependant, aucun mécanisme ne permet de relier causalement ces processus moléculaires ni de différencier ceux qui sont à l'origine du vieillissement de ceux qui n'en sont que des conséquences. Cela est dû notamment à une approche expérimentale limitée :

D'une part, les moyens classiques, utilisant des tests populationnels, ne parviennent pas à saisir la dynamique propre des processus observés. Ils ne peuvent que dire si ceux-ci sont affectés, en moyenne dans la population et dans le temps, ou non, et ne prennent pas en compte l'hétérogénéité entre les cellules.

D'autre part, il est possible de suivre des cellules uniques pendant toute leur vie en utilisant la microfluidique et la vidéomicroscopie long terme, pour mesurer la dynamique de processus en particulier et pouvoir les ordonner temporellement. Cependant, cette méthode reste à faible débit dû à des limitations techniques microfluidiques ainsi qu'à un débit d'analyse limité.

Résultats

Dès lors, un des projets de ma thèse a été de développer un système pour suivre des cellules uniques tout au long de leur vie, avec un débit élevé. Ce système est basé sur une puce microfluidique qui permet de piéger 30 000 cellules mères dans des microstructures et de disséquer automatiquement leurs cellules filles. Cette puce a été optimisée de façon à pouvoir conserver les cellules mères au sein du piège, quel que soit leur taille, ce qui était un défi technique non résolu par les puces existantes, sachant que le volume d'une cellule mère peut être multiplié par 10 lors du vieillissement. La puce a été aussi pensée pour rendre l'expérience plus simple à réaliser et plus robuste, en limitant les bouchons de cellule, les bulles d'air ou les contaminations grâce à un système de filtres.

Pour suivre ce grand nombre de cellules, nous avons développé un système de microscopie rapide basé sur une caméra à large champ, un objectif à faible grossissement, un filtre de fluorescence multibandes, et un système d'autofocus rapide.

Ainsi, une expérience typique génère 30000 vidéos de cellules uniques contenant des centaines d'images (<https://youtu.be/hQVNTbwbXo>). Néanmoins, les méthodes existantes pour analyser ce genre de données reposent sur l'annotation manuelle des images, limitant le débit de l'analyse. Pour pallier à cela, nous avons développé un logiciel basé sur l'apprentissage pour analyser automatiquement les vidéos, notamment pour détecter les événements pertinents tels que les divisions cellulaires ou la mort, et mesurer la taille ou la fluorescence des cellules (https://youtu.be/yvD_C8byeOE). Pour détecter les divisions et la mort, le système utilise une classification des images grâce à un Réseau Neuronal Convolutif travaillant sur les images individuelles de la vidéo, couplé à un réseau travaillant sur les séquences pour prendre en compte le lien temporel entre les images. Il utilise un réseau de type U-Net pour analyser les pixels des images individuelles afin de segmenter les cellules mère. Ainsi, le logiciel détecte les divisions et la mort avec une précision de 98% et permet

de suivre l'évolution de la taille de la cellule ou de marqueurs fluorescents en fonction du nombre de divisions effectuées. Il permet de gagner deux à trois ordres de grandeurs de débit d'analyse par rapport à une analyse manuelle. De plus, les réseaux de neurones de ce logiciel sont entraînaables avec des données personnalisées, et nous avons montré qu'il performait aussi bien avec des données issues d'autres laboratoires utilisant d'autres puces microfluidiques.

Un tel outil permet donc de mesurer les dynamiques d'un processus biologique grâce à un suivi temporel à haut débit de cellules uniques, et de cribler des marqueurs et des mutants de manière standardisée. Dès lors, il peut être utilisé au-delà du domaine du vieillissement, dans un but fondamental ou appliqué, sur des thèmes comme le cycle cellulaire, la quiescence. Ainsi, nous avons montré une preuve de principe en appliquant cet outil à l'étude de la réponse au stress, en récapitulant l'existence de plusieurs populations face à une gamme de doses de stress oxydant.

Partie biologique

Introduction

Parmi tous les facteurs de vieillissement identifiés, l'accumulation de cercle d'ADNr menant à de multiples dérégulations au sein de la cellule, représente un des modèles de vieillissement répliatif les plus aboutis. Chez *S. cerevisiae*, l'ADNr se présente sous la forme d'une suite de 150-200 répétitions présente dans le chromosome XII, de laquelle peut s'exciser une répétition sous la forme d'un cercle. Chaque répétition contenant une séquence de réplication autonome, ce cercle peut se répliquer à chaque division. De plus, ces cercles d'ADN restent au sein de la cellule mère et ne sont pas transmis à la fille. Dès lors, ils s'accumulent de manière exponentielle avec l'âge répliatif. Cependant, une des questions de ce modèle est de savoir si l'excision du premier cercle d'ADNr représente l'évènement élémentaire de la cascade menant au vieillissement, ou si cet évènement est une conséquence de l'âge. En d'autres termes, nous cherchons à savoir si la probabilité d'excision d'un cercle d'ADNr augmente avec l'âge ou reste inchangée, décrivant un processus stochastique.

Résultats

Pour répondre à cette question, j'ai utilisé une souche dans laquelle une des répétitions de gène d'ADNr était marquée avec un promoteur lié à une GFP. Ce rapporteur transcriptionnel permet ainsi de suivre l'augmentation exponentielle du nombre de cercles d'ADNr, si le gène

excisé est celui qui contient le marqueur. Dès lors, cet outil permet de mesurer le moment de l'excision, mais puisqu'une seule répétition parmi les 150-200 est marquée, cette mesure n'est possible que dans très peu de cellules.

Cependant, en utilisant la méthodologie développée précédemment et décrite dans la partie I. de ce résumé, nous avons pu analyser assez de cellules pour avoir la puissance statistique nécessaire et conclure que l'évènement d'excision d'un cercle d'ADNr suivait une loi de Poisson, c'est-à-dire que sa probabilité d'occurrence était constante avec l'âge. De plus, nous avons montré que cette probabilité était environ égale à 10% par division dans les cellules sauvages, et à 5% par division dans le mutant *fob1Δ* connu pour réduire la probabilité d'excision.

Cette découverte montre que le vieillissement répliatif peut être déclenché par un événement moléculaire ponctuel, contrairement au paradigme communément admis et anthropocentrique, définissant le vieillissement comme étant une défaillance progressive de processus parallèles. Pour valider ce modèle, il s'agit maintenant de cribler des mutants de longévité en utilisant la méthodologie développée, et de déterminer si la modification de leur durée de vie répliatrice est due à un effet sur la probabilité d'excision des cercles d'ADNr, ou s'ils survivent mieux aux effets de l'accumulation de ces cercles.

Chapitre 2 : Suivi de la dynamique de l'entrée en quiescence à l'échelle de la cellule unique

Introduction

La capacité de prolifération des micro-organismes est étroitement liée à la nature et à la disponibilité des nutriments dans leur habitat. La multiplication exponentielle des cellules conduit à l'épuisement ou à la modification de ces nutriments, et est donc liée à différentes phases prolifératives de la culture, allant jusqu'à l'arrêt de prolifération.

Par exemple, la levure bourgeonnante *S. cerevisiae* subit des transitions entre différentes phases métaboliques en raison de la consommation progressive de nutriments dans l'environnement. Une phase rapide de fermentation des sucres au cours de laquelle de l'éthanol est produit, est suivie d'une phase de respiration où les cellules consomment l'éthanol. Entre ces deux phases, les cellules subissent un arrêt de prolifération réversible appelé le *diauxic shift*. Après l'épuisement complet de toutes les sources de carbone, les cellules entrent dans un état d'arrêt de prolifération réversible, appelé quiescence, qui dure jusqu'à ce que de nouvelles sources de nutriments apparaissent. Par conséquent, l'état métabolique de *S. cerevisiae* est fortement dynamique et étroitement lié au remodelage continu de son environnement.

Cependant, ces changements sont associés à des réorganisations intracellulaires qui sont très hétérogènes d'une cellule à l'autre, et dépendant de la nature de la privation de nutriments, de la composition initiale du milieu, mais aussi de la vitesse de consommation des nutriments. Cependant, l'étude de la quiescence à l'échelle de la population ignore les hétérogénéités de cellule à cellule, tandis que l'observation de cellules uniques avec des stratégies classiques telles que la microfluidique, est incapable de prendre en compte la dynamique naturelle d'un milieu de culture puisqu'elles fonctionnent avec des privations abruptes de nutriments.

En d'autres termes, l'étude de l'entrée en quiescence naturelle nécessite à la fois un suivi longitudinal de cellules uniques, tout en permettant aux cellules d'avoir un impact collectif sur l'environnement.

Résultats

Pour cela, nous avons développé une méthodologie pour imager des cellules uniques de levure bourgeonnante au cours d'un cycle de vie non perturbé, de la phase fermentative à la fin de la quiescence, dans un environnement se dégradant de manière autonome. Des cellules

piégées dans une puce microfluidique d'observation sont constamment alimentées par le milieu d'une culture de cellules en croissance, subissant ainsi des conditions environnementales identiques. Pour éviter que les cellules du milieu de culture ne viennent envahir la puce microfluidique d'observation, nous avons mis au point un système de filtration pour séparer de manière continue les cellules de leur milieu, afin de ne perfuser que ce dernier.

Grâce à cela, nous avons montré une divergence abrupte de la population au moment du diauxic shift, où une fraction des cellules se retrouve incapable de passer à un métabolisme respiratoire et subit une entrée dans un état de pseudo-quiescence conduisant à une mort prématurée. De plus, nous avons montré que le pH interne de la cellule était directement lié à l'état métabolique de la cellule, et que les fluctuations de ce pH lors des différentes phases métaboliques conduisent à la formation de superassemblages protéiques. De plus, une fois en quiescence, le cytoplasme effectue une transition vers un état vitreux de manière abrupte et stochastique, certaines cellules transitionnant quelques minutes après l'arrêt de croissance, tandis que d'autres prennent plusieurs jours.

Au-delà de l'étude de l'entrée en quiescence, ce nouveau cadre expérimental ouvre la voie à une nouvelle approche de l'étude du destin cellulaire dans le cadre d'une dégradation autonome de l'environnement par la population.

Abstract

Aging is a natural phenomenon defined by a loss of fitness and an increase in mortality rate. Behind this simple phenomenologic description lies a complex mechanism involving many very dynamical biological processes acting at different scales. *Saccharomyces cerevisiae* is one of the simplest model organism to study aging. Yet, despite the dozens of hallmarks of aging and longevity genes identified, no precise mechanism can describe why a cell dies after a certain number of divisions. This is partly due to a limited experimental power, with populational assays not considering the heterogeneities between cells, while the current single-cell longitudinal approaches have a too low throughput, hence preventing to grasp the complexity of the phenomenon experimentally.

Therefore, we developed a framework based on microfluidics, fast-microscopy, and deep-learning to track single-cells throughout their lifespan, with a throughput increase of two orders of magnitude compared to existing systems. With that, it is possible to track and analyse more than 30000 cells per experiment and automatically detect relevant events such as cell divisions. Thus, one can screen markers and mutants in a standardized and systematic manner in order to capture the links and temporalities of the different processes of aging.

As an application, we sought to measure the statistics of an event thought trigger an cascade of leading to death. Interestingly, we found that this event was stochastic, suggesting that aging can arise from age-independent causes.

Keywords: Aging, single-cell, longitudinal tracking, homeostasis, division, yeast, microfluidics, deep-learning, stochasticity

Résumé court

Le vieillissement est un phénomène naturel défini par une dégradation des fonctions et une augmentation de la probabilité de mourir. Derrière cette description phénoménologique simple se cache un mécanisme complexe impliquant de nombreux processus biologiques dynamiques agissant à différentes échelles. *Saccharomyces cerevisiae* est l'un des organismes modèles les plus simples pour étudier le vieillissement. Pourtant, malgré les dizaines de marqueurs de vieillissement et de gènes de longévité identifiés, aucun mécanisme précis ne permet de décrire pourquoi une cellule meurt après avoir effectué un certain nombre de divisions. Cela est dû en partie à une puissance expérimentale limitée, les essais populationnels ne prenant pas en compte les hétérogénéités entre les cellules, tandis que les approches longitudinales à l'échelle de la cellule unique ont un débit trop faible actuellement. Il est alors difficile de lier temporellement et causalement les processus moléculaires menant à la mort.

Par conséquent, nous avons développé un système basé sur la microfluidique, la microscopie rapide et l'apprentissage profond pour suivre des cellules uniques tout au long de leur vie, augmentant le débit de deux ordres de grandeur par rapport aux systèmes existants. Il permet de suivre et d'analyser plus de 30000 cellules par expérience et de détecter automatiquement les événements pertinents tels que les divisions cellulaires. Ainsi, il est possible de cribler des marqueurs et des mutants de manière standardisée et systématique afin de saisir les liens et les temporalités des différents processus du vieillissement.

En guise d'application, nous avons cherché à mesurer les statistiques d'un événement connu pour déclencher une cascade d'événements conduisant à la mort. Nous avons constaté que cet événement avait la même probabilité quel que soit l'âge de la cellule, ce qui suggère que le vieillissement peut émerger de la stochasticité.

Mots clés: Vieillessement, cellule unique, suivi longitudinal, homéostasie, division, levure, microfluidique, apprentissage profond, stochasticité